

Université Paris Diderot
UFR de Physique

HABILITATION À DIRIGER LES RECHERCHES

présentée par

Jérôme NOVAK

RELATIVITÉ NUMÉRIQUE : MODÉLISATION DES ASTRES COMPACTS ET DES SOURCES D'ONDES GRAVITATIONNELLES

Soutenance prévue le 7 mai 2010, devant le jury composé de :

Mme. Isabelle GRENIER	présidente
M. Pierre BINETRUY	rapporteur
M. José M ^a IBAÑEZ	rapporteur
M. Philippe LE FLOCH	rapporteur
M. Luc BLANCHET	examineur
M. Christian KLEIN	examineur
M. David LANGLOIS	examineur

à la mémoire de mon père,

Dans le cadre professionnel, j'ai bénéficié de l'aide de très nombreuses personnes que j'essaie de remercier ci-dessous. Cependant, il est certain que j'en oublierai et je les prie de me pardonner.

Ma gratitude va d'abord à Éricourgoulhon, qui a été mon premier « contact » avec la relativité numérique en 1994. Depuis lors, mon admiration pour ses qualités scientifiques, pédagogiques et humaines n'a cessé de croître. Je suis, bien entendu, fortement reconnaissant à Silvano Bonazzola pour avoir la chance d'avoir travaillé avec lui et pour profiter de son expérience et ses conseils au quotidien. Je suis également très heureux d'avoir collaboré avec Philippe Grandclément et espère avoir à nouveau l'occasion de travailler sur un projet commun. Merci aux chercheurs du LUTH avec qui j'ai pu avoir de nombreuses discussions : Brandon Carter, dont la culture scientifique et générale est fascinante, mais aussi Claire Michaut et Fabrice Mottez. Enfin, un grand merci à Micaela Oertel pour ses explications de physique des particules, ses chocolats et une collaboration naissante qui, j'en suis sûr, sera très fructueuse.

Depuis mon séjour à l'Université de Valencia, j'ai gardé le contact avec l'« équipe espagnole » et, depuis de nombreuses années, j'ai l'immense plaisir de pouvoir compter sur José María Ibáñez comme collaborateur exceptionnel et aussi comme ami. C'est grâce à lui que j'ai pu nouer des liens scientifiques avec des chercheurs aussi inventifs que Toni Font ou Pablo Cerdá et, plus récemment, la jeune et très douée Isabel Cordero. Je les remercie tous pour toute la recherche que nous avons faite ensemble, pour leur aide et leur patience avec moi. Enfin, le plus Meudonnais des espagnols est sans doute José Luis Jaramillo à qui je tiens à exprimer ma plus sincère amitié, pour tout ce que nous avons fait ensemble (je ne compte pas seulement les articles !). À strictement parler, Harald Dimmelmeier est allemand, mais possède la flamme des espagnols : notre travail commun sur CoCoNuT m'a montré quelqu'un de très rigoureux qui sait être en même temps chaleureux et sympathique. Son départ pour AREVA m'a rendu triste, mais me rassure quant à la solidité des centrales nucléaires. Merci aussi à Reinhardt Prix et Greg Comer pour m'avoir initié à la superfluidité dans les étoiles à neutrons.

Il est clair que Nicolas Vasset restera comme le premier étudiant en thèse, et aussi quelqu'un avec qui j'ai réellement eu plaisir à travailler car il a l'étoffe d'un chercheur, avec des qualités humaines en plus que j'ai vraiment appréciées. J'ai aussi été très heureux de collaborer avec Jean-Louis Cornou et de voyager avec lui en Espagne ou en Sicile. Lap-Ming Lin a passé deux années au LUTH et je le remercie vivement pour son travail et sa disponibilité. José María Martín-García est venu plus récemment, et je suis heureux de l'expérience et de la rigueur qu'il a apportées.

Merci à Nathalie Deruelle pour m'avoir accueilli au DARC, puis à Jean-Michel Alimi pour avoir fait du LUTH non seulement un très bon laboratoire, mais aussi un lieu convivial. Je n'aurais sans doute pas été capable de réaliser le quart de ce que j'ai fait si je n'avais pas bénéficié de l'aide et du soutien des équipes administratives et informatique ; un énorme merci donc à Cécile Rosolen, Sylvie Gordon, Colette Ferreira, Stéphane Thomas, David Lépine, Virginie Hababou, Stéphane Méné et Jean-Yves Giot. Je crois que je ne suis jamais arrivé à mettre en défaut leur disponibilité ni leur gentillesse. Je n'ai pas encore eu l'occasion de travailler avec Fabrice Roy, mais j'espère que ce sera bientôt possible.

Je remercie enfin Pierre Binetruy, Philippe Le Floch et (encore !) José María Ibáñez pour avoir accepté la lourde tâche de rapporteur ; j'espère que ce manuscrit ne sera pas trop indigeste.

Table des matières

Remerciements	i
Curriculum vitæ	v
Activités d’encadrement	vii
Résumé	ix
EXPOSÉ DES RECHERCHES	1
Introduction	3
I Formulation des équations d’Einstein	7
1 Fully-constrained scheme (Bonazzola <i>et al.</i> 2004)	13
2 Mathematical issues in a fully-constrained... (Cordero-Carrión <i>et al.</i> 2008)	51
3 Improved constrained scheme... (Cordero-Carrión <i>et al.</i> 2009)	69
II Méthodes spectrales pour la relativité numérique	93
4 Spectral methods for numerical relativity (Grandclément & Novak 2009)	99
5 Absorbing boundary conditions... (Novak & Bonazzola 2004)	189
6 Divergence-free evolution... (Novak <i>et al.</i> 2010)	201
7 Apparent horizon finder (Lin & Novak 2007)	225

III Simulations d’astres compacts	237
8 “Mariage des maillages” (Dimmelmeier <i>et al.</i> 2005)	245
9 Rotating stars in Dirac gauge (Lin & Novak 2006)	293
10 Superfluid neutron stars (Prix <i>et al.</i> 2005)	311
11 Gyromagnetic ratio of relativistic stars (Novak & Marcq 2003)	341
12 Collapse of stable neutron stars (Novak 2001)	353
13 Kerr solution in Dirac gauge (Vasset <i>et al.</i> 2009)	365
Conclusions	389
Perspectives	391
Liste des publications	395
Bibliographie	399

Curriculum vitæ

État civil

Né le 8 décembre 1972 à Araraquara (Brésil), marié, deux enfants.

Situation actuelle

Chargé de recherche 1^{ère} classe au CNRS, affecté à l'UMR 8102
Laboratoire Univers et Théories
Observatoire de Paris

Situations précédentes

2002-2004 Chargé de recherche 2^{ème} classe à l'UMR 8102 du CNRS (LUTH, Meudon)

2000-2001 Chargé de recherche 2^{ème} classe à l'UMR 8629 du CNRS (Département d'Astrophysique Relativiste et de Cosmologie, Meudon)

1999-2000 Attaché Temporaire pour l'Enseignement et la Recherche à l'Université Paris 7

1998-1999 Post-doctorant au Département d'Astronomie et d'Astrophysique de l'Université de Valencia (Espagne)

Diplômes

- Doctorat de l'Université Paris 7, spécialité *Astrophysique et techniques spatiales* (1998), avec la mention *Très honorable avec Félicitations*
- D.E.A. d'Astrophysique et Techniques Spatiales (Université Paris 7, 1995), avec la mention *Très bien*
- Ingénieur de l'École Polytechnique (1994)

Coordonnées

e-mail : jerome.novak@obspm.fr

www : <http://luth.obspm.fr/minisite.php?nom=Novak>

tel : 01 45 07 75 82

fax : 01 45 07 79 71

Adresse postale : LUTH

Observatoire de Paris - Section de Meudon

5, place Jules Janssen

F-92195 Meudon Cedex

Activités d'encadrement

Encadrement

- Co-encadrement (avec M^{me} Micaela Oertel, LUTH) de M^{lle} Céline Guédé pour son **stage de M1** (Sciences de l'Univers et technologies spatiales, Observatoire de Paris) de mai à juin 2009 sur le thème *Le transport des neutrinos dans les supernovae*.
- Encadrement de la **thèse** de M. Nicolas Vasset, d'octobre 2006 au 30 juin 2009 sur le thème *Quelques aspects des horizons de trous noirs en relativité numérique* (dérogation obtenue auprès de l'Université Paris Diderot).
- Encadrement de M. Lap-Ming Lin, **post-doctorant** au LUTH entre septembre 2004 et août 2006.
- Encadrement de M. Nicolas Vasset pour son **stage de M2** (Sciences de la matière, ENS Lyon) d'avril à août 2006 sur le thème *Évolution dynamique d'un trou noir isolé*.
- Encadrement de M. Éric Cottalorda pour son **stage de DEA** (Astrophysique, Université de Strasbourg) de mars à juillet 2005 sur le thème *Recherche d'horizons apparents de trous noirs*.
- Co-encadrement (avec M. David Langlois, Institut d'Astrophysique de Paris) de M. Luis Perez Brea pour son **stage de DEA** (Physique théorique, ENS Paris) de février à mai 2004.
- Encadrement de M. Emmanuel Marcq pour son **stage de DEA** (Astrophysique et techniques spatiales, Observatoire de Paris) d'avril à juin 2002 sur le thème *Modélisation d'étoiles à neutrons axisymétriques chargées en rotation*.

Participation à l'enseignement

- Cours magistraux de programmation en C++ (8h/an) et travaux pratiques (16h/an) en DEA/M2 au Master de l'Observatoire de Paris.
- Encadrement de projets numériques (TP d'environ 20h/an) en formation post-M2 de l'École Doctorale d'Astronomie et Astrophysique d'Île-de-France, à l'Université d'Orsay (IDRIS).
- Examens oraux de mathématiques (colles, 60h/an) en première année de classes préparatoires aux grandes écoles au lycée Michelet, à Vanves.

Résumé

Mes travaux de recherche présentés ici concernent le domaine de la relativité numérique, c'est-à-dire les méthodes numériques de résolution des équations d'Einstein, appliquée aux ondes gravitationnelles et aux astres compacts. Le but est d'obtenir des prédictions théoriques (numériques) sur les ondes gravitationnelles émises par les trous noirs, étoiles à neutrons et supernovæ, ainsi que les caractéristiques de ces objets. La première partie est ainsi consacrée au développement d'un formalisme contraint des équations d'Einstein en vue d'une implémentation numériquement stable, évitant l'amplification des erreurs violant les contraintes. Les questions de structure mathématique et d'unicité des solutions des équations écrites dans cette formulation y sont étudiées. La deuxième partie traite des méthodes et techniques numériques que j'ai aidé à développer ; en particulier dans le cadre des méthodes spectrales pour lesquelles j'ai co-rédigé un article de revue. Plusieurs algorithmes sont présentés pour la simulation des ondes gravitationnelles : conditions au bord absorbantes pour les ondes quadrupolaires, méthode de résolution de l'équation d'onde tensorielle sous contrainte de divergence nulle et trouveur d'horizon apparent. Tous ces programmes numériques ont été implémentés dans la bibliothèque LORENE à laquelle j'ai contribué, que j'ai aidé à maintenir et à distribuer aux scientifiques intéressés. La dernière partie est dédiée aux modèles d'astres compacts obtenus numériquement. Plusieurs sujets y sont présentés, dont notamment les simulations d'effondrements stellaires avec rotation (code CoCoNuT), les modèles d'étoiles à neutrons avec champ magnétique ou à deux fluides (pour modéliser la superfluidité des neutrons), les effondrements d'étoiles à neutrons en trous noirs et les modèles de trous noirs en rotation. Une dernière partie présente les perspectives de ces travaux.

Abstract

The scientific studies which are presented here fall within the field of numerical relativity, meaning that they deal with computer methods devised to obtain numerical solutions of Einstein equations, applied to gravitational waves and compact objects. The goal is to obtain theoretical (numerical) predictions on the gravitational waves emitted by black holes, neutron stars and core-collapse supernovae, as well as on these objects. The first part is devoted to the development of a constrained formalism of Einstein equations allowing for a numerically stable implementation, i.e. showing no constraint-violating modes. The key points of mathematical structure of this formalism and uniqueness issues are also studied. The second part deals with the numerical methods that have been developed. In particular, a review on spectral methods in numerical relativity is given. Several useful algorithms for the simulations of gravitational waves are presented : absorbing boundary conditions for quadrupolar waves, a method for the solution of the tensor wave equation under the divergence-free constraint and the apparent horizon finder. All these numerical codes have been implemented in the LORENE library, to which I have contributed, maintained and helped interested scientists who wanted to use it. The last part gives results about numerical models of compact stars. Several subjects are presented, including rotating stellar core-collapse simulations (CoCoNuT code), neutron star models with a magnetic field or with two-fluids (to model neutron superfluidity), gravitational collapse of a neutron star to a black hole and rotating black hole models. The last part gives the outlook of those studies.

EXPOSÉ DES RECHERCHES

Introduction

Des quatre interactions fondamentales de la nature, la gravitation a été la première étudiée et modélisée, mais elle reste cependant moins bien comprise que les trois autres et, en particulier, il n'existe pas à ce jour de description quantique de la gravité. Ainsi, la théorie classique qui la décrit le mieux est la relativité générale et c'est dans le cadre de cette théorie que seront présentées les études de ce manuscrit. L'espace-temps est modélisé comme une variété quadri-dimensionnelle avec une métrique lorentzienne. Cette métrique est reliée au contenu en matière (tous les autres champs possédant de l'énergie) via les équations d'Einstein. Entre autres phénomènes, la relativité générale prédit l'existence et la propagation des *ondes gravitationnelles* comme étant une solution des équations d'Einstein du vide, obtenue en perturbant à l'ordre linéaire la solution sans champ gravitationnel (métrique plate, dite « de Minkowski »). Cette approche montre que les ondes gravitationnelles vérifient une équation des ondes tensorielle et qu'elles sont produites par des objets avec un très fort champ gravitationnel.

Les meilleurs sources sont a priori les *astres compacts* (abordés dans la partie III) : naines blanches, étoiles à neutrons et trous noirs, surtout lorsqu'ils forment une binaire. Ainsi, jusqu'à aujourd'hui les tests indirects les plus convaincants de l'existence des ondes gravitationnelles sont venus du chronométrage des pulsars binaires : ce sont des binaires d'astres compacts où l'un au moins est une étoile à neutrons émettant des pulses radio réguliers. Les mesures de ces ondes radio ont donné la preuve observationnelle que ces binaires perdaient du moment cinétique, emmené par les ondes gravitationnelles. L'accord quantitatif est excellent : l'évolution observée correspond à celle prédite par la relativité générale à 10^{-3} près [457]. Ces tests ont permis non seulement de vérifier que la théorie de la relativité générale modélise correctement l'interaction gravitationnelle, mais en plus qu'elle le fait mieux que d'autres théories comme les théories tenseur-scalaires [143]. Elle représente donc pour l'instant la meilleure théorie de la gravitation aux échelles du système solaire.

Afin d'obtenir des détections directes des ondes gravitationnelles, plusieurs instruments ont été réalisés, telles les barres résonnantes (voir par exemple [75]) et plus récemment, les détecteurs interférométriques tels Virgo [5] (Fig. 1) ou LIGO [2]. Malgré la mise en commun des données entre ces deux détecteurs aucune détection n'a été réalisée à ce jour, vraisemblablement car le taux d'événements dans les hautes fréquences auxquelles sont sensibles ces instruments est trop faible. En particulier, il n'existe aucune source « visible » en ondes électromagnétiques pour laquelle on soit sûr qu'elle serait détectable par Virgo/LIGO. Le projet spatial LISA [269] vise quant à lui à détecter des ondes gravitationnelles à plus basses fréquences avec, contrairement aux détecteurs terrestres du type Virgo/LIGO, un certain nombre de sources qui sont déjà

identifiées par leur signal électromagnétique.



FIG. 1 – Vue aérienne de l’interféromètre Virgo près de Pise (Italie). © EGO-Virgo / Photothèque du CNRS.

Le but de ces instruments n’est pas seulement d’obtenir une détection directe des ondes gravitationnelles, mais surtout d’effectuer à terme des observations d’intérêt physique et astrophysique. Par exemple, à partir des mesures de taux d’événements des coalescences de binaire, ou de la mesure des vitesses de rotations des objets compacts, il sera possible d’avoir des idées plus précises sur l’évolution stellaire et le taux de formation de ces systèmes. Ainsi aussi, en combinant les observations en ondes gravitationnelles avec les observations électromagnétiques à hautes énergies ou avec celles des neutrinos, on obtiendra des informations sur les propriétés de la matière à très haute densité au cœur des supernovae ou dans les étoiles à neutrons. Cela montre aussi que les astres compacts sont non seulement les sources les plus prometteuses de rayonnement gravitationnel, mais aussi des objets fascinants en soi, car ils sont le lieu de conditions physiques extrêmes : champ gravitationnel très intense, densité nucléaire, champ magnétique jusqu’à $10^{16}G$,...

La compréhension des astres compacts en tant que sources d’ondes gravitationnelles, mais aussi plus généralement comme objets astrophysiques nécessite donc des modèles physiques très riches qui, la plupart du temps, ne peuvent pas être calculés analytiquement. Il faut faire appel à l’outil numérique au moins partiellement, pour résoudre les multiples équations qui apparaissent dans ces modèles. Ce manuscrit présente ainsi trois parties qui s’inscrivent dans ce contexte d’étude des astres compacts et des ondes gravitationnelles à l’aide de la modélisation numérique. Il s’agit des travaux que j’ai effectués entre 2001 et 2009 au sein du Département d’Astrophysique Relativiste et Cosmologie (DARC), puis du Laboratoire Univers et Théories (LUTH) à l’Observatoire de Paris, section de Meudon. Les collaborateurs avec qui j’ai eu la chance de travailler ont été surtout mes collègues de Meudon : Silvano Bonazzola, Éric Gourgoulhon, Philippe Grandclément et Nicolas Vasset ; d’Espagne : Pablo Cerdá, Isabel Cordero, José María Ibáñez et José Luis Jaramillo ; et d’Allemagne : Harald Dimmelemeier. Le domaine

d'étude correspondant aux travaux exposés ci-après est souvent appelé « relativité numérique », et couvre plusieurs thèmes de recherche, depuis l'algorithmique et le développement de programmes numériques, jusqu'à l'astrophysique en passant par la magnéto-hydrodynamique.

Plan

Ce manuscrit comporte treize chapitres, qui correspondent chacun à un article publié (sauf le chapitre 6 est sous presse), mais ne sont pas présentés dans l'ordre chronologique ; ils sont en fait regroupés en trois parties. La première partie aborde les questions de formulation des équations d'Einstein avec, d'abord, le travail fondateur sur le formalisme contraint au chapitre 1, suivi d'une analyse plus mathématique de la partie hyperbolique de ce formalisme (chapitre 2) et d'une amélioration du formalisme après la découverte de problèmes d'unicité dans la partie elliptique des équations aux dérivées partielles (chapitre 3). Une fois les équations définies, les méthodes numériques utilisées pour les résoudre sont présentées dans la deuxième partie, et plus particulièrement au chapitre 4. Des détails importants sur le traitement des conditions aux bords sont décrits au chapitre 5 et une nouvelle technique pour la résolution de l'équation d'onde tensorielle avec condition de divergence nulle est donnée au chapitre 6. Cette équation est très importante car elle apparaît naturellement dans le formalisme contraint du chapitre 1. Enfin, l'implémentation d'un *trouveur d'horizon apparent* est décrite dans le chapitre 7. Il s'agit d'un outil extrêmement utile pour déterminer l'apparition ou l'évolution de trous noirs dans des espaces-temps numériques. La troisième partie donne les résultats d'études numériques d'astres compacts, avec d'abord l'effondrement gravitationnel d'un cœur d'étoile dégénéré produisant une étoile à neutrons (supernova gravitationnelle, chapitre 8), puis les études de modèles numériques d'étoiles à neutrons stationnaires en rotation (chapitre 9) et superfluides (chapitre 10). Le champ magnétique a été également pris en compte, avec l'étude du rapport gyromagnétique des étoiles compactes présentée au chapitre 11. Le travail correspondant au chapitre 12 étudie la possibilité de faire s'effondrer en trou noir des étoiles à neutrons stables en leur imprimant une poussée centripète, et essaie de relier ces évolutions avec les phénomènes critiques observés numériquement par Choptuik [117]. Le chapitre 13 clos le manuscrit avec la première implémentation numérique complète des conditions aux bords d'horizon isolé qui, avec la technique d'excision, permettent de simuler un trou noir dans le domaine de calcul.

Notations

Les notations et conventions employées sont en général les suivantes, il faut toutefois se référer à l'introduction de chaque article (chaque chapitre) pour les définitions spécifiques à ce chapitre :

- Les indices notés par des lettres grecques $\alpha, \beta, \dots, \mu, \nu, \dots$ prennent les valeurs de 0 à 3 et les indices latins à partir de i prennent les valeurs de 1 à 3.
- La signature de la métrique est $-+++$, la première coordonnée étant le temps.
- Les notations grasses \mathbf{u} indiquent qu'il s'agit d'un 4-tenseur u_α ou d'un 3-tenseur u_i .
- Pour les métriques à quatre dimensions, $g = -\det g_{\mu\nu}$ et à trois dimensions $\gamma = \det \gamma_{ij}$.

- Le symbole $\mathcal{L}_{\mathbf{v}}$ désigne la dérivée de Lie suivant le vecteur \mathbf{v} .
- Pour un tenseur $T^{\mu\nu}$ d'ordre 2, on note la trace $T = g_{\mu\nu}T^{\mu\nu}$, sans spécifier systématiquement la métrique utilisée, lorsqu'il n'y a pas d'ambiguïté.

Première partie

Formulation des équations d'Einstein

Une première étape pour la résolution numérique des équations d'Einstein est le choix de leur formulation. Très peu d'études numériques ont utilisé une formulation quadri-dimensionnelle, c'est-à-dire en utilisant directement des 4-tenseurs comme inconnues du système d'équations aux dérivées partielles représenté par les équations d'Einstein. De (très notables) exceptions sont les résultats de Pretorius sur les coalescences de binaires de trous noirs [373], basés sur un choix de jauge harmonique généralisée [374]. En général, une approche standard est de commencer par une décomposition 3 + 1, consistant à séparer les coordonnées de temps et d'espace, ce qui permet également de mettre les équations d'Einstein sous la forme d'un problème de Cauchy. Ce formalisme 3 + 1 a été introduit dans les années 1930-40 par André Lichnerowicz [291], puis développé et étudié par Yvonne Choquet-Bruhat dans les années 1950 [184]. Ces travaux ont ensuite été utilisés comme bases pour une approche hamiltonienne de la relativité générale [155], notamment avec le « formalisme ADM » [35]. Étant donnée la très grande importance de ce formalisme aujourd'hui pour la relativité numérique, voire bien au-delà, le lecteur intéressé est invité à consulter les récents ouvrages parus sur le sujet et, en particulier, le livre de Miguel Alcubierre [7] et les notes de cours d'Éricourgoulhon [214], ou de manière plus succincte, la section 1.2.1 page 17.

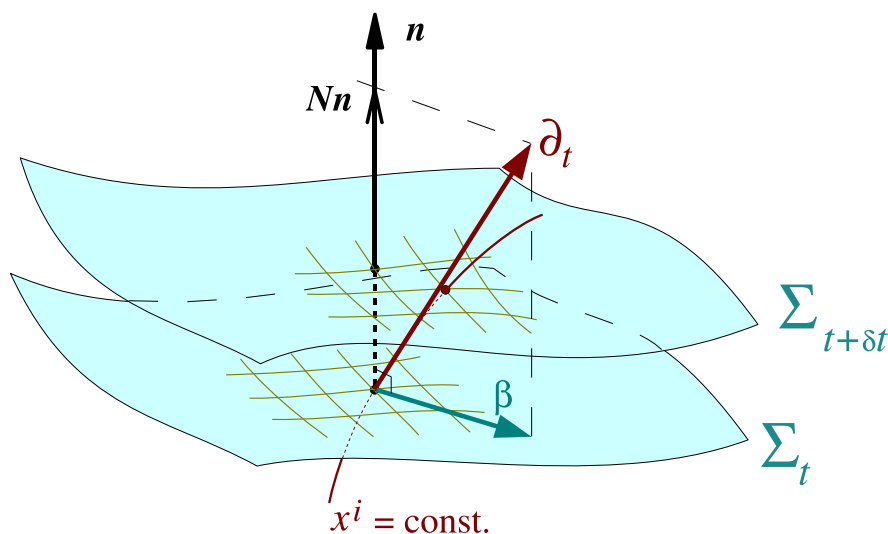


FIG. I.1 – Illustration du principe du feuilletage 3 + 1 : les feuilletes aux temps-coordonnées t et $t + \delta t$ sont représentés, avec le champ de vecteurs unitaires n^μ , normaux aux Σ_t et dirigés vers le futur. Le vecteur *shift* (β^i) représente la dérive des coordonnées spatiales $\{x^i\}_{i=1,2,3}$ et le *lapse* N le rapport entre le temps propre d'un observateur eulérien et le temps coordonnée t . Figure extraite de Gourgoulhon (2007) [214].

Concrètement, l'espace-temps à quatre dimensions est feuilleté par des 3-surfaces du genre espace Σ_t , indexées par le temps-coordonnée t , comme illustré sur la figure I.1, avec le champ de vecteurs n^μ , normaux aux Σ_t et dirigés vers le futur. Sur chacune des 3-surfaces est définie une 3-métrie γ_{ij} , décrivant la structure intrinsèque de celle-ci. L'évolution des coordonnées spatiales d'une 3-surface à l'autre est donnée par le 3-vecteur *shift* et la fonction *lapse* N mesure le rapport entre l'écoulement du temps propre d'un observateur eulérien (correspondant au

champ de vecteur \mathbf{n}) et le temps coordonnée t . Le passage de la 4-métrie $g_{\mu\nu}$ à ces quantités est ainsi donné par :

$$ds^2 = g_{\mu\nu} dx^\mu dx^\nu = -N^2 dt^2 + \gamma_{ij} (dx^i + \beta^i dt) (dx^j + \beta^j dt). \quad (1)$$

Une dernière quantité très importante dans ce cadre est la courbure extrinsèque (ou deuxième¹ forme fondamentale de chaque 3-surface) définie comme la dérivée de Lie, par rapport au vecteur n^μ de la 3-métrie γ_{ij} :

$$\mathbf{K} = -\frac{1}{2} \mathcal{L}_{\mathbf{n}} \gamma. \quad (2)$$

D'une manière similaire à la métrie, le 4-tenseur énergie-impulsion $T^{\mu\nu}$ entrant dans les équations d'Einstein est décomposé en grandeurs tridimensionnelles : E , J^i et S^{ij} (voir l'équation (1.6)).

Les équations d'Einstein sont projetées sur ces 3-surfaces, ainsi que sur la normale à ces 3-surfaces, donnée par le champ de vecteurs n^i . Les dix équations se retrouvent ainsi en deux catégories : quatre équations de contraintes et six équations d'évolution. En notant D_i la dérivée covariante, R_{ij} et R le tenseur et le scalaire de Ricci liés à la 3-métrie γ_{ij} , les contraintes s'écrivent :

$$R + K^2 - K_{ij} K^{ij} = 16\pi E \text{ (contrainte hamiltonienne)}, \quad (3)$$

$$D_j K^{ij} - D^i K = 8\pi J^i \text{ (contraintes impulsions)}. \quad (4)$$

Les six équations d'évolution prennent la forme :

$$\frac{\partial K_{ij}}{\partial t} - \mathcal{L}_{\beta} K_{ij} = -D_i D_j N + N R_{ij} - 2N K_{ik} K^k_j + N [K K_{ij} + 4\pi((S - E)\gamma_{ij} - 2S_{ij})]; \quad (5)$$

pour être complet, il faut leur ajouter la relation cinématique (2) :

$$K^{ij} = \frac{1}{2N} \left(\frac{\partial \gamma^{ij}}{\partial t} + D^i \beta^j + D^j \beta^i \right). \quad (6)$$

De manière analogue à l'électromagnétisme, lors de l'intégration des équations d'Einstein à partir de conditions initiales vérifiant les contraintes, celles-ci sont vérifiées au cours de l'évolution par cohérence du système d'équations aux dérivées partielles (grâce aux identités de Bianchi). Cela a conduit de nombreux groupes de relativité numérique à adopter des *formalismes libres*, c'est-à-dire dans lesquels les contraintes ne sont pas résolues au cours de l'intégration temporelle. Le formalisme libre le plus utilisé est communément appelé BSSN, pour Baumgarte-Shapiro [54], Shibata-Nakamura [421]. Cependant, un des problèmes lié à la discrétisation numérique, qui est apparu avec les formulations libres est la croissance exponentielle de modes violant les contraintes, et par conséquent les équations d'Einstein (voir par exemple la revue [428]).

Pour pallier ce problème, dans l'article Bonazzola *et al.* de 2004 (chapitre 1 et [73]), nous proposons un *formalisme contraint*, dans lequel toutes les équations de contraintes sont résolues

¹la première étant la 3-métrie γ_{ij}

à chaque instant, et seules deux équations d'évolution (sur six) sont considérées, correspondant aux deux degrés de polarisation des ondes gravitationnelles. Nous introduisons une généralisation de la jauge de Dirac et utilisons le feuilletage maximal comme choix de coordonnées. Bien que, par la suite, d'autres techniques ont permis de réduire l'impact des modes violant les contraintes dans l'implémentation des formalismes libres (par exemple les méthodes de pénalisation [232] et surtout la mise au point de jauges adaptés), il reste aujourd'hui important de pouvoir utiliser un tel formalisme contraint pour au moins trois raisons. La première est tout simplement le fait qu'aujourd'hui, presque tous les groupes de relativité numérique utilisent le même formalisme et les mêmes types de jauges. L'utilisation d'un formalisme vraiment différent pour les simulations permet d'avoir une vérification croisée des résultats, qui ne doivent bien évidemment pas dépendre de la formulation des équations, ni du choix de jauge. Le deuxième point qui est le plus important est que, malgré les techniques développées pour juguler les modes violant les contraintes, les formalismes libres peuvent présenter des dérives de l'erreur à long terme, pour lesquelles aucune solution n'existe à ce jour. Il est donc très important de disposer d'un schéma et de techniques numériques permettant une intégration des équations d'Einstein sur des intervalles de temps arbitraires. C'est dans cette direction que s'est inscrite notre démarche avec nos collaborateurs espagnols de l'Université de Valencia (Isabel Cordero-Carrión, Pablo Cerdá-Durán et José-Maria Ibañez). Un dernier point intéressant du formalisme contraint est le fait qu'il représente une généralisation simple et naturelle de l'approximation *conformément plate*, qui revient à dire que la 3-métrique des feuillet de genre espace de la décomposition 3 + 1 est reliée par un facteur conforme à la 3-métrique plate. Cette approximation a été introduite dans les années 1970 par Jim Isenberg [260], afin de supprimer les ondes gravitationnelles de l'espace-temps. Elle a été beaucoup utilisée par les groupes de relativité numérique pour calculer des conditions initiales (notamment pour les systèmes binaires, voir [481, 219]) quasi-stationnaires. Il est donc possible d'utiliser directement ces conditions initiales dans un code d'évolution utilisant le formalisme contraint.

C'est dans cette optique que nous avons étudié, dans l'article Cordero *et al.* de 2008 (chapitre 2 et [134]) les propriétés mathématiques des équations d'Einstein, exprimées dans le formalisme contraint. Dans ce cas, elles apparaissent comme un système d'équations aux dérivées partielles de type mixte hyperbolique-elliptique. Il a été montré que la partie hyperbolique ainsi obtenue formait un système décrivant l'évolution des degrés de liberté des ondes gravitationnelles, alors que la partie elliptique contenait le système des contraintes et la jauge. Cette partie hyperbolique, qui gouverne l'évolution de la déviation h^{ij} de la 3-métrique par rapport à la métrique plate, possède une structure hyperbolique bien définie grâce à la jauge de Dirac. En effet, ce choix est une condition suffisante pour que l'équation d'évolution pour le tenseur h^{ij} soit un système fortement hyperbolique, pour lequel nous avons trouvé une équivalence en terme de système hyperbolique d'équations de conservation. Cette équivalence est très intéressante pour l'implémentation numérique, si l'on veut utiliser des méthodes de type « Godunov ». De plus, l'étude des caractéristiques de ce système hyperbolique nous a permis de montrer que, dans le cas d'une frontière de domaine numérique d'intégration correspondant à l'horizon d'un trou noir, toutes les caractéristiques étaient sortantes, c'est-à-dire entrantes dans le trou noir. Ce résultat implique que, dans le cas de la simulation dynamique d'un trou noir dans ce formalisme, où l'on aura par ailleurs enlevé du domaine de calcul l'espace-temps correspondant à

l'intérieur de l'horizon (apparent), il ne sera pas nécessaire d'imposer de conditions sur ce bord pour le système hyperbolique. Bien que l'étude complète pour savoir si les équations d'Einstein sont bien posées dans ce formalisme n'ait pas été faite, ce travail a constitué un premier pas dans ce sens.

Un problème de convergence numérique de la partie elliptique du formalisme contraint est néanmoins apparue lors des simulations d'effondrement d'un paquet d'ondes gravitationnelles en trou noir. Cette question était connue depuis plusieurs années par les groupes utilisant l'approximation conformément plate pour la 3-métrique, lors de simulations d'effondrements gravitationnels [397]. Néanmoins, le fait que nous l'ayons rencontré dans le cas des équations d'Einstein complètes a confirmé que ce n'était pas lié à l'approximation de 3-métrique conformément plate, mais bien à la formulation des équations elliptiques. En effet, dans le cas d'un problème à symétrie sphérique, la 3-métrique peut être reliée à la 3-métrique plate de manière conforme en choisissant la jauge isotrope. Or, même dans ce cas où l'on ne fait pas d'approximation mais où toutes les équations d'Einstein sont bien résolues, le système d'équations ne converge pas pour un effondrement gravitationnel menant à un trou noir, lorsque la compacité du système fluide dépasse un certain seuil. Dans l'article Cordero *et al.* de 2009 (chapitre 3 et [135]), nous avons analysé ce phénomène en utilisant la théorie de stabilité des solutions d'équations aux dérivées partielles elliptiques non-linéaires, qui nous a permis d'identifier la source du problème. Nous avons ensuite reformulé les équations elliptiques du formalisme contraint, ainsi que celles de l'approximation conformément plate de la relativité générale (les deux systèmes sont très semblables). Nous avons enfin illustré l'efficacité de la nouvelle formulation dans le cas de l'effondrement gravitationnel d'une étoile à neutrons en rotation vers un trou noir. Dans cet exemple, nous avons comparé les résultats avec ceux de Baiotti *et al.* (2005) [41] et nous avons trouvé un accord excellent. Toutefois, dans le cas de l'approximation de la 3-métrique conformément plate, nous sommes obligés d'introduire une approximation supplémentaire, pour laquelle nous montrons qu'elle induit des erreurs plus faibles que l'approximation conformément plate elle-même. Ce qui est intéressant dans le cas étudié de l'effondrement de l'étoile à neutrons en trou noir, est que les résultats obtenus avec les deux approximations, sont en très bon accord avec les résultats obtenus en résolvant toutes les équations d'Einstein. Cela est un peu en contradiction avec l'intuition car l'état final de cet effondrement est un trou noir de Kerr, pour lequel il a été démontré que l'approximation conformément plate est inexacte. L'intérêt de ce résultat est de montrer qu'il est valide d'utiliser cette approximation pour la simulation des effondrements gravitationnels, ce qui peut réduire le temps de calcul nécessaire, pour l'utiliser dans d'autres parties du code (équation d'état réaliste, etc. ...).

Chapitre 1

A constrained scheme for Einstein equations based on Dirac gauge and spherical coordinates

Version publiée : S. Bonazzola, E.ourgoulhon, P. Grandclément et J. Novak, *Physical Review D* **70**, 104007 (2004).

Sommaire

1.1	Introduction and motivations	13
1.2	Covariant 3+1 conformal decomposition	17
1.3	Einstein equations in terms of the flat covariant derivative	22
1.4	Maximal slicing and Dirac gauge	26
1.5	A resolution scheme based on spherical coordinates	32
1.6	First results from a numerical implementation	44
1.7	Summary and conclusions	47
1.A	Degenerate elliptic operators on a black hole horizon	49

1.1 Introduction and motivations

Motivated by the construction of the detectors LIGO, GEO600, TAMA and VIRGO, as well as by the space project LISA, numerical studies of gravitational wave sources are numerous (see [55, 289] for recent reviews). The majority of them are performed within the framework of the so-called *3+1 formalism* of general relativity, also called *Cauchy formulation*, in which the spacetime is foliated by a family of spacelike hypersurfaces. We propose here a new strategy within this formalism, based on a constrained scheme and spherical coordinates, which is motivated as follows.

1.1.1 Motivations for a constrained scheme

In the 3+1 formalism, the Einstein equations are decomposed in a set of four *constraint equations* and a set of six *dynamical equations* [486, 55]. The constraint equations give rise to elliptic (or sometime parabolic) partial differential equations (PDE), whereas the PDE type of the dynamical equations depends on the choice of the coordinate system. Various strategies can then be contemplated: (i) *free evolution scheme*: solving the constraint equations only to get the initial data and performing the time evolution via the dynamical equations, without enforcing the constraints; (ii) *partially constrained scheme*: using some of the constraints to compute some of the metric components during the evolution and (iii) *fully constrained scheme*: solving the four constraint equations at each time step.

In the eighties, partially constrained schemes, with only the Hamiltonian constraint enforced, have been widely used in 2-D (axisymmetric) computations (e.g. Bardeen and Piran [47], Stark and Piran [440], Evans [165]). Still in the 2-D axisymmetric case, fully constrained schemes have been used by Evans [166] and Shapiro and Teukolsky [411] for non-rotating spacetimes, and by Abrahams, Cook, Shapiro and Teukolsky [4] for rotating ones. We also notice that the recent (2+1)+1 axisymmetric code of Choptuik *et al.* [118] is based on a constrained scheme too.

Regarding the 3-D case, almost all numerical studies to date are based on free evolution schemes¹. It turned out that the free evolution scheme directly applied to the standard 3+1 equations (sometimes called *ADM formulation*) failed due to the development of constraint-violating modes. An impressive amounts of works have then been devoted these last years to finding stable evolution schemes (see [428] for an extensive review and [296] for a very recent work in this area). Among them, a large number of authors have tried to introduce coordinates and auxiliary variables so that the dynamical equations become a first-order symmetric hyperbolic system. However these approaches have revealed very limited success in practice. Another approach has become very popular in the last few years: the so-called *BSSN formulation*, originally devised by Shibata and Nakamura [421] and re-introduced by Baumgarte and Shapiro [54]. It has shown a much improved stability with respect to the standard ADM formulation. Indeed the most successful computations in numerical relativity to date are based on that formulation (e.g. [424, 425]).

All the approaches mentioned above favor first-order hyperbolic equations with respect to elliptic equations. In particular, they employ a free-evolution scheme, avoiding to solve the (elliptic) constraint equations. The main reason is neither mathematical nor physical, but rather a technical one: for most numerical techniques, solving elliptic equations is CPU time expensive. In this article, we present an approach which is based on the opposite strategy, namely to use as much as possible elliptic equations and as few hyperbolic equations as possible. More precisely we propose to use a fully constrained-evolution scheme and to solve the minimum number of hyperbolic equations: the two wave equations corresponding to the two degrees of freedom of the gravitational field. The main advantages of this procedure are that (i) elliptic equations are much more stable than hyperbolic ones, in particular their mathematical well-posedness is usually established, (ii) the constraint-violating modes that plague the free-evolution schemes do not exist by construction in a fully constrained evolution, (iii) the equations describing stationary spacetimes are usually elliptic and are naturally recovered when taking the steady-state limit of the proposed scheme. Besides, let us point that some very efficient (i.e. requiring a modest CPU time) numerical techniques (based on spectral methods) are now available to solve elliptic equations [79, 228]. Very recently some scheme has been proposed in which the constraints, re-written as time evolution equations, are satisfied up to the time discretization error [202]. On the

¹an exception is the recent work [19], where some constrained evolution of a single isolated black hole is presented.

contrary, our scheme guarantees that the constraints are fulfilled within the precision of the *space* discretization error (which can have a much better accuracy, thanks to the use of spectral methods).

To achieve this aim, we use maximal slicing, as long as a generalization of Dirac gauge to curvilinear coordinates. This gauge fixes the spatial coordinates (x^i) in each hypersurface $t = \text{const}$. It has been introduced by Dirac in 1959 [156] as a way to fix the coordinates in the Hamiltonian formulation of general relativity, prior to its quantization (see [145] for a discussion). Dirac gauge has been discussed in the context of numerical relativity first by Smarr and York, in their search for a radiation gauge in general relativity [435]. But they disregarded it as being not covariant under coordinate transformation $(x^i) \mapsto (x^{i'})$ in the hypersurface $t = \text{const}$. They preferred the *minimal distortion gauge*, which is fully covariant and allows for an arbitrary choice of the coordinates (x^i) in the initial hypersurface. Here we show that if one introduces a flat 3-metric on each spatial hypersurface, in addition to the physical 3-metric induced by the spacetime metric, the Dirac gauge can be made covariant. This enables the use of curvilinear coordinates, whereas Dirac original formulation was only for Cartesian coordinates. However, contrary to the minimal distortion gauge, this generalized Dirac gauge still determines fully the coordinates in the initial slice (up to some inner boundary conditions if the slice contains some holes).

1.1.2 Motivations for spherical coordinates

Since the astrophysical objects we want to model (neutron stars and black holes) have spherical topology, it is natural to use spherical coordinates $(x^i) = (r, \theta, \varphi)$ to describe them. In particular, spherical coordinates and spherical components of tensor fields enable one to treat properly the boundary conditions (i) at the surface of fluid stars, as well as at some black hole (apparent) horizon, and (ii) at spatial infinity or at the edge of the computational domain. For a binary system, two systems of spherical coordinates (each centered on one of the objects) have proved to be successful in the treatment of binary neutron stars [218] and binary black holes [229].

Outer boundary conditions

For elliptic equations, spherical coordinates allow a natural $1/r$ compactification which permits to impose boundary conditions at spatial infinity [69, 228]. In this way, the imposed boundary conditions are exact.

For wave equations from a central source, a spherical boundary of the numerical domain of integration allows to set non-reflecting boundary conditions [341]. Moreover the use of spherical components of the metric tensor allows, in the Dirac gauge, an easy extraction of the wave components. This results from the asymptotic transverse and traceless (TT) behavior of Dirac gauge and the fact that a TT tensor wave propagating in the radial direction is well described with spherical components.

Black hole excision

Spherical coordinates clearly facilitate black hole excision. Moreover for stationary problems, one has usually to set the lapse to zero on some sphere $r = \text{const}$, in order to preserve the time-independent behavior of slicing of stationary spacetimes [219, 239]. As we discuss in Appendix 1.A, using spherical components of the metric tensor and shift vector is crucial is setting boundary condition on an excised 2-sphere with vanishing lapse function. In fact, because of the degeneracy of the operator acting on the above quantities when the lapse is zero, one can impose boundary conditions on certain components,

and not on the others. In Cartesian components (i.e. linear combinations of spherical components), the imposition of boundary conditions could not be done simply.

Fulfilling the Dirac gauge

We will show that, when using spherical coordinates, the Dirac gauge condition can be imposed easily on spherical *components* of the metric tensor. Indeed, we propose to use the Dirac gauge to compute directly some metric components from the other ones. This seems difficult with Cartesian components (even with spherical coordinates).

Spherical coordinates and numerical techniques

Despite the above strong advantages and although they have been widely used for 2-D (axisymmetric) computations [47, 440, 165, 166, 411, 4, 331, 88, 89], spherical coordinates are not well spread in 3-D numerical relativity. A few exceptions are the time evolution of pure gravitational wave spacetimes by Nakamura *et al.* [331]¹ and the attempts of computing 3-D stellar core collapse by Stark [439]. This situation is mostly due to the massive usage of finite difference methods, which have difficulties to treat the coordinate singularities on the axis $\theta = 0$ and $\theta = \pi$, and at the origin $r = 0$. On the contrary, spectral methods employed mostly in our group [72, 228] and Cornell group [361], deal without any difficulty with the singularities inherent to spherical coordinates. Let us note that in other fields of numerical simulation, like stellar hydrodynamics, spherical coordinates are well spread, for instance in the treatment of supernovae [148, 151].

1.1.3 Plan of the paper

We start the present study by introducing in Sec. 1.2 a conformal decomposition of the 3+1 Einstein equations which is fully covariant with respect to a background flat metric. This differs slightly from previous conformal decompositions (e.g. [421, 54]) by the fact that our conformal metric is a genuine tensor field, and not a tensor density. Then in Sec. 1.3 we re-write the conformal 3+1 Einstein equations in terms of the covariant derivative with respect to the flat background metric. This enables us to introduce the (generalized) Dirac gauge in Sec. 1.4 and to simplify accordingly the equations. We introduce as the basic object of our formulation the difference \mathbf{h} between the inverse conformal metric and the inverse flat metric. At the end of Sect. 1.4, we present an explicit wave equation for \mathbf{h} . In Sec. 1.5, we introduce spherical coordinates and explicit the equations in terms of tensor components with respect to an orthonormal spherical frame. We show how the Dirac gauge can then be used to deduce some metric components from the others in a quasi-algebraic way. The resolution of the dynamical 3+1 equations is then reduced to the resolution of two (scalar) wave equations. A numerical application is presented in Sec. 1.6, where it is shown that the proposed scheme can evolve stably pure gravitational wave spacetimes. Finally Sec. 1.7 gives the concluding remarks. This article is intended to be followed by another study which focuses on the treatment of boundary conditions at black hole horizon(s). Here we present only in Appendix 1.A a preliminary discussion about the type and the number of inner boundary conditions for black hole spacetimes.

¹Note that while Nakamura *et al.* [331] used spherical coordinates, they considered Cartesian components of the tensor fields.

1.2 Covariant 3+1 conformal decomposition

1.2.1 3+1 formalism

We refer the reader to [55] and [486] for an introduction to the 3+1 formalism of general relativity. Here we simply summarize a few key equations, in order mainly to fix the notations¹. The spacetime (or at least the part of it under study) is foliated by a family of spacelike hypersurfaces Σ_t , labeled by the time coordinate t . We denote by \mathbf{n} the future directed unit normal to Σ_t . By definition \mathbf{n} , considered as a 1-form, is parallel to the gradient of t :

$$\mathbf{n} = -Ndt. \quad (1.1)$$

The proportionality factor N is called the *lapse function*. It ensures that \mathbf{n} satisfies to the normalization relation $n_\mu n^\mu = -1$.

The metric γ induced by the spacetime metric \mathbf{g} onto each hypersurface Σ_t is given by the orthogonal projector onto Σ_t :

$$\gamma := \mathbf{g} + \mathbf{n} \otimes \mathbf{n}. \quad (1.2)$$

Since Σ_t is assumed to be spacelike, γ is a positive definite Riemannian metric. In the following, we call it the *3-metric* and denote by \mathbf{D} the covariant derivative associated with it. The second fundamental tensor characterizing the hypersurface Σ_t is its *extrinsic curvature* \mathbf{K} , given by the Lie derivative of γ along the normal vector \mathbf{n} :

$$\mathbf{K} := -\frac{1}{2}\mathcal{L}_{\mathbf{n}}\gamma. \quad (1.3)$$

One introduces on each hypersurface Σ_t a coordinate system $(x^i) = (x^1, x^2, x^3)$ which varies smoothly between neighboring hypersurfaces, so that $(x^\alpha) = (t, x^1, x^2, x^3)$ constitutes a well-behaved coordinate system of the whole spacetime². We denote by $(\partial/\partial x^\alpha) = (\partial/\partial t, \partial/\partial x^i) = (\partial/\partial t, \partial/\partial x^1, \partial/\partial x^2, \partial/\partial x^3)$ the natural vector basis associated with this coordinate system. The 3+1 decomposition of the basis vector $\partial/\partial t$ defines the *shift vector* β of the spatial coordinates (x^i) :

$$\frac{\partial}{\partial t} = N\mathbf{n} + \beta \quad \text{with} \quad \mathbf{n} \cdot \beta = 0. \quad (1.4)$$

The metric components $g_{\alpha\beta}$ with respect to the coordinate system (x^α) are expressed in terms of the lapse function N , the shift vector components β^i and the 3-metric components γ_{ij} according to

$$g_{\mu\nu} dx^\mu dx^\nu = -N^2 dt^2 + \gamma_{ij}(dx^i + \beta^i dt)(dx^j + \beta^j dt). \quad (1.5)$$

In the 3+1 formalism, the matter energy-momentum tensor \mathbf{T} is decomposed as

$$\mathbf{T} = E\mathbf{n} \otimes \mathbf{n} + \mathbf{n} \otimes \mathbf{J} + \mathbf{J} \otimes \mathbf{n} + \mathbf{S}, \quad (1.6)$$

where the energy density E , the momentum density \mathbf{J} and the strain tensor \mathbf{S} , all of them as measured by the observer of 4-velocity \mathbf{n} , are given by the following projections: $E := T_{\mu\nu}n^\mu n^\nu$, $J_\alpha := -\gamma_\alpha^\mu T_{\mu\nu}n^\nu$, $S_{\alpha\beta} := \gamma_\alpha^\mu \gamma_\beta^\nu T_{\mu\nu}$. By means of the Gauss and Codazzi relations, the Einstein

¹We use geometrized units for which $G = 1$ and $c = 1$; Greek indices run in $\{0, 1, 2, 3\}$, whereas Latin indices run in $\{1, 2, 3\}$ only.

²later on we will specify the coordinates (x^i) to be of spherical type, with $x^1 = r$, $x^2 = \theta$ and $x^3 = \varphi$, but at the present stage we keep (x^i) fully general.

field equation is equivalent to the following system of equations (see e.g. Eqs. (23), (24) and (39) of York [486]):

$$R + K^2 - K_{ij}K^{ij} = 16\pi E, \quad (1.7)$$

$$D_j K_i^j - D_i K = 8\pi J_i, \quad (1.8)$$

$$\begin{aligned} \frac{\partial}{\partial t} K_{ij} - \mathcal{L}_\beta K_{ij} = & -D_i D_j N + N [R_{ij} - 2K_{ik}K^k_j \\ & + K K_{ij} + 4\pi ((S - E)\gamma_{ij} - 2S_{ij})]. \end{aligned} \quad (1.9)$$

Equation (1.7) is called the *Hamiltonian constraint*, Eq. (1.8) the *momentum constraint* and Eqs. (1.9) the *dynamical equations*. In these equations K denotes the trace of the extrinsic curvature: $K := K^i_i$, $S := S^i_i$, R_{ij} the Ricci tensor associated with the 3-metric γ and $R := R^i_i$ the corresponding scalar curvature. These equations must be supplemented by the kinematical relation (1.3) between \mathbf{K} and γ :

$$\frac{\partial}{\partial t} \gamma_{ij} - \mathcal{L}_\beta \gamma_{ij} = -2N K_{ij}. \quad (1.10)$$

1.2.2 Conformal metric

York [485] has shown that the dynamical degrees of freedom of the gravitational field are carried by the conformal “metric” $\hat{\gamma}$ defined by

$$\hat{\gamma}_{ij} := \gamma^{-1/3} \gamma_{ij}, \quad (1.11)$$

where

$$\gamma := \det \gamma_{ij}. \quad (1.12)$$

The quantity defined by Eq. (1.11) is a tensor density of weight $-2/3$, which has unit determinant and which is invariant in any conformal transformation of γ_{ij} . It can be seen as representing the equivalence class of conformally related metrics to which the 3-metric γ belongs. The conformal “metric” (1.11) has been used notably in the BSSN formulation [421, 54], along with an “associated” covariant derivative $\hat{\mathbf{D}}$. However, since $\hat{\gamma}$ is a tensor density and not a tensor field, there is not a unique covariant derivative associated with it. In particular one has $\mathbf{D}\hat{\gamma} = 0$, so that the covariant derivative \mathbf{D} introduced in Sec. 1.2.1 is “associated” with $\hat{\gamma}$, in addition to $\hat{\mathbf{D}}$. As a consequence, some of the formulas presented in Refs. [421], [54] or [12] have a meaning only for Cartesian coordinates.

To clarify the meaning of $\hat{\mathbf{D}}$ and to allow for the use of spherical coordinates, we introduce an extra structure on the hypersurfaces Σ_t , namely a metric \mathbf{f} with the following properties: (i) \mathbf{f} has a vanishing Riemann tensor (flat metric), (ii) \mathbf{f} does not vary from one hypersurface to the next one along the spatial coordinates lines:

$$\frac{\partial}{\partial t} f_{ij} = 0, \quad (1.13)$$

and (iii) the asymptotic structure of the physical metric γ is given by \mathbf{f} :

$$\gamma_{ij} \sim f_{ij} \quad \text{at spatial infinity.} \quad (1.14)$$

This last relation expresses the asymptotic flatness of the hypersurfaces Σ_t , which we assume in this article.

The inverse metric is denoted by f^{ij} ¹: $f^{ik}f_{kj} = \delta^i_j$. We denote by \mathcal{D} the unique covariant derivative associated with \mathbf{f} : $\mathcal{D}_k f_{ij} = 0$ and define

$$\mathcal{D}^i := f^{ij}\mathcal{D}_j. \quad (1.15)$$

Thanks to the flat metric \mathbf{f} , we can properly define the *conformal metric* $\tilde{\gamma}$ as

$$\tilde{\gamma}_{ij} := \Psi^{-4}\gamma_{ij} \quad \text{or} \quad \gamma_{ij} =: \Psi^4\tilde{\gamma}_{ij}, \quad (1.16)$$

where the conformal factor Ψ is defined by

$$\Psi := \left(\frac{\gamma}{f}\right)^{1/12}, \quad (1.17)$$

γ and f being respectively the determinant of γ [cf. Eq. (1.12)] and the determinant of \mathbf{f} with respect to the coordinates (x^i) :

$$f := \det f_{ij}. \quad (1.18)$$

Being expressible as the quotient of two determinants, Ψ is a scalar field on Σ_t . Indeed a change of coordinates $(x^i) \mapsto (x^{i'})$ induces the following changes in the determinants: $\gamma' = (\det J)^2\gamma$ and $f' = (\det J)^2f$, where J denotes the Jacobian matrix $J^i_{i'} := \partial x^i/\partial x^{i'}$. It is then obvious that $\gamma'/f' = \gamma/f$, which shows the covariance of γ/f . Since Ψ is a scalar field, $\tilde{\gamma}$ defined by Eq. (1.16) is a tensor field on Σ_t and not a tensor density as the quantity defined by Eq. (1.11) and considered in the BSSN formulation [421, 54, 55]. Moreover, Ψ being always strictly positive (for γ and f are strictly positive), $\tilde{\gamma}$ is a Riemannian metric on Σ_t . Actually it is the member of the conformal equivalence class of γ which has the same determinant as the flat metric \mathbf{f} :

$$\det \tilde{\gamma}_{ij} = f. \quad (1.19)$$

In this respect, our approach agrees with the point of view of York in Ref. [487], who prefers to introduce a specific member of the conformal equivalence class of γ instead of manipulating tensor densities such as (1.11). In our case, we use the extra-structure \mathbf{f} to pick out the representative member of the conformal equivalence class by the requirement (1.19).

We define the *inverse conformal metric* $\tilde{\gamma}^{ij}$ by the requirement

$$\tilde{\gamma}_{ik}\tilde{\gamma}^{kj} = \delta_i^j, \quad (1.20)$$

which is equivalent to

$$\tilde{\gamma}^{ij} = \Psi^4\gamma^{ij} \quad \text{or} \quad \gamma^{ij} = \Psi^{-4}\tilde{\gamma}^{ij}. \quad (1.21)$$

Since $\tilde{\gamma}$ is a well defined metric on Σ_t , there is a unique covariant derivative associated with it, which we denote by $\tilde{\mathcal{D}}$: $\tilde{\mathcal{D}}_k\tilde{\gamma}_{ij} = 0$. The covariant derivatives $\tilde{\mathcal{D}}\mathbf{T}$ and $\mathcal{D}\mathbf{T}$ of any tensor field \mathbf{T} of type $\binom{p}{q}$ on Σ_t are related by the formula

$$\begin{aligned} \tilde{\mathcal{D}}_k T^{i_1 \dots i_p}_{j_1 \dots j_q} &= \mathcal{D}_k T^{i_1 \dots i_p}_{j_1 \dots j_q} + \sum_{r=1}^p \Delta^{i_r}_{lk} T^{i_1 \dots l \dots i_p}_{j_1 \dots j_q} \\ &\quad - \sum_{r=1}^q \Delta^l_{j_r k} T^{i_1 \dots i_p}_{j_1 \dots l \dots j_q}, \end{aligned} \quad (1.22)$$

¹Note that, in general one has $f^{ij} \neq \gamma^{ik}\gamma^{jl}f_{kl}$.

where Δ denotes the following type $\binom{1}{2}$ tensor field:

$$\Delta^k{}_{ij} := \frac{1}{2} \tilde{\gamma}^{kl} (\mathcal{D}_i \tilde{\gamma}_{lj} + \mathcal{D}_j \tilde{\gamma}_{il} - \mathcal{D}_l \tilde{\gamma}_{ij}). \quad (1.23)$$

$\Delta^k{}_{ij}$ can also be viewed as the difference between the Christoffel symbols¹ of \tilde{D}_i ($\tilde{\Gamma}^k{}_{ij}$) and those of \mathcal{D}_i ($\bar{\Gamma}^k{}_{ij}$):

$$\Delta^k{}_{ij} = \tilde{\Gamma}^k{}_{ij} - \bar{\Gamma}^k{}_{ij}. \quad (1.24)$$

The general formula for the variation of the determinant applied to the matrix $\tilde{\gamma}_{ij}$ writes, once combined with Eq. (1.19),

$$\delta \ln f = \delta \ln \tilde{\gamma} = \tilde{\gamma}^{ij} \delta \tilde{\gamma}_{ij}, \quad (1.25)$$

for any infinitesimal variation δ which obeys Leibniz rule. In the special case $\delta = \mathcal{D}_k$, we deduce immediately that

$$\tilde{\gamma}^{ij} \mathcal{D}_k \tilde{\gamma}_{ij} = 2\Delta^l{}_{kl} = 0. \quad (1.26)$$

A useful property of \tilde{D} is that the divergence with respect to it of any vector field V coincides with the divergence with respect to the flat covariant derivative \mathcal{D} :

$$\tilde{D}_k V^k = \mathcal{D}_k V^k. \quad (1.27)$$

This follows from the standard expression of the divergence in terms of partial derivatives with respect to the coordinates (x^i), and from Eq. (1.19).

1.2.3 Conformal decomposition

We represent the traceless part of the extrinsic curvature by

$$A^{ij} := \Psi^4 \left(K^{ij} - \frac{1}{3} K \gamma^{ij} \right). \quad (1.28)$$

Again, contrary to the A^{ij} of the BSSN formulation [421, 54], this quantity is a tensor field and not a tensor density. We introduce the following related type $\binom{0}{2}$ tensor field:

$$\tilde{A}_{ij} := \tilde{\gamma}_{ik} \tilde{\gamma}_{jl} A^{kl} = \Psi^{-4} \left(K_{ij} - \frac{1}{3} K \gamma_{ij} \right), \quad (1.29)$$

which can be seen as A^{ij} with the indices lowered by $\tilde{\gamma}_{ij}$, instead of γ_{ij} . Both A^{ij} and \tilde{A}_{ij} are traceless, in the sense that

$$\gamma_{ij} A^{ij} = \tilde{\gamma}_{ij} \tilde{A}^{ij} = 0 \quad \text{and} \quad \gamma^{ij} \tilde{A}_{ij} = \tilde{\gamma}^{ij} \tilde{A}_{ij} = 0. \quad (1.30)$$

The Ricci tensor R of the covariant derivative \mathcal{D} (associated with the physical 3-metric γ) is related to the Ricci tensor \tilde{R} of the covariant derivative \tilde{D} (associated with the conformal metric $\tilde{\gamma}$) by:

$$\begin{aligned} R_{ij} &= \tilde{R}_{ij} - 2\tilde{D}_i \tilde{D}_j \Phi + 4\tilde{D}_i \Phi \tilde{D}_j \Phi \\ &\quad - 2 \left(\tilde{D}^k \tilde{D}_k \Phi + 2\tilde{D}_k \Phi \tilde{D}^k \Phi \right) \tilde{\gamma}_{ij}, \end{aligned} \quad (1.31)$$

¹Recall that, while Christoffel symbols do not constitute the components of any tensor field, the difference between two sets of them does.

where

$$\Phi := \ln \Psi \quad (1.32)$$

and we have introduced the notation [in the same spirit as in Eq. (1.15)]

$$\tilde{D}^i := \tilde{\gamma}^{ij} \tilde{D}_j. \quad (1.33)$$

The trace of Eq. (1.31) gives

$$R = \Psi^{-4} \left(\tilde{R} - 8\tilde{D}_k \tilde{D}^k \Phi - 8\tilde{D}_k \Phi \tilde{D}^k \Phi \right), \quad (1.34)$$

where we have introduced the scalar curvature of the metric $\tilde{\gamma}_{ij}$:

$$\tilde{R} := \tilde{\gamma}^{ij} \tilde{R}_{ij}. \quad (1.35)$$

An equivalent form of Eq. (1.34) is $R = \Psi^{-4} \tilde{R} - 8\Psi^{-5} \tilde{D}_k \tilde{D}^k \Psi$, which agrees with Eq. (54) of York [486].

Thanks to Eq. (1.34), the Hamiltonian constraint (1.7) can be re-written

$$\tilde{D}_k \tilde{D}^k \Phi + \tilde{D}_k \Phi \tilde{D}^k \Phi = \frac{\tilde{R}}{8} - \Psi^4 \left(2\pi E + \frac{1}{8} \tilde{A}_{kl} A^{kl} - \frac{K^2}{12} \right). \quad (1.36)$$

This equation is equivalent to Eq. (70) of York [486]. The momentum constraint (1.8) becomes

$$\tilde{D}_j A^{ij} + 6A^{ij} \tilde{D}_j \Phi - \frac{2}{3} \tilde{D}^i K = 8\pi \Psi^4 J^i, \quad (1.37)$$

which agrees with Eq. (44) of Alcubierre et al. [10] in the special case of Cartesian coordinates (these Authors are using the quantity $\Phi' = \Phi + 1/12 \ln f$, with $f = 1$ in Cartesian coordinates).

The trace of the dynamical equation (1.9) [combined with the Hamiltonian constraint (1.7)] gives rise to an evolution equation for the trace K of the extrinsic curvature:

$$\begin{aligned} \frac{\partial K}{\partial t} - \beta^k \tilde{D}_k K &= -\Psi^{-4} \left(\tilde{D}_k \tilde{D}^k N + 2\tilde{D}_k \Phi \tilde{D}^k N \right) \\ &+ N \left[4\pi(E + S) + \tilde{A}_{kl} A^{kl} + \frac{K^2}{3} \right], \end{aligned} \quad (1.38)$$

whereas the traceless part of Eq. (1.9) becomes

$$\begin{aligned} \frac{\partial A^{ij}}{\partial t} - \mathcal{L}_\beta A^{ij} - \frac{2}{3} \tilde{D}_k \beta^k A^{ij} &= -\Psi^{-6} \left(\tilde{D}^i \tilde{D}^j Q - \frac{1}{3} \tilde{D}_k \tilde{D}^k Q \tilde{\gamma}^{ij} \right) \\ &+ \Psi^{-4} \left\{ N \left(\tilde{\gamma}^{ik} \tilde{\gamma}^{jl} \tilde{R}_{kl} + 8\tilde{D}^i \Phi \tilde{D}^j \Phi \right) + 4 \left(\tilde{D}^i \Phi \tilde{D}^j N + \tilde{D}^j \Phi \tilde{D}^i N \right) \right. \\ &\left. - \frac{1}{3} \left[N \left(\tilde{R} + 8\tilde{D}_k \Phi \tilde{D}^k \Phi \right) + 8\tilde{D}_k \Phi \tilde{D}^k N \right] \tilde{\gamma}^{ij} \right\} \\ &+ N \left[K A^{ij} + 2\tilde{\gamma}_{kl} A^{ik} A^{jl} - 8\pi \left(\Psi^4 S^{ij} - \frac{1}{3} S \tilde{\gamma}^{ij} \right) \right], \end{aligned} \quad (1.39)$$

where we have introduced the scalar field

$$Q := \Psi^2 N. \quad (1.40)$$

Q has the property to gather the second order derivatives of N and Ψ in Eq. (1.39). Moreover, in the stationary case, it has no asymptotic monopolar term (decaying like $1/r$), as discussed in [219]. An elliptic equation for Q is obtained by combining Eqs. (1.36) and (1.38):

$$\begin{aligned} \tilde{D}_k \tilde{D}^k Q &= \Psi^2 \left[\Psi^4 N \left(4\pi S + \frac{3}{4} \tilde{A}_{kl} A^{kl} + \frac{K^2}{2} \right) \right. \\ &\quad + N \left(\frac{1}{4} \tilde{R} + 2\tilde{D}_k \Phi \tilde{D}^k \Phi \right) + 2\tilde{D}_k \Phi \tilde{D}^k N \\ &\quad \left. - \Psi^4 \left(\frac{\partial K}{\partial t} - \beta^k \tilde{D}_k K \right) \right]. \end{aligned} \quad (1.41)$$

The trace and traceless parts of the kinematical relation (1.10) between \mathbf{K} and $\boldsymbol{\gamma}$ result respectively in

$$\frac{\partial \Psi}{\partial t} = \beta^k \tilde{D}_k \Psi + \frac{\Psi}{6} \left(\tilde{D}_k \beta^k - NK \right) \quad (1.42)$$

and

$$\frac{\partial \tilde{\gamma}^{ij}}{\partial t} - \mathcal{L}_{\beta} \tilde{\gamma}^{ij} - \frac{2}{3} \tilde{D}_k \beta^k \tilde{\gamma}^{ij} = 2NA^{ij}. \quad (1.43)$$

1.3 Einstein equations in terms of the flat covariant derivative

It is worth to write the Einstein equations, not in terms of the conformal covariant derivative $\tilde{\mathcal{D}}$, as done above, but in terms of the flat covariant derivative \mathcal{D} , because (i) numerical resolution usually proceeds through linear operators expressed in terms of \mathcal{D} (and deals with non-linearities via iterations), and (ii) the Dirac gauge we aim to use is expressed in terms of \mathcal{D} .

1.3.1 Ricci tensor of $\tilde{\mathcal{D}}$ in terms of the flat derivatives of $\tilde{\gamma}$

The Ricci tensor $\tilde{\mathbf{R}}$ of the covariant derivative $\tilde{\mathcal{D}}$ which appears in the equations of Sec. 1.2.3 can be expressed in terms of the flat covariant derivatives of the conformal metric $\tilde{\gamma}$ as

$$\begin{aligned} \tilde{R}_{ij} &= -\frac{1}{2} \tilde{\gamma}^{kl} (\mathcal{D}_k \mathcal{D}_l \tilde{\gamma}_{ij} - \mathcal{D}_k \mathcal{D}_i \tilde{\gamma}_{lj} - \mathcal{D}_k \mathcal{D}_j \tilde{\gamma}_{il}) \\ &\quad + \frac{1}{2} \mathcal{D}_k \tilde{\gamma}^{kl} (\mathcal{D}_i \tilde{\gamma}_{lj} + \mathcal{D}_j \tilde{\gamma}_{il} - \mathcal{D}_l \tilde{\gamma}_{ij}) \\ &\quad - \Delta^k_{il} \Delta^l_{jk}. \end{aligned} \quad (1.44)$$

This equation agrees with Eq. (2.17) of [421], provided it is restricted to Cartesian coordinates, for which $\mathcal{D}_i \rightarrow \partial_i$ and $\Delta^k_{ij} \rightarrow \tilde{\Gamma}^k_{ij}$. After some manipulations, Eq. (1.44) can be written as

$$\begin{aligned} \tilde{R}_{ij} &= -\frac{1}{2} \left(\tilde{\gamma}^{kl} \mathcal{D}_k \mathcal{D}_l \tilde{\gamma}_{ij} + \tilde{\gamma}_{ik} \mathcal{D}_j H^k + \tilde{\gamma}_{jk} \mathcal{D}_j H^k \right. \\ &\quad \left. + H^k \mathcal{D}_k \tilde{\gamma}_{ij} + \mathcal{D}_i \tilde{\gamma}^{kl} \mathcal{D}_k \tilde{\gamma}_{lj} + \mathcal{D}_j \tilde{\gamma}^{kl} \mathcal{D}_k \tilde{\gamma}_{il} \right) \\ &\quad - \Delta^k_{il} \Delta^l_{jk}, \end{aligned} \quad (1.45)$$

where we have introduced the vector field

$$H^i := \mathcal{D}_j \tilde{\gamma}^{ij} = -\tilde{\gamma}^{kl} \Delta^i_{kl} \quad (1.46)$$

[the second equality results from Eq. (1.23)]. If we restrict ourselves to Cartesian coordinates ($\mathcal{D}_i \rightarrow \partial_i$, $\Delta^i_{kl} \rightarrow \tilde{\Gamma}^i_{kl}$), the quantity H^i coincides with minus the ‘‘conformal connection functions’’ $\tilde{\Gamma}^i$ introduced by Baumgarte and Shapiro [54]: $\tilde{\Gamma}^i = -H^i$. Moreover after some rearrangements, the expression (1.45) for the Ricci tensor can be shown to agree with Eq. (22) of [54]. The motivation for the writing (1.45) of the Ricci tensor traces back to Nakamura, Oohara and Kojima [331]; it consists in letting appear a Laplacian acting on $\tilde{\gamma}_{ij}$ [first term on the right-hand side of Eq. (1.45)] and put all the other second order derivatives of $\tilde{\gamma}_{ij}$ into derivatives of H^i . This is very similar to the decomposition of the 4-dimensional Ricci tensor which motivates the introduction of harmonic coordinates; note that in general the principal part of the Ricci tensor contains 4 terms with second-order derivatives of the metric; we have only 3 in Eq. (1.45) because $\det \tilde{\gamma}_{ij} = f$.

Starting from Eq. (1.45), we obtain, after some computations, an expression of the Ricci tensor in terms of the flat covariant derivatives of $\tilde{\gamma}^{ij}$, instead of $\tilde{\gamma}_{ij}$:

$$\begin{aligned} \tilde{\gamma}^{ik} \tilde{\gamma}^{jl} \tilde{R}_{kl} &= \frac{1}{2} \left(\tilde{\gamma}^{kl} \mathcal{D}_k \mathcal{D}_l \tilde{\gamma}^{ij} - \tilde{\gamma}^{ik} \mathcal{D}_k H^j - \tilde{\gamma}^{jk} \mathcal{D}_k H^i + H^k \mathcal{D}_k \tilde{\gamma}^{ij} - \mathcal{D}_l \tilde{\gamma}^{ik} \mathcal{D}_k \tilde{\gamma}^{jl} \right. \\ &\quad - \tilde{\gamma}_{kl} \tilde{\gamma}^{mn} \mathcal{D}_m \tilde{\gamma}^{ik} \mathcal{D}_n \tilde{\gamma}^{jl} + \tilde{\gamma}^{ik} \tilde{\gamma}_{ml} \mathcal{D}_k \tilde{\gamma}^{mn} \mathcal{D}_n \tilde{\gamma}^{jl} + \tilde{\gamma}^{jl} \tilde{\gamma}_{kn} \mathcal{D}_l \tilde{\gamma}^{mn} \mathcal{D}_m \tilde{\gamma}^{ik} \\ &\quad \left. + \frac{1}{2} \tilde{\gamma}^{ik} \tilde{\gamma}^{jl} \mathcal{D}_k \tilde{\gamma}_{mn} \mathcal{D}_l \tilde{\gamma}^{mn} \right). \end{aligned} \quad (1.47)$$

If we restrict ourselves to Cartesian coordinates, the terms with second derivatives of $\tilde{\gamma}^{ij}$, i.e. the first three terms in the above equation, agree with Eq. (12) of [8].

The curvature scalar \tilde{R} defined from the Ricci tensor $\tilde{\mathbf{R}}$ by Eq. (1.35) is basically minus the flat divergence of \mathbf{H} plus some quadratic terms:

$$\tilde{R} = -\mathcal{D}_k H^k + \frac{1}{4} \tilde{\gamma}^{kl} \mathcal{D}_k \tilde{\gamma}^{ij} \mathcal{D}_l \tilde{\gamma}_{ij} - \frac{1}{2} \tilde{\gamma}^{kl} \mathcal{D}_k \tilde{\gamma}^{ij} \mathcal{D}_j \tilde{\gamma}_{il}. \quad (1.48)$$

1.3.2 Definition of the potentials h^{ij}

We will numerically solve not for the conformal metric $\tilde{\gamma}$ but for the deviation \mathbf{h} of the inverse conformal metric $\tilde{\gamma}^{ij}$ from the inverse flat metric, defined by the formula

$$\tilde{\gamma}^{ij} =: f^{ij} + h^{ij}. \quad (1.49)$$

\mathbf{h} is a symmetric tensor field on Σ_t of type $\binom{2}{0}$ (“twice contravariant tensor” h^{ij}) and we will manipulate it as such, without introducing any bilinear form (“twice covariant tensor” h_{ij}) dual to it.

The flat covariant derivatives of \mathbf{h} coincide with those of $\tilde{\gamma}^{ij}$: $\mathcal{D}_k \tilde{\gamma}^{ij} = \mathcal{D}_k h^{ij}$. In particular the vector field \mathbf{H} introduced in Eq. (1.46) is the flat divergence of \mathbf{h} :

$$H^i = \mathcal{D}_j h^{ij}. \quad (1.50)$$

Thanks to the splitting (1.49), we can express the differential operator $\tilde{\gamma}^{kl} \mathcal{D}_k \mathcal{D}_l$ which appears in the equations listed in Sec. 1.3.1 as $\tilde{\gamma}^{kl} \mathcal{D}_k \mathcal{D}_l = \Delta + h^{kl} \mathcal{D}_k \mathcal{D}_l$, where Δ is the Laplacian operator associated with the flat metric:

$$\Delta := f^{kl} \mathcal{D}_k \mathcal{D}_l = \mathcal{D}_k \mathcal{D}^k. \quad (1.51)$$

1.3.3 Einstein equations in terms of \mathbf{h} and \mathcal{D}

Inserting Eq. (1.48) into the combination (1.41) of the Hamiltonian constraint and the trace of the spatial part of the dynamical Einstein equations leads to

$$\begin{aligned} \Delta Q &= -h^{kl} \mathcal{D}_k \mathcal{D}_l Q - H^k \mathcal{D}_k Q + \Psi^6 \left[N \left(4\pi S + \frac{3}{4} \tilde{A}_{kl} A^{kl} + \frac{K^2}{2} \right) - \frac{\partial K}{\partial t} + \beta^k \mathcal{D}_k K \right] \\ &+ \Psi^2 \left[N \left(-\frac{1}{4} \mathcal{D}_k H^k + \frac{1}{16} \tilde{\gamma}^{kl} \mathcal{D}_k h^{ij} \mathcal{D}_l \tilde{\gamma}_{ij} - \frac{1}{8} \tilde{\gamma}^{kl} \mathcal{D}_k h^{ij} \mathcal{D}_j \tilde{\gamma}_{il} + 2\tilde{D}_k \Phi \tilde{D}^k \Phi \right) \right. \\ &\left. + 2\tilde{D}_k \Phi \tilde{D}^k N \right]. \end{aligned} \quad (1.52)$$

The momentum constraint (1.37) writes

$$\mathcal{D}_j A^{ij} + \Delta^i{}_{kl} A^{kl} + 6A^{ij} \mathcal{D}_j \Phi - \frac{2}{3} \tilde{\gamma}^{ij} \mathcal{D}_j K = 8\pi \Psi^4 J^i, \quad (1.53)$$

with the following expression for $\Delta^i{}_{kl}$, alternative to Eq. (1.23):

$$\Delta^k{}_{ij} = -\frac{1}{2} \left(\mathcal{D}^k \tilde{\gamma}_{ij} + h^{kl} \mathcal{D}_l \tilde{\gamma}_{ij} + \tilde{\gamma}_{il} \mathcal{D}_j h^{kl} + \tilde{\gamma}_{lj} \mathcal{D}_i h^{kl} \right). \quad (1.54)$$

Taking into account property (1.27), the trace relation (1.42) can be expressed as

$$\frac{\partial \Phi}{\partial t} - \beta^k \mathcal{D}_k \Phi = \frac{1}{6} \left(\mathcal{D}_k \beta^k - NK \right). \quad (1.55)$$

The combination (1.38) of the trace of the dynamical Einstein equations with the Hamiltonian constraint equations becomes

$$\begin{aligned} \frac{\partial K}{\partial t} - \beta^k \mathcal{D}_k K &= -\Psi^{-4} (\Delta N + h^{kl} \mathcal{D}_k \mathcal{D}_l N + H^k \mathcal{D}_k N \\ &+ 2\tilde{D}_k \Phi \tilde{D}^k N) + N \left[4\pi(E + S) + \tilde{A}_{kl} A^{kl} + \frac{K^2}{3} \right]. \end{aligned} \quad (1.56)$$

After some computations, the traceless kinematical relation (1.43) and the traceless part (1.39) of the dynamical Einstein equations become respectively

$$\frac{\partial h^{ij}}{\partial t} - \mathcal{L}_\beta h^{ij} - \frac{2}{3} \mathcal{D}_k \beta^k h^{ij} = 2N A^{ij} - (L\beta)^{ij}, \quad (1.57)$$

$$\begin{aligned} \frac{\partial A^{ij}}{\partial t} - \mathcal{L}_\beta A^{ij} - \frac{2}{3} \mathcal{D}_k \beta^k A^{ij} &= \frac{N}{2\Psi^4} \left(\Delta h^{ij} - \mathcal{D}^i H^j - \mathcal{D}^j H^i + \frac{2}{3} \mathcal{D}_k H^k f^{ij} \right) \\ &\quad - \frac{1}{2\Psi^6} \left(\mathcal{D}^i h^{jk} + \mathcal{D}^j h^{ik} - \mathcal{D}^k h^{ij} - \frac{2}{3} H^k f^{ij} \right) \mathcal{D}_k Q + \mathcal{S}^{ij}, \end{aligned} \quad (1.58)$$

where \mathcal{S}^{ij} is given by

$$\begin{aligned} \mathcal{S}^{ij} &:= \Psi^{-4} \left\{ N \left(\tilde{R}_*^{ij} + 8\tilde{D}^i \Phi \tilde{D}^j \Phi \right) + 4 \left(\tilde{D}^i \Phi \tilde{D}^j N + \tilde{D}^j \Phi \tilde{D}^i N \right) \right. \\ &\quad \left. - \frac{1}{3} \left[N \left((\tilde{R}_* + 8\tilde{D}_k \Phi \tilde{D}^k \Phi) \tilde{\gamma}^{ij} - \mathcal{D}_k H^k h^{ij} \right) + 8\tilde{D}_k \Phi \tilde{D}^k N \tilde{\gamma}^{ij} \right] \right\} \\ &\quad + N \left[K A^{ij} + 2\tilde{\gamma}_{kl} A^{ik} A^{jl} - 8\pi \left(\Psi^4 \mathcal{S}^{ij} - \frac{1}{3} S \tilde{\gamma}^{ij} \right) \right] \\ &\quad - \Psi^{-6} \left[\tilde{\gamma}^{ik} \tilde{\gamma}^{jl} \mathcal{D}_k \mathcal{D}_l Q + \frac{1}{2} \left(h^{ik} \mathcal{D}_k h^{lj} + h^{kj} \mathcal{D}_k h^{il} - h^{kl} \mathcal{D}_k h^{ij} \right) \mathcal{D}_l Q \right. \\ &\quad \left. - \frac{1}{3} \left(\tilde{\gamma}^{kl} \mathcal{D}_k \mathcal{D}_l Q \tilde{\gamma}^{ij} + H^k \mathcal{D}_k Q h^{ij} \right) \right], \end{aligned} \quad (1.59)$$

with

$$\begin{aligned} \tilde{R}_*^{ij} &:= \frac{1}{2} \left[h^{kl} \mathcal{D}_k \mathcal{D}_l h^{ij} - h^{ik} \mathcal{D}_k H^j - h^{jk} \mathcal{D}_k H^i + H^k \mathcal{D}_k h^{ij} - \mathcal{D}_l h^{ik} \mathcal{D}_k h^{jl} - \tilde{\gamma}_{kl} \tilde{\gamma}^{mn} \mathcal{D}_m h^{ik} \mathcal{D}_n h^{jl} \right. \\ &\quad \left. + \tilde{\gamma}_{ml} \mathcal{D}_k h^{mn} \left(\tilde{\gamma}^{ik} \mathcal{D}_m h^{jl} + \tilde{\gamma}^{jk} \mathcal{D}_m h^{il} \right) + \frac{1}{2} \tilde{\gamma}^{ik} \tilde{\gamma}^{jl} \mathcal{D}_k h^{mn} \mathcal{D}_l \tilde{\gamma}_{mn} \right], \end{aligned} \quad (1.60)$$

$$\tilde{R}_* := \frac{1}{4} \tilde{\gamma}^{kl} \mathcal{D}_k h^{mn} \mathcal{D}_l \tilde{\gamma}_{mn} - \frac{1}{2} \tilde{\gamma}^{kl} \mathcal{D}_k h^{mn} \mathcal{D}_n \tilde{\gamma}_{ml}. \quad (1.61)$$

Finally the notation $(L\beta)^{ij}$ in Eq. (1.57) stands for the conformal Killing operator associated with the flat metric \mathbf{f} and applied to the vector field β :

$$(L\beta)^{ij} := \mathcal{D}^i \beta^j + \mathcal{D}^j \beta^i - \frac{2}{3} \mathcal{D}_k \beta^k f^{ij}. \quad (1.62)$$

The writing (1.58) with the introduction of \mathcal{S}^{ij} by Eq. (1.59) is performed in order to single out the part which is linear in the first and second derivatives of h^{ij} (a term like $h^{kl} \mathcal{D}_k \mathcal{D}_l h^{ij}$ or $h^{ik} \mathcal{D}_k h^{lj} \mathcal{D}_l Q$ being considered as non-linear). In particular the quantities \tilde{R}_*^{ij} and \tilde{R}_* arise from the decomposition of the Ricci tensor (1.47) and Ricci scalar (1.48) in linear and quadratic parts:

$$\tilde{\gamma}^{ik} \tilde{\gamma}^{jl} \tilde{R}_{kl} = \frac{1}{2} (\Delta h^{ij} - \mathcal{D}^i H^j - \mathcal{D}^j H^i) + \tilde{R}_*^{ij}, \quad (1.63)$$

$$\tilde{R} = -\mathcal{D}_k H^k + \tilde{R}_*. \quad (1.64)$$

Consequently \mathcal{S}^{ij} contains no linear terms in the first and second-order spatial derivatives of h^{ij} . Regarding the time derivatives of h^{ij} (encoded in A^{ij}), it contains only one linear term, in NKA^{ij} . Note also that the covariant form $\tilde{\gamma}_{ij}$ of the conformal metric which appears in the expressions of \tilde{R}_*^{ij} and \tilde{R}_* is the inverse of the matrix $\tilde{\gamma}^{ij}$, and therefore can be expressed as a quadratic function of h^{ij} , thanks to the fact that $\tilde{\gamma} = f$.

1.4 Maximal slicing and Dirac gauge

1.4.1 Definitions and discussion

Let us now turn to the choice of coordinates, to fully specify the PDE system to be solved. First regarding the foliation Σ_t , we choose *maximal slicing*:

$$K = 0. \quad (1.65)$$

This well-known type of slicing has been introduced by Lichnerowicz [291] and popularized by York [486, 435]. It is often disregarded in 3-D numerical relativity because it leads to an elliptic equation for the lapse function (cf. discussion in Sec. 1.1.1). However it has very nice properties: beside the well-known singularity avoidance capability [434], it has been shown to be well adapted to the propagation of gravitational waves [435, 421].

Regarding the choice of the three coordinates (x^i) on each slice Σ_t , we consider the Dirac gauge. In Dirac's original definition [156], it corresponds to the requirement

$$\frac{\partial}{\partial x^j} \left(\gamma^{1/3} \gamma^{ij} \right) = 0. \quad (1.66)$$

This writing makes sense only with Cartesian type coordinates. In order to allow for any type of coordinates, we define the *generalized Dirac gauge* as

$$\mathcal{D}_j \left[\left(\frac{\gamma}{f} \right)^{1/3} \gamma^{ij} \right] = 0. \quad (1.67)$$

Obviously this covariant definition is made possible thanks to the introduction of the flat metric \mathbf{f} on Σ_t . We recognize in Eq. (1.67) the flat divergence of the conformal metric:

$$\mathcal{D}_j \tilde{\gamma}^{ij} = 0. \quad (1.68)$$

Since $\mathcal{D}_j f^{ij} = 0$, this condition is equivalent to the vanishing of the flat divergence of the potential h^{ij} :

$$\mathcal{D}_j h^{ij} = 0, \quad (1.69)$$

Another equivalent definition of the Dirac gauge is requiring that the vector \mathbf{H} vanishes [cf. Eq. (1.46)]:

$$H^i = 0. \quad (1.70)$$

As discussed in Sec. 1.1.1, the Dirac gauge has been considered as a candidate for a radiation gauge by Smarr and York [435] but disregarded in profit of the *minimal distortion gauge* which allows for any choice of coordinates in the initial slice. On the contrary Dirac gauge fully specifies (up to some

boundary conditions) the coordinates in the slices Σ_t , including the initial one. This property allows the search for stationary solutions of the proposed system of equations. In particular this allows to get quasi-stationary initial conditions for the time evolution. In this respect note that the numerous conformally flat initial data computed to date (see Ref. [55] for a review) automatically fulfill Dirac gauge, since the conformal flatness of the spatial metric γ is equivalent to the condition $\mathbf{h} = 0$.

Another strong motivation for choosing the Dirac gauge is that it simplifies drastically the principal linear part of the Ricci tensor $\tilde{\mathbf{R}}$ associated with the conformal metric: as seen on Eq. (1.47) or Eq. (1.60), this Ricci tensor, considered as a partial differential operator acting on \mathbf{h} reduces to the elliptic term $\tilde{\gamma}^{kl}\mathcal{D}_k\mathcal{D}_l h^{ij}$ in that gauge. Consequently, the second order part of the right hand side of Eq. (1.58) reduces to a flat Laplacian Δh^{ij} . This reduction of the Ricci tensor to a Laplacian has been the main motivation of the promotion of \mathbf{H} as an independent variable in the BSSN formulation [421, 54]. A related property of the Dirac gauge is that thanks to it, the curvature scalar \tilde{R} of the conformal metric does not contain any second order derivative of $\tilde{\gamma}^{ij}$ [set $H^k = 0$ in Eq. (1.48)].

Note that although Dirac gauge and minimal distortion gauge differ in the general case, both gauges result asymptotically in transverse-traceless (TT) coordinates (cf. Sec. IV of Ref. [435]), which are well adapted to the treatment of gravitational radiation. Both gauges are analogous to Coulomb gauge in electrodynamics. In 1994, Nakamura [329] has used a gauge, called *pseudo-minimal shear*, which is related to the Dirac gauge, for it writes $\mathcal{D}^j(\partial\tilde{\gamma}_{ij}/\partial t) = 0$, while Dirac gauge implies $\mathcal{D}_j(\partial\tilde{\gamma}_{ij}/\partial t) = 0$. Note however that this pseudo-minimal shear does not fix the coordinates on the initial time slice, contrary to Dirac gauge: as the minimal distortion condition, it only rules the time evolution of the coordinate system. The exact Dirac gauge has been employed recently in two numerical studies, by Kawamura, Oohara and Nakamura [273], who call it *the pseudo-minimal distortion condition*, and by Shibata, Uryu and Friedman [419].

Finally let us mention that Andersson and Moncrief [17] have shown recently that the Cauchy problem for 3+1 Einstein equations is locally strongly well posed for a coordinate system quite similar to maximal slicing + Dirac gauge, namely *constant mean curvature* ($K = t$) and *spatial harmonic coordinates* ($\mathcal{D}_j[(\gamma/f)^{1/2}\gamma^{ij}] = 0$).

1.4.2 Einstein equations within maximal slicing and Dirac gauge

Thanks to the choices (1.65) and (1.70), the combination (1.52) of the Hamiltonian constraint and the trace of the spatial part of the dynamical Einstein equations simplifies somewhat

$$\begin{aligned} \Delta Q = & -h^{kl}\mathcal{D}_k\mathcal{D}_l Q + \Psi^6 \left[N \left(4\pi S + \frac{3}{4}\tilde{A}_{kl}A^{kl} \right) \right] \\ & + 2\Psi^2 \left[N \left(\frac{\tilde{R}_*}{8} + \tilde{D}_k\Phi\tilde{D}^k\Phi \right) + \tilde{D}_k\Phi\tilde{D}^k N \right], \end{aligned} \quad (1.71)$$

where we have let appear the quadratic quantity \tilde{R}_* defined by Eq. (1.61). Note that thanks to Dirac gauge, the right hand side of the above equation does not contain any second order derivative of h^{ij} .

The momentum constraint (1.53) becomes

$$\mathcal{D}_j A^{ij} + \Delta^i{}_{kl} A^{kl} + 6A^{ij}\mathcal{D}_j\Phi = 8\pi\Psi^4 J^i. \quad (1.72)$$

Now, taking the (flat) divergence of Eq. (1.57) and using the fact that $\partial/\partial t$ commutes with \mathcal{D}_i , thanks to property (1.13), the Dirac gauge leads to an expression of the divergence of A^{ij} which does not

contain any time derivative of the shift vector nor any second derivative of h^{ij} :

$$\begin{aligned} \mathcal{D}_j A^{ij} = & -\frac{A^{ij}}{N} \mathcal{D}_j N + \frac{1}{2N} \left[\Delta \beta^i + \frac{1}{3} \mathcal{D}^i (\mathcal{D}_j \beta^j) \right. \\ & \left. + h^{kl} \mathcal{D}_k \mathcal{D}_l \beta^i + \frac{1}{3} h^{ik} \mathcal{D}_k (\mathcal{D}_l \beta^l) \right]. \end{aligned} \quad (1.73)$$

Inserting this relation into the momentum constraint equation (1.72) results in an elliptic equation for β :

$$\begin{aligned} \Delta \beta^i + \frac{1}{3} \mathcal{D}^i (\mathcal{D}_j \beta^j) = & 16\pi N \Psi^4 J^i + 2A^{ij} \mathcal{D}_j N \\ & - 12N A^{ij} \mathcal{D}_j \Phi - 2N \Delta^i{}_{kl} A^{kl} \\ & - h^{kl} \mathcal{D}_k \mathcal{D}_l \beta^i - \frac{1}{3} h^{ik} \mathcal{D}_k \mathcal{D}_l \beta^l. \end{aligned} \quad (1.74)$$

Thanks to maximal slicing, the kinematical trace relation (1.55) reduces to

$$\frac{\partial \Phi}{\partial t} - \beta^k \mathcal{D}_k \Phi = \frac{1}{6} \mathcal{D}_k \beta^k. \quad (1.75)$$

The combination (1.56) of the trace of the dynamical Einstein equations with the Hamiltonian constraint equations becomes an elliptic equation for the lapse function:

$$\begin{aligned} \Delta N = & \Psi^4 N \left[4\pi (E + S) + \tilde{A}_{kl} A^{kl} \right] - h^{kl} \mathcal{D}_k \mathcal{D}_l N \\ & - 2\tilde{D}_k \Phi \tilde{D}^k N. \end{aligned} \quad (1.76)$$

In Dirac gauge + maximal slicing, the time evolution system (1.57)-(1.58) becomes

$$\frac{\partial h^{ij}}{\partial t} - \mathcal{L}_\beta h^{ij} - \frac{2}{3} \mathcal{D}_k \beta^k h^{ij} = 2N A^{ij} - (L\beta)^{ij} \quad (1.77)$$

$$\begin{aligned} \frac{\partial A^{ij}}{\partial t} - \mathcal{L}_\beta A^{ij} - \frac{2}{3} \mathcal{D}_k \beta^k A^{ij} = & \frac{N}{2\Psi^4} \Delta h^{ij} + \mathcal{S}^{ij} \\ & - \frac{1}{2\Psi^6} \left(\mathcal{D}^i h^{jk} + \mathcal{D}^j h^{ik} - \mathcal{D}^k h^{ij} \right) \mathcal{D}_k Q, \end{aligned} \quad (1.78)$$

where \mathcal{S}^{ij} is slightly simplified to

$$\begin{aligned} \mathcal{S}^{ij} = & \Psi^{-4} \left\{ N \left(\tilde{R}_*^{ij} + 8\tilde{D}^i \Phi \tilde{D}^j \Phi \right) + 4 \left(\tilde{D}^i \Phi \tilde{D}^j N + \tilde{D}^j \Phi \tilde{D}^i N \right) - \frac{1}{3} \left[N \left((\tilde{R}_* + 8\tilde{D}_k \Phi \tilde{D}^k \Phi) \tilde{\gamma}^{ij} \right) \right. \right. \\ & \left. \left. + 8\tilde{D}_k \Phi \tilde{D}^k N \tilde{\gamma}^{ij} \right] \right\} + 2N \left[\tilde{\gamma}_{kl} A^{ik} A^{jl} - 4\pi \left(\Psi^4 \mathcal{S}^{ij} - \frac{1}{3} \mathcal{S} \tilde{\gamma}^{ij} \right) \right] \\ & - \Psi^{-6} \left[\tilde{\gamma}^{ik} \tilde{\gamma}^{jl} \mathcal{D}_k \mathcal{D}_l Q + \frac{1}{2} \left(h^{ik} \mathcal{D}_k h^{lj} + h^{kj} \mathcal{D}_k h^{il} - h^{kl} \mathcal{D}_k h^{ij} \right) \mathcal{D}_l Q - \frac{1}{3} \left(\tilde{\gamma}^{kl} \mathcal{D}_k \mathcal{D}_l Q \tilde{\gamma}^{ij} \right) \right] \end{aligned} \quad (1.79)$$

with

$$\begin{aligned} \tilde{R}_*^{ij} = & \frac{1}{2} \left[h^{kl} \mathcal{D}_k \mathcal{D}_l h^{ij} - \mathcal{D}_l h^{ik} \mathcal{D}_k h^{jl} - \tilde{\gamma}_{kl} \tilde{\gamma}^{mn} \mathcal{D}_m h^{ik} \mathcal{D}_n h^{jl} + \tilde{\gamma}_{nl} \mathcal{D}_k h^{mn} \left(\tilde{\gamma}^{ik} \mathcal{D}_m h^{jl} + \tilde{\gamma}^{jk} \mathcal{D}_m h^{il} \right) \right. \\ & \left. + \frac{1}{2} \tilde{\gamma}^{ik} \tilde{\gamma}^{jl} \mathcal{D}_k h^{mn} \mathcal{D}_l \tilde{\gamma}_{mn} \right]. \end{aligned} \quad (1.80)$$

The quadratic term \tilde{R}_* in Eq. (1.79) is unchanged and is given by Eq. (1.61). The Lie derivatives along the shift vector field β which appear in Eqs. (1.77) and (1.78) can be expressed in terms of the flat covariant derivative \mathcal{D} by the standard formula:

$$\mathcal{L}_\beta h^{ij} = \beta^k \mathcal{D}_k h^{ij} - h^{kj} \mathcal{D}_k \beta^i - h^{ik} \mathcal{D}_k \beta^j, \quad (1.81)$$

$$\mathcal{L}_\beta A^{ij} = \beta^k \mathcal{D}_k A^{ij} - A^{kj} \mathcal{D}_k \beta^i - A^{ik} \mathcal{D}_k \beta^j. \quad (1.82)$$

1.4.3 Wave equation for h^{ij}

As discussed in Sec. 1.4.1, one of the main motivations for using Dirac gauge is that it changes the second order operator acting on h^{ij} in Eq. (1.78) to a mere Laplacian. It is therefore tempting to write the first order time evolution system (1.77)-(1.78) as a (second order) wave equation for h^{ij} . Note that the first order operator $\partial/\partial t - \mathcal{L}_\beta$ which appear on the l.h.s. of the system (1.77)-(1.78) is nothing but the Lie derivative along the vector $N\mathbf{n}$. Its square is

$$\left(\frac{\partial}{\partial t} - \mathcal{L}_\beta \right)^2 h^{ij} = \frac{\partial^2 h^{ij}}{\partial t^2} - 2\mathcal{L}_\beta \frac{\partial h^{ij}}{\partial t} + \mathcal{L}_\beta \mathcal{L}_\beta h^{ij} - \mathcal{L}_{\dot{\beta}} h^{ij}, \quad (1.83)$$

with the short-hand notation

$$\dot{\beta}^i := \frac{\partial \beta^i}{\partial t}. \quad (1.84)$$

Applying the operator $\partial/\partial t - \mathcal{L}_\beta$ to Eq. (1.77) and inserting Eqs. (1.83) and (1.78) in the result leads to the wave equation

$$\begin{aligned} \frac{\partial^2 h^{ij}}{\partial t^2} - \frac{N^2}{\psi^4} \Delta h^{ij} - 2\mathcal{L}_\beta \frac{\partial h^{ij}}{\partial t} + \mathcal{L}_\beta \mathcal{L}_\beta h^{ij} = & \mathcal{L}_{\dot{\beta}} h^{ij} + \frac{4}{3} \mathcal{D}_k \beta^k \left(\frac{\partial}{\partial t} - \mathcal{L}_\beta \right) h^{ij} \\ & - \frac{N}{\Psi^6} \mathcal{D}_k Q \left(\mathcal{D}^i h^{jk} + \mathcal{D}^j h^{ik} - \mathcal{D}^k h^{ij} \right) \\ & + \frac{1}{N} \left[\left(\frac{\partial}{\partial t} - \mathcal{L}_\beta \right) N \right] \left[\left(\frac{\partial}{\partial t} - \mathcal{L}_\beta \right) h^{ij} - \frac{2}{3} \mathcal{D}_k \beta^k h^{ij} + (L\beta)^{ij} \right] \\ & + \frac{2}{3} \left[\left(\frac{\partial}{\partial t} - \mathcal{L}_\beta \right) \mathcal{D}_k \beta^k - \frac{2}{3} (\mathcal{D}_k \beta^k)^2 \right] h^{ij} \\ & + 2N \mathcal{S}^{ij} - \left(\frac{\partial}{\partial t} - \mathcal{L}_\beta \right) (L\beta)^{ij} + \frac{2}{3} \mathcal{D}_k \beta^k (L\beta)^{ij}. \end{aligned} \quad (1.85)$$

Note that the left-hand side of the above equation contains all the second-order derivatives (both in time and space) of h^{ij} , at the linear order. Actually the only second-order derivative of h^{ij} on the right-hand side is the non-linear term $h^{kl} \mathcal{D}_k \mathcal{D}_l h^{ij}$ contained in \mathcal{S}^{ij} via \tilde{R}_*^{ij} [cf. Eqs. (1.79) and (1.80)].

Let us rewrite Eq. (1.85) as a flat-space tensorial wave equation:

$$\square h^{ij} = \sigma^{ij} + (L\dot{\beta})^{ij}, \quad (1.86)$$

where \square denotes the d'Alembert operator associated with the flat metric \mathbf{f} [cf. Eq. (1.51)]:

$$\square := -\frac{\partial^2}{\partial t^2} + \Delta \quad (1.87)$$

and σ^{ij} is given by

$$\begin{aligned} \sigma^{ij} := & \left(1 - \frac{N^2}{\psi^4}\right) \Delta h^{ij} - 2\mathcal{L}\beta \frac{\partial h^{ij}}{\partial t} + \mathcal{L}\beta \mathcal{L}\beta h^{ij} - \mathcal{L}\dot{\beta} h^{ij} - \frac{4}{3} \mathcal{D}_k \beta^k \left(\frac{\partial}{\partial t} - \mathcal{L}\beta\right) h^{ij} \\ & + \frac{N}{\Psi^6} \mathcal{D}_k Q \left(\mathcal{D}^i h^{jk} + \mathcal{D}^j h^{ik} - \mathcal{D}^k h^{ij}\right) \\ & - \frac{1}{N} \left[\left(\frac{\partial}{\partial t} - \mathcal{L}\beta\right) N\right] \left[\left(\frac{\partial}{\partial t} - \mathcal{L}\beta\right) h^{ij} - \frac{2}{3} \mathcal{D}_k \beta^k h^{ij} + (L\beta)^{ij}\right] \\ & - \frac{2}{3} \left[\left(\frac{\partial}{\partial t} - \mathcal{L}\beta\right) \mathcal{D}_k \beta^k - \frac{2}{3} (\mathcal{D}_k \beta^k)^2\right] h^{ij} \\ & - 2N\mathcal{S}^{ij} - \mathcal{L}\beta (L\beta)^{ij} - \frac{2}{3} \mathcal{D}_k \beta^k (L\beta)^{ij}. \end{aligned} \quad (1.88)$$

Note that we have not included into σ^{ij} the term¹

$$\frac{\partial}{\partial t} (L\beta)^{ij} = (L\dot{\beta})^{ij} \quad (1.89)$$

which appears in the right-hand side of Eq. (1.85). Consequently this term appears explicitly in the right-hand side of Eq. (1.86).

At a given time step during the evolution, σ^{ij} is considered as a fixed source in Eq. (1.86), so that the problem is reduced to solving a flat space wave equation. Since \mathcal{D} and \square commute (thanks to the time-independence of \mathbf{f}), the source $\sigma^{ij} + (L\dot{\beta})^{ij}$ must be divergence-free in order for the solution h^{ij} of Eq. (1.86) to satisfy Dirac gauge (1.69). This means that one must have

$$\mathcal{D}_j (L\dot{\beta})^{ij} = -\mathcal{D}_j \sigma^{ij}, \quad (1.90)$$

or, from the definition (1.62) of the conformal Killing operator and the vanishing of \mathbf{f} 's Riemann tensor,

$$\Delta \dot{\beta}^i + \frac{1}{3} \mathcal{D}^i \left(\mathcal{D}_j \dot{\beta}^j\right) = -\mathcal{D}_j \sigma^{ij}. \quad (1.91)$$

The above elliptic equation fully determines $\dot{\beta}$ (up to some boundary conditions), and therefore, by direct time integration, β . This shows clearly that the shift vector propagates the Dirac spatial coordinates (x^i) from one slice Σ_t to the next one. Hence we recover the traditional interpretation of the shift vector. On the other side, β can be computed from the combination (1.74) of the momentum constraint and Dirac gauge condition. Both ways must yield the same result. However, from the numerical point of view, they may not be equivalent (due to numerical errors) and a strategy to compute the best value of β must be devised.

¹Eq. (1.89) holds thanks to the property (1.13).

Note that, since we reduce the time evolution problem to a second-order wave equation for h^{ij} , at each step, the extrinsic curvature term A^{ij} must be deduced from the time derivative of h^{ij} and the spatial derivatives of the shift vector by inverting Eq. (1.77):

$$A^{ij} = \frac{1}{2N} \left[(L\beta)^{ij} + \frac{\partial h^{ij}}{\partial t} - \mathcal{L}_\beta h^{ij} - \frac{2}{3} \mathcal{D}_k \beta^k h^{ij} \right]. \quad (1.92)$$

1.4.4 Transverse traceless decomposition

The generalized Dirac gauge, expressed as Eq. (1.69), makes the potential \mathbf{h} a transverse tensor field with respect to the metric \mathbf{f} . However, the trace of \mathbf{h} with respect to the metric \mathbf{f} ,

$$h := f_{ij} h^{ij}, \quad (1.93)$$

does not vanish in general, except in the linearized approximation. Therefore \mathbf{h} is not a transverse and traceless (TT) tensor field. Since this latter property would considerably help the treatment of the wave equation, we perform a TT decomposition of \mathbf{h} according to (see e.g. Sec. 7-4.2 of ADM [35])

$$h^{ij} =: \bar{h}^{ij} + \frac{1}{2} (h f^{ij} - \mathcal{D}^i \mathcal{D}^j \phi), \quad (1.94)$$

where ϕ is a solution of the Poisson equation

$$\Delta \phi = h \quad (1.95)$$

satisfying $\phi = 0$ at spatial infinity. Then the trace of the term $1/2 (h f^{ij} - \mathcal{D}^i \mathcal{D}^j \phi)$ on the right-hand side of Eq. (1.94) is equal to h . Moreover this term is divergence-free. We conclude that if \mathbf{h} is transverse (Dirac gauge), then $\bar{\mathbf{h}}$ defined by Eq. (1.94) is a TT tensor¹:

$$\mathcal{D}_j \bar{h}^{ij} = 0 \quad \text{and} \quad f_{ij} \bar{h}^{ij} = 0. \quad (1.96)$$

We then decompose Eq. (1.86) into a trace part, and a traceless one, to get

$$\square h = \sigma, \quad (1.97)$$

$$\square \bar{h}^{ij} = \bar{\sigma}^{ij} + (L\dot{\beta})^{ij}, \quad (1.98)$$

where $\sigma := f_{ij} \sigma^{ij}$ and $\bar{\sigma}^{ij}$ is the traceless part of σ^{ij} given by the decomposition analogous to (1.94):

$$\sigma^{ij} =: \bar{\sigma}^{ij} + \frac{1}{2} (\sigma f^{ij} - \mathcal{D}^i \mathcal{D}^j \Upsilon), \quad (1.99)$$

with $\Delta \Upsilon = \sigma$. Note that the quantity $(L\dot{\beta})^{ij}$ is trace-free by the very definition of operator L [Eq. (1.62)].

The search for the potentials h^{ij} can then proceed along the following steps: compute the trace σ of the effective source σ^{ij} [Eq. (1.88)] and solve the Poisson equation

$$\Delta \Upsilon = \sigma, \quad (1.100)$$

¹If we had removed the trace of \mathbf{h} in the “standard” way, by defining $\tilde{h}^{ij} := h^{ij} - \frac{1}{3} h f^{ij}$, the traceless part would not have been transverse.

with the boundary condition $\Upsilon = 0$ at spatial infinity. This leads to a regular solution for Υ because σ is a fast decaying source, due to the fact that Eq. (1.86) is the traceless part, with respect to the metric $\tilde{\gamma}$, of the dynamical Einstein equations and that $\tilde{\gamma} \sim \mathbf{f}$ asymptotically. The next step is to insert Υ and σ into Eq. (1.99) to compute $\bar{\sigma}^{ij}$. Then one has to solve the TT wave equation (1.98) for \bar{h}^{ij} . A resolution technique based on spherical coordinates and spherical tensor components will be presented in Sec. 1.5.3. Using this technique, the resolution of Eq. (1.98) is reduced to the resolution of two scalar d'Alembert equations. Then one may solve the scalar d'Alembert equation

$$\square\phi = \Upsilon \quad (1.101)$$

for ϕ and compute the trace h not by solving the d'Alembert equation (1.97) but directly as the Laplacian of ϕ [cf. Eq. (1.95)]. Inserting h and ϕ into Eq. (1.94) leads then to h^{ij} . An alternative approach to get h will be discussed in Sec. 1.5.4. It is algebraic [thus does not require to solve any d'Alembert equation like (1.97) or (1.101)] and has the advantage to enforce the condition on the determinant of $\tilde{\gamma}^{ij}$ [Eq. (1.19)].

1.5 A resolution scheme based on spherical coordinates

As discussed in Sec. 1.1.2, spherical coordinates have many advantages when treating neutron star or black hole spacetimes. Moreover, as we shall see below, the use of tensor components with respect to a spherical basis allow to compute three of the metric components $\tilde{\gamma}^{ij}$ directly from the Dirac gauge condition (1.68). In this section we therefore specialize the coordinates (x^i) on each hypersurface Σ_t to spherical ones. Moreover we expand all the tensor fields onto a spherical basis which is orthonormal with respect to the flat metric.

1.5.1 Spherical orthonormal basis

We introduce on Σ_t a coordinate system $x^i = (r, \theta, \varphi)$ of spherical type, i.e. r spans the range $[0, +\infty)$, θ the range $[0, \pi]$ (co-latitude angle), φ the range $[0, 2\pi)$ (azimuthal angle) and the components of the flat metric \mathbf{f} with respect to these coordinates are

$$f_{ij} = \text{diag}(1, r^2, r^2 \sin^2 \theta). \quad (1.102)$$

The determinant f [Eq. (1.18)] is then $f = r^4 \sin^2 \theta$.

From the natural vector basis associated with the coordinates (r, θ, φ) , $(\partial/\partial x^i) = (\partial/\partial r, \partial/\partial \theta, \partial/\partial \varphi)$, we construct the following vector fields:

$$\mathbf{e}_r := \frac{\partial}{\partial r}, \quad \mathbf{e}_\theta := \frac{1}{r} \frac{\partial}{\partial \theta}, \quad \mathbf{e}_\varphi := \frac{1}{r \sin \theta} \frac{\partial}{\partial \varphi}. \quad (1.103)$$

$(\mathbf{e}_{\hat{i}}) = (\mathbf{e}_r, \mathbf{e}_\theta, \mathbf{e}_\varphi)$ forms a basis of the vector space tangent to Σ_t . Moreover, this basis is orthonormal with respect to the flat metric \mathbf{f} : $f_{\hat{i}\hat{j}} = \text{diag}(1, 1, 1)$. Notice that we are denoting with a hat the generic indices \hat{i}, \hat{j}, \dots associated with this basis, but we denote by r, θ, φ (without a hat) indices of specific components on this basis.

Given a tensor field T of type $\binom{p}{q}$, the components of the covariant derivative $\mathcal{D}T$ in the orthonormal basis $e_{\hat{i}_1} \otimes \cdots \otimes e_{\hat{i}_p} \otimes \cdots \otimes e^{\hat{j}_1} \otimes \cdots \otimes e^{\hat{j}_q} \otimes e^{\hat{k}}$ are given by

$$\begin{aligned} \mathcal{D}_{\hat{k}} T_{\hat{j}_1 \dots \hat{j}_q}^{\hat{i}_1 \dots \hat{i}_p} &= e_{\hat{k}}^l \frac{\partial}{\partial x^l} T_{\hat{j}_1 \dots \hat{j}_q}^{\hat{i}_1 \dots \hat{i}_p} \\ &+ \sum_{r=1}^p \hat{\Gamma}_{\hat{l}\hat{k}}^{\hat{i}_r} T_{\hat{j}_1 \dots \hat{j}_q}^{\hat{i}_1 \dots \hat{l} \dots \hat{i}_p} \\ &- \sum_{r=1}^q \hat{\Gamma}_{\hat{j}_r \hat{k}}^{\hat{l}} T_{\hat{j}_1 \dots \hat{l} \dots \hat{j}_q}^{\hat{i}_1 \dots \hat{i}_p}, \end{aligned} \quad (1.104)$$

where $e_{\hat{k}}^l := \text{diag}(1, 1/r, 1/(r \sin \theta))$ is the change-of-basis matrix defined by Eq. (1.103), and the $\hat{\Gamma}_{\hat{i}\hat{j}}^{\hat{k}}$ are the connection coefficients of \mathcal{D} associated with the orthonormal frame $(e_{\hat{i}})$; these coefficients all vanish, except for

$$\begin{aligned} \hat{\Gamma}_{\theta\theta}^r &= -\hat{\Gamma}_{r\theta}^\theta = -r^{-1}, & \hat{\Gamma}_{\varphi\varphi}^r &= -\hat{\Gamma}_{r\varphi}^\varphi = -r^{-1}, \\ \hat{\Gamma}_{\varphi\varphi}^\theta &= -\hat{\Gamma}_{\theta\varphi}^\varphi = -(r \tan \theta)^{-1}. \end{aligned} \quad (1.105)$$

1.5.2 Resolution of elliptic equations

Scalar Poisson equations

We have to solve two scalar elliptic equations: the Hamiltonian constraint (combined with the trace of the dynamical Einstein equations) Eq. (1.71) for Q and the maximal slicing equation (1.76) for N . Both equations are not strictly Poisson equations since they contain Q and N on their right-hand side. Moreover the right-hand side of Eq. (1.71) is non-linear in Q (through $\Phi = (\ln N - \ln Q)/2$). Therefore these equations must be solved by iterations, solving for a Poisson equation at each step. Since we are using spherical coordinates, it is natural to perform an expansion on spherical harmonics $Y_\ell^m(\theta, \varphi)$. The resolution of the scalar Poisson equation is then reduced to the resolution of a system of second order ordinary differential equations in r for each couple (ℓ, m) . We refer the reader to Ref. [228] for further details.

Vector elliptic equation for the shift

As we have seen in Sec. 1.4.2, the Dirac gauge condition once inserted into the momentum constraint equation gives rise to the elliptic equation (1.74). Using the derivation formula (1.104) with the explicit values (1.105) of the connection coefficients, we obtain the following components of this equation with respect to the orthonormal frame $(e_{\hat{i}})$:

$$\frac{\partial^2 \beta^r}{\partial r^2} + \frac{2}{r} \frac{\partial \beta^r}{\partial r} + \frac{1}{r^2} \left(\Delta_{\theta\varphi} \beta^r - 2\beta^r - 2 \frac{\partial \beta^\theta}{\partial \theta} - 2 \frac{\beta^\theta}{\tan \theta} - \frac{2}{\sin \theta} \frac{\partial \beta^\varphi}{\partial \varphi} \right) + \frac{1}{3} \frac{\partial \theta}{\partial r} = S(\beta)^r \quad (1.106)$$

$$\frac{\partial^2 \beta^\theta}{\partial r^2} + \frac{2}{r} \frac{\partial \beta^\theta}{\partial r} + \frac{1}{r^2} \left(\Delta_{\theta\varphi} \beta^\theta + 2 \frac{\partial \beta^r}{\partial \theta} - \frac{\beta^\theta}{\sin^2 \theta} - 2 \frac{\cos \theta}{\sin^2 \theta} \frac{\partial \beta^\varphi}{\partial \varphi} \right) + \frac{1}{3r} \frac{\partial \theta}{\partial \theta} = S(\beta)^\theta \quad (1.107)$$

$$\begin{aligned} \frac{\partial^2 \beta^\varphi}{\partial r^2} + \frac{2}{r} \frac{\partial \beta^\varphi}{\partial r} + \frac{1}{r^2} \left(\Delta_{\theta\varphi} \beta^\varphi + \frac{2}{\sin \theta} \frac{\partial \beta^r}{\partial \varphi} + 2 \frac{\cos \theta}{\sin^2 \theta} \frac{\partial \beta^\theta}{\partial \varphi} - \frac{\beta^\varphi}{\sin^2 \theta} \right) + \frac{1}{3r \sin \theta} \frac{\partial \theta}{\partial \varphi} \\ = S(\beta)^\varphi, \end{aligned} \quad (1.108)$$

where $\Delta_{\theta\varphi}$ denotes the angular Laplacian:

$$\Delta_{\theta\varphi} := \frac{\partial^2}{\partial\theta^2} + \frac{1}{\tan\theta} \frac{\partial}{\partial\theta} + \frac{1}{\sin^2\theta} \frac{\partial^2}{\partial\varphi^2}, \quad (1.109)$$

$S(\boldsymbol{\beta})^{\hat{i}}$ stands for the right-hand side of Eq. (1.74) and $\theta := \mathcal{D}_k \beta^k$ is the divergence of $\boldsymbol{\beta}$ with respect to the flat connection \mathcal{D} . In terms of the components with respect to the orthonormal frame (\mathbf{e}_i), it reads

$$\theta = \frac{\partial\beta^r}{\partial r} + \frac{2\beta^r}{r} + \frac{1}{r} \left(\frac{\partial\beta^\theta}{\partial\theta} + \frac{\beta^\theta}{\tan\theta} + \frac{1}{\sin\theta} \frac{\partial\beta^\varphi}{\partial\varphi} \right). \quad (1.110)$$

As for the scalar elliptic equations for Q and N discussed above, the right-hand side $S(\boldsymbol{\beta})^{\hat{i}}$ of Eqs. (1.106)-(1.108) depend (linearly) on $\boldsymbol{\beta}$, both explicitly and via A^{ij} [see Eqs. (1.74) and (1.92)]. Thus an iterative resolution must be contemplated.

Equations (1.106)-(1.108) constitute a coupled system, since each equation contains all the components of $\boldsymbol{\beta}$. However, we can decouple the system by proceedings as follows. First, taking the (flat) divergence of this vector system, and taking into account that \mathcal{D} and Δ commute (flat metric), we get a scalar Poisson equation for θ only:

$$\Delta\theta = \frac{3}{4} \mathcal{D}_{\hat{k}} S(\boldsymbol{\beta})^{\hat{k}}. \quad (1.111)$$

Assuming this equation is solved for θ , we use Eq. (1.110) to replace the terms containing angular components in Eq. (1.106) to get a decoupled equation for β^r :

$$\begin{aligned} \frac{\partial^2\beta^r}{\partial r^2} + \frac{4}{r} \frac{\partial\beta^r}{\partial r} + \frac{2\beta^r}{r^2} + \frac{1}{r^2} \Delta_{\theta\varphi} \beta^r = \\ S(\boldsymbol{\beta})^r - \frac{1}{3} \frac{\partial\theta}{\partial r} + \frac{2}{r} \theta. \end{aligned} \quad (1.112)$$

This equation can be solved by expanding β^r in spherical harmonics. An alternative approach is to set

$$\chi := r\beta^r \quad (1.113)$$

which reduces Eq. (1.112) to an ordinary Poisson equation:

$$\Delta\chi = rS(\boldsymbol{\beta})^r - \frac{r}{3} \frac{\partial\theta}{\partial r} + 2\theta. \quad (1.114)$$

This is not surprising since χ is actually a scalar field on Σ_t : $\chi = f_{ij} r^i \beta^j$, where \mathbf{r} denotes the ‘‘position’’ vector field:

$$\mathbf{r} := r \mathbf{e}_r = x \mathbf{e}_x + y \mathbf{e}_y + z \mathbf{e}_z, \quad (1.115)$$

(x, y, z) and $(\mathbf{e}_x, \mathbf{e}_y, \mathbf{e}_z)$ being respectively the Cartesian coordinates and Cartesian frame canonically associated with the spherical coordinates (r, θ, φ) . Indeed, contrary to \mathbf{e}_r , which is singular at the origin $r = 0$, \mathbf{r} is a regular¹ vector field [this is obvious from the second equality in Eq. (1.115)]. Being the scalar product of $\boldsymbol{\beta}$ and \mathbf{r} (with respect to \mathbf{f}), χ is then a regular scalar.

¹As in Ref. [47], we define a *regular* tensor field as a tensor field whose components with respect to the Cartesian frame $(\mathbf{e}_x, \mathbf{e}_y, \mathbf{e}_z)$ are expandable in power series of x, y and z .

Let us now discuss the resolution of the angular part. We introduce a poloidal potential η and a toroidal potential μ such that $\boldsymbol{\beta}$ is expanded as (see also § 13.1 of Ref. [323] and § A.2.a of Ref. [478]):

$$\boldsymbol{\beta} = \beta^r \mathbf{e}_r + [r\mathcal{D}\eta - (\mathbf{e}_r \cdot \mathcal{D}\eta) \mathbf{r}] + \mathbf{r} \times \mathcal{D}\mu, \quad (1.116)$$

where the scalar product and the vectorial product are taken with respect to the flat metric \mathbf{f} . Note that the terms containing η and μ are by construction tangent to the sphere $r = \text{const}$ and that $\mathbf{r} \times \mathcal{D}\mu$ is nothing but the angular momentum operator of Quantum Mechanics applied to μ . An alternative expression is $\mathbf{r} \times \mathcal{D}\mu = -\mathcal{D} \times (\mu \mathbf{r})$. In term of components, Eq. (1.116) results in

$$\beta^\theta = \frac{\partial \eta}{\partial \theta} - \frac{1}{\sin \theta} \frac{\partial \mu}{\partial \varphi} \quad (1.117)$$

$$\beta^\varphi = \frac{1}{\sin \theta} \frac{\partial \eta}{\partial \varphi} + \frac{\partial \mu}{\partial \theta}. \quad (1.118)$$

It can be shown easily that the potentials η and μ obey to the following relations:

$$\Delta_{\theta\varphi} \eta = r\theta - r \frac{\partial \beta^r}{\partial r} - 2\beta^r \quad (1.119)$$

$$\begin{aligned} \Delta_{\theta\varphi} \mu &= \mathbf{r} \cdot (\mathcal{D} \times \boldsymbol{\beta}) \\ &= \frac{\partial \beta^\varphi}{\partial \theta} + \frac{\beta^\varphi}{\tan \theta} - \frac{1}{\sin \theta} \frac{\partial \beta^\theta}{\partial \varphi}. \end{aligned} \quad (1.120)$$

These formulas show that η and μ are uniquely defined (up to the addition of some function of r). θ , $\beta^r = \chi/r$ and the scalar $\mathbf{r} \cdot (\mathcal{D} \times \boldsymbol{\beta})$ being expandable in (scalar) spherical harmonics, Eqs. (1.119) and (1.120) show also that η and μ are expandable in spherical harmonics $Y_\ell^m(\theta, \varphi)$. The computation of η and μ from the components $(\beta^r, \beta^\theta, \beta^\varphi)$ can then be performed from Eqs. (1.119)-(1.120) by a mere division by $-\ell(\ell + 1)$ (eigenvalue of the operator $\Delta_{\theta\varphi}$ corresponding to the eigenfunction $Y_\ell^m(\theta, \varphi)$). In the following we call this type of computation a *quasi-algebraic* one.

By a straightforward computation, it can be shown that the part (1.107)-(1.108) of the original system is equivalent to the two Poisson equations

$$\Delta \eta = \eta_S - \frac{2\beta^r}{r^2} - \frac{1}{3} \frac{\theta}{r} \quad (1.121)$$

$$\Delta \mu = \mu_S, \quad (1.122)$$

where η_S and μ_S are the poloidal and toroidal potentials of the source $\mathcal{S}(\boldsymbol{\beta})$ [they can thus be determined from $\mathcal{S}(\boldsymbol{\beta})$ by formulas (1.119)-(1.120) with β^i replaced by $\mathcal{S}(\boldsymbol{\beta})^i$].

Having reduced the complicated coupled PDE system (1.106)-(1.108) to Poisson type equations (1.111), (1.112), (1.114), (1.121) and (1.122), various strategies can be devised to get the solution. In all of them, we take advantage of the fact that the Poisson equation (1.122) for the toroidal part is fully decoupled from the others to solve it first and hence get μ . Similarly the Poisson equation (1.111) for the divergence is decoupled from the other equations. So we can solve it to get θ . Then we plug θ on the right-hand side of Eq. (1.112) and solve it to get β^r . An alternative approach is to solve the Poisson equation (1.114) for χ and obtain β^r as χ/r . Then we have the following options: (i) deduce η from Eq. (1.119); (ii) solve the Poisson equation (1.121) to get η . Method (ii) requires to solve an additional Poisson equation, while method (i) requires only a division by $-\ell(\ell + 1)$ of the coefficients of spherical harmonics expansions, making a total of three scalar Poisson equations to solve the system. However method (i) involves the radial derivative of β^r which may result in a low order of differentiability of the numerical solution.

1.5.3 Resolution of the tensor wave equation

Spherical components

By means of the derivation formula (1.104) with the explicit values (1.105) of the connection coefficients, the tensor wave equation (1.98) can be written explicitly in terms of the components $\bar{h}^{\hat{i}\hat{j}}$ of the TT part of \mathbf{h} with respect to the orthonormal spherical basis:

$$-\frac{\partial^2 \bar{h}^{rr}}{\partial t^2} + \frac{\partial^2 \bar{h}^{rr}}{\partial r^2} + \frac{2}{r} \frac{\partial \bar{h}^{rr}}{\partial r} + \frac{1}{r^2} \left[\Delta_{\theta\varphi} \bar{h}^{rr} - 4\bar{h}^{rr} - 4 \frac{\partial \bar{h}^{r\theta}}{\partial \theta} - \frac{4\bar{h}^{r\theta}}{\tan \theta} - \frac{4}{\sin \theta} \frac{\partial \bar{h}^{r\varphi}}{\partial \varphi} + 2\bar{h}^{\theta\theta} + 2\bar{h}^{\varphi\varphi} \right] = \bar{S}^{rr}, \quad (1.123)$$

$$-\frac{\partial^2 \bar{h}^{r\theta}}{\partial t^2} + \frac{\partial^2 \bar{h}^{r\theta}}{\partial r^2} + \frac{2}{r} \frac{\partial \bar{h}^{r\theta}}{\partial r} + \frac{1}{r^2} \left[\Delta_{\theta\varphi} \bar{h}^{r\theta} - \left(4 + \frac{1}{\sin^2 \theta} \right) \bar{h}^{r\theta} + 2 \frac{\partial \bar{h}^{rr}}{\partial \theta} - 2 \frac{\partial \bar{h}^{\theta\theta}}{\partial \theta} - 2 \frac{\cos \theta}{\sin^2 \theta} \frac{\partial \bar{h}^{r\varphi}}{\partial \varphi} - \frac{2\bar{h}^{\theta\theta}}{\tan \theta} - \frac{2}{\sin \theta} \frac{\partial \bar{h}^{\theta\varphi}}{\partial \varphi} + \frac{2\bar{h}^{\varphi\varphi}}{\tan \theta} \right] = \bar{S}^{r\theta}, \quad (1.124)$$

$$-\frac{\partial^2 \bar{h}^{r\varphi}}{\partial t^2} + \frac{\partial^2 \bar{h}^{r\varphi}}{\partial r^2} + \frac{2}{r} \frac{\partial \bar{h}^{r\varphi}}{\partial r} + \frac{1}{r^2} \left[\Delta_{\theta\varphi} \bar{h}^{r\varphi} - \left(5 + \frac{1}{\tan^2 \theta} \right) \bar{h}^{r\varphi} + \frac{2}{\sin \theta} \frac{\partial \bar{h}^{rr}}{\partial \varphi} + 2 \frac{\cos \theta}{\sin^2 \theta} \frac{\partial \bar{h}^{r\theta}}{\partial \varphi} - 2 \frac{\partial \bar{h}^{\theta\varphi}}{\partial \theta} - \frac{2}{\sin \theta} \frac{\partial \bar{h}^{\varphi\varphi}}{\partial \varphi} - \frac{4\bar{h}^{\theta\varphi}}{\tan \theta} \right] = \bar{S}^{r\varphi}, \quad (1.125)$$

$$-\frac{\partial^2 \bar{h}^{\theta\theta}}{\partial t^2} + \frac{\partial^2 \bar{h}^{\theta\theta}}{\partial r^2} + \frac{2}{r} \frac{\partial \bar{h}^{\theta\theta}}{\partial r} + \frac{1}{r^2} \left[\Delta_{\theta\varphi} \bar{h}^{\theta\theta} - \frac{2\bar{h}^{\theta\theta}}{\sin^2 \theta} + 4 \frac{\partial \bar{h}^{r\theta}}{\partial \theta} - 4 \frac{\cos \theta}{\sin^2 \theta} \frac{\partial \bar{h}^{\theta\varphi}}{\partial \varphi} + 2\bar{h}^{rr} + \frac{2\bar{h}^{\varphi\varphi}}{\tan^2 \theta} \right] = \bar{S}^{\theta\theta}, \quad (1.126)$$

$$-\frac{\partial^2 \bar{h}^{\theta\varphi}}{\partial t^2} + \frac{\partial^2 \bar{h}^{\theta\varphi}}{\partial r^2} + \frac{2}{r} \frac{\partial \bar{h}^{\theta\varphi}}{\partial r} + \frac{1}{r^2} \left[\Delta_{\theta\varphi} \bar{h}^{\theta\varphi} - 2 \left(1 + \frac{2}{\tan^2 \theta} \right) \bar{h}^{\theta\varphi} + \frac{2}{\sin \theta} \frac{\partial \bar{h}^{r\theta}}{\partial \varphi} + 2 \frac{\partial \bar{h}^{r\varphi}}{\partial \theta} + 2 \frac{\cos \theta}{\sin^2 \theta} \left(\frac{\partial \bar{h}^{\theta\theta}}{\partial \varphi} - \frac{\partial \bar{h}^{\varphi\varphi}}{\partial \varphi} \right) - \frac{2\bar{h}^{r\varphi}}{\tan \theta} \right] = \bar{S}^{\theta\varphi}, \quad (1.127)$$

$$-\frac{\partial^2 \bar{h}^{\varphi\varphi}}{\partial t^2} + \frac{\partial^2 \bar{h}^{\varphi\varphi}}{\partial r^2} + \frac{2}{r} \frac{\partial \bar{h}^{\varphi\varphi}}{\partial r} + \frac{1}{r^2} \left[\Delta_{\theta\varphi} \bar{h}^{\varphi\varphi} - \frac{2\bar{h}^{\varphi\varphi}}{\sin^2 \theta} + \frac{4}{\sin \theta} \frac{\partial \bar{h}^{r\varphi}}{\partial \varphi} + 4 \frac{\cos \theta}{\sin^2 \theta} \frac{\partial \bar{h}^{\theta\varphi}}{\partial \varphi} + 2\bar{h}^{rr} + \frac{2\bar{h}^{\theta\theta}}{\tan^2 \theta} + \frac{4\bar{h}^{r\theta}}{\tan \theta} \right] = \bar{S}^{\varphi\varphi}, \quad (1.128)$$

where $\bar{S}^{\hat{i}\hat{j}}$ denotes the right-hand side of Eq. (1.98) : $\bar{S}^{\hat{i}\hat{j}} := \bar{\sigma}^{\hat{i}\hat{j}} + (L\dot{\beta})^{\hat{i}\hat{j}}$. These equations must be supplemented by the TT conditions [Eq. (1.96)], which read, in term of components with respect to

(e_i) ,

$$\frac{\partial \bar{h}^{rr}}{\partial r} + \frac{2\bar{h}^{rr}}{r} + \frac{1}{r} \left[\frac{\partial \bar{h}^{r\theta}}{\partial \theta} + \frac{1}{\sin \theta} \frac{\partial \bar{h}^{r\varphi}}{\partial \varphi} - \bar{h}^{\theta\theta} - \bar{h}^{\varphi\varphi} + \frac{\bar{h}^{r\theta}}{\tan \theta} \right] = 0 \quad (1.129)$$

$$\frac{\partial \bar{h}^{r\theta}}{\partial r} + \frac{3\bar{h}^{r\theta}}{r} + \frac{1}{r} \left[\frac{\partial \bar{h}^{\theta\theta}}{\partial \theta} + \frac{1}{\sin \theta} \frac{\partial \bar{h}^{\theta\varphi}}{\partial \varphi} + \frac{1}{\tan \theta} (\bar{h}^{\theta\theta} - \bar{h}^{\varphi\varphi}) \right] = 0 \quad (1.130)$$

$$\frac{\partial \bar{h}^{r\varphi}}{\partial r} + \frac{3\bar{h}^{r\varphi}}{r} + \frac{1}{r} \left[\frac{\partial \bar{h}^{\theta\varphi}}{\partial \theta} + \frac{1}{\sin \theta} \frac{\partial \bar{h}^{\varphi\varphi}}{\partial \varphi} + \frac{2\bar{h}^{\theta\varphi}}{\tan \theta} \right] = 0, \quad (1.131)$$

$$\bar{h}^{rr} + \bar{h}^{\theta\theta} + \bar{h}^{\varphi\varphi} = 0. \quad (1.132)$$

As discussed in Sec. 1.4.4, the TT conditions and the \square operator commute, so provided that the source \bar{S} is TT, the solution \bar{h} will also be TT.

For the steady state case ($\partial/\partial t = 0$) or for an implicit time scheme¹, we need to invert the full operator on the left hand side of the system (1.123)-(1.128). One immediately notices that this system couples all the components $h^{\hat{i}\hat{j}}$.

A natural idea to solve the system (1.123)-(1.128) would be to expand \bar{h} onto a a basis of *tensor* spherical harmonics. Notice that, contrarily to *scalar* spherical harmonics, there are several types of tensor ones (for a review, see [464]). A first family has been introduced by Mathews [313] and Zerilli [498]; they are called *pure orbital* harmonics in [464] and are eigenvectors of the angular Laplacian (1.109) acting on tensors. A second family is made of *pure spin* harmonics [384, 498] which are very well suited for describing gravitational radiation in the radiation zone (where one supposes that the wave vector is parallel to the radial direction). However, it should be realized that all families of tensor spherical harmonics are based on a longitudinal/transverse decomposition with a notion of *transversality* different from the one used here: in our acceptance, *transverse* means *divergence-free* [Eqs. (1.69) and (1.96)], whereas in tensor spherical harmonics literature, *transverse* means *orthogonal with respect to the radial vector e_r* . Asymptotically both notions coincide, but this is not the case at finite r . From the very definition of Dirac gauge [Eqs. (1.69)], it is clear that the notion of transversality relevant to our problem is the divergence-free one. As shown by Mathews [313] and explicated in the quadrupolar case by Teukolsky [460], it is possible a form linear combinations of tensor spherical harmonics which are divergence-free. We propose here a different route, which is actually simpler. We do not perform any expansion onto the tensor spherical harmonics, but use directly the traceless and divergence-free properties to reduce the tensor wave equation to two scalar wave equations, reflecting the two degree of freedoms of a TT symmetric tensor.

Before presenting this method, let us comment upon another tentative of decoupling the system (1.123)-(1.128) that one might naively contemplate. It would consist in solving separately each equation (1.123),..., (1.128) by treating as source the terms with $\bar{h}^{\hat{k}\hat{l}}$ ($k \neq i$ or $l \neq j$) so that only an operator acting on the component $\bar{h}^{\hat{i}\hat{j}}$ would appear on the left-hand side. Of course, since the other components of \bar{h} would be present on the right-hand side, such a method would require some iteration. However this method is not applicable, due to the bad behavior of the truncated operator (i.e. the operator which acts only on $\bar{h}^{\hat{i}\hat{j}}$ in the component $\hat{i}\hat{j}$): for a regular source, it gives a non-regular solution. Take for instance Eq. (1.123) in the stationary case ($\partial/\partial t = 0$): the operator acting on \bar{h}^{rr}

¹With Chebyshev spectral methods, the accumulation of collocation points near the boundaries implies a very severe Courant-Friedrich-Levy condition and in practice prohibits explicit schemes.

is

$$\mathcal{O}\bar{h}^{rr} := \frac{\partial^2 \bar{h}^{rr}}{\partial r^2} + \frac{2}{r} \frac{\partial \bar{h}^{rr}}{\partial r} + \frac{1}{r^2} (\Delta_{\theta\varphi} \bar{h}^{rr} - 4\bar{h}^{rr}). \quad (1.133)$$

Now $\bar{h}^{rr} = \chi/r^2$, where $\chi = f_{ik} f_{jl} \bar{h}^{ij} r^k r^l$ is a regular scalar field on Σ_t [see Eq. (1.142) below]. \bar{h}^{rr} is therefore expandable in scalar spherical harmonics $Y_\ell^m(\theta, \varphi)$. For a given (ℓ, m) , the behavior of \bar{h}^{rr} near the origin $r = 0$ must therefore be

$$\bar{h}^{rr} \sim r^n Y_\ell^m(\theta, \varphi), \quad (1.134)$$

where n is some positive integer, in order for \bar{h}^{rr} to be regular. Inserting this expression into Eq. (1.133) results in

$$\mathcal{O}\bar{h}^{rr} = [n(n-1) + 2n - \ell(\ell+1) - 4] r^{n-2} Y_\ell^m(\theta, \varphi). \quad (1.135)$$

Thus we get a regular solution of the homogeneous equation $\mathcal{O}\bar{h}^{rr} = 0$ near $r = 0$ only if, for any ℓ , there exists a strictly positive integer n such that $n^2 + n - \ell(\ell+1) - 4 = 0$. However in general, this last equation does not admit any integer solution n . The generalization to the time-dependent case is straightforward. Moreover, even if $r = 0$ is excluded from the computational domain (for example when treating black holes), a similar regularity problem appears in the other equations on the axis $\theta = 0$ or π .

Reduction to two scalar wave equations

As mentioned above, it is possible to use the four TT conditions (1.129)-(1.132) to decouple the system (1.123)-(1.128) and to reduce it to the resolution of two scalar wave equations.

A first way to proceed is to manipulate directly equations (1.123)-(1.132). For instance, inserting the first divergence-free condition (1.129) into (1.123) and using the traceless condition (1.132) results in the disappearing of the terms involving $\bar{h}^{r\theta}$, $\bar{h}^{r\varphi}$, $\bar{h}^{\theta\theta}$ and $\bar{h}^{\varphi\varphi}$:

$$-\frac{\partial^2 \bar{h}^{rr}}{\partial t^2} + \frac{\partial^2 \bar{h}^{rr}}{\partial r^2} + \frac{6}{r} \frac{\partial \bar{h}^{rr}}{\partial r} + \frac{1}{r^2} (\Delta_{\theta\varphi} \bar{h}^{rr} + 6\bar{h}^{rr}) = \bar{S}^{rr}. \quad (1.136)$$

To perform a more systematic treatment, as well as to gain some insight, it is worth to introduce the scalar product (with respect to \mathbf{f}) of $\bar{\mathbf{h}}$ with the position vector \mathbf{r} defined by Eq. (1.115):

$$V^i := f_{kl} \bar{h}^{ik} r^l, \quad (1.137)$$

or, in term of components,

$$V^{\hat{i}} = (r\bar{h}^{rr}, r\bar{h}^{r\theta}, r\bar{h}^{r\varphi}). \quad (1.138)$$

Note that the vector field \mathbf{V} thus defined is regular (for \mathbf{f} , $\bar{\mathbf{h}}$ and \mathbf{r} are regular tensor fields on Σ_t). From the identities $\square V^i = f_{kl} r^l \square \bar{h}^{ik} + 2\mathcal{D}_k \bar{h}^{ik}$ and $\mathcal{D}_i V^i = f_{kl} r^l \mathcal{D}_i \bar{h}^{ik} + f_{ij} \bar{h}^{ij}$ and the TT character of $\bar{\mathbf{h}}$, we deduce immediately that the $(rr, r\theta, r\varphi)$ part of the system (1.123)-(1.128) with the TT conditions (1.129)-(1.132) is equivalent to the vector wave equation

$$\square V^i = f_{kl} \bar{S}^{ik} r^l \quad \text{with} \quad \mathcal{D}_i V^i = 0. \quad (1.139)$$

Let us introduce the (regular) scalar field χ ¹ as the scalar product (with respect to \mathbf{f}) of \mathbf{r} and \mathbf{V} ,

$$\chi := f_{kl} r^k V^l = r V^r = r^2 \bar{h}^{rr}. \quad (1.140)$$

¹we use the same notation χ as for the decomposition of the shift vector in Sec. 1.5.2, assuming that no confusion may arise.

From the identity $\square\chi = f_{kl}r^k\square V^l + 2\mathcal{D}_kV^k$ and the divergence-free character of \mathbf{V} , we see that Eq. (1.139) implies the following scalar wave equation

$$\square\chi = r^2\bar{S}^{rr}. \quad (1.141)$$

Solving this equation immediately provides \bar{h}^{rr} by

$$\bar{h}^{rr} = \frac{\chi}{r^2}. \quad (1.142)$$

Note that inserting this last relation into Eq. (1.136) would have lead directly to Eq. (1.141).

We then proceed as for the vector Poisson equation treated in Sec. 1.5.2, namely we perform the radial/angular decomposition of \mathbf{V} following Eq. (1.116)¹:

$$\mathbf{V} = V^r\mathbf{e}_r + [r\mathcal{D}\eta - (\mathbf{e}_r \cdot \mathcal{D}\eta)\mathbf{r}] + \mathbf{r} \times \mathcal{D}\mu. \quad (1.143)$$

Combining the above equation with Eq. (1.138), we see that the potentials η and μ are related to the components $\bar{h}^{r\theta}$ and $\bar{h}^{\theta\theta}$ by

$$\bar{h}^{r\theta} = \frac{1}{r} \left(\frac{\partial\eta}{\partial\theta} - \frac{1}{\sin\theta} \frac{\partial\mu}{\partial\varphi} \right) \quad (1.144)$$

$$\bar{h}^{r\varphi} = \frac{1}{r} \left(\frac{1}{\sin\theta} \frac{\partial\eta}{\partial\varphi} + \frac{\partial\mu}{\partial\theta} \right). \quad (1.145)$$

Performing the same decomposition of the source, we get:

$$\bar{S}^{r\theta} = \frac{1}{r} \left(\frac{\partial\eta_{\bar{S}}}{\partial\theta} - \frac{1}{\sin\theta} \frac{\partial\mu_{\bar{S}}}{\partial\varphi} \right), \quad (1.146)$$

$$\bar{S}^{r\varphi} = \frac{1}{r} \left(\frac{1}{\sin\theta} \frac{\partial\eta_{\bar{S}}}{\partial\varphi} + \frac{\partial\mu_{\bar{S}}}{\partial\theta} \right). \quad (1.147)$$

Given $\bar{S}^{r\theta}$ and $\bar{S}^{r\varphi}$, $\eta_{\bar{S}}$ and $\mu_{\bar{S}}$ are computed from the analog of Eqs. (1.119)-(1.120) by

$$\Delta_{\theta\varphi}\eta_{\bar{S}} = r \left(\frac{\partial\bar{S}^{r\theta}}{\partial\theta} + \frac{\bar{S}^{r\theta}}{\tan\theta} + \frac{1}{\sin\theta} \frac{\partial\bar{S}^{r\varphi}}{\partial\varphi} \right) \quad (1.148)$$

$$\Delta_{\theta\varphi}\mu_{\bar{S}} = r \left(\frac{\partial\bar{S}^{r\varphi}}{\partial\theta} + \frac{\bar{S}^{r\varphi}}{\tan\theta} - \frac{1}{\sin\theta} \frac{\partial\bar{S}^{r\theta}}{\partial\varphi} \right). \quad (1.149)$$

As already discussed in Sec. 1.5.2, the potentials $\eta_{\bar{S}}$ and $\mu_{\bar{S}}$ are expandable in scalar spherical harmonics $Y_\ell^m(\theta, \varphi)$. Equations (1.148)-(1.149) are then algebraic ($\Delta_{\theta\varphi}u \rightarrow -\ell(\ell+1)u$) in terms of the coefficients of the spherical harmonics expansion.

The angular part of the vector wave equation (1.139) is equivalent to the following system, analogous to Eqs. (1.121)-(1.122) with $\theta = 0$ (since \mathbf{V} is divergence-free) and $V^r = r\bar{h}^{rr}$:

$$\square\eta = \eta_{\bar{S}} - \frac{2\bar{h}^{rr}}{r}, \quad (1.150)$$

$$\square\mu = \mu_{\bar{S}}. \quad (1.151)$$

¹again, we use the same notation η and μ as for the decomposition of β presented in Sec. 1.5.2, assuming that no confusion may arise.

We can see here that the equation for μ is fully decoupled from the other equations, contrarily to that for η which contains \bar{h}^{rr} . Actually the divergence-free condition $\mathcal{D}_i V^i = 0$ relates η to \bar{h}^{rr} by Eq. (1.119) (with $V^r = r\bar{h}^{rr} = \chi/r$):

$$\Delta_{\theta\varphi}\eta = -r \left(r \frac{\partial \bar{h}^{rr}}{\partial r} + 3\bar{h}^{rr} \right) = -\frac{\partial \chi}{\partial r} - \frac{\chi}{r}. \quad (1.152)$$

This last equation can be used to compute η , once \bar{h}^{rr} has been obtained as the solution of (1.136) [or from the system (1.141)-(1.142)], instead of solving the wave equation (1.150).

At this stage, there remains to compute the angular components $\bar{h}^{\theta\theta}$, $\bar{h}^{\theta\varphi}$ and $\bar{h}^{\varphi\varphi}$. They can be deduced fully from the other components, by means of the TT relations (1.130)-(1.132). Indeed, using the traceless condition (1.132), the transverse conditions (1.130) and (1.131) can be written as

$$\frac{\partial}{\partial \theta}(\sin^2 \theta \bar{h}^{\varphi\varphi}) - \frac{1}{\sin \theta} \frac{\partial}{\partial \varphi}(\sin^2 \theta \bar{h}^{\theta\varphi}) = T^\theta, \quad (1.153)$$

$$\frac{1}{\sin \theta} \frac{\partial}{\partial \varphi}(\sin^2 \theta \bar{h}^{\varphi\varphi}) + \frac{\partial}{\partial \theta}(\sin^2 \theta \bar{h}^{\theta\varphi}) = T^\varphi, \quad (1.154)$$

with

$$T^\theta := \sin^2 \theta \left(r \frac{\partial \bar{h}^{r\theta}}{\partial r} + 3\bar{h}^{r\theta} - \frac{\partial \bar{h}^{rr}}{\partial \theta} - \frac{\bar{h}^{rr}}{\tan \theta} \right), \quad (1.155)$$

$$T^\varphi := -\sin^2 \theta \left(r \frac{\partial \bar{h}^{r\varphi}}{\partial r} + 3\bar{h}^{r\varphi} \right). \quad (1.156)$$

Taking the angular divergence and the angular curl of Eqs. (1.153)-(1.154), as in Eqs. (1.148)-(1.149), we get the system

$$\Delta_{\theta\varphi}(\sin^2 \theta \bar{h}^{\varphi\varphi}) = \frac{\partial T^\theta}{\partial \theta} + \frac{T^\theta}{\tan \theta} + \frac{1}{\sin \theta} \frac{\partial T^\varphi}{\partial \varphi} \quad (1.157)$$

$$\Delta_{\theta\varphi}(\sin^2 \theta \bar{h}^{\theta\varphi}) = \frac{\partial T^\varphi}{\partial \theta} + \frac{T^\varphi}{\tan \theta} - \frac{1}{\sin \theta} \frac{\partial T^\theta}{\partial \varphi}. \quad (1.158)$$

Again, this system is algebraic in the spherical harmonics representation, and therefore can be easily solved to get $\sin^2 \theta \bar{h}^{\varphi\varphi}$ and $\sin^2 \theta \bar{h}^{\theta\varphi}$, after T^θ and T^φ have been evaluated by means of Eqs. (1.155)-(1.156). The components $\bar{h}^{\varphi\varphi}$ and $\bar{h}^{\theta\varphi}$ are then obtained by a division by $\sin^2 \theta$. Finally $\bar{h}^{\theta\theta}$ is obtained by the traceless condition (1.132):

$$\bar{h}^{\theta\theta} = -\bar{h}^{\varphi\varphi} - \bar{h}^{rr}. \quad (1.159)$$

In conclusion we propose to solve the tensor wave equation (1.98) by solving two scalar wave equations: for χ [Eq. (1.141)] and for μ [Eq. (1.151)]. \bar{h}^{rr} is then obtained by dividing χ by r^2 [Eq. (1.142)]. η is obtained from χ by the quasi-algebraic equation (1.152). From μ and η , we compute $\bar{h}^{r\theta}$ and $\bar{h}^{r\varphi}$ from Eqs. (1.144)-(1.145). Then solving the quasi-algebraic equations (1.157) and (1.158) gives $\bar{h}^{\varphi\varphi}$ and $\bar{h}^{\theta\varphi}$. Finally $\bar{h}^{\theta\theta}$ is computed by the traceless condition (1.159). The advantage of this procedure consists in solving only for two scalar wave equations which are linearly decoupled. This guarantees numerical stability, at least in the linear case.

Asymptotic behavior

Providing that the source \bar{S}^{ij} is decaying sufficiently fast, the general asymptotic outgoing solutions of the two scalar wave equations to be solved, Eqs. (1.141) and (1.151), have the form

$$\chi \sim \frac{1}{r} \mathcal{F}_\chi(t - r, \theta, \varphi) \quad \text{and} \quad \mu \sim \frac{1}{r} \mathcal{F}_\mu(t - r, \theta, \varphi), \quad (1.160)$$

where \mathcal{F}_χ and \mathcal{F}_μ are two bounded functions. From Eq. (1.152), we then get the following asymptotic behavior for the potential η :

$$\eta \sim \frac{1}{r} \mathcal{F}_\eta(t - r, \theta, \varphi), \quad (1.161)$$

where \mathcal{F}_η is a bounded function. The asymptotic behavior of the components \bar{h}^{rr} , $\bar{h}^{r\theta}$ and $\bar{h}^{r\varphi}$ follow immediately from Eqs. (1.142), (1.144) and (1.145):

$$\bar{h}^{rr} \sim \frac{1}{r^3} \mathcal{F}_\chi(t - r, \theta, \varphi), \quad (1.162)$$

$$\bar{h}^{r\theta} \sim \frac{1}{r^2} \mathcal{F}_1(t - r, \theta, \varphi), \quad (1.163)$$

$$\bar{h}^{r\varphi} \sim \frac{1}{r^2} \mathcal{F}_2(t - r, \theta, \varphi), \quad (1.164)$$

where \mathcal{F}_1 and \mathcal{F}_2 are two bounded functions. This faster than $O(1/r)$ decay shows that the $(\bar{h}^{rr}, \bar{h}^{r\theta}, \bar{h}^{r\varphi})$ part of $\bar{\mathbf{h}}$ does not transport any wave, as expected (cf. the asymptotic TT structure of Dirac gauge discussed in Sec. 1.4.1).

Thanks to the terms $r\partial\bar{h}^{r\theta}/\partial r$ and $r\partial\bar{h}^{r\varphi}/\partial r$ in Eqs. (1.155)-(1.156), it can be shown easily that the asymptotic behavior of $\bar{h}^{\theta\varphi}$ and $\bar{h}^{\varphi\varphi}$ deduced from Eqs. (1.162)-(1.164) are

$$\bar{h}^{\varphi\varphi} \sim -\frac{1}{r} h_+(t - r, \theta, \varphi) \quad \text{and} \quad \bar{h}^{\theta\varphi} \sim \frac{1}{r} h_\times(t - r, \theta, \varphi), \quad (1.165)$$

where h_+ and h_\times are two bounded functions. From Eqs. (1.159), (1.162) and (1.165), one gets

$$\bar{h}^{\theta\theta} \sim \frac{1}{r} h_+(t - r, \theta, \varphi). \quad (1.166)$$

Contemplating Eqs. (1.165) and (1.166), we recover the usual behavior of a radiating metric in the TT gauge, h_+ and h_\times being the two gravitational wave modes.

1.5.4 Computing the trace h by enforcing the unit value of the determinant of $\tilde{\gamma}^{\hat{i}\hat{j}}$

Having solved the TT wave equation for $\bar{\mathbf{h}}$, there remains to determine the trace $h = f_{ij}h^{ij}$ to reconstruct \mathbf{h} by Eq. (1.94), and then the conformal metric $\tilde{\gamma} = \mathbf{f} + \mathbf{h}$. h can be obtained by solving the scalar wave equation (1.97). However, h can also be computed in order to enforce a relation arising from the very definition of the conformal metric, namely that the determinant of the components $\tilde{\gamma}^{\hat{i}\hat{j}}$ is equal to the inverse of that of the flat metric: $\det \tilde{\gamma}^{\hat{i}\hat{j}} = f^{-1}$ [cf. Eq. (1.19)]. It is easy to show this is equivalent to the following requirement about the orthonormal components:

$$\det \tilde{\gamma}^{\hat{i}\hat{j}} = 1. \quad (1.167)$$

Replacing $\tilde{\gamma}^{\hat{i}\hat{j}}$ by $f^{\hat{i}\hat{j}} + h^{\hat{i}\hat{j}}$, this relation writes

$$\begin{vmatrix} 1 + h^{rr} & h^{r\theta} & h^{r\varphi} \\ h^{r\theta} & 1 + h^{\theta\theta} & h^{\theta\varphi} \\ h^{r\varphi} & h^{\theta\varphi} & 1 + h^{\varphi\varphi} \end{vmatrix} = 1. \quad (1.168)$$

Expanding the determinant and using $h = h^{rr} + h^{\theta\theta} + h^{\varphi\varphi}$ results in

$$\begin{aligned} h &= -h^{rr}h^{\theta\theta} - h^{rr}h^{\varphi\varphi} - h^{\theta\theta}h^{\varphi\varphi} + (h^{r\theta})^2 + (h^{r\varphi})^2 \\ &+ (h^{\theta\varphi})^2 - h^{rr}h^{\theta\theta}h^{\varphi\varphi} - 2h^{r\theta}h^{r\varphi}h^{\theta\varphi} + h^{rr}(h^{\theta\varphi})^2 \\ &+ h^{\theta\theta}(h^{r\varphi})^2 + h^{\varphi\varphi}(h^{r\theta})^2. \end{aligned} \quad (1.169)$$

This relation shows clearly that among the six components $h^{\hat{i}\hat{j}}$ only five of them are independent. The Dirac gauge adds three relations between the $h^{\hat{i}\hat{j}}$, leaving two independent components: the two dynamical degrees of freedom of the gravitational field. Equation (1.169) shows also that, at the linear order in $h^{\hat{i}\hat{j}}$, the condition $\det \tilde{\gamma}^{\hat{i}\hat{j}} = 1$ is equivalent to $h = 0$.

We propose to use Eq. (1.169) in a numerical code to compute h , in order to enforce the condition (1.167) by means of the following iterative procedure: initialize $h^{\hat{i}\hat{j}}$ by the TT part $\bar{h}^{\hat{i}\hat{j}}$ obtained as a solution of the wave equation (1.98); then (i) compute h from Eq. (1.169); (ii) solve the Poisson equation (1.95) to get ϕ ; (iii) insert the values of h and ϕ into Eq. (1.94) to get $h^{\hat{i}\hat{j}}$; (iv) go to (i). In practice, this procedure converges up to machine accuracy (sixteen digits) within at a few iterations.

1.5.5 A constrained scheme for Einstein equations

Let us sketch the constrained scheme we propose to solve the full 3-D time dependent Einstein equations. Our aim here is not to provide a detailed numerical algorithm, but to show how the Dirac gauge condition, in conjunction with the use of spherical coordinates, leads to a method of resolution in which the constraints are automatically satisfied and the time evolution equations are reduced to only two scalar wave equations.

At a given time step, one has to solve the two scalar Poisson equations (1.71) and (1.76) to get respectively Q and N , and therefore the conformal factor $\Psi = (Q/N)^{1/2}$. The Hamiltonian constraint is then automatically satisfied. We have outlined the resolution technique of these two scalar Poisson in Sec. 1.5.2. Let us stress here that a very efficient numerical technique to solve within spherical coordinates scalar Poisson equations with non-compact support has been presented in Ref. [228].

Then one has to solve the vector elliptic equation (1.74) to get the shift vector β , following the procedure presented in Sec. 1.5.2. The momentum constraint is then automatically satisfied.

The next equation to be solved is the TT tensor wave equation (1.98) for $\bar{\mathbf{h}}$, which arises from the Einstein dynamical equation (1.78). As detailed in Sec. 1.5.3, by fully exploiting the TT character of $\bar{\mathbf{h}}$, the resolution of this equation is reduced to the resolution of two scalar wave equations for two scalar potentials χ and μ [Eqs. (1.141) and (1.151)]. From χ and μ one can reconstruct all the components of $\bar{\mathbf{h}}$ by taking some derivatives or inverting some angular Laplacian (which reduces to a mere division by $-\ell(\ell + 1)$ on spherical harmonics expansions).

Then the trace h of \mathbf{h} is determined algebraically through Eq. (1.169) which ensures that $\det \tilde{\gamma}_{ij} = f$ [Eq. (1.19)]. From h and $\bar{\mathbf{h}}$, one reconstructs \mathbf{h} via Eq. (1.94), at the price of solving the Poisson equation (1.95) for ϕ .

Finally, from \mathbf{h} , β and N , one has to compute the conformal extrinsic curvature A^{ij} via Eq. (1.92).

In the above scheme, the only equations which are not satisfied by construction are (i) Eq. (1.75) which relates the time derivative of the conformal factor Ψ to the divergence of the shift vector β and (ii) Eq. (1.97) which is the trace part of the wave equation for \mathbf{h} . These two scalar equations must however be fulfilled by the solution and could be used as evaluators of the numerical error. Alternatively, Eq. (1.75) could be enforced as a condition on $\mathcal{D}_k\beta^k$ in the resolution of the elliptic equation (1.74) for β .

In the above discussion, we have not mentioned the inner boundary conditions to set on some excised black hole. This point is discussed briefly in Appendix 1.A and will be the main subject of a future study.

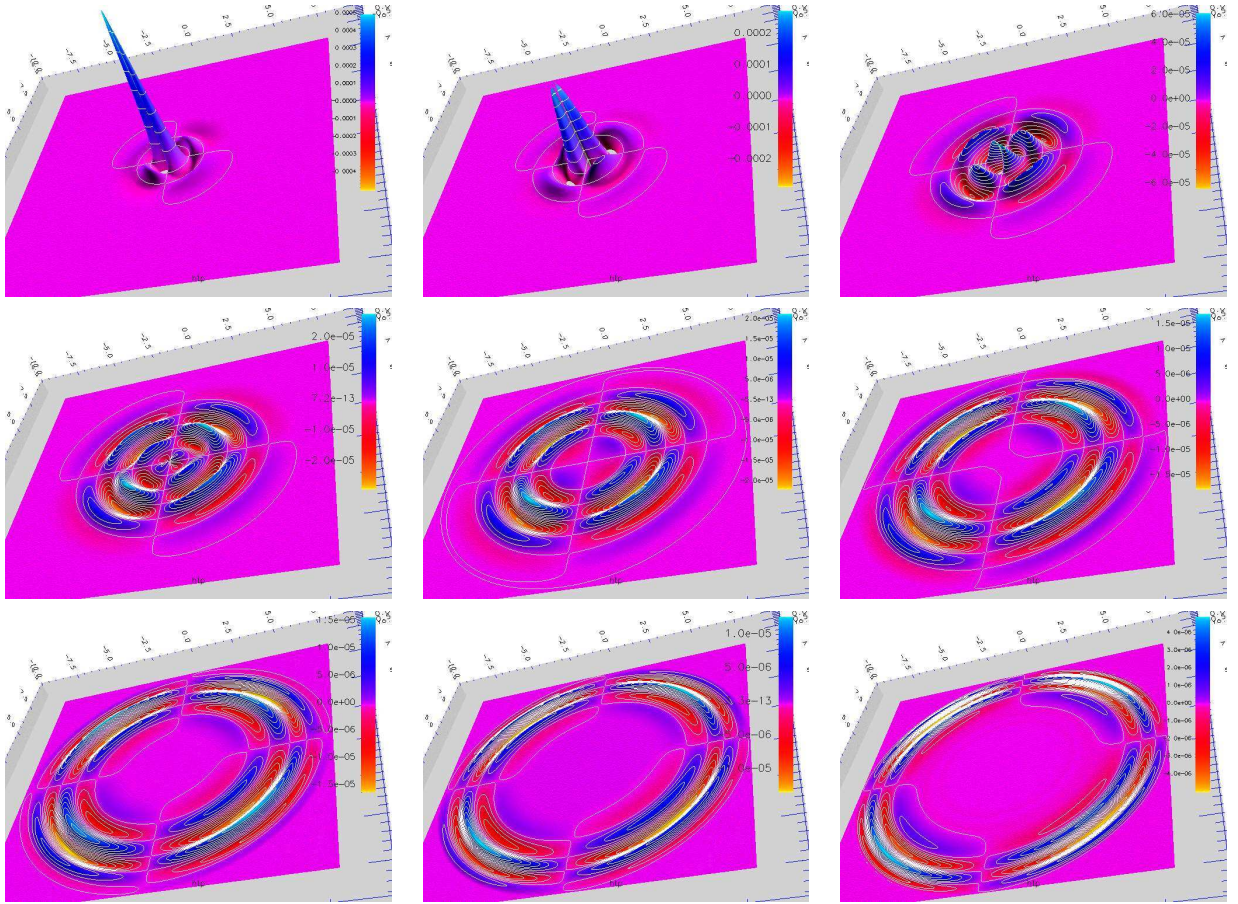


Figure 1.1: Evolution of the $h^{\varphi\varphi}$ component of \mathbf{h} in the plane $\theta = \pi/2$, between $t = 0$ (upper left) and $t = 8r_0$ (lower right). The various snapshots are separated by a constant time interval $\Delta t = r_0$. The size of the depicted square is $16r_0$, so that the wave extraction surface at $R_{\text{ext}} = 8r_0$ is given by the circle inscribed in this square.

1.6 First results from a numerical implementation

1.6.1 Short description of the code

We have implemented the constrained scheme given in Sec. 1.5.5 in a numerical code designed to evolve vacuum spacetimes within maximal slicing and Dirac gauge. The code is constructed upon the C++ library LORENE [216]. It uses multidomain spectral methods [69, 72] to solve the partial-differential equations within spherical coordinates. The scalar Poisson solver is that of Ref. [228], whereas the vector Poisson equation for the shift is solved via the method (ii) presented in Sec. 1.5.2. The scalar wave equations for χ and μ [Eqs. (1.141) and (1.151)] are integrated forward in time by means of the technique presented in Ref. [341], namely a second-order semi-implicit Crank-Nicholson scheme with efficient outgoing-wave boundary conditions. By “efficient” we mean that all wave modes with spherical harmonics indices $\ell = 0, 1$ and 2 are extracted at the outer boundary without any spurious reflection. This is far better than the Sommerfeld boundary condition commonly used in numerical relativity and which is valid only for the mode $\ell = 0$.

Various concentric shell-like domains are used, the outermost one being compactified, to bring spatial infinity to the computational domain. The compactified domain is employed to solve all the elliptic equations, allowing for the correct asymptotic flatness boundary conditions. On the contrary, the wave equations are solved only in the non-compactified domains, the outgoing-wave boundary condition [341] being imposed at the boundary between the last non-compactified shell and the compactified one. Further details upon the numerical code will be presented in a future publication.

1.6.2 Initial data and computational setting

We have employed the code to evolve pure 3-D gravitational wave spacetimes, as in the two BSSN articles [421, 54]. Initial data have been obtained by means of the *conformal thin sandwich* formalism [487, 364]. The freely specifiable parameters of this formalism are $\tilde{\gamma}$, $\partial\tilde{\gamma}/\partial t$, K and $\partial K/\partial t$. In accordance with our choice of maximal slicing, we set $K = 0$ and $\partial K/\partial t = 0$. Moreover, we use momentarily static data, $\partial\tilde{\gamma}/\partial t = 0$, along with a conformal metric $\tilde{\gamma}$ resulting from

$$\chi(t=0) = \frac{\chi_0}{2} r^2 \exp\left(-\frac{r^2}{r_0^2}\right) \sin^2\theta \sin 2\varphi \quad (1.170)$$

$$\mu(t=0) = 0. \quad (1.171)$$

The constant numbers χ_0 and r_0 parametrize respectively the amplitude and the width of the initial wave packet. Let us recall that, within Dirac gauge, the two scalars χ and μ fully specify \mathbf{h} and thus $\tilde{\gamma}$: (χ, μ) determine a unique TT tensor $\bar{\mathbf{h}}$ according to the decomposition presented in Sec. 1.5.3 and the full \mathbf{h} is reconstructed from the trace h computed in order to ensure $\det \tilde{\gamma}^{ij} = f^{-1}$, following the method given in Sec. 1.5.4. It can be shown that the metric defined by Eq. (1.170)-(1.171) corresponds to an even-parity Teukolsky wave [460] with $M = 2$. These initial data are similar to those used by Baumgarte and Shapiro [54] except theirs correspond to a $M = 0$ (axisymmetric) Teukolsky wave. In particular, we choose an amplitude $\chi_0 = 10^{-3}$ similar to that in Ref. [54].

A total of 6 numerical domains have been used: a spherical nucleus of radius $r = r_0$, surrounded by 4 spherical shells of outer radius $r = 2r_0, 4r_0, 6r_0$ and $8r_0$, and an external compactified domain of inner radius $r = 8r_0$. The outgoing wave boundary conditions discussed above are set at $r = 8r_0$, which we call the *wave extraction radius* R_{ext} . In particular, this means that we do not solve for \mathbf{h} for

$r > 8r_0$. Consequently we set \mathbf{h} to zero in the region $r > 8r_0$. More precisely, we perform a smooth matching of the value of \mathbf{h} at $r = 6r_0$ to zero at $r = 8r_0$. This means that we solving all the Einstein equations only for $r < 6r_0$. For $r \in [6r_0, \infty)$ we are solving the Einstein equations only for the lapse N , the shift vector β and the conformal factor Ψ , with \mathbf{h} set to zero in the $r > 8r_0$ part of their source terms. We take into account the symmetries present in the initial data (1.170)-(1.171): (i) symmetry with respect to the plane $\theta = \pi/2$ and (ii) symmetry with respect to the transformation $\varphi \mapsto \varphi + \pi$. Accordingly, the computational coordinate θ spans the interval $[0, \pi/2]$ only and φ the interval $[0, \pi)$. In each domain, the following numbers of collocations points (= numbers of polynomials in the spectral expansions) are used: $N_r \times N_\theta \times N_\varphi = 17 \times 9 \times 8$. The corresponding memory requirement is 260 MB. This modest value allows the computation to be performed on a laptop. We have used two different time steps $\delta t = 10^{-2}r_0$ and $\delta t = 5 \cdot 10^{-3}r_0$, to investigate the effects of time discretization.

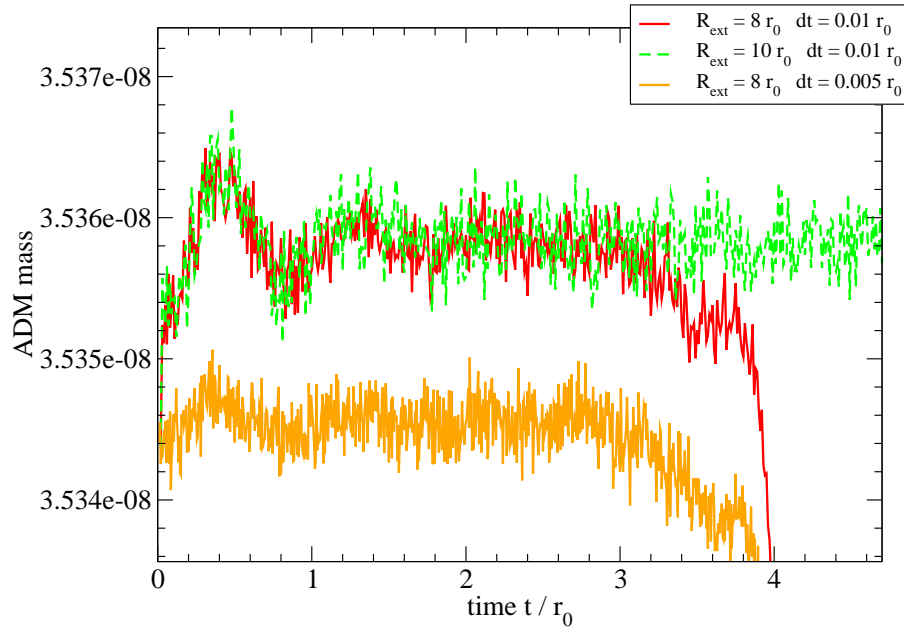


Figure 1.2: Evolution of the ADM mass for three different computational settings, corresponding to different values of the time step δt and the wave extraction radius R_{ext} .

1.6.3 Results

The time evolution of the component $h^{\varphi\varphi}$ of \mathbf{h} is shown in Fig. 1.1. All the wave packet leaves the computational domain $r < 8r_0$ around $t \sim 8r_0$ and we do not notice on Fig. 1.1 any spurious reflexion.

In order to test the code, we have monitored the ADM mass defined by

$$M_{\text{ADM}} = \frac{1}{16\pi} \oint_{\infty} \left[\mathcal{D}^j \gamma_{ij} - \mathcal{D}_i (f^{kl} \gamma_{kl}) \right] dS^i, \quad (1.172)$$

where the integral is taken over a sphere of radius $r = +\infty$ and where we have adapted the original definition [35] to general coordinates (i.e. non asymptotically Cartesian) by the explicit introduction of the flat metric \mathbf{f} . The above integral can be re-written in terms of the conformal metric and conformal

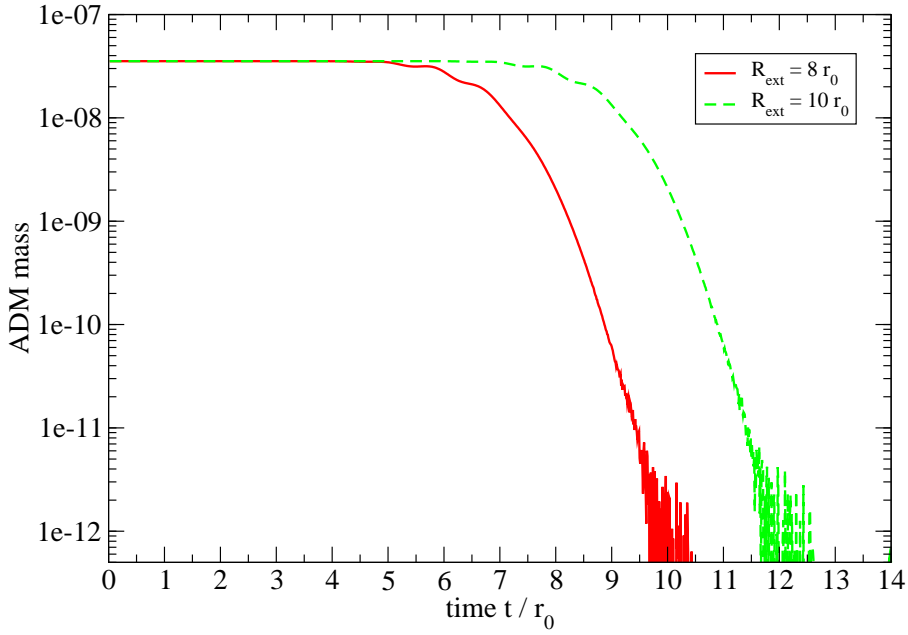


Figure 1.3: Evolution of the ADM mass (logarithmic scale, contrary to Fig. 1.2) for two different values of the wave extraction radius R_{ext} .

factor:

$$M_{\text{ADM}} = -\frac{1}{16\pi} \oint_{\infty} \left(8\mathcal{D}_i\Psi + f_{ij}\mathcal{D}_k h^{jk} - \mathcal{D}_i h \right) dS^i. \quad (1.173)$$

Within Dirac gauge, the second term in the integrand vanishes identically, whereas the last one does not contribute to the integral, due to the fast decay of h (at least $O(r^{-2})$) implied by Eq. (1.169). Therefore the expression for the ADM mass reduces to the flux of the gradient of the conformal factor:

$$M_{\text{ADM}} = -\frac{1}{2\pi} \oint_{\infty} \mathcal{D}_i\Psi dS^i. \quad (1.174)$$

Hence the expression of ADM mass in Dirac gauge is identical to the well known expression for conformally flat hypersurfaces. The evolution of the ADM mass computed by means of Eq. (1.174) (let us recall that the sphere at $r = \infty$ belongs to our computational domain) is presented in Fig. 1.2. For $t < 3r_0$, one sees that the ADM mass is conserved, as it should be, with an accuracy of four digits. Moreover, Fig. 1.2 shows that the main source of error in the ADM mass is the finite value of the time step δt . For $t > 3r_0$, the ADM mass starts to decrease, reflecting the fact that the wave is leaving the domain $r \leq R_{\text{ext}}$. Note that by increasing the wave extraction radius from $R_{\text{ext}} = 8r_0$ to $R_{\text{ext}} = 10r_0$, we get a conservation of the ADM mass up to $t \simeq 5r_0$ (dashed curved in Fig. 1.2). In Fig. 1.3, we present the evolution of the ADM mass on a longer timescale. We see clearly that, after remaining constant (the part shown in Fig. 1.2), the ADM mass decreases by four orders of magnitude after $t \simeq 10r_0$ (resp. $t \simeq 12r_0$) for the wave extraction radius $R_{\text{ext}} = 8r_0$ (resp. $R_{\text{ext}} = 10r_0$). The very small value of the ADM mass at late times demonstrates that all the wave packet has left the domain $r \leq R_{\text{ext}}$ and no spurious reflection has occurred. This is due to the efficient outgoing wave boundary conditions [341] set at the wave extraction radius.

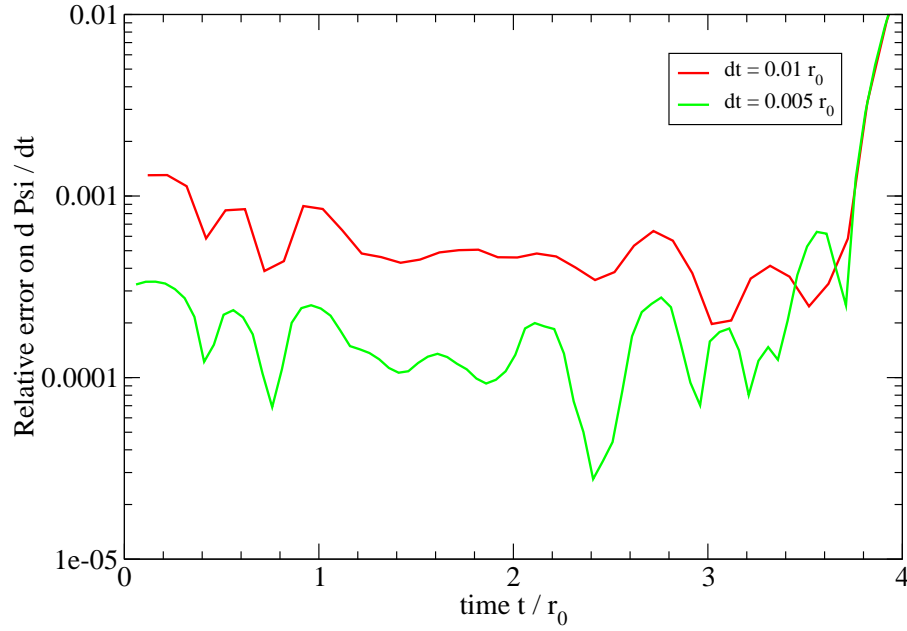


Figure 1.4: Relative error ε [Eq. (1.175)] on the time derivative of the conformal factor Ψ in the central domain ($r \leq r_0$).

Another test is provided by Eq. (1.75) which relates the time derivative of the conformal factor Ψ to the divergence of the shift vector β . As mentioned in Sec. 1.5.5, this equation must hold but is not enforced in our scheme. In a given numerical domain we define the relative error on Eq. (1.75) by

$$\varepsilon := \frac{|\partial\Phi/\partial t - \beta^k \mathcal{D}_k \Phi - \frac{1}{6} \mathcal{D}_k \beta^k|}{\max |\partial\Phi/\partial t| + \max |\beta^k \mathcal{D}_k \Phi + \frac{1}{6} \mathcal{D}_k \beta^k|}, \quad (1.175)$$

where the max are taken on the considered domain. We represent the value of ε in the domain where it is the largest, namely the nucleus ($r \leq r_0$), in Fig. 1.4. We see that Eq. (1.75) is actually very well satisfied. The error is in fact dominated by the time discretization (second order scheme), and is as low as a few 10^{-4} for $\delta t = 5 \cdot 10^{-3} r_0$. The increase of ε at $t \sim 4r_0$ is spurious and is due to the arrival of the wave packet in the wave extraction domain $6r_0 \leq r \leq 8r_0$.

To check the long term stability of the code, we have let it run well after the wave packet has leaved the area $r < 8r_0$, namely until $t = 400r_0$. This very long time scale is similar with that used in Ref. [54] to assess the stability of the BSSN scheme. We found no instability to develop. In particular the maximum value of the potential χ remains at the round-off error value of 10^{-12} that has been reached at $t \sim 40r_0$ (see Fig. 1.5).

1.7 Summary and conclusions

We have introduced on each hypersurface $t = \text{const}$ of the 3+1 formalism a flat 3-metric \mathbf{f} , in addition to the (physical) 3-metric γ induced by the spacetime 4-metric \mathbf{g} , in such a way that asymptotically both metrics coincide. This allows us to define properly the conformal metric $\tilde{\gamma}$ and not to stick to

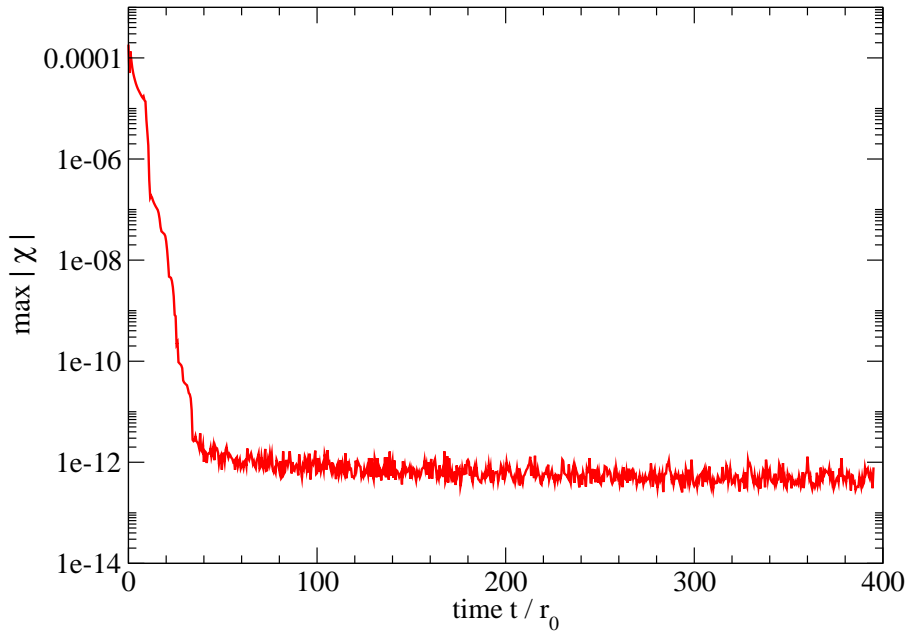


Figure 1.5: Evolution of the maximum of absolute value of the potential χ [Eq. (1.140)] for the long term run.

Cartesian coordinates. A flat metric is introduced anyway, more or less explicitly, when performing numerical computations. We have written the 3+1 equations entirely in terms of the covariant derivative associated with the flat metric \mathbf{f} .

The Dirac gauge is expressed simply in terms of this flat metric as the vanishing of the divergence *with respect to \mathbf{f}* of the conformal metric $\tilde{\gamma}$. Moreover in spherical components, the Dirac gauge reduces the resolution of the equations for $\tilde{\gamma}$ to two scalar wave equations. The remaining four components $\tilde{\gamma}^{ij}$ are then obtained from the condition $\det \tilde{\gamma}^{ij} = \det f^{ij}$ and the three components of the Dirac condition $\mathcal{D}_j \tilde{\gamma}^{ij} = 0$. This clearly shows that the gravitational field has two degrees of freedom and this exhibits the TT wave behavior of the metric at infinity. Let us stress that the usage of spherical coordinates and spherical components is essential for the reduction to two scalar wave equations. To our knowledge, this is the first time that a *differential* gauge is used to directly compute some of the metric components, thus decreasing the number of PDE to be solved. Previously, this was done only for *algebraic* gauges (i.e. setting some of the metric components to zero).

Contrary to e.g. the minimal distortion gauge [435] or the “Gamma-driver” gauge [14], the Dirac gauge completely fix the coordinates (up to some boundary conditions) in the initial hypersurface Σ_0 . This implies that initial data must be prepared within this gauge, which might be regarded as a drawback (for instance an analytic expression for the Kerr solution is not known in Dirac gauge). On the contrary, an advantage of the full coordinate fixing is to allow to compute stationary solutions by simply setting $\partial/\partial t = 0$ in the various equations. For instance, Shibata, Uryu and Friedman [419] have recently proposed to use the Dirac gauge to compute quasiequilibrium configurations of binary neutron stars.

In addition to the Dirac gauge, the use of the maximal slicing results in an elliptic equation for the lapse function. Another elliptic equation for the conformal factor Ψ (or equivalently for $Q := \Psi^2 N$) arises from the Hamiltonian constraint. The Dirac gauge itself, in conjunction with the momentum

constraint, results in an elliptic equation for the shift β . The maximal slicing relates the divergence of β to the time derivative of the conformal factor.

Solving the above equations implies that the four constraints are fulfilled by the solution. As already mentioned in the Introduction, some authors have proposed very recently a scheme in which the constraints, re-written as time evolution equations, are satisfied up to the time discretization errors [202]. On the contrary, in our scheme the constraints are fulfilled within the precision of the *space* discretization errors (which can be very low with a modest computational cost, thanks to spectral methods).

It is worth noticing that the five elliptic equations of the widely used Isenberg-Wilson-Mathews approximation to General Relativity [260, 261, 482] (see also Ref. [186]) are naturally recovered in our scheme by simply setting $\mathbf{h} = 0$: they are the equations for N , Q and β .

We have demonstrated the viability of the proposed constrained scheme by numerically computing the evolution of a gravitational wave packet in a vacuum spacetime. The numerical evolution has been found to be both very accurate and stable. We are also made confident by existing constrained schemes for vector equations which have proved to be successful: the divergence-free hydro scheme of Ref. [478] (the constraint being that the velocity field is divergence-free) and some MHD schemes in cylindrical coordinates [275] (the constraint being that the magnetic field is divergence-free).

In this paper we have focused on space slices with \mathbb{R}^3 topology, except for Appendix 1.A where we briefly discuss the properties of degenerate second order operators and the number of boundary conditions at the surface of excised holes with vanishing lapse. In a future work, we shall focus on black hole spacetimes.

APPENDIX

1.A Degenerate elliptic operators on a black hole horizon

In our view, a numerical scheme for black hole spacetimes should recover known stationary solutions in coordinate-time independent form (i.e. with the $\partial/\partial t$ coordinate vector coinciding with the Killing vector of stationarity). Indeed we require arbitrary long term evolution of steady state, or quasi-steady state, black hole spacetimes. For classical solutions (Kerr) in usual coordinates, this requirement results in a vanishing lapse on the horizon (see discussion in Refs. [219, 239]). Therefore we excise from our computational domain a sphere \mathcal{H} (or two spheres for binary systems) with $N = 0$ as a boundary condition on that sphere and choose spherical coordinates such that $r = 1$ on \mathcal{H} ¹.

In this case, the spatial operator acting on \mathbf{h} in Eq. (1.85) must not be merely the Laplacian Δ but

$$\blacktriangle h^{ij} := N\Delta h^{ij} - \mathcal{D}_k N \left(\mathcal{D}^i h^{jk} + \mathcal{D}^j h^{ik} - \mathcal{D}^k h^{ij} \right). \quad (1.176)$$

This operator is formed by writing $\mathcal{D}_k Q = \Psi^2 \mathcal{D}_k N + 2N\Psi \mathcal{D}_k \Psi$ in the right-hand side of Eq. (1.85) and gathering the $\mathcal{D}_k N$ term with the Δh^{ij} one. The operator \blacktriangle is degenerate, because of the vanishing of N at the boundary \mathcal{H} . Similarly, the operator acting on the shift vector β is degenerate on \mathcal{H} (cf. Eq. (1.74) with A^{ij} given by Eq. (1.92) which contains a division by the lapse N). Letting the

¹For a binary system, we introduce two coordinate systems, each centered on one hole, cf. [229]

unknown u be a component of h^{ij} or β^i , these equations are of the kind

$$N\Delta u + \epsilon \mathcal{D}_i N \mathcal{D}^i u = S, \quad (1.177)$$

with the associated homogeneous equation

$$N\Delta u + \epsilon \mathcal{D}_i N \mathcal{D}^i u = 0, \quad (1.178)$$

where $N = 0$ and $\partial N / \partial r > 0$ at $r = 1$, $\epsilon = \pm 1$ and S is some effective source. Since Eq. (1.177) is linear, a solution is a linear combination of a particular solution and a homogeneous solution, i.e. a solution of Eq. (1.178). In the non-degenerate case, since Eq. (1.178) is of second order, we have two independent homogeneous solutions, which allow us to impose two boundary conditions. In the degenerate case ($N = 0$ at $r = 1$), the number of regular homogeneous solutions depends upon the sign of ϵ : two for $\epsilon = -1$ and only one for $\epsilon = +1$. To illustrate this, let us consider the following one-dimensional second order equation analogue to Eq. (1.178) with $x = r - 1$:

$$x \frac{d^2 u}{dx^2} + \epsilon \frac{du}{dx} = 0, \quad \text{with } x \in [0, 1]. \quad (1.179)$$

The involved second-order operator is clearly degenerate at $x = 0$. For $\epsilon = -1$, we have two independent homogeneous solutions:

$$u_1(x) = \text{const} \quad \text{and} \quad u_2(x) = x^2, \quad (1.180)$$

whereas for $\epsilon = 1$, the two independent homogeneous solutions are

$$u_1(x) = \text{const} \quad \text{and} \quad u_2(x) = \ln x. \quad (1.181)$$

The last one is clearly not regular at $x = 0$, so that in this case, one can use only one homogeneous solution to satisfy a Dirichlet boundary condition.

This behavior of the degenerate operator can also be understood by considering the parabolic (heat-like) equation associated with Eq. (1.178):

$$\frac{\partial u}{\partial t} = N\Delta u + \epsilon \mathcal{D}_i N \mathcal{D}^i u. \quad (1.182)$$

The solution of the elliptic equation (1.178) is the eigenfunction corresponding to the zero eigenvalue of the spatial operator acting on the right-hand side of Eq. (1.182). In other words, the solution u we search for is the relaxed solution of the heat-like equation (1.182). When $N \rightarrow 0$, Eq. (1.182) becomes an advection equation near $r = 1$, for which the number of boundary conditions at $r = 1$ is zero or one depending whether the ‘‘effective velocity’’ $-\epsilon \mathcal{D}_i N = -\epsilon \frac{\partial N}{\partial r} \mathbf{e}_r$ is ingoing or outgoing at the boundary $r = 1$.

For the spherical components of the shift vector, we have $\epsilon = -1$, so that a boundary condition can always be given at $r = 1$, in addition to the boundary condition at $r = \infty$. Regarding the spherical components of the metric potential h^{ij} , $\epsilon = 1$ for h^{rr} , which means that no boundary condition can be set at $r = 1$ in addition to $h^{rr} = 0$ at $r = \infty$. On the contrary, $\epsilon = -1$ for the potential μ introduced in Eqs. (1.144)-(1.145). These points shall be studied more in details in a future work. It is worth to mention that the boundary conditions for h^{ij} at $r = 1$ determine fully the coordinates within the Dirac gauge.

Chapitre 2

Mathematical issues in a fully-constrained formulation of Einstein equations

Version publiée : I. Cordero-Carrión, J. M. Ibáñez, E.ourgoulhon, J. L. Jaramillo, et J. Novak, *Physical Review D* **77**, 084007 (2008).

Sommaire

2.1	A Fully-Constrained evolution scheme	51
2.2	First-order reduction of the reduced system in the FCF	57
2.3	Characteristic structure of the reduced system	59
2.4	Dirac gauge and system of conservation laws	63
2.5	Dirac system	64
2.6	Discussion.	67

2.1 A Fully-Constrained evolution scheme

A second-order fully-constrained evolution formalism for the Einstein equations has been proposed in Ref. [73]. This evolution scheme, that will be referred in the following as Fully-Constrained Formulation (FCF), is based on a conformal 3+1 formulation of General Relativity and makes use of an elliptic condition for the choice of spatial coordinates, a *generalized Dirac gauge*, and a maximal condition for the slicing. The enforcement of the constraints along the evolution together with the elliptic nature of the employed gauge conditions, translates the FCF formalism into a mixed elliptic-hyperbolic Partial Differential Equations (PDE) system, consisting in five quasi-linear elliptic equations coupled with a tensorial second-order in time and in space evolution equation for the conformal metric. In this article, we aim at gaining insight on some mathematical issues associated with this PDE system and, in particular, assessing the hyperbolicity of the tensorial evolution part. A good understanding of the mathematical structure of the system will be crucial in the context of full 3D numerical relativity simulations, since the choice of state-of-the-art numerical tools will be adapted to the specific structures

of the whole system governing the evolution of matter fields in a dynamical space-time: spectral methods for the elliptic subsystem [230], and modern high-resolution shock-capturing techniques for the hyperbolic part [311, 176]. The implementation of the scheme in [73] will naturally extend previous works —following the Conformal Flatness Condition (CFC) approach of Isenberg-Wilson-Mathews [260, 481]— devoted to the study of some relevant astrophysical sources of gravitational radiation [147, 148, 149, 151].

2.1.1 Gauge reduction, PDE evolution systems and well-posedness

The gauge character of General Relativity (GR) strongly conditions any attempt of finding a solution by solving a Partial Differential Equations (PDE) problem. In its standard formulation through the Einstein equation

$$R_{\mu\nu} - \frac{1}{2}R g_{\mu\nu} = 8\pi T_{\mu\nu}, \quad (2.1)$$

solutions are given in terms of spacetime geometries $(\mathcal{M}, g_{\mu\nu})$, i.e. classes of Lorentzian metrics $g_{\mu\nu}$ equivalent under diffeomorphisms of \mathcal{M} , rather than by specific 4-metrics in some particular coordinate system. As a consequence of this, any attempt to cast (2.1) as a standard PDE system necessarily must go through a *gauge reduction* process. This fixing of the gauge involves four different (differential) systems: i) the *reduced* system, whose solution provides the metric in a given coordinate system, ii) the *constraint system*, consequence of the gauge character of the theory and that characterizes the solution manifold, iii) the *gauge system*, which fixes the coordinate chart and permits to write the reduced system as a standard PDE problem, and iv) the *subsidiary system*, guaranteeing the overall consistency along the evolution and, in particular, between the reduced and gauge systems. The mathematical consistency of the evolution formalism involves two aspects. First, one must assess the analytic well-posedness of the PDE system that is actually solved during the evolution, that we will refer to in the following as the *evolution PDE system*, that includes the *reduced system* but possibly other additional PDEs. Second, one must guarantee the fulfillment of the *subsidiary system* during the evolution.

As in other evolution formalisms based on the Initial Value problem for the Einstein equation [190], the constrained system in the FCF scheme follows from the Gauss-Codazzi-Ricci conditions

$$\begin{aligned} {}^{(3)}R - K_{ij}K^{ij} + K^2 &= 16\pi\rho \\ D_j (K^{ij} - \gamma^{ij}K) &= 8\pi J^i, \end{aligned} \quad (2.2)$$

i.e. the Hamiltonian and momentum constraints in the 3+1 formulation (ρ is the energy density and J^i the current vector) which are elliptic in nature. The currently most successful numerical evolution formalisms are *free* schemes in which the constraint system (2.2) is not enforced during the evolution. This is the case of certain generalized harmonic formalisms [374, 232] and the 3+1 BSSN (from Baumgarte, Shapiro, Shibata and Nakamura; see references [421, 54]) used in recent binary black hole breakthroughs [373, 101, 44, 375] and in fully 3D evolution of binary neutron stars (see e.g. [424]). In these free schemes, the corresponding evolution PDE system is formed by the respective reduced systems together with some additional evolution equations to fix the harmonic gauge sources, in the case generalized harmonic schemes, or the lapse function and shift vector, in the BSSN case. No elliptic equation is solved during the evolution and standard hyperbolic techniques can in principle be used to assess the well-posedness of the evolution system (cf. in this sense [233] for the case of the BSSN system). In contrast, the FCF here discussed actually incorporates the constraints to

the evolution PDE system. Moreover, the use of the above-mentioned elliptic gauge conditions adds additional elliptic equations during the evolution. The resulting FCF scheme presents some interesting properties as compared with free evolution schemes. Apart from the absence of constraint violations (an issue under control in current BSSN and generalized harmonic formulations), we can highlight the following features (cf. [73] for a more complete discussion): first, the FCF naturally generalizes (as commented above) the successful scheme employed in the CFC approximation to General Relativity; second, it permits to read the gravitational waveforms directly from the metric components; third, the scheme can be straightforwardly adapted to the extraction of gravitational radiation at null infinity by making use of hyperboloidal 3-slices implemented by means of a *constant mean curvature* elliptic gauge condition; and fourth, it provides a well-suited framework for the formulation of realistic (approximate) prescriptions in the construction of quasi-stationary astrophysically configurations [471]. However, the well-posedness analysis of such a mixed elliptic-hyperbolic system can be a formidable problem, since part of the dynamics related to the characteristic fields in the hyperbolic part is encoded in fields obtained only once the elliptic part is solved. Even though analyses of such systems exist in the GR literature (see e.g. Refs.[119, 120, 121] and particularly Ref. [17]) they deal with free evolution systems, in which the elliptic part follows only from the gauge conditions. The well-posedness analysis of the complete elliptic-hyperbolic system in the FCF scheme, which in addition includes the constraints, is beyond the scope of this work and we will mainly focus on the hyperbolicity analysis of the tensorial evolution equation. Before referring to the additional issues related to the subsidiary system, we must provide some details about the FCF formalism.

2.1.2 Brief review of the FCF scheme

Following Ref. [73], we consider a standard 3+1 decomposition of an asymptotically flat spacetime $(\mathcal{M}, g_{\mu\nu})$ in terms of a foliation by spacelike hypersurfaces (Σ_t) . We denote the unit timelike normal vector to the spacelike slice Σ_t by n^μ , the spatial 3-metric by $\gamma_{\mu\nu}$, i.e. $\gamma_{\mu\nu} = g_{\mu\nu} + n_\mu n_\nu$, and adopt the following sign convention for the extrinsic curvature: $K_{\mu\nu} = -\frac{1}{2}\mathcal{L}_n\gamma_{\mu\nu}$. The evolution vector $t^\mu \equiv (\partial_t)^\mu$ is decomposed in terms of the lapse function N and the shift vector β^μ , as $t^\mu = Nn^\mu + \beta^\mu$.

Under this 3+1 decomposition, Einstein equation (2.1) splits into the 3+1 constraints in (2.2) and a set of evolution equations for the extrinsic curvature that, together with the kinematical relation defining the extrinsic curvature, constitute the 3+1 evolution equations

$$\begin{aligned} (\partial_t - \mathcal{L}_\beta)\gamma_{ij} &= -2NK_{ij} \\ (\partial_t - \mathcal{L}_\beta)K_{ij} &= -D_i D_j N + N \left\{ {}^{(3)}R_{ij} + KK_{ij} - 2K_i^k K_{kj} + 4\pi[(S - E)\gamma_{ij} - 2S_{ij}] \right\} . \end{aligned} \quad (2.3)$$

This is a first-order in time and second-order in space evolution system for (γ_{ij}, K^{ij}) .

The first specific element in the FCF scheme is the introduction of a *time independent* fiducial flat metric f_{ij} , which satisfies $\mathcal{L}_t f_{ij} = \partial_t f_{ij} = 0$. This rigid structure is chosen to coincide with γ_{ij} at spatial infinity, capturing its asymptotic Euclidean character, and permits to work with tensor quantities rather than with tensor densities. We will denote by \mathcal{D}_i the Levi-Civita connection associated with f_{ij} .

Conformal decomposition. As a step forward in the reduction process to the PDE system in the present FCF, we perform a conformal decomposition of the 3+1 fields:

$$\gamma_{ij} = \Psi^4 \tilde{\gamma}_{ij} \quad , \quad K^{ij} = \Psi^4 \tilde{A}^{ij} + \frac{1}{3} K \gamma^{ij} \quad , \quad (2.4)$$

where $K = \gamma^{ij}K_{ij}$, the representative $\tilde{\gamma}_{ij}$ of the conformal class of the 3-metric is chosen to satisfy the unimodular condition $\det(\tilde{\gamma}_{ij}) = \det(f_{ij})$, and the traceless part \tilde{A}^{ij} of the extrinsic curvature is decomposed as

$$\tilde{A}^{ij} = \frac{1}{2N} \left(\tilde{D}^i \beta^j + \tilde{D}^j \beta^i - \frac{2}{3} \tilde{D}_k \beta^k \tilde{\gamma}^{ij} + \partial_t \tilde{\gamma}^{ij} \right), \quad (2.5)$$

with \tilde{D}_i the Levi-Civita connection associated with $\tilde{\gamma}_{ij}$. Finally, in the following we will denote by h^{ij} the deviation of the conformal metric from the flat fiducial metric, i.e.

$$h^{ij} := \tilde{\gamma}^{ij} - f^{ij}. \quad (2.6)$$

Using these conformal decompositions of γ_{ij} and K^{ij} , the 3+1 constraints (2.2) and evolution system (2.3) can be expressed in terms of the basic variables $h^{ij}, \Psi, N, \beta^i, K$. Before giving more explicit expressions, let us remove the gauge freedom.

Gauge system. Following the prescriptions in [73], namely maximal slicing and the so-called generalized Dirac gauge, we choose

$$K = 0, \quad H^i := \mathcal{D}_k \tilde{\gamma}^{ki} = 0, \quad (2.7)$$

These gauge conditions fix the coordinates, even in the initial slice, up to boundary terms (see e.g. sections 9.3. and 9.4. in [214]). These two relations define the gauge system in the FCF scheme. Since the gauge system is meant to hold at all times, the following conditions must also be satisfied

$$\dot{K} = 0, \quad \partial_t \left(\mathcal{D}_k \tilde{\gamma}^{ki} \right) = 0. \quad (2.8)$$

The FCF scheme actually enforces the first of these conditions, $\dot{K} = 0$, during the evolution. Taking the trace in the second equation in (2.3), and using the Hamiltonian constraint that is also enforced during the evolution (see below), an elliptic equation for the lapse follows

$$\tilde{D}_k \tilde{D}^k N + 2\tilde{D}_k \ln \Psi \tilde{D}^k N = S_N[N, \Psi, \beta^i, \tilde{\gamma}_{ij}]. \quad (2.9)$$

Main or reduced system. In the FCF scheme in Ref. [73] the reduced system is a second-order in time and second-order in space evolution system for the deviation tensor h^{ij} . This is obtained by: i) combining equations in (2.3) into a single second-order in time equation; ii) inserting in it the conformal decompositions (2.4) and (2.5), and iii) imposing the gauges (2.7). The resulting expression is formally written as (see next section for a detailed account):

$$\frac{\partial^2 h^{ij}}{\partial t^2} - \frac{N^2}{\Psi^4} \tilde{\gamma}^{kl} \mathcal{D}_k \mathcal{D}_l h^{ij} - 2\mathcal{L}_\beta \frac{\partial h^{ij}}{\partial t} + \mathcal{L}_\beta \mathcal{L}_\beta h^{ij} = S_h^{ij}, \quad (2.10)$$

where the source S_h^{ij} does not contain second derivatives of h^{ij} . Use of the Dirac gauge results in the wave-like form of this equation, since it eliminates certain second derivatives of the type $\mathcal{D}^i \mathcal{D}_k h^{kj}$ coming from the expression of the Ricci tensor.

Constrained system. The Hamiltonian constraint in (2.2) can be written as an elliptic equation for the conformal factor Ψ :

$$\tilde{D}_k \tilde{D}^k \Psi - \frac{{}^3\tilde{R}}{8} \Psi = S_\Psi[\Psi, N, \beta^i, \tilde{\gamma}_{ij}]. \quad (2.11)$$

Again $S_\Psi[\Psi, N, \beta^i, \tilde{\gamma}_{ij}]$ represents a non-linear source. Momentum constraint poses a more subtle issue. In Ref. [73] an elliptic equation for the shift vector is deduced using *both* the momentum constraint and the preservation in time of the Dirac gauge (second relation in (2.8)):

$$\tilde{D}_k \tilde{D}^k \beta^i + \frac{1}{3} \tilde{D}^i \tilde{D}_k \beta^k + {}^3\tilde{R}^i{}_k \beta^k = S_\beta^i[\Psi, N, \beta^i, \tilde{\gamma}_{ij}] \quad (2.12)$$

An equation for the shift could be derived from the momentum constraint alone, but the coupling to the tensorial equation (2.10) would become more complicated due to the presence of a mixed time-space second-order derivative of h^{ij} . This term is eliminated by the use of a Dirac, or a similar, gauge.

Alternatively, an elliptic equation for the shift can be drawn from the preservation of the Dirac gauge alone, renouncing, therefore, to the fully-constrained character of the scheme —e.g. this is the strategy in Ref. [17], but using a spatial harmonic gauge condition instead of the Dirac one. At the end of the day, the choice (2.12) in the FCF scheme provides an elliptic equation for the shift that enforces the momentum constraint, *as long as the Dirac gauge is satisfied*.

FCF evolution PDE system. The mixed elliptic-hyperbolic PDE system that evolves some initial data given on an Cauchy slice is formed by: a) Eqs. (2.9), (2.11) and (2.12), the elliptic part, and b) Eq. (2.10), the wave-like tensorial equation. As we have pointed out, we will not consider here the well-posedness analysis of the whole system. To give an idea of the involved difficulties, we note that the elliptic part is very similar to the Extended Conformal Thin Sandwich (XCTS) [364, 358] employed in the construction of initial data, though here it is solved all along the evolution. Even the restriction to the elliptic subsystem represents a very hard problem, as it is illustrated by the lack of the existence results for the XCTS system and the preliminary numerical [365] (see also [265]) and analytical [53, 480] results pointing towards a generic non-uniqueness of the elliptic system. For these reasons, we will focus on the study of the hyperbolicity of the tensorial evolution equation (2.10), understanding this as a necessary condition for the overall well-posedness.

Subsidiary system. The resolution of the PDE evolution system only guarantees the consistency between the reduced and gauge systems as far as the slicing condition is regarded, since equation (2.9) for the lapse is indeed enforced. This is in principle not the case for the Dirac gauge. More dramatically, if the Dirac gauge is actually not satisfied, the FCF scheme is not really fully-constrained, since in that situation Eq. (2.12) no longer enforces the momentum constraint. A control of the evolution of the Dirac gauge is therefore crucial in the scheme. A wave-like equation for $\mathcal{D}_k h^{ki}$ can be obtained by taking the divergence of the tensorial Eq. (2.10). The vanishing of $\mathcal{D}_k h^{ki}$ in the evolution would then follow from the initial conditions $\mathcal{D}_k h^{ki} = 0$ and $\partial_t (\mathcal{D}_k h^{ki} = 0) = 0$ imposed in the construction of the initial data, and the satisfaction of Eq. (91) in Ref. [73] for $\dot{\beta}^i$. The latter can be considered as the *subsidiary system* in the FCF scheme.

2.1.3 Specific objectives and organization

Though the wave character of Eq. (2.10) essentially guarantees its hyperbolicity, we aim here at developing a more detailed analysis. This is motivated by the need of controlling the characteristics in initial boundary problems and also when trying to make use of first-order techniques employed in matter evolutions. Our main specific goal in this article is the development of a hyperbolicity analysis of a *first-order* version of the evolution part in the FCF formalism, where N , Ψ and β^i are considered as fixed parameters. In particular, we aim at obtaining explicit expressions for the characteristic fields and speeds. As pointed out above, this point represents a fundamental ingredient in the study of the appropriate boundary conditions if boundaries are present in the integration domain. This constitutes only a preliminary study of the well-posedness of the evolution system since no stability analysis whatsoever will be considered. Certainly further analysis is required. However, in the absence of a full treatment and being ultimately motivated by practical numerical implementations needs, the level of rigor and completeness in this article is adapted to the achievement of limited but concrete results.

On behalf of self-consistency, and in spite of the lack of a fully rigorous treatment of the FCF subsidiary system, we also aim at discussing certain (numerical) algorithms devised to guarantee the fulfillment of the Dirac gauge along the evolution. Though this is not the substitute of a formal proof it provides, on the one hand, support for the coherence among the reduced, gauge and constrained systems. On the other hand, and more importantly from a practical point of view, the implementation of the FCF scheme is then guaranteed to be fully-constrained, even in numerical implementations where errors can occur even if analytic well-posedness has been established.

The article is organized as follows. Section 2.2 presents first-order formulation of the FCF scheme, more concretely of its reduced system. In section 2.3 the characteristic structure of the reduced system is analyzed, with a brief application to inner boundaries in excised black hole spacetime evolutions. Section 2.4 discusses the possibility of writing the first-order reduced FCF system as a system of conservation laws, by making explicit use of the Dirac gauge. In section 2.5 two different manners of enforcing the Dirac gauge in the evolution are introduced, providing key support for overall consistency and guaranteeing the fully-constrained character of the scheme. Finally section 2.6 concludes with a discussion of the results.

2.2 First-order reduction of the reduced system in the FCF

Equations governing the evolution of h^{ij} in the FCF are:

$$\begin{aligned}
& \frac{\partial^2 h^{ij}}{\partial t^2} - \frac{N^2}{\psi^4} \tilde{\gamma}^{kl} \mathcal{D}_k \mathcal{D}_l h^{ij} - 2\mathcal{L}_\beta \frac{\partial h^{ij}}{\partial t} + \mathcal{L}_\beta \mathcal{L}_\beta h^{ij} = \mathcal{L}_\beta h^{ij} + \frac{4}{3} \mathcal{D}_k \beta^k \left(\frac{\partial}{\partial t} - \mathcal{L}_\beta \right) h^{ij} \\
& - \frac{N}{\psi^6} \mathcal{D}_k Q \left(\mathcal{D}^i h^{jk} + \mathcal{D}^j h^{ik} - \mathcal{D}^k h^{ij} \right) + \left[\left(\frac{\partial}{\partial t} - \mathcal{L}_\beta \right) \ln N \right] \left[\left(\frac{\partial}{\partial t} - \mathcal{L}_\beta \right) h^{ij} \right. \\
& \left. - \frac{2}{3} \mathcal{D}_k \beta^k h^{ij} + (L\beta)^{ij} \right] + \frac{2}{3} \left[\left(\frac{\partial}{\partial t} - \mathcal{L}_\beta \right) \mathcal{D}_k \beta^k - \frac{2}{3} \left(\mathcal{D}_k \beta^k \right)^2 \right] h^{ij} \\
& - \left(\frac{\partial}{\partial t} - \mathcal{L}_\beta \right) (L\beta)^{ij} + \frac{2}{3} \mathcal{D}_k \beta^k (L\beta)^{ij} + 2N\psi^{-4} Z^{ij} \\
& - 2N\psi^{-6} \left[\tilde{\gamma}^{ik} \tilde{\gamma}^{jl} \mathcal{D}_k \mathcal{D}_l Q + \frac{1}{2} \left(h^{ik} \mathcal{D}_l h^{lj} + h^{jk} \mathcal{D}_k h^{il} - h^{kl} \mathcal{D}_k h^{ij} \right) \mathcal{D}_l Q - \frac{1}{3} \tilde{\gamma}^{ij} \tilde{\gamma}^{kl} \mathcal{D}_k \mathcal{D}_l Q \right] \\
& + (2N)^2 \left[\tilde{\gamma}_{kl} A^{ik} A^{jl} - 4\pi \left(\psi^4 S^{ij} - \frac{1}{3} S \tilde{\gamma}^{ij} \right) \right], \tag{2.13}
\end{aligned}$$

where S^{ij} and S are, respectively, the spatial components of the stress tensor $S_{\alpha\beta} := \gamma_\alpha^\mu \gamma_\beta^\nu T_{\mu\nu}$, associated with the matter energy-momentum tensor $T_{\mu\nu}$, and its trace. $(L\beta)^{ij}$ is the conformal Killing operator associated with the flat metric f_{ij} acting on the vector field β^i :

$$(L\beta)^{ij} := \mathcal{D}^i \beta^j + \mathcal{D}^j \beta^i - \frac{2}{3} \mathcal{D}_k \beta^k f^{ij}, \tag{2.14}$$

and the auxiliary quantities Q and Z^{ij} are

$$Q := N\psi^2, \tag{2.15}$$

$$\begin{aligned}
Z^{ij} &= N \left[\tilde{R}_*^{ij} + 8\psi^{-2} \left(\tilde{\gamma}^{ik} \mathcal{D}_k \psi \right) \left(\tilde{\gamma}^{jl} \mathcal{D}_l \psi \right) \right] \\
&+ 4\psi^{-1} \left(\tilde{\gamma}^{ik} \mathcal{D}_k \psi \right) \left(\tilde{\gamma}^{jl} \mathcal{D}_l N \right) + 4\psi^{-1} \left(\tilde{\gamma}^{jk} \mathcal{D}_k \psi \right) \left(\tilde{\gamma}^{il} \mathcal{D}_l N \right) \\
&- \frac{1}{3} N \left[\tilde{R}_* + 8\psi^{-2} \mathcal{D}_k \psi \left(\tilde{\gamma}^{kl} \mathcal{D}_l \psi \right) \right] \tilde{\gamma}^{ij} - \frac{8}{3} \psi^{-1} \mathcal{D}_k \psi \left(\tilde{\gamma}^{kl} \mathcal{D}_k N \right) \tilde{\gamma}^{ij}. \tag{2.16}
\end{aligned}$$

The symmetric tensor \tilde{R}_*^{ij} is defined by

$$\begin{aligned}
\tilde{R}_*^{ij} &:= \frac{1}{2} \left[-\mathcal{D}_l h^{ik} \mathcal{D}_k h^{jl} - \tilde{\gamma}_{kl} \tilde{\gamma}^{mn} \mathcal{D}_m h^{ik} \mathcal{D}_n h^{jl} + \tilde{\gamma}^{nl} \mathcal{D}_k h^{mn} \left(\tilde{\gamma}^{ik} \mathcal{D}_m h^{jl} + \tilde{\gamma}^{jk} \mathcal{D}_m h^{il} \right) \right] \\
&+ \frac{1}{4} \tilde{\gamma}^{ik} \tilde{\gamma}^{jl} \mathcal{D}_k h^{mn} \mathcal{D}_l \tilde{\gamma}_{mn}, \tag{2.17}
\end{aligned}$$

and the scalar \tilde{R}_* is

$$\tilde{R}_* := \frac{1}{4} \tilde{\gamma}^{kl} \mathcal{D}_k h^{mn} \mathcal{D}_l \tilde{\gamma}_{mn} - \frac{1}{2} \tilde{\gamma}^{kl} \mathcal{D}_k h^{mn} \mathcal{D}_n \tilde{\gamma}_{mn}. \tag{2.18}$$

Let us write Eqs. (2.13) as a first-order system, by introducing the following auxiliary variables:

$$u^{ij} := \frac{\partial h^{ij}}{\partial t}, \quad (2.19)$$

$$w_k^{ij} := \mathcal{D}_k h^{ij}. \quad (2.20)$$

With these new variables the system for h^{ij} can be cast into

$$\frac{\partial u^{ij}}{\partial t} - \frac{N^2}{\psi^4} \tilde{\gamma}^{kl} \mathcal{D}_k w_l^{ij} - 2\beta^k \mathcal{D}_k u^{ij} + \beta^k \beta^l \mathcal{D}_k w_l^{ij} = \phi^{ij} \left(\beta^k, N, \psi, \partial_\mu \beta^k, \partial_\mu N, \partial_\mu \psi, h^{ij}, u^{ij}, w_k^{ij} \right), \quad (2.21)$$

where ϕ^{ij} are source terms which do not contain partial derivatives of u^{ij} or w_k^{ij} . From definition (2.20) we obtain

$$\frac{\partial w_k^{ij}}{\partial t} = \mathcal{D}_k u^{ij}, \quad (2.22)$$

where we have taken into account that $\partial_t f^{ij} = 0$. In terms of the above new auxiliary variables, the system of Eqs. (2.19, 2.21, 2.22), can be written as:

$$\frac{\partial \bar{\mathbf{v}}}{\partial t} + \mathbf{A}^l \mathcal{D}_l \bar{\mathbf{v}} = \mathbf{g} \left(\beta^k, N, \psi, \partial_\mu \beta^k, \partial_\mu N, \partial_\mu \psi, h^{ij}, u^{ij}, w_k^{ij} \right), \quad (2.23)$$

where the vector $\bar{\mathbf{v}}$ is:

$$\bar{\mathbf{v}} = \begin{pmatrix} (h^{ij}) \\ (u^{ij}) \\ (w_k^{ij}) \end{pmatrix}, \quad (2.24)$$

and the source \mathbf{g} is

$$\mathbf{g} \left(\beta^k, N, \psi, \partial_\mu \beta^k, \partial_\mu N, \partial_\mu \psi, h^{ij}, u^{ij}, w_k^{ij} \right) = \begin{pmatrix} (u^{ij}) \\ (\phi^{ij}) \\ (0) \end{pmatrix}. \quad (2.25)$$

In these equations, $\bar{\mathbf{v}}$ and \mathbf{g} are vectors of dimension 30, as it results from the symmetry properties of h^{ij} , u^{ij} , and w_k^{ij} . Let us remind that, besides the above symmetry properties, the following algebraic constraints have to be satisfied: i) $\det \tilde{\gamma}_{ij} = \det f_{ij}$; and $w_i^{ij} = 0$, which is equivalent to Dirac's gauge. In order to write the matrices of the system in a simple way, the following auxiliary quantities are defined:

$$q^{ij} := \beta^i \beta^j - N^2 \psi^{-4} \tilde{\gamma}^{ij}, \quad (2.26)$$

$$Q^i := (q^{1i} \quad q^{2i} \quad q^{3i}), \quad (2.27)$$

$$-\delta^i := \begin{pmatrix} -\delta_1^i \\ -\delta_2^i \\ -\delta_3^i \end{pmatrix}. \quad (2.28)$$

- *Case 3:* $\zeta_i q^{ij} = 0, \forall j = 1, 2, 3$. This is a stronger case than the previous one. Again from the definition of q^{ij} , we have:

$$\zeta_i (\beta^i \beta^j - N^2 \psi^{-4} \tilde{\gamma}^{ij}) = 0 \Leftrightarrow (\zeta_i \beta^i) \beta^j = N^2 \zeta^j. \quad (2.37)$$

From this, and the decomposition $\beta^i = (\beta^\parallel) \zeta^i + (\beta^\perp)^i$, it follows:

$$\zeta_i q^{ij} = 0 \Leftrightarrow (\beta^\perp)^i = 0 \quad \text{and} \quad (\beta^\parallel)^2 = N^2 \quad (2.38)$$

This is just a stronger version of the second case above.

As a consequence of the above analysis we can set up the following lemma.

Lemma 3: The (right-)eigenvectors associated with the matrix $\mathbf{A}^l \zeta_l$ define a complete system iff i) the lapse N does not vanish, and ii) the projection of the evolution vector onto the plane spanned by n^μ and ζ^μ , i.e. $(t^\parallel)^\mu = N n^\mu + b_\beta \zeta^\mu$, is non-null, i.e. $(\beta^\parallel)^2 \neq N^2$.

In the eigenvalue problem (2.30), ζ^i stands for an arbitrary spatial vector. In particular, we can always choose $\zeta^i = \beta^i$. In that case, the degeneracy condition in cases 2 and 3 above reduces to $\beta^i \beta_i = N^2$. This happens if the vector t^μ becomes null. Moreover, if the vector t^μ is spacelike then we are in case 2, since then there exists a vector ζ^i (in fact, a cone obtained by the rotation of the non-vanishing β^i by an appropriate angle) such that the projection of β^i onto that ζ^i , referred to as $(\beta^\parallel)^i$, satisfies $(\beta^\parallel)^i (\beta^\parallel)_i = (\zeta_i \beta^i)^2 = N^2$. We conclude:

Proposition 1 : The system (2.23) is strongly hyperbolic if t^μ is timelike, i.e. if $N \neq 0$ and $N^2 - \beta^i \beta_i > 0$.

In some particular cases, degeneracy in the eigenvalues can occur. In particular, it could happen that one of the eigenvalues λ_+ or λ_- coincides with λ_0 . These degeneracies can appear where:

$$\lambda_+^{(\zeta)} \lambda_-^{(\zeta)} = 0 \Leftrightarrow (\beta^\mu \zeta_\mu)^2 = N^2 (\zeta^\mu \zeta_\mu). \quad (2.39)$$

Again, one can consider ζ^i to be unitary. Hence, either λ_+ or λ_- vanishes when $(\beta^\parallel)^2 = N^2$. As seen in (2.36), in this case the system of eigenvectors is incomplete.

Another relevant property is the following:

Proposition 2: All the characteristic fields associated with the eigenvalue problem (2.30) are linearly degenerate, i.e., they satisfy the following condition:

$$\mathbf{D} \lambda_p(\bar{v}) \cdot r_p(\bar{v}) = 0, \quad (2.40)$$

where r_p is the eigenvector associated to the eigenvalue λ_p , and the operator \mathbf{D} is defined in the space of the variables of the system.

This shows the good behaviour of the Dirac gauge since, in the language from fluid dynamics, it means that no shocks can be propagated along these curves, in particular gauge shocks. Hence, if there were discontinuities, they have to be contact discontinuities.

Regarding the characteristics speeds $\lambda_\pm^{(\zeta)}$ we have:

Corollary 1: The non-zero eigenvalues associated with ζ^i correspond to the coordinate velocity of light.

This feature, which is an expected result, can be shown by considering a unitary ζ^i and a curve whose spatial part points in the ζ^i direction: $\frac{dx^i}{dt} = \left| \frac{dx^i}{dt} \right| \zeta^i$. Using the 3+1 expression of the metric, the vanishing of the line element of the curve, where the component of β^i in the ζ^i direction is considered, is imposed. It follows, using the expression for $\lambda^{(\zeta)}$ in (2.31) that $\lambda^{(\zeta)} = \left| \frac{dx}{dt} \right|$.

2.3.1 Application to inner boundary conditions

The explicit expressions (2.31) for the characteristic speeds are specially useful in the assessment of the boundary conditions to be imposed on a given border. We illustrate this by considering inner boundaries in the context of excised black hole spacetimes. Before doing so, let us underline that the FCF can be employed in combination with any of the standard techniques dealing with the black hole singularity in numerical evolutions of black hole spacetimes, namely *excision*, *punctures* or *stuffed black holes*. However, the excision technique is favoured if (the elliptic subsystem of) the FCF is implemented by means of spectral methods. Focusing on the excision approach, let us denote by \mathcal{S}_t the inner sphere employed as inner boundary at a given spacelike slice Σ_t , and by \mathcal{H} the worldtube hypersurface generated along the evolution by *piling up* the different \mathcal{S}_t . A natural expectation is that no inner boundary conditions should be prescribed for radiation fields on inner superluminal (growing) inner boundaries. This would avoid the need to incorporate boundary conditions in the well-posedness analysis of the associated initial boundary value problem. From this reason, spacelike inner hypersurfaces \mathcal{H} are good candidates for inner boundary conditions. However, this general idea must be assessed in the context of every specific evolution scheme. In our particular case, we must check that characteristic speeds (2.31) are outgoing (with respect to the integration domain). The tangent vector h^μ to \mathcal{H} which is normal to each \mathcal{S}_t , and transports \mathcal{S}_t into $\mathcal{S}_{t+\delta t}$, can be written as

$$h^\mu = Nn^\mu + h_s s^\mu, \quad (2.41)$$

where s^μ is the normal vector to \mathcal{S}_t , lying on Σ_t and pointing toward spatial infinity. Then, since the norm of h^μ is given by $h^\mu h_\mu = -N^2 + h_s^2$, it follows that \mathcal{H} is spacelike as long as $b > N$. Choosing a coordinate system adapted to \mathcal{H} , i.e. where all the spheres \mathcal{S}_t stay at the same coordinate position—say $r = \text{const} = r_o$ —it follows that $h_s = \beta^i s_i \equiv \beta^\perp$. In this case, \mathcal{H} is spacelike as long as $\beta^\perp > N$. Evaluating expression (2.31) for $\zeta^i = s^i$, it follows

$$\lambda_\pm^{(s)} = -\beta^\perp \pm N \quad (2.42)$$

From this it follows that:

Corollary 2: For a coordinate system adapted to a spacelike inner worldtube \mathcal{H} , where $\beta^\perp > N$, no ingoing radiative modes flow into the integration domain Σ_t at the excision surface.

Under these conditions no inner boundary conditions whatsoever must be prescribed for the hyperbolic part. Of course, it is not obvious how to choose dynamically an inner boundary \mathcal{H} that is guaranteed to be spacelike during the evolution. A proposal in this line has been presented in [268] in the context of the dynamical trapping horizon framework (see e.g. Ref. [222]). Quasi-local approaches to black hole horizons aim at modeling the boundary of a black hole region as world-tubes of apparent horizons (\mathcal{S}_t). Dynamical horizons provide a geometric prescription for \mathcal{H} that is guaranteed to be spacelike, as long as the black hole is dynamical, and remain inside the event horizon, if cosmic censorship holds. The corresponding geometric dynamical horizon characterization is enforced as an inner boundary condition on the elliptic part of the FCF, in particular on the shift equation (2.12). This shows the key interplay between elliptic and hyperbolic modes in the coupled fully-constrained PDE evolution system. Note however that, according to Proposition 1, the hyperbolic evolution system ceases to be strongly hyperbolic. In fact, the evolution vector t^μ , tangent to \mathcal{H} in the adapted coordinate system, becomes spacelike in a finite region. This can be bypassed by adopting a coordinate system in which the coordinate radii of the \mathcal{S}_t slices grow in time: $r = r(t) \neq 0$, where $r(t)$ is appropriately *chosen*. In this case, $h_s = \beta^\perp$ holds no longer, and this relation is rather substituted by

and the *parentheses* in the subindices represent a symmetric sum, e.g., $w_{(1}^{ij}\delta_2^l) = w_1^{ij}\delta_2^l + w_2^{ij}\delta_1^l$.

These matrices have the same eigenvalues as the matrices \mathbf{A}^l . The corresponding eigenvectors are different but they keep the same fundamental properties as the ones associated to the matrices \mathbf{A}^l , namely they define a complete system. Hence, the following lemma is in order:

Proposition 3: Taking advantage of Dirac's gauge, it is possible to convert the hyperbolic part of the coupled elliptic-hyperbolic system of the FCF formalism, into a (strongly) hyperbolic system of conservation laws (with sources).

2.5 Preservation of the Dirac gauge in the evolution: the Dirac system

The importance of the enforcement of the Dirac gauge during the evolution in time has already been stressed in the introduction. In this section we give a brief description of some numerical algorithms that can be used to fulfill the Dirac gauge, when solving the reduced system (2.10). In particular, we do not intend to provide a formal proof of the consistency of the method. Because of the unimodularity of the conformal metric $\tilde{\gamma}_{ij}$, the symmetric tensor h^{ij} has only five degrees of freedom. For simplicity, here we shall illustrate the scheme by considering the case where the trace $h = f_{ij}h^{ij} = 0$. The unimodular condition would be satisfied by an iteration on the value of the trace, as described in [73]. We consider the particular case of spherical polar coordinate system (r, θ, φ) , and note by Δ the flat Laplace operator, i.e.

$$\Delta := \mathcal{D}_i \mathcal{D}^i = \frac{\partial^2}{\partial r^2} + \frac{2}{r} \frac{\partial}{\partial r} + \frac{1}{r^2} \Delta_{\theta\varphi} \quad , \quad (2.47)$$

where $\Delta_{\theta\varphi}$ involves only angular derivatives. Thus, the problem to be solved can be written as a wave equation with constraints

$$\left(\frac{\partial^2}{\partial t^2} - \Delta \right) h^{ij} = \mathcal{S}^{ij} \quad , \quad (2.48)$$

$$\mathcal{D}_j h^{ij} = 0 \quad , \quad (2.49)$$

$$h = 0 \quad ; \quad (2.50)$$

where the source \mathcal{S}^{ij} gathers all the other terms of Eqs. (2.13), including the shift terms in the differential operator. The structure of the differential operator in the left-hand side is here simplified with respect to the full evolution one of Sec. 2.2, in order to focus on the propagation aspects, which are already contained in the simple wave operator. The full evolution operator can also be handled with a similar technique, but involving more technical justifications. The system (2.48)-(2.50) can be seen as the evolution of two scalar fields, two dynamical degrees of freedom, from which one recovers the full tensor h^{ij} using the trace and divergence-free conditions. To gain insight, it is helpful to decompose the tensor on a basis of Mathews-Zerilli [313, 498] tensorial spherical harmonics. We use the basis of six families of *pure-spin tensor harmonics* as referred to by Thorne [464], with the same notations: $\mathbf{T}^{L_0, \ell m}$, $\mathbf{T}^{E_1, \ell m}$, $\mathbf{T}^{B_1, \ell m}$, $\mathbf{T}^{E_2, \ell m}$, $\mathbf{T}^{B_2, \ell m}$, $\mathbf{T}^{T_0, \ell m}$. If we note the coefficients of h^{ij} in this basis $(c^{L_0, \ell m}, c^{E_1, \ell m}, c^{B_1, \ell m}, c^{E_2, \ell m}, c^{B_2, \ell m}, c^{T_0, \ell m})$, we can define for any rank 2 symmetric tensor the

following six scalar fields:

$$\begin{aligned}
L_0 &:= \sum_{\ell,m} c^{L_0,\ell m} Y_{\ell m} = h^{rr}, \\
\eta &:= \sum_{\ell \geq 1, m} c^{E_1,\ell m} Y_{\ell m}, \\
\mu &:= \sum_{\ell \geq 1, m} c^{B_1,\ell m} Y_{\ell m}, \\
\mathcal{W} &:= \sum_{\ell \geq 2, m} c^{E_2,\ell m} Y_{\ell m}, \\
\mathcal{X} &:= \sum_{\ell \geq 2, m} c^{B_2,\ell m} Y_{\ell m}, \\
T_0 &:= \sum_{\ell,m} c^{T_0,\ell m} Y_{\ell m}, \tag{2.51}
\end{aligned}$$

where $Y_{\ell m}(\theta, \varphi)$ are the scalar spherical harmonics, which are eigenfunctions of the angular Laplace operator $\Delta_{\theta\varphi} Y_{\ell m} = -\ell(\ell+1)Y_{\ell m}$. Note that there is a one-to-one relation between the six components of h^{ij} and these six scalar fields. The trace condition (2.50) simply turns into $T_0 + h^{rr} = 0$, therefore we shall replace T_0 with $-h^{rr}$ in all forthcoming expressions. The divergence-free conditions (2.49) turn into:

$$\frac{\partial h^{rr}}{\partial r} + \frac{3h^{rr}}{r} + \frac{1}{r} \Delta_{\theta\varphi} \eta = 0, \tag{2.52}$$

$$\frac{\partial \eta}{\partial r} + \frac{3\eta}{r} + (\Delta_{\theta\varphi} + 2) \frac{\mathcal{W}}{r} - \frac{h^{rr}}{2r} = 0, \tag{2.53}$$

$$\frac{\partial \mu}{\partial r} + \frac{3\mu}{r} + (\Delta_{\theta\varphi} + 2) \frac{\mathcal{X}}{r} = 0; \tag{2.54}$$

where all the angular derivatives are expressed in terms of $\Delta_{\theta\varphi}$, introduced in Eq. (2.47).

A first way to solve the system (2.48)-(2.50) has been described in Ref. [73] and uses evolution equations for h^{rr} and μ , from which other scalar fields are deduced through the gauge equations (2.52)-(2.54) as solutions of the angular Laplace operator, with radial derivatives as sources. However, this method has the great disadvantage of requiring the computation of two radial derivatives to get h^{ij} , when the source \mathcal{S}^{ij} already contains second-order radial derivatives of h^{ij} . This fourth-order derivation introduces a great amount of numerical noise, which has been observed to rapidly spoil the numerical integration. An alternative way is to evolve two other scalar fields and then to integrate (or solve PDEs coming from) the Dirac gauge condition to obtain the others. Unfortunately, this is not possible using only the six scalar fields (2.51), but one can devise the following procedure in a similar spirit.

Any rank 2 symmetric tensor T^{ij} can be split into two pieces:

$$T^{ij} = \left(\hat{L}V \right)^{ij} + \tilde{T}^{ij} \equiv \mathcal{D}^i V^j + \mathcal{D}^j V^i + \tilde{T}^{ij}, \tag{2.55}$$

with $\mathcal{D}_j \tilde{T}^{ij} = 0$. For a given T^{ij} the divergence of Eq. (2.55) allows for the determination of the vector V^i through the elliptic PDE

$$\mathcal{D}^k \mathcal{D}_k V^i + \mathcal{D}^i \mathcal{D}_j V^j = \mathcal{D}_j T^{ij}, \tag{2.56}$$

where V^i is fixed up to isometries of f_{ij} , which are set by the choice of boundary conditions. If we now return to the case $T^{ij} = h^{ij}$ and consider only asymptotically flat spatial metric defined on \mathbb{R}^3 —no holes—the Dirac gauge condition (2.49) is equivalent to having $V^i = 0$, since there are no Euclidean symmetries vanishing at infinity. If one similarly seeks three scalar fields (A, B, C) such that:

$$A = B = C = 0 \iff \tilde{T}^{ij} = 0, \quad (2.57)$$

one can check that a solution is:

$$A = \frac{\partial \mathcal{X}}{\partial r} - \frac{\mu}{r}, \quad (2.58)$$

$$B = \frac{\partial \mathcal{W}}{\partial r} - \frac{\Delta_{\theta\varphi} \mathcal{W}}{2r} - \frac{\eta}{r} - \frac{h^{rr}}{4r}, \quad (2.59)$$

$$C = \frac{\partial h^{rr}}{\partial r} + \frac{3h^{rr}}{r} + 2\Delta_{\theta\varphi} \left(\frac{\partial \mathcal{W}}{\partial r} + \frac{\mathcal{W}}{r} \right). \quad (2.60)$$

In the present case where the trace (or the determinant) is given, B and C are actually coupled and it is sufficient to consider:

$$\begin{aligned} \tilde{B} &= \sum_{\ell, m} \tilde{B}^{\ell m} Y_{\ell m}, \text{ with} \\ \tilde{B}^{\ell m} &= (\ell + 2) \left(\frac{\partial \mathcal{W}}{\partial r} + \ell \frac{\mathcal{W}}{r} \right) - \frac{2\eta}{r} - \frac{1}{2(\ell + 1)} \left(\frac{\partial h^{rr}}{\partial r} + (\ell + 4) \frac{h^{rr}}{r} \right), \end{aligned} \quad (2.61)$$

to recover B and C using the trace. A nice property of A and \tilde{B} is that, when expressed in terms of these potentials related to h^{ij} , the tensor Poisson equation, with F^{ij} being a symmetric-tensor representing a source:

$$\Delta h^{ij} = F^{ij} \quad (2.62)$$

has a rather simple form. Namely, if we define F^A and $F^{\tilde{B}}$ as the scalar potentials similar to A and \tilde{B} , but deduced from F^{ij} , a consequence of Eq. (2.62) is:

$$\begin{aligned} \Delta A &= F^A, \\ \tilde{\Delta} \tilde{B} &= F^{\tilde{B}}, \end{aligned} \quad (2.63)$$

with

$$\tilde{\Delta} := \frac{\partial^2}{\partial r^2} + \frac{2}{r} \frac{\partial}{\partial r} + \frac{1}{r^2} \tilde{\Delta}_{\theta\varphi} \quad \text{and} \quad \tilde{\Delta}_{\theta\varphi} Y_{\ell m} := -\ell(\ell - 1) Y_{\ell m}. \quad (2.64)$$

Obviously, a very similar property holds for the wave equation (2.48). Therefore, a way of solving numerically the constrained system of Eqs. (2.48)-(2.50), by making use of the potentials A and B , is the following. With the source \mathcal{S}^{ij} and h^{ij} known at the initial hypersurface, it is possible to deduce the potentials \mathcal{S}^A and $\mathcal{S}^{\tilde{B}}$ of the source and thus to advance the potentials A and \tilde{B} of h^{ij} to next time-step through the evolution equations

$$\begin{aligned} \left(\frac{\partial^2}{\partial t^2} - \Delta \right) A &= \mathcal{S}^A, \\ \left(\frac{\partial^2}{\partial t^2} - \tilde{\Delta} \right) \tilde{B} &= \mathcal{S}^{\tilde{B}}. \end{aligned} \quad (2.65)$$

Then the six scalar fields (2.51) can be computed by solving the PDE system formed by the following five elliptic equations: the definitions of A and \tilde{B} , i.e. Eqs. (2.58) and (2.61), together with the Dirac gauge conditions (2.52)-(2.54) plus the trace-free condition (2.50) —used to get T_0 . All the components of h^{ij} can be finally recovered by taking angular derivatives of the scalar fields defined in Eqs. (2.51). With this algorithm, only two scalar potentials, A and \tilde{B} , are evolved in time. The whole tensor is deduced from these potentials and the gauge and trace conditions. Note that, when decomposing all the scalar fields onto a spherical harmonics function basis, the elliptic system of five PDEs described above reduces to a system of coupled *ordinary* differential equations in the radial coordinate r .

With either of these approaches (the one described here or that presented in Ref. [73]) it is possible to evolve two scalar potentials using hyperbolic wave-like operators and recover the symmetric tensor h^{ij} through an elliptic system of PDEs obtained from the gauge conditions. A numerical implementation of these techniques being beyond the scope of the present article, we have here only exhibited both algorithms in order to show that it is, in principle, possible to build-up the whole conformal metric from the gauge conditions, while being consistent with the evolution equations. This might inversely be linked toward the property of the Dirac gauge system being preserved by the 3+1 evolution system. Future numerical developments in these directions shall certainly bring better insight into the problem.

2.6 Discussion.

All evolution formalisms for the resolution of Einstein equations as an initial value boundary problem exploit the intrinsic hyperbolicity of Eqs. (2.1), although the associated evolution systems are not necessarily hyperbolic from the PDE theory point of view [188]. In the present case of the FCF formalism [73], Einstein equations result in a coupled elliptic-hyperbolic PDE system. The hyperbolic part PDE evolution system consists of the *reduced system*, governing the evolution of the gravitational degrees of freedom, whereas the elliptic part is formed by the *constrained system* and part of the *gauge system* (maximal slicing equation). In fact, in the context of the algorithms presented in section 2.5, the elliptic Dirac system, Eqs. (2.52)-(2.54), can be actually seen as a part of the PDE evolution system. In summary, the evolution PDE system is formed by the reduced, constraint, and gauge systems, whereas the fulfillment of the subsidiary system, represented by Eq. (91) in Ref. [73] for β^i , can be used as a control test of the scheme along the evolution. We have carried out a first analysis of the mathematical structure of the PDE evolution system paying particular attention to the equations (2.10) governing the evolution for the deviation h^{ij} of the conformal metric from the flat fiducial one f_{ij} , i.e. $h^{ij} = \tilde{\gamma}^{ij} - f^{ij}$. Dirac's gauge plays an important role in getting a well defined hyperbolic structure. This elliptic gauge is close in spirit and properties to other gauges employed in the literature, like the *spatial harmonic* gauge in [17], the *minimal distortion* introduced by York & Smarr, the *new minimal distortion* gauge introduced by Jantzen & York, or the numerically motivated *pseudo-minimal distortion* gauge by Nakamura, *approximate minimal distortion* by Shibata or the *Gamma freezing* (cf. Secs. 9.3. and 9.4 in Ref. [214] for a review of them). In particular, all of them can be written as elliptic equations on the shift vector β^i . The Dirac gauge fixes spatial coordinates in the evolution (including on the initial data, as the *spatial harmonic gauge* does) up to boundary conditions. For boundary conditions (enforced when solving the elliptic PDE for β^i) such that the evolution vector is timelike, the Dirac gauge provides a sufficient condition for the strong hyperbolicity of Eq. (2.10). Moreover, using this gauge it is possible to derive a *flux vector* in terms of which the first-order system of equations, equivalent to (2.10), has the structure of a hyperbolic

system of conservation laws (with sources). Likewise, the analysis of the characteristics sheds light on the prescription of inner boundary conditions on a spacelike inner cylinder, when employing an excision approach to black hole evolutions. More generally, maximal and Dirac gauges can be relaxed to admit more general gauges, while preserving the hyperbolic properties of the system but possibly complicating the structure of the sources.

Having said this, it is clear that further analysis is necessary. First, particular attention should be paid to the source terms in equation (2.13). They can introduce, in the so-called stiff case, new characteristic time scales (relaxation times in the language of fluid dynamics) which may be much smaller than the CFL (Courant-Friedrichs-Lewy) numerical time step (see, e.g., [271, 394, 318]). In particular, authors in reference [271] have studied general hyperbolic systems with supercharacteristic relaxations, and they shown in which conditions a source term can be damping or, on the contrary, enforces growth of instabilities. Looking, in our case, at the quantity R_*^{ij} (Eq. (2.17)), one can notice the presence of quadratic terms in the w_k^{ij} ; it suggests that huge spatial gradients of h^{jk} can introduce some degree of stiffness in the source terms. Second, nothing has been said about the possible outer boundary conditions to be prescribed when studying the initial boundary value problem with an outer timelike cylinder. Certainly, in this case the well-posedness analysis is more complicate. However, thanks the enforcement of the constraint along the evolution, there is no need of devising specific constraint preserving boundary conditions, and Sommerfeld-like conditions as in [341, 96] can be straightforwardly employed. Third, nothing has been said about the elliptic part and its coupling with the hyperbolic subsystem. On the one hand, this coupling is crucial in the overall well-posedness of the problem, as clearly illustrated in the inner boundary conditions issue, where inner boundary conditions on the elliptic part determine the ingoing or outgoing nature of the characteristics in the hyperbolic part. On the other hand, the analysis of the elliptic system by itself represents an outstanding challenge. This is illustrated by the XCTS elliptic system [364, 358] referred to in Section 2.1.2, very closely related to the FCF elliptic subsystem. We note that, in this case, no results on existence are available and very little is known on uniqueness, where recent numerical [365, 265] and analytical works [53, 480] works point toward the essential non-uniqueness of the system (related to a wrong sign in the differential operator of the maximal slicing equation). Fourth, nothing has been said about consequences on well-posedness of coupling matter equations to the gravitational degrees of freedom.

Although our analysis is far from being exhaustive, it has the advantage of giving some clues about which numerical strategies are the most convenient in order to solve Einstein equations in the FCF formalism. In this sense, we have attempted to obtain some limited but concrete results, rather than remained frozen by the “non-attainability” of complete and fully rigorous results.

Chapitre 3

Improved constrained scheme for the Einstein equations : An approach to the uniqueness issue

Version publiée : I. Cordero-Carrión, P. Cerdá-Durán, H. Dimmelmeier, J. L. Jaramillo, J. Novak et E.ourgoulhon, *Physical Review D* **79**, 024017 (2009).

Sommaire

3.1	Introduction	69
3.2	The fully constrained formalism and CFC	71
3.3	The new scheme in the conformally flat case	75
3.4	Numerical results	79
3.5	Generalization to the fully constrained formalism	85
3.6	Discussion	87
3.A	Consistency of the approximation	90

3.1 Introduction

The recent years have seen the successful application of numerical codes to accurately calculate the spacetimes of compact astrophysical objects like collapsing stellar cores, (proto-)neutron stars, and black holes. Most of these codes are based on the $3 + 1$ formalism of general relativity (see, e.g., [486, 7, 214] for reviews). They typically fall into two classes. One approach relies on the *free evolution* of the $3 + 1$ Einstein equations, recast in order to cure long-term stability problems. Here the constraint equations are only solved initially, and closely monitored at each timestep to control the accuracy of the numerical solution.

Alternatively, formulations based on a *constrained evolution*, where the constraints are solved in parallel with evolution equations, have proven to be successful as well. Such approaches exhibit the advantage that the solution cannot violate the constraints by definition (within the accuracy of the numerical scheme). In particular, the conformally flat approximation [260, 482] (hereafter CFC) of the

full Einstein equations, which constitutes a fully constrained formulation, has shown to yield long-term stable evolutions of such astrophysical scenarios (see, e.g., [149, 345, 397, 3]). However, apart from computational challenges, arising from the need to frequently solve the elliptic constraint equations, constrained formulations suffer from mathematical non-uniqueness problems when the configuration becomes too compact. In the case of the collapse of a stellar core or a (proto-)neutron star to a black hole, such a situation is encountered already before the apparent horizon forms. This issue has in the past been prohibitive to successfully applying such formulations in numerical simulations of a wide range of astrophysical problems.

The non-uniqueness of solutions stems from the non-linearity of the constraint equations and has been studied within the so-called *extended conformal thin sandwich (XCTS)* [487, 364, 358] approach to the initial data problem in general relativity. In Ref. [365] a parabolic branching was numerically found in the solutions to the XCTS equations for perturbations of Minkowski spacetime, providing the first evidence of non-uniqueness in this elliptic system. First analytical studies have been carried out in [53, 480], finding support for the genericity of this non-uniqueness behavior. More specifically, the XCTS elliptic system is formed by the Einstein constraint equations in a *conformal thin sandwich (CTS)* decomposition [487] supplemented with an additional elliptic equation for the lapse function, which follows from the maximal slicing condition. Although no general results on existence and uniqueness for the XCTS system are available (in contrast to the CTS case and similar elliptic systems encompassing only the constraints; see, e.g., [347, 348, 486, 487, 364]), the analysis in [53] strongly suggests the presence of a *wrong* sign in a certain term of the lapse equation as the culprit for the loss of uniqueness, essentially because it spoils the application of a maximum principle to guarantee uniqueness. Moreover, in these circumstances (namely, the existence of a non-trivial kernel for the XCTS elliptic operator) it is shown in [480] that the parabolic behavior found in [365] is indeed generic.

Certain constrained evolution formalisms which incorporate elliptic gauges in their schemes contain elliptic subsystems which share essential points with the XCTS equations. Non-uniqueness in the elliptic subsystem is certainly an issue for the well-posedness of the whole elliptic-hyperbolic evolution system. In numerical implementations this can depend on the employed numerical scheme, in particular on its capability to remain *close* to one of the solutions, at least as long as the solution stays sufficiently apart from the branching point. In fact, constrained or partially constrained evolutions have shown to be robust in a variety of contexts (see, e.g., the references in [389] and Sec. 5.2.2 of [267]). However, the problems described above have also emerged, for instance in the axisymmetric case in [118, 387] (see also [392]). The analysis in [389] concludes that the reason behind the failures in these axisymmetric formulations is in fact related to the presence of *wrong* signs or, more precisely, to the *indefinite* character of certain non-linear Helmholtz-like equations present in the scheme (see [389] for details and also for a parallel numerical discussion in terms of a class of relaxation methods for the convergence of the elliptic solvers). Regarding the full three-dimensional case, fully constrained formalisms have been presented in [73, 134].

The goal of the present work is to discuss a scheme addressing the non-uniqueness issues of XCTS-like elliptic systems in the full three-dimensional case, with astrophysical applications as our main motivation. Having the analysis of the fully constrained formalism (hereafter *FCF*) of [73, 134] as our ultimate aim, we focus on an approximation in the spirit of the CFC approximation by Isenberg, Wilson, and Mathews [260, 481]. This methodological choice is justified since the CFC scheme already contains the relevant elliptic system of FCF, but in a setting in which potential additional problematic issues related to the FCF hyperbolic part do not mix up with the specific problem we are addressing here. Therefore, we discuss in detail a modification of the CFC scheme (in the presence of matter)

where maximum-principle lines of reasoning can be used to infer the uniqueness of the solutions. We investigate numerically the performance of the new CFC scheme and finally indicate the main lines for its generalization to the full Einstein FCF case.

The article is organized as follows. In Sec. 3.2 we review the FCF and CFC formalisms, and then discuss the limitations found in the numerical implementations of the latter. In Sec. 3.3 we introduce the modification of the CFC scheme aiming at solving the uniqueness issues, and present various numerical tests of the new scheme in Sec. 3.4. In Sec. 3.5 the guidelines for the generalization to the FCF case are discussed and conclusions are drawn in Sec. 3.6. In Appendix 3.A we justify a further approximation assumed in Sec. 3.3 which is consistent with the CFC setting. Throughout the paper we use the signature $(-, +, +, +)$ for the spacetime metric and units in which $c = G = M_\odot = 1$. Greek indices run from 0 to 3 whereas Latin ones from 1 to 3 only.

3.2 The fully constrained formalism and the conformal flatness condition

3.2.1 A brief review of the fully constrained formalism

Given an asymptotically flat spacetime $(\mathcal{M}, g_{\mu\nu})$ we consider a 3+1 splitting by spacelike hypersurfaces Σ_t , denoting timelike unit normals to Σ_t by n^μ . The data on each spacelike hypersurface Σ_t are given by the pair (γ_{ij}, K^{ij}) , where $\gamma_{\mu\nu} = g_{\mu\nu} + n_\mu n_\nu$ is the Riemannian metric induced on Σ_t . We choose the convention $K_{\mu\nu} = -\frac{1}{2}\mathcal{L}_n \gamma_{\mu\nu}$ for the extrinsic curvature. With the lapse function N and the shift vector β^i , the Lorentzian metric $g_{\mu\nu}$ can be expressed in coordinates (x^μ) as

$$g_{\mu\nu} dx^\mu dx^\nu = -N^2 dt^2 + \gamma_{ij}(dx^i + \beta^i dt)(dx^j + \beta^j dt). \quad (3.1)$$

On the other hand, we can write

$$2NK^{ij} = \partial_t \gamma^{ij} + D^i \beta^j + D^j \beta^i, \quad (3.2)$$

where D_i is the Levi–Civita connection associated with $\gamma_{\mu\nu}$ and $\partial_t \gamma^{ij}$ represents the Lie derivative with respect to the evolution vector $t^\mu := (\partial_t)^\mu = Nn^\mu + \beta^\mu$. As in [73] we introduce a *time independent* flat metric f_{ij} , which satisfies $\mathcal{L}_t f_{ij} = \partial_t f_{ij} = 0$ and coincides with γ_{ij} at spatial infinity. We define $\gamma := \det \gamma_{ij}$ and $f := \det f_{ij}$. This fiducial metric permits the use of tensor quantities rather than tensor densities. The next step in the formulation of [73] is the conformal decomposition of the 3 + 1 fields. First, a representative $\tilde{\gamma}_{ij}$ in the conformal class of γ_{ij} is chosen, so we can write

$$\gamma_{ij} = \psi^4 \tilde{\gamma}_{ij}, \quad K^{ij} = \psi^{\zeta-8} \tilde{A}^{ij} + \frac{1}{3} K \gamma^{ij}, \quad (3.3)$$

where $K = \gamma^{ij} K_{ij}$ and $\tilde{\gamma} := \det \tilde{\gamma}_{ij}$, and $\zeta \in \mathbb{R}$. In Ref. [73], the choice $\zeta = 4$ was adopted, leading to the following expression of \tilde{A}^{ij} in terms of the lapse N and shift β^i :

$$\tilde{A}^{ij} = \frac{1}{2N} \left(\tilde{D}^i \beta^j + \tilde{D}^j \beta^i - \frac{2}{3} \tilde{D}_k \beta^k \tilde{\gamma}^{ij} + \partial_t \tilde{\gamma}^{ij} \right), \quad (3.4)$$

\tilde{D}_i being the Levi–Civita connection associated with $\tilde{\gamma}_{ij}$. This is in the spirit of the decomposition employed in the (X)CTS approach to initial data. Regarding the choice of representative of the

conformal metric $\tilde{\gamma}_{ij}$, a unimodular condition $\tilde{\gamma} = f$ was adopted in [73], so that $\psi = (\gamma/f)^{1/12}$. The deviation of the conformal metric from the flat fiducial metric is denoted by h^{ij} , i.e.

$$h^{ij} := \tilde{\gamma}^{ij} - f^{ij}. \quad (3.5)$$

Once the 3+1 conformal decomposition is performed, a choice of gauge is needed in order to properly reformulate the Einstein equations as partial differential equations. The prescriptions in [73] are *maximal slicing* and the so-called *generalized Dirac gauge*,

$$K = 0, \quad \mathcal{D}_k \tilde{\gamma}^{ki} = 0, \quad (3.6)$$

where \mathcal{D}_k stands for the Levi-Civita connection associated with the flat metric f_{ij} . The Einstein equations become then a coupled elliptic-hyperbolic system to be solved for the basic variables h^{ij} , ψ , N , and β^i [73].

Expressing the differential operators in terms of the connection of the flat metric, the elliptic part can be written as

$$\begin{aligned} \Delta\psi &= -2\pi E\psi^5 - h^{kl}\mathcal{D}_k\mathcal{D}_l\psi + \psi\frac{\tilde{R}}{8} \\ &\quad - \frac{\psi^5}{8(2N)^2}\tilde{\gamma}_{ik}\tilde{\gamma}_{jl}\left[(L\beta)^{ij} + \frac{\partial h^{ij}}{\partial t} - \mathcal{L}\beta h^{ij} - \frac{2}{3}\mathcal{D}_k\beta^k h^{ij}\right] \\ &\quad \times \left[(L\beta)^{kl} + \frac{\partial h^{kl}}{\partial t} - \mathcal{L}\beta h^{kl} - \frac{2}{3}\mathcal{D}_m\beta^m h^{kl}\right], \end{aligned} \quad (3.7)$$

$$\begin{aligned} \Delta(N\psi) &= 2N\psi^5\pi(E + 2S) + N\psi\frac{\tilde{R}}{8} - h^{kl}\mathcal{D}_k\mathcal{D}_l(N\psi) \\ &\quad + \frac{7}{32}\frac{\psi^6}{(N\psi)}\tilde{\gamma}_{ik}\tilde{\gamma}_{jl}\left[(L\beta)^{ij} + \frac{\partial h^{ij}}{\partial t} - \mathcal{L}\beta h^{ij} - \frac{2}{3}\mathcal{D}_k\beta^k h^{ij}\right] \\ &\quad \times \left[(L\beta)^{kl} + \frac{\partial h^{kl}}{\partial t} - \mathcal{L}\beta h^{kl} - \frac{2}{3}\mathcal{D}_k\beta^k h^{kl}\right], \end{aligned} \quad (3.8)$$

$$\begin{aligned} \Delta\beta^i + \frac{1}{3}\mathcal{D}^i\mathcal{D}_j\beta^j &= 16\pi N\psi^4 S^i - h^{kl}\mathcal{D}_k\mathcal{D}_l\beta^i - \frac{1}{3}h^{ik}\mathcal{D}_k\mathcal{D}_l\beta^l + \frac{\psi^6}{N}\mathcal{D}_j\left(\frac{N}{\psi^6}\right)\left[(L\beta)^{ij}\right] \\ &\quad + \frac{\psi^6}{N}\mathcal{D}_j\left(\frac{N}{\psi^6}\right)\left[\frac{\partial h^{ij}}{\partial t} - \mathcal{L}\beta h^{ij} - \frac{2}{3}\mathcal{D}_k\beta^k h^{ij}\right] - 2N\Delta_{kl}^i\tilde{A}^{kl}, \end{aligned} \quad (3.9)$$

where Δ stands for the flat Laplacian ($\Delta := f^{ij}\mathcal{D}_i\mathcal{D}_j$), E , S^i and S are respectively the energy density, momentum density and trace of the stress tensor, all measured by the observer of 4-velocity n^μ (Eulerian observer): in terms of the energy-momentum tensor $T_{\mu\nu}$, $E := T_{\mu\nu}n^\mu n^\nu$, $S^i := -\gamma^{i\mu}T_{\mu\nu}n^\nu$, and $S := \gamma^{ij}S_{ij}$, with $S_{ij} := T_{\mu\nu}\gamma^\mu{}_i\gamma^\nu{}_j$. Furthermore,

$$\tilde{R} = \frac{1}{4}\tilde{\gamma}^{kl}\mathcal{D}_k h^{mn}\mathcal{D}_l\tilde{\gamma}_{mn} - \frac{1}{2}\tilde{\gamma}^{kl}\mathcal{D}_k h^{mn}\mathcal{D}_n\tilde{\gamma}_{ml}, \quad (3.10)$$

$$(L\beta)^{ij} := \mathcal{D}^i\beta^j + \mathcal{D}^j\beta^i - \frac{2}{3}f^{ij}\mathcal{D}_k\beta^k, \quad (3.11)$$

$$\Delta_{ij}^k := \frac{1}{2}\tilde{\gamma}^{kl}(\mathcal{D}_i\tilde{\gamma}_{lj} + \mathcal{D}_j\tilde{\gamma}_{il} - \mathcal{D}_l\tilde{\gamma}_{ij}). \quad (3.12)$$

Equation (3.7) follows from the Hamiltonian constraint, whereas Eq. (3.9) results from the momentum constraint together with the preservation of the Dirac gauge in time. Equation (3.8) corresponds to the preservation in time of the maximal slicing condition, $\partial K/\partial t = 0$. Note that expression (3.10) for the Ricci scalar of the conformal metric does not involve any second order derivative of the metric; this property follows from Dirac gauge [73]. The resulting elliptic subsystem coincides with the XCTS system [364], except from the field chosen to solve the maximal slicing equation: Eq. (3.8) above is to be solved for $N\psi$, whereas in [364] the *conformal lapse* $\tilde{N} := N\psi^{-6}$ is employed instead. This affects directly the value (and in particular the sign) of the power of the conformal factor in the non-linear terms of Eqs. (3.7)–(3.8). More generally, one could define a generic rescaling of the lapse, $N = \tilde{N}\psi^a$, such that the choice in [364] corresponds to $a = 6$, whereas the choice in Eq. (3.8) above corresponds to $a = -1$ (see [265] for the general equations in the vacuum case). An important remark is the absence of a choice of a such that the factors multiplying ψ and \tilde{N} on the right hand side of the linearized versions of Eqs. (3.7) and (3.8) present both a positive sign. In the presence of matter, terms multiplying the energy density E also contribute to these sign difficulties, though in this case they can be fixed by an appropriate conformal rescaling of the energy density (see later). An additional concern in a generic evolution scenario is the sign of \tilde{R} , also relevant in the linearized equations. Implications of this issue are discussed in Sec. 3.3.

The Einstein equations in the form of the elliptic equations (3.7)–(3.9) and the hyperbolic equation for h^{ij} as given in Ref. [73] are to be solved together with the hydrodynamic equations,

$$\nabla_\mu(\rho u^\mu) = 0, \quad (3.13)$$

$$\nabla_\mu T^\mu{}_\nu = 0, \quad (3.14)$$

where ∇^μ is the Levi-Civita connection associated with the metric $g_{\mu\nu}$, ρ is the rest-mass (baryon mass) density, and u^μ is the 4-velocity of the fluid.

3.2.2 The conformal flatness approximation

If the hyperbolic part of the FCF system is not solved, but rather the condition $h^{ij} = 0$ is imposed, the resulting 3-metric γ_{ij} is conformally flat, and the CFC approximation is recovered. Therefore, FCF is a natural generalization of the CFC approximation. The latter has been used in many astrophysical applications like the rotational collapse of cores of massive stars [149, 151, 351, 115] or supermassive stars [397], the phase-transition-induced collapse of rotating neutron stars to hybrid quark stars [3], equilibrium models of rotating neutron stars [131, 152], as well as for binary neutron star merger [481, 345, 346, 170]. The elliptic subsystem of the FCF, Eqs. (3.7)–(3.9), reduces in CFC to

$$\Delta\psi = -2\pi\psi^{-1} \left[E^* + \frac{\psi^6 K_{ij} K^{ij}}{16\pi} \right], \quad (3.15)$$

$$\Delta(N\psi) = 2\pi N\psi^{-1} \left[E^* + 2S^* + \frac{7\psi^6 K^{ij} K_{ij}}{16\pi} \right], \quad (3.16)$$

$$\Delta\beta^i + \frac{1}{3}\mathcal{D}^i\mathcal{D}_j\beta^j = 16\pi N\psi^{-2}(S^*)^i + 2\psi^{10} K^{ij}\mathcal{D}_j\frac{N}{\psi^6}, \quad (3.17)$$

where the following rescaled matter quantities have been introduced, following York [486]:

$$E^* := \sqrt{\gamma/f} E = \psi^6 E, \quad (3.18)$$

$$S^* := \sqrt{\gamma/f} S = \psi^6 S, \quad (3.19)$$

$$(S^*)_i := \sqrt{\gamma/f} S_i = \psi^6 S_i. \quad (3.20)$$

Equations (3.15) and (3.16) inherit the local non-uniqueness problems already present in the FCF equations. Although the sign problems specifically related to the energy density terms are solved by the conformal rescaling of the components of the energy-momentum tensor and the CFC eliminates the \tilde{R} term, problems related to the $K_{ij}K^{ij}$ term remain in the scalar CFC equations. This is apparent once the extrinsic curvature is expressed in terms of the lapse and the shift.

Conformal rescaling of the hydrodynamical variables are not only relevant for local uniqueness issues. The hydrodynamic equations (3.13)–(3.14) can be formulated as a first-order hyperbolic system of conservation equations for the quantities $(D^*, (S^*)_i, E^*)$ [46, 177], where, similarly to Eqs. (3.18)–(3.20), $D^* := \psi^6 D$, $D := Nu^0 \rho$ being the baryon mass density as measured by the Eulerian observer. We can thus consider E^* and $(S^*)_i$ as known variables in the computation of the CFC metric. Note that these quantities differ from E and S_i by a factor ψ^6 , and hence it is not possible to compute the non-starred quantities before knowing the value of ψ . If the energy-momentum tensor represents a fluid, then the source of Eq. (3.16) cannot be explicitly expressed in terms of $(D^*, (S^*)_i, E^*)$, the reason for that being the dependence of S^* on the pressure P . The pressure can only be computed in terms of the “primitive” quantities, e.g., as a function $P(\rho, \epsilon)$ of the rest-mass density and the specific internal energy ϵ . The primitive quantities are in general recovered from (D, S_i, E) implicitly by means of an iteration algorithm. So far, two solutions of the problem related to the fact that S^* directly contains P have been used in numerical simulations performed using the CFC approximation.

The first approach [481] is to consider P , and hence also S^* , as an implicit function of ψ . Then Eqs. (3.15)–(3.17) can be solved as a coupled set of non-linear equations using a fixed-point iteration algorithm. The convergence of the algorithm to the correct solution depends not only on the proximity of the initial seed metric to the solution, but also on the uniqueness of this solution. The latter point is extensively discussed in Sec. 3.3. Furthermore, one problem of this approach is the necessity of performing the recovery of the primitive variables, which is numerically a time consuming procedure, to compute the pressure during each fixed point iteration. Due to the uniqueness problem, this approach can be only successfully applied in numerical simulations for at most moderately strong gravity (like stellar core collapse to a neutron star or inspiral and initial merger phase of binary neutron stars), but fails for more compact configurations like the collapse of a stellar core or a neutron star to a black hole. For such scenarios with very strong gravity, one finds convergence of the metric to a physically incorrect solution of the equations or even non-convergence of the algorithm.

A second approach to the recovery algorithm problem is the attempt to calculate P independently of the CFC equations. This can be achieved by computing the conformal factor by means of the evolution equation

$$\frac{\partial \psi'}{\partial t} = \frac{\psi'}{6} \mathcal{D}_k \beta^k. \quad (3.21)$$

The conformal factor ψ' obtained in this way is analytically identical to the ψ from Eqs. (3.15)–(3.17), but here we use a different notation to keep track of the way it is computed. The value of ψ' is solely used to evaluate P , and the coupled system of Eqs. (3.15)–(3.17) is solved for determining ψ , N , and β^i . Although this approach allows to avoid the problem of recovering the primitive variables at each iteration, it also suffers from the convergence problem, and the simulation of configurations with very strong gravity is still not feasible. Furthermore, new complications are introduced by the fact of using two differently computed values, ψ and ψ' , of the same quantity. For some scenarios like the formation of a black hole from stellar collapse, the numerical values of these two quantities during the evolution of the system start to diverge significantly at some point. We find that this inconsistency cannot be avoided, since any attempt to artificially synchronize both values leads to numerical instabilities.

3.3 The new scheme in the conformally flat case

3.3.1 Uniqueness of the elliptic equations and convergence of elliptic solvers

Well-posed elliptic partial differential systems admit non-unique solutions whenever the associated differential operator has a non-trivial kernel. When discussing sufficient conditions guaranteeing uniqueness, it is illustrative to first consider the case of a scalar elliptic equation. In particular, for the class of scalar elliptic equations for the function u of the form

$$\Delta u + hu^p = g, \quad (3.22)$$

where h and g are known functions independent of u , a maximum principle can be used to prove local uniqueness of the solutions as long as the sign of the exponent p is different from the sign of the proper function h [381, 486, 458, 164].

In the CFC case, we are not dealing with a single scalar elliptic equation, but rather with the coupled non-linear elliptic system (3.15)-(3.17). Therefore, assessing if the scalar equations (3.15) and (3.16) do present the good signs for the application of a maximum principle is an important step for understanding the uniqueness properties of the whole system. However, as pointed out in the previous section, the CFC equations for the conformal factor and the lapse possess the wrong signs in the quadratic extrinsic curvature terms (once everything is expressed in terms of the lapse and the shift). This problem can be fixed in Eq. (3.15) by an appropriate rescaling of the lapse, $N = \tilde{N}\psi^6$, but this strategy does not solve the problem for the lapse equation (cf. the discussion on the conformal lapse \tilde{N} in Sec. 3.2.1). Therefore we cannot use the maximum principle to infer local uniqueness of the solutions to the CFC equations. In these conditions of potential non-unique solutions, convergence to a non-desirable solution may happen. As mentioned in the introduction, this pathology has been illustrated using simple analytical examples of scalar equations of the type (3.22) in [53], as well as in numerical implementations of the vacuum Einstein constraints in the XCTS approach [365] and certain constrained evolution formalisms (see, e.g., [389]).

In the context of the CFC approximation this sign issue has also appeared, in particular associated with the “recovery algorithm” problem discussed in Sec. 3.2.2 since it involves the evaluation of the conformal factor. Non-unique solutions of ψ , either due to the use of the non-conformally rescaled E or the quadratic extrinsic curvature term, spoil the convergence of the algorithm when density and thus compactness increases. We again emphasize that a possible synchronization of ψ and ψ' does not solve the problem in general, since numerical instabilities eventually arise at sufficiently high compactness.

3.3.2 Numerical examples

The non-uniqueness of solutions has also been observed in FCF, as described in the following example. Let us consider a vacuum spacetime, with initial data formed by a Gaussian wave packet, as in [73], but with much higher amplitude $\chi_0 = 0.9$ instead of $\chi_0 = 10^{-3}$ in [73] (see the latter reference for notations). The integration technique and numerical settings are the same as in [73], but contrary to the results for small amplitude obtained in that reference, the wave packet does not disperse to infinity and instead starts to collapse. Fig. 3.1 displays the time evolution of the central lapse N_c at $r = 0$ and of the system’s ADM mass M_{ADM} , which in the present conformal decomposition can be

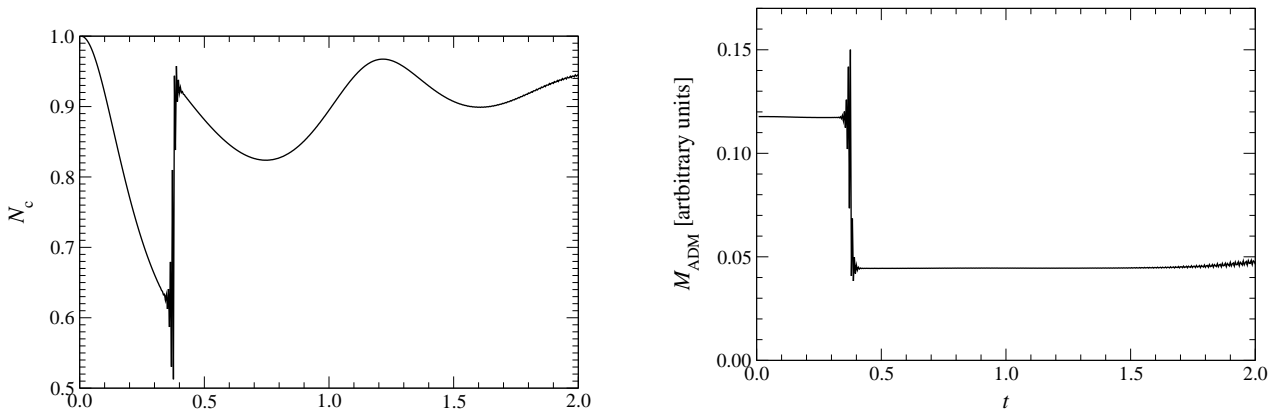


Figure 3.1: Time evolution of the central lapse N_c (left panel) and the ADM mass M_{ADM} (right panel) for a collapsing packet of gravitational waves, using the integration scheme proposed in [73]. The unit of t is given by the initial width of the wave packet

expressed as

$$\begin{aligned}
 M_{\text{ADM}} &= -\frac{1}{2\pi} \oint_{\infty} \left(\mathcal{D}_i \psi - \frac{1}{8} \mathcal{D}^j \tilde{\gamma}_{ij} \right) d\mathcal{A}^i \\
 &= -\frac{1}{2\pi} \oint_{\infty} \mathcal{D}_i \psi d\mathcal{A}^i,
 \end{aligned} \tag{3.23}$$

where the integral is taken over a sphere of radius $r = \infty$ and the second equality follows from the use of Dirac gauge [Eq. (3.6)].

The very sudden change at $t \simeq 0.4$ in both the central lapse and the ADM mass, which is also present in, e.g., the central conformal factor ψ_c , originates from the convergence of the elliptic system (3.7)–(3.9) to another solution with a different (unphysical) value of the ADM mass. The good conservation of M_{ADM} and the smooth evolution of N_c for $t \gtrsim 0.4$ indicate that this other solution remains stable until $t \simeq 2$, when high-frequency oscillations appear. These oscillations may be due to the overall inconsistency of the system, destabilizing the whole scheme. On the other hand, the time evolution of h^{ij} does not show any such type of behavior, and h^{ij} exhibits a continuous radial profile at all times. This is numerical evidence that, also for the full Einstein case (i.e. without approximation) the generalized elliptic equations suffer from a similar convergence problem as in the CFC case.

The same subject is also exemplified when one tries to calculate the spacetime metric for an equilibrium neutron star model from the unstable branch using either Eqs. (3.7)–(3.9) in the FCF case or Eqs. (3.15)–(3.17) in the CFC approximation. Even for the simple setup of a polytrope with adiabatic index $\Gamma = 2$ in spherical symmetry, those metric equations yield – when converging at all – a grossly incorrect solution if the matter quantities (D, S_i, E) in the source terms are held fixed. Both the metric components as well as the ADM mass can deviate from the physical solution by several ten percent, even though that incorrect metric satisfies the asymptotic flatness condition. The reason why programs for constructing rotating relativistic neutron star models like the KEH code [283], the RNS code [445], or the BGSM code [67] are not obstructed by this non-uniqueness problem apparently is that they all utilize an iteration over both the metric and the hydrodynamic equations *simultaneously*, thereby allowing the matter quantities to change during the calculation of the metric.

We want to stress here that these non-convergence issues in the CFC case are not related to the approximation that is made. If one considers this system in the spherical (one-dimensional) case, CFC is no longer an approximation, but is the choice of the so-called isotropic gauge. Even then, the elliptic system (3.15)-(3.17) no longer converges to the proper (physical) solution.

3.3.3 The new scheme and its theoretical properties

Despite the above mentioned convergence problems, numerically simulating the physical problem of spherical collapse to a black hole in isotropic coordinates has been successfully studied by Shapiro and Teukolsky in [410]. Due to the spherical symmetry, there exists only one independent component of the extrinsic curvature. It is then possible to compute directly a conformal extrinsic curvature, $\psi^6 K_r^r$, from the conserved hydrodynamical variables. The elliptic equation for ψ then decouples from the other elliptic equations by introducing this conformal extrinsic curvature and using the conserved hydrodynamical variables in the source. This source term presents no problem for proving local uniqueness and the equation for ψ always converges to the physically correct solution. Once the conformal factor, the extrinsic curvature (from the conformal factor and the conformal extrinsic curvature) and the conserved hydrodynamical variables are known, the elliptic equation for $N\psi$ can be solved and, again, the source exhibits no local uniqueness problem. This follows from the fact that the extrinsic curvature is not expressed in terms of the lapse and the shift. This contrasts with the CFC equation (3.16) where a division by N^2 occurs in the last term when the extrinsic curvature is expressed in terms of its constituents N , ψ , and β^i . In addition, there is no necessity of using ψ' . Finally, the elliptic equation for the shift vector can be solved. In summary, no problems of instabilities or divergence are encountered.

We now generalize this scheme to the CFC case in three dimensions. This involves the use of two different conformal decompositions of the extrinsic curvature. That is, first, two different conformal rescaling and, second, two different decompositions of the traceless part into longitudinal and transverse parts. Adopting maximal slicing, $K = 0$, a generic conformal decomposition can be written as

$$K^{ij} = \psi^{\zeta-8} (A^{(\zeta)})^{ij} := \psi^{\zeta-8} \left(\frac{1}{\sigma} (LX)^{ij} + A_{\text{TT}}^{ij} \right), \quad (3.24)$$

where ζ is a free parameter and σ a free function, A_{TT}^{ij} is transverse traceless and L in the conformal Killing operator defined by Eq. (3.11). We implicitly make use of a flat conformal metric, with respect to which A_{TT}^{ij} is transverse although, in principle it would be more general to use the metric $\tilde{\gamma}^{ij}$ and the conformal Killing operator associated with it, \tilde{L} . But such a decomposition would introduce many technical difficulties in our treatment. In particular, it is numerically easier to handle tensors which are divergence-free with respect to the flat metric in the generalization to FCF. The vector X^i , on which L is acting, is therefore called the *longitudinal part* of $(A^{(\zeta)})^{ij}$. The first decomposition we use is the one introduced in Eqs. (3.3)–(3.4) with the choice $\zeta = 4$ and $\sigma = 2N$. This corresponds to a CTS-like decomposition of the traceless part, so that X^i is given by the shift vector β^i and A_{TT}^{ij} can be expressed in terms of the time derivative of the conformal metric. We denote this traceless part as $\tilde{A}^{ij} := (A^{(4)})^{ij}$. In the CFC approximation this becomes

$$K^{ij} = \psi^{-4} \tilde{A}^{ij}, \quad \tilde{A}^{ij} = \frac{1}{2N} (L\beta)^{ij}. \quad (3.25)$$

The second conformal decomposition,

$$K^{ij} = \psi^{-10} \hat{A}^{ij}, \quad \hat{A}^{ij} = (LX)^{ij} + \hat{A}_{\text{TT}}^{ij}, \quad (3.26)$$

refers to $\zeta = -2$ and $\sigma = 1$. It rather corresponds to a conformal transverse traceless (CTT) decomposition of the traceless part of extrinsic curvature introduced by Lichnerowicz [291]. Notice that we have defined $\hat{A}^{ij} := (A^{(-2)})^{ij}$, not to be confused with $\tilde{A}^{ij} := (A^{(4)})^{ij}$. The relation between \hat{A}^{ij} and \tilde{A}^{ij} is given by

$$\hat{A}^{ij} = \psi^{10} K^{ij} = \psi^6 \tilde{A}^{ij}. \quad (3.27)$$

In terms of \hat{A}^{ij} , the CFC momentum constraint can be written as

$$\mathcal{D}_j \hat{A}^{ij} = 8\pi\psi^{10} S^i = 8\pi\psi^6 f^{ij} S_j = 8\pi f^{ij} S_j^*. \quad (3.28)$$

Consistency between the CTT-like decomposition (3.26) and the CTS-like one (3.25) generically requires a non-vanishing transverse part \hat{A}_{TT}^{ij} in Eq. (3.26). However, as it is shown in Appendix 3.A, this \hat{A}_{TT}^{ij} is smaller in amplitude than the non-conformal part h^{ij} of the spatial metric and \hat{A}^{ij} can be approximated on the CFC approximation level as

$$\hat{A}^{ij} \approx (LX)^{ij} = \mathcal{D}^i X^j + \mathcal{D}^j X^i - \frac{2}{3} \mathcal{D}_k X^k f^{ij}. \quad (3.29)$$

From Eqs. (3.26) and (3.28), an elliptic equation for the vector X^i can be derived,

$$\Delta X^i + \frac{1}{3} \mathcal{D}^i \mathcal{D}_j X^j = 8\pi f^{ij} S_j^*, \quad (3.30)$$

from which X^i can be obtained. With this vector field, one can calculate the tensor \hat{A}^{ij} via (3.29). Notice that in the case of spherical symmetry, $\hat{A}^{rr} = \psi^{10} K^{rr} = \psi^6 K_r^r$ is the quantity used by Shapiro and Teukolsky [410].

The elliptic equation for the conformal factor can be rewritten in terms of the conserved hydrodynamical variables and \hat{A}^{ij} :

$$\Delta\psi = -2\pi\psi^{-1} E^* - \psi^{-7} \frac{f_{il} f_{jm} \hat{A}^{lm} \hat{A}^{ij}}{8}. \quad (3.31)$$

This equation can be solved in order to obtain the conformal factor. Once the conformal factor is known, the procedure to implicitly recover the primitive variables from the conserved ones is possible, the pressure P can be computed using the equation of state, and therefore S^* is at hand. The elliptic equation for $N\psi$ can be reformulated by means of the conserved hydrodynamical variables, \hat{A}^{ij} , and the conformal factor:

$$\Delta(\psi N) = 2\pi N\psi^{-1} (E^* + 2S^*) + N\psi^{-7} \frac{7f_{il} f_{jm} \hat{A}^{lm} \hat{A}^{ij}}{8}. \quad (3.32)$$

From this equation $N\psi$ can then be obtained, and consequently the lapse function N . Note that, since \hat{A}^{ij} is already known at this step, no division by N^2 spoils the good sign for the maximum principle.

Using the relation between the two conformal decompositions of the extrinsic curvature, $\hat{A}^{ij} = \psi^6 \tilde{A}^{ij}$, Eq. (3.25) can be expressed as $(L\beta)^{ij} = 2N\psi^{-6} \hat{A}^{ij}$. Taking the divergence we arrive at an elliptic equation for the shift vector,

$$\Delta\beta^i + \frac{1}{3} \mathcal{D}^i (\mathcal{D}_j \beta^j) = \mathcal{D}_j (2N\psi^{-6} \hat{A}^{ij}), \quad (3.33)$$

where the source is completely known. This elliptic equation can be solved in order to obtain the shift vector β^i consistent with $\partial_t \tilde{\gamma}_{ij} = 0$, as required by the CFC approximation.

In this recast of the CFC equations an extra elliptic vectorial equation for the vector field X^i is introduced. However, now the signs of the exponents of ψ and N are compatible with the maximum principle for scalar elliptic equations, and the problem is *linearization stable*. While this does not guarantee *global* uniqueness of the solutions, it provides a sufficient result for *local* uniqueness. This strongly relies on the fact that the system decouples in a hierarchical way, which we summarize here once more:

1. With the hydrodynamical conserved quantities at hand, solve Eq. (3.30) for X^i , and thus for \hat{A}^{ij} .
2. Solve Eq. (3.31) for ψ , where local uniqueness is now guaranteed. Then S^* can be calculated consistently.
3. Solve Eq. (3.32) for $N\psi$, a linear equation where the maximum principle can be applied and uniqueness and existence follow with appropriate boundary conditions.
4. As the source of Eq. (3.33) is then fully known, solve it for β^i .

Note that this scheme is similar to that used by Shibata and Uryū [426] to compute initial data for black hole - neutron star binaries. We will discuss this point further in Sec. 3.6.2.

The new CFC metric equations presented here not only allow to evolve the hydrodynamical equations and recover the metric variables from the elliptic equations in a consistent way (no auxiliary quantity ψ' is needed). It also permits to introduce initial perturbations in the hydrodynamical variables (strictly speaking in the conserved quantities) in a set of previously calculated initial data and directly delivers the correct values for the metric. It is even possible to perturb only the primitive quantities, and consistently resolve for the metric by iterating until the conformal factor ψ , which links the primitive to the conserved quantities, converges. We find that such an iteration method fails for sufficiently strong gravity if the original CFC formulation is used.

3.4 Numerical results

We recapitulate that the original CFC formulation exhibits serious convergence problems when dealing with highly compact configurations such as nascent black holes. This weakness of the original formalism is noticeable in the fact that no simulations of rotational collapse to a black hole substantially beyond the formation of the apparent horizon have been performed so far in CFC. Furthermore, already some scenarios which do not involve the formation of a black hole are feasible with the old formulation only if procedures like using Eq. (3.21) with all associated problems and inconsistencies are employed. An example is the migration of a neutron star model from the stable to the unstable branch, which is a standard test for relativistic hydrodynamics codes. In contrast, the new CFC scheme presented in this work solves all problems which prevented performing such simulations in the past. In order to show the suitability of the new scheme we present the results of numerical simulations of the migration test and of the rotational collapse to a black hole.

Table 3.1: Initial models used in the migration test and the rotational collapse to a black hole. $\rho_{c,i}$ is the initial central rest-mass density, Ω_i is the initial angular velocity, $r_{p,i}/r_{e,i}$ is the initial ratio of polar to equatorial coordinate radius, M_{ADM} is the gravitational ADM mass, and J is the total angular momentum (which is conserved in CFC during the evolution in the axisymmetric case). Units in which $G = c = M_{\odot} = 1$ are used.

Model	$\rho_{c,i}$ [10^{-3}]	Ω_i [10^{-2}]	$r_{p,i}/r_{e,i}$	$r_{e,i}$	M_{ADM}	J/M_{ADM}^2
SU	8.000	0	1.00	4.267	1.447	0
SS	1.346	0	1.00	7.999	1.424	0
D1	3.280	1.73	0.95	5.947	1.665	0.207
D2	3.189	2.88	0.85	6.336	1.727	0.362
D3	3.134	3.55	0.75	6.839	1.796	0.468
D4	3.116	3.95	0.65	7.611	1.859	0.542

3.4.1 Model setup

The numerical simulations presented here are performed using the numerical code CoCoNuT [148, 151]. This code solves the evolution of the hydrodynamics equations coupled to the elliptic equations for the spacetime metric in the CFC approximation. Standard high-resolution shock-capturing schemes are used in the hydrodynamic evolution, while spectral methods are employed to solve the metric equations. The code is based on spherical polar coordinates, and for the tests presented here we assume axisymmetry and symmetry with respect to the equatorial plane. Note that the metric equations presented in this paper are covariant. Thus the formalism can be used for any coordinate basis as well as without any symmetry conditions.

The initial models are general relativistic $\Gamma = 2$ polytropes in equilibrium with a polytropic constant $K = 100$. The models are chosen to be situated on the unstable branch, i.e. $\partial M_{\text{ADM}}/\partial \rho_c < 0$, where ρ_c is the central rest-mass density. Therefore, any perturbation of the star induces either the collapse to a black hole or the migration to a configuration of the same baryon mass on the stable branch. Table 3.1 shows the main features of these initial models. Models D1 to D4 are uniformly rotating models which are identical to those presented in [41]. The model labeled SU is a spherical model, while model SS is the counterpart model with the same baryon mass but located on the stable branch. The equilibrium rotating star models in Dirac gauge (the axisymmetric and stationary limit of FCF) used here are described in [293], and are computed using the LORENE [216] library. We map the hydrodynamic and metric quantities to the CFC code neglecting the $h^{ij} \sim 10^{-3}$ terms, which are negligible due to their smallness. Alternatively, we compute CFC equilibrium initial models. In this case we find that the differences with respect to the FCF models are small ($\sim 0.1\%$) for representative metric and hydrodynamic quantities initially and during the evolution, and therefore we discuss only the FCF initial models here.

The hydrodynamic equation are discretized on the finite difference grid with $n_r \times n_\theta$ grid points. The radial grid size is Δr_0 for the innermost cell and increases geometrically outwards, while the angular grid is equidistantly spaced. The metric equations are solved on a spectral grid consisting

of $n_d - 1$ radial domains distributed such as to cover homogeneously the finite difference grid and a compactified exterior domain extending to radial infinity. On the spectral grid we resolve each radial domain with 33 collocation points. The spherical model needs only one angular collocation point, while we use 17 angular points for the rotating models.

We track the location of the apparent horizon by means of a three-dimensional spectral apparent horizon finder, described in detail and tested in [294]. The apparent horizon location is given by a function $\mathcal{H}(r, \theta)$, which is decomposed into a set of spherical harmonics. The coefficients of \mathcal{H} in this basis are computed iteratively, in order to satisfy the condition that the expansion in the outgoing null direction vanishes at the apparent horizon location.

3.4.2 Migration of unstable neutron stars to the stable branch

The first test we consider is the migration of a neutron star model in equilibrium from the unstable branch to the stable branch, which is a standard but still demanding test for general relativistic hydrodynamics codes, as it involves the dynamic transition between two very compact equilibrium states. This test has been performed in the past in full general relativistic simulations [181]. We start the evolution with the non-rotating equilibrium model labeled SU. Since it belongs to the unstable branch, any perturbation from exact equilibrium (which can for instance be caused by discretization errors) leads either to a collapse or to an expansion to a new equilibrium configuration of the same baryon mass on the stable branch. The corresponding equilibrium configuration with the same baryon mass, model SS, has smaller ADM mass than the initial system (see Table 3.1). Therefore, to preserve the ADM mass, the final configuration cannot be exactly the equilibrium model SS. The energy difference between models SU and SS should be transformed into kinetic energy, remaining in the final object in the form of pulsations.

In our case the numerical truncation error is sufficient to trigger the migration. Since the final neutron star on the stable branch is larger than the initial model (see Table 3.1) the outer boundary of the finite difference grid is chosen to be 4.5 times the radius of the model SS. We perform two simulations on a finite difference grid with 150 or 300 radial cells and $\Delta r_0 = 0.022$ or 0.012, respectively. We use $n_d = 6$ radial domains for the spectral grid. We evolve the system with either a polytropic or an ideal gas equation of state.

Figure 3.2 shows the time evolution of the central values of the rest-mass density and the lapse. As the star expands, ρ_c decreases while N_c grows until the new stable equilibrium configuration is reached. In the polytropic case, there are no physical mechanisms to damp the strong pulsations, and the final state resembles a star oscillating around the equilibrium configuration until numerical dissipation finally damps the oscillations. This can be seen in the pulsating values of rest-mass density and lapse around the value corresponding to the equilibrium model on the stable branch (solid horizontal line in Fig. 3.2).

In the ideal gas case, shock waves are formed at every pulsation which dissipate kinetic energy into thermal energy, thereby damping the oscillations. As these shocks reach the surface of the star, a small amount of mass is expelled from the star and matter is ejected outwards into the surrounding artificial low-density atmosphere until it is lost from the grid across the outer numerical boundary. We approximately compute the escape velocity as $v_e = \sqrt{2U} \approx \sqrt{\psi^2 - 1}$, where U is the Newtonian potential. This formula is not exact in general relativity, but it should be sufficiently accurate near the outer numerical boundary where gravity is weaker. We find that the shock waves leaving the computational domain exceed the escape velocity and therefore the lost mass is gravitationally unbounded. We also check that these results are not affected by changing the resolution or setting the outer boundary

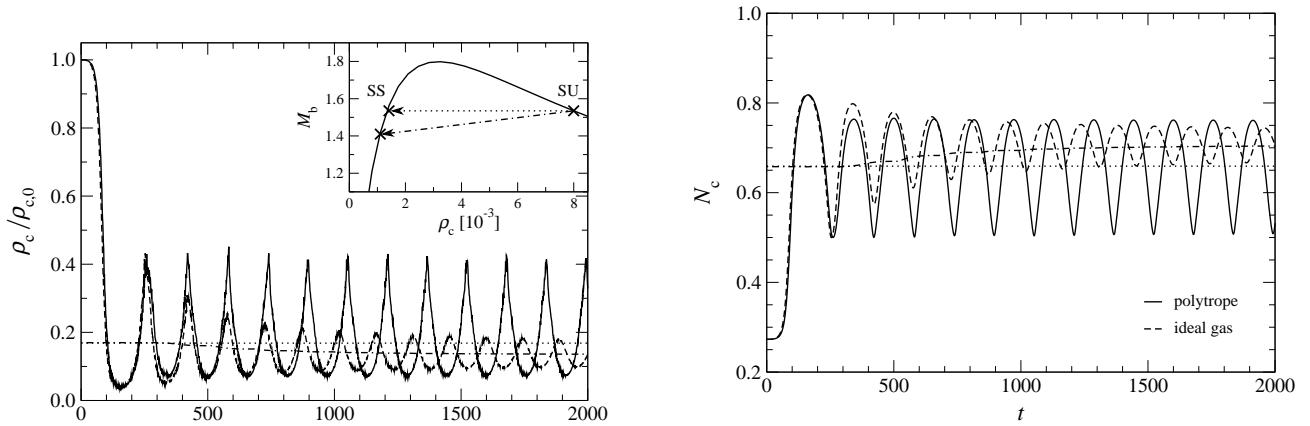


Figure 3.2: Time evolution of the central rest-mass density ρ_c (left panel) and the central lapse N_c (right panel) for the migration of the unstable neutron star model SU to the stable branch, with either a polytropic (solid lines) or an ideal gas (dashed lines) equation of state. The dotted horizontal lines mark the value of ρ_c and N_c for the equilibrium configuration SS from the stable branch with the same baryon mass M_b as model SU, while the dash-dotted lines are obtained from a series of equilibrium models where mass shedding, like in the migration model with an ideal gas equation of state, is taken into account. In the inset the baryon mass M_b versus ρ_c relation for this model setup is displayed. The models SU (the initial model) and SS (the final state for a polytropic equation of state) as well as the final state for an ideal gas equation of state are marked. The arrows symbolize the respective migration paths.

twice as far away. As the oscillations are damped, the shocks become weaker and the mass expelled at each oscillation is smaller. At the end of the simulation the star has lost about 10% of its initial baryon mass approaching a state of constant baryon mass. As a consequence, the final equilibrium configuration on the stable branch is not the model SS anymore but the corresponding model from the stable branch with lower baryon mass and central density. In Fig. 3.2 we plot the central rest-mass density and lapse of a series of equilibrium models on the stable branch corresponding to the baryon mass remaining in the computational domain at each time. It can be seen that these values deviate with time from model SS and fit the final state in the hydrodynamical evolution of the star.

As a by-product of this study we draw reader's attention to the consistency (as it should be) between the amplitude and the frequency of the oscillations. The period of these oscillations is approximately of the order of the hydrodynamical characteristic time τ_ρ , which decreases with density like $\tau_\rho \approx \rho^{-1/2}$. In the polytropic case, the maxima of the oscillations in ρ_c are systematically higher than in the ideal gas case. Consequently, the characteristic time is shorter than in the ideal gas case, as Fig. 3.2 shows. A second property worth to be pointed out is that the low numerical viscosity of our code is responsible for maintaining a nearly constant amplitude of the oscillations (in the polytropic case) during many characteristic times.

Our simulations are consistent with the results from a fully relativistic three-dimensional code in [181]. Similar simulations of this test with the original, unmodified CFC scheme lead from the start to a completely incorrect solution with a grossly wrong ADM mass. When running with the new improved CFC scheme, we obtain a $M_{\text{ADM}} = 1.451M_\odot$ and initial values for the conformal factor and lapse of $\psi_c = 1.561$ and $\alpha_c = 0.273$, respectively. On the other hand, with the unmodified conventional

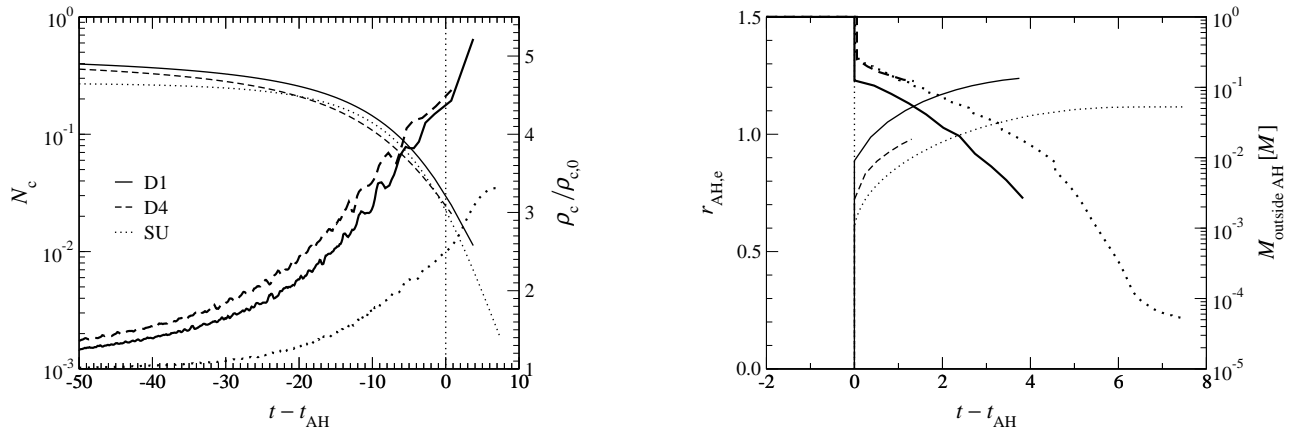


Figure 3.3: Collapse to a black hole for the spherical model SU, and the rotating models D1 and D4. The left panel shows the time evolution of the central lapse N_c (thin lines) and the central rest-mass density ρ_c relative to the initial value $\rho_{c,0}$ (thick lines). The right panel shows the time evolution of the apparent horizon radius $r_{\text{AH},e}$ in the equatorial plane (thin lines) and the rest mass $M_{\text{outside AH}}$ remaining outside the apparent horizon relative to the total rest mass M (thick lines). The dashed vertical lines mark the time when the apparent horizon first appears. If the axes of the lower panel were exchanged, the resulting plot would resemble the typical spacetime diagram of a star collapsing to a black hole.

CFC scheme, the metric solver already initially converges to a solution with $M_{\text{ADM}} = 0.647M_{\odot}$ (55%), $\psi_c = 1.221$ (61%) and $\alpha_c = 0.532$ (63%), where the relative differences to the physically correct solution are given in parentheses.

As presented in [309] the migration test can be successfully simulated using the old CFC scheme, if one resorts to additionally solving the evolution equation (3.21) for the conformal factor (which would lead to large inconsistencies in scenarios with higher compactness but still yields acceptable results for the standard migration case). Already here the superiority of the new, fully consistent CFC scheme, which does not depend on such scenario-dependent amendments, becomes apparent.

3.4.3 Collapse of unstable neutron stars to a black hole

As the second test we present the collapse of a (spherical or rotating) neutron star model to a black hole. Following [41] we trigger the collapse to a black hole by reducing the polytropic constant K by 2% in the initial models D1 to D4. Alternatively, in the spherical model SU we increase the rest-mass density by 0.1%, which yields a similar dynamic evolution. However, since the models are initially in equilibrium, the total collapse *time* depends strongly on the perturbation applied. In these collapse cases, the outer boundary of the finite difference grid is 20% larger than the star radius. For the spherical model SU, we perform two simulations using 150 or 300 radial cells and $\Delta r_0 \sim 10^{-3}$ or 10^{-4} , respectively, to assess the resolution dependence of our simulations. For the rotating models D1 to D4 the grid is made up of 150×20 and 150×40 cells, with the same radial grid spacing as in the spherical model. We choose $n_d = 8$ radial domains for the spectral grid. As in [41] we use a polytropic equation of state in the evolution.

The top panel of Fig. 3.3 shows the evolution of the rest-mass density and lapse at the center.

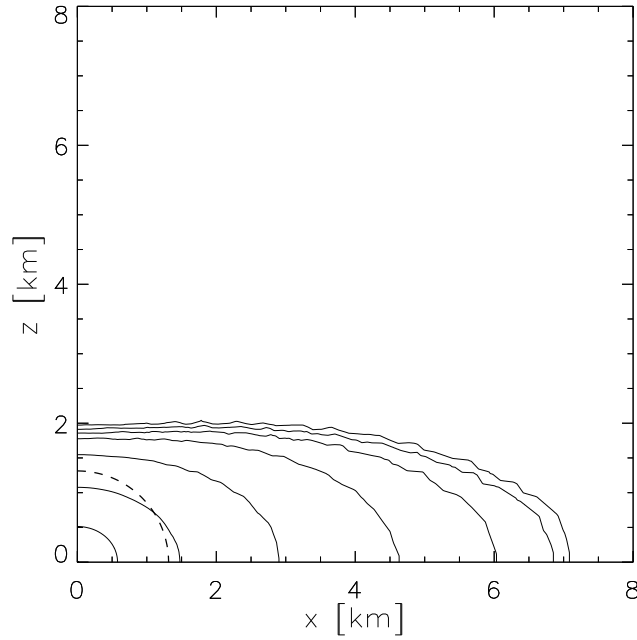


Figure 3.4: Isocontours of the rest-mass density for model D4 after the apparent horizon first appears at $t = 129.9$. The dashed line shows the location of the apparent horizon.

Since for the maximal slicing condition the singularity cannot be reached in a finite time, N_c rapidly approaches zero once the apparent horizon has formed. In parallel, ρ_c grows, which results in a decrease of the numerical time step due to the Courant condition applied to the innermost grid cell. We terminate the evolution as the central regions of the collapsing star inside the apparent horizon become increasingly badly resolved on the regular grid and thus numerical errors grow. We check in model SU that by refining the radial resolution we are able to follow the collapse to even higher densities. Therefore, the only limitation to perform a stable evolution after the apparent horizon formation is the numerical resolution used. Note, however, that the spatial gauge condition is fixed in CFC, and thus we are not able to utilize the common method of exploiting the gauge freedom for the radial component of the shift vector in order to effectively increase the central resolution.

In the bottom panel of Fig. 3.3 we display the time evolution of the apparent horizon radius. As expected, the apparent horizon appears at a finite radius and already encompasses a significant fraction of the total mass of the star ($\sim 70-80\%$) at that time. Afterwards its radius grows as the surrounding matter falls inside beyond the horizon. The fraction of rest mass remaining outside the horizon is also plotted in the figure. In the rotating case the apparent horizon is slightly non-spherical. The ratio of polar to equatorial proper circumferential radius of the apparent horizon at the end of the simulation is $R_p/R_e = 0.998-0.978$ for models D1 to D4, where $R_e := \int_0^{2\pi} \sqrt{g_{\varphi\varphi}} d\varphi / (2\pi)$ and $R_p := \int_0^\pi \sqrt{g_{\theta\theta}} d\theta / \pi$.

Since we cannot reasonably determine the location of the event horizon, as this would require the evolution of spacetime until the black hole has become practically stationary, we utilize the apparent horizon radius to estimate the mass of the newly formed black hole. Following the prescription in [41] we use the expression $M_{\text{BH}} = R_e/2$. Note that this formula is only strictly valid for a stationary Kerr black hole. In our case, however, first of all some (albeit a small) amount of matter is still

outside the horizon and the black hole is still dynamically evolving, and secondly the metric of a Kerr black hole is not conformally flat [196]. Still, according to [41] this approximation (excluding the effects of CFC) introduces an error in the mass estimate of only $\sim 2\%$. For the spherical model the estimated value for M_{BH} at the end of the simulation agrees within 0.5% with the ADM mass M_{ADM} of the initial model, while in the rotating models D1 to D3 the error is $\leq 4\%$. In all these cases the above formula overestimates the black hole mass. Due to its rapid rotation and the resulting strong centrifugal forces, in model D4 the collapse deviates significantly from sphericity, leading to a strongly oblate form of the density stratification. Consequently, we still find a non-negligible amount of matter outside the apparent horizon at the end of the simulation (about 12% of the total rest mass). Therefore the value for M_{BH} is 8.2% smaller than M_{ADM} . In Fig. 3.4 we present the distribution of the rest-mass density and the location of the apparent horizon at the end of the simulation for this particular model. Since the time evolution is limited by our chosen, still computationally affordable grid resolution in the central region we are not able to evolve this model to times when a disk forms as in [41]. Nevertheless, all other quantities qualitatively agree with the results in that work, although we refrain from performing a more detailed comparison due to the respective differences in the gauge of the two formulations used in [41] and in this study, respectively.

In the near future we plan to carry out an exhaustive analysis of the scenario of a collapse to a black hole by comparing on one hand the CFC formulation with FCF (see Sec. 3.5), and on the other hand by comparing FCF with other (*free evolution*) formulations. The difficulties induced by the use of different gauges can be overcome by using gauge-invariant quantities for comparison and analyzing their behavior as a function of proper time.

3.5 Generalization to the fully constrained formalism

The ideas presented in Sec. 3.3 can be generalized to the FCF approach of the full Einstein equations described in Sec. 3.2.1.

As shown in [134], the hyperbolic part of FCF can be split into a first order system. The reformulation of the CFC equations presented in Sec. 3.3 relies on the rescaled extrinsic curvature \hat{A}^{ij} given by Eq. (3.27). Consequently, we write the FCF hyperbolic part as a first order system in (h^{ij}, \hat{A}^{ij}) , instead of first order system in $(h^{ij}, \partial h^{ij}/\partial t)$ as in [134], arriving at

$$\frac{\partial h^{ij}}{\partial t} = 2N\psi^{-6}\hat{A}^{ij} + \beta^k w_k^{ij} - \tilde{\gamma}^{ik}\mathcal{D}_k\beta^j - \tilde{\gamma}^{kj}\mathcal{D}_k\beta^i + \frac{2}{3}\tilde{\gamma}^{ij}\mathcal{D}_k\beta^k, \quad (3.34)$$

$$\begin{aligned} \frac{\partial \hat{A}^{ij}}{\partial t} = & -\mathcal{D}_k \left(-\frac{N\psi^2}{2}\tilde{\gamma}^{kl}w_l^{ij} - \beta^k\hat{A}^{ij} \right) - \hat{A}^{kj}\mathcal{D}_k\beta^i - \hat{A}^{ik}\mathcal{D}_k\beta^j + \frac{2}{3}\hat{A}^{ij}\mathcal{D}_k\beta^k \\ & + 2N\psi^{-6}\tilde{\gamma}_{kl}\hat{A}^{ik}\hat{A}^{jl} - 8\pi N\psi^6 \left(\psi^4 S^{ij} - \frac{S\tilde{\gamma}^{ij}}{3} \right) + N \left(\psi^2 \tilde{R}_*^{ij} + 8\tilde{\gamma}^{ik}\tilde{\gamma}^{jl}\mathcal{D}_k\psi\mathcal{D}_l\psi \right) \\ & + 4\psi \left(\tilde{\gamma}^{ik}\tilde{\gamma}^{jl}\mathcal{D}_k\psi\mathcal{D}_l N + \tilde{\gamma}^{ik}\tilde{\gamma}^{jl}\mathcal{D}_k N\mathcal{D}_l\psi \right) \\ & - \frac{1}{3} \left[N \left(\psi^2 \tilde{R} + 8\tilde{\gamma}^{kl}\mathcal{D}_k\psi\mathcal{D}_l\psi \right) + 8\psi\tilde{\gamma}^{kl}\mathcal{D}_k\psi\mathcal{D}_l N \right] \tilde{\gamma}^{ij} \\ & - \frac{1}{2} \left(\tilde{\gamma}^{ik}w_k^{lj} + \tilde{\gamma}^{kj}w_k^{il} \right) \mathcal{D}_l(N\psi^2) - \tilde{\gamma}^{ik}\tilde{\gamma}^{jl}\mathcal{D}_k\mathcal{D}_l(N\psi^2) + \frac{1}{3}\tilde{\gamma}^{ij}\tilde{\gamma}^{kl}\mathcal{D}_k\mathcal{D}_l(N\psi^2), \quad (3.35) \end{aligned}$$

where

$$w_k^{ij} := \mathcal{D}_k h^{ij}, \quad (3.36)$$

$$\tilde{R}_*^{ij} := \frac{1}{2} \left[-w_l^{ik} w_k^{jl} - \tilde{\gamma}_{kl} \tilde{\gamma}^{mn} w_m^{ik} w_n^{jl} + \tilde{\gamma}_{nl} w_k^{mn} \left(\tilde{\gamma}^{ik} w_m^{jl} + \tilde{\gamma}^{jk} w_m^{il} \right) \right] + \frac{1}{4} \tilde{\gamma}^{ik} \tilde{\gamma}^{jl} w_k^{mn} \mathcal{D}_l \tilde{\gamma}_{mn}. \quad (3.37)$$

The system is closed by adding the equation

$$\begin{aligned} \frac{\partial w_k^{ij}}{\partial t} - \mathcal{D}_k \left(\beta^l w_l^{ij} + 2N\psi^{-6} \hat{A}^{ij} \right) &= -w_k^{il} \mathcal{D}_l \beta^j - \tilde{\gamma}^{il} \mathcal{D}_k \mathcal{D}_l \beta^j - w_k^{lj} \mathcal{D}_l \beta^i - \tilde{\gamma}^{lj} \mathcal{D}_k \mathcal{D}_l \beta^i + \frac{2}{3} \tilde{\gamma}^{ij} \mathcal{D}_k \mathcal{D}_l \beta^l \\ &\quad + \frac{2}{3} w_k^{ij} \mathcal{D}_l \beta^l, \end{aligned} \quad (3.38)$$

which is derived from applying partial derivatives with respect to t in the definition of w_k^{ij} . Moreover, the system observes the constraint of Dirac gauge, $w_i^{ij} = 0$ [Eq. (3.6)], and for the determinant of the conformal metric, we obtain $\tilde{\gamma} = f$. The first order system given by Eqs. (3.34)–(3.38) has the same properties regarding hyperbolicity and existence of fluxes as the one in [134]. It has the advantage over the second order system for h^{ij} proposed in Ref. [73] of getting rid of partial derivatives with respect to t of the lapse N , the shift β^i , or the conformal factor ψ .

The elliptic part of FCF can be rewritten, using the tensor \hat{A}^{ij} , as

$$\tilde{\gamma}^{kl} \mathcal{D}_k \mathcal{D}_l \psi = -2\pi\psi^{-1} E^* - \frac{\tilde{\gamma}_{il} \tilde{\gamma}_{jm} \hat{A}^{lm} \hat{A}^{ij}}{8\psi^7} + \frac{\psi \tilde{R}}{8}, \quad (3.39)$$

$$\tilde{\gamma}^{kl} \mathcal{D}_k \mathcal{D}_l (N\psi) = \left[2\pi\psi^{-2} (E^* + 2S^*) + \left(\frac{7\tilde{\gamma}_{il} \tilde{\gamma}_{jm} \hat{A}^{lm} \hat{A}^{ij}}{8\psi^8} + \frac{\tilde{R}}{8} \right) \right] (N\psi), \quad (3.40)$$

$$\tilde{\gamma}^{kl} \mathcal{D}_k \mathcal{D}_l \beta^i + \frac{1}{3} \tilde{\gamma}^{ik} \mathcal{D}_k \mathcal{D}_l \beta^l = 16\pi N\psi^{-6} \tilde{\gamma}^{ij} (S^*)_j + \hat{A}^{ij} \mathcal{D}_j (2N\psi^{-6}) - 2N\psi^{-6} \Delta_{kl}^i \hat{A}^{kl}. \quad (3.41)$$

The strategy to evolve the two symmetric tensors h^{ij} and \hat{A}^{ij} relies on a decomposition of these tensors in longitudinal and transverse traceless parts. The longitudinal parts (divergences with respect to the flat metric) are either known a priori or are determined by the elliptic equations. More specifically, the divergence of h^{ij} vanishes according to the Dirac gauge, whereas the divergence of \hat{A}^{ij} is determined by the momentum constraint (3.42) – see below. Consequently, focus is placed on the transverse traceless parts of these tensors. The latter are described in a pure-spin tensor harmonic decomposition, as it has been discussed in a previous article [134]. In particular, each transverse traceless tensor is fully expressed in terms of two scalar potentials (named A and \tilde{B} in [134]) that are evolved according to evolution equations obtained from the transverse traceless parts of Eqs. (3.34) and (3.35) for h^{ij} and \hat{A}^{ij} , respectively, by applying consistently the decomposition in [134]. Once the scalar potentials on the next time slice are determined, the tensors h^{ij} and \hat{A}_{TT}^{ij} can be reconstructed completely, satisfying the divergence-free conditions. This fully fixes h^{ij} , whereas in the case of \hat{A}^{ij} the longitudinal part is computed in a very similar way to the CFC case, i.e. by determining the vector X^i from the momentum constraint as described hereafter.

From Eq. (3.26), the momentum constraint can be written as

$$\mathcal{D}_j \hat{A}^{ij} = 8\pi \tilde{\gamma}^{ij} (S^*)_j - \Delta_{kl}^i \hat{A}^{kl}, \quad (3.42)$$

which is equivalent to the following elliptic equation for X^i :

$$\begin{aligned} \mathcal{D}_j \mathcal{D}^j X^i + \frac{1}{3} \mathcal{D}^i \mathcal{D}_k X^k + \tilde{\gamma}^{im} \left(\mathcal{D}_k \tilde{\gamma}_{ml} - \frac{\mathcal{D}_m \tilde{\gamma}_{kl}}{2} \right) \times \\ \left(\mathcal{D}^k X^l + \mathcal{D}^l X^k - \frac{2}{3} f^{kl} \mathcal{D}_p X^p \right) = \\ 8\pi \tilde{\gamma}^{ij} (S^*)_j - \tilde{\gamma}^{im} \left(\mathcal{D}_k \tilde{\gamma}_{ml} - \frac{\mathcal{D}_m \tilde{\gamma}_{kl}}{2} \right) \hat{A}_{\text{TT}}^{kl}. \end{aligned} \quad (3.43)$$

This elliptic equation for the vector X^i is linear. Since h^{ij} and \hat{A}_{TT}^{ij} have been calculated previously, we can solve the elliptic equation (3.43) to obtain the vector X^i . With this method, the Dirac gauge and the momentum constraint are guaranteed to be satisfied. Then, \hat{A}^{ij} is reconstructed from \hat{A}_{TT}^{ij} and X^i on the new time slice.

At this point, since the tensors h^{ij} and \hat{A}^{ij} are known, we can follow exactly the same scheme as in the CFC case to solve in a hierarchical way the elliptic equations. First the conformal factor is obtained from Eq. (3.39), then the lapse function from Eq. (3.40), and finally the shift vector is acquired from Eq. (3.41). These equations are decoupled in the order mentioned. No sign problems are exhibited in the scalar elliptic equation and therefore the maximum principle can be applied. A minor concern is associated with the sign of the term \tilde{R} in Eq. (3.39), but unique solutions also exist for negative conformal Ricci scalars (closely related to \tilde{R}). Note that, contrary to the CFC case, here no (additional) approximation has been made: it is simply a new scheme to write down FCF, where the elliptic part is better behaved from the point of view of local uniqueness. Numerical simulations with this FCF scheme will be presented in a future publication.

3.6 Discussion

3.6.1 Summary

We have presented an approach to the solution of the uniqueness issues appearing in certain constrained formulations of Einstein equations. We have illustrated the problem and its solution through a detailed analytical and numerical study of a waveless approximation that retains all the involved essential features.

More specifically, we have reformulated XCTS-like elliptic systems appearing in constrained evolution schemes of the Einstein equations like FCF of [73, 134], as well as in the CFC approximation [260, 482]. Such systems require the simultaneous solution of the constraints, in particular the momentum constraint for the shift, together with a maximal slicing condition for the lapse. The resulting elliptic system presents potential local non-uniqueness problems, and numerical implementations have indeed encountered such obstacles. The original CFC formulation has not been able to cope with these problems, suffering from convergence of the system to unphysical solutions or non-convergence at all in high density regimes. We have suggested that these problems are not due to the approximative nature of CFC, since FCF in the variant of [73, 134], which is a natural generalization of CFC to the non-conformally flat case, also suffers from the same problems. In order to address these issues, and first focusing on the simpler CFC case, we have considered the conformal rescaling of the traceless part of the extrinsic curvature, resulting in the expression for \hat{A}^{ij} in Eq. (3.27), which is a rescaling different from the respective ones employed in FCF and the CFC approximation, but coincides with the one in

the XCTS approach of [487, 364]. This is motivated by the work of Shapiro and Teukolsky [410], who simulated the collapse of a neutron star model using such a reformulation of the CFC metric equations (however restricted to spherical symmetry in their case) and apparently did not encounter any of the problems described above. Extending their approach to three dimensions, we have decomposed \hat{A}^{ij} into longitudinal and transverse parts as in the CTT formulation of the constraint equations (3.29). The divergence (i.e. the longitudinal part) of this tensor is determined by the momentum constraints, Eqs. (3.28) in the CFC case, just as in the CTT formulation. In the CFC scheme, we have neglected the transverse part of this tensor, as the order of its error is higher than the one arising from the CFC approximation itself. In the non-approximate FCF case, the transverse part of \hat{A}^{ij} is determined by an evolution equation. Once the conformal extrinsic curvature is obtained it can be employed in the Hamiltonian equation to calculate the conformal factor ψ . The lapse is then fixed through the maximal slicing condition, and the resulting equation allows the application of a maximum principle uniqueness argument. Finally, the shift is found through the kinematical relationship defining the extrinsic curvature, leading to Eq. (3.33).

By performing a variety of tests, we have provided evidence that the problem of convergence to an unphysical solution of the metric equations (or even complete non-convergence) in the original formulation of the CFC scheme is fully cured by our new reformulation. Not only numerical results in the original CFC scheme (in the at most moderately gravitationally compact regime where that system still yields physically correct solutions) can be reproduced by the new formulation but, more importantly, the new numerical results presented here exhibit the proper numerical and physical behavior even for highly compact configurations. For the first time, it has been possible to successfully perform both the migration test and the collapse of a neutron star to a black hole in the CFC case in a consistent way. Our new formulation thus facilitates simulations in the high density regime of those scenarios where CFC is still a reasonably fair approximation, that is, for systems which are not too far from sphericity like stellar gravitational collapse.

3.6.2 Comparison with previous works

As compared to the original CFC formulation by Isenberg [260] and Mathews and Wilson [482], the scheme presented here is augmented by an additional vector elliptic equation for X^i , while the elliptic character of the system of metric equations is preserved. The new scheme reformulates the CFC approximation in a CTT shape (one scalar and one vector elliptic equation), and then solves for the lapse and the shift (one additional scalar and one vector elliptic equation). In contrast, the original CFC scheme employed an (X)CTS approach where, together with two scalar elliptic equations, only one vector elliptic equation was present. In contrast to the original scheme, the elliptic system in the new formulation not only corrects the problem of local uniqueness in the scalar elliptic equations, but also introduces a hierarchical structure that decouples the system in one direction.

In the context of the conformally flat approximation, the same “augmented CFC” scheme as that discussed here has been introduced already by Saijo [397] to compute gravitational collapse of differentially rotating supermassive stars. However, in this work the inconsistency between Eq. (3.25) and Eq. (3.29), i.e. setting to zero the transverse traceless part of \hat{A}^{ij} , has not been pointed out. On the contrary, we have analyzed this inconsistency in detail (cf. Appendix 3.A) and have shown that it leads to an error of the same order as that of the CFC approximation. In addition, we have shown here that the introduction of the vector potential X^i is the key ingredient for solving the non-uniqueness issue.

The same scheme, but without the conformal rescaling of the matter quantities, has also been

used recently by Shibata and Uryū [426] in the context of computing initial data. As in [397], the inconsistency resulting from setting to zero the transverse traceless part of \hat{A}^{ij} and the uniqueness issue are not discussed in their work. We emphasize that these studies [397, 426] do not discuss the extension of the new scheme to the non-conformally flat case, as done here.

Let us also mention that the augmented CFC scheme presented here can be regarded as a hybrid mixture between some of the waveless approximation theories (WAT) proposed by Isenberg [260]. In fact, the CFC approximation using the two choices $\tilde{\gamma}_{ij} = f_{ij}$ and $\partial_t \tilde{\gamma}_{ij} = 0$ [as employed in Eq. (3.33)] corresponds to version WAT-I. On the other hand, the approximation $\hat{A}_{\text{TT}}^{ij} = 0$ used in Eq. (3.29) is in the spirit of the vanishing transverse traceless part of the extrinsic curvature in the (coupled) version WAT-II (although WAT-II refers to the physical extrinsic curvature, whereas here we have dealt with the conformal one). As mentioned above, both assumptions are consistent at the considered level of approximation as shown in Appendix 3.A.

Regarding the complete constrained evolution of the Einstein equations, we have generalized the ideas presented here for the CFC case to the elliptic part of FCF. In previous studies [73, 134], the hyperbolic part of Einstein equations resulted in a wave-type equation for the tensor h^{ij} , representing the deviation of the 3-metric from conformal flatness. With the introduction of \hat{A}^{ij} we have recovered here a first-order evolution system, analogous to the standard Hamiltonian 3 + 1 system, in which we have however retained only the divergence-free terms. Thus, for both h^{ij} and \hat{A}^{ij} , the transverse (divergence-free) parts are evolved by this system, while the longitudinal parts are fixed either by the gauge (for h^{ij}), or by the momentum constraint (for \hat{A}^{ij}). Numerical results for this case will be presented in future studies.

We finally comment on the recent work by Rinne [389], where uniqueness problems appearing in certain constrained and partially constrained schemes for vacuum axisymmetric Einstein equations [118, 200] are addressed. As in the present case, uniqueness issues related to the Hamiltonian constraint equation are solved by adopting an appropriate rescaling the extrinsic curvature. On the other hand, problems associated with the slicing condition are tracked to the substitution in that equation of the extrinsic curvature by its kinematical expression in terms of the (shift and the) lapse. The latter spoils the uniqueness properties by reversing the sign of the relevant term in the slicing equation. This problem is solved by enlarging the elliptic system with an additional vector so as to re-express the relevant components of the extrinsic curvature without resorting to the lapse. The resulting elliptic system presents also a hierarchical structure. Although the spirit of such approach is close to the one here presented, the specific manner of introducing the additional vector variable in [389] critically relies on the two-dimensionality of the axisymmetric problem (specifically, on a choice of a particular gauge and on the fact that vectors and rank-two traceless symmetric tensors have the same number components in two dimensions, a property lost in three dimensions). On the contrary, the introduction of the vector X^i through the CTT decomposition (3.29) is properly devised to work in three dimensions. Relevant related discussions in the three-dimensional context can be found in Sec. 3.4 of [389], where the relation between non-uniqueness problems in XCTS and axisymmetric constrained evolution schemes is discussed.

APPENDIX

3.A Consistency of the approximation

In the derivation of the new formalism we make use of the fact that $(LX)^{ij} \approx \hat{A}^{ij}$ in CFC. We show next that this assumption is completely consistent at the accuracy level of the CFC approximation. In the first place, we need to estimate the error of the CFC approximation itself. By definition the CFC 3-metric deviates linearly with h^{ij} from the (exact) FCF case. It can be easily shown from the FCF equations (3.39)-(3.41) that the metric quantities behave as

$$\psi = \psi_{\text{CFC}} + \mathcal{O}(h), \quad (3.44)$$

$$N = N_{\text{CFC}} + \mathcal{O}(h), \quad (3.45)$$

$$\beta^i = \beta_{\text{CFC}}^i + \mathcal{O}(h). \quad (3.46)$$

Therefore h^{ij} can be used as an estimator for the error of the CFC approximation.

Two limits in which CFC is exact will be considered. First, in spherical symmetry the CFC metric system is an exact reformulation of the Einstein equations since $h^{ij} = 0$ in the FCF metric. If the system is close to spherical symmetry (i.e. spheroidal), and if we are able to define a quasi-spherical surface of the system (e.g., the surface of a star or the apparent horizon of a BH) then the equatorial and polar circumferential proper radius, R_e and R_p , can be computed, and we can define the ellipticity of the system as

$$e^2 := 1 - R_p^2/R_e^2. \quad (3.47)$$

Close to sphericity e^2 scales linearly with h^{ij} , and we can ensure that the error of CFC is $h^{ij} \sim \mathcal{O}(e^2)$. The second limit to consider is if a post-Newtonian expansion of the gravitational sources is possible, i.e. if the post-Newtonian parameter $\max(v^2/c^2, GM/Lc^2) < 1$, where v , M , and L are the typical velocity, mass, and length of the system, respectively. In this case the CFC metric behaves like the first post-Newtonian approximation [281, 114], i.e.

$$\psi = \psi_{\text{CFC}} + \mathcal{O}(1/c^4), \quad (3.48)$$

$$N = N_{\text{CFC}} + \mathcal{O}(1/c^4), \quad (3.49)$$

$$c\beta^i = c\beta_{\text{CFC}}^i + \mathcal{O}(1/c^4). \quad (3.50)$$

Note that, for clarity, we explicitly retain powers of the speed of light c as factors in the equations throughout this appendix. In the case that both limits are valid, i.e. close to sphericity and in the post-Newtonian expansion, the non-conformally-flat part of the 3-metric behaves like $h^{ij} \sim \mathcal{O}(e^2/c^4)$. The next step is to compute the behavior of the CFC metric if we assume $(LX)^{ij} \approx \hat{A}^{ij}$, considering the two limiting cases introduced above.

In the spherically symmetric case the relation $(LX)^{ij} = \hat{A}^{ij}$ is trivially fulfilled. Therefore the behavior for a quasi-spherical configuration is also $h^{ij} \sim \mathcal{O}(e^2)$ even if $\hat{A}_{\text{TT}}^{ij} = 0$ is assumed. This limit in the approximation is very important, since it is independent of the strength of the gravitational field. For example it allows us to evolve black holes, with the only condition that h^{ij} should be small, i.e. close to the sphericity.

To check the approximation in the post-Newtonian limit we need to compare β_{CFC}^i and X^i . This can be done by means of the post-Newtonian expansion of the sources of Eqs. (3.17) and (3.30), respectively,

$$\Delta\beta_{\text{CFC}}^i + \frac{1}{3}\mathcal{D}^i\mathcal{D}_j\beta_{\text{CFC}}^j = 16\pi S^{*i} + \mathcal{O}(1/c^7), \quad (3.51)$$

$$\Delta X^i + \frac{1}{3}\mathcal{D}^i\mathcal{D}_j X^j = 8\pi S^{*i} + \mathcal{O}(1/c^7). \quad (3.52)$$

From the comparison of Eqs. (3.51) and (3.52) we obtain that

$$c^3 \frac{\beta_{\text{CFC}}^i}{2} = c^3 X^i + \mathcal{O}(1/c^2). \quad (3.53)$$

Thus \hat{A}^{ij} can be computed in terms of X^i as

$$c^4 \hat{A}^{ij} = \frac{\psi_{\text{CFC}}^6}{2N_{\text{CFC}}} c^4 (L\beta_{\text{CFC}})^{ij} = c^4 (LX)^{ij} + \mathcal{O}(1/c^2), \quad (3.54)$$

where we make use of $\psi_{\text{CFC}}^6/N_{\text{CFC}} = 1 + \mathcal{O}(1/c^2)$. The effect of using $(LX)^{ij}$ instead of \hat{A}^{ij} in the calculation of the CFC metric can be seen in the expressions

$$\begin{aligned} \psi_{\text{CFC}} &= \Delta_{\text{s}}^{-1} \mathcal{S}_{(\psi)}(N_{\text{CFC}}, \psi_{\text{CFC}}, \hat{A}^{ij}) \\ &= \Delta_{\text{s}}^{-1} \mathcal{S}_{(\psi)}(N_{\text{CFC}}, \psi_{\text{CFC}}, (LX)^{ij}) + \mathcal{O}(1/c^8), \end{aligned} \quad (3.55)$$

$$\begin{aligned} N_{\text{CFC}} &= \psi_{\text{CFC}}^{-1} \Delta_{\text{s}}^{-1} \mathcal{S}_{(N\psi)}(N_{\text{CFC}}, \psi_{\text{CFC}}, \hat{A}^{ij}) \\ &= \psi_{\text{CFC}}^{-1} \Delta_{\text{s}}^{-1} \mathcal{S}_{(N\psi)}(N_{\text{CFC}}, \psi_{\text{CFC}}, (LX)^{ij}) + \mathcal{O}(1/c^8), \end{aligned} \quad (3.56)$$

$$\begin{aligned} c\beta_{\text{CFC}}^i &= c\Delta_{\text{v}}^{-1} \mathcal{S}_{(\beta)}(N_{\text{CFC}}, \psi_{\text{CFC}}, \hat{A}^{ij}) \\ &= c\Delta_{\text{v}}^{-1} \mathcal{S}_{(\beta)}(N_{\text{CFC}}, \psi_{\text{CFC}}, (LX)^{ij}) + \mathcal{O}(1/c^6). \end{aligned} \quad (3.57)$$

where $\mathcal{S}_{(\psi)}$, $\mathcal{S}_{(N\psi)}$ and $\mathcal{S}_{(\beta)}$ are the sources of Eqs. (3.31)–(3.33), and Δ_{s}^{-1} and Δ_{v}^{-1} are just the inverse operators appearing in the right-hand-side of these equations (for the scalars ψ and $N\psi$, and for the vector β^i , respectively). When comparing Eqs. (3.56)–(3.50) with Eqs. (3.48)–(3.50), it becomes obvious that in all cases the error introduced by making the approximation $(LX)^{ij} \approx \hat{A}^{ij}$ is smaller than the error of the CFC approximation itself.

As an illustration of the above properties, we study the influence of the \hat{A}_{TT}^{ij} term in Eq. (3.29) when computing rotating neutron star models with a polytropic $\Gamma = 2$ equation of state. This model setup contains the initial models used in Sec. 3.4. They assume axial symmetry and stationarity, in combination with rigid rotation. We build a sequence of rotating polytropes with increasing rotation frequencies, while keeping the central enthalpy fixed, which produces models of increasing masses from $M = 1.33 M_{\odot}$ (no rotation), to $M = 1.57 M_{\odot}$ (the Kepler limit; see below). For all these models, we use three gravitational field schemes: the exact Einstein equations using the stationary ansatz in FCF, and the two approximate ones, regular CFC and CFC neglecting the term \hat{A}_{TT}^{ij} in Eq. (3.29). The results are displayed on a logarithmic scale in Fig. 3.5. In the top panel we show the maximal amplitudes of \hat{A}_{TT}^{ij} (relatively to \hat{A}^{ij}) in both FCF and regular CFC, as functions of the ellipticity e defined in Eq. (3.47). This quantity is physically and numerically limited by the minimal rotational period at the so-called mass-shedding limit (or Kepler limit), when centrifugal forces exactly balance gravitational and pressure forces at the star's equator. In the FCF case we plot the maximal amplitude of h^{ij} . This quantity is dimensionless and represents the deviation of the 3-metric from conformal flatness, which can be interpreted as the relative error one makes in the metric when using CFC instead of FCF. Note that this error on computing \hat{A}^{ij} by discarding the \hat{A}_{TT}^{ij} term in the CFC approximation is roughly of the same magnitude as the error on the metric in the CFC case. All these quantities decrease like $\mathcal{O}(e^2)$ as expected, except for stars rotating close to the Kepler limit. Indeed, the development in powers e is equivalent to a slow-rotation approximation (see, e.g., [240])

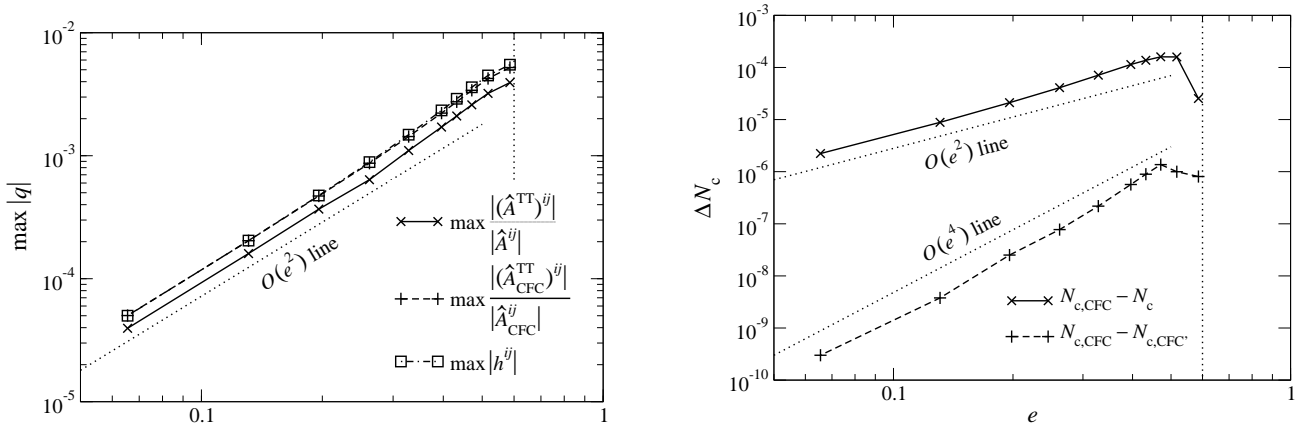


Figure 3.5: Consistency of the approximation for rotating neutron star models. In the left panel $\max |\hat{A}_{\text{TT}}^{ij} / \hat{A}^{ij}|$ for FCF (solid line) and CFC (dashed line) as well as the maximum deviation from conformal flatness $\max |h^{ij}|$ for FCF (dash-dotted line) are plotted against the ellipticity e . The right panel shows the absolute difference $|N_{c,\text{CFC}} - N_c|$ in the central value of the lapse between CFC and FCF (solid line) and the absolute difference $|N_{c,\text{CFC}} - N_{c,\text{CFC}'}|$ between regular CFC and CFC neglecting \hat{A}_{TT}^{ij} in Eq. (3.29) (dashed line). The Kepler limit is marked by vertical dotted lines, while the slanted dotted lines represent the order of accuracy with respect to powers of e .

by perturbing spherically symmetric configurations and, when comparing these slow-rotation results to numerical “exact” ones for rigidly rotating stars (see, e.g., [379] in the two-fluids case), one sees that they usually agree extremely well, excepted very close to the Kepler limit, where this “perturbed spherical symmetry” approach is no longer valid. Finally, because \hat{A}^{ij} appears as a quadratic source term in the Poisson-like equations (3.15, 3.16), the overall errors on the lapse N or the conformal factor ψ are even smaller, as shown in the bottom panel of Fig. 3.5. In the case of the central value N_c of the lapse, the error due to the CFC approximation is maximal at the Kepler limit and $\lesssim 10^{-4}$ for the studied sequence. The error which is then due to neglecting \hat{A}_{TT}^{ij} within the CFC scheme amounts to $\lesssim 10^{-6}$ and decreases faster than the error due to the CFC approximation, namely as $\mathcal{O}(e^4)$, again except near the Kepler limit. Our tests thus show that for stationary rotating neutron star models this additional approximation induces an error which falls within the overall CFC approximation.

Deuxième partie

Méthodes spectrales pour la relativité
numérique

Les équations d'Einstein se présentent comme un système d'équations aux dérivées partielles (EDP) couplées et non-linéaires, dépendant des quatre coordonnées de temps et d'espace. Ainsi, le formalisme contraint présenté dans la partie I se traduit par un système couplant cinq EDP elliptiques du second ordre, deux EDP hyperboliques du second ordre et le système d'EDP pour la jauge de Dirac (5 équations du premier ordre, qui seront explicitées dans le chapitre 6). Cette complexité, même avec une jauge « plus simple », fait qu'il n'existe que très peu de solutions exactes des équations d'Einstein qui soient pertinentes pour l'astrophysique. Une première méthode pour obtenir des solutions approchées est de faire des développements perturbatifs de type “post-Newtonien” [62], qui se sont révélés très puissants pour le problème des ondes gravitationnelles provenant de la phase spirillante des binaires d'astres compacts. Cependant, ce type de techniques est limité par l'hypothèse que les astres sont bien représentés par des points matériels. Si l'on cherche à modéliser la fin de l'événement de fusion de la binaire ou résoudre les équations pour la matière venant de la conservation du tenseur impulsion-énergie (équation de l'hydrodynamique, équations de Maxwell, ...), il est clair qu'il faut alors utiliser des méthodes numériques de résolution d'EDP. Il s'agit du champ de recherche de la *relativité numérique*, dont le but est de développer les techniques numériques les plus performantes afin de pouvoir simuler les systèmes physiques possédant un champ gravitationnel intense (nécessitant la relativité générale pour une bonne description). Plusieurs techniques numériques peuvent être mises à contribution pour résoudre les EDP de ces modèles, qui incluent souvent les équations de l'hydrodynamique, magnéto-hydrodynamique, ...

Alors que la plupart des groupes de relativité numérique utilisaient les méthodes aux différences finies, ce sont Silvano Bonazzola et Jean-Alain Marck qui ont introduit les méthodes spectrales en relativité numérique dans les années 1980 [66, 78]. Ces méthodes avaient été développées et présentées à la fin des années 1970 [210], avec l'idée de base qui est de représenter une fonction, non pas par un ensemble de ses valeurs en un nombre fini de points de grille, mais par un ensemble de coefficients dans une base fonctionnelle donnée. La définition d'une grille reste nécessaire pour le calcul de ces coefficients et pour l'évaluation d'opérateurs non-linéaires. L'exemple le plus simple est l'utilisation de séries tronquées de Fourier pour la représentation de fonctions périodiques. Dans les cas non-périodiques, on utilise une base de polynômes orthogonaux, comme les polynômes de Tchebychev, de Legendre ou, plus généralement, des fonctions solutions d'un problème de Sturm-Liouville singulier. Le grand avantage est qu'il faut, en général, beaucoup moins de coefficients que de valeurs sur des points de grilles pour bien décrire une fonction sur un intervalle, calculer sa dérivée, etc... Cela permet de réduire la mémoire utilisée par les programmes et de pouvoir facilement aborder des problèmes à trois dimensions. Le principal inconvénient est la non-convergence de ces méthodes dans les cas où la fonction que l'on veut représenter est discontinue (phénomène de Gibbs).

Depuis le début des années 2000, d'autres groupes de relativité numérique ont commencé à adopter les méthodes spectrales ; en particulier le groupe de Caltech-Cornell qui a réussi récemment à effectuer les simulations les plus précises de binaires de trous noirs [405]. Par ailleurs, des approches « multi-méthodes » combinant les méthodes spectrales avec d'autres ont été utilisées : méthodes spectrales pour le champ gravitationnel et, dans le cadre du projet CoCoNuT [150], méthodes de Godunov (ou capture de choc) pour l'hydrodynamique relativiste [342, 151, 150], ou des méthodes Lagrangiennes (smoothed particle hydrodynamics) pour

les coalescences de binaires d'étoiles à neutrons [170]. Ainsi, il est apparu intéressant de rédiger un article de revue sur les méthodes spectrales en relativité numérique, et nous avons eu la chance, Philippe Grandclément et moi-même, d'être invité pour le réaliser [230]. Cet article tente de faire le point sur les travaux de relativité numérique qui utilisent les méthodes spectrales, ainsi que de donner quelques informations et démonstrations sur ces méthodes numériques elles-mêmes (voir chapitre 4).

De manière plus pratique, en collaboration avec Éricourgoulhon, Philippe Grandclément et Jean-Alain Marck, nous avons développé la bibliothèque numérique LORENE [216] pour la résolution numérique des équations d'Einstein (mais aussi d'autres équations de physique théorique), en utilisant les méthodes spectrales. Cette bibliothèque est aujourd'hui sous licence publique de type GNU, c'est-à-dire qu'elle est librement téléchargeable depuis sa page web [216] ; elle est écrite en C++, qui est un langage de programmation orienté objet. Nous avons mis en place une liste de diffusion et organisé une école internationale de formation à son utilisation en novembre 2005.

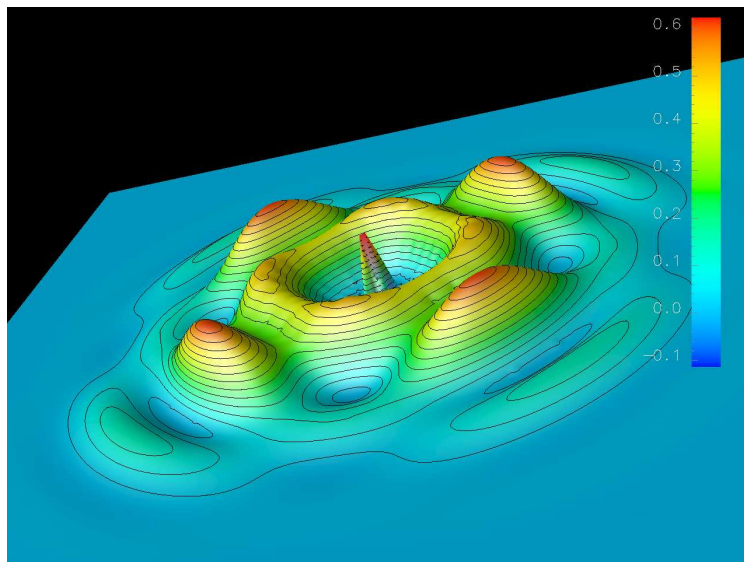


FIG. II.1 – Scalaire de courbure dans le plan équatorial d'une onde gravitationnelle se propageant dans le vide. Le code d'évolution utilise le formalisme contraint et les méthodes spectrales, de la bibliothèque LORENE.

En revanche, le travail qui est présenté dans les chapitres 5–7 et qui a été publié correspond à deux autres aspects liés à l'utilisation des méthodes spectrales en relativité numérique : le développement d'algorithmes d'analyse numérique nécessaires à la relativité générale et celui d'outils spécifiques, en particulier pour le diagnostic des résultats. En ce qui concerne le premier point, avec Silvano Bonazzola, nous nous sommes penchés sur les problèmes de conditions aux bords absorbantes pour l'équation de propagation des ondes gravitationnelles [341]. En effet, contrairement aux équations elliptiques, il n'est pas possible d'effectuer simplement un changement de coordonnée spatiale de type $u = 1/r$, afin de ramener le domaine d'intégration infini dans un intervalle fini. Il faut donc, en général, imposer des conditions aux bords « trans-

parentes » pour que les ondes puissent quitter le domaine de calcul numérique sans être réfléchies par le bord artificiel. Nous avons donc présenté de telles conditions aux bords, en les implémentant et testant sur des exemples simples. Ces conditions sont maintenant utilisées comme standard dans les simulations utilisant LORENE. Cependant, plusieurs études ont depuis montré des conditions aux bords plus sophistiquées [96, 388, 95, 390, 391], et il serait sans doute judicieux de considérer l'implémentation de ces nouvelles prescriptions, bien qu'elles soient relativement compliquées à mettre en œuvre.

Toujours en analyse numérique, un algorithme adapté à la résolution de l'équation des ondes pour un tenseur symétrique, avec la contrainte de divergence nulle a été développé [340]. Ce problème, qui est la généralisation aux tenseurs d'ordres 2 des équations pour le champ vectoriel magnétique, est central dans le formalisme contraint décrit dans les chapitres 1–3, où le tenseur h^{ij} représentant la déviation de la 3-métrie par rapport à la métrie plate vérifie une équation d'évolution de type « onde » avec, en plus la condition de jauge qui est la divergence nulle. Il s'agit, bien évidemment d'un système sur-déterminé, pour lequel il faut choisir les bonnes équations à résoudre pour que toutes soient néanmoins vérifiées. Une première approche relativement simple avait été présentée dans l'article de Bonazzola *et al.* de 2004 [73], mais dans de nombreuses applications, les résultats étaient entachés d'un trop grand bruit numérique. Il était donc nécessaire de revoir complètement l'algorithme en cherchant les degrés de libertés scalaires associés au tenseur h^{ij} . Cela permet d'effectuer une intégration relativement aisée de l'équation des ondes en termes de ces scalaires, puis de reconstruire à chaque pas de temps le tenseur complet par les conditions de divergence nulle et les définitions des scalaires. Cette approche a été implémentée dans la bibliothèque LORENE [216].

Enfin, outil numérique important a été développé avec M. Lap-Ming Lin, post-doctorant dans notre groupe, concernant la recherche d'horizons apparents dans les espaces-temps provenant de simulations numériques [294], voir chapitre 7. Les horizons apparents sont des objets très intéressants pour les simulations numériques, à plus d'un titre. D'abord, en supposant vraie la conjecture de censure cosmique, la présence d'un horizon apparent implique nécessairement la présence d'un horizon des événements autour de celui-ci. Cela est donc une preuve de la présence de trou noir dans les données numériques, avant l'apparition éventuelle de la singularité centrale, qui de toute manière ne peut être décrite correctement sur ordinateur. Ensuite, le fait de connaître avec précision la position d'un horizon apparent et la métrie induite sur sa surface permet de déduire de nombreuses propriétés sur le trou noir qu'il représente : masse, moment cinétique ou écart à la situation stationnaire. Nous avons ainsi présenté un nouvel algorithme permettant de trouver, dans un espace-temps numérique, la position d'un horizon apparent en coordonnées sphériques. Cet algorithme itératif utilise les méthodes spectrales et une décomposition de la partie angulaire des fonctions sur la base des harmoniques sphériques. Nous avons montré que cet algorithme était très robuste et plus rapide que ceux précédemment publiés et utilisés dans la communauté en lui faisant passer des tests sur les solutions analytiques. Il a été implémenté dans la bibliothèque numérique LORENE [216], ainsi que dans le programme CoCoNuT [150].

Chapitre 4

Spectral methods for numerical relativity

Version publiée : P. Grandclément et J. Novak, *Living Reviews in Relativity* **12**, 1 (2009).

Sommaire

4.1	Introduction	99
4.2	Concepts in One Dimension	105
4.3	Multidimensional Cases	130
4.4	Time-Dependent Problems	141
4.5	Stationary Computations and Initial Data	159
4.6	Dynamic Evolution of Relativistic Systems	173
4.7	Conclusions	186

4.1 Introduction

Einstein's equations represent a complicated set of nonlinear partial differential equations for which some exact [61] or approximate [62] analytical solutions are known. But these solutions are not always suitable for physically or astrophysically interesting systems, which require an accurate description of their relativistic gravitational field without any assumption on the symmetry or with the presence of matter fields, for instance. Therefore, many efforts have been undertaken to solve Einstein's equations with the help of computers in order to model relativistic astrophysical objects. Within this field of *numerical relativity*, several numerical methods have been experimented with and a large variety are currently being used. Among them, *spectral methods* are now increasingly popular and the goal of this review is to give an overview (at the moment it is written or updated) of the methods themselves, the groups using them and the results obtained. Although some of the theoretical framework of spectral methods is given in Sections 4.2 to 4.4, more details can be found in the books by Gottlieb and Orszag [210], Canuto et al. [102, 103, 104], Fornberg [182], Boyd [85] and Hesthaven et al. [250]. While these references have, of course, been used for writing this review, they may also help the interested reader to get a deeper understanding of the subject. This review is organized as follows: hereafter

in the introduction, we briefly introduce spectral methods, their usage in computational physics and give a simple example. Section 4.2 gives important notions concerning polynomial interpolation and the solution of ordinary differential equations (ODE) with spectral methods. Multidomain approach is also introduced there, whereas some multidimensional techniques are described in Section 4.3. The cases of time-dependent partial differential equations (PDE) are treated in Section 4.4. The last two sections then review results obtained using spectral methods: for stationary configurations and initial data (Section 4.5), and for the time evolution (Section 4.6) of stars, gravitational waves and black holes.

4.1.1 About spectral methods

When doing simulations and solving PDEs, one faces the problem of representing and deriving functions on a computer, which deals only with (finite) integers. Let us take a simple example of a function $f : [-1, 1] \rightarrow \mathbb{R}$. The most straightforward way to approximate its derivative is through *finite-difference methods*: first one must setup a *grid*

$$\{x_i\}_{i=0\dots N} \subset [-1, 1]$$

of $N + 1$ points in the interval, and represent f by its $N + 1$ values on these grid points

$$\{f_i = f(x_i)\}_{i=0\dots N}.$$

Then, the (approximate) representation of the derivative f' shall be, for instance,

$$\forall i < N, f'_i = f'(x_i) \simeq \frac{f_{i+1} - f_i}{x_{i+1} - x_i}. \quad (4.1)$$

If we suppose an equidistant grid, so that $\forall i < N, x_{i+1} - x_i = \Delta x = 1/N$, the error in the approximation (4.1) will decay as Δx (first-order scheme). One can imagine higher-order schemes, with more points involved for the computation of each derivative and, for a scheme of order n , the accuracy can vary as $(\Delta x)^n = 1/N^n$.

Spectral methods represent an alternate way: the function f is no longer represented through its values on a finite number of grid points, but using its coefficients (coordinates) $\{c_i\}_{i=0\dots N}$ in a finite basis of known functions $\{\Phi_i\}_{i=0\dots N}$

$$f(x) \simeq \sum_{i=0}^N c_i \Phi_i(x). \quad (4.2)$$

A relatively simple case is, for instance, when $f(x)$ is a periodic function of period two, and the $\Phi_{2i}(x) = \cos(\pi i x)$, $\Phi_{2i+1}(x) = \sin(\pi i x)$ are trigonometric functions. Equation (4.2) is then nothing but the truncated Fourier decomposition of f . In general, derivatives can be computed from the c_i 's, with the knowledge of the expression for each derivative $\Phi'_i(x)$ as a function of $\{\Phi_i\}_{i=0\dots N}$. The decomposition (4.2) is approximate in the sense that $\{\Phi_i\}_{i=0\dots N}$ represent a complete basis of some finite-dimensional functional space, whereas f usually belongs to some other infinite-dimensional space. Moreover, the coefficients c_i are computed with finite accuracy. Among the major advantages of using spectral methods is the rapid decay of the error (faster than any power of $1/N$, and in practice often exponential e^{-N}), for well-behaved functions (see Section 4.2.4); one, therefore, has an *infinite*-order scheme.

In a more formal and mathematical way, it is useful to work within the methods of weighted residuals (MWR, see also Section 4.2.5). Let us consider the PDE

$$Lu(x) = s(x) \quad x \in U \subset \mathbb{R}^d, \quad (4.3)$$

$$Bu(x) = 0 \quad x \in \partial U, \quad (4.4)$$

where L is a linear operator, B the operator defining the boundary conditions and s is a source term. A function \bar{u} is said to be a *numerical solution* of this PDE if it satisfies the boundary conditions (4.4) and makes “small” the residual

$$R = L\bar{u} - s. \quad (4.5)$$

If the solution is searched for in a finite-dimensional subspace of some given Hilbert space (any relevant L^2_U space) in terms of the expansion (4.2), then the functions $\{\Phi_i(x)\}_{i=0\dots N}$ are called *trial functions* and, in addition, the choice of a set of *test functions* $\{\xi_i(x)\}_{i=0\dots N}$ defines the notion of smallness for the residual by means of the Hilbert space scalar product

$$\forall i = 0\dots N, \quad (\xi_i, R) = 0. \quad (4.6)$$

Within this framework, various numerical methods can be classified according to the choice of the trial functions:

- **Finite differences:** the trial functions are overlapping local polynomials of fixed order (lower than N).
- **Finite elements:** the trial functions are local smooth functions, which are nonzero, only on subdomains of U .
- **Spectral methods:** the trial functions are global smooth functions on U .

Various choices of the test functions define different types of spectral methods, as detailed in Section 4.2.5. Usual choices for the trial functions are (truncated) Fourier series, spherical harmonics or orthogonal families of polynomials.

4.1.2 Spectral methods in physics

We do not give here all the fields of physics in which spectral methods are employed, but sketching the variety of equations and physical models that have been simulated with such techniques. Spectral methods originally appeared in numerical fluid dynamics, where large spectral hydrodynamic codes have been regularly used to study turbulence and transition to the turbulence since the seventies. For fully resolved, direct numerical calculations of Navier–Stokes equations, spectral methods were often preferred for their high accuracy. Historically, they also allowed for two or three-dimensional simulations of fluid flows, because of their reasonable computer memory requirements. Many applications of spectral methods in fluid dynamics have been discussed by Canuto et al. [102, 104], and the techniques developed in that field are of some interest to numerical relativity.

From pure fluid-dynamics simulations, spectral methods have rapidly been used in connected fields of research: geophysics [412], meteorology and climate modeling [459]. In this last research category, global circulation models are used as boundary conditions to more specific (lower-scale) models, with improved micro-physics. In this way, spectral methods are only a part of the global numerical model,

combined with other techniques to bring the highest accuracy, for a given computational power. A solution to the Maxwell equations can, of course, also be obtained with spectral methods and therefore, magneto-hydrodynamics (MHD) have been studied with these techniques (see, e.g., Hollerbach [253]). This has been the case in astrophysics too, where, for example, spectral three-dimensional numerical models of solar magnetic dynamo action realized by turbulent convection have been computed [93]. And Kompaneet's equation, describing the evolution of photon distribution function in a plasma bath at thermal equilibrium within the Fokker-Planck approximation, has been solved using spectral methods to model the X-ray emission of *Her X-1* [66, 72]. In simulations of cosmological structure formation or galaxy evolution, many N-body codes rely on a spectral solver for the computation of the gravitational force by the *particle-mesh* algorithm. The mass corresponding to each particle is decomposed onto neighboring grid points, thus defining a density field. The Poisson equation giving the Newtonian gravitational potential is then usually solved in Fourier space for both fields [252].

To our knowledge, the first published result of the numerical solution of Einstein's equations, using spectral methods, is the spherically-symmetric collapse of a neutron star to a black hole by Gourgoulhon in 1991 [211]. He used spectral methods as they were developed in the Meudon group by Bonazzola and Marck [79]. Later studies of quickly-rotating neutron stars [67] (stationary axisymmetric models), the collapse of a neutron star in tensor-scalar theory of gravity [337] (spherically-symmetric dynamic spacetime), and quasiequilibrium configurations of neutron star binaries [71] and of black holes [229] (three-dimensional and stationary spacetimes) have grown in complexity, up to the three-dimensional time-dependent numerical solution of Einstein's equations [73]. On the other hand, the first fully three-dimensional evolution of the whole Einstein system was achieved in 2001 by Kidder et al. [277], where a single black hole was evolved to $t \simeq 600 M - 1300 M$ using excision techniques. They used spectral methods as developed in the Cornell/Caltech group by Kidder et al. [279] and Pfeiffer et al. [361]. Since then, they have focused on the evolution of black-hole-binary systems, which has recently been simulated up to merger and ring down by Scheel et al. [405]. Other groups (for instance Ansorg et al. [30], Bartnik and Norton [49], Frauendiener [185] and Tichy [466]) have also used spectral methods to solve Einstein's equations; Sections 4.5 and 4.6 are devoted to a more detailed review of these works.

4.1.3 A simple example

Before entering the details of spectral methods in Sections 4.2, 4.3 and 4.4, let us give here their spirit with the simple example of the Poisson equation in a spherical shell:

$$\Delta\phi = \sigma, \tag{4.7}$$

where Δ is the Laplace operator (4.93) expressed in spherical coordinates (r, θ, φ) (see also Section 4.3.2). We want to solve Equation (4.7) in the domain where $0 < R_{\min} \leq r \leq R_{\max}$, $\theta \in [0, \pi]$, $\varphi \in [0, 2\pi)$. This Poisson equation naturally arises in numerical relativity when, for example, solving for initial conditions or the Hamiltonian constraint in the 3+1 formalism [214]: the linear part of these equations can be cast in form (4.7), and the nonlinearities put into the source σ , with an iterative scheme on ϕ .

First, the angular parts of both fields are decomposed into a (finite) set of spherical harmonics $\{Y_\ell^m\}$ (see Section 4.3.2):

$$\sigma(r, \theta, \varphi) \simeq \sum_{\ell=0}^{\ell_{\max}} \sum_{m=-\ell}^{m=\ell} s_{\ell m}(r) Y_\ell^m(\theta, \varphi), \tag{4.8}$$

with a similar formula relating ϕ to the radial functions $f_{\ell m}(r)$. Because spherical harmonics are eigenfunctions of the angular part of the Laplace operator, the Poisson equation can be equivalently solved as a set of ordinary differential equations for each couple (ℓ, m) , in terms of the coordinate r :

$$\forall(\ell, m), \quad \frac{d^2 f_{\ell m}}{dr^2} + \frac{2}{r} \frac{df_{\ell m}}{dr} - \frac{\ell(\ell+1)f_{\ell m}}{r^2} = s_{\ell m}(r). \quad (4.9)$$

We then map

$$\begin{aligned} [R_{\min}, R_{\max}] &\rightarrow [-1, 1] \\ r &\mapsto \xi = \frac{2r - R_{\max} - R_{\min}}{R_{\max} - R_{\min}}, \end{aligned} \quad (4.10)$$

and decompose each field in a (finite) basis of Chebyshev polynomials $\{T_i\}_{i=0\dots N}$ (see Section 4.2.4):

$$\begin{aligned} s_{\ell m}(\xi) &= \sum_{i=0}^N c_{i\ell m} T_i(\xi), \\ f_{\ell m}(\xi) &= \sum_{i=0}^N a_{i\ell m} T_i(\xi). \end{aligned} \quad (4.11)$$

Each function $f_{\ell m}(r)$ can be regarded as a column-vector $A_{\ell m}$ of its $N+1$ coefficients $a_{i\ell m}$ in this basis; the linear differential operator on the left-hand side of Equation (4.9) being, thus, a matrix $L_{\ell m}$ acting on the vector:

$$L_{\ell m} A_{\ell m} = S_{\ell m}, \quad (4.12)$$

with $S_{\ell m}$ being the vector of the $N+1$ coefficients $c_{i\ell m}$ of $s_{\ell m}(r)$. This matrix can be computed from the recurrence relations fulfilled by the Chebyshev polynomials and their derivatives (see Section 4.2.4 for details).

The matrix L is singular because problem (4.7) is ill posed. One must indeed specify boundary conditions at $r = R_{\min}$ and $r = R_{\max}$. For simplicity, let us suppose

$$\forall(\theta, \varphi), \quad \phi(r = R_{\min}, \theta, \varphi) = \phi(r = R_{\max}, \theta, \varphi) = 0. \quad (4.13)$$

To impose these boundary conditions, we adopt the tau methods (see Section 4.2.5): we build the matrix \bar{L} , taking L and replacing the last two lines by the boundary conditions, expressed in terms of the coefficients from the properties of Chebyshev polynomials:

$$\forall(\ell, m), \quad \sum_{i=0}^N (-1)^i a_{i\ell m} = \sum_{i=0}^N a_{i\ell m} = 0. \quad (4.14)$$

Equations (4.14) are equivalent to boundary conditions (4.13), within the considered spectral approximation, and they represent the last two lines of \bar{L} , which can now be inverted and give the coefficients of the solution ϕ .

If one summarizes the steps:

1. Setup an adapted grid for the computation of spectral coefficients (e.g., equidistant in the angular directions and Chebyshev–Gauss–Lobatto collocation points; see Section 4.2.4).

2. Get the values of the source σ on these grid points.
3. Perform a spherical-harmonics transform (for example, using some available library [322]), followed by the Chebyshev transform (using a Fast Fourier Transform (FFT), or a Gauss–Lobatto quadrature) of the source σ .
4. For each couple of values (ℓ, m) , build the corresponding matrix \bar{L} with the boundary conditions, and invert the system (using any available linear-algebra package) with the coefficients of σ as the right-hand side.
5. Perform the inverse spectral transform to get the values of ϕ on the grid points from its coefficients.

A numerical implementation of this algorithm has been reported by Grandclément et al. [228], who have observed that the error decayed as $e^{-\ell_{\max}} \cdot e^{-N}$, provided that the source σ was smooth. Machine round-off accuracy can be reached with $\ell_{\max} \sim N \sim 30$, which makes the matrix inversions of step 4 very cheap in terms of CPU and the whole method affordable in terms of memory usage. These are the main advantages of using spectral methods, as shall be shown in the following sections.

4.2 Concepts in One Dimension

In this section the basic concept of spectral methods in one spatial dimension is presented. Some general properties of the approximation of functions by polynomials are introduced. The main formulae of the spectral expansion are then given and two sets of polynomials are discussed (Legendre and Chebyshev polynomials). A particular emphasis is put on convergence properties (i.e., the way the spectral approximation converges to the real function).

In Section 4.2.5, three different methods of solving an ordinary differential equation (ODE) are exhibited and applied to a simple problem. Section 4.2.6 is concerned with multidomain techniques. After giving some motivations for the use of multidomain decomposition, four different implementations are discussed, as well as their respective merits. One simple example is given, which uses only two domains.

For problems in more than one dimension see Section 4.3.

4.2.1 Best polynomial approximation

Polynomials are the only functions that a computer can exactly evaluate and so it is natural to try to approximate any function by a polynomial. When considering spectral methods, we use global polynomials on a few domains. This is to be contrasted with finite difference schemes, for instance, where only local polynomials are considered.

In this particular section, real functions of $[-1, 1]$ are considered. A theorem due to Weierstrass (see for instance [137]) states that the set \mathbb{P} of all polynomials is a dense subspace of all the continuous functions on $[-1, 1]$, with the norm $\|\cdot\|_\infty$. This maximum norm is defined as

$$\|f\|_\infty = \max_{x \in [-1, 1]} |f(x)|. \quad (4.15)$$

This means that, for any continuous function f of $[-1, 1]$, there exists a sequence of polynomials (p_i) , $i \in \mathbb{N}$ that converges *uniformly* towards f :

$$\lim_{i \rightarrow \infty} \|f - p_i\|_\infty = 0. \quad (4.16)$$

This theorem shows that it is probably a good idea to approximate continuous functions by polynomials.

Given a continuous function f , the best polynomial approximation of degree N , is the polynomial p_N^* that minimizes the norm of the difference between f and itself:

$$\|f - p_N^*\|_\infty = \min \{ \|f - p\|_\infty, p \in \mathbb{P}_N \}. \quad (4.17)$$

Chebyshev alternate theorem states that for any continuous function f , p_N^* is unique (theorem 9.1 of [382] and theorem 23 of [316]). There exist $N + 2$ points $x_i \in [-1, 1]$ such that the error is exactly attained at those points in an alternate manner:

$$f(x_i) - p_N^*(x_i) = (-1)^{i+\delta} \|f - p_N^*\|_\infty, \quad (4.18)$$

where $\delta = 0$ or $\delta = 1$. An example of a function and its best polynomial approximation is shown in Figure 4.1.

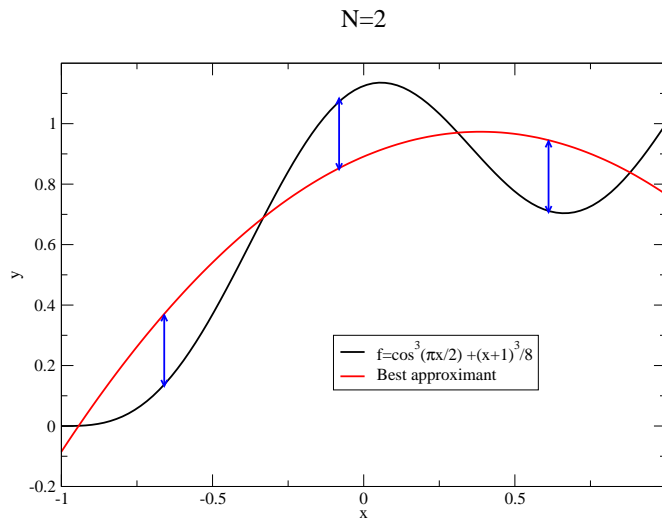


Figure 4.1: Function $f = \cos^3(\pi x/2) + (x+1)^3/8$ (black curve) and its best approximation of degree 2 (red curve). The blue arrows denote the four points where the maximum error is attained.

4.2.2 Interpolation on a grid

A *grid* X on the interval $[-1, 1]$ is a set of $N + 1$ points $x_i \in [-1, 1]$, $0 \leq i \leq N$. These points are called the *nodes* of the grid X .

Let us consider a continuous function f and a family of grids X with $N + 1$ nodes x_i . Then, there exists a unique polynomial of degree N , $I_N^X f$, that coincides with f at each node:

$$I_N^X f(x_i) = f(x_i) \quad 0 \leq i \leq N. \quad (4.19)$$

$I_N^X f$ is called the interpolant of f through the grid X . $I_N^X f$ can be expressed in terms of the Lagrange cardinal polynomials:

$$I_N^X f = \sum_{i=0}^N f(x_i) \ell_i^X(x), \quad (4.20)$$

where ℓ_i^X are the Lagrange cardinal polynomials. By definition, ℓ_i^X is the unique polynomial of degree N that vanishes at all nodes of the grid X , *except* at x_i , where it is equal to one. It is easy to show that the Lagrange cardinal polynomials can be written as

$$\ell_i^X(x) = \prod_{j=0, j \neq i}^N \frac{x - x_j}{x_i - x_j}. \quad (4.21)$$

Figure 4.2 shows some examples of Lagrange cardinal polynomials. An example of a function and its interpolant on a uniform grid can be seen in Figure 4.3.

Thanks to Chebyshev alternate theorem, one can see that the best approximation of degree N is an interpolant of the function at $N + 1$ nodes. However, in general, the associated grid is not known.

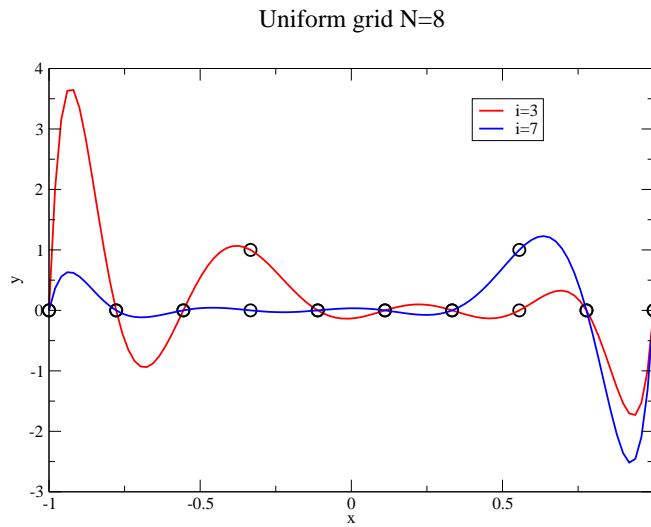


Figure 4.2: Lagrange cardinal polynomials ℓ_3^X (red curve) and ℓ_7^X on an uniform grid with $N = 8$. The black circles denote the nodes of the grid.

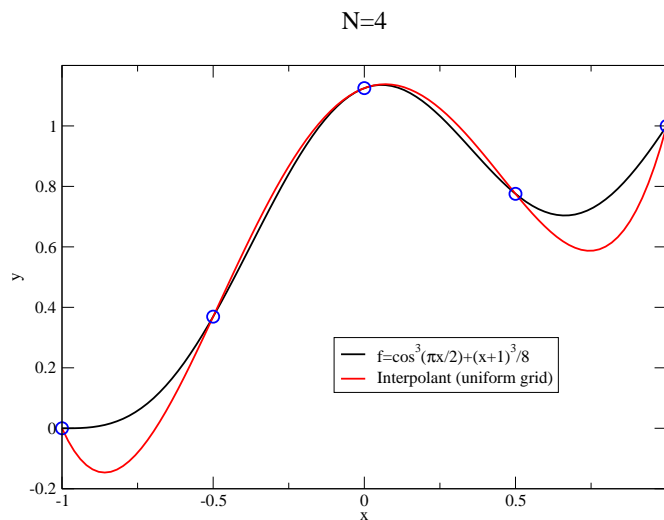


Figure 4.3: Function $f = \cos^3(\pi x/2) + (x+1)^3/8$ (black curve) and its interpolant (red curve) on a uniform grid of five nodes. The blue circles show the position of the nodes.

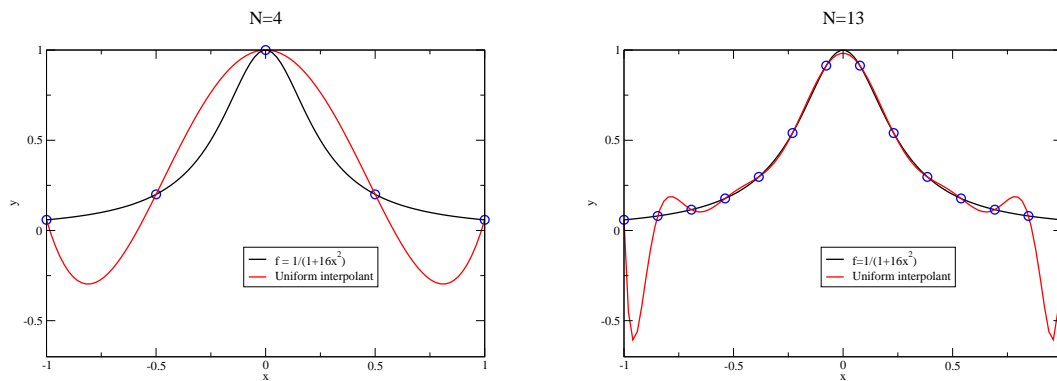


Figure 4.4: Function $f = \frac{1}{1+16x^2}$ (black curve) and its interpolant (red curve) on a uniform grid of five nodes (left panel) and 14 nodes (right panel). The blue circles show the position of the nodes.

The difference between the error made by interpolating on a given grid X can be compared to the smallest possible error for the best approximation. One can show that (see Prop. 7.1 of [382]):

$$\|f - I_N^X f\|_\infty \leq (1 + \Lambda_N(X)) \|f - p_N^*\|_\infty, \quad (4.22)$$

where Λ is the *Lebesgue constant* of the grid X and is defined as:

$$\Lambda_N(X) = \max_{x \in [-1,1]} \sum_{i=0}^N |\ell_i^X(x)|. \quad (4.23)$$

A theorem by Erdős [163] states that, for any choice of grid X , there exists a constant $C > 0$ such that:

$$\Lambda_N(X) > \frac{2}{\pi} \ln(N+1) - C. \quad (4.24)$$

It immediately follows that $\Lambda_N \rightarrow \infty$ when $N \rightarrow \infty$. This is related to a result from 1914 by Faber [168] that states that for any grid, there always exists at least one continuous function f , whose interpolant does not converge uniformly to f . An example of such failure of convergence is shown in Figure 4.4, where the convergence of the interpolant to the function $f = \frac{1}{1+16x^2}$ is clearly nonuniform (see the behavior near the boundaries of the interval). This is known as the Runge phenomenon.

Moreover, a theorem by Cauchy (theorem 7.2 of [382]) states that, for all functions $f \in \mathcal{C}^{(N+1)}$, the interpolation error on a grid X of $N+1$ nodes is given by

$$f(x) - I_N^X f(x) = \frac{f^{(N+1)}(\epsilon)}{(N+1)!} w_{N+1}^X(x), \quad (4.25)$$

where $\epsilon \in [-1, 1]$. w_{N+1}^X is the nodal polynomial of X , being the only polynomial of degree $N+1$, with a leading coefficient of 1, and that vanishes on the nodes of X . It is then easy to show that

$$w_{N+1}^X(x) = \prod_{i=0}^N (x - x_i). \quad (4.26)$$

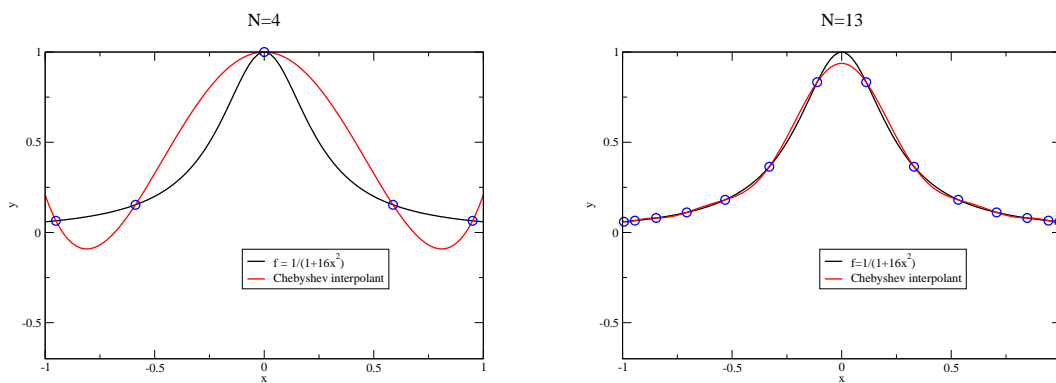


Figure 4.5: Same as Figure 4.4 but using a grid based on the zeros of Chebyshev polynomials. The Runge phenomenon is no longer present.

In Equation (4.25), one has a priori no control on the term involving f^{N+1} . For a given function, it can be rather large and this is indeed the case for the function f shown in Figure 4.4 (one can check, for instance, that $|f^{N+1}(1)|$ becomes larger and larger). However, one can hope to minimize the interpolation error by choosing a grid such that the nodal polynomial is as small as possible. A theorem by Chebyshev states that this choice is unique and is given by a grid, whose nodes are the zeros of the Chebyshev polynomial T_{N+1} (see Section 4.2.3 for more details on Chebyshev polynomials). With such a grid, one can achieve

$$\|w_{N+1}^X\|_\infty = \frac{1}{2^N}, \quad (4.27)$$

which is the smallest possible value (see Equation (18), Section 4.2, Chapter 5 of [259]). So, a grid based on nodes of Chebyshev polynomials can be expected to perform better than a standard uniform one. This is what can be seen in Figure 4.5, which shows the same function and its interpolants as in Figure 4.4, but with a Chebyshev grid. Clearly, the Runge phenomenon is no longer present. One can check that, for this choice of function f , the uniform convergence of the interpolant to the function is recovered. This is because $\|w_{N+1}^X\|_\infty$ decreases faster than $f^{N+1}/(N+1)!$ increases. Of course, Faber's result implies that this cannot be true for all the functions. There still must exist some functions for which the interpolant does not converge uniformly to the function itself (it is actually the class of functions that are not absolutely continuous, like the Cantor function).

4.2.3 Polynomial interpolation

Orthogonal polynomials

Spectral methods are often based on the notion of *orthogonal polynomials*. In order to define orthogonality, one must define the scalar product of two functions on an interval $[-1, 1]$. Let us consider a positive function w of $[-1, 1]$ called the *measure*. The scalar product of f and g with respect to this measure is defined as:

$$(f, g)_w = \int_{x \in [-1, 1]} f(x) g(x) w(x) dx. \quad (4.28)$$

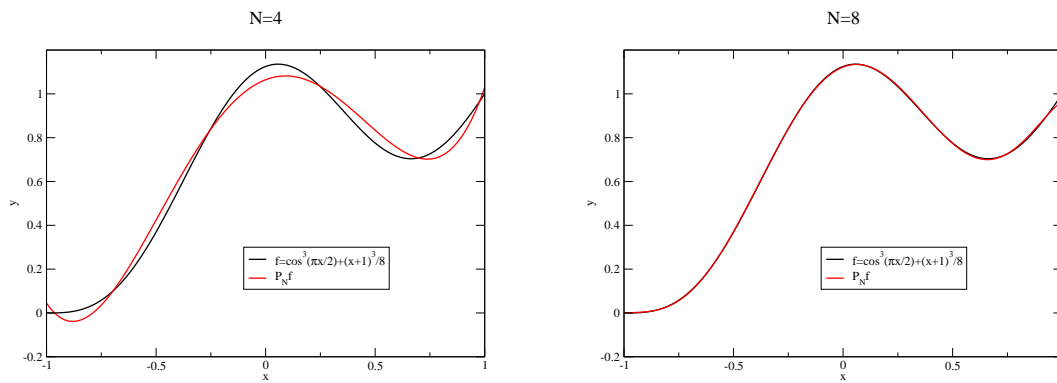


Figure 4.6: Function $f = \cos^3(\pi x/2) + (x+1)^3/8$ (black curve) and its projection on Chebyshev polynomials (red curve), for $N = 4$ (left panel) and $N = 8$ (right panel).

A basis of P_N is then a set of $N + 1$ polynomials $\{p_n\}_{n=0\dots N}$. p_n is of degree n and the polynomials are orthogonal: $(p_i, p_j)_w = 0$ for $i \neq j$.

The projection $P_N f$ of a function f on this basis is then

$$P_N f = \sum_{n=0}^N \hat{f}_n p_n, \quad (4.29)$$

where the coefficients of the projection are given by

$$\hat{f}_n = \frac{(f, p_n)}{(p_n, p_n)}. \quad (4.30)$$

The difference between f and its projection goes to zero when N increases:

$$\|f - P_N f\|_\infty \rightarrow 0 \quad \text{when} \quad N \rightarrow \infty. \quad (4.31)$$

Figure 4.6 shows the function $f = \cos^3(\pi x/2) + (x+1)^3/8$ and its projection on Chebyshev polynomials (see Section 4.2.4) for $N = 4$ and $N = 8$, illustrating the rapid convergence of $P_N f$ to f .

At first sight, the projection seems to be an interesting means of numerically representing a function. However, in practice this is not the case. Indeed, to determine the projection of a function, one needs to compute the integrals (4.30), which requires the evaluation of f at a great number of points, making the whole numerical scheme impractical.

Gaussian quadratures

The main theorem of Gaussian quadratures (see for instance [103]) states that, given a measure w , there exist $N + 1$ positive real numbers w_n and $N + 1$ real numbers $x_n \in [-1, 1]$ such that:

$$\forall f \in \mathbb{P}_{2N+\delta}, \quad \int_{[-1,1]} f(x) w(x) dx = \sum_{n=0}^N f(x_n) w_n. \quad (4.32)$$

The w_n are called the *weights* and the x_n are the collocation points. The integer δ can take several values depending on the exact quadrature considered:

- Gauss quadrature: $\delta = 1$.
- Gauss–Radau: $\delta = 0$ and $x_0 = -1$.
- Gauss–Lobatto: $\delta = -1$ and $x_0 = -1, x_N = 1$.

Gauss quadrature is the best choice because it applies to polynomials of higher degree but Gauss–Lobatto quadrature is often more useful for numerical purposes because the outermost collocation points coincide with the boundaries of the interval, making it easier to impose matching or boundary conditions. More detailed results and demonstrations about those quadratures can be found for instance in [103].

Spectral interpolation

As already stated in 4.2.3, the main drawback of projecting a function in terms of orthogonal polynomials comes from the difficulty to compute the integrals (4.30). The idea of spectral methods is to approximate the coefficients of the projection by making use of Gaussian quadratures. By doing so, one can define the *interpolant* of a function f by

$$I_N f = \sum_{n=0}^N \tilde{f}_n p_n(x), \quad (4.33)$$

where

$$\tilde{f}_n = \frac{1}{\gamma_n} \sum_{i=0}^N f(x_i) p_n(x_i) w_i \quad \text{and} \quad \gamma_n = \sum_{i=0}^N p_n^2(x_i) w_i. \quad (4.34)$$

The \tilde{f}_n exactly coincides with the coefficients \hat{f}_n , if the Gaussian quadrature is applicable for computing Equation (4.30), that is, for all $f \in \mathbb{P}_{N+\delta}$. So, in general, $I_N f \neq P_N f$ and the difference between the two is called the *aliasing error*. The advantage of using \tilde{f}_n is that they are computed by estimating f at the $N + 1$ collocation points only.

One can show that $I_N f$ and f coincide at the collocation points: $I_N f(x_i) = f(x_i)$ so that I_N interpolates f on the grid, whose nodes are the collocation points. Figure 4.7 shows the function $f = \cos^3(\pi/2) + (x + 1)^3/8$ and its spectral interpolation using Chebyshev polynomials, for $N = 4$ and $N = 6$.

Two equivalent descriptions

The description of a function f in terms of its spectral interpolation can be given in two different, but equivalent spaces:

- in the configuration space, if the function is described by its value at the $N + 1$ collocation points $f(x_i)$;
- in the coefficient space, if one works with the $N + 1$ coefficients \tilde{f}_i .

There is a bijection between both spaces and the following relations enable us to go from one to the other:

- the coefficients can be computed from the values of $f(x_i)$ using Equation (4.34);

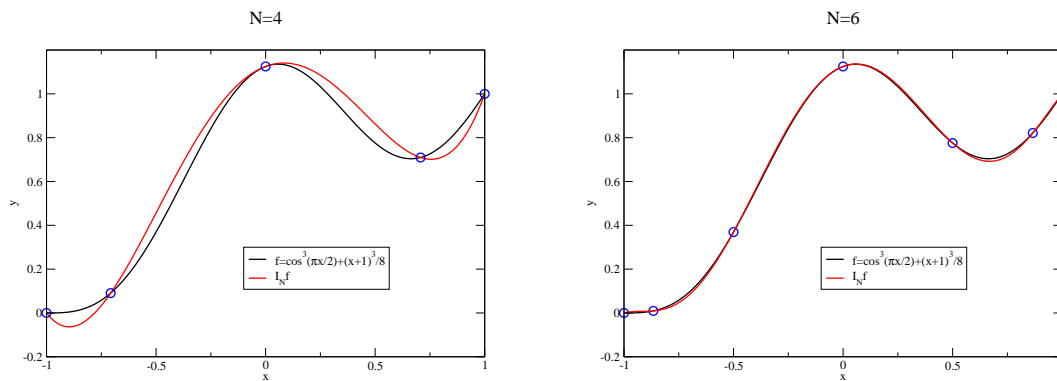


Figure 4.7: Function $f = \cos^3(\pi x/2) + (x+1)^3/8$ (black curve) and its interpolant $I_N f$ on Chebyshev polynomials (red curve), for $N = 4$ (left panel) and $N = 6$ (right panel). The collocation points are denoted by the blue circles and correspond to Gauss–Lobatto quadrature.

- the values at the collocation points are expressed in terms of the coefficients by making use of the definition of the interpolant (4.33):

$$f(x_i) = \sum_{n=0}^N \tilde{f}_n p_n(x_i). \quad (4.35)$$

Depending on the operation one has to perform on a given function, it may be more clever to work in one space or the other. For instance, the square root of a function is very easily given in the collocation space by $\sqrt{f(x_i)}$, whereas the derivative can be computed in the coefficient space if, and this is generally the case, the derivatives of the basis polynomials are known, by $f'(x) = \sum_{n=0}^N \tilde{f}_n p'_n(x)$.

4.2.4 Usual polynomials

Sturm–Liouville problems and convergence

The Sturm–Liouville problems are eigenvalue problems of the form:

$$-(pu')' + qu = \lambda w, \quad (4.36)$$

on the interval $[-1, 1]$. p , q and w are real-valued functions such that:

- $p(x)$ is continuously differentiable, strictly positive and continuous at $x = \pm 1$.
- $q(x)$ is continuous, non-negative and bounded.
- $w(x)$ is continuous, non-negative and integrable.

The solutions are then the eigenvalues λ_i and the eigenfunctions $u_i(x)$. The eigenfunctions are orthogonal with respect to the measure w :

$$\int_{-1}^1 u_m(x) u_n(x) w(x) dx = 0 \quad \text{for } m \neq n. \quad (4.37)$$

Singular Sturm–Liouville problems are particularly important for spectral methods. A Sturm–Liouville problem is singular if and only if the function p vanishes at the boundaries $x = \pm 1$. One can show, that if the functions of the spectral basis are chosen to be the solutions of a singular Sturm–Liouville problem, then the convergence of the function to its interpolant is faster than any power law of N , N being the order of the expansion (see Section 5.2 of [103]). One talks about spectral convergence. Let us be precise in saying that this does not necessarily imply that the convergence is exponential. Convergence properties are discussed in more detail for Legendre and Chebyshev polynomials in Section 4.2.4.

Conversely, it can be shown that spectral convergence is not ensured when considering solutions of regular Sturm–Liouville problems [103].

In what follows, two usual types of solutions of singular Sturm–Liouville problems are considered: Legendre and Chebyshev polynomials.

Legendre polynomials

Legendre polynomials P_n are eigenfunctions of the following singular Sturm–Liouville problem:

$$((1-x^2)P_n')' + n(n+1)P_n = 0. \quad (4.38)$$

In the notations of Equation (4.36), $p = 1 - x^2$, $q = 0$, $w = 1$ and $\lambda_n = -n(n+1)$.

It follows that Legendre polynomials are orthogonal on $[-1, 1]$ with respect to the measure $w(x) = 1$. Moreover, the scalar product of two polynomials is given by:

$$(P_n, P_m) = \int_{-1}^1 P_n P_m dx = \frac{2}{2n+1} \delta_{mn}. \quad (4.39)$$

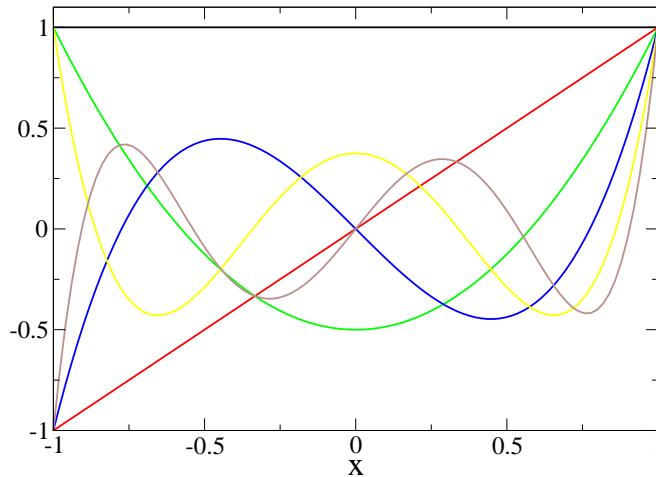
Starting from $P_0 = 1$ and $P_1 = x$, the successive polynomials can be computed by the following recurrence expression:

$$(n+1)P_{n+1}(x) = (2n+1)xP_n(x) - nP_{n-1}(x). \quad (4.40)$$

Among the various properties of Legendre polynomials, one can note that i) P_n has the same parity as n . ii) P_n is of degree n . iii) $P_n(\pm 1) = (\pm 1)^n$. iv) P_n has exactly n zeros on $[-1, 1]$. The first polynomials are shown in Figure 4.8.

The weights and locations of the collocation points associated with Legendre polynomials depend on the choice of quadrature.

- Legendre–Gauss: x_i are the nodes of P_{N+1} and $w_i = \frac{2}{(1-x_i^2)[P'_{N+1}(x_i)]^2}$.
- Legendre–Gauss–Radau: $x_0 = -1$ and x_i are the nodes of $P_N + P_{N+1}$. The weights are given by $w_0 = \frac{2}{(N+1)^2}$ and $w_i = \frac{1}{(N+1)^2}$.


 Figure 4.8: First Legendre polynomials, from P_0 to P_5 .

- Legendre–Gauss–Lobatto: $x_0 = -1$, $x_N = 1$ and x_i are the nodes of P'_N . The weights are $w_i = \frac{2}{N(N+1)} \frac{1}{[P'_N(x_i)]^2}$.

These values have no analytic expression, but they can be computed numerically in an efficient way.

Some elementary operations can easily be performed on the coefficient space. Let us assume that a function f is given by its coefficients a_n so that $f = \sum_{n=0}^N a_n P_n$. Then, the coefficients b_n of

$Hf = \sum_{n=0}^N b_n P_n$ can be found as a function of a_n , for various operators H . For instance,

- if H is multiplication by x then:

$$b_n = \frac{n}{2n-1} a_{n-1} + \frac{n+1}{2n+3} a_{n+1} \quad (n \geq 1); \quad (4.41)$$

- if H is the derivative:

$$b_n = (2n+1) \sum_{p=n+1, p+n \text{ odd}}^N a_p; \quad (4.42)$$

- if H is the second derivative:

$$b_n = (n+1/2) \sum_{p=n+2, p+n \text{ even}}^N [p(p+1) - n(n+1)] a_p. \quad (4.43)$$

These kind of relations enable one to represent the action of H as a matrix acting on the vector of a_n , the product being the coefficients of Hf , i.e. the b_n .

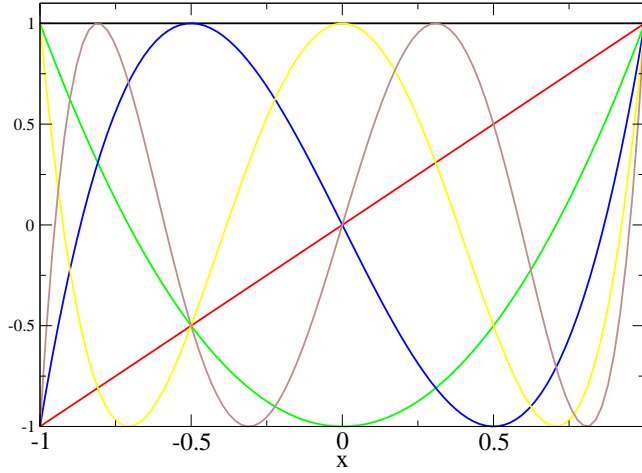


Figure 4.9: First Chebyshev polynomials, from T_0 to T_5 .

Chebyshev polynomials

Chebyshev polynomials T_n are eigenfunctions of the following singular Sturm-Liouville problem:

$$\left(\sqrt{1-x^2}T_n'\right)' + \frac{n}{\sqrt{1-x^2}}T_n = 0. \quad (4.44)$$

In the notation of Equation (4.36), $p = \sqrt{1-x^2}$, $q = 0$, $w = 1/\sqrt{1-x^2}$ and $\lambda_n = -n$.

It follows that Chebyshev polynomials are orthogonal on $[-1, 1]$ with respect to the measure $w = 1/\sqrt{1-x^2}$ and the scalar product of two polynomials is

$$(T_n, T_m) = \int_{-1}^1 \frac{T_n T_m}{\sqrt{1-x^2}} dx = \frac{\pi}{2} (1 + \delta_{0n}) \delta_{mn}. \quad (4.45)$$

Given that $T_0 = 1$ and $T_1 = x$, the higher-order polynomials can be obtained by making use of the recurrence

$$T_{n+1}(x) = 2xT_n(x) - T_{n-1}(x). \quad (4.46)$$

This implies the following simple properties: i) T_n has the same parity as n ; ii) T_n is of degree n ; iii) $T_n(\pm 1) = (\pm 1)^n$; iv) T_n has exactly n zeros on $[-1, 1]$. The first polynomials are shown in Figure 4.9.

Contrary to the Legendre case, both the weights and positions of the collocation points are given by analytic formulae:

- Chebyshev–Gauss: $x_i = \cos \frac{(2i+1)\pi}{2N+2}$ and $w_i = \frac{\pi}{N+1}$.
- Chebyshev–Gauss–Radau: $x_i = \cos \frac{2\pi i}{2N+1}$. The weights are $w_0 = \frac{\pi}{2N+1}$ and $w_i = \frac{2\pi}{2N+1}$.

- Chebyshev–Gauss–Lobatto: $x_i = \cos \frac{\pi i}{N}$. The weights are $w_0 = w_N = \frac{\pi}{2N}$ and $w_i = \frac{\pi}{N}$.

As for the Legendre case, the action of various linear operators H can be expressed in the coefficient space. This means that the coefficients b_n of Hf are given as functions of the coefficients a_n of f . For instance,

- if H is multiplication by x :

$$b_n = \frac{1}{2} [(1 + \delta_{0n-1}) a_{n-1} + a_{n+1}] \quad (n \geq 1); \quad (4.47)$$

- if H is the derivative:

$$b_n = \frac{2}{(1 + \delta_{0n})} \sum_{p=n+1, p+n \text{ odd}}^N p a_p; \quad (4.48)$$

- if H is the second derivative:

$$b_n = \frac{1}{(1 + \delta_{0n})} \sum_{p=n+2, p+n \text{ even}}^N p(p^2 - n^2) a_p. \quad (4.49)$$

Convergence properties

One of the main advantages of spectral methods is the very fast convergence of the interpolant $I_N f$ to the function f , at least for smooth enough functions. Let us consider a \mathcal{C}^m function f ; one can place the following upper bounds on the difference between f and its interpolant $I_N f$:

- For Legendre:

$$\|I_N f - f\|_{L^2} \leq \frac{C_1}{N^{m-1/2}} \sum_{k=0}^m \|f^{(k)}\|_{L^2}. \quad (4.50)$$

- For Chebyshev:

$$\|I_N f - f\|_{L_w^2} \leq \frac{C_2}{N^m} \sum_{k=0}^m \|f^{(k)}\|_{L_w^2}. \quad (4.51)$$

$$\|I_N f - f\|_{\infty} \leq \frac{C_3}{N^{m-1/2}} \sum_{k=0}^m \|f^{(k)}\|_{L_w^2}. \quad (4.52)$$

The C_i are positive constants. An interesting limit of the above estimates concerns a \mathcal{C}^∞ function. One can then see that the difference between f and $I_N f$ decays faster than any power of N . This is *spectral convergence*. Let us be precise in saying that this does not necessarily imply that the error decays exponentially (think about $\exp(-\sqrt{N})$, for instance). Exponential convergence is achieved only for analytic functions, i.e. functions that are locally given by a convergent power series.

An example of this very fast convergence is shown in Figure 4.10. The error clearly decays exponentially, the function being analytic, until it reaches the level of machine precision, 10^{-14} (one is working in double precision in this particular case). Figure 4.10 illustrates the fact that, with spectral methods, very good accuracy can be reached with only a moderate number of coefficients.

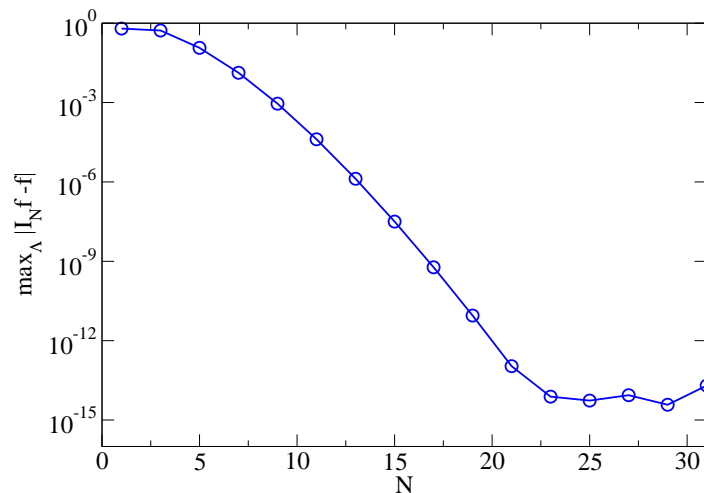


Figure 4.10: Maximum difference between $f = \cos^3(\pi x/2) + (x+1)^3/8$ and its interpolant $I_N f$, as a function of N .

If the function is less regular (i.e. not C^∞), the error only decays as a power law, thus making the use of spectral method less appealing. It can easily be seen in the worst possible case: that of a discontinuous function. In this case, the estimates (4.50-4.52) do not even ensure convergence. Figure 4.11 shows a step function and its interpolant for various values of N . One can see that the maximum difference between the function and its interpolant does not go to zero even when N is increasing. This is known as the Gibbs phenomenon.

Finally, Equation (4.52) shows that, if $m > 0$, the interpolant converges uniformly to the function. Continuous functions that do not converge uniformly to their interpolant, whose existence has been shown by Faber [168] (see Section 4.2.2), must belong to the C^0 functions. Indeed, for the case $m = 0$, Equation (4.52) does not prove convergence (neither do Equations (4.50) or (4.51)).

Trigonometric functions

A detailed presentation of the theory of Fourier transforms is beyond the scope of this work. However, there is a close link between *discrete Fourier transforms* and their spectral interpolation, which is briefly outlined here. More detail can be found, for instance, in [103].

The Fourier transform Pf of a function f of $[0, 2\pi]$ is given by:

$$Pf(x) = a_0 + \sum_{n=1}^{\infty} a_n \cos(nx) + \sum_{n=1}^{\infty} b_n \sin(nx). \quad (4.53)$$

The Fourier transform is known to converge rather rapidly to the function itself, if f is periodic. However, the coefficients a_n and b_n are given by integrals of the form $\int_0^{2\pi} f(x) \cos(nx) dx$, that cannot easily be computed (as was the case for the projection of a function on orthogonal polynomials in Section 4.2.3).

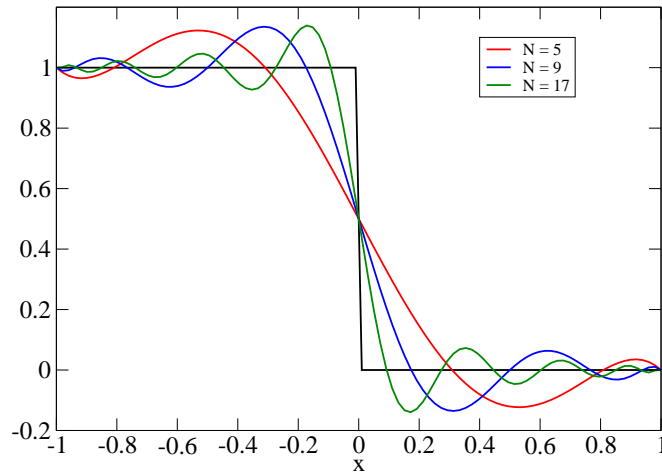


Figure 4.11: Step function (black curve) and its interpolant, for various values of N .

The solution to this problem is also very similar to the use of the Gaussian quadratures. Let us introduce $N + 1$ collocation points $x_i = 2\pi i/(N + 1)$. Then the *discrete Fourier coefficients* with respect to those points are:

$$\tilde{a}_0 = \frac{1}{N} \sum_{k=1}^N f(x_k), \quad (4.54)$$

$$\tilde{a}_n = \frac{2}{N} \sum_{k=1}^N f(x_k) \cos(nx_k), \quad (4.55)$$

$$\tilde{b}_n = \frac{2}{N} \sum_{k=1}^N f(x_k) \sin(nx_k) \quad (4.56)$$

and the interpolant $I_N f$ is then given by:

$$I_N f(x) = \tilde{a}_0 + \sum_{n=1}^N \tilde{a}_n \cos(nx) + \sum_{n=1}^N \tilde{b}_n \sin(nx). \quad (4.57)$$

The approximation made by using discrete coefficients in place of real ones is of the same nature as the one made when computing coefficients of projection (4.30) by means of the Gaussian quadratures. Let us mention that, in the case of a discrete Fourier transform, the first and last collocation points lie on the boundaries of the interval, as for a Gauss-Lobatto quadrature. As for the polynomial interpolation, the convergence of $I_N f$ to f is spectral for all periodic and C^∞ functions.

Choice of basis

For periodic functions of $[0, 2\pi[$, the discrete Fourier transform is the natural choice of basis. If the considered function has also some symmetries, one can use a subset of the trigonometric polynomials.

For instance, if the function is i) periodic on $[0, 2\pi[$ and is also odd with respect to $x = \pi$, then it can be expanded in terms of sines only. If the function is not periodic, then it is natural to expand it either in Chebyshev or Legendre polynomials. Using Legendre polynomials can be motivated by the fact that the associated measure is very simple: $w(x) = 1$. The multidomain technique presented in Section 4.2.6 is one particular example in which such a property is required. In practice, Legendre and Chebyshev polynomials usually give very similar results.

4.2.5 Spectral methods for ODEs

The weighted residual method

Let us consider a differential equation of the form

$$Lu(x) = S(x), \quad x \in [-1, 1], \quad (4.58)$$

where L is a linear second-order differential operator. The problem admits a unique solution once appropriate boundary conditions are prescribed at $x = 1$ and $x = -1$. Typically, one can specify i) the value of u (Dirichlet-type) ii) the value of its derivative $\partial_x u$ (Neumann-type) iii) a linear combination of both (Robin-type).

As for the elementary operations presented in Section 4.2.4 and 4.2.4, the action of L on u can be expressed by a matrix L_{ij} . If the coefficients of u with respect to a given basis are the \tilde{u}_i , then the coefficients of Lu are

$$\sum_{j=0}^N L_{ij} \tilde{u}_j. \quad (4.59)$$

Usually, L_{ij} can easily be computed by combining the action of elementary operations like the second derivative, the first derivative, multiplication or division by x (see Sections 4.2.4 and 4.2.4 for some examples).

A function u is an admissible solution to the problem if and only if i) it fulfills the boundary conditions exactly (up to machine accuracy) ii) it makes the *residual* $R = Lu - S$ small. In the weighted residual method, one considers a set of $N + 1$ test functions $\{\xi_n\}_{n=0\dots N}$ on $[-1, 1]$. The smallness of R is enforced by demanding that

$$(R, \xi_k) = 0, \quad \forall k \leq N. \quad (4.60)$$

As N increases, the obtained solution gets closer and closer to the real one. Depending on the choice of the test functions and the way the boundary conditions are enforced, one gets various solvers. Three classical examples are presented below.

The tau method

In this particular method, the test functions coincide with the basis used for the spectral expansion, for instance the Chebyshev polynomials. Let us denote \tilde{u}_i and \tilde{s}_i the coefficients of the solution u and of the source S , respectively.

Given the expression of Lu in the coefficient space (4.59) and the fact that the basis polynomials are orthogonal, the residual equations (4.60) are expressed as

$$\sum_{i=0}^N L_{ni} \tilde{u}_i = \tilde{s}_n, \quad \forall n \leq N, \quad (4.61)$$

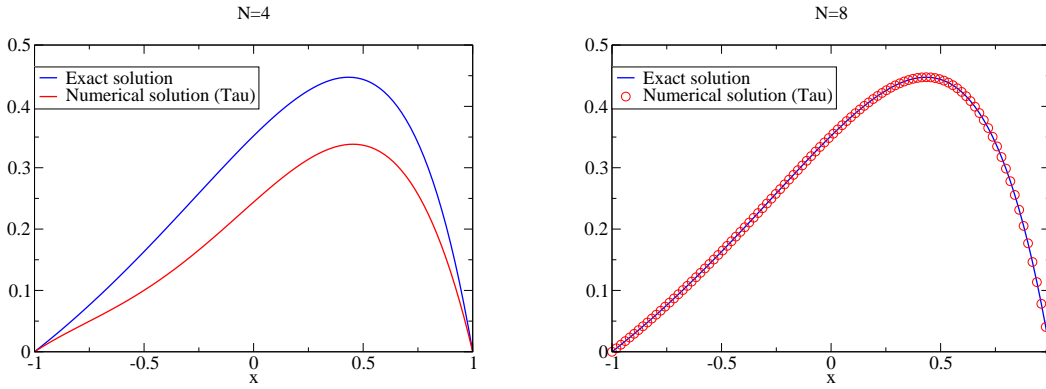


Figure 4.12: Exact solution (4.64) of Equation (4.62) (blue curve) and the numerical solution (red curve) computed by means of a tau method, for $N = 4$ (left panel) and $N = 8$ (right panel).

the unknowns being the \tilde{u}_i . However, as such, this system does not admit a unique solution, due to the homogeneous solutions of L (i.e. the matrix associated with L is not invertible) and one has to impose boundary conditions. In the tau method, this is done by relaxing the *last two* equations (4.61) (i.e. for $n = N - 1$ and $n = N$) and replacing them by the boundary conditions at $x = -1$ and $x = 1$.

The tau method thus ensures that Lu and S have the same coefficients, excepting the last ones. If the functions are smooth, then their coefficients should decrease in a spectral manner and so the “forgotten” conditions are less and less stringent as N increases, ensuring that the computed solution converges rapidly to the real one.

As an illustration, let us consider the following equation:

$$\frac{d^2u}{dx^2} - 4\frac{du}{dx} + 4u = \exp(x) - \frac{4e}{(1+x^2)} \quad (4.62)$$

with the following boundary conditions:

$$u(x = -1) = 0 \quad \text{and} \quad u(x = 1) = 0. \quad (4.63)$$

The exact solution is analytic and is given by

$$u(x) = \exp(x) - \frac{\sinh(1)}{\sinh(2)} \exp(2x) - \frac{e}{(1+x^2)}. \quad (4.64)$$

Figure 4.12 shows the exact solution and the numerical one, for two different values of N . One can note that the numerical solution converges rapidly to the exact one, the two being almost indistinguishable for N as small as $N = 8$. The numerical solution exactly fulfills the boundary conditions, no matter the value of N .

The collocation method

The collocation method is very similar to the tau method. They only differ in the choice of test functions. Indeed, in the collocation method one uses continuous functions that are zero at all but one

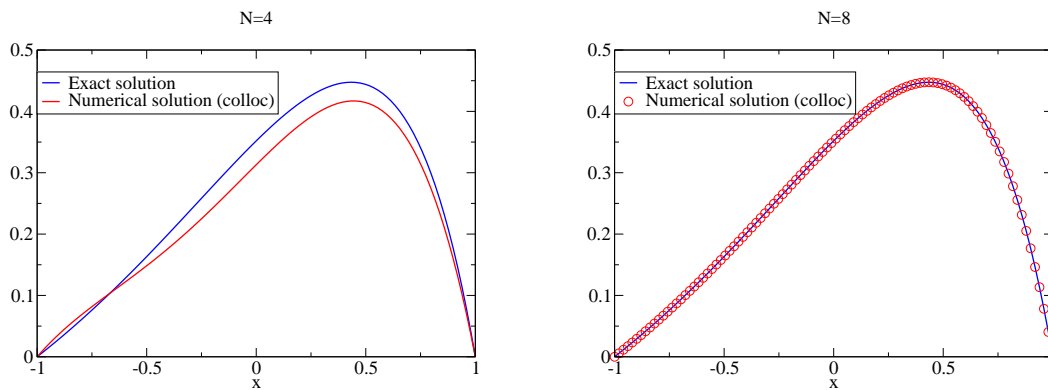


Figure 4.13: Exact solution (4.64) of Equation (4.62) (blue curve) and the numerical solution (red curve) computed by means of a collocation method, for $N = 4$ (left panel) and $N = 8$ (right panel).

collocation point. They are indeed the Lagrange cardinal polynomials already seen in Section 4.2.2 and can be written as $\xi_i(x_j) = \delta_{ij}$. With such test functions, the residual equations (4.60) are

$$Lu(x_n) = S(x_n), \quad \forall n \leq N. \quad (4.65)$$

The value of Lu at each collocation point is easily expressed in terms of \tilde{u} by making use of (4.59) and one gets

$$\sum_{i=0}^N \sum_{j=0}^N L_{ij} \tilde{u}_j T_i(x_n) = S(x_n), \quad \forall n \leq N. \quad (4.66)$$

Let us note that, even if the collocation method imposes that Lu and S coincide at each collocation point, the unknowns of the system written in the form (4.66) are the coefficients \tilde{u}_n and not $u(x_n)$. As for the tau method, system (4.66) is not invertible and boundary conditions must be enforced by additional equations. In this case, the relaxed conditions are the two associated with the outermost points, i.e. $n = 0$ and $n = N$, which are replaced by appropriate boundary conditions to get an invertible system.

Figure 4.13 shows both the exact and numerical solutions for Equation (4.62).

Galerkin method

The basic idea of the Galerkin method is to seek the solution u as a sum of polynomials G_i that *individually* verify the boundary conditions. Doing so, u automatically fulfills those conditions and they do not have to be imposed by additional equations. Such polynomials constitute a Galerkin basis of the problem. For practical reasons, it is better to choose a Galerkin basis that can easily be expressed in terms of the original orthogonal polynomials.

For instance, with boundary conditions (4.63), one can choose:

$$G_{2k}(x) = T_{2k+2}(x) - T_0(x) \quad (4.67)$$

$$G_{2k+1}(x) = T_{2k+3}(x) - T_1(x). \quad (4.68)$$

More generally, the Galerkin basis relates to the usual ones by means of a transformation matrix

$$G_i = \sum_{j=0}^N M_{ji} T_j, \quad \forall i \leq N-2. \quad (4.69)$$

Let us mention that the matrix M is not square. Indeed, to maintain the same degree of approximation, one can consider only $N-1$ Galerkin polynomials, due to the two additional conditions they have to fulfill (see, for instance, Equations (4.67-4.68)). One can also note that, in general, the G_i are *not* orthogonal polynomials.

The solution u is sought in terms of the coefficients \tilde{u}_i^G on the Galerkin basis:

$$u(x) = \sum_{k=0}^{N-2} \tilde{u}_k^G G_k(x). \quad (4.70)$$

By making use of Equations (4.59) and (4.69) one can express Lu in terms of \tilde{u}_i^G :

$$Lu(x) = \sum_{k=0}^{N-2} \tilde{u}_k^G \sum_{i=0}^N \sum_{j=0}^N M_{jk} L_{ij} T_i(x). \quad (4.71)$$

The test functions used in the Galerkin method are the G_i themselves, so that the residual system reads:

$$(Lu, G_n) = (S, G_n), \quad \forall n \leq N-2, \quad (4.72)$$

where the left-hand side is computed by means of Equation (4.71) and by expressing the G_i in terms of the T_i with Equation (4.69). Concerning the right-hand side, the source itself *is not* expanded in terms of the Galerkin basis, given that it does not fulfill the boundary conditions. Putting all the pieces together, the Galerkin system reads:

$$\sum_{k=0}^{N-2} \tilde{u}_k^G \sum_{i=0}^N \sum_{j=0}^N M_{in} M_{jk} L_{ij} (T_i|T_i) = \sum_{i=0}^N M_{in} \tilde{s}_i (T_i|T_i), \quad \forall n \leq N-2. \quad (4.73)$$

This is a system of $N-1$ equations for the $N-1$ unknowns \tilde{u}_i^G and it can be directly solved, because it is well posed. Once the \tilde{u}_i^G are known, one can obtain the solution in terms of the usual basis by making, once again, use of the transformation matrix:

$$u(x) = \sum_{i=0}^N \left(\sum_{n=0}^{N-2} M_{in} \tilde{u}_n^G \right) T_i. \quad (4.74)$$

The solution obtained by the application of this method to Equation (4.62) is shown in Figure 4.14.

Optimal methods

A spectral method is said to be optimal if it does not introduce an additional error to the error that would be introduced by interpolating the exact solution of a given equation.

Let us call u_{exact} such an exact solution, unknown in general. Its interpolant is $I_N u_{\text{exact}}$ and the numerical solution of the equation is u_{num} . The numerical method is then optimal if and only if $\|I_N u_{\text{exact}} - u_{\text{exact}}\|_{\infty}$ and $\|u_{\text{num}} - u_{\text{exact}}\|_{\infty}$ behave in the same manner when $N \rightarrow \infty$.

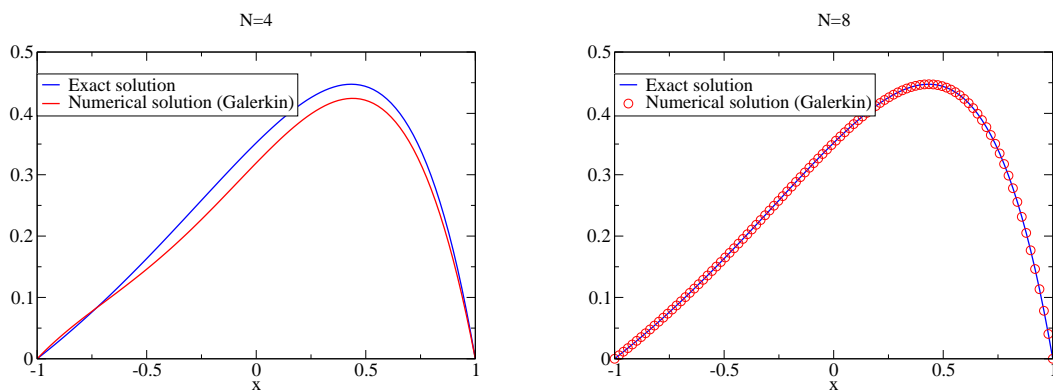


Figure 4.14: Exact solution (4.64) of Equation (4.62) (blue curve) and the numerical solution (red curve) computed by means of the Galerkin method, for $N = 4$ (left panel) and $N = 8$ (right panel).

In general, optimality is difficult to check because both u_{exact} and its interpolant are unknown. However, for the test problem proposed in Section 4.2.5 this can be done. Figure 4.15 shows the maximum relative difference between the exact solution (4.64) and its interpolant and the various numerical solutions. All the curves behave in the same manner as N increases, indicating that the three methods previously presented are optimal (at least for this particular case).

4.2.6 Multidomain techniques for ODEs

Motivations and setting

As seen in Section 4.2.4, spectral methods are very efficient when dealing with C^∞ functions. However, they lose some of their appeal when dealing with less regular functions, the convergence to the exact functions being substantially slower. Nevertheless, the physicist has sometimes to deal with such functions. This is the case for the density jump at the surface of strange stars or the formation of shocks, to mention only two examples. In order to maintain spectral convergence, one then needs to introduce several computational domains such that the various discontinuities of the functions lie at the interface between the domains. Doing so *in each domain* means that one only deals with C^∞ functions.

Multidomain techniques can also be valuable when dealing with a physical space either too complicated or too large to be described by a single domain. Related to that, one can also use several domains to increase the resolution in some parts of the space where more precision is required. This can easily be done by using a different number of basis functions in different domains. One then talks about fixed-mesh refinement.

Efficient parallel processing may also require that several domains be used. Indeed, one could set a solver, dealing with each domain on a given processor, and interprocessor communication would then only be used for matching the solution across the various domains. The algorithm of Section 4.2.6 is well adapted to such purposes.

In the following, four different multidomain methods are presented to solve an equation of the type

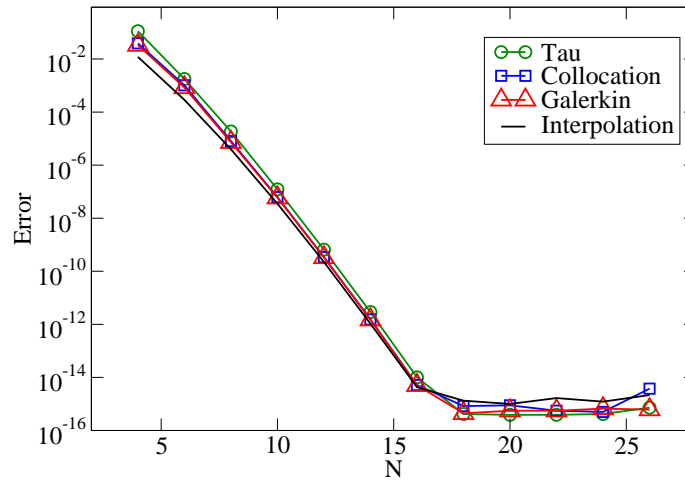


Figure 4.15: The difference between the exact solution (4.64) of Equation (4.62) and its interpolant (black curve) and between the exact and numerical solutions for i) the tau method (green curve and circle symbols) ii) the collocation method (blue curve and square symbols) iii) the Galerkin method (red curve and triangle symbols).

$Lu = S$ on $[-1, 1]$. L is a second-order linear operator and S is a given source function. Appropriate boundary conditions are given at the boundaries $x = -1$ and $x = 1$.

For simplicity the physical space is split into two domains:

- first domain: $x \leq 0$ described by $x_1 = 2x + 1$, $x_1 \in [-1, 1]$,
- second domain: $x \geq 0$ described by $x_2 = 2x - 1$, $x_2 \in [-1, 1]$.

If $x \leq 0$, a function u is described by its interpolant in terms of x_1 : $I_N u(x) = \sum_{i=0}^N \tilde{u}_i^1 T_i(x_1(x))$.

The same is true for $x \geq 0$ with respect to the variable x_2 . Such a set-up is obviously appropriate to deal with problems where discontinuities occur at $x = 0$, that is $x_1 = 1$ and $x_2 = -1$.

The multidomain tau method

As for the standard tau method (see Section 4.2.5) and in each domain, the test functions are the basis polynomials and one writes the associated residual equations. For instance, in the domain $x \leq 0$ one gets:

$$(T_n, R) = 0 \implies \sum_{i=0}^N L_{ni} \tilde{u}_i^1 = \tilde{s}_n^1 \quad \forall n \leq N, \quad (4.75)$$

\tilde{s}^1 being the coefficients of the source and L_{ij} the matrix representation of the operator. As for the one-domain case, one relaxes the last two equations, keeping only $N - 1$ equations. The same is done in the second domain.

Two supplementary equations are enforced to ensure that the boundary conditions are fulfilled. Finally, the operator L being of second order, one needs to ensure that the solution *and* its first derivative are continuous at the interface $x = 0$. This translates to a set of two additional equations involving both domains.

So, one considers

- $N - 1$ residual equations in the first domain,
- $N - 1$ residual equations in the second domain,
- 2 boundary conditions,
- 2 matching conditions,

for a total of $2N + 2$ equations. The unknowns are the coefficients of u in both domains (i.e. the \tilde{u}_i^1 and the \tilde{u}_i^2), that is $2N + 2$ unknowns. The system is well posed and admits a unique solution.

Multidomain collocation method

As for the standard collocation method (see Section 4.2.5) and in each domain, the test functions are the Lagrange cardinal polynomials. For instance, in the domain $x \leq 0$ one gets:

$$\sum_{i=0}^N \sum_{j=0}^N L_{ij} \tilde{u}_j^1 T_i(x_{1n}) = S(x_{1n}) \quad \forall n \leq N, \quad (4.76)$$

L_{ij} being the matrix representation of the operator and x_{1n} the n^{th} collocation point in the first domain. As for the one-domain case, one relaxes the two equations corresponding to the boundaries of the domain, keeping only $N - 1$ equations. The same is done in the second domain.

Two supplementary equations are enforced to ensure that the boundary conditions are fulfilled. Finally, the operator L being second order, one needs to ensure that the solution *and* its first derivative are continuous at the interface $x = 0$. This translates to a set of two additional equations involving the coefficients in both domains.

So, one considers

- $N - 1$ residual equations in the first domain,
- $N - 1$ residual equations in the second domain,
- 2 boundary conditions,
- 2 matching conditions,

for a total of $2N + 2$ equations. The unknowns are the coefficients of u in both domains (i.e. the \tilde{u}_i^1 and the \tilde{u}_i^2), that is $2N + 2$ unknowns. The system is well posed and admits a unique solution.

Method based on homogeneous solutions

The method described here proceeds in two steps. First, particular solutions are computed in each domain. Then, appropriate linear combinations with the homogeneous solutions of the operator L are performed to ensure continuity and impose boundary conditions.

In order to compute particular solutions, one can rely on any of the methods described in Section 4.2.5. The boundary conditions at the boundary of each domain can be chosen (almost) arbitrarily. For instance, one can use in each domain a collocation method to solve $Lu = S$, demanding that the particular solution u_{part} is zero at both ends of each interval.

Then, in order to have a solution over the whole space, one needs to add homogeneous solutions to the particular ones. In general, the operator L is second order and admits two independent homogeneous solutions g and h in each domain. Let us note that, in some cases, additional regularity conditions can reduce the number of available homogeneous solutions. The homogeneous solutions can either be computed analytically if the operator L is simple enough or numerically, but one must then have a method for solving $Lu = 0$.

In each domain, the physical solution is a combination of the particular solution and homogeneous ones of the type:

$$u = u_{\text{part}} + \alpha g + \beta h, \tag{4.77}$$

where α and β are constants that must be determined. In the two domains case, we are left with four unknowns. The system of equations they must satisfy is composed of i) two equations for the boundary conditions ii) two equations for the matching of u and its first derivative across the boundary between the two domains. The obtained system is called the matching system and generally admits a unique solution.

Variational method

Contrary to previously presented methods, the variational one is only applicable with Legendre polynomials. Indeed, the method requires that the measure be $w(x) = 1$. It is also useful to extract the second-order term of the operator L and to rewrite it as $Lu = u'' + H$, H being first order only.

In each domain, one writes the residual equation explicitly:

$$(\xi, R) = 0 \implies \int \xi u'' dx + \int \xi (Hu) dx = \int \xi S dx. \tag{4.78}$$

The term involving the second derivative of u is then integrated by parts:

$$[\xi u'] - \int \xi' u' dx + \int \xi (Hu) dx = \int \xi S dx. \tag{4.79}$$

The test functions are the same as the ones used for the collocation method, i.e. functions being zero at all but one collocation point, in both domains ($d = 1, 2$): $\xi_i(x_{dj}) = \delta_{ij}$. By making use of the Gauss quadratures, the various parts of Equation (4.79) can be expressed as ($d = 1, 2$ indicates the

domain):

$$\int \xi'_n u' dx = \sum_{i=0}^N \xi'_n(x_{di}) u'(x_{di}) w_i = \sum_{i=0}^N \sum_{j=0}^N D_{ij} D_{in} w_i u(x_{dj}), \quad (4.80)$$

$$\int \xi_n (Hu) dx = \sum_{i=0}^N \xi_n(x_{di}) (Hu)(x_{di}) w_i = w_n \sum_{i=0}^N H_{ni} u(x_{di}), \quad (4.81)$$

$$\int \xi_n S dx = \sum_{i=0}^N \xi_n(x_{di}) S(x_{di}) w_i = S(x_{dn}) w_n, \quad (4.82)$$

where D_{ij} (or H_{ij} , respectively) represents the action of the derivative (or of H , respectively) in the configuration space

$$g'(x_{dk}) = \sum_{j=0}^N D_{kj} g(x_{dj}), \quad (4.83)$$

$$(Hg)(x_{dk}) = \sum_{j=0}^N H_{kj} g(x_{dj}). \quad (4.84)$$

For points *strictly* inside each domain, the integrated term $[\xi u']$ of Equation (4.79) vanishes and one gets equations of the form:

$$-\sum_{i=0}^N \sum_{j=0}^N D_{ij} D_{in} w_i u(x_{dj}) + w_n \sum_{i=0}^N H_{ni} u(x_{di}) = S(x_{dn}) w_n. \quad (4.85)$$

This is a set of $N - 1$ equations for each domains ($d = 1, 2$). In the above form, the unknowns are the $u(x_{di})$, i.e. the solution is sought in the configuration space.

As usual, two additional equations are provided by appropriate boundary conditions at both ends of the global domain. One also gets an additional condition by matching the solution across the boundary between the two domains.

The last equation of the system is the matching of the first derivative of the solution. However, instead of writing it “explicitly”, this is done by making use of the integrated term in Equation (4.79) and this is actually the crucial step of the whole method. Applying Equation (4.79) to the last point x_{1N} of the first domain, one gets:

$$u'(x_1 = 1) = \sum_{i=0}^N \sum_{j=0}^N D_{ij} D_{iN} w_i u(x_{1j}) - w_N \sum_{i=0}^N H_{Ni} u(x_{1i}) + S(x_{1N}) w_N. \quad (4.86)$$

The same can be done with the first point of the second domain to get $u'(x_2 = -1)$, and the last equation of the system is obtained by demanding that $u'(x_1 = 1) = u'(x_2 = -1)$ and relates the values of u in both domains.

Before finishing with the variational method, it may be worthwhile to explain why Legendre polynomials are used. Suppose one wants to work with Chebyshev polynomials instead. The measure is then $w(x) = \frac{1}{\sqrt{1-x^2}}$. When one integrates the term containing u'' by parts, one gets

$$\int -u'' f w dx = [-u' f w] + \int u' f' w dx. \quad (4.87)$$

Because the measure is divergent at the boundaries, it is difficult, if not impossible, to isolate the term in u' . On the other hand, this is precisely the term that is needed to impose the appropriate matching of the solution.

Merits of the various methods

From a numerical point of view, the method based on an explicit matching using the homogeneous solutions is somewhat different from the two others. Indeed, one must solve several systems in a row and each one is of the same size as the number of points in one domain. This splitting of the different domains can also be useful for designing parallel codes. On the contrary, for both the variational and the tau method one must solve only one system, but its size is the same as the number of points in a whole space, which can be quite large for many domains settings. However, those two methods do not require one to compute the homogeneous solutions, computation that could be tricky depending on the operators involved and the number of dimensions.

The variational method may seem more difficult to implement and is only applicable with Legendre polynomials. However, on mathematical grounds, it is the only method that is demonstrated to be optimal. Moreover, some examples have been found in which the others methods are not optimal. It remains true that the variational method is very dependent on both the shape of the domains and the type of equation that needs to be solved.

The choice of one method or another thus depends on the particular situation. As for the mono-domain space, for simple test problems the results are very similar. Figure 4.16 shows the maximum error between the analytic solution and the numeric one for the four different methods. All errors decay exponentially and reach machine accuracy within roughly the same number of points.

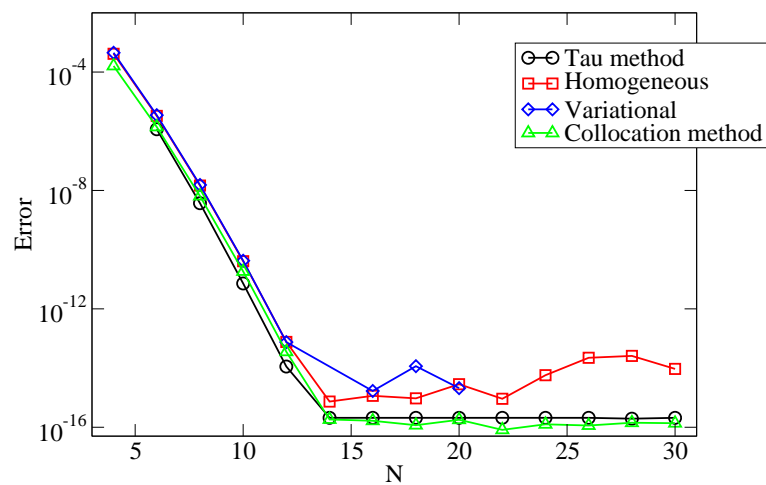


Figure 4.16: Difference between the exact and numerical solutions of the following test problem. $\frac{d^2u}{dx^2} + 4u = S$, with $S(x < 0) = 1$ and $S(x > 0) = 0$. The boundary conditions are $u(x = -1) = 0$ and $u(x = 1) = 0$. The black curve and circles denote results from the multidomain tau method, the red curve and squares from the method based on the homogeneous solutions, the blue curve and diamonds from the variational one, and the green curve and triangles from the collocation method.

4.3 Multidimensional Cases

In principle, the generalization to more than one dimension is rather straightforward if one uses the tensor product. Let us first take an example, with the spectral representation of a scalar function $f(x, y)$ defined on the square $(x, y) \in [-1, 1] \times [-1, 1]$ in terms of Chebyshev polynomials. One simply writes

$$f(x, y) = \sum_{i=0}^M \sum_{j=0}^N a_{ij} T_i(x) T_j(y), \quad (4.88)$$

with T_i being the Chebyshev polynomial of degree i . The partial differential operators can also be generalized as being linear operators acting on the space $\mathbb{P}_M \otimes \mathbb{P}_N$. Simple linear partial differential equations (PDE) can be solved by one of the methods presented in Section 4.2.5 (Galerkin, tau or collocation), on this MN -dimensional space. The development (4.88) can of course be generalized to any dimension. Some special PDE and spectral basis examples, where the differential equation decouples for some of the coordinates, will be given in Section 4.3.2.

4.3.1 Spatial coordinate systems

Most of the interesting problems in numerical relativity involve asymmetries that require the use of a full set of three-dimensional coordinates. We briefly review several coordinate sets (all orthogonal) that have been used in numerical relativity with spectral methods. They are described through the line element ds^2 of the flat metric in the coordinates we discuss.

- **Cartesian (rectangular) coordinates** are of course the simplest and most straightforward to implement; the line element reads $ds^2 = dx^2 + dy^2 + dz^2$. These coordinates are regular in all space, with vanishing connection, which makes them easy to use, since all differential operators have simple expressions and the associated triad is also perfectly regular. They are particularly well adapted to cube-like domains, see for instance [357, 361] and [185] in the case of toroidal topology.
- **Circular cylindrical coordinates** have a line element $ds^2 = d\rho^2 + \rho^2 d\phi^2 + dz^2$ and exhibit a coordinate singularity on the z -axis ($\rho = 0$). The associated triad being also singular for $\rho = 0$, regular vector or tensor fields have components that are multivalued (depending on ϕ) at any point of the z -axis. As for the spherical coordinates, this can be handled quite easily with spectral methods. This coordinate system can be useful for axisymmetric or rotating systems, see [30].
- **Spherical (polar) coordinates** will be discussed in more detail in Section 4.3.2. Their line element reads $ds^2 = dr^2 + r^2 d\theta^2 + r^2 \sin^2 \theta d\varphi^2$, showing a coordinate singularity at the origin ($r = 0$) and on the axis for which $\theta = 0, \pi$. They are very useful in numerical relativity for the numerous sphere-like objects under study (stars, black hole horizons) and have mostly been implemented for shell-like domains [72, 228, 357, 466] and for spheres including the origin [79, 228].
- **Prolate spheroidal coordinates** consist of a system of confocal ellipses and hyperbolae, describing an (x, z) -plane, and an angle φ giving the position as a rotation with respect to the focal axis [284]. The line element is $ds^2 = a^2 (\sinh^2 \mu + \sin^2 \nu) (d\mu^2 + d\nu^2) + a^2 \sinh^2 \mu \sin^2 \nu d\varphi^2$.

The foci are situated at $z = \pm a$ and represent coordinate singularities for $\mu = 0$ and $\nu = 0, \pi$. These coordinates have been used in [33] with black-hole-puncture data at the foci.

- **Bispherical coordinates** are obtained by the rotation of bipolar coordinates around the focal axis, with a line element $ds^2 = a^2 (\cosh \eta - \cos \chi)^{-2} (d\eta^2 + d\chi^2 + \sin^2 \chi d\varphi^2)$. As with prolate spheroidal coordinates, the foci situated at $z = \pm a$ ($\eta \rightarrow \pm\infty, \chi = 0, \pi$) and more generally, the focal axis, exhibit coordinate singularities. Still, the surfaces of constant η are spheres situated in the $z > 0 (< 0)$ region for $\eta > 0 (< 0)$, respectively. Thus, these coordinates are very well adapted for the study of binary systems and in particular for excision treatment of black hole binaries [27].

Mappings

Choosing a smart set of coordinates is not the end of the story. As for finite elements, one would like to be able to cover some complicated geometries, like distorted stars, tori, etc... or even to be able to cover the whole space. The reason for this last point is that, in numerical relativity, one often deals with isolated systems for which boundary conditions are only known at spatial infinity. A quite simple choice is to perform a mapping from *numerical coordinates* to *physical coordinates*, generalizing the change of coordinates to $[-1, 1]$, when using families of orthonormal polynomials or to $[0, 2\pi]$ for Fourier series.

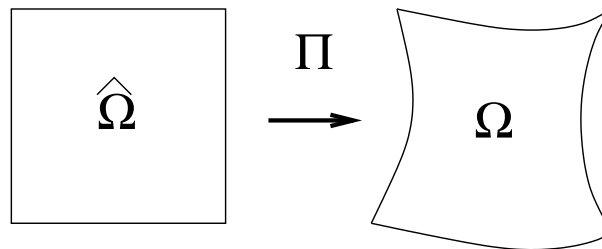


Figure 4.17: Regular deformation of the $[-1, 1] \times [-1, 1]$ square.

An example of how to map the $[-1, 1] \times [-1, 1]$ domain can be taken from Canuto et al. [102], and is illustrated in Figure 4.17: once the mappings from the four sides (boundaries) of $\hat{\Omega}$ to the four sides of Ω are known, one can construct a two-dimensional regular mapping Π , which preserves orthogonality and simple operators (see Chapter 3.5 of [102]).

The case where the boundaries of the considered domain are not known at the beginning of the computation can also be treated in a spectral way. In the case where this surface corresponds to the surface of a neutron star, two approaches have been used. First, in Bonazzola et al. [69], the star (and therefore the domain) is supposed to be “star-like”, meaning that there exists a point from which it is possible to reach any point on the surface by straight lines that are all contained inside the star. To such a point is associated the origin of a spherical system of coordinates, so that it is a spherical domain, which is regularly deformed to coincide with the shape of the star. This is done within an iterative scheme, at every step, once the position of the surface has been determined. Then, another approach has been developed by Ansorg et al. [30] using cylindrical coordinates. It is a square in the plane (ρ, z) , which is mapped onto the domain describing the interior of the star. This mapping involves an unknown function, which is itself decomposed in terms of a basis of Chebyshev

polynomials, so that its coefficients are part of the global vector of unknowns (as the density and gravitational field coefficients).

In the case of black-hole–binary systems, Scheel et al. [404] have developed horizon-tracking coordinates using results from control theory. They define a control parameter as the relative drift of the black hole position, and they design a feedback control system with the requirement that the adjustment they make on the coordinates be sufficiently smooth that they do not spoil the overall Einstein solver. In addition, they use a dual-coordinate approach, so that they can construct a co-moving coordinate map, which tracks both orbital and radial motion of the black holes and allows them to successfully evolve the binary. The evolutions simulated in [404] are found to be unstable, when using a single rotating-coordinate frame. We note here as well the work of Bonazzola et al. [74], where another option is explored: the *stroboscopic* technique of matching between an inner rotating domain and an outer inertial one.

Spatial compactification

As stated above, the mappings can also be used to include spatial infinity into the computational domain. Such a *compactification* technique is not tied to spectral methods and has already been used with finite-difference methods in numerical relativity by, e.g., Pretorius [374]. However, due to the relatively low number of degrees of freedom necessary to describe a spatial domain within spectral methods, it is easier within this framework to use some resources to describe spatial infinity and its neighborhood. Many choices are possible to do so, either directly choosing a family of well-behaved functions on an unbounded interval, for example the Hermite functions (see, e.g., Section 17.4 in Boyd [85]), or making use of standard polynomial families, but with an adapted mapping. A first example within numerical relativity was given by Bonazzola et al. [67] with the simple inverse mapping in spherical coordinates.

$$r = \frac{1}{\alpha(x-1)}, \quad x \in [-1, 1]. \quad (4.89)$$

This inverse mapping for spherical “shells” has also been used by Kidder and Finn [279], Pfeiffer et al. [361, 357], and Ansorg et al. in cylindrical [30] and spheroidal [33] coordinates. Many more elaborated techniques are discussed in Chapter 17 of Boyd [85], but to our knowledge, none have been used in numerical relativity yet. Finally, it is important to point out that, in general, the simple compactification of spatial infinity is not well adapted to solving hyperbolic PDEs and the above mentioned examples were solving only for elliptic equations (initial data, see Section 4.5). For instance, the simple wave equation (4.126) is not invariant under the mapping (4.89), as has been shown, e.g., by Sommerfeld (see [436], Section 23.E). Intuitively, it is easy to see that when compactifying only spatial coordinates for a wave-like equation, the distance between two neighboring grid points becomes larger than the wavelength, which makes the wave poorly resolved after a finite time of propagation on the numerical grid. For hyperbolic equations, it is therefore usually preferable to impose physically and mathematically well-motivated boundary conditions at a finite radius (see, e.g., Friedrich and Nagy [189], Rinne [388] or Buchman and Sarbach [95]).

Patching in more than one dimension

The multidomain (or multipatch) technique has been presented in Section 4.2.6 for one spatial dimension. In Bonazzola et al. [72] and Grandclément et al. [228], the three-dimensional spatial domains consist of spheres (or star-shaped regions) and spherical shells, across which the solution can be

matched as in one-dimensional problems (only through the radial dependence). In general, when performing a matching in two or three spatial dimensions, the reconstruction of the global solution across all domains might need some more care to clearly write down the matching conditions (see, e.g., [357], where overlapping as well as nonoverlapping domains are used at the same time). For example in two dimensions, one of the problems that might arise is the counting of matching conditions for corners of rectangular domains, when such a corner is shared among more than three domains. In the case of a PDE where matching conditions must be imposed on the value of the solution, as well as on its normal derivative (Poisson or wave equation), it is sufficient to impose continuity of either normal derivative at the corner, the jump in the other normal derivative being spectrally small (see Chapter 13 of Canuto et al. [102]).

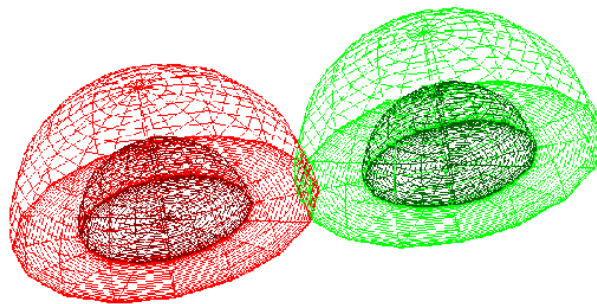


Figure 4.18: Two sets of spherical domains describing a neutron star or black hole binary system. Each set is surrounded by a compactified domain of the type (4.89), which is not displayed

A now typical problem in numerical relativity is the study of binary systems (see also Sections 4.5.5 and 4.6.3) for which two sets of spherical shells have been used by Gourgoulhon et al. [218], as displayed in Figure 4.18. Different approaches have been proposed by Kidder et al. [276], and used by Pfeiffer [357] and Scheel et al. [404] where spherical shells and rectangular boxes are combined together to form a grid adapted to black hole binary study. Even more sophisticated setups to model fluid flows in complicated tubes can be found in [306].

Multiple domains can thus be used to adapt the numerical grid to the interesting part (manifold) of the coordinate space; they can be seen as a technique close to the spectral element method [355]. Moreover, it is also a way to increase spatial resolution in some parts of the computational domain where one expects strong gradients to occur: adding a small domain with many degrees of freedom is the analog of fixed-mesh refinement for finite-differences.

4.3.2 Spherical coordinates and harmonics

Spherical coordinates (see Figure 4.19) are well adapted for the study of many problems in numerical relativity. Those include the numerical modeling of isolated astrophysical single objects, like a neutron star or a black hole. Indeed, stars' surfaces have sphere-like shapes and black hole horizons have this topology as well, which is best described in spherical coordinates (eventually through a mapping, see Section 4.3.1). As these are isolated systems in general relativity, the exact boundary conditions are imposed at infinity, requiring a compactification of space, which is here achieved with the compactification of the radial coordinate r only.

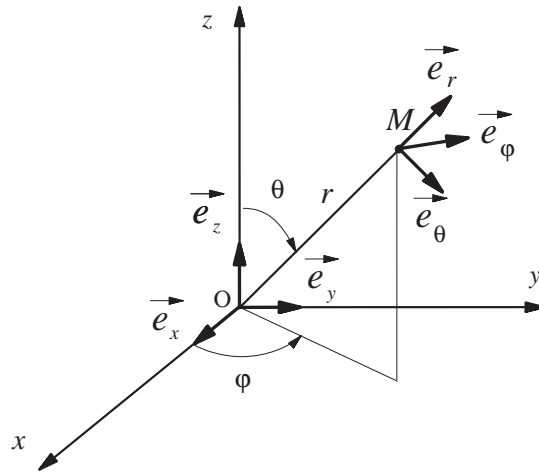


Figure 4.19: Definition of spherical coordinates (r, θ, φ) of a point M and associated triad $(\vec{e}_r, \vec{e}_\theta, \vec{e}_\varphi)$, with respect to the Cartesian ones.

When the numerical grid does not extend to infinity, e.g., when solving for a hyperbolic PDE, the boundary defined by $r = \text{const}$ is a smooth surface, on which boundary conditions are much easier to impose. Finally, *spherical harmonics*, which are strongly linked with these coordinates, can simplify a lot the solution of Poisson-like or wave-like equations. On the other hand, there are some technical problems linked with this set of coordinates, as detailed hereafter, but spectral methods can handle them in a very efficient way.

Coordinate singularities

The transformation from spherical (r, θ, φ) to Cartesian coordinates (x, y, z) is obtained by

$$x = r \sin \theta \cos \varphi, \quad (4.90)$$

$$y = r \sin \theta \sin \varphi, \quad (4.91)$$

$$z = r \cos \theta. \quad (4.92)$$

One immediately sees that the origin $r = 0 \iff x = y = z = 0$ is singular in spherical coordinates because neither θ nor φ can be uniquely defined. The same happens for the z -axis, where $\theta = 0$ or π , and φ cannot be defined. Among the consequences is the singularity of some usual differential operators, like, for instance, the Laplace operator

$$\Delta = \frac{\partial^2}{\partial r^2} + \frac{2}{r} \frac{\partial}{\partial r} + \frac{1}{r^2} \left(\frac{\partial^2}{\partial \theta^2} + \frac{1}{\tan \theta} \frac{\partial}{\partial \theta} + \frac{1}{\sin^2 \theta} \frac{\partial^2}{\partial \varphi^2} \right). \quad (4.93)$$

Here, the divisions by r at the center, or by $\sin \theta$ on the z -axis look singular. On the other hand, the Laplace operator, expressed in Cartesian coordinates, is a perfectly regular one and, if it is applied to a *regular* function, should give a well-defined result. The same should be true if one uses spherical coordinates: the operator (4.93) applied to a regular function should yield a regular result. This means that a regular function of spherical coordinates must have a particular behavior at the origin and on

the axis, so that the divisions by r or $\sin \theta$ appearing in regular operators are always well defined. If one considers an analytic function in (regular) Cartesian coordinates $f(x, y, z)$, it can be expanded as a series of powers of x, y and z , near the origin

$$f(x, y, z) = \sum_{n,p,q} a_{npq} x^n y^p z^q. \quad (4.94)$$

Placing the coordinate definitions (4.90)-(4.92) into this expression gives

$$f(r, \theta, \varphi) = \sum_{n,p,q} a_{npq} r^{n+p+q} \cos^q \theta \sin^{n+p} \theta \cos^n \varphi \sin^p \varphi; \quad (4.95)$$

and rearranging the terms in φ :

$$f(r, \theta, \varphi) = \sum_{m,p,q} b_{mpq} r^{|m|+2p+q} \sin^{|m|+2p} \theta \cos^q \theta e^{im\varphi}. \quad (4.96)$$

With some transformations of trigonometric functions in θ , one can express the angular part in terms of spherical harmonics $Y_\ell^m(\theta, \varphi)$, see Section 4.3.2, with $\ell = |m| + 2p + q$ and obtain the two following regularity conditions, for a given couple (ℓ, m) :

- near $\theta = 0$, a regular scalar field is equivalent to $f(\theta) \sim \sin^{|m|} \theta$,
- near $r = 0$, a regular scalar field is equivalent to $f(r) \sim r^\ell$.

In addition, the r -dependence translates into a Taylor series near the origin, with the same parity as ℓ . More details in the case of polar (2D) coordinates are given in Chapter 18 of Boyd [85].

If we go back to the evaluation of the Laplace operator (4.93), it is now clear that the result is always regular, at least for $\ell \geq 2$ and $m \geq 2$. We detail the cases of $\ell = 0$ and $\ell = 1$, using the fact that spherical harmonics are eigenfunctions of the angular part of the Laplace operator (see Equation (4.103)). For $\ell = 0$ the scalar field f is reduced to a Taylor series of only even powers of r , therefore the first derivative contains only odd powers and can be safely divided by r . Once decomposed on spherical harmonics, the angular part of the Laplace operator (4.93) acting on the $\ell = 1$ component reads $-2/r^2$, which is a problem only for the first term of the Taylor expansion. On the other hand, this term cancels with the $\frac{2}{r} \frac{\partial}{\partial r}$, providing a regular result. This is the general behavior of many differential operators in spherical coordinates: when applied to a regular field, the *full* operator gives a regular result, but *single terms* of this operator may give singular results when computed separately, the singularities canceling between two different terms.

As this may seem an argument against the use of spherical coordinates, let us stress that spectral methods are very powerful in evaluating such operators, keeping everything finite. As an example, we use Chebyshev polynomials in ξ for the expansion of the field $f(r = \alpha\xi)$, α being a positive constant. From the Chebyshev polynomial recurrence relation (4.46), one has

$$\forall n > 0, \quad \frac{T_{n+1}(\xi)}{\xi} = 2T_n(\xi) - \frac{T_{n-1}(\xi)}{\xi}, \quad (4.97)$$

which recursively gives the coefficients of

$$g(\xi) = \frac{f(\xi) - f(0)}{\xi}, \quad (4.98)$$

from those of $f(\xi)$. The computation of this *finite part* $g(\xi)$ is always a regular and linear operation on the vector of coefficients. Thus, the singular terms of a regular operator are never computed, but the result is a good one, as if the cancellation of such terms had occurred. Moreover, from the parity conditions it is possible to use only even or odd Chebyshev polynomials, which simplifies the expressions and saves computer time and memory. Of course, relations similar to Equation (4.97) exist for other families of orthonormal polynomials, as well as relations that divide by $\sin \theta$ a function developed on a Fourier basis. The combination of spectral methods and spherical coordinates is thus a powerful tool for accurately describing regular fields and differential operators inside a sphere [79]. To our knowledge, this is the first reference showing that it is possible to solve PDEs with spectral methods inside a sphere, including the three-dimensional coordinate singularity at the origin.

Spherical harmonics

Spherical harmonics are the pure angular functions

$$Y_\ell^m(\theta, \varphi) = \sqrt{\frac{2\ell+1}{4\pi} \frac{(\ell-m)!}{(\ell+m)!}} P_\ell^m(\cos \theta) e^{im\varphi}, \quad (4.99)$$

where $\ell \geq 0$ and $|m| \leq \ell$. $P_\ell^m(\cos \theta)$ are the associated Legendre functions defined by

$$P_\ell^m(x) = \frac{(\ell+m)!}{(\ell-m)!} \frac{1}{2^\ell \ell! \sqrt{(1-x^2)^m}} \frac{d^{\ell-m}}{dx^{\ell-m}} (1-x^2)^\ell, \quad (4.100)$$

for $m \geq 0$. The relation

$$P_\ell^{-m}(x) = \frac{(\ell-m)!}{(\ell+m)!} P_\ell^m(x) \quad (4.101)$$

gives the associated Legendre functions for negative m ; note that the normalization factors can vary in the literature. This family of functions have two very important properties. First, they represent an orthogonal set of regular functions defined on the sphere; thus, any regular scalar field $f(\theta, \varphi)$ defined on the sphere can be decomposed into spherical harmonics

$$f(\theta, \varphi) = \sum_{\ell=0}^{+\infty} \sum_{m=-\ell}^{m=\ell} f_{\ell m} Y_\ell^m(\theta, \varphi). \quad (4.102)$$

Since the harmonics are regular, they automatically take care of the coordinate singularity on the z -axis. Then, they are eigenfunctions of the angular part of the Laplace operator (noted here as $\Delta_{\theta\varphi}$):

$$\forall(\ell, m) \quad \Delta_{\theta\varphi} Y_\ell^m(\theta, \varphi) := \frac{\partial^2 Y_\ell^m}{\partial \theta^2} + \frac{1}{\tan \theta} \frac{\partial Y_\ell^m}{\partial \theta} + \frac{1}{\sin^2 \theta} \frac{\partial^2 Y_\ell^m}{\partial \varphi^2} = -\ell(\ell+1) Y_\ell^m(\theta, \varphi), \quad (4.103)$$

the associated eigenvalues being $-\ell(\ell+1)$.

The first property makes the description of scalar fields on spheres very easy: spherical harmonics are used as a decomposition basis within spectral methods, for instance in geophysics or meteorology, and by some groups in numerical relativity [49, 228, 466]. However, they could be more broadly used in numerical relativity, for example for Cauchy-characteristic evolution or matching [483, 40], where a single coordinate chart on the sphere might help in matching quantities. They can also help to describe star-like surfaces being defined by $r = h(\theta, \varphi)$ as event or apparent horizons [330, 51, 9]. The search

for apparent horizons is also made easier: since the function h verifies a two-dimensional Poisson-like equation, the linear part can be solved directly, just by dividing by $-\ell(\ell + 1)$ in the coefficient space.

The second property makes the Poisson equation,

$$\Delta\phi(r, \theta, \varphi) = \sigma(r, \theta, \varphi), \quad (4.104)$$

very easy to solve (see Section 4.1.3). If the source σ and the unknown ϕ are decomposed into spherical harmonics, the equation transforms into a set of *ordinary* differential equations for the coefficients (see also [228]):

$$\forall(\ell, m) \quad \frac{d^2\phi_{\ell m}}{dr^2} + \frac{2}{r} \frac{d\phi_{\ell m}}{dr} - \frac{\ell(\ell + 1)\phi_{\ell m}}{r^2} = \sigma_{\ell m}. \quad (4.105)$$

Then, any ODE solver can be used for the radial coordinate: spectral methods, of course, (see Section 4.2.5), but others have been used as well (see *e.g.*, Bartnik et al. [48, 49]). The same technique can be used to advance in time the wave equation with an implicit scheme and Chebyshev-tau method for the radial coordinate [79, 341].

The use of spherical-harmonics decomposition can be regarded as a basic spectral method, like Fourier decomposition. There are, therefore, publicly available “spherical harmonics transforms”, which consist of a Fourier transform in the φ -direction and a successive Fourier and Legendre transform in the θ -direction. A rather efficient one is the SpharmonicsKit/S2Kit [322], but writing one’s own functions is also possible [216].

Tensor components

All the discussion in Sections 4.3.1–4.3.2 has been restricted to scalar fields. For vector, or more generally tensor fields in three spatial dimensions, a vector basis (triad) must be specified to express the components. At this point, it is very important to stress that the choice of the basis is independent of the choice of coordinates. Therefore, the most straightforward and simple choice, even if one is using spherical coordinates, is the Cartesian triad $(\mathbf{e}_x = \frac{\partial}{\partial x}, \mathbf{e}_y = \frac{\partial}{\partial y}, \mathbf{e}_z = \frac{\partial}{\partial z})$. With this basis, from a numerical point of view, all tensor components can be regarded as scalars and therefore, a regular tensor can be defined as a tensor field, whose components with respect to this Cartesian frame are expandable in powers of x, y and z (as in Bardeen and Piran [47]). Manipulations and solutions of PDEs for such tensor fields in spherical coordinates are generalizations of the techniques for scalar fields. In particular, when using the multidomain approach with domains having different shapes and coordinates, it is much easier to match Cartesian components of tensor fields. Examples of use of Cartesian components of tensor fields in numerical relativity include the vector Poisson equation [228] or, more generally, the solution of elliptic systems arising in numerical relativity [361]. In the case of the evolution of the unconstrained Einstein system, the use of Cartesian tensor components is the general option, as it is done by the Caltech/Cornell group [277, 404].

The use of an *orthonormal spherical basis* $(\mathbf{e}_r = \frac{\partial}{\partial r}, \mathbf{e}_\theta = \frac{1}{r} \frac{\partial}{\partial \theta}, \mathbf{e}_\varphi = \frac{1}{r \sin \theta} \frac{\partial}{\partial \varphi})$ (see. Figure 4.19) requires more care. The interested reader can find more details in the work of Bonazzola et al. [79, 73]. Nevertheless, there are systems in general relativity in which spherical components of tensors can be useful:

- When doing excision for the simulation of black holes, the boundary conditions on the excised sphere for elliptic equations (initial data) may be better formulated in terms of spherical components for the shift or the three-metric [129, 222, 265]. In particular, the component that is normal to the excised surface is easily identified with the radial component.

- Still, in the 3+1 approach, the extraction of gravitational radiation in the wave zone is made easier if the perturbation to the metric is expressed in spherical components, because the transverse part is then straightforward to obtain [464].

Problems arise because of the singular nature of the basis itself, in addition to the spherical coordinate singularities. The consequences are first that each component is a multivalued function at the origin $r = 0$ or on the z -axis, and then that components of a given tensor are not independent from one another, meaning that one cannot, in general, specify each component independently or set it to zero, keeping the tensor field regular. As an example, we consider the gradient $V^i = \nabla^i \phi$ of the scalar field $\phi = x$, where x is the usual first Cartesian coordinate field. This gradient expressed in Cartesian components is a regular vector field $V^x = 1$, $V^y = 0$, $V^z = 0$. The spherical components of \mathbf{V} read

$$\begin{aligned} V^r &= \sin \theta \cos \varphi, \\ V^\theta &= \cos \theta \cos \varphi, \\ V^\varphi &= -\sin \varphi, \end{aligned} \quad (4.106)$$

which are all multidefined at the origin, and the last two on the z -axis. In addition, if V^θ is set to zero, one sees that the resulting vector field is no longer regular: for example the square of its norm is multidefined, which is not a good property for a scalar field. As for the singularities of spherical coordinates, these difficulties can be properly handled with spectral methods, provided that the decomposition bases are carefully chosen.

The other drawback of spherical coordinates is that the usual partial differential operators mix the components. This is due to the nonvanishing connection coefficients associated with the spherical flat metric [73]. For example, the vector Laplace operator ($\nabla_j \nabla^j V^i$) reads

$$\frac{\partial^2 V^r}{\partial r^2} + \frac{2}{r} \frac{\partial V^r}{\partial r} + \frac{1}{r^2} \left(\Delta_{\theta\varphi} V^r - 2V^r - 2 \frac{\partial V^\theta}{\partial \theta} - 2 \frac{V^\theta}{\tan \theta} - \frac{2}{\sin \theta} \frac{\partial V^\varphi}{\partial \varphi} \right) \quad (4.107)$$

$$\frac{\partial^2 V^\theta}{\partial r^2} + \frac{2}{r} \frac{\partial V^\theta}{\partial r} + \frac{1}{r^2} \left(\Delta_{\theta\varphi} V^\theta + 2 \frac{\partial V^r}{\partial \theta} - \frac{V^\theta}{\sin^2 \theta} - 2 \frac{\cos \theta}{\sin^2 \theta} \frac{\partial V^\varphi}{\partial \varphi} \right) \quad (4.108)$$

$$\frac{\partial^2 V^\varphi}{\partial r^2} + \frac{2}{r} \frac{\partial V^\varphi}{\partial r} + \frac{1}{r^2} \left(\Delta_{\theta\varphi} V^\varphi + \frac{2}{\sin \theta} \frac{\partial V^r}{\partial \varphi} + 2 \frac{\cos \theta}{\sin^2 \theta} \frac{\partial V^\theta}{\partial \varphi} - \frac{V^\varphi}{\sin^2 \theta} \right), \quad (4.109)$$

with $\Delta_{\theta\varphi}$ defined in Equation (4.103). In particular, the r -component (4.107) of the operator involves the other two components. This can make the resolution of a vector Poisson equation, which naturally arises in the initial data problem [127] of numerical relativity, technically more complicated, and the technique using scalar spherical harmonics (Section 4.3.2) is no longer valid. One possibility can be to use vector, and more generally tensor [313, 498, 464, 92], spherical harmonics as the decomposition basis. Another technique might be to build from the spherical components regular scalar fields, which can have a similar physical relevance to the problem. In the vector case, one can think of the following expressions

$$\Theta = \nabla_i V^i, \quad \chi = r_i V^i, \quad \mu = r^i \epsilon_{ijk} \nabla^j V^k, \quad (4.110)$$

where $\mathbf{r} = r \mathbf{e}_r$ denotes the position vector and ϵ_{ijk} the third-rank fully-antisymmetric tensor. These scalars are the divergence, r -component and curl of the vector field. The reader can verify that a Poisson equation for V^i transforms into three equations for these scalars, expandable in terms of scalar spherical harmonics. The reason that these fields may be more interesting than Cartesian components is that they can have more physical or geometric meaning.

4.3.3 Going further

The development of spectral methods linked with the problems arising in the field of numerical relativity has always been active and continues to be. Among the various directions of research one can foresee, quite interesting ones might be the beginning of higher-dimensional studies and the development of better-adapted mappings and domains, within the spirit of going from pure spectral methods to spectral elements [355, 60].

More than three spatial dimensions

There has been some interest in the numerical study of black holes in higher dimensions, as well as with compactified extra dimensions [437], as in brane world models [429, 286]; recently, some simulations of the head-on collision of two black holes have already been undertaken [489]. With the relatively low number of degrees of freedom per dimension needed, spectral methods should be very efficient in simulations involving four spatial dimensions or more. Here we give starting points to implement four-dimensional (as needed by, e.g., brane world models) spatial representation with spectral methods. The simplest approach is to take Cartesian coordinates (x, y, z, w) , but a generalization of spherical coordinates $(r, \theta, \varphi, \xi)$ is also possible and necessitates less computational resources. The additional angle ξ is defined in $[0, \pi]$ with the following relations with Cartesian coordinates

$$\begin{aligned} x &= r \sin \theta \cos \varphi \sin \xi, \\ y &= r \sin \theta \sin \varphi \sin \xi, \\ z &= r \cos \theta \sin \xi, \\ w &= r \cos \xi. \end{aligned}$$

The four-dimensional flat Laplace operator appearing in constraint equations [429] reads

$$\Delta_4 \phi = \frac{\partial^2 \phi}{\partial r^2} + \frac{3}{r} \frac{\partial \phi}{\partial r} + \frac{1}{r^2} \left(\frac{\partial^2 \phi}{\partial \xi^2} + \frac{2}{\tan \xi} \frac{\partial \phi}{\partial \xi} + \frac{1}{\sin^2 \xi} \Delta_{\theta\varphi} \phi \right), \quad (4.111)$$

where $\Delta_{\theta\varphi}$ is the two-dimensional angular Laplace operator (4.103). As in the three-dimensional case, it is convenient to use the eigenfunctions of the angular part, which are here

$$G_k^\ell(\cos \xi) P_\ell^m(\cos \theta) e^{im\varphi}, \quad (4.112)$$

with k, ℓ, m integers such that $|m| \leq \ell \leq k$. $P_\ell^m(x)$ are the associated Legendre functions defined by Equation (4.100). $G_k^\ell(x)$ are the associated Gegenbauer functions

$$G_k^\ell(\cos \xi) = (\sin^\ell \xi) G_k^{(\ell)}(\cos \xi) \text{ with } G_k^{(\ell)}(x) = \frac{d^\ell G_k(x)}{dx^\ell}, \quad (4.113)$$

where $G_k(x)$ is the k -th Gegenbauer polynomial $C_k^{(\lambda)}$ with $\lambda = 1$, as the G_k are also a particular case of Jacobi polynomials with $\alpha = \beta = 1/2$ (see, for example, [284]). Jacobi polynomials are also solutions of a singular Sturm-Liouville problem, which ensures fast convergence properties (see Section 4.2.4). The $G_k(x)$ fulfill recurrence relations that make them easy to implement as a spectral decomposition basis, like the Legendre polynomials. These eigenfunctions are associated with the eigenvalues $-k(k+2)$:

$$\Delta_4 \left(G_k^\ell(\cos \xi) P_\ell^m(\cos \theta) e^{im\varphi} \right) = -k(k+2) G_k^\ell(\cos \xi) P_\ell^m(\cos \theta) e^{im\varphi}. \quad (4.114)$$

So, as in 3+1 dimensions, after decomposing in such a basis, the Poisson equation turns into a collection of ODEs in the coordinate r . This type of construction might be generalized to even higher dimensions, with a choice of the appropriate type of Jacobi polynomials for every new introduced angular coordinate.

4.4 Time-Dependent Problems

From a relativistic point of view, the time coordinate could be treated in the same way as spatial coordinates and one should be able to achieve spectral accuracy for the time representation of a spacetime function $f(t, x, y, z)$ and its derivatives. Unfortunately, this does not seem to be the case and we are neither aware of any efficient algorithm dealing with the time coordinate, nor of any published successful code solving any of the PDEs coming from Einstein's equations, with the recent exception of the 1+1 dimensional study by Hennig and Ansorg [246]. Why is time playing such a special role? It is not easy to find in the literature on spectral methods a complete and comprehensive study. A first standard explanation is the difficulty, in general, of predicting the exact time interval on which one wants to study the time evolution. In addition, time discretization errors in both finite difference techniques and spectral methods are typically much smaller than spatial ones. Finally, one must keep in mind that, contrary to finite difference techniques, spectral methods store all global information about a function over the whole time interval. Therefore, one reason may be that there are strong memory and CPU limitations to fully three-dimensional simulations; it is already very CPU and memory consuming to describe a complete field depending on 3+1 coordinates, even with fewer degrees of freedom, as is the case for spectral methods. But the strongest limitation is the fact that, in the full 3+1 dimensional case, the matrix representing a differential operator would be very big; it would therefore be very time consuming to invert it in a general case, even with iterative methods.

More details on the standard, finite-difference techniques for time discretization are given in Section 4.4.1. Due to the technical complexity of a general stability analysis, we restrict the discussion of this section to the eigenvalue stability (Section 4.4.1) with the following approach: the eigenvalues of spatial operator matrices must fall within the stability region of the time-marching scheme. Although this condition is only a necessary one and, in general, is not sufficient, it provides very useful guidelines for selecting time-integration schemes. A discussion of the imposition of boundary conditions in time-dependent problems is given in Section 4.4.2. Section 4.4.3 then details the stability analysis of spatial discretization schemes, with the examples of heat and advection equations, before the details of a fully-discrete analysis are given for a simple case (Section 4.4.4).

4.4.1 Time discretization

There have been very few theoretical developments in spectral time discretization, with the exception of Ierley et al. [257], where the authors have applied spectral methods in time to the study of the Korteweg de Vries and Burger equations, using Fourier series in space and Chebyshev polynomials for the time coordinates. Ierley et al. [257] observe a timestepping restriction: they have to employ multidomain and patching techniques (see Section 4.2.6) for the time interval, with the size of each subdomain being roughly given by the Courant–Friedrichs–Lewy (CFL) condition. Therefore, the most common approach for time representation are finite-difference techniques, which allow for the use of many well-established time-marching schemes, and the method of lines (for other methods, including fractional stepping, see Fornberg [182]). Let us write the general form of a first-order-in-time linear PDE:

$$\forall t \geq 0, \quad \forall x \in [-1, 1], \quad \frac{\partial u(x, t)}{\partial t} = Lu(x, t), \quad (4.115)$$

where L is a linear operator containing only derivatives with respect to the spatial coordinate x . For every value of time t , the spectral approximation $u_N(x, t)$ is a function of only one spatial dimension belonging to some finite-dimensional subspace of the suitable Hilbert space \mathcal{H} , with the given L_w^2 spatial

norm, associated for example with the scalar product and the weight w introduced in Section 4.2.3. Formally, the solution of Equation (4.115) can be written as:

$$\forall x \in [-1, 1], \quad u(x, t) = e^{Lt}u(x, 0). \quad (4.116)$$

In practice, to integrate time-dependent problems one can use spectral methods to calculate spatial derivatives and standard finite-difference schemes to advance in time.

Method of lines

At every instant t , one can represent the function $u_N(x, t)$ by a finite set $U_N(t)$, composed of its time-dependent spectral coefficients or its values at the collocation points. We denote L_N the spectral approximation to the operator L , together with the boundary conditions, if the tau or collocation method is used. L_N is, therefore, represented as an $N \times N$ matrix. This is the *method of lines*, which allows one to reduce a PDE to an ODE, after discretization in all but one dimensions. The advantage is that many ODE integration schemes are known (Runge-Kutta, symplectic integrators, ...) and can be used here. We shall suppose an equally-spaced grid in time, with the timestep noted Δt and $U_N^J = U_N(J \times \Delta t)$.

In order to step from U_N^J to U_N^{J+1} , one has essentially two possibilities: explicit and implicit schemes. In an *explicit scheme*, the action of the spatial operator L_N on $U_N^K|_{K \leq J}$ must be computed to explicitly get the new values of the field (either spatial spectral coefficients or values at collocation points). A simple example is the *forward Euler method*:

$$U_N^{J+1} = U_N^J + \Delta t L_N U_N^J, \quad (4.117)$$

which is first order and for which, as for any explicit schemes, the timestep is limited by the CFL condition. The imposition of boundary conditions is discussed in Section 4.4.2. With an *implicit scheme* one must solve for a boundary value problem in term of U_N^{J+1} at each timestep: it can be performed in the same way as for the solution of the elliptic equation (4.62) presented in Section 4.2.5. The simplest example is the *backward Euler method*:

$$U_N^{J+1} = U_N^J + \Delta t L_N U_N^{J+1}, \quad (4.118)$$

which can be re-written as an equation for the unknown U_N^{J+1} :

$$(I + \Delta t L_N) U_N^{J+1} = U_N^J,$$

where I is the identity operator. Both schemes have different stability properties, which can be analyzed as follows. Assuming that L_N can be diagonalized in the sense of the definition given in (4.4.1), the stability study can be reduced to the study of the collection of scalar ODE problems

$$\frac{\partial U_N}{\partial t} = \lambda_i U_N, \quad (4.119)$$

where λ_i is any of the eigenvalues of L_N in the sense of Equation (4.123).

Stability

The basic definition of *stability* for an ODE integration scheme is that, if the timestep is lower than some threshold, then $\|U_N^J\| \leq Ae^{KJ\Delta t}$, with constants A and K independent of the timestep. This is perhaps not the most appropriate definition, since in practice one often deals with bounded functions and an exponential growth in time would not be acceptable. Therefore, an integration scheme is said to be *absolutely stable* (or asymptotically stable), if $\|U_N^J\|$ remains bounded, $\forall J \geq 0$. This property depends on a particular value of the product $\lambda_i \times \Delta t$. For each time integration scheme, the *region of absolute stability* is the set of the complex plane containing all the $\lambda_i \Delta t$ for which the scheme is absolutely stable.

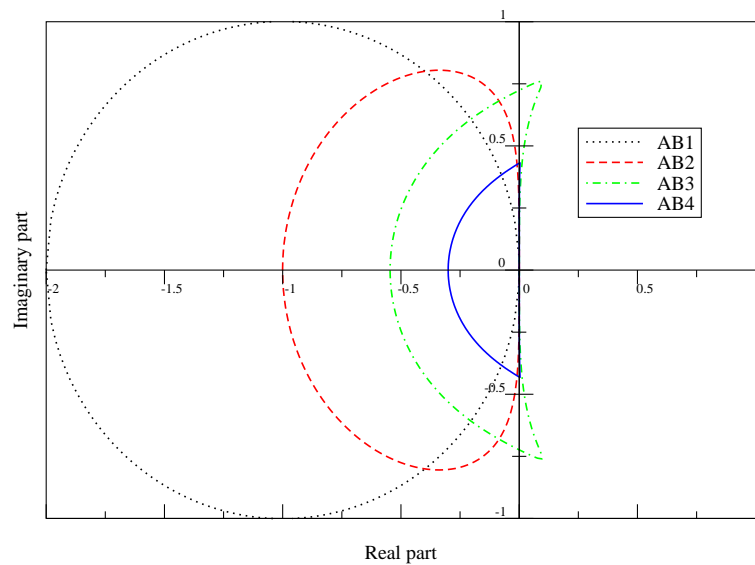


Figure 4.20: Regions of absolute stability for the Adams–Bashforth integration schemes of order one to four.

Finally, a scheme is said to be *A-stable* if its region of absolute stability contains the half complex plane of numbers with negative real part. It is clear that no explicit scheme can be *A-stable* due to the CFL condition. It has been shown by Dahlquist [138] that there is no linear multistep method of order higher than two, which is *A-stable*. Thus implicit methods are also limited in timestep size, if more than second-order accurate. In addition, Dahlquist [138] shows that the most accurate second-order *A-stable* scheme is the trapezoidal one (also called Crank–Nicolson, or second-order Adams–Moulton scheme)

$$U_N^{J+1} = U_N^J + \frac{\Delta t}{2} \left(L_N U_N^{J+1} + L_N U_N^J \right). \quad (4.120)$$

Figures 4.20 and 4.21 display the absolute stability regions for the Adams–Bashforth and Runge–Kutta families of explicit schemes (see, for instance, [102]). For a given type of spatial linear operator, the requirement on the timestep usually comes from the largest (in modulus) eigenvalue of the operator. For example, in the case of the advection equation on $[-1, 1]$, with a Dirichlet boundary condition,

$$\begin{aligned} Lu &= \frac{\partial u}{\partial x}, \\ \forall t, \quad u(1, t) &= 0, \end{aligned} \quad (4.121)$$

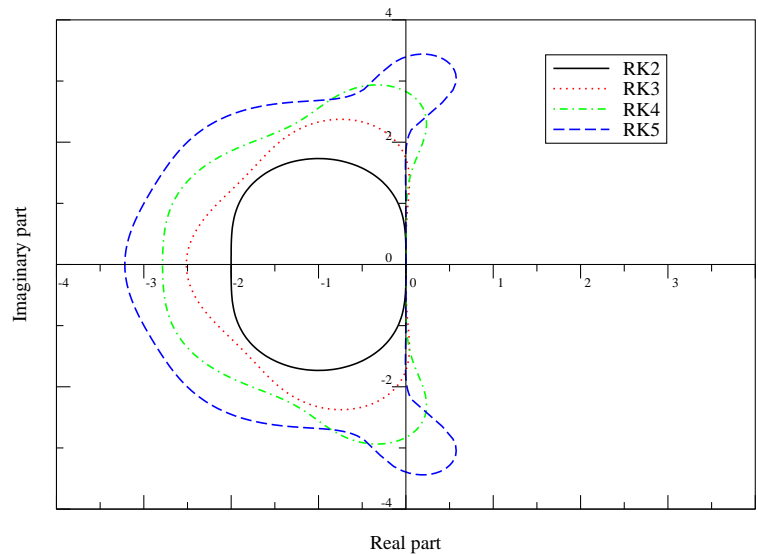


Figure 4.21: Regions of absolute stability for the Runge–Kutta integration schemes of order two to five. Note that the size of the region increases with order.

and using a Chebyshev-tau method, one can see that the largest eigenvalue of L_N grows in modulus as N^2 . Therefore, for any of the schemes considered in Figures 4.20 and 4.21, the timestep has a restriction of the type

$$\Delta t \lesssim O(N^{-2}), \quad (4.122)$$

which can be related to the usual CFL condition by the fact that the minimal distance between two points of a (N -point) Chebyshev grid decreases like $O(N^{-2})$. Due to the above mentioned *Second Dahlquist barrier* [138], implicit time marching schemes of order higher than two also have such a limitation.

Spectrum of simple spatial operators

An important issue in determining the absolute stability of a time-marching scheme for the solution of a given PDE is the computation of the spectrum (λ_i) of the discretized spatial operator L_N (4.119). As a matter of fact, these eigenvalues are those of the matrix representation of L_N , together with the necessary boundary conditions for the problem to be well posed (e.g., $\mathcal{B}_N u = 0$). If one denotes b the number of such boundary conditions, each eigenvalue λ_i (here, in the case of the tau method) is defined by the existence of a non-null set of coefficients $\{c_j\}_{1 \leq j \leq N}$ such that

$$\begin{aligned} (\forall j) 1 \leq j \leq N - b, \quad (L_N u)_j &= \lambda_i c_j, \\ \mathcal{B}_N u &= 0. \end{aligned} \quad (4.123)$$

As an example, let us consider the case of the advection equation (first-order spatial derivative) with a Dirichlet boundary condition, solved with the Chebyshev-tau method (4.121). Because of the definition of the problem (4.123), there are $N - 1$ “eigenvalues”, which can be computed, after a small transformation, using any standard linear algebra package. For instance, it is possible, making use of

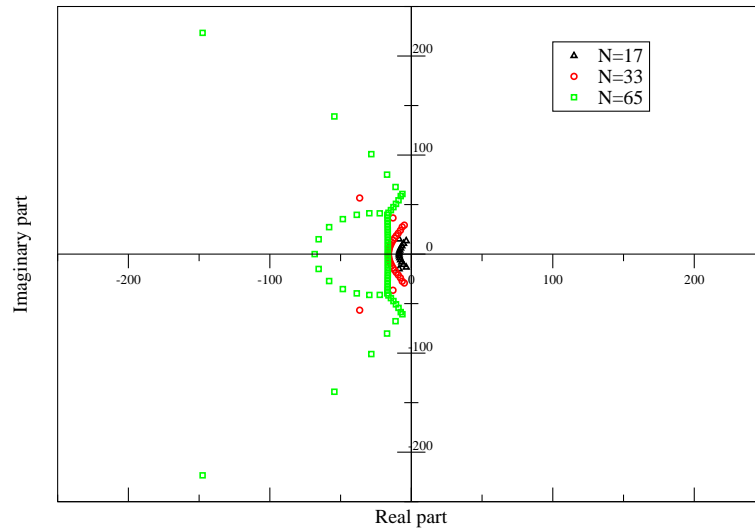


Figure 4.22: Eigenvalues of the first derivative-tau operator (4.123) for Chebyshev polynomials. The largest (in modulus) eigenvalue is not displayed; this one is real, negative and goes as $O(N^2)$.

the boundary condition, to express the last coefficient as a combination of the other ones

$$c_N = - \sum_{j=1}^{N-1} c_j. \quad (4.124)$$

One is thus left with the usual eigenvalue problem for an $(N - 1) \times (N - 1)$ matrix. Results are displayed in Figure 4.22 for three values of N . Real parts are all negative: the eigenvalue that is not displayed lies on the negative part of the real axis and is much larger in modulus (it is growing as $O(N^2)$) than the $N - 1$ others.

This way of determining the spectrum can be, of course, generalized to any linear spatial operator, for any spectral basis, as well as to the collocation and Galerkin methods. Intuitively from CFL-type limitations, one can see that in the case of the heat equation ($Lu = \partial^2 u / \partial x^2$), explicit time-integration schemes (or any scheme that is not A -stable) will have a severe timestep limitation of the type

$$\Delta t \lesssim O(N^{-4}), \quad (4.125)$$

for both a Chebyshev or Legendre decomposition basis. Finally, one can decompose a higher-order-in-time PDE into a first-order system and then use one of the above proposed schemes. In the particular case of the wave equation,

$$\frac{\partial^2 u}{\partial t^2} = \frac{\partial^2 u}{\partial x^2}, \quad (4.126)$$

it is possible to write a second-order Crank-Nicolson scheme directly [341]:

$$U_N^{J+1} = 2U_N^J - U_N^{J-1} + \frac{\Delta t^2}{2} \left(\frac{\partial^2 U_N^{J+1}}{\partial x^2} + \frac{\partial^2 U_N^{J-1}}{\partial x^2} \right). \quad (4.127)$$

Since this scheme is A -stable, there is no limitation on the timestep Δt , but for explicit or higher-order schemes this limitation would be $\Delta t \lesssim O(N^{-2})$, as for the advection equation. The solution of such an implicit scheme is obtained as that of a boundary value problem at each timestep.

Semi-implicit schemes

It is sometimes possible to use a combination of implicit and explicit schemes to loosen a timestep restriction of the type (4.122). Let us consider, as an example, the advection equation with nonconstant velocity on $[-1, 1]$,

$$\frac{\partial u}{\partial t} = v(x) \frac{\partial u}{\partial x}, \quad (4.128)$$

with the relevant boundary conditions, which shall in general depend on the sign of $v(x)$. If, on the one hand, the stability condition for explicit time schemes (4.122) is too strong, and on the other hand an implicit scheme is too lengthy to implement or to use (because of the nonconstant coefficient $v(x)$), then it is interesting to consider the semi-implicit two-step method (see also [210])

$$\begin{aligned} U_N^{J+1/2} - \frac{\Delta t}{2} L_N^- U_N^{J+1/2} &= U_N^J + \frac{\Delta t}{2} (L_N - L_N^-) U_N^J, \\ U_N^{J+1} - \frac{\Delta t}{2} L_N^+ U_N^{J+1} &= U_N^{J+1/2} + \frac{\Delta t}{2} (L_N - L_N^+) U_N^{J+1/2}, \end{aligned} \quad (4.129)$$

where L_N^+ and L_N^- are respectively the spectral approximations to the constant operators $-v(1)\partial/\partial x$ and $-v(-1)\partial/\partial x$, together with the relevant boundary conditions (if any). This scheme is absolutely stable if

$$\Delta t \lesssim \frac{1}{N \max |v(x)|}. \quad (4.130)$$

With this type of scheme, the propagation of the wave at the boundary of the interval is treated implicitly, whereas the scheme is still explicit in the interior. The implementation of the implicit part, for which one needs to solve a boundary-value problem, is much easier than for the initial operator (4.128) because of the presence of only constant-coefficient operators. This technique is quite helpful in the case of more severe timestep restrictions (4.125), for example for a variable coefficient heat equation.

4.4.2 Imposition of boundary conditions

The time-dependent PDE (4.115) can be written as a system of ODEs in time either for the time-dependent spectral coefficients $\{c_i(t)\}_{i=0\dots N}$ of the unknown function $u(x, t)$ (Galerkin or tau methods), or for the time-dependent values at collocation points $\{u(x_i, t)\}_{i=0\dots N}$ (collocation method). Implicit time-marching schemes (like the backward Euler scheme (4.118)) are technically very similar to a succession of boundary-value problems, as for elliptic equations or Equation (4.62) described in Section 4.2.5. The coefficients (or the values at collocation points) are determined at each new timestep by inversion of the matrix of type $I + \Delta t L$ or its higher-order generalization. To represent a well-posed problem, this matrix needs, in general, the incorporation of boundary conditions, for tau and collocation methods. Galerkin methods are not so useful if the boundary conditions are time dependent: this would require the construction of a new Galerkin basis at each new timestep, which is too complicated and/or time consuming. We shall therefore discuss in the following sections the imposition of boundary conditions for explicit time schemes, with the tau or collocation methods.

Strong enforcement

The standard technique is to enforce the boundary conditions exactly, i.e. up to machine precision. Let us suppose here that the time-dependent PDE (4.115), which we want to solve, is well posed with boundary condition

$$\forall t \geq 0, \quad u(x = 1, t) = b(t), \quad (4.131)$$

where $b(t)$ is a given function. We give here some examples, with the forward Euler scheme (4.117) for time discretization.

In the **collocation method**, the values of the approximate solution at (Gauss–Lobatto type) collocation points $\{x_i\}_{i=0\dots N}$ are determined by a system of equations:

$$\begin{aligned} \forall i = 0 \dots N - 1, \quad U_N^{J+1}(x_i) &= U_N^J(x_i) + \Delta t (L_N U_N^J)(x = x_i), \\ U_N^{J+1}(x = x_N = 1) &= b((J + 1)\Delta t), \end{aligned} \quad (4.132)$$

where the value at the boundary ($x = 1$) is directly set to be the boundary condition.

In the **tau method**, the vector U_N^J is composed of the $N + 1$ coefficients $\{c_i(J \times \Delta t)\}_{i=0\dots N}$ at the J -th timestep. If we denote by $(L_N U_N^J)_i$ the i -th coefficient of L_N applied to U_N^J , then the vector of coefficients $\{c_i\}_{i=0\dots N}$ is advanced in time through the system:

$$\begin{aligned} \forall i = 0 \dots N - 1, \quad c_i((J + 1) \times \Delta t) &= c_i(J \times \Delta t) + \Delta t (L_N U_N^J)_i \\ c_N((J + 1) \times \Delta t) &= b((J + 1)\Delta t) - \sum_{k=0}^{N-1} c_k, \end{aligned} \quad (4.133)$$

the last equality ensures the boundary condition in the coefficient space.

Penalty approach

As shown in the previous examples, the standard technique consists of neglecting the solution to the PDE for one degree of freedom, in configuration or coefficient space, and using this degree of freedom in order to impose the boundary condition. However, it is interesting to try and impose a linear combination of both the PDE and the boundary condition on this last degree of freedom, as is shown by the next simple example. We consider the simple (time-independent) integration over the interval $x \in [-1, 1]$:

$$\frac{du}{dx} = \sin(x - 1), \quad \text{and } u(1) = 0, \quad (4.134)$$

where $u(x)$ is the unknown function. Using a standard Chebyshev relation (4.160) collocation method (see Section 4.2.5), we look for an approximate solution u_N as a polynomial of degree N verifying

$$\begin{aligned} \forall i = 0 \dots N - 1, \quad \frac{du_N}{dx}(x_i) &= \sin(x_i - 1), \\ \frac{du_N}{dx}(x_N = 1) &= 0, \end{aligned}$$

where $\{x_i\}_{i=0\dots N}$ are the Chebyshev–Gauss–Lobatto collocation points.

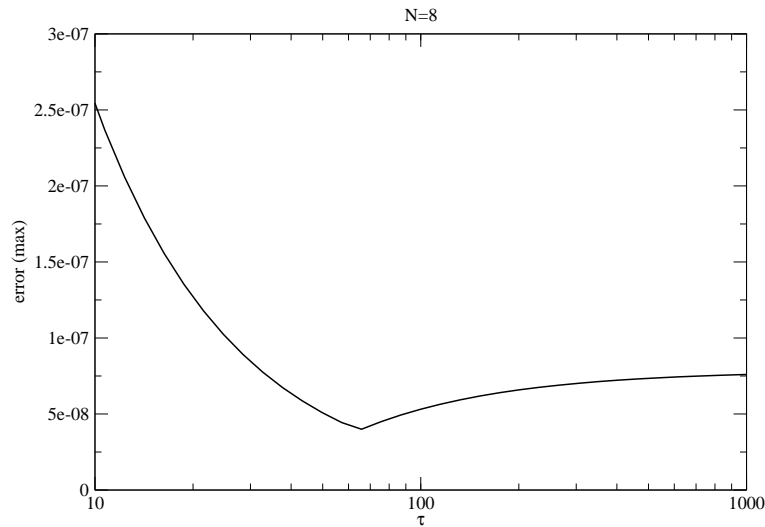


Figure 4.23: Behavior of the error in the solution of the differential equation (4.134), as a function of the parameter τ entering the numerical scheme (4.135).

We now adopt another procedure that takes into account the differential equation at the boundary as well as the boundary condition, with u_N verifying (remember that $x_N = 1$):

$$\begin{aligned} \forall i = 0 \dots N - 1, \quad \frac{du_N}{dx}(x_i) &= \sin(x_i - 1), \\ \frac{du_N}{dx}(x_N) - \tau u_N(x_N) &= \sin(x_N - 1), \end{aligned} \quad (4.135)$$

where $\tau > 0$ is a constant; one notices when taking the limit $\tau \rightarrow +\infty$, that both systems become equivalent. The discrepancy between the numerical and analytical solutions is displayed in Figure 4.23, as a function of that parameter τ , when using $N = 8$. It is clear from that figure that there exists a finite value of τ ($\tau_{\min} \simeq 70$) for which the error is minimal and, in particular, lower than the error obtained by the standard technique. Numerical evidence indicates that $\tau_{\min} \sim N^2$. This is a simple example of *weakly imposed* boundary conditions, with a *penalty term* added to the system. The idea of imposing boundary conditions up to the order of the numerical scheme was first proposed by Funaro and Gottlieb [195] and can be efficiently used for time-dependent problems, as illustrated by the following example. For a more detailed description, we refer the interested reader to the review article by Hesthaven [249].

Let us consider the linear advection equation

$$\forall x \in [-1, 1], \forall t \geq 0, \quad \frac{\partial u}{\partial t} = \frac{\partial u}{\partial x} \quad (4.136)$$

$$\forall t \geq 0, \quad u(1, t) = f(t), \quad (4.137)$$

where $f(t)$ is a given function. We look for a Legendre collocation method to obtain a solution, and define the polynomial $Q^-(x)$, which vanishes on the Legendre–Gauss–Lobatto grid points, except at the boundary $x = 1$:

$$Q^-(x) = \frac{(1+x)P'_N(x)}{2P'_N(1)}.$$

Thus, the Legendre collocation *penalty method* uniquely defines a polynomial $u_N(x, t)$ through its values at Legendre–Gauss–Lobatto collocation points $\{x_i\}_{i=0\dots N}$

$$\forall i = 0 \dots N, \quad \left. \frac{\partial u_N}{\partial t} \right|_{x=x_i} = \left. \frac{\partial u_N}{\partial x} \right|_{x=x_i} - \tau Q^-(x_i) (u_N(1, t) - f(t)), \quad (4.138)$$

where τ is a free parameter as in Equation (4.135). For all the grid points, except the boundary one, this is the same as the standard Legendre collocation method ($\forall i = 0 \dots N-1, Q^-(x_i) = 0$). At the boundary point $x = x_N = 1$, one has a linear combination of the advection equation and the boundary condition. Contrary to the case of the simple integration (4.135), the parameter τ here cannot be too small: in the limit $\tau \rightarrow 0$, the problem is ill posed and the numerical solution diverges. On the other hand, we still recover the standard (strong) imposition of boundary conditions when $\tau \rightarrow +\infty$. With the requirement that the approximation be asymptotically stable, we get for the discrete energy estimate (see the details of this technique in Section 4.4.3) the requirement

$$\frac{1}{2} \frac{d}{dt} \|u_N(t)\|^2 = \sum_{i=0}^N u_N(x_i, t) \left. \frac{\partial u_N}{\partial x} \right|_{x=x_i} w_i - \tau u_N^2(t, x_N) w_N \leq 0.$$

Using the property of Gauss–Lobatto quadrature rule (with the Legendre–Gauss–Lobatto weights w_i), and after an integration by parts, the stability is obtained if

$$\tau \geq \frac{1}{2w_N} \geq \frac{N(N+1)}{4}. \quad (4.139)$$

It is also possible to treat more complex boundary conditions, as described in Hesthaven and Gottlieb [251] in the case of Robin-type boundary conditions (see Section 4.2.5 for a definition). Specific conditions for the penalty coefficient τ are derived, but the technique is the same: for each boundary, a penalty term is added, which is proportional to the error on the boundary condition at the considered time. Thus, nonlinear boundary operators can also be incorporated easily (see, e.g., the case of the Burgers equation in [249]). The generalization to multidomain solutions is straightforward: each domain is considered as an isolated one, which requires boundary conditions at every timestep. The condition is imposed through the penalty term containing the difference between the junction conditions. This approach has very strong links with the variational method presented in Section 4.2.6 in the case of time-independent problems. A more detailed discussion of the *weak* imposition of boundary conditions is given in Canuto et al. (Section 3.7 of [103] and Section 5.3 of [104] for multidomain methods).

4.4.3 Discretization in space: stability and convergence

After dealing with temporal discretization, we now turn to another fundamental question of numerical analysis of initial value problems, which is to find conditions under which the discrete (spatial) approximation $u_N(x, t)$ converges to the right solution $u(x, t)$ of the PDE (4.115) as $N \rightarrow \infty$ and $t \in [0, T]$. The time derivative term is treated formally, as one would treat a source term on the right-hand side, that we do not consider here, for better clarity.

A given spatial scheme of solving the PDE is said to be *convergent* if any numerical approximation $u_N(x, t)$, obtained through this scheme, to the solution $u(x, t)$

$$\|P_N u - u_N\|_{L_w^2} \rightarrow 0 \text{ as } N \rightarrow \infty. \quad (4.140)$$

Two more concepts are helpful in the convergence analysis of numerical schemes:

- *consistency*: an approximation to the PDE (4.115) is consistent if $\forall v \in \mathcal{H}$ both

$$\left. \begin{aligned} \|P_N(Lv - L_N v)\|_{L_w^2} &\rightarrow 0 \\ \|P_N v - v_N\|_{L_w^2} &\rightarrow 0 \end{aligned} \right\} \text{as } N \rightarrow \infty; \quad (4.141)$$

- *stability*: with the formal notations of Equation (4.116), an approximation to the PDE (4.115) is stable if

$$\forall N, \quad \|e^{L_N t}\| = \sup_v \frac{\|e^{L_N t} v\|_{L_w^2}}{\|v\|_{L_w^2}} \leq C(t), \quad (4.142)$$

where $C(t)$ is independent of N and bounded for $t \in [0, T]$.

Lax–Richtmyer theorem

The direct proof of convergence of a given scheme is usually very difficult to obtain. Therefore, a natural approach is to use the *Lax–Richtmyer equivalence theorem*: “a consistent approximation to a well-posed linear problem is stable if and only if it is convergent”. Thus, the study of convergence of discrete approximations can be reduced to the study of their stability, assuming they are consistent. Hereafter, we sketch out the proof of this equivalence theorem.

The time-evolution PDE (4.115) is approximated by

$$\frac{\partial u_N}{\partial t} = L_N u_N. \quad (4.143)$$

To show that stability implies convergence, we subtract it from the exact solution (4.115)

$$\frac{\partial (u - u_N)}{\partial t} = L_N (u - u_N) + Lu - L_N u,$$

and obtain, after integration, (the dependence on the space coordinate x is skipped)

$$u(t) - u_N(t) = e^{L_N t} [u(0) - u_N(0)] + \int_0^t e^{L_N(t-s)} [Lu(s) - L_N u(s)] ds. \quad (4.144)$$

Using the stability property (4.142), the norm (L_w^2) of this equation implies

$$\|u(t) - u_N(t)\| \leq C(t) \|u(0) - u_N(0)\| + \int_0^t C(t-s) \|Lu(s) - L_N u(s)\| ds. \quad (4.145)$$

Since the spatial approximation scheme is consistent and $C(t)$ is a bounded function independent of N , for a given $t \in [0, T]$ the left-hand side goes to zero as $N \rightarrow \infty$, which proves the convergence.

Conversely, to show that convergence implies stability, we use the triangle inequality to get

$$0 \leq \| \|e^{L_N t} u\| - \|e^{L t} u\| \| \leq \|e^{L_N t} u - e^{L t} u\| \rightarrow 0.$$

From the well-posedness $\|e^{L t} u\|$ is bounded and therefore $\|e^{L_N t} u\|$ is bounded as well, independent of N .

The simplest stability criterion is the *von Neumann stability condition*: if we define the adjoint L^* of the operator L , using the inner product, with weight w of the Hilbert space

$$\forall (u, v) \in \mathcal{H}, \quad (u, Lv)_w = (L^* u, v)_w,$$

then the matrix representation L_N^* of L^* is also the adjoint of the matrix representation of L_N . The operator L_N is said to be normal if it commutes with its adjoint L_N^* . The von Neumann stability condition states that, for normal operators, if there exists a constant K independent of N , such that

$$\forall i, 1 \leq i \leq N, \quad \operatorname{Re}(\lambda_i) < K, \quad (4.146)$$

with (λ_i) being the eigenvalues of the matrix L_N , then the scheme is stable. This condition provides an operational technique for checking the stability of normal approximations. Unfortunately, spectral approximations using orthogonal polynomials have, in general, strongly non-normal matrices L_N and therefore, the von Neumann condition cannot be applied. Some exceptions include Fourier-based spectral approximations for periodic problems.

Energy estimates for stability

The most straightforward technique for establishing the stability of spectral schemes is the *energy method*: it is based on choosing the approximate solution itself as a test function in the evaluation of residual (4.60). However, this technique only provides a sufficient condition and, in particular, crude energy estimates indicating that a spectral scheme might be unstable can be very misleading for non-normal evolution operators (see the example in Section 8 of Gottlieb and Orszag [210]).

Some sufficient conditions on the spatial operator L and its approximation L_N are used in the literature to obtain energy estimates and stability criteria, including:

- If the operator L is *semibounded*:

$$\exists \gamma, \quad L + L^* \leq \gamma I, \quad (4.147)$$

where I is the identity operator.

- In the parabolic case, if L satisfies the *coercivity condition* (see also Chapter 6.5 of Canuto et al. [103]¹):

$$\exists A > 0, \forall (u, v), \quad |(Lu, v)| \leq A \|u\| \|v\|, \quad (4.148)$$

and the *continuity condition*:

$$\exists \alpha > 0, \forall u, \quad (Lu, u) \leq -\alpha \|u\|^2. \quad (4.149)$$

- In the hyperbolic case, if there exists a constant $C > 0$ such that

$$\forall u, \quad \|Lu\| \leq C \|u\|, \quad (4.150)$$

and if the operator verifies the *negativity condition*:

$$\forall u, \quad (Lu, u) \leq 0. \quad (4.151)$$

As an illustration, we now consider a Galerkin method applied to the solution of Equation (4.115), in which the operator L is semibounded, following the definition (4.147). The discrete solution u_N is such that the residual (4.60) estimated on the approximate solution u_N itself verifies

$$\left(\frac{\partial u_N}{\partial t} - Lu_N, u_N \right)_w = 0. \quad (4.152)$$

¹Note the difference in sign convention between [103] and here.

Separating the time derivative and the spatial operator:

$$\frac{1}{2} \frac{d}{dt} \|u_N(t)\|_w^2 = \frac{1}{2} ((L + L^*)u_N(t), u_N(t))_w,$$

which shows that the “energy”

$$\|u_N(t)\|^2 \leq e^{\gamma t} \|u_N(0)\|^2 \quad (4.153)$$

grows at most exponentially with time. Since $u_N(t) = e^{L_N t} u_N(0)$ for any $u_N(0)$, we obtain

$$\|e^{L_N t}\| \leq e^{\frac{1}{2}\gamma t}, \quad (4.154)$$

which gives stability and therefore convergence, provided that the approximation is consistent (thanks to the Lax–Richtmyer theorem).

Examples: heat equation and advection equation

Heat equation

We first study the linear heat equation

$$\frac{\partial u}{\partial t} - \frac{\partial^2 u}{\partial x^2} = 0, \quad \text{with } -1 < x < 1, t > 0, \quad (4.155)$$

with homogeneous Dirichlet boundary conditions

$$\forall t \geq 0, \quad u(-1, t) = u(1, t) = 0, \quad (4.156)$$

and initial condition

$$\forall -1 \leq x \leq 1, \quad u(x, 0) = u^0(x). \quad (4.157)$$

In the semidiscrete approach, the Chebyshev collocation method for this problem (see Section 4.2.5) can be devised as follows: the spectral solution $u_N(t > 0)$ is a polynomial of degree N on the interval $[-1, 1]$, vanishing at the endpoints. On the other Chebyshev–Gauss–Lobatto collocation points $\{x_k\}_{k=1 \dots N-1}$ (see Section 4.2.4), $u_N(t)$ is defined through the collocation equations

$$\forall k = 1 \dots N-1, \quad \frac{\partial u}{\partial t}(x_k, t) - \frac{\partial^2 u}{\partial x^2}(x_k, t) = 0, \quad (4.158)$$

which are time ODEs (discussed in Section 4.4.1) with the initial conditions

$$\forall k = 0 \dots N, \quad u_N(x_k, 0) = u^0(x_k). \quad (4.159)$$

We will now discuss the stability of such a scheme, with the computation of the energy bound to the solution. Multiplying the k -th equation of the system (4.158) by $u_N(x_k, t)w_k$, where $\{w_k\}_{k=0 \dots N}$ are the discrete weights of the Chebyshev–Gauss–Lobatto quadrature (Section 4.2.4), and summing over k , one gets:

$$\frac{1}{2} \frac{d}{dt} \sum_{k=0}^N (u_N(x_k, t))^2 w_k - \sum_{k=0}^N \frac{\partial^2 u_N}{\partial x^2}(x_k, t) u_N(x_k, t) w_k = 0. \quad (4.160)$$

Boundary points ($k = 0, N$) have been included in the sum since u_N is zero there due to boundary conditions. The product $u_N \times \partial^2 u_N / \partial x^2$ is a polynomial of degree $2N - 2$, so the quadrature formula is exact

$$\sum_{k=0}^N \frac{\partial^2 u_N}{\partial x^2}(x_k, t) u_N(x_k, t) w_k = \int_{-1}^1 \frac{\partial^2 u_N}{\partial x^2}(x_k, t) u_N(x_k, t) w(x) dx, \quad (4.161)$$

and integrating by parts twice, one gets the relation

$$\int_{-1}^1 \frac{\partial^2 u_N}{\partial x^2}(x_k, t) u_N(x_k, t) w(x) dx = \int_{-1}^1 \left(\frac{\partial u_N}{\partial x} \right)^2 w(x) dx - \frac{1}{2} \int_{-1}^1 u_N^2 \frac{\partial^2 w}{\partial x^2} dx. \quad (4.162)$$

By the properties of the Chebyshev weight

$$\frac{\partial^2 w}{\partial x^2} - \frac{2}{w} \left(\frac{\partial w}{\partial x} \right)^2 = 0 \quad \text{and} \quad \frac{\partial^2 w}{\partial x^2} = (1 + 2x^2) w^5, \quad (4.163)$$

it is possible to show that

$$\int_{-1}^1 u_N^2 \frac{\partial^2 w}{\partial x^2} dx \leq 3 \int_{-1}^1 u_N^2 w^5 dx \leq 6 \int_{-1}^1 \frac{\partial^2 u_N}{\partial x^2}(x_k, t) u_N(x_k, t) w(x) dx, \quad (4.164)$$

and thus that

$$\int_{-1}^1 \frac{\partial^2 u_N}{\partial x^2}(x_k, t) u_N(x_k, t) w(x) dx \geq \frac{1}{4} \int_{-1}^1 \left(\frac{\partial u_N}{\partial x} \right)^2 w(x) dx \geq 0. \quad (4.165)$$

Therefore, integrating relation (4.160) over the time interval $[0, t]$, one obtains

$$\sum_{k=0}^N (u_N(x_k, t))^2 w_k \leq \sum_{k=0}^N (u^0(x_k))^2 w_k \leq 2 \max_{x \in [0, 1]} |u^0(x)|^2. \quad (4.166)$$

The left-hand side represents the discrete norm of $u_N(t)^2$, but since this is a polynomial of degree $2N$, one cannot apply the Gauss–Lobatto rule. Nevertheless, it has been shown (see, e.g., Section 5.3 of Canuto et al. [103]) that discrete and L_w^2 -norms are uniformly equivalent, therefore:

$$\int_{-1}^1 (u_N(x, t))^2 w(x) \leq 2 \max_{x \in [0, 1]} |u^0(x)|^2, \quad (4.167)$$

which proves the stability of the Chebyshev collocation method for the heat equation. Convergence can again be deduced from the Lax–Richtmyer theorem, but a detailed analysis cf. Section 6.5.1 of Canuto et al. [103]) shows that the numerical solution obtained by the method described here converges to the true solution and one can obtain the convergence rate. If the solution $u(x, t)$ is m -times differentiable with respect to the spatial coordinate x (see Section 4.2.4) the energy norm of the error decays as N^{1-m} . In particular, if the solution is C^∞ , the error decays faster than any power of N .

Advection equation

We now study the Legendre-tau approximation to the simple advection equation

$$\frac{\partial u}{\partial t} + \frac{\partial u}{\partial x} = 0, \quad \text{with } -1 < x < 1, t > 0, \quad (4.168)$$

with homogeneous Dirichlet boundary condition

$$\forall t \geq 0, \quad u(-1, t) = 0, \quad (4.169)$$

and initial condition

$$\forall -1 \leq x \leq 1, \quad u(x, 0) = u^0(x). \quad (4.170)$$

If we seek the solution as the truncated Legendre series:

$$u_N(x, t) = \sum_{i=0}^N a_i(t) P_i(x)$$

by the tau method, then u_N satisfies the equation:

$$\frac{\partial u_N}{\partial t} + \frac{\partial u_N}{\partial x} = \tau_N(t) P_N(x). \quad (4.171)$$

Equating coefficients of P_N on both sides of (4.171), we get

$$\tau_N = \frac{da_N}{dt}.$$

Applying the L_w^2 scalar product with u_N to both sides of Equation (4.171), we obtain

$$\frac{1}{2} \frac{\partial}{\partial t} (\|u_N\|^2 - a_N^2) = - \int_{-1}^1 u \frac{\partial u_N}{\partial x} dx = -\frac{1}{2} u_N^2(1) \leq 0,$$

which implies the following inequality:

$$\frac{d}{dt} \sum_{i=0}^{N-1} a_i^2 \leq 0. \quad (4.172)$$

Finally, $a_N(t)$ is bounded because it is determined in terms of $\{a_i\}_{i=0 \dots N-1}$ from the boundary condition (4.169), and thus, stability is proved. In the same way as before, for the heat equation, it is possible to derive a bound for the error $\|u(x, t) - u_N(x, t)\|$, if the solution $u(x, t)$ is m -times differentiable with respect to the spatial coordinate x ; the energy norm of the error decays like N^{1-m} (see also Section 6.5.2 of Canuto et al. [103]). In particular, if the solution is C^∞ , the error decays faster than any power of N .

4.4.4 Fully-discrete analysis

Stability issues have been discussed separately for time (Section 4.4.1) and space (Section 4.4.3) discretizations. The global picture (*fully discrete analysis*), taking into account both discretizations is, in general, very difficult to study. However, it is possible in some particular cases to address

the problem and in the following lines, we shall perform a fully discrete analysis of the advection equation (4.168), using a Legendre collocation method in space and a forward Euler scheme in time. Using the notation of Section 4.4.1

$$\forall x \in [-1, 1], \quad U_N^{J+1}(x) = U_N^J(x) - \Delta t \frac{\partial U_N^J}{\partial x} + \Delta t \frac{\partial U_N^J}{\partial x} \Big|_{x=-1} \frac{P_{N+1}(x)}{P_{N+1}(-1)}, \quad (4.173)$$

where the last term imposes the boundary condition $\forall J, \quad U_N^J(x = -1) = 0$. We consider this relation at the Legendre–Gauss collocation points $(\{x_i\}_{i=0\dots N})$, which are zeros of $P_{N+1}(x)$; the square of this expression taken at these collocation points gives

$$\forall i \in [0, N], \quad \left(U_N^{J+1}(x_i) \right)^2 = \left(U_N^J(x_i) \right)^2 + \Delta t^2 \left(\frac{\partial U_N^J}{\partial x} \Big|_{x=x_i} \right)^2 - 2\Delta t U_N^J(x_i) \frac{\partial U_N^J}{\partial x} \Big|_{x=x_i}.$$

We multiply by $(1 - x_i)w_i$, where $\{w_i\}_{i=0\dots N}$ are the Legendre–Gauss weights, and sum over i to obtain

$$\begin{aligned} \sum_{i=0}^N (1 - x_i) \left(U_N^{J+1}(x_i) \right)^2 w_i &= \sum_{i=0}^N (1 - x_i) \left(U_N^J(x_i) \right)^2 w_i - 2\Delta t \sum_{i=0}^N (1 - x_i) U_N^J(x_i) w_i \frac{\partial U_N^J}{\partial x} \Big|_{x=x_i} \\ &+ \Delta t^2 \sum_{i=0}^N \left(\frac{\partial U_N^J}{\partial x} \Big|_{x=x_i} \right)^2 (1 - x_i) w_i. \end{aligned}$$

For stability we require that a certain discrete energy of U_N^J be bounded in time:

$$\sum_{i=0}^N (1 - x_i) \left(U_N^{J+1}(x_i) \right)^2 w_i \leq \sum_{i=0}^N (1 - x_i) \left(U_N^J(x_i) \right)^2 w_i, \quad (4.174)$$

which means that

$$\Delta t^2 \sum_{i=0}^N \left(\frac{\partial U_N^J}{\partial x} \Big|_{x=x_i} \right)^2 (1 - x_i) w_i - 2\Delta t \sum_{i=0}^N (1 - x_i) U_N^J(x_i) w_i \frac{\partial U_N^J}{\partial x} \Big|_{x=x_i} \leq 0.$$

With the exactness of the Legendre–Gauss quadrature rule for polynomials of degree lower than $2N+1$, we have

$$\sum_{i=0}^N \left(\frac{\partial U_N^J}{\partial x} \Big|_{x=x_i} \right)^2 (1 - x_i) w_i = \int_{-1}^1 \left(\frac{\partial U_N^J}{\partial x} \right)^2 (1 - x) dx,$$

and, with an additional integration by parts,

$$\sum_{i=0}^N (1 - x_i) U_N^J(x_i) w_i \frac{\partial U_N^J}{\partial x} \Big|_{x=x_i} = \int_{-1}^1 (1 - x) U_N^J \frac{\partial U_N^J}{\partial x} dx = \frac{1}{2} \int_{-1}^1 (U_N^J(x))^2 dx.$$

The stability condition obtained from energy analysis translates into an upper bound for the timestep, which can be seen as an accurate estimate of the CFL restriction on the timestep:

$$\Delta t \leq \frac{\int_{-1}^1 (U_N^J(x))^2 dx}{\int_{-1}^1 \left(\frac{\partial U_N^J}{\partial x} \right)^2 (1 - x) dx} \simeq \mathcal{O} \left(\frac{1}{N^2} \right). \quad (4.175)$$

Strong stability-preserving methods

The above fully-discrete analysis must, in principle, be performed for every time-marching scheme. Therefore, it is very convenient to have a way of extending the results from the first-order Euler method to higher-order methods. *Strong stability-preserving* Runge–Kutta and multistep methods preserve these kinds of stability properties, including those following from nonlinear stability analysis. A general review of the subject has been done by Shu [431], and we list some results here.

If we consider the general time ODE:

$$\frac{dU_N}{dt} = L_N U_N, \quad (4.176)$$

arising from the spatial discretization of the PDE (4.115), we suppose that, after discretization in time using the first-order forward Euler scheme, the strong stability requirement $\|U_N^{J+1}\| \leq \|U_N^J\|$ gives a CFL restriction of the type (4.175)

$$\Delta t \leq \Delta t_{FE}. \quad (4.177)$$

We can then write an s -stage Runge–Kutta method in the form

$$\begin{aligned} U_N^{(0)} &= U_N^J, \\ U_N^{(i)} &= \sum_{k=0}^{i-1} \left(\alpha_{i,k} + \Delta t \beta_{i,k} L_N U_N^{(k)} \right), \quad i = 1, \dots, s, \\ U_N^{J+1} &= U_N^{(s)}, \end{aligned}$$

and see that, as long as $\alpha_{i,k} \geq 0$ and $\beta_{i,k} \geq 0$, all of the intermediate stages are simply convex combinations of forward Euler operators. If this method is strongly stable for L_N , under the condition (4.177), then the intermediate stages can be bounded and the Runge–Kutta scheme is stable under the CFL condition

$$\Delta t \leq c \Delta t_{FE}, \quad c = \min_{i,k} \frac{\alpha_{i,k}}{\beta_{i,k}}. \quad (4.178)$$

In the same manner, one can devise strong stability-preserving explicit multistep methods of the form

$$U_N^{J+1} = \sum_{i=1}^s \left(\alpha_i U_N^{J+1-i} + \Delta t \beta_i L_N U_N^{J+1-i} \right),$$

which can also be cast into convex combinations of forward Euler steps and, therefore, these multistep methods are also stable, provided that

$$\Delta t \leq c \Delta t_{FE}, \quad c = \min_i \frac{\alpha_i}{\beta_i}. \quad (4.179)$$

Examples of useful coefficients for Runge–Kutta and multistep strong stability-preserving methods can be found in [431, 250]. The best of these methods are those for which the CFL coefficient c is as large as possible.

4.4.5 Going further: High-order time schemes

When using spectral methods in time-dependent problems, it is sometimes frustrating to have such accurate numerical techniques for the evaluation of spatial derivatives and the integration of elliptic PDEs, while the time derivatives and hyperbolic PDEs do not benefit from spectral convergence. Some tentative studies are being undertaken in order to represent the time interval by spectral methods as well [246]. In their spherically-symmetric study of the wave equation in Minkowski spacetime, Hennig and Ansorg have applied spectral methods to both spatial and time coordinates. Moreover, they have used a conformal compactification of Minkowski spacetime, making the wave equation singular at null infinity. They have obtained nicely accurate and spectrally convergent solutions, even to a nonlinear wave equation. If these techniques can be applied in general three-dimensional simulations, it would really be a great improvement.

Nevertheless, there are other, more sophisticated and accurate time-integration techniques that are currently being investigated for several stiff PDEs [270], including Korteweg–de Vries and nonlinear Schrödinger equations [280]. Many such PDEs share the properties of being stiff (very different time scales/characteristic frequencies) and combining low-order nonlinear terms with higher-order linear terms. Einstein’s evolution equations can also be written in such a way [73]. Let us consider a PDE

$$\frac{\partial u}{\partial t} = Lu + \mathcal{N}u, \quad (4.180)$$

using the notation of Section 4.4.1 and \mathcal{N} as a nonlinear spatial operator. Following the same notation and within spectral approximation, one recovers

$$\frac{\partial U_N}{\partial t} = L_N U_N + \mathcal{N}_N U_N. \quad (4.181)$$

We will now describe five methods of solving this type of ODE (see also [270]):

- **Implicit-explicit** techniques use an explicit multistep scheme to advance the nonlinear part \mathcal{N}_N , and an implicit one for the linear part.
- **Split-step** techniques are effective when the equation splits into two equations, which can be directly integrated (see [280] for examples with the nonlinear Schrödinger and Korteweg-de Vries equations).
- **Integrating factor** is a change of variable that allows for the exact solution of the linear part

$$V_N = e^{-L_N t} U_N, \quad (4.182)$$

and explicit multistep method for the integration of the new nonlinear part

$$\frac{\partial V_N}{\partial t} = e^{-L_N t} \mathcal{N}_N e^{L_N t} V_N. \quad (4.183)$$

- **Sliders** can be seen as an extension of the implicit-explicit method described above. In addition to splitting the problem into a linear and nonlinear part, the linear part itself is split into two or three regions (in Fourier space), depending on the wavenumber. Then, different numerical schemes are used for different groups of wavenumbers: implicit schemes for high wavenumbers and explicit high-order methods for low wavenumbers. This method is restricted to Fourier spectral techniques in space.

- **Exponential time-differencing** techniques have been known for some time in computational electrodynamics. These methods are similar to the integrating factor technique, but one considers the *exact* equation over one timestep

$$U_N^{J+1} = e^{L_N \Delta t} U_N^J + e^{L_N \Delta t} \int_0^{\Delta t} e^{-L_N \tau} \mathcal{N}_N(U_N(N\Delta t + \tau), N\Delta t + \tau) d\tau. \quad (4.184)$$

Various orders for these schemes come from the approximation order of the integral. For example Kassam and Trefethen [270] consider a fourth-order Runge–Kutta type approximation to this integral, where the difficulty comes from the accurate computation of functions, that suffer from cancellation errors.

4.5 Stationary Computations and Initial Data

4.5.1 Introduction

In this section, we restrict ourselves to problems in which time does not appear explicitly. This is especially the case for systems, that are stationary, like neutron stars in rotation or binary systems in circular orbits. The computation of initial data also falls into this class, given that it consists in finding a particular solution of Einstein's equations *at a given time* only. Indeed, when using the standard 3+1 decomposition of spacetime, the initial data that are passed to the evolution equations cannot be totally arbitrary and must satisfy a set of equations called Einstein's constraint equations. For more details of the initial data problem we refer to the review by Cook [127]. So, in treating the problems considered here, one may forget about the issues specific to time presented in Section 4.4.

It must be said that spectral methods are not the only technique that has been successfully used to generate stationary spacetimes. [52, 472, 128, 314] give some examples of this, especially in the case of binary systems, for neutron stars or black holes. More references can be found in [127].

4.5.2 Single compact stars

The computation of the structure of stationary compact stars dates back to 1939 with the famous solution of Tolman–Oppenheimer–Volkoff. During the last few years, the need for accurate models has become more pressing, especially with the coming online of gravitational wave detectors, which could help to probe the interior of such compact stars. Isolated stars in rotation are essentially axisymmetric, but some physical effects can induce a symmetry breaking that could lead to the emission of gravitational waves. In the following, we will review some computations that aim at including some of these effects, such as spontaneous symmetry breaking, the inclusion of magnetic fields, the effects of exotic dense matter (mainly with strange quarks) and the influence of an interior composed of two different superfluids.

Formalisms

The first computation of models of relativistic rotating stars in general relativity, by means of spectral methods, is presented in [67]. The equations are solved in spherical coordinates (see Section 4.3.2). Doing so, the fields only depend on the azimuthal angle θ and on the radius r . The fields are expanded in terms of spherical harmonics with respect to the angle and in Chebyshev polynomials with respect to r . The use of spherical harmonics is a natural way of dealing with the coordinate singularity on the z -axis. In [67] the whole space is divided into two spherical domains, the outer one extending up to infinity by making use of the compactification in $1/r$ seen in Section 4.3.1. With such a setting, Einstein's equations reduce to a set of four elliptic equations with sources extending up to infinity that are solved using a version of the algorithm based on matching with the homogeneous solutions (presented in Section 4.2.6) for each spherical harmonic. The system is complete once a description of the matter is given. The simplest choice is to consider a polytropic fluid, with or without a magnetic field. The system is solved by iteration.

In [67], a particular emphasis is put on various methods to measure the accuracy of the code. For nonrotating stars, the error is found to decrease exponentially, as the number of coefficients increases (see Figures 5 and 6 of [67]). However, for fast-rotating configurations, the error only decays as a power law (see Figure 7 of [67]). This comes from the fact that quantities like the energy density are

no longer C^∞ across the star's surface. Nevertheless, the results are in good agreement (to 0.1%) with those obtained by other numerical methods, as can be seen in [344].

Spectral convergence can be recovered by using surface-adapted coordinates as first done in [77]. A regular mapping of the numerical coordinates to the physical ones is introduced, so that the surface of the star lies at the boundary between two domains (see Section 4.3.1). For polytropes with $\gamma < 2$, this is sufficient to recover spectral convergence (see Figures 5 and 6 of [69]). However, for $\gamma > 2$, some quantities are still diverging at the surface but the convergence can be made closer and closer to the spectral one by analytically regularizing the density (see Section IV of [69]). Doing so, the error decreases as a power law, but the decrease can be made arbitrary fast at the cost of increasing the number of operations and so the computational time.

Up until 2006, neutron stars were computed using quasi-isotropic coordinates. However, in order to use these configurations as initial data for evolutionary codes, it may be useful to allow for other choices. Among the possible gauges, Dirac's is one of the most promising [73]. In [293] models of rotating neutron stars in the Dirac gauge are computed for both polytropic and realistic equations of state. Contrary to the quasi-isotropic coordinates, the use of this new gauge implies that one must solve one tensor-like Poisson equation. Configurations obtained with the two different formalisms are shown to be in very good agreement.

Rotating neutron star models

Even before adapted mappings were available, interesting results could be obtained. In [399, 400], models of rotating neutron stars with various equations of state have been computed. Among the most surprising findings is the existence of supra-massive stars. These stars do not connect to the nonrotating limit. Indeed, their high mass can only be supported by the presence of a centrifugal force. One of the remarkable features of such stars is the fact that they actually spin up when they lose angular momentum, contrary to what is observed for normal stars. This effect can also be seen for neutron stars containing hyperons and, thus, a softer equation of state [493]. Let us mention that, in this case, the stability analysis of the configurations required the great precision that spectral methods with adapted coordinates could provide.

It is known that isolated pulsars spin down due to magnetic braking. As the rotational frequency decreases, it is possible that the star will encounter a transition from one state of matter to another. Stationary rotating models have been used to determine the properties of such transitions [494, 495, 496]. A puzzling result is that the amount of energy released in a first-order phase transition does not depend on the orbital velocity of the star and is the same as for nonrotating ones. This is shown to be the case for both weak [495] and strong [496] first-order transitions.

Spontaneous symmetry breaking

It is known that stars can undergo spontaneous symmetry breaking when rotating fast enough. When such a phenomenon occurs, triaxial configurations are formed that are potential emitters of gravitational waves. The departure from axisymmetry is studied in two papers by the Meudon group [68, 70]. The idea of the method is to start from an axisymmetric neutron star configuration and to follow the growth or decay of triaxial instabilities. This work reaffirms well-established results from the Newtonian regime and presents the first results in general relativity for various equations of states. For a few of them, the frequency at which symmetry breaking occurs lies in the frequency band of the LIGO and Virgo detectors.

In 2002, this work was extended [207] by making use of surface-fitting coordinates. This enabled the authors to obtain results in the incompressible case by properly dealing with discontinuities lying at the surface of the star. Classical results in the incompressible case are, thus, recovered and it is found that the inclusion of relativity has only a moderate effect. Indeed, the critical ratio between the kinetic energy and the absolute gravitational energy $T/|W|$ at which the triaxial instability occurs is only 30% larger for relativistic stars, with respect to their classical counterparts.

If relativistic effects only slightly stabilize stars, the same is not true for differential rotation. Indeed, in [398], the authors study various rotation profiles and equations of state using the same technique as in [68, 70] to determine the onset of instability. It appears that the critical value of $T/|W|$ can be almost twice as high as for uniformly rotating stars.

Configurations with magnetic fields

Even if magnetic fields are strong in neutron stars, the structure of the object is not affected until it reaches huge values, on the order of at least 10^{10} T. In [64], models of rapidly-rotating stars with poloidal fields are constructed for various equations of state. The magnetic effects are taken into account consistently by solving the appropriate Maxwell equations, as well as by means of spectral methods. The maximum mass of highly-magnetized neutrons stars is found to be higher by 13-29 % than for nonmagnetized stars. The magnetic field induces an additional pressure, which can help to support more massive stars, thus explaining this increase.

The presence of a magnetic field can also lead to the deformation of a neutron star. Such deformation could lead to the formation of a triaxial configuration, which would then emit gravitational waves. In [77] the emitted signal is computed. Typically the system radiates at two frequencies: Ω and 2Ω where Ω is the angular velocity of the star.

In more recent work by the Meudon group [343], magnetized configurations have been computed using coordinates matched to the surface of the star, thus making the computation much more accurate. Gyromagnetic ratios of rapidly-rotating neutron stars of various equations of state are obtained. The limit of a ratio of $g = 2$ value for a charged black hole is never reached.

Strange stars

It is possible that the fundamental state of nuclear matter is not the ordinary matter but rather a plasma of deconfined quarks u , d and s , called *strange matter*. If this is the case, neutron stars should rather be called strange stars. The main difference between these two types of compact stars is that strange ones are somewhat smaller and thus more compact. In particular, they support higher rotation rates. There is a strong density jump at the surface of a strange star and surface-fitting coordinates are required in order to deal with it.

Fast rotating models of strange stars are computed in [217, 203]. Due to higher compactness, it is found that strange stars can rotate significantly faster than their neutron star counterparts. The attained $T/|W|$ can be twice as large. As in the neutron star case, supermassive configurations that spin up with angular momentum loss are found. The influence of strange matter on the emission of gravitational waves is studied in [205] where viscosity effects and triaxial instabilities are carefully taken into account.

It is believed that millisecond pulsars have been spun up by accreting matter from a companion. However, the details of this mechanism depend on the nature of the compact object. In [492], the

differences between accretion onto a neutron star and onto a strange star are investigated, using 2D stationary models computed by spectral methods.

Quasiperiodic oscillations

Quasiperiodic oscillations (QPOs) are observed in the kHz regime and are believed to be the signature of matter falling into a compact object. In the standard picture, the frequency of the QPOs is that of the last stable orbit around the compact object. Let us mention that the presence of a last stable orbit around an extended body is not an effect of relativity but can also be seen in the Newtonian regime, as shown in [497].

The precise structure of the accreting object has a great influence on the QPO. In a series of papers [490, 204, 16, 58], comparisons are made between observations and various compact star models that could account for QPOs.

Using a multidomain approach, strange stars with a crust can also be computed [491], one domain describing the interior of the star and another the crust. It is shown that the presence of the crust could change the value of the QPO by up to 20%.

More complex configurations

In this section, objects in more exotic configurations are presented. This is an illustration of both the complexity of neutron stars physics and the ability of spectral methods to deal with complicated systems.

The observation of glitches in isolated pulsars is consistent with the presence of a superfluid interior. The simplest model considers two fluids, one composed of neutrons and the other of protons and electrons, both components being superfluids. However, these two components could have different velocities, in particular different rotation rates. Such configurations are computed in [379]. A multidomain setting is crucial to be able to follow the two different fluids because the components do not have the same shape. Among the various results obtained, let us mention the confirmation of the existence of prolate-oblate configurations.

Neutron stars are usually assumed to be at zero temperature. However, this approximation is known to no longer be true for newborn neutron stars just after the supernova. Models of newborn neutron stars in uniform rotations are constructed in [224] using an extension of the code developed in [67]. Various hypothesis about the interior (different lepton numbers, isothermal versus isentropic) are considered. Sequences of fixed baryon mass and angular momentum are constructed. Such sequences approximate the evolution of the protoneutron star into a cold neutron star. The results have been extended to differentially-rotating protoneutron stars in [225].

The effect of finite temperature is also investigated in [476]. The authors found that newborn neutron stars are unlikely to undergo bar mode instability, but that the secular ones could take place and result in a significant emission of gravitational waves. Another interesting result of [476] is the existence of toroidal-like configurations, which appear for a broad range of parameters and before the mass-shedding limit. In such cases, the surface of the star is highly deformed and surface-fitting coordinates are required.

Axisymmetric rotating neutron stars have also been computed by a code developed by Ansong et al. [29, 30]. This code is based on Lewis–Papapetrou coordinates (ρ, ξ) , which are closely related to the usual cylindrical coordinates. Typically, space is decomposed into two domains: one

for the interior of the star and another for the exterior, which extends up to spatial infinity. Compactification of space and surface-fitting mappings are used. Both variables are expanded in terms of Chebyshev polynomials. Instead of solving the equations harmonic by harmonic and then iterating, as is done by the Meudon group, the equations are written with a collocation method (see Section 4.2.5) and solved as one single system. The price to pay is that the size of the system is somewhat larger (i.e. in m^2 , m being the total number of coefficients for each coordinate). The system is solved by means of the Newton–Raphson method. At each step, the linear system is solved using iterative techniques with preconditioning. With this method, impressive accuracy is reached.

The coordinates used in [29, 30] are more general than the ones used by the Meudon group, especially with respect to their surface-fitting capabilities. They can account for more complicated configurations and, in particular, highly-distorted matter distribution can be obtained. This is shown in [32, 31], where relativistic axisymmetric toroidal configurations of matter, known as the Dyson rings, are computed. Such rings are obtained up to the mass-shedding limit. Transition to the limit of an extreme Kerr black hole is also discussed.

4.5.3 Single black holes

Compared to the compact star case, single black holes have not been studied very much. This is probably because the structure of a stationary black hole is somewhat simpler than the one of a compact star. However, as will be seen, there are still properties that must be investigated.

Spacetimes containing a single black hole constitute a good benchmark for numerical methods, a lot of results being known analytically. In [279], the authors have implemented a spectral solver and applied it to various test problems. The solver itself is two dimensional and thus applicable only to axisymmetric systems. There is a single domain that consists of the whole space outside a sphere of given radius (i.e. the black hole). Space is compactified by using the standard variable $1/r$. The two physical variables (r, θ) are mapped onto squares in \mathbb{R}^2 and then expanded in terms of Chebyshev polynomials. The equations are written using a 2D collocation method (see Section 4.2.5) and the resulting system is solved by an iterative algorithm (here Richardson’s method with preconditioning). This solver is applied to solve Einstein’s constraint equations for three different systems: i) a single black hole ii) a single black hole with angular momentum iii) a black hole plus Brill waves. In all three cases, spectral convergence is achieved and accuracy on the order of 10^{-10} is reached with 30 points in each dimension.

A black hole is somewhat simpler than a neutron star, in the sense that there is no need for a description of matter (no equation of state, for instance). However, in some formalisms, the presence of a black hole is enforced by imposing a nontrivial solution on a surface (typically a sphere). The basic idea is to demand that the surface be a trapped surface. Such surfaces are known to lie inside event horizons and so are consistent with the presence of a black hole. Discussions about such boundary conditions can be found in [129]. However, in nonstationary cases, the set of equations to be used is not easy to derive. The authors of [265] implement various sets of boundary conditions to investigate their properties. Two different and independent spectral codes are used. Both codes are very close to those used in the case of neutron stars, one of them based on LORENE library [216] (see Section 4.5.2) and the other one developed by Ansorg and sharing a lot a features with [29, 30]. Such numerical tools have proved useful in clarifying the properties of some sets of boundary conditions that could be imposed on black hole horizons.

The reverse problem is also important in the context of numerical relativity. In some cases one needs to know if a given configuration contains a trapped surface and if it can be located at each

timestep. Several algorithms have been proposed in the past to find the locus at which the expansion of the outgoing light rays vanishes (thus defining the trapped surface). Even if the term is not used explicitly, the first application of spectral expansions to this problem is detailed in [51]. The various fields are expanded in a basis of symmetric trace-free tensors. The algorithm is applied to spacetimes containing one or two black holes. However, results seem to indicate that high order expansions are required to locate horizons with a sufficient precision.

More recently, another code [294] using spectral methods has been used to locate apparent horizons. It is based on the LORENE library with its standard setting, i.e. a multidomain decomposition of space and spherical coordinates (see Section 4.5.2 for more details). The horizon finder has been successfully tested on known configurations, like Kerr–Schild black holes. The use of spectral methods makes it both fast and accurate. Even if the code uses only one set of spherical coordinates (hence its presentation in this section), it can be applied to situations with more than one black hole, like the well-known Brill–Lindquist data [91].

4.5.4 Rings around black holes

The problem of uniformly rotating rings surrounding a black hole can be viewed as an intermediate step between one-body axisymmetric configurations and the two body problem. Indeed, even if one has to deal with two components, the problem is still axisymmetric. In [34], configurations of a black hole surrounded by a uniformly rotating ring of matter are computed in general relativity. The matter is assumed to be a perfect fluid. To solve the equations, space is divided into five computational domains. One of them describes the ring itself, another one the region around the black hole and another extends up to infinity. The two other domains are used to connect those regions. One of the difficulties is that the surface of the ring is not known a priori and so the domains must be dynamically adapted to its surface. Cylindrical-type coordinates are used and, in each domain, are mapped onto squares of numerical coordinates. The actual mappings depend on the domain and can be found in Section IV of [34].

Numerical coordinates are expanded in terms of Chebyshev polynomials. The system to be solved is obtained by writing Einstein’s equations in collocation space including regularity conditions on the axis and appropriate boundary conditions on both the horizon of the black hole and at spatial infinity. As in [29, 30], the system is solved iteratively, using the Newton–Raphson method.

Both the Newtonian and relativistic configurations are computed. The ratio between the mass of the black hole and the mass of the ring is varied from zero (no black hole) to 144. The inner mass shedding of the ring can be obtained. One of the most interesting results is the existence of configurations for which the ratio J_c/M_c^2 of the black hole angular momentum and the square of its mass exceeds one, contrary to what can be achieved for an isolated black hole.

4.5.5 Compact star binaries

Formalism

Systems consisting of two compact objects are known to emit gravitational waves. Due to this emission, no closed orbits can exist and the objects follow a spiral-like trajectory. This implies that such systems have no symmetries that can be taken into account and full time evolutions should be made. However, when the objects are relatively far apart, the emission of gravitational waves is small and the inspiral slow. In this regime, one can hope to approximate the real trajectory with a sequence of closed orbits.

Moreover, the emission of gravitational waves is known to efficiently circularize eccentric orbits so that only circular orbits are usually considered.

So, a lot of effort has been devoted to the computation of circular orbits in general relativity. This can be done by demanding that the system admit a helical Killing vector $\partial_t + \Omega\partial_\varphi$, Ω being the orbital angular velocity of the system. Roughly speaking, this means that advancing in time is equivalent to turning the system around its axis. Working in the corotating frame, one is left with a time-independent problem.

Additional approximations must be made in order to avoid any diverging quantities. Indeed, when using helical symmetry, the system has an infinite lifetime and can fill the whole space with gravitational waves, thus causing quantities like the total mass to be infinite. To deal with that, various techniques can be used, the simplest one consisting of preventing the appearance of any gravitational waves. This is usually done by demanding that the *spatial metric* be conformally flat. This is not a choice of coordinates but a true approximation that has a priori no reason to be verified. Indeed, even for a single rotating black hole, one can not find coordinates in which the spatial three-metric is conformally flat, so that we do not expect it to be the case for binary systems. However, comparisons with post-Newtonian results or non-conformally-flat results tend to indicate that this approximation is relatively good.

Under these assumptions, Einstein's equations reduce to a set of five elliptic equations for the lapse, the conformal factor and the shift vector. These equations encompass both the Hamiltonian and momentum constraint equations and the trace of the evolution equations. To close the system, one must provide a description of the matter. It is commonly admitted that the fluid is irrotational, the viscosity in neutron stars being too small to synchronize the motion of the fluid with the orbital motion. It follows that the motion of the fluid is described by an additional elliptic equation for the potential of the flow. The matter terms entering the equations via the stress-energy tensor can then be computed, once an equation of state is given. An evolutionary sequence can be obtained by varying the separation between the stars.

Numerical procedure

Up to now, only the Meudon group has solved these equations by means of spectral methods in the case of two neutron stars. Two sets of domains are used, one centered on each star. Each set consists of sphere-like domains that match the surface of the star and extend up to infinity. Functions are expanded in terms of spherical harmonics with respect to the angles (θ, φ) and Chebyshev polynomials with respect to the radial coordinates. Each Poisson equation $\Delta N = S_N$ is split into two parts $\Delta N_1 = S_{N_1}$ and $\Delta N_2 = S_{N_2}$, such that $S_N = S_{N_1} + S_{N_2}$ and $N = N_1 + N_2$. The splitting is, of course, not unique and only requires that S_{N_i} be mainly centered around star i so that it is well described by spherical coordinates around it. The equation labeled i is then solved using domains centered on the appropriate star. The splittings used for the various equations can be found explicitly in Section IV-C of [218].

The elliptic equations are solved using the standard approach by the Meudon group found in [228]. For each spherical harmonic, the equation is solved using the tau method and the matching between the various domains is made using the homogeneous solutions method (see Section 4.2.6). The whole system of equations is solved by iteration and most of the computational time is spent when quantities are passed from one set of domains to the other by means of a spectral summation (this requires N^6 operations, N being the number of collocation points in one dimension). A complete and precise description of the overall procedure can be found in [218].

Neutron star binaries

The first sequence of irrotational neutron star binaries computed by spectral means is shown in [72]. Both stars are assumed to be polytropes with an index $\gamma = 2$. The results are in good agreement with those obtained simultaneously by other groups with other numerical techniques (see, for instance, [52, 472]). One of the important points that has been clarified by [72] concerns the evolution of the central density of the stars. Indeed, at the end of the 1990s, there was a claim that both stars could individually collapse to black holes before coalescence, due to the increase of central density as the two objects spiral towards each other. Should that have been true, this would have had a great impact on the emitted gravitational wave signal. However, it turned out that this came from a mistake in the computation of one of the matter terms. The correct behavior, confirmed by various groups and in particular by [72], is a decrease in central density as the stars get closer and closer (see Figure I of [72]).

If the first sequence computed by spectral methods is shown in [72], the complete description and validation of the method are given in [218]. Convergence of the results with respect to the number of collocation points is exhibited. Global quantities like the total energy or angular momentum are plotted as a function of the separation and show remarkable agreement with results coming from analytical methods (see Figures 8–15 of [218]). Relativistic configurations are also shown to converge to their Newtonian counterparts when the compactness of the stars is small (see Figures 16–20 of [218]).

Newtonian configurations of compact stars with various equations of state are computed for both equal masses [449] and various mass ratios [454]. One of the main results of the computations concerns the nature of the end point of the sequence. For equal masses, the sequence ends at contact for synchronized binaries and at mass shedding for irrotational configurations. This is to be contrasted with the non-equal-mass case, in which the sequence always ends at the mass shedding limit of the smallest object.

Properties of the sequences in the relativistic regime are discussed in [455, 456]. In [455] sequences with $\gamma = 2$ are computed for various compactness and mass ratios for both synchronized and irrotational binaries. The nature of the end point of the sequences is discussed and similar behavior to the Newtonian regime is observed. The existence of a configuration of maximum binding energy is also discussed. Such existence could have observational implications because it could be an indication of the onset of a dynamic instability. Sequences of polytropes with various indexes ranging from 1.8 to 2.2 are discussed in [456]. In particular, the authors are lead to conjecture that, if a configuration of maximum binding energy is observed in the Newtonian regime, it will also be observed in conformal relativity for the same set of parameters.

In [169] the authors derive from the sequences computed in [455] a method to constrain the compactness of the stars from the observations. Indeed, from the results in [455] one can easily determine the energy emitted in gravitational waves per interval of frequency (i.e. the power spectrum of the signal). For large separation, that is, for small frequencies, the curves follow the Newtonian. However, there is a break frequency at the higher end (see Figure 2 of [169]). The location of this frequency depends mainly on the compactness of the stars. More precisely, the more compact the stars are, the higher the break frequency is. Should such frequency be observed by the gravitational wave detectors, this could help to put constraints on the compactness of the neutron stars and, thus, on the equation of state of such objects.

Extensions

The framework of [218] is applied to more realistic neutron stars in [57]. In this work, the equations of state are more realistic than simple polytropes. Indeed, three different equations are considered for the interior, all based on different microscopic models. The crust is also modeled. For all the models, the end point of the evolution seems to be given by the mass shedding limit. However, the frequency at which the shedding occurs depends rather strongly on the EOS. The results are in good agreement with post-Newtonian ones, until hydrodynamic effects begin to be dominant. This occurs at frequencies in the range of 500–1000 Hz, depending on the EOS.

Sequences of strange star binaries have also been computed [292]. Contrary to the neutron star case, matter density does not vanish at the surface of the stars and one really needs to use surface-fitting domains to avoid any Gibbs phenomenon that would spoil the convergence of the overall procedure. Sequences are computed for both synchronized and irrotational binaries and a configuration of maximum binding energy is attained in both cases. This is not surprising: strange stars are more compact than neutron stars and are less likely to be tidally destroyed before reaching the extremum of energy, making it easier to attain dynamic instability. More detailed results on both neutron star and strange star binaries are discussed in [206, 208].

All the work presented above was done in the conformal flatness approximation. As already stated in Section 4.5.5, this is only an approximation and one expects that the true conformal three-metric will depart from flatness. However, in order to maintain asymptotic flatness of spacetime, one needs to get rid of the gravitational wave content. One such waveless approximation is presented in [423] and implemented in [471]. Two independent codes are used, one of them being an extension of the work described in [218]. The number of equations to be solved is then greater than in conformal flatness (one has to solve for the conformal metric), but the algorithms are essentially the same. It turns out that the deviation from conformal flatness is rather small. The new configurations are slightly further from post-Newtonian results than the conformally-flat ones, which is rather counter-intuitive and might be linked to a difference in the definition of the waveless approximations.

4.5.6 Black-hole–binary systems

Digging the holes

Though the computation of black hole binaries in circular orbit has a lot of common features with the neutron star case, there are also some differences that need to be addressed. In at least one aspect, black holes are much simpler objects because they are a solution of Einstein’s equations without matter. So the whole issue of investigating various equations of state is irrelevant and there is no need to solve any equation for the matter. However, there is a price to pay and one must find a way to impose the presence of black holes in the spacetime. Two ideas have been proposed.

In the *puncture method*, the full spacetime contains three asymptotically-flat regions. One is located at $r = \infty$ and the other two at two points, $M1$ and $M2$, which are called the punctures. The presence of flat regions near the punctures is enforced by demanding that some quantities, like the conformal factor, diverge at those points (typically as $1/r$). The discontinuities are taken out analytically and the equations are solved numerically for the regular parts in the whole space. This idea dates back to the work of Brill and Lindquist [91], at least in the case of black holes initially at rest. The puncture approach has been successfully applied to the computation of quasicircular orbits by means of spectral methods in [33].

The *apparent horizon method* relies on initial works by Misner [319] and Lindquist [300]. In this case, the space has only two asymptotically-flat regions. One can show that this is equivalent to solving Einstein's equations outside two spheres on which boundary conditions must be imposed. The boundary conditions are based on the concept of trapped surfaces and apparent horizons. The physical state of the black holes are precisely encoded in the boundary conditions.

First configurations

The first configurations of black hole binaries computed by means of spectral methods can be found in [229]. The formalism and various hypotheses are given in the companion paper [219]. The assumptions are very similar to those used for neutron star binaries (see Section 4.5.5). Helical symmetry is enforced and conformal flatness assumed. The holes are described by the apparent horizon technique. However, the boundary conditions used have been shown to be only approximately valid, up to a rather good accuracy. This effect is discussed in the original paper [229] and further explored by Cook in [129]. The numerical techniques are very similar to the ones employed for neutron-star-binary configurations (see Section 4.5.5). Two sets of spherical domains are used, one for each black hole. Boundary conditions are imposed on the surface between the nucleus and the first shell. Both sets extend up to infinity using a compactification in $1/r$.

For the first time, good agreement was found between numerical results and post-Newtonian ones. A detailed comparison can be found in [142]. In particular, the location of the energy minimum is shown to coincide to within a few percent. This improvement with respect to previous numerical work is mainly due to a difference in the physical hypothesis (i.e. the use of helical symmetry). One important product of [229] is the use of a new criterion to determine the appropriate value of the orbital angular velocity Ω . Indeed, for neutron stars, this is done by demanding that the fluid of both stars be in equilibrium [218]. This, of course, is not applicable for black holes. Instead, in [219, 229] it is proposed that one find Ω by demanding that the ADM mass and the Komar-like mass coincide. Without going into too much detail, this amounts to demanding that, far from the binary and at first order in $1/r$, the metric behave like the Schwarzschild. It is shown in [219] that it can be linked to a relativistic virial theorem. Since then it has been shown that this criterion can also be used for neutron stars [456] and that it is equivalent to the use of a variational principle called *the effective potential method* [128, 50, 359, 113], where the binding energy is minimized with respect to Ω .

Further investigation

More recently, two other spectral codes have been developed in the context of black hole binaries and successfully applied to address some of the issues raised by the work of [219, 229].

One of these codes comes from the Caltech/Cornell group of Pfeiffer et al. and is described extensively in [361, 357]. The code is multidomain and two main types of domains are used i) square domains in which each Cartesian-like coordinate is expanded in terms of Chebyshev polynomials and ii) spherical domains in which spherical harmonics are used for the angles (θ, φ) and Chebyshev polynomials for the radial coordinate. Space can be compactified by standard use of the variable $1/r$. The two types of domains can be set up in various manners to accommodate the desired geometry. When using both square and spherical domains, there are regions of space that belong to more than one domain. This is to be contrasted with work by the Meudon group in which different domains are only touching but not overlapping. The algorithm of [361] solves differential equations by using a multidimensional collocation method. The size of the resulting system is roughly equal to the

number of collocation points. It is then solved iteratively via a Newton–Raphson algorithm with a line search. At each step of the Newton–Raphson method, the linear system is solved by means of an iterative scheme (typically GMRES). This inner iterative solver requires careful preconditioning to work properly. Various tests are passed by the code in [361], in which elliptic equations and systems are solved in either spherical or bispherical topologies. In the cases presented, the error decays spectrally.

In [360] the code is used to investigate different ways of solving the constraint equations. Three different decompositions are used: the conformal TT one, the physical TT one and the thin-sandwich decomposition. When solving for the constraint equations only, one must also choose some *freely specifiable* variables, which describe the physical state of the system. In [360], these specifiable variables are fixed using a superposition of two Kerr–Schild black holes. The net result of [360] is that global quantities, like the total energy, are very sensitive to the choice of decomposition. The variation of total energy can be as large as 5%, which is the order of the energy released by gravitational waves. It is also shown that the choice of extrinsic curvature tensor is more crucial than the one of conformal metric, in accordance with an underlying result of [229]. Let us point that the equations derived from the helical Killing vector approach in [219, 229] are equivalent to the ones obtained by making use of the thin-sandwich decomposition of the constraints. The freely specifiable variables are obtained by both the imposition of the helical Killing symmetry and by solving an additional equation for the lapse function (resulting in the *extended thin-sandwich* formalism).

In [133] the boundary conditions based on the apparent horizon formalism [129] are implemented and tested numerically in the case of one and two black holes. In the latter case, the main difference from [229] lies in the use of more elaborate and better boundary conditions on the horizons of the black holes. By allowing for a nonvanishing lapse on the horizons, the authors of [133] solve the constraint equations exactly. This is to be contrasted with [229], where the momentum constraint equation is only solved up to a small correction. Both results show rather good agreement. This is not surprising as the correction used by the Meudon group was known to be small (see Figures 10 and 11 of [229]). More results are presented in [113], for both corotating and irrotational black holes. An important result of [113] is the comparison of the two criteria for determining the orbital angular velocity Ω . They indeed show that the *effective potential method* first introduced in [128] and the method based on the virial theorem proposed in [219] are in very good agreement.

By slightly extending the boundary conditions used in [113], the authors of [363] propose to reduce the eccentricity of the black-hole–binary configurations. This is done by giving the black holes a small radial velocity by modifying the boundary condition on the shift vector. The code and other equations are the same as in [113]. Time evolution of the obtained initial data does show that this technique can reduce the eccentricity of the binary. However, the effect on the emitted gravitational wave is small and probably unimportant.

Another application of the Caltech/Cornell solver can be found in [305], where the emphasis is put on nearly maximum spinning black holes. Initial data are constructed for both single black holes and binaries. Three families of initial data are investigated. Using a formalism based on the Kerr–Schild spacetime, the authors are able to reach spins as large as $a = 0.9998$. Such nearly-maximum spinning black holes may be relevant from the astrophysical point of view. Evolutions of these data are also discussed there.

The other spectral code used to compute configurations of black hole binaries comes from An-sorg [27]. It shares a lot of features with the code developed by the same author in the context of rotating stars [29, 30] already discussed in Section 4.5.2. Space is decomposed into two domains. One of them lies just outside the horizons of the black holes and bispherical-like coordinates are used.

The other domain extends up to infinity and an appropriate mapping is used in order to avoid the singularity of the bispherical coordinates at spatial infinity (see Section IV of [27]). The angle of the bispherical coordinates (i.e. the angle around the x-axis joining the two black holes) is expanded in terms of a Fourier series and the two other coordinates in terms of Chebyshev polynomials. As in [34, 361], the partial differential equations are solved using a collocation method and the resulting system is solved by the Newton–Raphson method. Once again the linear system coming from the Jacobian is solved by an iterative scheme with preconditioning. The code is used to compute essentially the same configuration as those shown in [113]. An interesting point of [27] is the detailed investigation of the convergence of the results with increased resolution. As can be seen in Figure 4 of [27], the error initially decreases exponentially, but, for high number of points, it seems that the error follows only a power law. This is an indication that some non- \mathcal{C}^∞ fields must be present. It is conjectured in [27] that this comes from logarithm terms that cannot be dealt with properly with a compactification in $1/r$. The same kind of effect is investigated in some detail in [228], where some criteria for the appearance of such terms are discussed.

A code very similar to the one used in [27] has also been used to compute spacetimes with black holes using the puncture approach [33]. Given that the black holes are no longer described by their horizons, one does not need to impose inner boundary conditions. The absence of this requirement enables the author of [33] to use a single domain to describe the whole space, from the puncture up to infinity. The other features of the spectral solver are the same as in [27]. This method has been successfully applied to the computation of black-hole–binary configurations in the puncture framework. The authors have, in particular, investigated high mass ratios between the bodies and compared their results with the ones given in the test-mass limit around a Schwarzschild black hole. The discrepancy is found to be on the order of 50% for the total energy. It is believed that this comes from the fact that the mass of each puncture cannot be directly related to the local black hole mass (see discussion in Section VII of [33]).

Finally, let us mention that the algorithms developed by Ansorg in [29, 30, 33, 27] have all been unified in [28] to accommodate any type of binaries. Various domain decompositions are exhibited that can be used to represent neutron stars, excised black holes or puncture black holes, with the compactification of space. The algorithms are shown to be applicable to limiting cases such as large mass ratios.

4.5.7 Black-hole–neutron-star binaries

Until recently binaries consisting of a neutron star and a black hole received fewer attention than other types of systems. It was believed, and this was partially true, that this case could easily be handled once the cases of neutron star and black hole binaries were understood. However, such binaries are of evident observational interest and could be the most promising source of gravitational waves for ground-based detectors [59].

The first application of spectral methods to black-hole–neutron-star binaries can be found in [450]. The main approximation is to consider that the black hole is not influenced by the neutron star. Technically, this means that Einstein’s equations are split into two parts (i.e. as for neutron star binaries 4.5.5). However, the part of the fields associated with the black hole is fixed to its analytical value. As the fields are not solved for the black-hole part, the results should depend on the actual splitting, the equations being nonlinear. The part of the fields associated with the neutron star are solved using the standard setting for the Meudon group. Of course, this whole procedure is only valid if the black hole is much more massive than the neutron star and this is why [450] is limited to mass

ratios of 10. In this particular case, it is shown that the results depend, to the level of a few percent, on the choice of splitting, which is a measure of the reached accuracy. It is also shown that the state of rotation of the star (i.e. synchronized or irrotational) has little influence on the results.

In [451] the equations of the extended thin-sandwich formulation are solved consistently. As for the neutron-star–binary case, two sets of spherical coordinates are used, one centered around each object. The freely specifiable variables are derived from the Kerr–Schild approach. Configurations are obtained with a moderate mass ratio of five. However, the agreement with post-Newtonian results is not very good and the data seem to be rather noisy (especially the deformation of the star).

Quasiequilibrium configurations based on a helical Killing vector and conformal flatness have been obtained independently by [226] and [452]. Both codes are based on the LORENE library [216] and use two sets of spherical coordinates. They differ mainly in their choice of boundary conditions for the black hole. However, it is shown in the erratum of [226] that the results match pretty well and are in very good agreement with post-Newtonian results. Mass ratios ranging from 1 to 10 are obtained in [452] and the emitted energy spectra are estimated. The work of [452] has been extended in [453], where the parameter space of the binary is extensively explored. In particular, the authors determine whether the end point of the sequences is due to an instability or to the mass-shedding limit. It turns out that the star is more likely to reach the mass-shedding limit if it is less compact and if the mass ratio between the black hole and the star is important, as expected.

More recently, the Caltech/Cornell group has applied the spectral solver of [361, 357] in order to compute black-hole–neutron-star configurations [183]. Some extensions have been made to enable the code to deal with matter by making use of surface-fitting coordinates. Thanks to the domain decomposition used (analogous to the one of [361, 357]), the authors of [183] can reach an estimated accuracy 5×10^{-5} , which is better than the precision of previous works (by roughly an order of magnitude). Configurations with one spinning black hole and configurations with reduced eccentricity are also presented, along the lines of [363].

4.5.8 Spacetimes with waves

[362] presents a method to produce initial data configurations containing waves. Given a fixed background metric, it shows how to superimpose a given gravitational wave content. The equations are solved numerically using a multidomain spectral code based on [361, 357]. Space is covered by various sphere-like shells and is described up to infinity. When no black hole is present, the origin is covered by a square domain because regularity conditions at the origin, in spherical coordinates, are not handled by [361, 357]. Such a setting is used to generate spacetimes containing i) pure quadrupolar waves ii) flat space with an ingoing pulse and iii) a single black hole superimposed with an ingoing quadrupolar wave.

4.5.9 Hyperboloidal initial data

If the 3+1 decomposition is the most widely used for numerical relativity, some other possibilities have been proposed, with possibly better features. In particular, one can vary the foliation of spacetime to get *hyperboloidal data*. With such a setting, at infinity spacetime is foliated by light cones instead of spatial hypersurfaces, which makes the extraction of gravitational waves, in principle, easier.

In [185], Frauendiener is interested in generating hyperboloidal initial-data sets from data in physical space. The technique proceeds in two steps. First a nonlinear partial differential equation (the Yamabe equation) must be solved to determine the appropriate conformal factor ω . Then, the data

are constructed by dividing some quantities by this ω . This second step involves an additional difficulty: ω vanishes at infinity but the ratios are finite and smooth. It is demonstrated in [185] that spectral methods can deal with these two steps. Some symmetry is assumed so that the problem reduces to a two-dimensional one. The first variable is periodic and expanded in terms of a Fourier series, whereas Chebyshev polynomials are used for the other. The Yamabe equation is solved using an iterative scheme based on Richardson's iteration procedure. The construction of the fields, and hence the division by a field vanishing at infinity, is then handled by making use of the nonlocal nature of the spectral expansion (i.e. by working in the coefficient space; see Section 4 of [185] for more details).

4.6 Dynamic Evolution of Relativistic Systems

The modeling of time-dependent physical systems is traditionally the ultimate goal in numerical simulations. Within the field of numerical relativity, the need for studies of dynamic systems is even more pronounced because of the search for gravitational wave patterns. Unfortunately, as presented in Section 4.4.1, there is no efficient spectral time discretization yet and one normally uses finite-order time-differentiation schemes. Therefore, in order to get high temporal accuracy, one must use high-order explicit time-marching schemes (e.g., fourth or sixth-order Runge–Kutta [86]). This requires quite a lot of computational power and might explain why, except for gravitational collapse [211, 337], very few studies using spectral methods have dealt with dynamic situations until the Caltech/Cornell group began to use spectral methods in numerical relativity in the early part of this century [276, 277]. This group now has a very well-developed pseudospectral collocation code, “Spectral Einstein Code” (SpEC), for the solution of full three-dimensional dynamic Einstein equations.

In this section, we review the status of numerical simulations that use spectral methods in some fields of general relativity and relativistic astrophysics. Although we may give at the beginning of each section a very short introduction to the context of the relevant numerical simulations, our point is not to give detailed descriptions of them, as dedicated reviews exist for most of the themes presented here and the interested reader should consult them for details of the physics and comparisons with other numerical and analytic techniques. Among the systems that have been studied, one can find gravitational collapse [194] (supernova core collapse or collapse of a neutron star to a black hole), oscillations of relativistic stars [442, 282] and evolution of “vacuum” spacetimes. These include the cases of pure gravitational waves or scalar fields, evolving in the vicinity of a black hole or as (self-gravitating) perturbations of Minkowski flat spacetime. Finally, we will discuss the situation of compact binary [370, 62] spectral numerical simulations.

4.6.1 Single Stars

The numerical study of the evolution of stars in general relativity involves two parts: first, one must solve for the evolution of matter (relativistic hydrodynamics, see [176]), and second, one must compute the new configuration of the gravitational field. Whereas spectral-methods based codes are now able to study quite well the second part (see Section 4.6.2), the first has not benefited from the efforts of groups using spectral methods in the past decade. Thus, one faces a paradox: spectral methods have been primarily developed for the simulation of hydrodynamic systems (see Section 4.1.2), but they are not often used for relativistic hydrodynamics. This might be understood as a consequence of the general problem of spectral methods to deal with discontinuous fields and supersonic flows: the Gibbs phenomenon (see Section 4.2.4). Relativistic flows in astrophysics are often supersonic and therefore contain shocks. Although some techniques have been devised to deal with them in one-dimensional studies (see, e.g., [80]), there has been no convincing multidimensional convincing work. Another problem of multidimensional relativistic hydrodynamics that can spoil rapid convergence properties is sharp density profiles near neutron star surfaces. These can imply a diverging or discontinuous radial derivative of the density, thus slowing down the convergence of the spectral series.

Supernova core collapse

The physical scenario studied here is the formation of a neutron star from the gravitational collapse of a degenerate stellar core. This core can be thought of as the iron core of a massive star at the end

of its evolution (standard mechanism of type II supernova). The degeneracy pressure of the electrons can no longer support the gravity and the collapse occurs. When the central density reaches nuclear values, the strong interaction stiffens the equation of state, stopping the collapse in the central region and generating a strong shock. This mechanism has long been thought to be a powerful source of gravitational radiation, but recent simulations show that the efficiency is much lower than previously estimated [153, 423]. The first numerical study of this problem was the spherically-symmetric approach by May and White [315] using artificial viscosity to damp the spurious numerical oscillations caused by the presence of shock waves in the flow solution. Currently, state-of-the-art codes use more sophisticated High-Resolution Shock-Capturing (HRSC) schemes or High-Resolution Central (HRC) schemes (for details on these techniques, see the review by Font [176]). The first axisymmetric fully (general) relativistic simulations of the core collapse scenario were done by Shibata [416] and Shibata and Sekiguchi [423], which used HRSC schemes and a parametric equation of state. More recently, magnetohydrodynamic effects have been taken into account in the axisymmetric core collapse by Shibata et al. [420] using HRC schemes. Three-dimensional core collapse simulations, including a more realistic equation of state and deleptonization scheme have been performed within the CACTUS-CARPET-WHISKY [15, 41] framework by Ott et al. [352, 351]. These simulations have been compared with those of the CoCoNuT code (see [148, 151] and later in this section). A more detailed historical presentation can be found in the *Living Review* by Fryer and New [194].

The appearance of a strong hydrodynamic shock is, in principle, a serious problem to numerical models using spectral methods. Nevertheless, a first preliminary study in spherical symmetry and the Newtonian theory of gravity was undertaken in 1986 by Bonazzola and Marck [78], with the use of “natural” viscosity. The authors show a mass conservation to a level better than 10^{-4} using one domain with only 33 Chebyshev polynomials. In 1993, the same authors performed the first three-dimensional simulation (still in Newtonian theory) of the pre-bounce phase [81], giving a computation of the gravitational wave amplitude, which was shown to be lower than standard estimates. Moreover, they showed that for a given mass, the gravitational wave amplitude depends only on the deformation of the core. These three-dimensional simulations were made possible thanks to the use of spectral methods, particularly for the solution of the Poisson equation for the gravitational potential.

Thus, shock waves pose a problem to spectral codes and have either been smoothed with spectral vanishing viscosity [235] or ignored by the code stopping before their appearance. Another idea developed first between the Meudon and Valencia groups was to use more appropriate techniques for the simulation of shock waves: namely the High-Resolution Shock-Capturing techniques, also known as Godunov methods (see the *Living Reviews* by Martí and Müller [311] and by Font [176]). On the other hand, one wants to keep the fewest degrees of freedom required by spectral methods for an accurate-enough description of functions, in particular for the solution of elliptic equations or for the representation of more regular fields, such as gravitational ones. Indeed, even in the case where a hydrodynamic shock is present, since it only appears as a source for the metric in Einstein’s equations, the resulting gravitational field is at least C^1 and the spectral series do converge, although slower than in the smooth case. Moreover, in a multidomain approach, if the shock is contained within only one such domain, it is then necessary to increase resolution in only this particular domain and it is still possible to keep the overall number of coefficients lower than the number of points for the HRSC scheme. The combination of both types of methods (HRSC and spectral) was first achieved in 2000 by Novak and Ibáñez [342]. They studied a spherically-symmetric core collapse in tensor-scalar theory of gravity, which is a more general theory than general relativity and allows *a priori* for monopolar gravitational waves. The system of PDEs to be solved resembles that of general relativity, with the addition of a

scalar nonlinear wave equation for the monopolar dynamic degree of freedom. It was solved by spectral methods, whereas the relativistic hydrodynamics equations were solved by Godunov techniques. Two grids were used, associated to each numerical technique, and interpolations between the two were done at every timestep. Although strong shocks were present in this simulation, they were sharply resolved with HRSC techniques and the gravitational field represented through spectral methods did not exhibit any Gibbs-like oscillations. Monopolar gravitational waveforms could, thus, be given. In collaboration with the Garching relativistic hydrodynamics group, this numerical technique was extended in 2005 to three dimensions, but in the *conformally-flat approximation* of general relativity (see Sections 4.5.5 and 4.5.6) by Dimmelmeier et al. [151]. This approach using spectral methods for the gravitational field computation is now sometimes referred to as the “Marriage des Maillages” (French for “grid wedding”) and is currently employed by the core-collapse code CoCoNuT of Dimmelmeier et al. [148, 151] to study general relativistic simulations of protoneutron stars, with a microphysical equation of state as well as an approximate description of deleptonization [153].

Collapse to a black hole

Stellar collapse to a black hole has been widely studied, starting with spherically-symmetric computations; in the case of dust (matter with no pressure), an analytical solution by Oppenheimer and Snyder [349] was found in 1939. Pioneering numerical works by Nakamura and Sato [332, 333] studied the axisymmetric general relativistic collapse to a black hole; Stark and Piran [440] gave the gravitational wave emission from such a collapse in the formalism of Bardeen and Piran [47]. Fully general relativistic collapse simulations in axisymmetry have also been performed by Shibata [415], and the first three-dimensional calculations of gravitational-wave emission from the collapse of rotating stars to black holes was done by Baiotti et al. [41]. Recently, Stephens et al. [441] developed an evolution code for the coupled Einstein–Maxwell–MHD equations, with application to the collapse to a black hole of a magnetized, differentially-rotating neutron star.

To our knowledge, all studies of the collapse to a black hole, which use spectral methods are currently restricted to spherical symmetry. However, in this case and contrary to the core-collapse scenario, there is *a priori* no shock wave appearing in the evolution of the system and spectral methods are highly accurate at modeling the hydrodynamics as well. Thus, assuming spherical symmetry, the equations giving the gravitational field are very simple, first because of Birkhoff’s theorem, which gives the gravitational field outside the star, and then from the absence of any dynamic degree of freedom in the gravitational field. For example, when choosing the radial (Schwarzschild) gauge and polar slicing, Einstein’s equations, expressed within 3+1 formalism, turn into two first-order constraints, which are simply solved by integrating with respect to the radial coordinate (see [211]).

In the work of Gourgoulhon [211] a Chebyshev-tau method is used. The evolution equations for the relativistic fluid variables are integrated with a semi-implicit time scheme and a quasi-Lagrangian grid: the boundary of the grid is comoving with the surface of the star, but the grid points remain the usual Gauss–Lobatto collocation points (Section 4.2.3). Due to the singularity-avoiding gauge choice, the collapsing star ends in the “frozen-star” state, with the collapse of the lapse. This induces strong gradients on the metric potentials, but the code is able to follow the collapse down to very small values of the lapse, at less than 10^{-6} . The code is very accurate at determining whether a star at equilibrium is unstable, by triggering the physical instability from numerical noise at very low level. This property was later used by Gourgoulhon et al. [215] to study the stability of equilibrium configurations of neutron stars near the maximal mass, taking into account the effect of weak interaction processes. The addition of an inward velocity field to the initial equilibrium configurations enabled Gourgoulhon [212]

to partially answer the question of the minimal mass of black holes: can the effective mass-energy potential barrier associated with stable equilibrium states be penetrated by stars with substantial inward radial kinetic energy? In [212], Gourgoulhon was able to form a black hole with a starting neutron star that was 10% less massive than the usual maximal mass.

The spectral numerical code developed by Gourgoulhon [211] has been extended to also simulate the propagation of neutrinos, coming from the thermal effect and nonequilibrium weak interaction processes. With this tool, Gourgoulhon and Haensel [221] have simulated the neutrino bursts coming from the collapse of neutron stars, with different equations of state. Another modification of this spectral code has been done by Novak [337], extending the theory of gravity to tensor-scalar theories. This allowed for the simulation of monopolar gravitational waves coming from the spherically-symmetric collapse of a neutron star to a black hole [337]. From a technical point of view, the solution of a nonlinear wave equation on curved spacetime has been added to the numerical model. It uses an implicit second-order Crank–Nicolson scheme for the linear terms and an explicit scheme for the nonlinear part. In addition, as for the hydrodynamics, the wave equation is solved on a grid, partly comoving with the fluid. The evolution of the scalar field shows that the collapsing neutron star has “expelled” all of its scalar charge before the appearance of the black hole.

Relativistic stellar pulsations

Oscillations of relativistic stars are often studied as a time-independent, linear eigenvalue problem [282]. Nevertheless, numerical approaches via time evolutions have proved to bring interesting results, as obtained by Font et al. [181] for the first quasiradial mode frequencies of rapidly-rotating stars in full general relativity. Nonlinear evolution of the gravitational-radiation–driven instability in the r -modes of neutron stars has been studied by many authors (for a presentation of the physical problem, see Section 13 of [23]). In particular, the first study of nonlinear r -modes in rapidly-rotating relativistic stars, via three-dimensional general-relativistic hydrodynamic evolutions has been done by Stergioulas and Font [444]. Different approaches to numerical hydrodynamic simulations in Newtonian gravity have been attempted by Lindblom et al. [295], with an additional braking term, as by Villain and Bonazzola [478] (see the following).

Because of their very high accuracy, spectral methods are able to track dynamic instabilities in the evolution of equilibrium neutron star configurations, as shown in section 4.6.1 by the work of Gourgoulhon et al. [211, 215]. In this work, when the initial data represents a stable neutron star, some oscillations appear, which corresponds to the first fundamental mode of the star. As another illustration of the accuracy, let us mention the work of Novak [336], who followed the dynamic evolution of *unstable* neutron stars in the tensor-scalar theory of gravity. The instability is linked with the possibility for these stars of undergoing some “spontaneous scalarization”, meaning that they could gain a very high scalar charge, whereas the scalar field would be very weak (or even null) outside the star. Thus, for a given number of baryons, there would be three equilibria for a star: two stable ones with high scalar charges (opposite in sign) and an unstable one with a weak scalar charge. Starting from this last one, the evolution code described in [337] was able to follow the transition to a stable equilibrium, with several hundreds of damped oscillations for the star. This damping is due to the emission of monopolar gravitational waves, which carry away the star’s kinetic energy. The final state corresponds to the equilibrium configuration, independently computed by a simple code solving the generalized Tolman–Oppenheimer–Volkoff system with a scalar field, up to 1% error, after more than 50,000 timesteps. These studies could be undertaken with spectral methods because in these scenarios the flow remains subsonic and one does not expect any shock to be formed.

It is therefore quite natural to try and simulate stellar pulsations using spectral methods. Unfortunately, there have been only a few such studies, which are detailed in the following. Lockitch et al. [304] have studied the inertial modes of slowly-rotating stars in full general relativity. They wrote down perturbation equations in the form of a system of ordinary differential equations, thanks to a decomposition into vector and tensor spherical harmonics. This system is then a nonlinear eigenvalue problem for the dimensionless mode frequency in the rotating frame. Equilibrium and perturbation variables are then expanded in terms of a basis of Chebyshev polynomials, taking into account the coordinate singularity at the origin and parity requirements. The authors were therefore able to determine the values of the mode frequency, making the whole system singular and looked for eigenfunctions, through their spectral decomposition. They found that inertial modes were slightly stabilized by relativistic effects.

A different and maybe more natural approach, namely the time integration of the evolution equations, has been undertaken by Villain et al. [478, 477] with a spectral magnetohydrodynamics code in spherical coordinates. The code solves the linearized Euler or Navier–Stokes equations, with the anelastic approximation. This approximation, which is widely used in other fields of astrophysics and atmospheric physics, consists in neglecting acoustic waves by assuming that time derivatives of the pressure and the density perturbations are negligible. It allows for a characteristic time, which is not set by acoustic propagation time, but is much longer and the timestep can be chosen so as to follow the inertial modes themselves. In their 2002 paper [478], Villain et al. study inertial modes (i.e. modes whose restoring force is the Coriolis force, among which the r -modes [23]) in slowly rotating polytropes with $\gamma = 2$ in the linear regime. First, this is done in the framework of Newtonian gravity, where the anelastic approximation implies that the Eulerian perturbations of the gravitational potential do not play any role in the velocity perturbations. Second, they study the relativistic case, but with the *Cowling approximation*, meaning again that the metric perturbations are discarded. In both regimes and trying different boundary conditions for the velocity field at the surface of the star, they note the appearance of a polar part of the mode and the “concentration of the motion” near the surface, showing up in less than 15 periods of the linear r -mode. A more recent work [477] deals with the study of gravity modes, in addition to inertial modes, in neutron stars. The interesting point of this work is the use of a quite realistic equation of state for nuclear matter, which is valid even when beta equilibrium is broken. The authors were, thus, able to show that the coupling between polar and axial modes is increasing with the rotation of the star, and that the coupling of inertial modes with gravity modes in nonbarotropic stars can produce fast energy exchanges between polar and axial parts of the fluid motion. From a numerical point of view, one of the key ingredients is the solution of the vector heat equation, coming from the Euler or Navier–Stokes equations. This is done by a poloidal-toroidal [83] decomposition of the velocity field into two scalar potentials, which is very natural in spectral methods. Moreover, to ensure correct analytical behavior at the origin, all scalar quantities are projected at each timestep to a modified Legendre function basis.

More recently, a complete nonlinear study of rotating star pulsations has been set by Dimmelmeier et al. [152]. They used the general relativistic code CoCoNuT (see above, Section 4.6.1) in axial symmetry, with an HRSC hydrodynamic solver, and spectral methods for the simplified Einstein equations (conformally-flat three metric). They noted that the conformal flatness condition did not have much effect on the dynamics when comparing with the Cowling approximation. Nevertheless, they found that differential rotation was shifting the modes to lower frequencies and they confirmed the existence of the mass-shedding-induced damping of pulsations.

4.6.2 Vacuum and black hole evolutions

If one wants to simulate the most interesting astrophysical sources of gravitational radiation, one must have a code able to follow, in a stable manner, gravitational waves themselves on a background spacetime. It has been observed by all numerical relativity groups that the stability of a numerical code, which solves Einstein's field equations, not only depends on the numerical algorithm, but also on the particular formulation of the equations. Successes in the simulations of binary systems of compact objects in general relativity (see Section 4.6.3) are also due to numerous studies and advances in the formulations of Einstein's equations. The methods known at present that work for the numerical evolution of binaries are the *generalized harmonic coordinate* method [187, 199, 374] and the *BSSN* method (for Baumgarte–Shapiro–Shibata–Nakamura [54, 421]). In particular, these two formulations of the field equations have the important property that *constraint violating modes* (see discussion following) stay at a reasonable level during the evolution. Use of the generalized harmonic gauge requires constraint damping terms; and a particular method suited for harmonic evolution, which was proposed by Gundlach et al. [232], enabled Pretorius to evolve black hole spacetimes [374, 373].

It is, therefore, a crucial step to devise such a stable formulation, and more particularly with spectral methods, because they add very little numerical dissipation and thus, even the smallest instability is not dissipated away and can grow to an unacceptable level. The situation becomes even more complicated with the setup of an artificial numerical boundary at a finite distance from the source, needing appropriate boundary conditions to control the physical wave content, and possibly to limit the growth of unstable modes. All these points have been extensively studied since 2000 by the Caltech/Cornell groups and their pseudospectral collocation code SpEC [279, 277, 402, 403, 296, 255, 278, 297, 86]; they were followed in 2004 by the Meudon group [73] and in 2006 by Tichy [466].

Next, it is necessary to be able to evolve black holes. Successful simulations of black hole binaries have been performed using the *black-hole puncture technique* [101, 44]. Unfortunately, the dynamic part of Einstein fields are not regular at the puncture points and it seems difficult to regularize them so as to avoid any Gibbs-like phenomenon using spectral methods. Therefore, punctures are not generally used for spectral implementations; instead the excision technique is employed, removing part of the coordinate space inside the apparent horizon. There is no need for boundary conditions on this new artificial boundary, provided that one uses a free-evolution scheme [402], solving only hyperbolic equations. In the considered scheme, and for hydrodynamic equations as well, one does not need to impose any boundary condition, nor do any special treatment on the excision boundary, contrary to finite difference techniques, where one must construct special one-sided differencing stencils. On the other hand, with a constrained scheme, elliptic-type equations are to be solved [73] and, as for initial data (see Sections 4.5.3 and 4.5.6), boundary conditions must be provided, e.g., on the apparent horizon, from the dynamic horizon formalism [223].

Finally, good outer boundary conditions, which are at the same time mathematically well posed, consistent with the constraints and prevent as much as possible reflections of outgoing waves, must be devised. In that respect, quite complete boundary conditions have been obtained by Buchman and Sarbach [95].

Formulation and boundary conditions

Several formulations have been proposed in the literature for the numerical solution of Einstein's equations using spectral methods. The standard one is the 3+1 (a.k.a. Arnowitt–Deser–Misner – ADM) formalism of general relativity [35, 486] (for a comprehensive introduction, see the lecture

notes byourgoulhon [214]), which has been reformulated into the BSSN [54, 421] for better stability. But first, let us mention an alternative *characteristic* approach based on expanding null hypersurfaces foliated by metric two-spheres developed by Bartnik [48]. This formalism allows for a simple analysis of the characteristic structure of the equations and uses the standard “edth” ($\bar{\delta}$) operator on S^2 to express angular derivatives. Therefore, Bartnik and Norton [49] use spin-weighted spherical harmonics (see Section 4.3.2) to numerically describe metric fields.

Coming back to the 3+1 formalism, Einstein’s equations split into two subsets of equations. First, the *dynamic* equations specifying the way the gravitational field evolves from one timeslice to the next; then, the *constraint* equations, which must be fulfilled on each timeslice. Still, it is well known that for the Einstein system, as well as for Maxwell’s equations of electromagnetism, if the constraints are verified on the initial timeslice, then the dynamic equations guarantee that they shall be verified in the future of that timeslice. Unfortunately, when numerically doing such *free* evolution, i.e. solving only for the dynamic equations, small violations of the constraints due to round-off errors appear to grow exponentially (for an illustration with spectral methods, see, e.g., [402, 466]). The opposite strategy is to discard some of the evolution equations, keeping the equations for the two physical dynamic degrees of freedom of the gravitational field, and to solve for the four constraint equations: this is a *constrained* evolution [73].

The advantages of the free evolution schemes are that they usually allow one to write Einstein’s equations in the form of a strongly- or symmetric-hyperbolic system, for which there are many mathematical theorems of existence and well-posedness. In addition, it is possible to analyze such systems in terms of characteristics, which can give very clear and easy-to-implement boundary conditions [278]. Using finite-difference numerical methods, it is also very CPU-time consuming to solve for constraint equations, which are elliptic in type, but this is not the case with spectral methods. On the other hand, constrained evolution schemes have, by definition, the advantage of not being subject to constraint-violation modes. Besides, the equations describing stationary spacetimes are usually elliptic and are naturally recovered when taking the steady-state limit of such schemes. Finally, elliptic PDEs usually do not exhibit instabilities and are known to be well posed. To be more precise, constrained evolution using spectral methods has been implemented by the Meudon group [73], within the framework of the BSSN formulation. Free-evolution schemes have been used by Tichy [466] (with the BSSN formulation) and by the Caltech/Cornell group, which has developed their Kidder–Scheel–Teukolsky (KST) scheme [277] and have later used the Generalized-Harmonic (GH) scheme [297]. The KST scheme is, in fact, a 12-parameter family of hyperbolic formulations of Einstein’s equations, which can be fine tuned in order to stabilize the evolution of, e.g., black hole spacetimes [402].

Even when doing so, constraint-violating modes grow exponentially and three ways of controlling their growth have been studied by the Caltech/Cornell group. First, the addition of multiples of the constraints to the evolution system in order to minimize this growth. The parameters linked with these additional terms are then adjusted to control the evolution of the constraint norm. This generalized version of the dynamic constraint control method used by Tiglio et al. [468] has been presented by Lindblom et al. [296] and tested on a particular representation of the Maxwell equations. Second, Lindblom et al. [296] devised constraint preserving boundary conditions from those of Calabrese et al. [100], where the idea was to get maximally dissipative boundary conditions on the *constraint evolution* equations [296, 278]. This second option appeared to be more efficient, but still did not completely eliminate the instabilities. Finally, bulk constraint violations cannot be controlled by constraint-preserving boundary conditions alone, so Holst et al. [255] derived techniques to project at each timestep the solution of the dynamic equations onto the constraint submanifold of solutions.

This method necessitates the solution of a covariant inhomogeneous Helmholtz equation to determine the optimal projection. Nevertheless, the most efficient technique seems to be the use of the GH formulation, which also incorporates multiples of the constraints, thus exponentially suppressing bulk constraint violation, together with constraint-preserving boundary conditions [297].

Boundary conditions are not only important for the control of the constraint-violation modes in free evolutions. Because they cannot be imposed at spatial infinity (see Section 4.3.1), they must be completely transparent to gravitational waves and prevent any physical wave from entering the computational domain. A first study of interest for numerical relativity was done by Novak and Bonazzola [341], in which gravitational waves are considered in the wave zone, as perturbations of flat spacetime. The specificity of gravitational waves is that they start at the quadrupole level ($\ell = 2$) in terms of spherical harmonics expansion. Standard radiative boundary conditions (known as Sommerfeld boundary conditions [436]) being accurate only for the $\ell = 0$ component, a generalization of these boundary conditions has been done to include quadrupolar terms [341]. They strongly rely on the spectral decomposition of the radiative field in terms of spherical harmonics and on spherical coordinates. More specific boundary conditions for the Einstein system, in order to control the influx of the radiative part of the Weyl tensor, have been devised by Kidder et al. [278] for the KST formulation, generalizing earlier work by Stewart [446] and Calabrese et al. [100]. They were then adapted to the GH formulation by Lindblom et al. [297]. Rinne [388] has studied the well-posedness of the initial-boundary-value problem of the GH formulation of Einstein's equations. He has considered first-order boundary conditions, which essentially control the incoming gravitational radiation through the incoming fields of the Weyl tensor. He has also tested the stability of the whole system with a collocation pseudospectral code simulating a Minkowski or Schwarzschild perturbed spacetime. Generalizing previous works, a hierarchy of absorbing boundary conditions has been introduced by Buchman and Sarbach [95], which have then been implemented in the Caltech/Cornell SpEC code by Ruiz et al. [395], together with new sets of absorbing and constraint-preserving conditions in the generalized harmonic gauge. Ruiz et al. have shown that their second-order conditions can control the incoming gravitational radiation, up to a certain point. In addition, they have analyzed the well-posedness of the initial-boundary-value problems arising from these boundary conditions. Rinne et al. [390] have compared various methods for treating outer boundary conditions. They have used the SpEC code to estimate the reflections caused by the artificial boundary, as well as the constraint violation it can generate.

Gauges and wave evolution

The final ingredient before performing a numerical simulation of the dynamic Einstein system is the gauge choice. For example, the analytical study of the linearized gravitational wave in vacuum has been done with the harmonic gauge, for which the coordinates $\{x^\mu\}$ verify the scalar covariant wave equation

$$H_\mu = g_{\mu\nu} \nabla_\sigma \nabla^\sigma x^\nu = 0. \quad (4.185)$$

This is the definition of the form H_μ , where $g_{\mu\nu}$ is the metric and ∇_σ the associated covariant derivative. Recent work by the Caltech/Cornell group uses the GH formulation in which the gauge choice is achieved through the specification of H_μ as an arbitrary function of $\{x^\mu\}$ and $g_{\mu\nu}$, which can be set, for instance, to its initial value [404]. Still, it is with the KST formulation, and with the lapse and shift set from the analytic values, that Boyle et al. [86] have submitted the Caltech/Cornell SpEC code to the “Mexico City tests” [13]. These are a series of basic numerical relativity code tests to verify their accuracy and stability, including small amplitude linear plane wave, gauge wave and Gowdy spacetime

evolutions. These tests have been passed by the Caltech-Cornell code using a Fourier basis for all three Cartesian coordinates and a fourth-order Runge-Kutta timestepping scheme. In the particular case of the linear plane wave, Boyle et al. [86] exhibit the proper error behavior, which increases as the square of the wave amplitude, because all nonlinear terms are neglected in this test. The authors have also shown that the use of filtering of the spherical harmonics coefficients was very effective in reducing nonlinear aliasing instabilities. Gauge drivers for the GH formulation of Einstein's equations have been devised by Lindblom et al. [298]. They provide an elegant way of imposing gauge conditions that preserve hyperbolicity for many standard gauge conditions. These drivers have been tested with the SpEC code.

Within the constrained formulation of Einstein's equations, the Meudon group has introduced a generalization of the Dirac gauge to any type of spatial coordinates [73]. Considering the conformal 3+1 decomposition of Einstein's equations, the Dirac gauge requires that the conformal three-metric $\tilde{\gamma}^{ij}$ (such that $\det \tilde{\gamma}^{ij} = 1$) be divergence-free with respect to the flat three-metric (defined as the asymptotic structure of the three-metric and with the associated covariant derivative \bar{D})

$$\bar{D}_i \tilde{\gamma}^{ij} = 0. \quad (4.186)$$

The time coordinate is set by the standard maximal slicing condition. These conditions turn out to be *dynamic* gauge conditions: the lapse and the shift are determined through the solution of elliptic PDEs at each timestep. With this setting, Bonazzola et al. have studied the propagation of a three-dimensional gravitational wave, i.e. the solution of the fully nonlinear Einstein equations in vacuum. Their multidomain spectral code based on the LORENE library [216] was able to follow the wave using spherical coordinates, including the (coordinate) singular origin, and to let it out of the numerical grid with transparent boundary conditions [341]. Evolution was performed with a second-order semi-implicit Crank–Nicolson time scheme, and the elliptic system of constraint equations was solved iteratively. Since only two evolution equations were solved (out of six), the others were used as error indicators and proved the awaited second-order time convergence. A preliminary analysis of the mathematical structure of the evolution part of this formalism done by Cordero et al. [134] has shown that the choice of Dirac's gauge for the spatial coordinates guarantees the strongly hyperbolic character of that system as a system of conservation laws.

Black hole spacetimes

As stated at the beginning of Section 4.6.2, the detailed strategy to perform numerical simulations of black hole spacetimes depends on the chosen formulation. With the characteristic approach, Bartnik and Norton [49] modeled gravitational waves propagating on a black hole spacetime in spherical coordinates, but with a null coordinate $z = t - r$. Interestingly, they combined a spectral decomposition on spin-weighted spherical harmonics for the angular coordinates and an eighth-order scheme using spline convolution to calculate derivatives in the r or z direction. Integration in these directions was done with a fourth or eighth-order Runge–Kutta method. For the spectral part, they had to use Orszag's 2/3 rule [102] for antialiasing. This code achieved a global accuracy of 10^{-5} and was able to evolve the black hole spacetime up to $z = 55 M$. More recently, Tichy has evolved a Schwarzschild black hole in Kerr–Schild coordinates in the BSSN formulation, up to $t \simeq 100 M$ [466]. He used spherical coordinates in a shell-like domain, excising the interior of the black hole. The expansion functions are Chebyshev polynomials for the radial direction, and Fourier series for the angular ones.

Most successful simulations in this domain have been performed by the Caltech/Cornell group, who seem to be able to stably evolve forever not only a Schwarzschild, but also a Kerr black hole

perturbed by a gravitational wave pulse [297], using their GH formulation with constraint-damping and constraint-preserving boundary conditions. However, several attempts had been reported by this group before, starting with the spherically-symmetric evolution of a Schwarzschild black hole by Kidder et al. [276]. Problems had arisen when trying three-dimensional simulations of such physical systems with the new parameterized KST formalism [277]. Using spherical coordinates in a shell-like domain, the authors decomposed the fields (or Cartesian components for tensor fields) on a Chebyshev radial base and scalar spherical harmonics. The integration in time was done using a fourth-order Runge–Kutta scheme and the gauge variables were assumed to keep their analytical initial values. The evolution was limited by the growth of constraint-violating modes at $t \sim 1000 M$. With a fine-tuning of the parameters of the KST scheme, Scheel et al. [402] have been able to extend the lifetime of the numerical simulations to about $8000 M$. On the other hand, when studying the behavior of a dynamic scalar field on a fixed Kerr background, Scheel et al. [403] managed to get nice results on the late time decay of this scalar field. They had to eliminate high-frequency numerical instabilities, with a filter on the spherical harmonics basis, following again Orszag’s 2/3 rule [102] and truncating the last third of the coefficients. It is interesting to note that no filtering was necessary on the radial (Chebyshev) basis functions. A more complicated filtering rule has been applied by Kidder et al. [278] when trying to limit the growth of constraint-violation in three-dimensional numerical evolutions of black hole spacetimes with appropriate boundary conditions. They have set to zero the spherical harmonics terms with $\ell \geq \ell_{\max} - 3$ in the *tensor* spherical harmonics expansion of the dynamic fields. The stable evolutions reported by Lindblom et al. [297], thus, might be due to the following three ingredients:

- GH formalism, exponentially suppressing all small short-wavelength constraint violations,
- constraint-preserving boundary conditions,
- the filtering of spherical harmonics spectral coefficients.

4.6.3 Binary systems

As seen in Section 4.6.2, not many groups using spectral methods are able to solve all the three-dimensional Einstein equations in a stable way. When dealing with black holes, the situation is even worse. Only very recently, the Caltech/Cornell group succeeded in following 16 orbits, merger and ring-down of an equal-mass nonspinning black-hole–binary system [405]. Moreover, we can report on three recent partial results in the field using spectral methods, dealing with each type of binary system (neutron stars and/or black holes) and leaving space for future study in this rapidly evolving field. We note, of course, that successful numerical evolutions of such systems have been performed with other numerical methods, which we very briefly summarize here. The first successful fully-relativistic simulation of neutron star binaries was obtained by Shibata et al. [418, 417] and now, more groups are also able to study such systems: the Louisiana State University (LSU) group [18] and the Albert Einstein Institute (AEI, Golm) group [42]. We should also mention here the more microphysically-detailed simulations by Oechslin and Janka [346], although with the conformally-flat approximation, and those of Liu et al. [303] evolving magnetized neutron star binaries. Shibata and Uryū [426, 427] have successfully evolved black-hole–neutron-star binaries using the puncture technique for the modeling of the black hole. As far as black hole binary systems are concerned, after many years of hard work and codes evolving the binary system for a restricted time, a first stable simulation up to the merger phase has been performed by Pretorius [373], who used general harmonic coordinates together

with constraint-damping terms and a compactification of spatial infinity. He also used the excision technique for a region surrounding the singularity inside the horizon. This first success was followed a few months later by the Texas/Brownsville group [101] and the NASA/Goddard group [44], using very different techniques, namely BSSN with moving punctures and “1+log” slicing together with a “T-driver” shift condition. These techniques have rapidly become standards for many other groups, which are now able to stably evolve black hole binaries, such as the AEI/LSU collaboration [368], the group in Jena [209], that at Pennsylvania State University [247] and at Florida Atlantic University [467]. The results have reached a high level of confidence and it is possible to compare gravitational waveforms obtained from numerical evolution with post-Newtonian template families [354].

Neutron star binaries

Numerical simulations of the final stage of inspiral and merger of neutron star binaries have been performed by Faber et al. [170], who used spectral methods in spherical coordinates (based on LORENE library [216]) to solve Einstein’s equations in the conformally-flat approximation (see Sections 4.5 and 4.6.1). The hydrodynamic evolution has been computed using a Lagrangian smoothed particle hydrodynamics (SPH) code. As for the initial conditions described in Section 4.5.5, the equations for the gravitational field reduce, in the case of the conformally-flat approximation, to a set of five nonlinear coupled elliptic (Poisson-type) PDEs. The considered fields (lapse, shift and conformal factor) are “split” into two parts, each component being associated with one of the stars in the binary. Although this splitting is not unique, the result obtained is independent from it, because the equations with the complete fields are solved iteratively, for each timestep. Boundary conditions are imposed on each solution of the field equations at radial infinity thanks to a multidomain decomposition and a $u = 1/r$ compactification in the last domain. The authors used $\sim 10^5$ SPH particles for each run, with an estimated accuracy level of 1–2%. Most of the CPU time was spent in calculating the values of quantities known from their spectral representation, at SPH particle positions. Another difficulty has been the determination of the domain boundary containing each neutron star, avoiding any Gibbs phenomena. Because the conformally-flat approximation discards gravitational waves, the dissipative effects of gravitational radiation back reaction were added by hand. The authors used the slow-motion approximation [481] to induce a shrinking of the binary systems, and the gravitational waves were calculated with the lowest-order quadrupole formulae. The code has passed many tests and, in particular, it has evolved several quasiequilibrium binary configurations without adding the radiation reaction force with resulting orbits that were nearly circular (change in separation lower than 4%). The code was thus able to follow irrotational neutron star binaries, including radiation reaction effects, up to the merger and the formation of a differentially rotating remnant, which is stable against immediate gravitational collapse for reasonably stiff equations of state. All the results agreed pretty well with previous relativistic calculations.

Black-hole–neutron-star binaries

A similar combination of numerical techniques has been used by Faber et al. [171] to compute the dynamic evolution of merging black-hole–neutron-star binaries. In addition to the conformally-flat approximation and similar to Taniguchi et al. [451], Faber et al. [171] considered only the case of an extremely large mass ratio between the black hole and the neutron star, thus holding the black hole position fixed and restricting the spectral computational grid to the neighborhood of the neutron star. The metric describing the space surrounding the black hole was thus, supposed to keep the form of a

Schwarzschild black hole in isotropic coordinates. The neutron star was restricted to low compactness (only a few percent) in order to have systems that disrupt well outside the last stable orbit. The system was considered to be in corotation and, just as for neutron star binaries, the gravitational radiation reaction was added by hand. As stated above, the numerical methods used SPH discretization to treat dynamic evolution of matter, and the spectral library LORENE [216] to solve the Einstein field Poisson-like equations in the conformally-flat approximation. But here, the spectral domains associated with the neutron star did not extend to radial infinity (no compactified domain) and approximate boundary conditions were imposed, using a multipole expansion of the fields. The main reason being that the black hole central singularity could not be well described on the neutron star grid.

Faber et al. [171] have studied the evolution of neutron-star–black-hole binaries with different polytropic indices for the neutron star matter equation of state, the initial data being obtained as solutions of the conformal thin-sandwich decomposition of Einstein’s equations. They found that, at least for some systems, the mass transfer from the neutron star to the black hole plays an important role in the dynamics of the system. For most of these systems, the onset of tidal disruption occurred outside the last stable orbit, contrary to what had been previously proposed in analytical models. Moreover, they have not found any evidence for significant shocks within the body of the neutron star. This star possibly expanded during the mass loss, eventually losing mass outward and inward provided that it was not too far within the last stable orbit. Although the major part of released matter remained bound to the black hole, a significant fraction could be ejected with sufficient velocity to become unbound from the binary system.

Black hole binaries

Encouraging results concerning black-hole–binary simulations with spectral methods have been first obtained by Scheel et al. [404]. They have used two coordinate frames to describe the motion of black holes in the spectral grid. Indeed, when using excision techniques (punctures are not regular enough to be well represented by spectral methods), excision boundaries are fixed on the numerical grid. This can cause severe problems when, due to the movement of the black hole, the excision surface becomes timelike and the whole evolution problem becomes ill-posed in the absence of boundary conditions. One solution seems to be the use of comoving coordinates, but the authors report that the GH formulation they use appear to be unstable with this setting. They, therefore, consider a first system of inertial coordinates (with respect to spatial infinity) to define the tensor components in the triad associated with these coordinates, and a second system of comoving (in some sense) coordinates. In the case of their black-hole–binary tests [404], they define the comoving coordinates dynamically, with a feedback control system that adjusts the moving coordinate frame to control the location of each apparent horizon center.

The spectral code uses 44 domains of different types (spherical and cylindrical shells, rectangular blocks) to describe the binary system. Most of the numerical strategy to integrate Einstein’s equations is taken from the tests on the GH formulation of Lindblom et al. [297] and has already been detailed in Section 4.6.2. The important technical ingredient detailed by Scheel et al. [404] is the particular filtering of tensor fields in terms of spherical harmonics. The dual-coordinate-frame representation can mix the tensor’s spherical harmonic components. So, in their filtering of the highest-order tensor spherical-harmonic coefficients, Scheel et al. [404] had to take into account this mixing by transforming spatial tensors into a rotating-frame tensor spherical-harmonic basis before filtering and then transforming back to an inertial frame basis. This method allowed them to evolve black-hole–binary spacetimes for more than four orbits, until $t \gtrsim 600 M_{\text{ADM}}$.

However, a central problem has been the capability of the code to follow the merger phase, and even though the code was able to compute the inspiral quite accurately, it used to fail just before the black holes merged. The problem was that, when the black holes came close to each other, their horizons became extremely distorted and strong gradients would develop in the dynamic fields. This has been explained as a gauge effect, coming from the incapacity of the gauge condition to react and change the geometry when the two black holes begin to interact strongly, and can be seen as a coordinate singularity developing close to the merger. Nevertheless, a cure has been found, as explained in Scheel et al. [405]. The original gauge is kept until some given time and then smoothly changed to a new one, based on the gauge treatment by Pretorius [374, 373] (for the lapse): the gauge source function is evolved through a damped, driven wave equation, which drives the lapse toward unity and the shift vector toward zero near the horizons. Thus, the horizons expand in coordinate space and the dynamic fields are smoothed out near the horizons, preventing gauge singularities from developing. With this transition of the gauge condition, the evolution of the black holes can be tracked until the formation of a common horizon encompassing both black holes. Then, the evolution of this single-distorted dynamic black hole is achieved by first interpolating all variables onto a new computational domain containing only one excised region, then by choosing a new comoving coordinate system, and finally by again modifying the gauge condition to drive the shift vector to a time-independent state.

These new gauge conditions have allowed Scheel et al. [405] to follow the inspiral during 16 orbits, and the merger and ring-down phase of an equal-mass nonspinning black-hole–binary system. They were able to compute the mass and the spin of the final black hole with very high accuracy (10^{-5} and 10^{-4} relative accuracy for the mass and spin, respectively), and to extract the physical waveform accurately to 0.01 radians in phase. This is the first spectral numerical simulation of the full evolution of a black-hole–binary system.

4.7 Conclusions

We would like to conclude our overview of spectral methods in numerical relativity by pointing out a few items that we feel are particularly interesting.

4.7.1 Strengths and weaknesses

The main advantage of spectral methods, especially with respect to finite difference ones, is the very rapid convergence of the numerical approximation to the real function. This implies that very high accuracy can usually be reached with only a moderate number of points. This obviously makes the codes both faster and less demanding on memory. Various examples of convergence can be found in Section 4.2. However, this rapid convergence is only achieved for C^∞ functions. Indeed, when the functions are less continuous, spurious oscillations appear and the convergence only follows a power law. In the case of discontinuous functions, this is known as the Gibbs phenomenon (see the extreme case of Figure 4.11). Gibbs-like phenomena are very likely to prevent codes from converging or to make time evolutions unstable. So spectral methods must rely heavily on the domain decomposition of space and the domains must be chosen so that the various discontinuities lie at the boundaries. Because of this, spectral methods are usually more difficult to implement than standard finite differences (see, for instance, the intricate mappings of [28]). The situation is even more complicated when the surfaces of discontinuities are not known in advance or have complicated shapes.

Spectral methods are also very efficient at dealing with problems that are related to coordinate singularities. Indeed, if the basis functions fulfill the regularity requirements, then all the functions will automatically satisfy them. In particular, it makes the use of spherical coordinates much easier than with other methods, as explained in Section 4.3.2.

Another nice feature is the fact that a function can be represented either by its coefficients or its values at the collocation points. Depending on the operation one has to perform, it is easier to work with the one representation or the other. When working in the coefficient space, one takes full advantage of the nonlocality of the spectral representation. A lot of operations that would be difficult otherwise can then be easily performed, like computing the ratio of two quantities vanishing at the same point (see, for instance, [185]).

4.7.2 Combination with other methods

Spectral methods have also demonstrated that they can be a valuable tool when combined with other methods. For instance, when shocks are present, spectral methods alone have trouble dealing with discontinuities at the shock interface. However, this can be efficiently dealt with using Godunov methods. Such a combination has already been successfully applied to the simulation of the oscillations of compact stars in [152] and of core collapse [352].

Spectral methods have also been used in conjunction with a description of the fluid based on SPH (smoothed particle hydrodynamics) in the case of neutron star binaries [170] and for the merger of a neutron star with a black hole [171]. In both cases, the fluid is described by an ensemble of particles to which forces are applied. Such technique can account for complicated fluid configurations, like the spiral arms that are formed during the merger. Such arms would be tricky to follow by means of spectral methods alone. On the other hand, the equations describing gravity are nicely solved by spectral solvers.

4.7.3 Future developments

Finally, we would like to point out a few directions could lead to interesting results. Of course, we are not aware of what the other groups have planned for the future.

Appropriate choice of coordinates is evidently important. However, for binary systems, rather few results have been obtained using the natural choice of bispherical coordinates. So far, variations of such coordinates have only been used by Ansorg and collaborators and only in the context of initial data [33, 27, 28]. We believe that applying these coordinates, or similar coordinates, to evolutionary codes could lead to interesting results, in terms of both speed and accuracy.

The application of spectral methods to theories more complicated than general relativity is also imaginable. One of the possible fields of application is the study of branes, where there is an additional dimension to spacetime. The fact that spectral methods are accurate with relatively few degrees of freedom makes them a good candidate for simulating systems with extra dimensions. The addition of gauge fields is also something that could be studied with spectral methods, to investigate the possibility of “hairy” black holes, for instance. Of course, these are just a few ideas of what the future applications of spectral methods to the field of relativity might be.

Chapitre 5

Absorbing boundary conditions for simulation of gravitational waves with spectral methods in spherical coordinates

Version publiée : J. Novak et S. Bonazzola, *Journal of Computational Physics* **197**, pp.186-196 (2004).

Sommaire

5.1	Introduction	189
5.2	Absorbing boundary conditions	191
5.3	Numerical experiments	194
5.4	Conclusions	198

5.1 Introduction

5.1.1 Wave equations in General Relativity

The determination of numerical solutions of the Einstein equations is the scope of *numerical relativity*. It is a fundamental issue not only for the determination of gravitational wave signals for detector data analysis, but also for the study of the properties of relativistic astrophysical objects [339]. Within numerical relativity studies, the most commonly used formulation of the Einstein equations is the so-called “3+1” formalism (also called *Cauchy formalism* [486]) in which space-time is foliated by a family of space-like hypersurfaces Σ_t , which are described by their 3-metric γ_{ij} . The 4-metric $g_{\mu\nu}$ is then described in terms of γ_{ij} , a 3-vector N^i (called *shift*) and a scalar N (called *lapse*). In this formalism, the Einstein equations can be decomposed into a set of four constraint equations and six second-order dynamical equations. Solving the Einstein equations then turns to be a Cauchy problem of evolution under constraints and there remains the freedom to choose the time coordinate (slicing)

and the spatial gauge.

For example, the choice of *maximal slicing* for the time coordinate (see [435]) converts the constraint equations to scalar form and a vectorial Poisson-like equation, for which a numerical method for solution has been presented in [228]. As far as evolution equations are concerned, they consist of six non-linear scalar wave equations in curved space-time, with the additional choice of the *Dirac* gauge [435]. The whole system is a mixed initial value-boundary problem, and this paper deals with boundary conditions for the time evolution equations. Indeed, a simpler problem is considered: the initial value-boundary problem for a linear and flat scalar wave equation:

$$\square\phi(t, r, \theta, \varphi) = \sigma(t, r, \theta, \varphi) \quad (5.1)$$

where

$$\square\phi = \frac{\partial^2\phi}{\partial t^2} - \frac{\partial^2\phi}{\partial r^2} - \frac{2}{r} \frac{\partial\phi}{\partial r} - \frac{1}{r^2} \left(\frac{\partial^2\phi}{\partial\theta^2} + \frac{1}{\tan\theta} \frac{\partial\phi}{\partial\theta} + \frac{1}{\sin^2\theta} \frac{\partial^2\phi}{\partial\varphi^2} \right)$$

is the usual flat scalar d'Alembert operator in spherical coordinates (r, θ, φ) and σ is a source. To solve a more general problem in curved space-time, like for example:

$$\frac{\partial^2\phi}{\partial t^2} - \mu^2(t, r)\Delta\phi = \phi^2, \quad (5.2)$$

one can put non-linear terms to the source σ and represent at each time-step the metric function μ^2 by a polynomial (semi-implicit scheme, see [337] for an example in spherical symmetry).

5.1.2 Motivations for general quadrupolar absorbing boundary conditions

The study of the simple wave equation and its properties concerning quadrupolar waves is more than a toy-model for numerical relativity. There are many degrees of freedom in the formulation of the Einstein equations and in the gauge choice. It is not clear which of these formulations are well-posed or numerically stable [191]. It is therefore important to have numerical tools that are general in the sense that they can be used within the framework of various formulations and gauges. Still, in many cases, the dynamical degrees of freedom of the gravitational field can be described by wave-like propagation equations in curved space-time. On the other hand, since we are mainly interested in the gravitational wave signal, which has a quadrupolar dominant term, we have to make high precision numerical models (including boundary conditions) to study this mode, as well as lower multipoles.

These statements can be illustrated as follows. One of the main sources we want to study are binaries of two compact objects (neutron star or black hole) orbiting around each other. Gravitational waves take away angular momentum and the system coalesces. In some perturbative approach, the terms corresponding to this “braking force” result from a subtle cancellation between terms of much higher amplitude [62]. In numerical non-perturbative studies, the same phenomenon may happen and, if the dominant modes of the wave are not computed with enough precision, the angular momentum loss may be strongly overestimated. Moreover, the time-scale for coalescence is much larger than the orbital period and the system is almost stationary.

There has been many interesting developments concerning absorbing boundaries in the last years, with the Perfectly Matched Layers (PML, see [248] and [302]) which consist in surrounding the true domain of interest by an absorbing layer where the wave is damped. These methods may not be the best-suited for our problems since, as stated above, we might have to change the formulation of

the equations we want to solve. Moreover, the main problem we want to address is the simulation of quadrupolar waves and, as it will be shown later in this paper, with our formulation it is possible to have a clear control on the behavior of these quadrupolar waves. Finally, this formulation is straightforward to implement and very little CPU time consuming in the context of spectral methods and spherical coordinates, which we are already using to solve elliptic partial differential equations (PDE) arising in numerical relativity (scalar and vectorial ones, see [228]). The development and implementation of the PML techniques for our problem would require much more work and computing time, whereas it is not guaranteed at all it would give better results. For all these reasons we chose to develop a new formulation of the Bayliss and Turkel [56] boundary conditions, particularly well suited for using with spectral methods and spherical coordinates.

The paper deals with this new formulation as well as numerical tests. It is organized as follows. First, Sec. 5.2 presents boundary conditions: it briefly recalls main results from Bayliss and Turkel (5.2.1) and we then derive the formulation adapted up to quadrupolar modes of the wave (5.2.2). Then, Sec. 5.3 briefly describes spectral methods in spherical coordinates that were used (5.3.1) and details the numerical results (5.3.2). Finally, Sec. 5.4 gives a summary and some concluding remarks.

5.2 Absorbing boundary conditions

An important difference between the solution of the wave equation and that of the Poisson equation (as in [228]) is the fact that boundary conditions cannot be imposed at infinity, since one cannot use “compactification”, i.e. a change of variable of the type $u = 1/r$. This type of compactification is not compatible with an hyperbolic PDE, see [436]. One has to construct an artificial boundary and impose conditions on this surface to simulate an infinite domain. These conditions should therefore give no reflection of the wave, that could spuriously act on the evolution of the system studied inside the numerical grid. The boundary conditions have to *absorb* all the waves that are coming to the outer limit of the grid. The general *condition of radiation* is derived e.g. in [436], and defined as

$$\lim_{r \rightarrow \infty} \left(\frac{\partial}{\partial r} + \frac{\partial}{\partial t} \right) (r\phi) = 0. \quad (5.3)$$

At a finite distance $r = R$ the condition, which is then approximate, reads

$$\frac{\partial \phi}{\partial t} + \frac{\phi}{R} + \frac{\partial \phi}{\partial r} \Big|_{r=R} = 0, \quad (5.4)$$

which will be hereafter referred as the “Sommerfeld condition” and is exact only for pure monopolar waves. A completely general and exact boundary condition for the wave equation on an artificial spherical boundary has recently been derived by Aladl *et al.* [6] and involves an infinite series of inverse Fourier transforms of the solution. This condition may not be suitable for direct numerical implementation for which Aladl *et al.* derived a truncated approximate condition.

5.2.1 Asymptotic expansion in terms of multipolar momenta

A rather general method to impose non-reflecting boundary conditions is to construct a sequence of boundary conditions that, for each new term, are in some sense giving better results. Some of the possibilities to define “better” are when the reflected wave decreases:

- as the incident wave approaches in a direction closer to some preferred direction(s) (see e.g. [162]),
- for shorter wavelengths,
- as the position of artificial boundary goes to infinity.

This last approach is the most relevant to the problem of solving the Einstein equation for isolated systems. It is also a way of expanding condition (5.3) in terms of asymptotic series, which has been studied in [56], where a sequence of recursive boundary conditions is derived. Let us recall here some of their results.

A radiating solution of (5.1) with the source $\sigma = 0$ can be written as the following expansion:

$$\phi(t, r, \theta, \varphi) = \sum_{k=1}^{\infty} \frac{f_k(t-r, \theta, \varphi)}{r^k}. \quad (5.5)$$

The operators acting on a function $f(t, r, \theta, \varphi)$ are recursively defined by:

$$B_1 f = \frac{\partial f}{\partial t} + \frac{\partial f}{\partial r} + \frac{f}{r}, \quad (5.6)$$

$$B_{n+1} f = \left(\frac{\partial}{\partial t} + \frac{\partial}{\partial r} + \frac{2n+1}{r} \right) B_n f. \quad (5.7)$$

The family of boundary conditions then reads:

$$B_n \phi|_{r=R} = 0. \quad (5.8)$$

In [56], it is shown that, following from (5.5), a radiating solution of the wave equation verifies:

$$B_n \phi = O\left(\frac{1}{r^{2n+1}}\right), \quad (5.9)$$

which in particular means that condition (5.8) is an asymptotic one in powers of $1/r$. The condition $B_1 \phi = 0$ is same as the Sommerfeld condition (5.4) and the same as the first approximation in terms of the angle between the direction of propagation of the wave and the normal to the boundary, derived in [162].

Finally, using expression (5.5) one can verify that the operator B_n annihilates the first n terms of the expansion. Thinking in terms of spherical harmonics, this means that condition (5.8) is exact if the wave carries only terms with $l \leq n-1$. In other words, the reflection coefficients for all modes lower than n are zero. Since we are interested in the study of gravitational wave emission by isolated systems, it is of great importance to have a very accurate description of the quadrupolar part of the waves, which is dominant. Therefore, if the $l=2$ part of the gravitational wave is well described, higher-order terms may not play such an important role in the dynamical evolution of the system. The situation then is not so bad even if only an approximate boundary condition is imposed for those terms with $l \geq 3$. Moreover, the error on the function scales like $1/R^{n+1}$ so, if we impose

$$B_3 \phi|_{r=R} = 0, \quad (5.10)$$

we have an exact boundary condition for the main contribution to the gravitational wave and an error going to zero as $O(1/R^4)$. When developing this expression, one gets:

$$\left(\frac{\partial^3}{\partial t^3} + 3 \frac{\partial^3}{\partial t^2 \partial r} + 9 \frac{1}{r} \frac{\partial^2}{\partial t^2} + 3 \frac{\partial^3}{\partial t \partial r^2} + 18 \frac{1}{r^2} \frac{\partial}{\partial t} + 18 \frac{1}{r} \frac{\partial^2}{\partial t \partial r} + \frac{\partial^3}{\partial r^3} + 9 \frac{1}{r} \frac{\partial^2}{\partial r^2} + 18 \frac{1}{r^2} \frac{\partial}{\partial r} + 6 \frac{1}{r^3} \right) \phi \Big|_{r=R} = 0. \quad (5.11)$$

5.2.2 New formulation for quadrupolar terms

Starting from (5.11) and considering that ϕ is a solution of the wave equation (5.1), we replace second radial derivatives with:

$$\frac{\partial^2 \phi}{\partial r^2} = \frac{\partial^2 \phi}{\partial t^2} - \frac{2}{r} \frac{\partial \phi}{\partial r} - \frac{1}{r^2} \Delta_{\text{ang}} \phi, \quad (5.12)$$

where:

$$\Delta_{\text{ang}} \phi = \frac{\partial^2 \phi}{\partial \theta^2} + \frac{1}{\tan \theta} \frac{\partial \phi}{\partial \theta} + \frac{1}{\sin^2 \theta} \frac{\partial^2 \phi}{\partial \varphi^2} \quad (5.13)$$

is the angular part of the Laplace operator. We are making here the assumption that, at the outer boundary of the grid ($r = R$), the source term σ of (5.1) is negligible. This is a very good approximation for our studies of isolated systems and is also the assumption made when writing a solution to the wave equation in the form (5.5). For example, the third order radial derivative is replaced with

$$\frac{\partial^3 \phi}{\partial r^3} = \frac{\partial^3 \phi}{\partial t^2 \partial r} + \frac{2}{r^3} \Delta_{\text{ang}} \phi - \frac{1}{r^2} \Delta_{\text{ang}} \frac{\partial \phi}{\partial r} + \frac{2}{r^2} \frac{\partial \phi}{\partial r} - \frac{2}{r} \frac{\partial^2 \phi}{\partial r^2}; \quad (5.14)$$

and the second-order radial derivatives of the last term (combined with its counterpart term in (5.11)) is replaced once more using (5.12). The boundary condition is then written as:

$$B_3 \phi = \left(4 \frac{\partial^3}{\partial t^3} + 4 \frac{\partial^3}{\partial t^2 \partial r} + 16 \frac{1}{r} \frac{\partial^2}{\partial t^2} + 18 \frac{1}{r^2} \frac{\partial}{\partial t} + 12 \frac{1}{r} \frac{\partial^2}{\partial t \partial r} + 6 \frac{1}{r^2} \frac{\partial}{\partial r} + \frac{3}{r^2} \Delta_{\text{ang}} \frac{\partial}{\partial t} - \frac{1}{r^2} \Delta_{\text{ang}} \frac{\partial}{\partial r} - \frac{5}{r^3} \Delta_{\text{ang}} + \frac{6}{r^3} \right) \phi. \quad (5.15)$$

We use the auxiliary function ξ :

$$\forall(t, \theta, \varphi), \quad B_1 \phi|_{r=R} = \left(\frac{\partial}{\partial t} + \frac{\partial}{\partial r} + \frac{1}{r} \right) \phi(t, r, \theta, \varphi) \Big|_{r=R} = \xi(t, \theta, \varphi), \quad (5.16)$$

which is defined on the sphere at $r = R$. Inserting this definition into the boundary condition $B_3 \phi|_{r=R} = 0$, with Eq. (5.15), one gets:

$$\frac{\partial^2 \xi}{\partial t^2} - \frac{3}{4R^2} \Delta_{\text{ang}} \xi + \frac{3}{R} \frac{\partial \xi}{\partial t} + \frac{3\xi}{2R^2} = \frac{1}{2R^2} \Delta_{\text{ang}} \left(\frac{\phi}{R} - \frac{\partial \phi}{\partial r} \Big|_{r=R} \right); \quad (5.17)$$

which is a wave-like equation on the outer boundary of the grid, with some source term, equal to zero if the solution ϕ is spherically symmetric. The boundary condition (5.10) is now equivalent to the system (5.16)-(5.17). Written in this way, this formulation can be regarded as a perturbation of the Sommerfeld boundary condition ($B_1 \phi = 0$) given by (5.16). The main advantages are that it can be very easily implemented using spectral methods and spherical coordinates (see Sec. 5.3.1) and that mixed derivatives have almost disappeared: there is only one remaining as a source of (5.17).

5.3 Numerical experiments

5.3.1 Implementation using spectral methods and spherical coordinates

Spectral methods ([210], [102], for a review see [85]) are a very powerful approach for the solution of a PDE and, in particular, they are able to represent functions and their spatial derivatives with very high accuracy. As presented in [72], we decompose scalar fields on spherical harmonics $Y_l^m(\theta, \varphi)$, for the angular part:

$$\phi(t, r, \theta, \varphi) = \sum_{l=0}^L \sum_{m=-l}^l \phi_{lm}(t, r) Y_l^m(\theta, \varphi), \quad (5.18)$$

and on even Chebyshev polynomials ($T_{2k}(x = r/R)$) for the radial part of each $\phi_{lm}(t, r)$. Time derivatives are evaluated using finite-difference methods. Since Chebyshev collocation points are spaced by a distance of order $1/N^2$, (where N is the highest degree of the Chebyshev polynomials used for the radial decomposition) near grid boundaries, the Courant condition on the time step for explicit integration schemes of the wave equation (5.1) also varies like $1/N^2$. This condition is very restrictive and it is therefore necessary to use an implicit scheme. We use the Crank-Nicholson scheme, which is unconditionally stable, as shown by various authors (see e.g. [210]). This scheme is second-order in time and the smoothing of the solution due to implicit time-stepping remains lower than the other errors discussed hereafter. This implicit scheme results in a boundary-value problem for ϕ at each time-step. The solution to this problem is obtained by inverting the resulting spatial operator acting on ϕ using the tau method. Its matrix (in Chebyshev coefficient space) has a condition number that is rapidly increasing with N . This can be alleviated by the use of preconditioning matrices, obtained from finite-differences operators (see [102]).

At the beginning of time integration, we suppose that ϕ satisfies the Sommerfeld boundary condition (5.4), that is $\forall(\theta, \varphi) \xi(t = 0, \theta, \varphi) = 0$. ξ is then calculated at next time-step using (5.17). This is done very easily since the angular parts of ϕ and ξ are decomposed on the basis of spherical harmonics; each component $\xi_{lm}(t)$ is the solution of a simple ODE in time, which is integrated using the same Crank-Nicholson scheme as for the main wave equation (5.1), with boundary conditions such that ξ is periodic on the sphere. This is already verified by the Y_l^m (Galerkin method). We get, with δt being the time-step, $\phi_{lm}^J(r) = \phi_{lm}(t + J\delta t, r)$ and $\xi_{lm}^J = \xi_{lm}(J\delta t)$:

$$\begin{aligned} \frac{\xi_{lm}^{J+1} - 2\xi_{lm}^J + \xi_{lm}^{J-1}}{\delta t^2} + \frac{3l(l+1)}{8R^2} (\xi_{lm}^{J+1} + \xi_{lm}^{J-1}) + \frac{3}{R} \frac{\xi_{lm}^{J+1} - \xi_{lm}^{J-1}}{2\delta t} \\ + \frac{3}{4R^2} (\xi_{lm}^{J+1} + \xi_{lm}^{J-1}) = \frac{l(l+1)}{2R^2} \left(\frac{\phi_{lm}^J(R)}{R} - \frac{\partial \phi_{lm}^J}{\partial r} \Big|_{r=R} \right). \end{aligned}$$

This equation in ξ_{lm}^{J+1} is solved and, for each pair (l, m) , we impose for ϕ_{lm}^{J+1}

$$\left(\frac{\partial}{\partial t} + \frac{\partial}{\partial r} + \frac{1}{r} \right) \phi_{lm}^{J+1}(r) \Big|_{r=R} = \xi_{lm}^{J+1},$$

which looks like a modification of the condition (5.4).

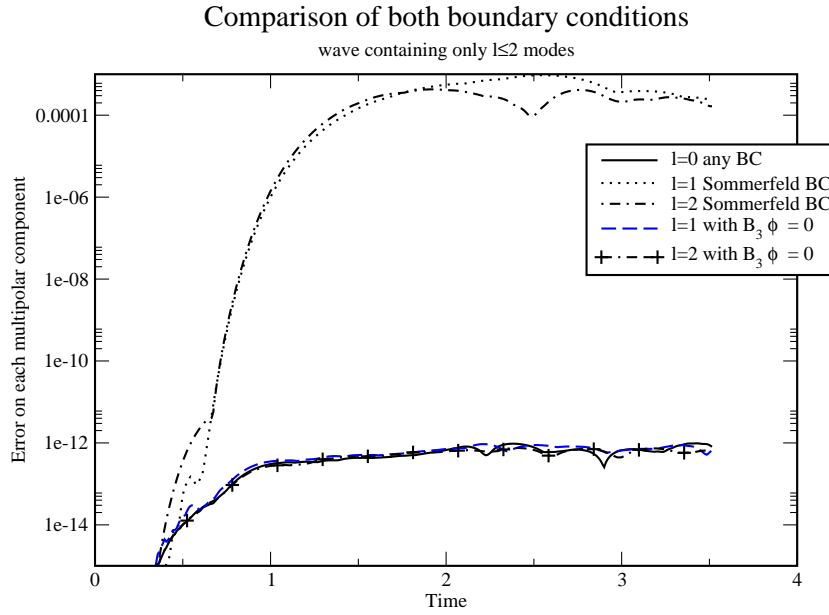


Figure 5.1: Comparison between the efficiencies of $B_1\phi = 0$ (5.4) and $B_3\phi = 0$ (5.16) for $l \leq 2$ modes. The source of the wave equation is defined in Eqs. (5.19) and (5.20). We took $R = 1.2$, a time-step $\delta t = 10^{-6}$, 33 polynomials for radial decomposition, 5 for θ and 4 for φ .

5.3.2 Tests on outgoing waves

The Sommerfeld boundary condition (5.4) is an exact condition, even at finite distance from the source, when only considering monopolar waves. In order to test our implementation of absorbing boundary condition (5.8), we compared its efficiency in being transparent to waves carrying only monopolar, dipolar and quadrupolar terms, to the efficiency of the Sommerfeld boundary condition for monopolar waves. We started with $\phi = 0$ at $t = 0$ and then solved Eq. (5.1) with

$$\begin{aligned} \sigma(t, r, \theta, \varphi) &= S(r, \theta, \varphi) e^{-1/t^2} e^{-1/(t-1)^2} & 0 \leq t \leq 1 \\ \sigma(t, r, \theta, \varphi) &= 0 \text{ otherwise,} \end{aligned} \quad (5.19)$$

with $S(r, \theta, \varphi)$ null for $r > R$.

In all cases, we performed a first calculation with a very large grid (considered as infinite, we checked with various values of the radius that the result in the interval $0 \leq r \leq R$ would be the same), so that in the time interval $[0, 2R + 1]$ the wave would not reach the boundary, on which we imposed an homogeneous boundary condition¹. This gave us the reference solution crossing the $r = R$ sphere without any reflection. We then solved again the same problem, but on a grid of radius R , imposing Sommerfeld boundary conditions $B_1\phi = 0$ (5.4), or our quadrupolar boundary conditions $B_3\phi = 0$ through the system (5.16)-(5.17). The L_1 norm of the relative difference between the functions obtained on the small grid and the reference solution was taken as the error.

¹results obtained here did not depend on the nature of boundary conditions

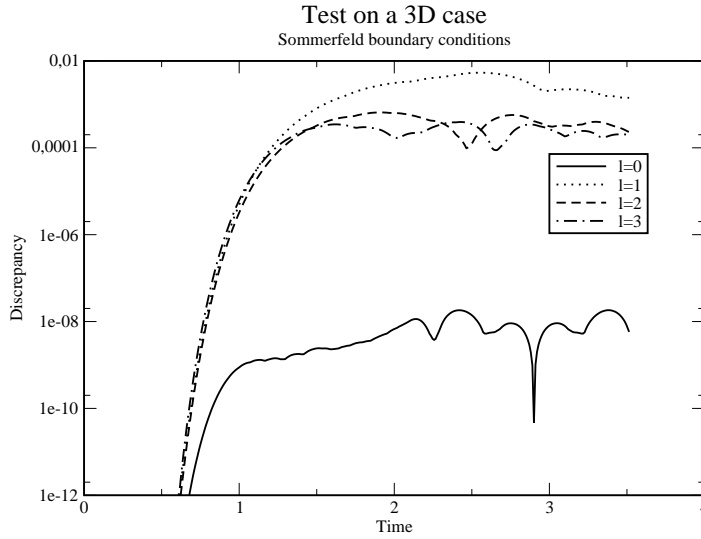


Figure 5.2: Time evolution of the first four modes of the wave generated by the source defined in Eqs. (5.19) and (5.21); using $B_1\phi = 0$ (5.4). We took $R = 1.2$, a time-step $\delta t = 10^{-4}$, 33 polynomials for radial decomposition, 17 for θ and 16 for φ .

$l \leq 2$ case

First, we took

$$S(r, \theta, \varphi) = \left(e^{-r^2} - e^{-R^2} \right) \left(r^2 \cos^2 \theta + r \sin \theta \cos \varphi \right), \quad (5.20)$$

which contains only $l \leq 2$ modes. Figure 5.1 shows the relative efficiency of $B_3\phi = 0$ (5.16) condition to $B_1\phi = 0$ (5.4) for all three modes present in the wave generated by (5.20). For the monopolar ($l = 0$) mode, the evolution of the error would be the same for both types of boundary conditions, within one percent of difference on the error. As far as the discrepancy for dipolar and quadrupolar modes is concerned, one can see that it drops from 10^{-4} with Sommerfeld boundary condition, to 10^{-12} with $B_3\phi = 0$ (5.16). This lower level is the same as for the monopolar mode with the Sommerfeld boundary condition. We have checked that all solutions had converged with respect to the number of spectral coefficients and to the time-step. The error level at 10^{-12} is then mainly due to the condition number of the matrix operator we invert (see Sec. 5.3.1 above). We here conclude that our formulation of $B_3\phi = 0$ (5.16) is as efficient for waves containing only $l \leq 2$ modes as the Sommerfeld boundary condition (5.4) for monopolar waves.

Waves containing higher multipoles

The study has been extended to a more general source σ which contains *a priori* all multipolar terms:

$$S(r, \theta, \varphi) = \left(e^{-r^2} - e^{-R^2} \right) \left(e^{-4(x-0.7)^2} + e^{-3(x+0.5)^2} \right). \quad (5.21)$$

Of course, in numerical implementation, only a finite number of these terms are represented. The geometry of this source can be related to the distribution of mass in the case of a binary system of gravitating bodies, which is one of the main astrophysical sources of gravitational radiation we try to

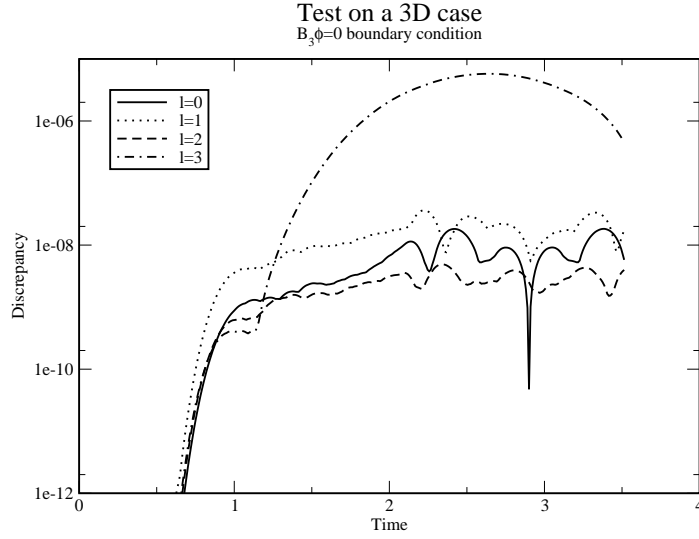


Figure 5.3: Time evolution of the first four modes of the wave generated by the source defined in Eqs. (5.19) and (5.21); using $B_3\phi = 0$ (5.16) as the boundary condition. We took $R = 1.2$, a time-step $\delta t = 10^{-4}$, 33 polynomials for radial decomposition, 17 for θ and 16 for φ .

model. Let us make a comparison between the errors obtained, on the one hand with the condition $B_1\phi = 0$ (Figure 5.2), and on the other hand with $B_3\phi = 0$ (Figure 5.3).

As in the case in Figure 5.1, the error in the monopolar component remains roughly the same, regardless of whether one uses boundary condition (5.4) or (5.16). The errors for the dipolar and quadrupolar components also exhibit similar properties: the use of condition (5.16) causes these errors to be of the same magnitude as the error in the monopolar term. In the case of Figure 5.3, this level is higher than on Figure 5.1 because a longer time-step has been used. Finally, we have also plotted the discrepancies between the reference and test solutions for the $l = 3$ multipole. Following [56], the boundary condition $B_3\phi = 0$ is not exact for this component. Nevertheless, one can see a reduction in the error for this component. This can be understood using the result of [56] which shows that the condition $B_3\phi = 0$ cancels the first 3 terms in the asymptotic development in powers of $1/r$ of the solution ϕ (5.9). Then, since a given multipolar term l_0 is present in terms like $1/r^n$ with $n \leq l_0$ (see e.g. [436]), it is clear that the condition $B_3\phi = 0$ is supposed to cancel all terms decaying slower than $1/r^4$ in the $l \geq 3$ mode. Thus, the error displayed on Figure 5.4 is three orders of magnitude lower with the condition $B_3\phi = 0$ than with $B_1\phi = 0$.

We have checked this point, namely that the maximal error over the time interval would decrease like $1/R^4$, where R is the distance at which the boundary conditions were imposed. We have also checked that the error decreased both exponentially with the number of coefficients used in r, θ or φ , as one would expect for spectral methods, and like δt^2 (second-order time integration scheme). Figure 5.4 shows the overall error as a function of time for both boundary conditions used. Comparing Figure 5.4 with figures 5.2 and 5.3, one can see that most of the error comes from the $l = 1$ term when using $B_1\phi = 0$ boundary condition, and from the $l = 3$ term when using $B_3\phi = 0$. Finally, the computational cost of this enhanced boundary condition is very low with this new approach. For the tests presented here, the difference in CPU time would be of about 10%. This is linked with the fact

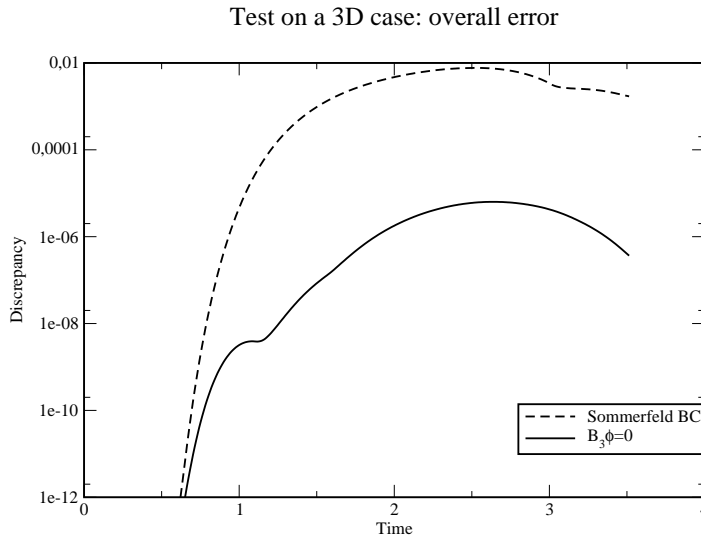


Figure 5.4: Time evolution of the error made in the computation of the wave generated by the source defined in Eqs. (5.19) and (5.21); using $B_1\phi = 0$ (5.4) and $B_3\phi = 0$ (5.16). We took $R = 1.2$, a time-step $\delta t = 10^{-4}$, 33 polynomials for radial decomposition, 17 for θ and 16 for φ .

that our formulation (5.16) is a perturbation of the Sommerfeld boundary condition (5.4), where the quantity $\xi_{lm}(t)$ is obtained by simple (ordinary differential equation) integration.

5.4 Conclusions

The purpose of this paper has been to provide a boundary condition that is well-adapted for the simulation of astrophysical sources of gravitational radiation, whose dominant modes are quadrupolar. We took the series of boundary conditions derived by Bayliss and Turkel [56], truncated at quadrupolar order, and derived a new formulation of that third-order condition in terms of a first-order condition (resembling the classical radiation one), combined with a wave-like equation on the outer boundary of the integration domain. This formulation is simple in the sense that mixed derivatives are (almost) absent.

The numerical implementation using spectral methods and spherical coordinates is straightforward and this formulation of high-order boundary conditions requires only a little more CPU time (less than 10% in our tests) than the simplest first-order condition (5.4). We have verified that our implementation of this boundary condition had the same efficiency with respect to transparency for dipolar and quadrupolar waves as the Sommerfeld condition (5.4) for monopolar waves. The precision increases very rapidly (like $1/R^4$) as one imposes the boundary condition further from the source of radiation. These two points are of great interest for the simulation of gravitational radiation from isolated astrophysical sources.

As an alternative, one can cite that more accurate results may be obtained using the so-called 2+2 formalism in the wave zone [154] and matching it to the results in 3+1 formalism¹ near the source.

¹this is the *characteristic-Cauchy* matching, CCM

Our approach is different, much simpler to implement and should give accurate enough results for the Einstein equations.

Chapitre 6

A spectral method for the wave equation of divergence-free vectors and symmetric tensors inside a sphere

Version publiée : J. Novak, J.-L. Cornou et N. Vasset, *Journal of Computational Physics* **229**, pp. 399-414 (2010).

Sommaire

6.1	Introduction	201
6.2	Vector case	204
6.3	Symmetric tensor case	208
6.4	Boundary conditions	214
6.5	Numerical tests	218
6.6	Concluding remarks	222

6.1 Introduction

Evolution partial differential equations (PDE) for vector fields under the divergence-free constraint appear in many physical models. Similar problems are to be solved with second-rank tensor fields. In most of these equations, if the initial data and boundary conditions satisfy the divergence-free condition, then the solution on a given time interval is divergence-free too. But from the numerical point of view, things can be more complicated and round-off errors can create undesired solutions, which may then trigger growing unphysical modes. Therefore, in the case of vector fields, several methods for the numerical solution of such PDEs have been devised, such as the constraint transport method [167] or the toroidal-poloidal decomposition [160, 310]. The aim of this paper is to present a new method for the case of symmetric tensor fields, which appear in general relativity within the so-called 3+1 approach [7], keeping in mind the vector case for which the method can be closely related to the toroidal-poloidal approach. We first give motivations for the numerical study of divergence-free vectors and tensors in Secs. 6.1.1 and 6.1.2; we briefly introduce our notations and conventions for

spherical coordinates and grid in Sec. 6.1.3. The case of the vector divergence-free evolution is studied in Sec. 6.2, and the link with the poloidal-toroidal decomposition is detailed in Sec. 6.2.3. We then turn to the symmetric tensor case in Sec. 6.3 with the particular traceless condition in Sec. 6.3.3. A discussion of the treatment of boundary conditions is given in Sec. 6.4, with the particular point of inner boundary conditions (Sec. 6.4.3). Finally, some numerical experiments are reported in Sec. 6.5 to support our algorithms and concluding remarks are given in Sec. 6.6.

6.1.1 Divergence-free vector fields in relativistic magneto-hydrodynamics

In classical electrodynamics, the magnetic field is known to be divergence-free since Maxwell's equations. This result can be extended to general relativistic electrodynamics as well. In classical hydrodynamics, the continuity equation can be expressed as $\partial_t \rho + \nabla \cdot (\rho \mathbf{u}) = 0$, where ρ is the mass density of the fluid, and \mathbf{u} its velocity. Various approximations give rise to divergence-free vectors. Incompressible fluids have constant density along flow lines and therefore verify that their velocity field \mathbf{u} is divergence-free. Water is probably the most common example of an incompressible fluid. In an astrophysical context, the incompressible approximation can lead to a pretty good approximation of the behavior of compressible fluid provided that the flow's Mach number is much smaller than unity. Another useful hydrodynamic approximation is the anelastic approximation, which essentially consists in filtering out the sound waves, whose extremely short time scale would otherwise force the use of an impractically small time step for numerical purposes. In general-relativistic magneto-hydrodynamics, the anelastic approximation takes the form $\nabla \cdot (\rho \Gamma \mathbf{u}) = 0$, where \mathbf{u} is the coordinate fluid velocity, Γ the Lorentz factor of the fluid, and ρ its rest-mass density.

Divergence-free vectors have given rise to a large literature in numerical simulations. For example, while using an induction equation to numerically evolve a magnetic field, there is no guarantee that the divergence of the updated magnetic field is numerically conserved. The most common methods to conserve divergences in hyperbolic systems are constrained transport methods, projection methods or hyperbolic divergence cleaning methods (see [470] for a review).

6.1.2 Divergence-free symmetric tensors in general relativity

The basic formalism of general relativity uses four-dimensional objects and, in particular, symmetric four-tensors as the metric or the stress-energy tensor. A choice of the gauge, which comes naturally to describe the propagation of gravitational waves is the *harmonic gauge* (e.g. [144]), for which the divergence of the four-metric is zero. The 3+1 formalism (see [7] for a review) is an approach to general relativity introducing a slicing of the four-dimensional spacetime by three-dimensional spacelike surfaces, which have a Riemannian induced three-metric. With this formalism, the four-dimensional tensors of general relativity are projected onto these three-surfaces as three-dimensional tensors. Consequently, the choice of the gauge on the three-surface is a major issue for the computation of the solutions of Einstein's equations.

The divergence-free condition on the conformal three-metric has already been put forward by Dirac [156] in Cartesian coordinates, and generalized to any type of coordinates in [73]. This conformal three-metric obeys an evolution equation which can be cast into a wave-like propagation equation. Far from any strong source of gravitational field, this evolution equation tends to a tensor wave equation, under the gauge constraint. With the choice of the generalized Dirac gauge this translates into the

system we study in Sec. 6.3, with the addition of one extra constraint: the fact that the determinant of the conformal metric must be one (Eq. (167) of [73]).

The choice of spherical coordinates and components comes naturally with the study of isolated spheroidal objects as relativistic stars or black holes. Moreover, boundary conditions for the metric or for the hydrodynamics equations can be better expressed and implemented using tensor or vector components in the spherical basis. The numerical simulations of astrophysically relevant objects in general relativity must therefore be able to deal with the evolution of divergence-free symmetric tensors, in spherical coordinates and components. A particular care must be given to the fulfillment of the divergence-free condition, since this additional constraint sets the spatial gauge on the spacetime.

6.1.3 Spherical components and coordinates

In the following, unless specified, all the vector and tensor fields shall be functions of the four space-time coordinates $\mathbf{V}(t, r, \theta, \varphi)$ and $\mathbf{h}(t, r, \theta, \varphi)$, where (r, θ, φ) are the polar spherical coordinates. The associated spherical *orthonormal* basis is defined as:

$$\mathbf{e}_r = \frac{\partial}{\partial r}, \quad \mathbf{e}_\theta = \frac{1}{r} \frac{\partial}{\partial \theta}, \quad \mathbf{e}_\varphi = \frac{1}{r \sin \theta} \frac{\partial}{\partial \varphi}. \quad (6.1)$$

The vector and symmetric tensor fields shall be described by their contravariant components $\{V^r, V^\theta, V^\varphi\}$ and $\{h^{rr}, h^{r\theta}, h^{r\varphi}, h^{\theta\theta}, h^{\theta\varphi}, h^{\varphi\varphi}\}$, using this spherical basis:

$$\mathbf{V} = \sum_{i=r,\theta,\varphi} V^i \mathbf{e}_i, \quad \mathbf{h} = \sum_{i=r,\theta,\varphi} \sum_{j=r,\theta,\varphi} h^{ij} \mathbf{e}_i \otimes \mathbf{e}_j. \quad (6.2)$$

The scalar Laplace operator acting on a field $\phi(r, \theta, \varphi)$ is written:

$$\Delta \phi = \frac{\partial^2 \phi}{\partial r^2} + \frac{2}{r} \frac{\partial \phi}{\partial r} + \frac{1}{r^2} \Delta_{\theta\varphi} \phi, \quad (6.3)$$

where $\Delta_{\theta\varphi}$ is the angular part of the Laplace operator, containing only derivatives with respect to θ or φ :

$$\Delta_{\theta\varphi} \phi = \frac{\partial^2 \phi}{\partial \theta^2} + \frac{\cos \theta}{\sin \theta} \frac{\partial \phi}{\partial \theta} + \frac{1}{\sin^2 \theta} \frac{\partial^2 \phi}{\partial \varphi^2}. \quad (6.4)$$

We now introduce scalar spherical harmonics, defined on the sphere as (see Sec. 18.11 of [85] for more details)

$$\forall \ell \geq 0, \forall m, 0 \leq m \leq \ell, \quad Y_\ell^m(\theta, \varphi) = e^{im\varphi} P_\ell^m(\cos \theta), \quad (6.5)$$

where P_ℓ^m is the associated Legendre function. For negative m , spherical harmonics are defined

$$\forall m, -\ell \leq m < 0, \quad Y_\ell^m(\theta, \varphi) = (-1)^m e^{im\varphi} P_\ell^{|m|}(\cos \theta). \quad (6.6)$$

Their two main properties used in this study are that they form a complete basis for the development of regular scalar functions on the sphere, and that they are eigenfunctions of the angular Laplace operator:

$$\forall (\ell, m), \quad \Delta_{\theta\varphi} Y_\ell^m = -\ell(\ell + 1) Y_\ell^m. \quad (6.7)$$

6.2 Vector case

We look for the solution of the following initial-boundary value problem of unknown vector \mathbf{V} , inside a sphere of (constant) radius R , thus $\forall(\theta, \varphi)$:

$$\forall t \geq 0, \forall r < R, \quad \frac{\partial^2 \mathbf{V}}{\partial t^2} = \Delta \mathbf{V}, \quad (6.8)$$

$$\forall t \geq 0, \forall r \leq R, \quad \nabla \cdot \mathbf{V} = 0, \quad (6.9)$$

$$\forall r \leq R, \quad \mathbf{V}(0, r, \theta, \varphi) = \mathbf{v}_0(r, \theta, \varphi),$$

$$\forall r \leq R, \quad \left. \frac{\partial \mathbf{V}}{\partial t} \right|_{t=0} = \mathbf{w}_0(r, \theta, \varphi),$$

$$\forall t \geq 0, \quad \mathbf{V}(t, R, \theta, \varphi) = \mathbf{b}_0(t, \theta, \varphi). \quad (6.10)$$

\mathbf{v}_0 , \mathbf{w}_0 and \mathbf{b}_0 are given regular functions for initial data and boundary conditions, respectively. Δ is the vector Laplace operator, which in spherical coordinates and in the contravariant representation (6.2) using the orthonormal basis (6.1) reads:

$$(\Delta \mathbf{V})^r = \frac{\partial^2 V^r}{\partial r^2} + \frac{4}{r} \frac{\partial V^r}{\partial r} + \frac{2V^r}{r^2} + \frac{1}{r^2} \Delta_{\theta\varphi} V^r - \frac{2}{r} \Theta, \quad (6.11)$$

$$(\Delta \mathbf{V})^\theta = \frac{\partial^2 V^\theta}{\partial r^2} + \frac{2}{r} \frac{\partial V^\theta}{\partial r} + \frac{1}{r^2} \left(\Delta_{\theta\varphi} V^\theta + 2 \frac{\partial V^r}{\partial \theta} - \frac{V^\theta}{\sin^2 \theta} - 2 \frac{\cos \theta}{\sin^2 \theta} \frac{\partial V^\varphi}{\partial \varphi} \right),$$

$$(\Delta \mathbf{V})^\varphi = \frac{\partial^2 V^\varphi}{\partial r^2} + \frac{2}{r} \frac{\partial V^\varphi}{\partial r} + \frac{1}{r^2} \left(\Delta_{\theta\varphi} V^\varphi + \frac{2}{\sin \theta} \frac{\partial V^r}{\partial \varphi} + 2 \frac{\cos \theta}{\sin^2 \theta} \frac{\partial V^\theta}{\partial \varphi} - \frac{V^\varphi}{\sin^2 \theta} \right),$$

with the divergence Θ

$$\Theta \equiv \nabla \cdot \mathbf{V} = \frac{\partial V^r}{\partial r} + \frac{2V^r}{r} + \frac{1}{r} \left(\frac{\partial V^\theta}{\partial \theta} + \frac{V^\theta}{\tan \theta} + \frac{1}{\sin \theta} \frac{\partial V^\varphi}{\partial \varphi} \right). \quad (6.12)$$

One can remark that a necessary condition for this system to be well-posed is that

$$\nabla \cdot \mathbf{v}_0 = \nabla \cdot \mathbf{w}_0 = 0. \quad (6.13)$$

In addition, the boundary setting at $r = R$ is actually overdetermined: the three conditions are not independent because of the divergence constraint. This aspect of the problem will be developed in more details in Sec. 6.4.1.

In the rest of this Section, we devise a method to verify both equations (6.8) and (6.9). This technique is similar to that presented in [74] with the difference that we motivate it by the use of vector spherical harmonics, and can easily be related to the poloidal-toroidal decomposition method, as discussed in Sec. 6.2.3.

6.2.1 Decomposition on vector spherical harmonics

The first step is to decompose the angular dependence of the vector field \mathbf{V} onto a basis of *pure spin vector harmonics* (see [464] for a review):

$$\mathbf{V}(t, r, \theta, \varphi) = \sum_{\ell, m} \left(E^{\ell m}(t, r) \mathbf{Y}_{\ell m}^E + B^{\ell m}(t, r) \mathbf{Y}_{\ell m}^B + R^{\ell m}(t, r) \mathbf{Y}_{\ell m}^R \right), \quad (6.14)$$

defined from the scalar spherical harmonics as

$$\forall \ell > 0, \forall -\ell \leq m \leq \ell, \mathbf{Y}_{\ell m}^E = r \nabla Y_{\ell}^m, \quad (6.15)$$

$$\forall \ell > 0, \forall -\ell \leq m \leq \ell, \mathbf{Y}_{\ell m}^B = \mathbf{e}_r \times \mathbf{Y}_{\ell m}^E, \quad (6.16)$$

$$\forall \ell \geq 0, \forall -\ell \leq m \leq \ell, \mathbf{Y}_{\ell m}^R = Y_{\ell}^m \mathbf{e}_r; \quad (6.17)$$

where ∇ is the gradient in the orthonormal basis (6.1). Note that both $\mathbf{Y}_{\ell m}^E$ and $\mathbf{Y}_{\ell m}^B$ are purely transverse, whereas $\mathbf{Y}_{\ell m}^R$ is purely radial. From this decomposition, we define the *pure spin* components of \mathbf{V} by summing all the multipoles with *scalar* spherical harmonics (6.5):

$$V^{\eta}(t, r, \theta, \varphi) = \sum_{\ell, m} E^{\ell m} Y_{\ell}^m, \quad (6.18)$$

$$V^{\mu}(t, r, \theta, \varphi) = \sum_{\ell, m} B^{\ell m} Y_{\ell}^m, \quad (6.19)$$

the last one being the usual r -component

$$\sum_{\ell, m} R^{\ell m} Y_{\ell}^m = V^r. \quad (6.20)$$

The advantages of these pure spin components are first, that by construction they can be expanded onto the scalar spherical harmonic basis, and second, that angular derivatives appearing in all equations considered transform into the angular Laplace operator (6.7).

To be more explicit, (V^{η}, V^{μ}) can be related to the vector spherical components by (see also [73]):

$$\begin{aligned} V^{\theta} &= \frac{\partial V^{\eta}}{\partial \theta} - \frac{1}{\sin \theta} \frac{\partial V^{\mu}}{\partial \varphi}, \\ V^{\varphi} &= \frac{1}{\sin \theta} \frac{\partial V^{\eta}}{\partial \varphi} + \frac{\partial V^{\mu}}{\partial \theta}; \end{aligned} \quad (6.21)$$

and inversely

$$\Delta_{\theta\varphi} V^{\eta} = \frac{\partial V^{\theta}}{\partial \theta} + \frac{V^{\theta}}{\tan \theta} + \frac{1}{\sin \theta} \frac{\partial V^{\varphi}}{\partial \varphi}, \quad (6.22)$$

$$\Delta_{\theta\varphi} V^{\mu} = \frac{\partial V^{\varphi}}{\partial \theta} + \frac{V^{\varphi}}{\tan \theta} - \frac{1}{\sin \theta} \frac{\partial V^{\theta}}{\partial \varphi}. \quad (6.23)$$

Let us here point out that the angular Laplace operator $\Delta_{\theta\varphi}$ is diagonal with respect to the functional basis of spherical harmonics and, therefore, the above relations can directly be used to obtain V^{η} and V^{μ} .

Thus, if the fields are defined on the whole sphere $\theta \in [0, \pi]$, $\varphi \in [0, 2\pi]$, it is possible to transform the usual components $(V^{\theta}, V^{\varphi})$ to the pure spin ones (V^{η}, V^{μ}) by this one-to-one transformation, up to a constant ($\ell = 0$ part) for V^{η} and V^{μ} . Since this constant is not relevant, it shall be set to zero and disregarded in the following. Therefore, a vector field shall be represented equivalently by its usual spherical components or by (V^r, V^{η}, V^{μ}) .

6.2.2 Divergence-free degrees of freedom

From the vector spherical harmonic decomposition, we now compute two scalar fields that represent the divergence-free degrees of freedom of a vector. We start from the divergence of a general vector \mathbf{W} , expressed in terms of pure spin components:

$$\Theta = \frac{\partial W^r}{\partial r} + 2\frac{W^r}{r} + \frac{1}{r}\Delta_{\theta\varphi}W^\eta; \quad (6.24)$$

where W^η has been computed for the vector \mathbf{W} from Eq. (6.22). This shows that the divergence of \mathbf{W} does not depend on the pure spin component W^μ . On the other hand, it is well-known that any sufficiently smooth and rapidly decaying vector field \mathbf{W} can be (uniquely on \mathbb{R}^3) decomposed as a sum of a gradient and a divergence-free part (Helmholtz's theorem)

$$\mathbf{W} = \nabla\phi + \mathbf{D}_0, \quad (6.25)$$

with $\nabla \cdot \mathbf{D}_0 = 0$. From the formula (6.23), one can check that the component W^μ only depends on \mathbf{D}_0 . Next, taking the curl of \mathbf{W} and, in particular, combining the θ - and φ - components of this curl, one has that $\partial_r W^\eta + \frac{W^\eta}{r} - \frac{W^r}{r}$ has the same property of being invariant under the addition of any gradient field to \mathbf{W} , thus depends only on \mathbf{D}_0 . Therefore, we define the potential

$$A = \frac{\partial W^\eta}{\partial r} + \frac{W^\eta}{r} - \frac{W^r}{r}. \quad (6.26)$$

As a consequence, we have that

$$\mathbf{D}_0 = 0 \iff W^\mu = 0 \text{ and } A = 0. \quad (6.27)$$

We have thus identified two scalar degrees of freedom for a divergence-free vector field, which can be easily related to the well-known poloidal-toroidal decomposition (Sec. 6.2.3), but have the advantage of being generalizable to the symmetric tensor case.

We now write the wave equation (6.8) in terms of V^μ and A (computed from V^r and V^η). It is first interesting to examine the pure spin components of the vector Laplace operator (6.11):

$$(\Delta \mathbf{V})^\eta = \Delta V^\eta + 2\frac{V^r}{r^2}, \quad (6.28)$$

$$(\Delta \mathbf{V})^\mu = \Delta V^\mu; \quad (6.29)$$

one sees that the equation for V^μ decouples from the system, therefore Eq. (6.8) implies that

$$\frac{\partial^2 V^\mu}{\partial t^2} = \Delta V^\mu. \quad (6.30)$$

Forming then from (6.11) and (6.28) an equation for the potential A , which is a consequence of the original wave equation (6.8), we obtain

$$\frac{\partial^2 A}{\partial t^2} = \Delta A. \quad (6.31)$$

We are left with two scalar wave equations, (6.30) and (6.31), for the divergence-free part of the vector field \mathbf{V} . The recovery of the full vector field shall be discussed in Sec. 6.2.4; the treatment of boundary conditions shall be presented in Sec. 6.4.1.

6.2.3 Link with poloidal-toroidal decomposition

According to the classical poloidal-toroidal decomposition, a divergence-free vector field \mathbf{F} can be considered to be generated by two scalar potentials Φ and Ψ , via

$$\mathbf{F} = \nabla \times (\Psi \mathbf{k}) + \nabla \times \nabla \times (\Phi \mathbf{k}) \quad (6.32)$$

Here, \mathbf{k} is a unit vector, called the pilot vector, which is chosen according to the geometry of the problem considered. In [83, 84], \mathbf{k} is chosen to be \mathbf{e}_z in cylindrical coordinates. One can also find the decomposition $\mathbf{F} = \nabla \times (A(r, \theta) \mathbf{e}_\varphi) + B(r, \theta) \mathbf{e}_\varphi$ when considering axisymmetric solenoidal fields (see for example [254]). The latter representation makes A appear clearly as a poloidal component, and B as a toroidal component. In order to link the general poloidal-toroidal formalism to our previous potentials, we chose $\mathbf{k} = \mathbf{e}_r$ in spherical coordinates (sometimes called the Mie decomposition, see [158]). Then, one can show that

$$\mathbf{F} = -\frac{1}{r^2} \Delta_{\theta\varphi} \Phi \mathbf{e}_r + \frac{1}{r} \left(\frac{1}{\sin \theta} \partial_\varphi \Psi + \partial_\theta \partial_r \Phi \right) \mathbf{e}_\theta + \frac{1}{r} \left(-\partial_\theta \Psi + \frac{1}{\sin \theta} \partial_\varphi \partial_r \Phi \right) \mathbf{e}_\varphi \quad (6.33)$$

Hence, we can identify the former pure spin components F^η and F^μ through

$$\begin{aligned} F^\eta &= \frac{1}{r} \partial_r \Phi \\ F^\mu &= -\frac{1}{r} \Psi \end{aligned}$$

Therefore, the potential A is linked to the potential Φ via

$$A = \frac{1}{r} \partial_r^2 \Phi + \frac{1}{r^3} \Delta_{\theta\varphi} \Phi = \Delta \left(\frac{\Phi}{r} \right) \quad (6.34)$$

which gives us a compatibility condition

$$\Delta_{\theta\varphi} A = -\Delta(rF^r) \quad (6.35)$$

The latter equation expresses that $\partial_r(r^2\Theta) = 0$ for the original vector. Since our vector is a regular function of coordinates, it expresses that $\Theta = 0$.

One can also show the following relations

$$\begin{aligned} \mathbf{e}_r \cdot \nabla \times \mathbf{F} &= \frac{1}{r} \Delta_{\theta\varphi} F^\mu \\ \mathbf{e}_r \cdot \nabla \times \nabla \times \mathbf{F} &= \frac{1}{r} \Delta_{\theta\varphi} A \end{aligned}$$

6.2.4 Integration scheme

We defer to Sec. 6.5.1 the numerical details about the integration procedure, and we sketch here the various steps. From the result of Sec. 6.2.2, the problem (6.8)-(6.9) can be transformed into two initial-value boundary problems, for the component V^μ (6.30) and the potential A (6.31) respectively. Initial data can be deduced from \mathbf{v}_0 and \mathbf{w}_0 , so that $V^\mu(t=0)$ and $\partial V^\mu/\partial t(t=0)$ are the μ -components of, respectively, \mathbf{v}_0 and \mathbf{w}_0 . The same is true for the A potential. The determination of boundary conditions from the knowledge of \mathbf{b}_0 shall be discussed in Sec. 6.4. We therefore assume here that

we have computed the component V^μ and the potential A , inside the sphere of radius R , for a given interval $[0, T]$, and we show how to recover the whole vector \mathbf{V} .

The pure spin components (V^r, V^η) of the vector \mathbf{V} are obtained by solving the system of PDEs composed by the definition of the potential A (6.26), together with the divergence-free condition (6.24). From their definitions (6.18)-(6.20), it is clear that the angular parts of both V^r and V^η can be decomposed onto the basis of scalar spherical harmonics, and therefore A as well:

$$A(t, r, \theta, \varphi) = \sum_{\ell, m} A^{\ell m}(t, r) Y_\ell^m(\theta, \varphi). \quad (6.36)$$

We are left with the following set of systems of ordinary differential equations in the r -coordinate:

$$\forall \ell > 0, \forall m \quad -\ell \leq m \leq \ell, \quad \begin{cases} \frac{\partial R^{\ell m}}{\partial r} + 2\frac{R^{\ell m}}{r} - \frac{\ell(\ell+1)}{r} E^{\ell m} = 0 \\ \frac{\partial E^{\ell m}}{\partial r} + \frac{E^{\ell m}}{r} - \frac{R^{\ell m}}{r} = A^{\ell m} \end{cases}. \quad (6.37)$$

The potential A being given, the pure spin components V^r and V^η are obtained from this system, with the boundary conditions discussed in Sec. 6.4.1. The μ -component is already known too, so it is possible to compute the spherical components of $\mathbf{V} \forall t \in [0, T]$, from Eqs. (6.21). Note that all angular derivatives present in this system (6.37) are only in the form of the angular Laplace operator $\Delta_{\theta\varphi}$ (6.4). It must also be emphasized that the divergence-free condition is not enforced in terms of spherical components (Eq. (6.12)), but in terms of pure spin components. Thus, if the value of the divergence is numerically checked, it shall be higher than machine precision, because of the numerical derivatives one must compute to pass from pure spin to spherical components (Eqs. (6.21)).

The properties of the system (6.37) are easy to study. Substituting $R^{\ell m}$ in the first line by its expression as a function of $E^{\ell m}$ and $A^{\ell m}$ (obtained from the second line), one gets a simple Poisson equation:

$$\Delta \left(r E^{\ell m} \right) = r \frac{\partial A^{\ell m}}{\partial r} + 2 A^{\ell m}. \quad (6.38)$$

The discussion about boundary conditions, homogeneous solutions and regularity for $r = 0$ and $r \rightarrow \infty$ are immediately deduced from those of the Poisson equation (see e.g. [228]).

In the case where a source \mathbf{S} is present on the right-hand side of the problem (6.8), the method of imposing $\nabla \cdot \mathbf{V} = 0$ can be generalized by adding sources to Eqs. (6.30)-(6.31), which are deduced from \mathbf{S} . Indeed, it is easy to show that the source for the equation for V^μ is the pure spin μ -component of \mathbf{S} and the source for the equation for A is the equivalent potential computed from \mathbf{S} pure spin components, using formula (6.26). Note that an integrability condition for this problem is that the source be divergence-free too. Therefore, for a well-posed problem, any gradient term present in \mathbf{S} can be considered as spurious and is naturally removed by this method, since the μ -component and the A potential are both insensitive to the gradient parts.

6.3 Symmetric tensor case

Similarly to the vector case studied in Sec. 6.2, we look here for the solution of an initial-boundary value problem of unknown symmetric tensor \mathbf{h} , inside a sphere of radius R . As explained in Sec. 6.1.3, the symmetric tensor \mathbf{h} shall be represented by its contravariant components $h^{ij}(=h^{ji})$, where the

indices run from 1(r) to 3(φ); moreover, we suppose that all components of \mathbf{h} decay to zero at least as fast as $1/r$, as $r \rightarrow \infty$. We shall also use the Einstein summation convention over repeated indices.

Thus the problem is written, $\forall(\theta, \varphi)$:

$$\forall t \geq 0, \forall r < R, \quad \frac{\partial^2 h^{ij}}{\partial t^2} = \Delta h^{ij}, \quad (6.39)$$

$$\forall t \geq 0, \forall r \leq R, \quad \nabla_j h^{ij} = 0, \quad (6.40)$$

$$\forall r \leq R, \quad h^{ij}(0, r, \theta, \varphi) = \alpha_0^{ij}(r, \theta, \varphi),$$

$$\forall r \leq R, \quad \left. \frac{\partial h^{ij}}{\partial t} \right|_{t=0} = \gamma_0^{ij}(r, \theta, \varphi),$$

$$\forall t \geq 0, \quad h^{ij}(t, R, \theta, \varphi) = \beta_0^{ij}(t, \theta, \varphi). \quad (6.41)$$

The tensors $\alpha_0^{ij}, \gamma_0^{ij}$ and β_0^{ij} are given regular functions for initial data and boundary conditions, respectively. The full expression of the tensor Laplace operator in spherical coordinates and in the orthonormal spherical basis (6.1) is given by Eqs. (123)-(128) of [73] and shall not be recalled here. We point out again that the boundary setting at $r = R$ is overdetermined: this is discussed in more detail in Sec. 6.4.2.

We introduce the vector \mathbf{H} , defined as the divergence of h^{ij} and given in the spherical contravariant components (6.2) by:

$$H^i \equiv \nabla_j h^{ij} \iff \begin{cases} H^r = \frac{\partial h^{rr}}{\partial r} + \frac{2h^{rr}}{r} + \frac{1}{r} \left(\frac{\partial h^{r\theta}}{\partial \theta} + \frac{1}{\sin \theta} \frac{\partial h^{r\varphi}}{\partial \varphi} - h^{\theta\theta} - h^{\varphi\varphi} + \frac{h^{r\theta}}{\tan \theta} \right), \\ H^\theta = \frac{\partial h^{r\theta}}{\partial r} + \frac{3h^{r\theta}}{r} + \frac{1}{r} \left(\frac{\partial h^{\theta\theta}}{\partial \theta} + \frac{1}{\sin \theta} \frac{\partial h^{\theta\varphi}}{\partial \varphi} + \frac{1}{\tan \theta} (h^{\theta\theta} - h^{\varphi\varphi}) \right), \\ H^\varphi = \frac{\partial h^{r\varphi}}{\partial r} + \frac{3h^{r\varphi}}{r} + \frac{1}{r} \left(\frac{\partial h^{\theta\varphi}}{\partial \theta} + \frac{1}{\sin \theta} \frac{\partial h^{\varphi\varphi}}{\partial \varphi} + \frac{2h^{\theta\varphi}}{\tan \theta} \right) = 0. \end{cases} \quad (6.42)$$

We now detail, in the rest of this Section, a method to verify both evolution equation (6.39) and the divergence-free constraint (6.40).

6.3.1 Decomposition on tensor spherical harmonics

As in the vector case (Sec. 6.2.1), we start by decomposing the angular dependence of the tensor field h^{ij} onto *pure spin tensor harmonics*, introduced by [313] and [498] (we again use the notations of [464]):

$$\mathbf{h}(t, r, \theta, \varphi) = \sum_{\ell, m} \left(L_0^{\ell m} \mathbf{T}_{\ell m}^{L_0} + T_0^{\ell m} \mathbf{T}_{\ell m}^{T_0} + E_1^{\ell m} \mathbf{T}_{\ell m}^{E_1} + B_1^{\ell m} \mathbf{T}_{\ell m}^{B_1} + E_2^{\ell m} \mathbf{T}_{\ell m}^{E_2} + B_2^{\ell m} \mathbf{T}_{\ell m}^{B_2} \right), \quad (6.43)$$

where $(L_0^{\ell m}, T_0^{\ell m}, E_1^{\ell m}, B_1^{\ell m}, E_2^{\ell m}, B_2^{\ell m})$ are all functions of only (t, r) . Complete definitions and properties of this set of tensor harmonics can be found in [464]. Note that these harmonics have been devised in order to describe gravitational radiation, far from any source. In that respect, the most relevant harmonics are \mathbf{T}^{E_2} and \mathbf{T}^{B_2} , since they are transverse and traceless. The pure spin components

of the tensor \mathbf{h} are defined as:

$$h^{rr}(t, r, \theta, \varphi) = \sum_{\ell, m} L_0^{\ell m} Y_\ell^m, \quad (6.44)$$

$$h^\tau(t, r, \theta, \varphi) = \sum_{\ell, m} T_0^{\ell m} Y_\ell^m, \quad (6.45)$$

$$h^\eta(t, r, \theta, \varphi) = \sum_{\ell, m} E_1^{\ell m} Y_\ell^m, \quad (6.46)$$

$$h^\mu(t, r, \theta, \varphi) = \sum_{\ell, m} B_1^{\ell m} Y_\ell^m, \quad (6.47)$$

$$h^{\mathcal{W}}(t, r, \theta, \varphi) = \sum_{\ell, m} E_2^{\ell m} Y_\ell^m, \quad (6.48)$$

$$h^{\mathcal{X}}(t, r, \theta, \varphi) = \sum_{\ell, m} B_2^{\ell m} Y_\ell^m. \quad (6.49)$$

Explicit relations between the last five components and the usual spherical components (6.2) are now given.

$$h^\tau = h^{\theta\theta} + h^{\varphi\varphi} \quad (6.50)$$

is transverse; and the total trace is simply given by

$$h = h^{rr} + h^\tau. \quad (6.51)$$

In the following we shall use either the component h^τ or the trace. The components h^η and h^μ have similar formulas to those of the vector pure spin components, as $\{h^{ri}\}_{i=1,2,3}$ can be seen as a vector:

$$h^{r\theta} = \frac{\partial h^\eta}{\partial \theta} - \frac{1}{\sin \theta} \frac{\partial h^\mu}{\partial \varphi}, \quad (6.52)$$

$$h^{r\varphi} = \frac{1}{\sin \theta} \frac{\partial h^\eta}{\partial \varphi} + \frac{\partial h^\mu}{\partial \theta};$$

the reverse formula being similar to Eqs. (6.22) and (6.23), they are not recalled here. Finally, the last two components are obtained by:

$$P \equiv \frac{(h^{\theta\theta} - h^{\varphi\varphi})}{2} = \frac{\partial^2 h^{\mathcal{W}}}{\partial \theta^2} - \frac{1}{\tan \theta} \frac{\partial h^{\mathcal{W}}}{\partial \theta} - \frac{1}{\sin^2 \theta} \frac{\partial^2 h^{\mathcal{W}}}{\partial \varphi^2} - 2 \frac{\partial}{\partial \theta} \left(\frac{1}{\sin \theta} \frac{\partial h^{\mathcal{X}}}{\partial \varphi} \right), \quad (6.53)$$

$$h^{\theta\varphi} = \frac{\partial^2 h^{\mathcal{X}}}{\partial \theta^2} - \frac{1}{\tan \theta} \frac{\partial h^{\mathcal{X}}}{\partial \theta} - \frac{1}{\sin^2 \theta} \frac{\partial^2 h^{\mathcal{X}}}{\partial \varphi^2} + 2 \frac{\partial}{\partial \theta} \left(\frac{1}{\sin \theta} \frac{\partial h^{\mathcal{W}}}{\partial \varphi} \right);$$

and the inverse relations are given by:

$$\Delta_{\theta\varphi} (\Delta_{\theta\varphi} + 2) h^{\mathcal{W}} = \frac{\partial^2 P}{\partial \theta^2} + \frac{3}{\tan \theta} \frac{\partial P}{\partial \theta} - \frac{1}{\sin^2 \theta} \frac{\partial^2 P}{\partial \varphi^2} - 2P + \frac{2}{\sin \theta} \frac{\partial}{\partial \varphi} \left(\frac{\partial h^{\theta\varphi}}{\partial \theta} + \frac{h^{\theta\varphi}}{\tan \theta} \right), \quad (6.54)$$

$$\Delta_{\theta\varphi} (\Delta_{\theta\varphi} + 2) h^{\mathcal{X}} = \frac{\partial^2 h^{\theta\varphi}}{\partial \theta^2} + \frac{3}{\tan \theta} \frac{\partial h^{\theta\varphi}}{\partial \theta} - \frac{1}{\sin^2 \theta} \frac{\partial^2 h^{\theta\varphi}}{\partial \varphi^2} - 2h^{\theta\varphi} - \frac{2}{\sin \theta} \frac{\partial}{\partial \varphi} \left(\frac{\partial P}{\partial \theta} + \frac{P}{\tan \theta} \right). \quad (6.55)$$

Here as for the vector case, the h^η and h^μ components do not contain any relevant $\ell = 0$ term, whereas $h^{\mathcal{W}}$ and $h^{\mathcal{X}}$ contain neither $\ell = 0$, nor $\ell = 1$ terms, as expected for transverse traceless parts of the tensor \mathbf{h} . We shall use any set of components of the tensor \mathbf{h} : either the usual ones $\{h^{ij}\}$, using the spherical basis, or the pure spin ones $\{h^{rr}, h^\tau$ (or h), $h^\eta, h^\mu, h^{\mathcal{W}}, h^{\mathcal{X}}\}$.

6.3.2 Divergence-free degrees of freedom

The vector \mathbf{H} defined as the divergence of \mathbf{h} in Eq. (6.42) can be expanded in terms of vector pure spin components, which are then written as functions of the tensor pure spin components of \mathbf{h} (we use the trace h instead of h^τ):

$$H^r = \frac{\partial h^{rr}}{\partial r} + \frac{3h^{rr}}{r} + \frac{1}{r} (\Delta_{\theta\varphi} h^\eta - h), \quad (6.56)$$

$$H^\eta = \Delta_{\theta\varphi} \left[\frac{\partial h^\eta}{\partial r} + \frac{3h^\eta}{r} + \frac{1}{r} \left((\Delta_{\theta\varphi} + 2) h^\mathcal{W} + \frac{h - h^{rr}}{2} \right) \right], \quad (6.57)$$

$$H^\mu = \Delta_{\theta\varphi} \left[\frac{\partial h^\mu}{\partial r} + \frac{3h^\mu}{r} + \frac{1}{r} (\Delta_{\theta\varphi} + 2) h^\mathcal{X} \right]. \quad (6.58)$$

A possible generalization of the Helmholtz theorem to the symmetric tensor case is that, for any sufficiently smooth and rapidly decaying symmetric tensor field \mathbf{T} , one can find a unique (on \mathbb{R}^3) decomposition of the form

$$T^{ij} = \nabla^i L^j + \nabla^j L^i + h_0^{ij}, \quad (6.59)$$

with $\nabla_j h_0^{ij} = 0$. With these definitions, $\nabla_j T^{ij} = 0 \iff L^i = 0$ which means that, from the six scalar degrees of freedom of the symmetric tensor T^{ij} , the three longitudinal ones can be represented by the three components of the vector \mathbf{L} . Therefore, the divergence-free symmetric tensor h_0^{ij} has only three scalar degrees of freedom that we exhibit hereafter.

One can check that the three scalar potentials defined by

$$\mathcal{A} = \frac{\partial T^\mathcal{X}}{\partial r} - \frac{T^\mu}{r}, \quad (6.60)$$

$$\mathcal{B} = \frac{\partial T^\mathcal{W}}{\partial r} - \frac{1}{2r} \Delta_{\theta\varphi} T^\mathcal{W} - \frac{T^\eta}{r} + \frac{T - T^{rr}}{4r}, \quad (6.61)$$

$$\mathcal{C} = \frac{\partial T}{\partial r} - \frac{\partial T^{rr}}{\partial r} + \frac{T}{r} - \frac{3T^{rr}}{r} - 2\Delta_{\theta\varphi} \left(\frac{\partial T^\mathcal{W}}{\partial r} + \frac{T^\mathcal{W}}{r} \right), \quad (6.62)$$

satisfy the property

$$\mathcal{A} = \mathcal{B} = \mathcal{C} = 0 \iff \mathbf{h}_0 = 0, \quad (6.63)$$

and represent the three divergence-free scalar degrees of freedom of a symmetric tensor.

In order to write the wave equation (6.39) in terms of these potentials, we first express the pure spin components of the tensor Laplace operator acting on a general symmetric tensor \mathbf{h} :

$$(\Delta \mathbf{h})^{rr} = \Delta h^{rr} - \frac{6h^{rr}}{r^2} - \frac{4}{r^2} \Delta_{\theta\varphi} h^\eta + \frac{2h}{r^2} \quad (6.64)$$

$$(\Delta \mathbf{h})^\eta = \Delta h^\eta + \frac{2}{r} \frac{\partial h^\eta}{\partial r} + \frac{2h^\eta}{r^2} - \frac{2}{r} \left(\frac{\partial h^\eta}{\partial r} + \frac{3h^\eta}{r} + (\Delta_{\theta\varphi} + 2) \frac{h^\mathcal{W}}{r} + \frac{1}{2r} h - \frac{3}{2r} h^{rr} \right), \quad (6.65)$$

$$(\Delta \mathbf{h})^\mu = \Delta h^\mu + \frac{2}{r} \frac{\partial h^\mu}{\partial r} + \frac{2h^\mu}{r^2} - \frac{2}{r} \left(\frac{\partial h^\mu}{\partial r} + \frac{3h^\mu}{r} + (\Delta_{\theta\varphi} + 2) \frac{h^\mathcal{X}}{r} \right), \quad (6.66)$$

$$(\Delta \mathbf{h})^\mathcal{W} = \Delta h^\mathcal{W} + \frac{2h^\mathcal{W}}{r^2} + \frac{2h^\eta}{r^2}, \quad (6.67)$$

$$(\Delta \mathbf{h})^\mathcal{X} = \Delta h^\mathcal{X} + \frac{2h^\mathcal{X}}{r^2} + \frac{2h^\mu}{r^2}, \quad (6.68)$$

$$\text{trace of } \Delta \mathbf{h} = \Delta h. \quad (6.69)$$

The term between parentheses in Eq. (6.66) is exactly zero in the case of a divergence-free tensor, as it represents the μ -component of the vector \mathbf{H} (6.58). The similar term in Eq. (6.65) reduces to $-h^{rr}/r$, when using $H^\eta = 0$ with Eq. (6.57). We can now write evolution equations, implied by the original tensor wave equation (6.39):

$$\frac{\partial^2 \mathcal{A}}{\partial t^2} = \Delta \mathcal{A}, \quad (6.70)$$

$$\frac{\partial^2 \mathcal{B}}{\partial t^2} = \Delta \mathcal{B} - \frac{\mathcal{C}}{2r^2}, \quad (6.71)$$

$$\frac{\partial^2 \mathcal{C}}{\partial t^2} = \Delta \mathcal{C} + \frac{2\mathcal{C}}{r^2} + \frac{8\Delta_{\theta\varphi}\mathcal{B}}{r^2}. \quad (6.72)$$

The situation is therefore slightly more complicated than in the vector case with Eqs. (6.30)-(6.31). Indeed, the two potentials \mathcal{B} and \mathcal{C} are coupled, but it is possible to define new potentials satisfying decoupled wave-like evolution equations. We first write the scalar spherical harmonic decomposition of \mathcal{A} , \mathcal{B} and \mathcal{C} :

$$\mathcal{A}(t, r, \theta, \varphi) = \sum_{\ell, m} \mathcal{A}^{\ell m}(t, r) Y_\ell^m(\theta, \varphi),$$

$$\mathcal{B}(t, r, \theta, \varphi) = \sum_{\ell, m} \mathcal{B}^{\ell m}(t, r) Y_\ell^m(\theta, \varphi),$$

$$\mathcal{C}(t, r, \theta, \varphi) = \sum_{\ell, m} \mathcal{C}^{\ell m}(t, r) Y_\ell^m(\theta, \varphi).$$

Then, we define new potentials $\tilde{\mathcal{B}}$ and $\hat{\mathcal{C}}$ as:

$$\tilde{\mathcal{B}}(t, r, \theta, \varphi) = \sum_{\ell, m} \left(2\mathcal{B}^{\ell m}(t, r) + \frac{\mathcal{C}^{\ell m}(t, r)}{2(\ell+1)} \right) Y_\ell^m(\theta, \varphi), \quad (6.73)$$

$$\hat{\mathcal{C}}(t, r, \theta, \varphi) = \sum_{\ell, m} \left(\mathcal{C}^{\ell m}(t, r) - 4\ell\mathcal{B}^{\ell m}(t, r) \right) Y_\ell^m(\theta, \varphi). \quad (6.74)$$

The Eqs. (6.71)-(6.72) are transformed into:

$$\frac{\partial^2 \tilde{\mathcal{B}}}{\partial t^2} = \tilde{\Delta} \tilde{\mathcal{B}}, \quad (6.75)$$

$$\frac{\partial^2 \hat{\mathcal{C}}}{\partial t^2} = \hat{\Delta} \hat{\mathcal{C}}; \quad (6.76)$$

with, for any scalar field $f(r, \theta, \varphi) = \sum_{(\ell, m)} f^{\ell m}(r) Y_\ell^m(\theta, \varphi)$, the operators defined as:

$$\tilde{\Delta} f = \frac{\partial^2 f}{\partial r^2} + \frac{2}{r} \frac{\partial f}{\partial r} + \frac{1}{r^2} \left[\sum_{\ell m} -\ell(\ell-1) f^{\ell m} Y_\ell^m \right], \quad (6.77)$$

$$\hat{\Delta} f = \frac{\partial^2 f}{\partial r^2} + \frac{2}{r} \frac{\partial f}{\partial r} + \frac{1}{r^2} \left[\sum_{\ell m} -(\ell+1)(\ell+2) f^{\ell m} Y_\ell^m \right]. \quad (6.78)$$

These two operators are very similar to the usual Laplace operator, but in the angular part $\Delta_{\theta\varphi}$, they contain a shift of, respectively -1 and $+1$ in the multipolar number ℓ , for $\tilde{\Delta}$ and $\hat{\Delta}$. We thus have obtained three evolution wave-like equations (6.70), (6.75) and (6.76) for the three scalar degrees of freedom of a divergence-free symmetric tensor.

6.3.3 Traceless case

As presented in Sec. 6.1.2, some evolution problems of symmetric tensors in general relativity can have another constraint, in addition to the divergence-free condition already studied (6.40). This is the condition of determinant one for the conformal metric which turns into an algebraic condition (Eq. (169) of [73]), and is enforced by iteratively solving a Poisson equation with the trace of the tensor as a source, as described in Sec. V.D of [73]. Therefore, in the following the trace of the unknown tensor \mathbf{h} is assumed to be known.

The fact that the trace h (6.51) of a divergence-free symmetric tensor is fixed reduces *a priori* the number of scalar degrees of freedom to two. For instance, we here show that if the trace is given, the scalar potentials \mathcal{B} and \mathcal{C} are linked. We take the partial derivative with respect to r of the definition of \mathcal{C} (6.62) and \mathcal{B} (6.61) to obtain:

$$\frac{\partial \mathcal{C}}{\partial r} + \frac{2\mathcal{C}}{r} + 2\Delta_{\theta\varphi} \left(\frac{\partial \mathcal{B}}{\partial r} + \frac{3\mathcal{B}}{r} - \frac{\mathcal{C}}{4r} \right) = \Delta h. \quad (6.79)$$

Therefore, if h and \mathcal{C} are given, it is possible to integrate this relation with respect to the r -coordinate to obtain \mathcal{B} (which we have assumed to converge to 0 as $r \rightarrow \infty$). Because of the definitions (6.73)-(6.74), $\tilde{\mathcal{B}}$ and $\hat{\mathcal{C}}$ are also linked together if the trace is given.

We shall assume in the following that this trace is zero. All the equations presented hereafter can easily be generalized to the non-zero (given) trace case, taking the general form of the equations of Sec. 6.3.2. We shall therefore use only two scalar potentials, namely \mathcal{A} and $\tilde{\mathcal{B}}$ to describe a general traceless divergence-free symmetric tensor.

6.3.4 Integration scheme

Similarly to what has been done in the beginning of this section, we consider the homogeneous wave equation for a symmetric tensor (6.39), under the constraints that the tensor be divergence-free (6.40) and traceless ($h = 0$). We have seen in Sec. 6.3.3 that it was necessary to solve for at least the two wave-like evolution equations (6.70) and (6.75). We describe now how to obtain the whole tensor, once $\mathcal{A}(t, r, \theta, \varphi)$ and $\tilde{\mathcal{B}}(t, r, \theta, \varphi)$ are known.

In order to obtain first the six pure spin components (actually, their spherical harmonic decompositions (6.44)-(6.49)) of \mathbf{h} at any time t , we use the following six equations: the traceless condition, the three divergence-free conditions and the definitions of \mathcal{A} and $\tilde{\mathcal{B}}$. They represent two systems of coupled differential equations in the r -coordinate, that we express in terms of the tensor spherical harmonic components (6.43). The first one comes from the definition of \mathcal{A} (6.60) and the $H^\mu = 0$ condition (6.58); it couples the μ - and the \mathcal{X} -components of \mathbf{h} :

$$\frac{\partial B_2^{\ell m}}{\partial r} - \frac{B_1^{\ell m}}{r} = \mathcal{A}^{\ell m}, \quad (6.80)$$

$$\frac{\partial B_1^{\ell m}}{\partial r} + \frac{3B_1^{\ell m}}{r} + \frac{2 - \ell(\ell + 1)B_2^{\ell m}}{r} = 0. \quad (6.81)$$

This system has two unknown functions $B_1^{\ell m}$ and $B_2^{\ell m}$, whereas $\mathcal{A}^{\ell m}$ is obtained from the time evolution of $\mathcal{A}(t, r, \theta, \varphi)$.

The second one comes from the definition of $\tilde{\mathcal{B}}$ (6.73) and the two $H^r = H^\eta = 0$ conditions (6.56)-(6.57); it couples the rr -, η - and \mathcal{W} -components:

$$(\ell + 2) \frac{\partial E_2^{\ell m}}{\partial r} + \ell(\ell + 2) \frac{E_2^{\ell m}}{r} - \frac{2E_1^{\ell m}}{r} - \frac{1}{2(\ell + 1)} \frac{\partial L_0^{\ell m}}{\partial r} - \frac{\ell + 4}{\ell + 1} \frac{L_0^{\ell m}}{2r} = \tilde{\mathcal{B}}^{\ell m}, \quad (6.82)$$

$$\frac{\partial L_0^{\ell m}}{\partial r} + \frac{3L_0^{\ell m}}{r} - \frac{\ell(\ell + 1)E_1^{\ell m}}{r} = 0, \quad (6.83)$$

$$\frac{\partial E_1^{\ell m}}{\partial r} + \frac{3E_1^{\ell m}}{r} - \frac{L_0^{\ell m}}{2r} + \frac{2 - \ell(\ell + 1)E_2^{\ell m}}{r} = 0. \quad (6.84)$$

Here, the unknowns are $L_0^{\ell m}$, $E_1^{\ell m}$ and $E_2^{\ell m}$ and $\tilde{\mathcal{B}}^{\ell m}$ is known from the evolution of $\tilde{\mathcal{B}}(t, r, \theta, \varphi)$.

When looking at a more general setting, the trace h appears only in the second system. If we combine Eq. (6.80) with Eq. (6.81), we obtain a Poisson equation for the unknown rh^χ , with \mathcal{A} and its radial derivative as a source. As for the vector case, this system can be solved using, for example, the spectral scalar Poisson solver described in [228], and one obtains the pure spin components h^μ and h^χ .

Such an argument cannot be used for the second system, but a search for homogeneous solutions gives that, for a given ℓ , the simple powers of r :

$$r^{\ell-2}, \frac{1}{r^{\ell+3}} \text{ and } \frac{1}{r^{\ell+1}} \quad (6.85)$$

represent a basis of the kernel of the system (6.82)-(6.84). With this information, one can devise a simple spectral method to solve this system (see Sec. 6.5.1) and obtain the pure spin components h^{rr} , h^η and $h^\mathcal{W}$. With the traceless condition, one can also recover h^τ from h^{rr} , and finally use Eqs. (6.52)-(6.53) to get the spherical components of \mathbf{h} .

6.4 Boundary conditions

6.4.1 Vector system

We discuss here the spatial boundary conditions to be used during our procedure, so that we recover the unknown vector field at any time-step. The source of the vector wave equation is put to zero for the sake of clarity; but the reasoning would be exactly the same in the general case.

As pointed out in Sec. 6.2.4, the recovery of the vector field at each time-step will require two different operations: first, we use the two scalar wave equations (6.31) and (6.30) to recover A and V^μ . Two boundary conditions, set at the outer sphere (the boundary of our computation domain), will then be needed for these quantities. The second step will consist of the inversion of the differential system (6.37), to obtain the pure spin components V^r and V^η . This system is, in terms of the structure of the space of homogeneous solutions, mathematically equivalent to a Poisson problem (see Eq. (6.38)); its inversion will then also require an additional boundary condition.

From the setting of our problem presented at the beginning of Sec. 6.2, we can impose Dirichlet boundary conditions for the 3 pure spin components on the outer sphere. The condition on V^μ enables us to recover the value of the entire field on our computational domain, through the direct resolution of (6.30). Once we obtain the value of the field A on our domain, we can use a condition on either V^r or V^η to invert the system (6.37), and retrieve the additional spin components.

There remains the necessity of imposing a boundary condition on A to solve Eq. (6.31). This cannot be done using condition at $r = R$ in (6.10) and the definition (6.26), because $\frac{\partial V^\eta}{\partial r}$ must be specified. To overcome this difficulty, we exhibit here algebraic relations that link the value of A at the boundary and time derivatives of the pure spin components. These will be compatibility conditions, derived only from the structure of our problem. We express radial derivatives of equations (6.24) and (6.26), respectively, to obtain, using relations (6.11) and (6.28), the following identities (see also Eq. (6.35)):

$$\frac{1}{r} \Delta_{\theta\varphi} A = -\frac{\partial^2 V^r}{\partial t^2}, \quad (6.86)$$

$$\frac{\partial A}{\partial r} + \frac{A}{r} = \frac{\partial^2 V^\eta}{\partial t^2}. \quad (6.87)$$

Those equations are derived using only the fact that our vector field satisfies the wave equation and is divergence-free. From the knowledge of the vector field at the boundary, we can impose either of these two relations as boundary conditions for A ; the first being of Dirichlet type for each spherical harmonic of A , the second of Robin type. This way we are able to solve equation (6.31), and complete our resolution scheme.

Let us finally note that our boundary problem is, as one could guess, actually overdetermined: there is no need to know the value of the entire vector field on the outer sphere. It can be easily seen that, if one only has access to the boundary values of V^μ and V^r , or V^μ and V^η , the boundary conditions for all equations can be provided. This also gives us insight about what would happen if we set up a numerical problem in which spatial boundary conditions are not consistent with a solution of Eqs. (6.8, 6.9); this could occur for example because of numerical rounding errors or simply a physical boundary prescription which is not compatible with a divergence-free vector field. Our method will then still provide a solution that is divergence-free and which satisfies Eqs. (6.8, 6.9); however only the boundary conditions that are directly enforced will be satisfied. For example, if we choose in our scheme to enforce boundary conditions on V^μ and V^η , the outer boundary conditions that are satisfied at each time-step are actually of the form (we keep the notation of (6.10)):

$$\begin{aligned} \forall t \geq 0, \quad V^\mu(t, R, \theta, \varphi) &= b_0^\mu(t, \theta, \varphi), \\ V^\eta(t, R, \theta, \varphi) &= b_0^\eta(t, \theta, \varphi), \\ \frac{\partial V^r(t, R, \theta, \varphi)}{\partial r} + \frac{2}{r} V^r(t, R, \theta, \varphi) &= -\frac{1}{r} \Delta_{\theta\varphi} b_0^\eta(t, \theta, \varphi). \end{aligned} \quad (6.88)$$

The last condition is directly derived from the vanishing of the divergence (Eq. (6.24)) at the boundary. Let us note that we do not even impose a Dirichlet condition on V^r as was originally intended. We may then not satisfy all the boundary conditions we wished to prescribe at first. This may also depend on the boundary value we choose to use for the inversion of the system (6.37).

We do not treat alternative cases for the boundary problem (for which the knowledge of the vector field on the outer sphere could be substituted by, for example, the knowledge of its first radial derivative); but a similar approach would also provide expressions for the boundary conditions of all the equations tackled in our scheme.

6.4.2 Tensor system

The tensor problem presents itself in a similar way to the vector case, only with a few additional difficulties. As seen in Sec. 6.3.4, we can separate the problem into two parts; the first consists in

retrieving the field \mathcal{A} from Eq (6.70), and then get the spin components h^μ and h^χ . In a similar way, we compute the value of $\tilde{\mathcal{B}}$ from Eq. (6.75), so that we obtain the fields h^{rr} , $h^{\mathcal{V}}$ and h^η from the inversion of the system (6.82, 6.83, 6.84). The field h^r is deduced from the traceless hypothesis. The tensor field is then entirely determined.

As in the vector case, the solution of wave equations for \mathcal{A} and $\tilde{\mathcal{B}}$ requires one boundary condition for each equation. The elliptic system (6.80, 6.81) is also quite similar to that for the vector case, and its space of homogeneous solutions is also equivalent to that of a single Poisson equation. One boundary condition is also required; it will be chosen as a Dirichlet condition on either h^μ or h^χ , according to the setting of our problem (6.41).

For the elliptic system (6.82, 6.83, 6.84), the homogeneous solutions have been characterized in Sec. 6.3.4. The only basis vector of the kernel of solutions that is regular in our computation domain is, for any $\ell \geq 2$, the solution $r^{\ell-2}$. The other two vectors of the kernel basis are not regular at the origin of spherical coordinates. This means, from a basic point of view, that one boundary condition will be sufficient at the outer sphere. It will be provided, again according to our problem setting, as a Dirichlet condition on any of the fields h^{rr} , h^η or $h^{\mathcal{V}}$.

The last boundary problem concerns the fields \mathcal{A} and $\tilde{\mathcal{B}}$. They will be handled the same way as in the vector case. We take the radial derivatives of the equations (6.58) and (6.60), using the elliptic equations (6.66) and (6.68), to obtain the following compatibility conditions:

$$(\Delta_{\theta\varphi} + 2)\mathcal{A} = -\frac{\partial^2 h^\mu}{\partial t^2}, \quad (6.89)$$

$$\frac{\partial \mathcal{A}}{\partial r} + 2\frac{\mathcal{A}}{r} = \frac{\partial^2 h^\chi}{\partial t^2}, \quad (6.90)$$

These are again derived using only the divergence-free property of the vector field as well as the verification of the main wave equation. Using the known value of, respectively, h^μ and h^χ at the outer boundary, we obtain either a Dirichlet boundary condition for each spherical harmonic from the first relation, or a Robin condition with the second one. Again those identities have been obtained only from the equations of our problem and the definitions of the variables we use.

Taking the same path for the second part of the problem, we express radial derivatives of Eqs. (6.56), (6.57), (6.61) and (6.62) to obtain respectively, and for each spherical harmonic, the following relations:

$$\frac{\partial^2 L_0^{\ell m}}{\partial t^2} = -\frac{1}{(2\ell+1)r} \left[\frac{(\ell+1)(\ell+2)}{2} \hat{\mathcal{C}}^{\ell m} - \ell(\ell+1)(\ell-1) \tilde{\mathcal{B}}^{\ell m} \right] \quad (6.91)$$

$$\frac{\partial^2 E_1^{\ell m}}{\partial t^2} = \frac{1}{(2\ell+1)r} \left[(\ell+1)(\ell-1) \tilde{\mathcal{B}}^{\ell m} + \frac{\ell+2}{2} \hat{\mathcal{C}}^{\ell m} \right] \quad (6.92)$$

$$\frac{\partial^2 E_2^{\ell m}}{\partial t^2} = \frac{1}{2\ell+1} \left[\frac{(\ell+1)}{2} \frac{\partial \tilde{\mathcal{B}}^{\ell m}}{\partial r} - \frac{1}{4} \frac{\partial \hat{\mathcal{C}}^{\ell m}}{\partial r} - \frac{(\ell+1)(\ell+2)}{2} \frac{\tilde{\mathcal{B}}^{\ell m}}{r} - \frac{\ell-3}{4} \frac{\hat{\mathcal{C}}^{\ell m}}{r} \right] \quad (6.93)$$

$$\begin{aligned} \frac{\partial^2 (L_0^{\ell m} + T_0^{\ell m})}{\partial t^2} &= \frac{1}{2\ell+1} \left[\frac{(\ell+1)(\ell+2)}{2} \frac{\partial \hat{\mathcal{C}}^{\ell m}}{\partial r} - \ell(\ell+1)(\ell+2) \frac{\partial \tilde{\mathcal{B}}^{\ell m}}{\partial r} + \ell(\ell+1)(\ell-1)^2 \frac{\tilde{\mathcal{B}}^{\ell m}}{r} \right. \\ &\quad \left. + \frac{1}{2}(\ell+1) [\ell(\ell-3) + \ell + 4] \frac{\hat{\mathcal{C}}^{\ell m}}{r} \right]. \end{aligned} \quad (6.94)$$

When expressing the vanishing of the trace, the last equation can be transformed into:

$$\begin{aligned} \frac{\partial^2 E_2^{\ell m}}{\partial t^2} &= \frac{1}{2\ell(\ell+1)(2\ell+1)} \left[(\ell+1) \frac{\partial \hat{\mathcal{C}}^{\ell m}}{\partial r} + 2\ell(\ell+1) \frac{\partial \tilde{\mathcal{B}}^{\ell m}}{\partial r} + \frac{(\ell+1)(\ell+4)}{2} \frac{\hat{\mathcal{C}}^{\ell m}}{r} \right. \\ &\quad \left. - \ell(\ell+1)(\ell-3) \frac{\tilde{\mathcal{B}}^{\ell m}}{r} \right]. \end{aligned} \quad (6.95)$$

Although those equations involve both the fields $\tilde{\mathcal{B}}$ and $\hat{\mathcal{C}}$, one can easily see that combining them can lead to conditions on the field $\tilde{\mathcal{B}}$ only. For example, the combination of (6.91) and (6.92) provides, for each index ℓ :

$$\tilde{\mathcal{B}}^{\ell m} = \frac{r}{(\ell+1)(\ell-1)} \left[\frac{\partial^2 L_0^{\ell m}}{\partial t^2} + (\ell+1) \frac{\partial^2 E_1^{\ell m}}{\partial t^2} \right], \quad (6.96)$$

which is interpreted as a Dirichlet boundary condition for $\tilde{\mathcal{B}}$. Robin boundary conditions can be obtained from the combination of Eqs. (6.93), (6.94), and either (6.91) or (6.92). The tensor boundary problem is then entirely solved; tests for some of the boundary conditions derived here are presented in Sec. 6.5. Let us note again that this problem is overdetermined: concerning the first system, the knowledge of a Dirichlet condition on either only h^μ , or only $h^\mathcal{X}$ suffices to provide boundary conditions for \mathcal{A} and the system (6.80, 6.81). For the part of the algorithm related to $\tilde{\mathcal{B}}$, we easily see that Dirichlet conditions for any two of the spin components h^{rr} , h^η and $h^\mathcal{V}$ are sufficient to solve the boundary problem.

We finally point out that, in the same fashion as in the vector case, if the value β_0^{ij} imposed as a Dirichlet condition for the tensor at the outer boundary (Eq. (6.41)) is not consistent with the system, the boundary conditions actually imposed on our scheme will be slightly different: only the Dirichlet conditions for the pure spin components that are explicitly enforced will be satisfied. Other boundary values will only express the coherence with respect to the fact that the solution is indeed divergence free. As done in Sec. 6.4.1, it is possible to express other boundary conditions enforced in practice by using the expression for the tensor divergence \mathbf{H} as a function of the pure spin components.

6.4.3 Working in a shell: inner boundary conditions

We say a few words here about the resolution of the tensorial problem when our computation domain is no longer an entire sphere, but is instead bounded on the interior at a finite coordinate radius $r = R_{\text{in}} > 0$. We add in our setting the condition that, $\forall (\theta, \varphi)$:

$$\forall t \geq 0, \quad h^{ij}(t, R_{\text{in}}, \theta, \varphi) = \zeta_0^{ij}(t, \theta, \varphi).$$

Physical information is then also provided at the internal boundary (this is, again, an overdetermined set of boundary conditions). This new geometry will imply the need for two inner boundary conditions to be imposed for the wave equations on \mathcal{A} and in $\tilde{\mathcal{B}}$. These are easily found using the results of the last section and the knowledge of Dirichlet boundary conditions on the inner and outer sphere for all components. The system (6.80, 6.81) also needs an additional (inner) boundary condition, imposed on either h^μ or $h^\mathcal{X}$. There is, however, a slight subtlety concerning the triple system (6.82, 6.83, 6.84). As seen in Sec. 6.3.4, the kernel of solutions to this system is of dimension 3, and since our computational domain no longer includes $r = 0$, all 3 basis vectors of this kernel are regular in our domain.

This means that 3 boundary conditions have to be imposed overall for inverting this system (in contrast with the sphere case, where we only imposed one). Those three conditions are imposed here on either h^{rr} , h^η or $h^{\mathcal{V}}$ on each limit of the domain. We have *a priori* the freedom to choose which boundary conditions we want to impose, and where to impose them; numerical experimentation would be required to indicate whether or not there are preferable choices.

To conclude this section, we mention also the work of [475] where the authors used the formalism presented in this paper to solve a tensor elliptic equation that is part of a formulation of the Einstein equations. The resolution was made on a 3-space excised by a sphere of fixed coordinate radius, where the tensor equation possessed a weak singularity property (see [236]). The boundary condition problem was treated a little bit differently, as all boundary conditions imposed were either emanating from the very structure of the problem, or were not needed at all. This is a consequence of the particular behavior of that operator at the boundary; on this setting for the domain geometry, one boundary condition was imposed to invert the system in h^μ and h^χ , and two for the system involving h^{rr} , h^η and $h^{\mathcal{V}}$.

6.5 Numerical tests

6.5.1 Spectral methods in a sphere

The numerical schemes presented in previous sections have been implemented using a multi-domain spectral method in spherical coordinates (see e.g. [85, 250], for general presentations and [230] for a more detailed description in the case of numerical relativity). We have used the LORENE numerical library [216], with scalar fields decomposed onto a basis of Chebyshev polynomials, in several domains, for the r -coordinate, Fourier series for the φ -coordinate and either Fourier or associated Legendre functions for the θ -coordinate ($P_\ell^m(\cos\theta)$, see Sec. 6.1.3). This last option is obviously needed by our algorithms, which strongly rely on spherical harmonics decompositions and on the angular part of the Laplace operator $\Delta_{\theta\varphi}$. The other basis of decomposition (Fourier) is quite useful for computing angular derivatives $\partial/\partial\theta$ and operators such as $1/\sin\theta$, appearing in e.g. (6.21) or (6.52). The coordinate singularity on the z -axis ($\theta = 0, \pi$) is naturally handled by the spherical harmonic decomposition basis. We cope with the coordinate singularity at the origin ($r = 0$), using an even/odd radial decomposition basis (only even/odd Chebyshev polynomials), depending on the parity of the multipole ℓ (see [79] and Sec. 3.2 of [230]). The complete regularity requirement would be that, for each multipole ℓ the radial Taylor expansion of a regular function should include only r^p with $p \geq \ell$. We have found however that the simpler parity prescription described above is in practice sufficient for the study of the wave or Poisson equations performed here.

The wave equations (6.30)-(6.31) and (6.70)-(6.75) are integrated numerically by writing them as first-order systems:

$$\frac{\partial^2 \phi}{\partial t^2} = \Delta \phi \iff \begin{cases} \frac{\partial \phi}{\partial t} = \psi, \\ \frac{\partial \psi}{\partial t} = \Delta \phi. \end{cases} \quad (6.97)$$

After discretization in the angular coordinates using spherical harmonics, we then use a third-order Adams-Bashforth (explicit) time-stepping scheme with a fixed time-step dt and a Chebyshev-tau technique in the radial coordinate. The differential systems for the computation of pure spin components from the divergence-free degrees of freedom, as system (6.37) in the vector case, or systems (6.80)-

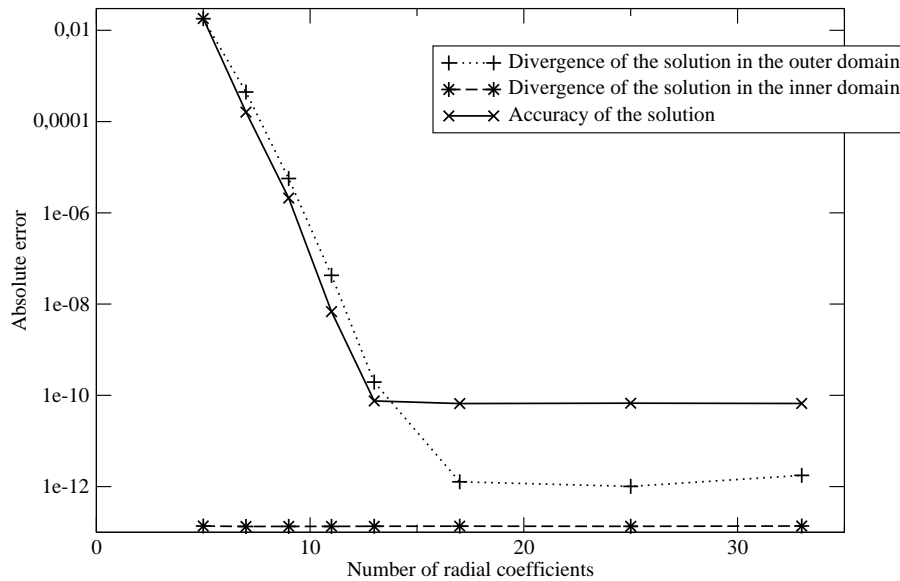


Figure 6.1: Decay of the errors (difference with theoretical solution and divergence of the numerical solution) for the vector wave equation, as a function of the number of radial Chebyshev coefficients N_r used in each domain. Other settings are $R = 6$, $dt = 0,00032$, $N_\theta = 17$, $N_\varphi = 4$.

(6.84) in the tensor case, are solved at every time-step in the Chebyshev coefficient space. A tau method is used to match together the solutions across the domains, and to impose the boundary conditions at $r = R$.

6.5.2 Vector wave equation

We consider here the numerical solution of the problem (6.8)-(6.10), with $v_0^i(r, \theta, \varphi)$ given by its Cartesian components by (with $z = r \cos(\theta)$):

$$v_0^x = -v_0^y = \cos(z), \quad (6.98)$$

the other component is zero. Thus, the vector v_0^i is clearly divergence-free. With appropriate boundary conditions, the solution of the problem (6.8)-(6.10) is (still in Cartesian components) simple to express:

$$V^x(t, r, \theta, \varphi) = -V^y(t, r, \theta, \varphi) = \cos(t) \cos(z), \quad (6.99)$$

the other component being zero. The vector wave equation is solved through the two scalar wave equations for the potentials A and the component V^μ as explained in Sec. 6.2.4. From Eq. (6.99), we know the values of $b_0^i(t, \theta, \varphi)$ appearing in Eq. (6.10) as Dirichlet boundary conditions and we can deduce its pure spin components ($b_0^r, b_0^\theta, b_0^\mu$). These are used to obtain Dirichlet boundary conditions for the evolution equations for A and μ , as described in Sec.6.4.1 using Eq. (6.86) for A . Finally, the elliptic system (6.37) is solved with the appropriate Dirichlet boundary condition given by the spin component b_0^r (see also Sec. 6.4.1).

We use the numerical techniques given in Sec. 6.5.1, with two domains, and numbers of points in each direction given by $(N_r, N_\theta, N_\varphi)$. We have integrated the vector wave equation over the time

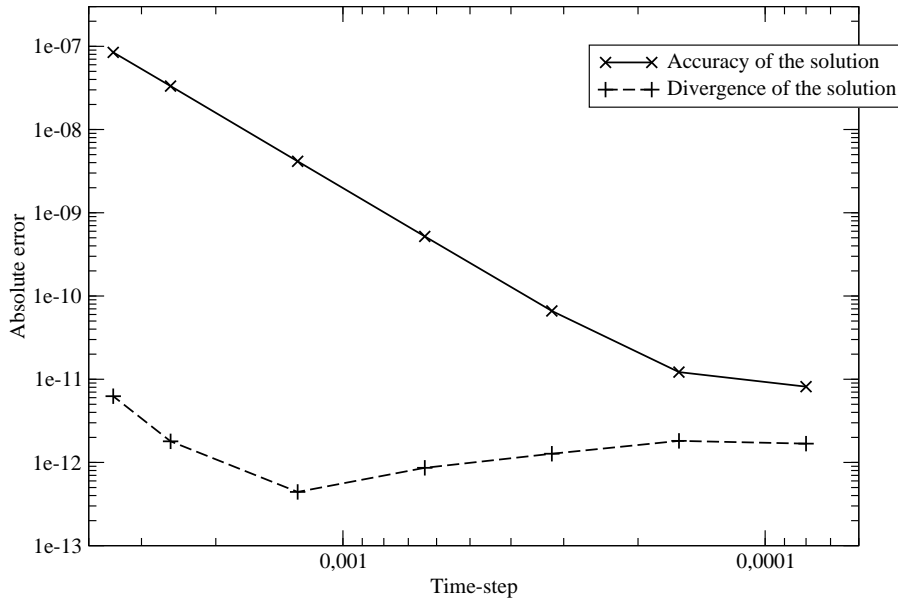


Figure 6.2: Decay of the errors (difference with theoretical solution and divergence of the numerical solution) for the vector wave equation, as a function of the time-step dt . Other settings are $R = 6$, $N_r = 17$, $N_\theta = 17$, $N_\varphi = 4$.

interval $t \in [0, 2\pi]$ and looked at the maximum in time of two quantities to estimate the accuracy of the solution. First, the difference between the numerical solution and the theoretical one (6.99), rotated to spherical basis (6.1), is computed. Then, the divergence of the numerical solution, expressed in the spherical basis is also monitored. Note that, even though all the Cartesian components of V^i do not depend on the azimuthal angle φ , the spherical components do depend on φ and we have always used four points in the φ -direction.

In Fig. 6.1, we observe as expected an exponential convergence of both the discrepancy between the theoretical and numerical solutions (maximum over all grid points and all components) as functions of the number of spectral coefficients used in the radial direction N_r , all other parameters being fixed. The same behavior has been observed when keeping N_r fixed and varying N_θ . Besides, we observe an exponential decay of the divergence of the solution in the second (or outer) domain, whereas the divergence of the solution in the first (central) domain remains constant to the radial precision. This is due to the matching across domains and imposition of boundary conditions, which can be seen as a modification of the solution of the system (6.37) by the addition of a linear combination of homogeneous solutions. These homogeneous solutions of the system (6.37) are, for each multipole ℓ , $r^{\ell-1}$ and $1/r^{\ell+2}$. The latter being singular at $r = 0$ is not relevant in the central domain. The $r^{\ell-1}$ function is a polynomial and is well represented in the first domain, whereas in the second domain, we also need to resolve $1/r^{\ell+2}$, which is poorly approximated for low values of N_r .

On the other hand, when varying the time-step dt , the difference between the numerical and exact solutions decreases as $\mathcal{O}(dt^3)$ (see Fig. 6.2), as expected for a third-order scheme. Another feature verified in Fig. 6.2 is the fact that the divergence of the solution is (almost) independent of the time-step, being thus only a function of the spatial resolution. The best accuracy observed in Fig. 6.1 is limited by angular resolution and the fact that the divergence is computed using spherical components

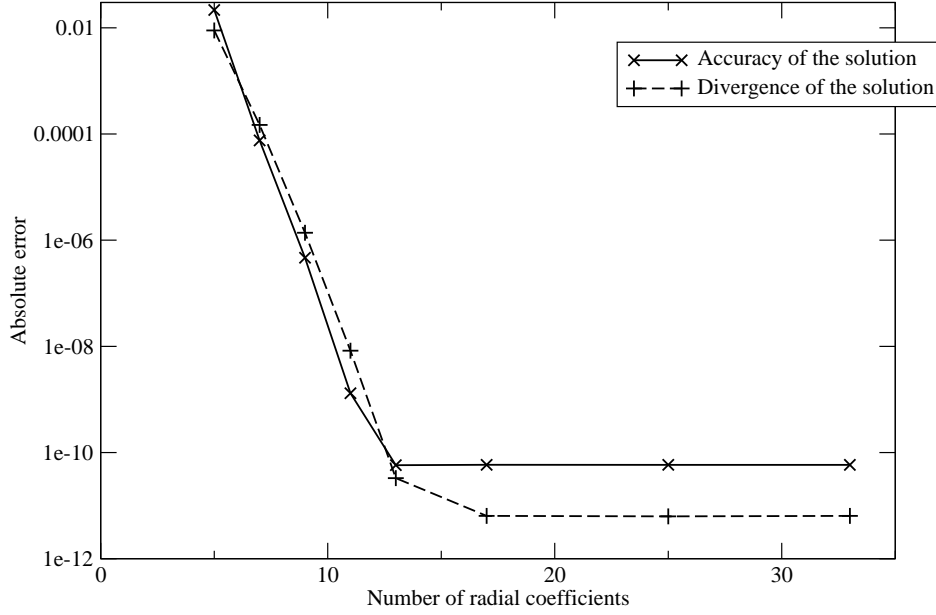


Figure 6.3: Decay of the errors (difference with theoretical solution and divergence of the numerical solution) for the tensor wave equation, as a function of the number of radial Chebyshev coefficients N_r used in each domain. Other settings are $R = 6$, $dt = 0.00032$, $N_\theta = 17$, $N_\varphi = 4$.

(Eq. 6.12), whereas the divergence-free constraint is imposed using pure spin components (Eq. 6.24). Therefore, the computation of derivatives in Eqs. (6.21) to obtain the spherical components introduces additional numerical noise, depending on the angular resolution.

6.5.3 Divergence-free and traceless tensor wave equation

Similarly to Sec. 6.5.2, we consider here the numerical solution of the problem (6.39)-(6.41), with $\alpha_0^{ij}(r, \theta, \varphi)$ given in the Cartesian basis by (with $z = r \cos(\theta)$):

$$\alpha_0^{xx} = -\alpha_0^{yy} = \cos(z), \quad (6.100)$$

all the other components are zero. Thus the tensor α_0^{ij} is clearly symmetric, divergence-free and trace-free. With $\gamma_0^{ij} = 0$ and appropriate boundary conditions, the solution of the problem (6.39)-(6.41) is (still in Cartesian components) simple to express:

$$h^{xx}(t, r, \theta, \varphi) = -h^{yy}(t, r, \theta, \varphi) = \cos(t) \cos(z), \quad (6.101)$$

all the other components being zero. The tensor wave equation is solved through the two scalar wave-like equations for the potentials \mathcal{A} and $\tilde{\mathcal{B}}$ as explained in Sec. 6.3.4. From Eq. (6.101), we know the

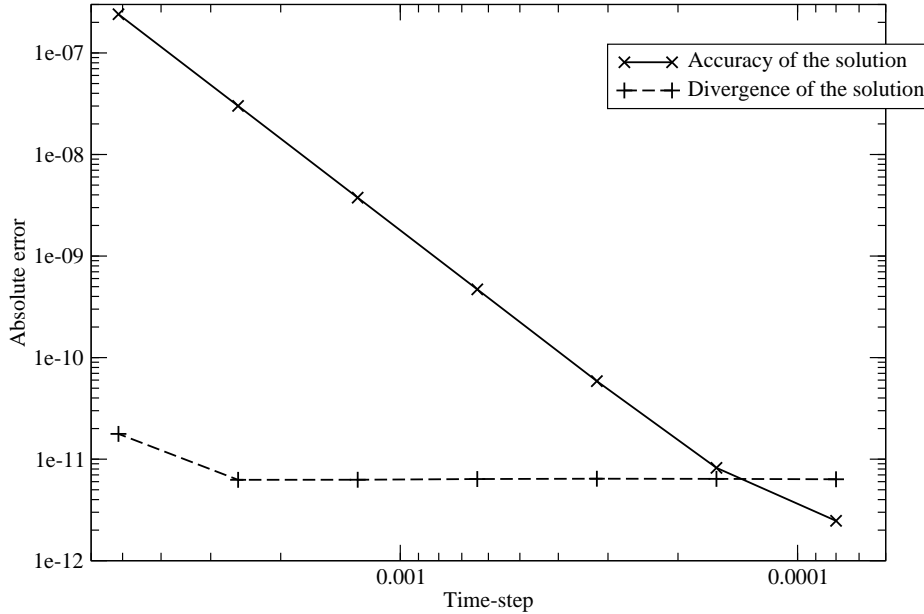


Figure 6.4: Decay of the errors (difference with theoretical solution and divergence of the numerical solution) for the tensor wave equation, as a function of the time-step dt . Other settings are $R = 6$, $N_r = 17$, $N_\theta = 17$, $N_\varphi = 4$.

values of $\beta_0^{ij}(t, \theta, \varphi)$ appearing in Eq. (6.41) as Dirichlet boundary conditions and we can deduce its pure spin components $(\beta_0^{rr}, \beta_0^\eta, \beta_0^\mu)$. These are used to obtain Dirichlet boundary conditions for the evolution equations for \mathcal{A} and $\tilde{\mathcal{B}}$, as described in Sec. 6.4.2 using Eqs. (6.89) and (6.96), respectively. Finally, the elliptic systems (6.80)-(6.84) are solved with the appropriate Dirichlet boundary conditions given by the spin components of β_0^{ij} , namely β_0^{rr} and β_0^μ . We have integrated the tensor wave equation following the same procedure as in Sec. 6.5.2. results are displayed in Figs. 6.3 and 6.4, where we observe as expected an exponential convergence of both the discrepancy between the theoretical and numerical solutions, and the divergence of the numerical, as functions of N_r . When varying the time-step dt , the difference between the numerical and exact solutions decreases as $\mathcal{O}(dt^3)$, as expected. Here again, the divergence of the solution is (almost) independent of the time-step, being thus only a function of the spatial resolution, from the same reasons as in the vector case.

6.6 Concluding remarks

We have described a new numerical method for solving the wave equation of a rank-two symmetric tensor on a spherical grid, ensuring the divergence-free condition on this tensor. In order to describe this method, we have first addressed the vector case, for which we have reformulated the poloidal-toroidal decomposition in spherical components. This approach, which relies on a decomposition

onto vector spherical harmonics was then generalized to the case of a symmetric tensor. Through numerical tests of the vector and tensor wave evolution in a sphere using spectral explicit time schemes, we have observed that this method was convergent and accurate. In particular, the level at which the divergence-free condition is violated is determined only by the spatial discretization and does not depend on the time-step, as expected. This method strongly relies on the decomposition onto spherical harmonic spectral bases, but is not bound to spectral methods for the representation of the radial coordinate.

The discussion in Sec. 6.4 gave us the compatibility conditions (6.86), (6.89) (6.96), which are necessary to obtain boundary conditions for the additional scalar field equations, representing the evolution of the divergence-free degrees of freedom of our objects $(A, \mathcal{A}, \tilde{\mathcal{B}})$. The numerical tests performed in this study have dealt only with simple Dirichlet boundary conditions. However, it would be rather straightforward to generalize them to more complex boundary conditions, which are needed in realistic simulations of gravitational waves [288, 341, 391].

In this respect, an interesting issue would probably be the general well-posed nature of these boundary conditions with respect to our scheme, and how the modifications for these conditions with this method, sketched in Sec.6.4.1 and 6.4.2, would alter the physical behavior of the solution. One could for example think of a Robin-like boundary setting linked to an outer wave-absorbing condition (as in [341]), instead of the Dirichlet setting studied here; the fact that boundary conditions may be only partially verified could have an effect on how this required feature at the boundary would be described eventually in our scheme. The same type of questions arise in a more general case, where the source terms of the equations are non-vanishing: these sources would also require well-posedness conditions (i.e. a vanishing divergence for the wave equation). If this requirement is not satisfied (because of the iteration procedure or numerical errors), although the problem is then mathematically ill-posed, our scheme will still converge: it provides us with a solution of the wave equation with a source that is basically the divergence-free part of the original ill-posed source. The influence of this feature on the general stability and physical relevance of the procedure is an open issue.

Future studies include the simulations of perturbed black hole spacetimes, with the extraction of gravitational waves, and the solution of general-relativistic magneto-hydrodynamics in the case of a rotating neutron star.

Chapitre 7

A new spectral apparent horizon finder for 3D numerical relativity

Version publiée : L.-M. Lin et J. Novak, *Classical and Quantum Gravity* **24**, pp.2665-2676 (2007).

Sommaire

7.1	Introduction	225
7.2	Notations and definitions	226
7.3	The Nakamura <i>et al.</i> algorithm	227
7.4	Our algorithm	228
7.5	Tests	230
7.6	Conclusions	235

7.1 Introduction

Apparent horizons play an important role in numerical relativity for spacetimes containing black hole(s). Being defined locally in time (see section 7.2), the apparent horizon(s) can readily be computed from the data on each hypersurface during a numerical evolution in $3 + 1$ numerical relativity. In contrast, the event horizon is a global property and can be determined approximately only when the spacetime has essentially settled down to a stationary state. Once the spacetime has settled down, the event horizon can be found at all previous times by integrating null geodesics backwards in time (e.g., [256, 25, 290, 146]). As it (if exists) must be inside an event horizon [242], the apparent horizon is an important tool to track the location and movement of black hole(s) in a numerically generated spacetime. Furthermore, the surface of an apparent horizon also provides a natural boundary within which the spacetime region can be excised from the computational domain in order to handle the physical singularities inside a black hole [461, 408] (see also Unruh as cited in [461] and e.g. [12, 101, 474, 43] for black hole simulations without excision). In the new concept of a “dynamical horizon” (see [39, 82] for reviews), apparent horizons are essentially the cross sections of the (three-dimensional spacelike) dynamical horizon on the hypersurfaces. It has recently been shown in this context that the areas of the apparent horizons satisfy a causal evolution equation and give a positive

bulk viscosity in a viscous fluid analogy [222]. This is in contrast to the event horizon which yields a noncausal evolution and a negative bulk viscosity.

A wide variety of algorithms for finding apparent horizons have been proposed in the past decade. We refer the reader to the review article by Thornburg [463] (and references therein) for details. In this paper, we present a new apparent horizon finder which is based on spectral methods. While spectral-method based algorithm for finding apparent horizons was first proposed by Nakamura *et al.* [330] more than twenty years ago, our new approach does not suffer from the same weakness as in the Nakamura *et al.* algorithm: namely the $\ell = 0$ coefficient of the spherical harmonics decomposition of the apparent-horizon's surface needed to be determined by a root-finding procedure. Hence, our algorithm leads to a more robust and efficient spectral apparent horizon finder. We have tested our finder with analytic solutions for single and two black-hole spacetimes. Our finder is as efficient as the currently fastest algorithms developed by Schnetter [406] and Thornburg [462].

This paper is organized as follows. In section 7.2 we present the notations and various definitions. In section 7.3 we briefly review the Nakamura *et al.* algorithm; we describe our spectral algorithm and the numerical procedure in section 7.4. Section 7.5 presents tests with analytic solutions to assess the accuracy, robustness, and efficiency of our finder. Finally, we summarize our results in section 7.6. Latin (Greek) indices go from 1 to 3 (0 to 3).

7.2 Notations and definitions

Given a spacelike hypersurface Σ with future-pointing unit normal n^μ , the 3-metric $\gamma_{\mu\nu}$ induced by the spacetime metric $g_{\mu\nu}$ onto Σ is

$$\gamma_{\mu\nu} := g_{\mu\nu} + n_\mu n_\nu. \quad (7.1)$$

Let S be a closed smooth (two-dimensional) surface embedded in Σ , and let s^μ be the outward-pointing unit normal of S , which is spacelike and also normal to n^μ (i.e., $s_\mu s^\mu = 1$ and $s_\mu n^\mu = 0$). The 3-metric $\gamma_{\mu\nu}$ now induces a 2-metric on S :

$$m_{\mu\nu} := \gamma_{\mu\nu} - s_\mu s_\nu. \quad (7.2)$$

Let k^μ be the tangents of the outgoing future-pointing null geodesic whose projection on Σ is orthogonal to S . We have (up to an overall factor)

$$k^\mu = s^\mu + n^\mu, \quad (7.3)$$

on the 2-surface S .

The expansion of the outgoing null geodesics is

$$\Theta = \nabla_\mu k^\mu, \quad (7.4)$$

where ∇_μ is the covariant derivative associated with $g_{\mu\nu}$. In terms of three-dimensional quantities, on the 2-surface S , the expansion can be written as (see, e.g., [55])

$$\Theta = D_i s^i - K + s^i s^j K_{ij}, \quad (7.5)$$

where D_i is the covariant derivative associated with γ_{ij} , K_{ij} is the extrinsic curvature of Σ , and K is the trace of K_{ij} . The expansion can also be written as

$$\Theta = m^{ij} (D_i s_j - K_{ij}). \quad (7.6)$$

The 2-surface S is called a marginally trapped surface if $\Theta = 0$ everywhere on S . We shall call here the outermost of such surfaces (which is a marginally outer trapped surface - MOTS) the apparent horizon.

To parameterize the apparent horizon, we assume that the topology of S is a 2-sphere, and S is star-shaped around the coordinate origin $r = 0$, which means that for every point M inside S , the straight line connecting the origin to M is entirely inside S [69]. The position of the apparent horizon can then be represented as

$$F(r, \theta, \varphi) := r - h(\theta, \varphi) = 0, \quad (7.7)$$

where (r, θ, φ) are the standard spherical coordinates. The function h measures the coordinate distance to the horizon's surface in the direction (θ, φ) . With this parametrization, the unit normal s^i is given by

$$s^i = \frac{D^i F}{(\gamma^{ij} D_i F D_j F)^{1/2}} := \frac{D^i F}{|DF|}, \quad (7.8)$$

where $D^i := \gamma^{ij} D_j$. The expansion (equation (7.6)) becomes

$$\Theta = m^{ij} \left(\frac{D_i D_j F}{|DF|} - K_{ij} \right), \quad (7.9)$$

where the condition $m^{ij} s_j = 0$ has been used.

7.3 The Nakamura *et al.* algorithm

In this section, we give a brief review of the algorithm adopted by Nakamura *et al.* [330] for finding apparent horizon based on spectral methods. They expand h in spherical harmonics:

$$h(\theta, \varphi) = \sum_{\ell=0}^{\ell_{\max}} \sum_{m=-\ell}^{\ell} a_{\ell m} Y_{\ell}^m(\theta, \varphi). \quad (7.10)$$

They rewrite the apparent horizon equation $\Theta = 0$ as¹

$$\Delta_{\theta\varphi} h = \rho\Theta + \Delta_{\theta\varphi} h, \quad (7.11)$$

where $\Delta_{\theta\varphi}$ is the flat Laplacian operator on a 2-sphere defined by

$$\Delta_{\theta\varphi} h := h_{,\theta\theta} + \cot\theta h_{,\theta} + \sin^{-2}\theta h_{,\varphi\varphi}. \quad (7.12)$$

The positive scalar function ρ is chosen such that the term $h_{,\theta\theta}$ cancels on the right hand side (RHS). Using the fact that the Y_{ℓ}^m are an orthogonal set of eigenfunctions of $\Delta_{\theta\varphi}$:

$$\Delta_{\theta\varphi} Y_{\ell}^m = -\ell(\ell+1) Y_{\ell}^m, \quad (7.13)$$

we obtain the relation (with $d\Omega = \sin\theta d\theta d\varphi$)

$$-\ell(\ell+1) a_{\ell m} = \int_S Y_{\ell}^{m*} (\rho\Theta + \Delta_{\theta\varphi} h) d\Omega. \quad (7.14)$$

¹We follow the notation of Gundlach [231].

This equation can be used to solve for the coefficients $a_{\ell m}$ via an iteration procedure. However, the value of a_{00} has to be determined at each iteration step by solving for the root of

$$\int_S Y_0^{0*} (\rho\Theta + \Delta_{\theta\varphi} h) d\Omega = 0. \quad (7.15)$$

The main disadvantage of the above scheme is that the coefficient a_{00} has to be determined separately by equation (7.15). As pointed out by Gundlach [231], solving equation (7.15) by any iteration method is as computationally expensive as many steps of the main iteration loop. Furthermore, equation (7.15) may have multiple roots or none. In those cases, each root or each minimum (if there is no root) should be investigated separately [274]. This clearly reduces the efficiency of the algorithm significantly.

7.4 Our algorithm

7.4.1 Master equation for apparent horizon

Our spectral-method based algorithm uses a similar ansatz (7.11) as Nakamura *et al.* [330]. The main difference is that we do not need to determine a_{00} separately. Hence, this leads to a more robust and efficient apparent horizon finder based solely on spectral method¹.

To begin, we first introduce a flat metric f_{ij} on the hypersurface Σ . The components of the flat metric with respect to the spherical coordinates (r, θ, φ) , and the associated natural basis $(\frac{\partial}{\partial r}, \frac{\partial}{\partial \theta}, \frac{\partial}{\partial \varphi})$, are $f_{ij} = \text{diag}(1, r^2, r^2 \sin^2 \theta)$. Let \mathcal{D}_i be the covariant derivative associated with f_{ij} . The expansion function Θ (equation (7.9)) can now be written as

$$\Theta = (\gamma^{ij} - s^i s^j) [|DF|^{-1} (\mathcal{D}_i \mathcal{D}_j F - \Delta_{ij}^m \mathcal{D}_m F) - K_{ij}], \quad (7.16)$$

where the tensor field Δ_{ij}^m is defined by

$$\Delta_{ij}^m := \frac{1}{2} \gamma^{mn} (\mathcal{D}_i \gamma_{jn} + \mathcal{D}_j \gamma_{in} - \mathcal{D}_n \gamma_{ij}). \quad (7.17)$$

We have also used the following relation between the two covariant derivatives D_i and \mathcal{D}_i :

$$D_i V_j = \mathcal{D}_i V_j - \Delta_{ij}^m V_m, \quad (7.18)$$

where V^j is an arbitrary 3-vector on Σ_t .

Motivated by the recently proposed fully constrained-evolution scheme for numerical relativity [73], we define a conformal factor Ψ by

$$\Psi := \left(\frac{\det \gamma_{ij}}{\det f_{ij}} \right)^{1/12}, \quad (7.19)$$

and also a tensor field h^{ij} by

$$\gamma^{ij} = \Psi^{-4} (f^{ij} + h^{ij}). \quad (7.20)$$

¹See [231] for Gundlach's "fast flow" algorithm which combines the spectral algorithm of Nakamura *et al.* and the so-called curvature flow method (see also [463] for discussion).

We also expand all tensor fields onto the following spherical basis:

$$\mathbf{e}_{\hat{r}} := \frac{\partial}{\partial r}, \quad \mathbf{e}_{\hat{\theta}} := \frac{1}{r} \frac{\partial}{\partial \theta}, \quad \mathbf{e}_{\hat{\varphi}} := \frac{1}{r \sin \theta} \frac{\partial}{\partial \varphi}. \quad (7.21)$$

This basis is orthonormal with respect to the flat metric: $f_{\hat{i}\hat{j}} = \text{diag}(1, 1, 1)$. Here and afterwards we denote the tensor indices associated with this basis with a hat. The expansion function now becomes

$$\begin{aligned} \Theta &= \Psi^{-4} |DF|^{-1} f^{\hat{i}\hat{j}} \mathcal{D}_{\hat{i}} \mathcal{D}_{\hat{j}} F + \left(\Psi^{-4} h^{\hat{i}\hat{j}} - s^{\hat{i}} s^{\hat{j}} \right) |DF|^{-1} \mathcal{D}_{\hat{i}} \mathcal{D}_{\hat{j}} F \\ &\quad - \left(\gamma^{\hat{i}\hat{j}} - s^{\hat{i}} s^{\hat{j}} \right) \left(|DF|^{-1} \Delta_{\hat{i}\hat{j}}^{\hat{m}} \mathcal{D}_{\hat{m}} F + K_{\hat{i}\hat{j}} \right). \end{aligned} \quad (7.22)$$

Now let us consider the first term on the RHS of this equation:

$$\begin{aligned} \Psi^{-4} |DF|^{-1} f^{\hat{i}\hat{j}} \mathcal{D}_{\hat{i}} \mathcal{D}_{\hat{j}} F &= \Psi^{-4} |DF|^{-1} (\mathcal{D}_{\hat{r}} \mathcal{D}_{\hat{r}} F + \mathcal{D}_{\hat{\theta}} \mathcal{D}_{\hat{\theta}} F + \mathcal{D}_{\hat{\varphi}} \mathcal{D}_{\hat{\varphi}} F) \\ &= \frac{-1}{\Psi^4 |DF| r^2} (h_{,\theta\theta} + \cot \theta h_{,\theta} + \sin^{-2} \theta h_{,\varphi\varphi} - 2r) \\ &= \frac{-1}{\Psi^4 |DF| h^2} (\Delta_{\theta\varphi} h - 2h), \end{aligned} \quad (7.23)$$

where we have set $r = h(\theta, \varphi)$ for the apparent horizon in the last equality. In equation (7.23), we have used the following relation for the components of the covariant derivative $\mathcal{D}_{\hat{j}}$ of a 3-vector $V^{\hat{i}}$ in the orthonormal basis $\{\mathbf{e}_{\hat{i}}\}$:

$$\mathcal{D}_{\hat{j}} V_{\hat{i}} = e_{\hat{j}}^k \frac{\partial}{\partial x^k} V_{\hat{i}} - \hat{\Gamma}_{\hat{i}\hat{j}}^{\hat{k}} V_{\hat{k}}, \quad (7.24)$$

where $e_{\hat{j}}^k := \text{diag}[1, 1/r, 1/(r \sin \theta)]$. The $\hat{\Gamma}_{\hat{i}\hat{j}}^{\hat{k}}$ are the connection coefficients of $\mathcal{D}_{\hat{k}}$ associated with $\{\mathbf{e}_{\hat{i}}\}$. The non-vanishing components are

$$\hat{\Gamma}_{\hat{\theta}\hat{\theta}}^{\hat{r}} = -\hat{\Gamma}_{\hat{r}\hat{\theta}}^{\hat{\theta}} = -\frac{1}{r}, \quad \hat{\Gamma}_{\hat{\varphi}\hat{\varphi}}^{\hat{r}} = -\hat{\Gamma}_{\hat{r}\hat{\varphi}}^{\hat{\varphi}} = -\frac{1}{r}, \quad \hat{\Gamma}_{\hat{\varphi}\hat{\varphi}}^{\hat{\theta}} = -\hat{\Gamma}_{\hat{\theta}\hat{\varphi}}^{\hat{\varphi}} = \frac{-1}{r \tan \theta}. \quad (7.25)$$

Equations (7.22) and (7.23) suggest that, instead of the ansatz (7.11) as taken by Nakamura *et al.*, it is more appropriate to rewrite the apparent horizon equation $\Theta = 0$ as

$$\Delta_{\theta\varphi} h - 2h = \lambda \Theta + \Delta_{\theta\varphi} h - 2h, \quad (7.26)$$

where the scalar function λ is chosen to be $\lambda = \Psi^4 |DF| h^2$ such that the combination $\Delta_{\theta\varphi} h - 2h$ cancels on the RHS of this equation. Hence, the master equation that we solve in our algorithm is

$$\begin{aligned} \Delta_{\theta\varphi} h - 2h &= \Psi^4 |DF| h^2 \left[\left(\Psi^{-4} h^{\hat{i}\hat{j}} - s^{\hat{i}} s^{\hat{j}} \right) |DF|^{-1} \mathcal{D}_{\hat{i}} \mathcal{D}_{\hat{j}} F \right. \\ &\quad \left. - \left(\gamma^{\hat{i}\hat{j}} - s^{\hat{i}} s^{\hat{j}} \right) \left(|DF|^{-1} \Delta_{\hat{i}\hat{j}}^{\hat{m}} \mathcal{D}_{\hat{m}} F + K_{\hat{i}\hat{j}} \right) \right]. \end{aligned} \quad (7.27)$$

The expansion coefficients are now determined by solving the following equation iteratively:

$$a_{\ell m} = \frac{-1}{\ell(\ell+1)+2} \int_S Y_{\ell}^{m*} (\lambda \Theta + \Delta_{\theta\varphi} h - 2h) d\Omega. \quad (7.28)$$

This equation applies for all $\ell \geq 0$, and hence a_{00} is not treated specially. In Ref. [413], Shibata developed an apparent horizon finder based essentially on the same form of equation (7.26). However, he solved the equation using finite-differencing method without pointing out the key advantage that, if solved by spectral method, the coefficient a_{00} (as determined by our equation (7.28) and his equation (1.3) in [413]) does not need to be solved by a root-finding procedure. In this work, we solve the algorithm for the first time with spectral method. The difference between equations (7.28) and (7.14) leads to a dramatic improvement in the efficiency and robustness of spectral-method based algorithms for finding apparent horizons.

7.4.2 Numerical procedure

For given 3-metric γ_{ij} and extrinsic curvature K_{ij} on a hypersurface Σ , equation (7.27) represents a nonlinear elliptic equation for the function h . We solve this equation iteratively by considering the RHS of the equation as a source term for the linear operator $\Delta_{\theta\varphi} - 2$ acting on h . We use a multidomain spectral method to solve the elliptic equation [69, 72]. The code is constructed upon the C++ library LORENE [216], and is publicly available.

The numerical iteration procedure is briefly described here. Assume that the data $(\gamma_{\hat{i}\hat{j}}, K_{\hat{i}\hat{j}})$ are given on Σ . The conformal factor Ψ and the tensor field $h^{\hat{i}\hat{j}}$ are then calculated by equations (7.19) and (7.20) respectively. Assume that an initial guess for the function $h(\theta, \varphi)$ is chosen (equivalently for the spectral coefficients $a_{\ell m}$). The iteration processes as follows:

1. At the n -th iteration step, the function $h^{(n)}$ is determined by the coefficients $a_{\ell m}^{(n)}$ (with the superscript (n) labels the iteration steps). The level-set function F and the unit normal vector s^i are then obtained from $h^{(n)}$ (see section 7.2).
2. The spectral coefficients at the next iteration step are calculated by equation (7.28):

$$a_{\ell m}^{(n+1)} = \frac{-1}{\ell(\ell+1)+2} \int_S Y_\ell^{m*} S^{(n)} d\Omega, \quad (7.29)$$

where $S^{(n)}$ represents the RHS of equation (7.27) evaluated from $a_{\ell m}^{(n)}$. The new function $h^{(n+1)}$ is then obtained from $a_{\ell m}^{(n+1)}$ by equation (7.10).

3. The difference between $h^{(n+1)}$ and $h^{(n)}$ is calculated. The iteration procedure continues until the maximum value of the difference throughout the whole angular grid (θ_i, φ_j) is smaller than some prescribed value ϵ_h .

7.5 Tests

7.5.1 Kerr-Schild data

As a first test of the apparent horizon finder, we use a single black hole in Kerr-Schild coordinates (see, e.g., [320]) to study its convergence properties and robustness. Let M and a denote respectively the mass and spin parameter of the black hole. In the standard spherical coordinates (r, θ, φ) , the polar and equatorial coordinate radii of the apparent horizon are given by

$$r_{\text{po}} = \bar{r}, \quad r_{\text{eq}} = \sqrt{\bar{r}^2 + a^2}, \quad (7.30)$$

Table 7.1: Convergence test for a Kerr-Schild black hole with $M = 1$ and $a = 0.9$. Listed are the number of radial collocation points in each domain N_r , the fractional errors in the polar (equatorial) coordinate radius $\Delta r_{\text{po}}/r_{\text{po}}$ ($\Delta r_{\text{eq}}/r_{\text{eq}}$) and area $\Delta A/A$, the maximum remaining error of the expansion function $\Delta\Theta_{\text{max}}$ on the horizon, and the run times. We use $N_\theta = (N_r + 1)/2$ points in the polar direction and $N_\varphi = 1$ in the azimuthal direction. We set the iteration parameter $\epsilon_h = 10^{-10}$.

N_r	$\Delta r_{\text{po}}/r_{\text{po}}$	$\Delta r_{\text{eq}}/r_{\text{eq}}$	$\Delta A/A$	$\Delta\Theta_{\text{max}}$	Time (s)
13	2.360×10^{-5}	8.003×10^{-6}	1.276×10^{-5}	4.240×10^{-3}	0.507
17	1.693×10^{-6}	9.705×10^{-8}	1.605×10^{-6}	5.333×10^{-4}	0.747
21	1.580×10^{-7}	2.145×10^{-8}	1.788×10^{-7}	6.574×10^{-5}	1.129
25	1.692×10^{-8}	4.235×10^{-9}	2.045×10^{-8}	8.033×10^{-6}	1.615
33	1.067×10^{-10}	1.707×10^{-10}	4.733×10^{-10}	1.559×10^{-7}	3.059
37	1.649×10^{-10}	1.325×10^{-10}	2.863×10^{-10}	2.383×10^{-8}	4.286
41	1.590×10^{-10}	1.053×10^{-10}	2.154×10^{-10}	3.790×10^{-9}	5.722

where $\bar{r} = M + \sqrt{M^2 - a^2}$. The area is given by

$$A = 4\pi (\bar{r}^2 + a^2). \quad (7.31)$$

We first test the convergence property of the code with respect to increasing number of collocation points from runs with a black hole of $M = 1$ and $a = 0.9$. The polar radius of the apparent horizon is $r_{\text{po}} \approx 1.436$ and the equatorial radius is $r_{\text{eq}} \approx 1.695$. The analytic data (γ_{ij}, K_{ij}) are set on the numerical grid points of the computational domain ranging from $r = 1$ to $r = 5$, which is covered by three spectral domains. The boundary between the first and the second domain is at $r = r_{12} = 1.5$, whereas that between the second and the third domain is at $r = r_{23} = 2.5$. In each domain, we use $(N_r, N_\theta, N_\varphi)$ collocation points. We also enforce a symmetry with respect to the equatorial plane. The initial guess for h is a sphere at $r = 3$.

Table 7.1 shows the results for increasing N_r , with $N_\theta = (N_r + 1)/2$ and $N_\varphi = 1$. We choose the iteration parameter $\epsilon_h = 10^{-10}$ in this test (see section 7.4.2). In the table, for each N_r , we list the fractional errors in the polar (equatorial) coordinate radius $\Delta r_{\text{po}}/r_{\text{po}}$ ($\Delta r_{\text{eq}}/r_{\text{eq}}$) and area $\Delta A/A$, the maximum remaining error in the expansion function $\Delta\Theta_{\text{max}}$ on the horizon's surface, and the run times¹. The error in the area is defined by $\Delta A/A := |(A_{\text{ana}} - A_{\text{num}})/A_{\text{ana}}|$, where the analytic result A_{ana} is given by equation (7.31) and the numerical result is calculated by the integral

$$A_{\text{num}} = \int_S \sqrt{\hat{q}} h^2 \sin \theta d\theta d\varphi, \quad (7.32)$$

with \hat{q} being the determinant of the 2-metric on the apparent-horizon's surface (expanded onto the

¹The run times correspond to the CPU time the code took to locate the apparent horizon on a 2 GHz Intel Core Duo processor. The best-fitted curve suggests that the scaling of the run time is close to N_θ^2 , which comes from the computation of discrete Legendre transforms.

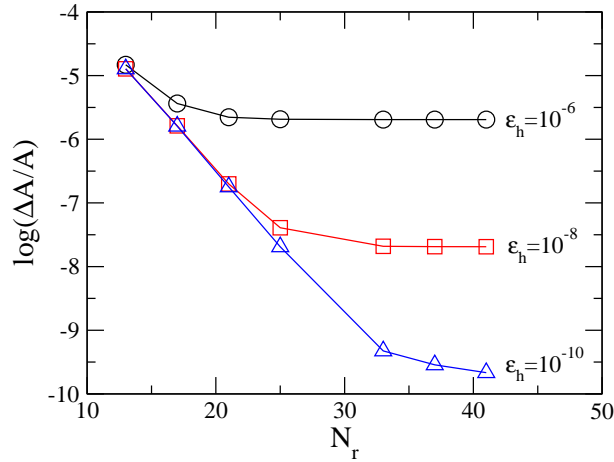


Figure 7.1: Convergence towards zero of the fractional error in the area $\Delta A/A$ with the number of collocation points for three different choices of the iteration parameter ϵ_h .

basis $\{\mathbf{e}_i\}$). Explicitly, in terms of a general 3-metric γ_{ij} , A_{num} is given by

$$A_{\text{num}} = \int_0^{2\pi} \int_0^\pi [(\gamma_{\hat{r}\hat{r}}h_\theta^2 + 2\gamma_{\hat{r}\hat{\theta}}hh_{,\theta} + \gamma_{\hat{\theta}\hat{\theta}}h^2) (\gamma_{\hat{r}\hat{r}}h_\varphi^2 + 2\gamma_{\hat{r}\hat{\varphi}}hh_{,\varphi} \sin\theta + \gamma_{\hat{\varphi}\hat{\varphi}}h^2 \sin^2\theta) - (\gamma_{\hat{r}\hat{r}}h_\theta h_{,\varphi} + \gamma_{\hat{r}\hat{\theta}}hh_{,\varphi} + \gamma_{\hat{r}\hat{\varphi}}hh_{,\theta} \sin\theta + \gamma_{\hat{\theta}\hat{\varphi}}h^2 \sin\theta)^2]^{1/2} d\theta d\varphi. \quad (7.33)$$

In figure 7.1 we plot $\Delta A/A$ against N_r to show explicitly the convergence behavior of the finder for three different choices of ϵ_h . It can be seen that the error $\Delta A/A$ converges exponentially towards zero with the number of points, as expected for spectral methods, until the accuracy is limited by the choice of ϵ_h . Furthermore, we also see that the number of iterations to a given error level ϵ_h is essentially independent of the value of ℓ_{max} used in equation (7.10). This agrees with the conclusions obtained from the original Nakamura *et al.*'s algorithm (or its modifications) as investigated by Kembal and Bishop [274].

Next we test the robustness of our finder by performing runs with different initial guesses for h . We use the same black hole as above ($M = 1, a = 0.9$), but with a larger computational domain ranging from $r = 1$ to $r = 10$. The boundaries between the different spectral domains are $r_{12} = 2.5$ and $r_{23} = 5.5$. In general, we set up an initial guess for h to be the surface of an ellipsoid given by

$$\frac{x^2}{a^2} + \frac{y^2}{b^2} + \frac{z^2}{c^2} = 1, \quad (7.34)$$

where (x, y, z) are the Cartesian coordinates relating to the spherical coordinates (r, θ, φ) in the standard way. The constants (a, b, c) are freely chosen. The initial guess used for the results listed in table 7.1 corresponds to $a = b = c = 3$. Table 7.2 contains the results for five different initial guesses. Case A corresponds to a sphere with a coordinate radius which is about five times away from the horizon's surface. On the other hand, the initial surface for case B is a sphere located entirely inside the apparent horizon. The initial guess for case C is an ellipsoid enclosing the horizon. Finally, cases D and E represent initial surfaces which cross the horizon. The results show that our finder can locate the apparent horizon to the same accuracy with all the five (quite generic) choices of (a, b, c) .

Table 7.2: Robustness test for the same black hole used in table 7.1. The polar coordinate radius of the apparent horizon is $r_{\text{po}} \approx 1.436$ and the equatorial coordinate radius is $r_{\text{eq}} \approx 1.695$. The initial guess for the 2-surface h is given by the surface of an ellipsoid with axes (a, b, c) defined in equation (7.34). We use collocation points $N_r = 25$ and $N_\theta = 13$ for all the five cases considered, but $N_\varphi = 1$ (4) for cases A and B (C-E).

Case	(a, b, c)	$\Delta A/A$ (10^{-6})
A	(8, 8, 8)	4.04871
B	(1.2, 1.2, 1.2)	4.04905
C	(4, 6, 8)	4.04875
D	(2, 3, 1.2)	4.04910
E	(1.2, 1.5, 2)	4.04909

One of the main requirements of an apparent horizon finder is speed. This is in particular an important issue if the finder has to run frequently during a simulation. In order to compare the speed of our finder with some other commonly used methods, we take the data given by Schnetter [406].

In table 5 of [406] Schnetter compared the run times to locate the apparent horizon of a Kerr-Schild black hole with $M = 1$ and $a = 0.6$ for his elliptic method and two other methods, namely the fast-flow [231] and minimization [26] algorithms. The fastest case (0.5 s on a 1.2 GHz processor) was obtained by his elliptic method with the initial guess being a sphere at $r = 2$. The error in the area is $\Delta A/A = 9 \times 10^{-3}$ (according to table 4 of [406]). For comparison, the fast-flow and minimization algorithms took more than 10 s and 90 s respectively in the test [406].

We have performed tests with the same black hole and initial guess, and found that our finder took 0.129 s (on our 2 GHz processor) to locate the horizon to the accuracy $\Delta A/A = 2 \times 10^{-5}$ using the resolution $(N_r, N_\theta, N_\varphi) = (7, 5, 1)$ with $\epsilon_h = 10^{-8}$. We have also used Thornburg's finder AHFINDERDIRECT [462] (which is implemented within the CACTUS computational toolkit [15]) to perform the same test using Cartesian grid resolutions $(N_x, N_y, N_z) = (31, 31, 19)$ with $\Delta x = \Delta y = \Delta z = 0.2$ in bitant symmetry. We found that his finder took 1.004 s (on our 2 GHz processor) to locate the apparent horizon to the accuracy $\Delta A/A = 3 \times 10^{-4}$.

We note that the above test does not represent a direct comparison between the different algorithms because of the different grid structures (Cartesian vs spherical coordinates), code implementations, memory usage, and computer systems. Nevertheless, we can conclude that for this particular test, to obtain about the same accuracy level, our spectral-method based finder is as efficient as the finders developed by Schnetter [406] and Thornburg [462].

7.5.2 Brill-Lindquist data

In this part, we test our finder using the Brill-Lindquist data [91]. This is a classic test involving multiple black holes used in numerical relativity. The 3-metric is conformally flat, $\gamma_{ij} = \phi^4 f_{ij}$, and is time symmetric (i.e., $K_{ij} = 0$). For two black holes, ϕ is given by

$$\phi = 1 + \frac{M_1}{2|\vec{r} - \vec{r}_1|} + \frac{M_2}{2|\vec{r} - \vec{r}_2|}, \quad (7.35)$$

Table 7.3: Schwarzschild black hole offset from the coordinate origin. The hole is located at the Cartesian coordinates $(d/\sqrt{2}, d/\sqrt{2}, 0)$. Listed are the offset d , the fractional error in the area $\Delta A/A$, and the maximum remaining error of the expansion function on the horizon $\Delta\Theta_{\max}$.

d	$\Delta A/A$	$\Delta\Theta_{\max}$
0.1	9×10^{-6}	3×10^{-3}
0.2	3×10^{-6}	5×10^{-3}
0.3	2×10^{-6}	2×10^{-2}
0.4	1×10^{-4}	5×10^{-2}

where M_i ($i = 1, 2$) is the mass of the i th black hole and the \vec{r}_i are the coordinate positions of the holes.

We first begin with a single black hole ($M_2 = 0$), in which case the problem is equivalent to a Schwarzschild black hole in isotropic coordinates offset from the coordinate origin. The apparent horizon is a coordinate sphere of radius $M_1/2$ with respect to the center of the hole. The area of the horizon is $A = 16\pi M_1^2$. We set $M_1 = 1$ and the coordinate position of the hole at $\vec{r}_1 = (x_1, y_1, z_1) = (d/\sqrt{2}, d/\sqrt{2}, 0)$. We have varied d in order to verify that our finder also works when the center of the spherical harmonics is offset from the center of the horizon. Table 7.3 lists the results for four different values of d . The initial guesses are always $a = b = c = 1$ in equation (7.34). We use three spectral domains to cover the spatial slice up to $r = 1.5$, with collocation points $(N_r, N_\theta, N_\varphi) = (33, 17, 16)$ in each domain. The boundaries between the domains are $r_{12} = 0.5$ and $r_{23} = 0.8$. Similar to [231, 274], we see that the accuracy drops quite significantly for very distorted surfaces with respect to the coordinate origin. In particular, the error in the area $\Delta A/A$ increases by almost two orders of magnitude when d increases from 0.3 to 0.4; this error could be reduced using higher grid resolution¹. Nevertheless, it is worth to point out that the original Nakamura *et al.* spectral algorithm [330] would not produce any results for $d = 0.3$ and 0.4 because equation (7.15) has no roots [274]. We also see that the results are essentially independent of the direction of the offset.

Next we turn to a Brill-Lindquist data for two black holes of equal mass. In particular, we take $M_1 = M_2 = 1$ in the test. The data forms a one-parameter family parameterized by the coordinate separation d between the holes. When they are far apart, each hole has an individual apparent horizon. For small separation, there is a single common apparent horizon enclosing both holes. Determining the critical separation at which the common horizon appears in this two black hole spacetime is a standard test problem for apparent horizon finders. The critical separation obtained originally by Brill and Lindquist is $d_c = 1.56$ [91], while more recent results suggest that $d_c \approx 1.53$ (e.g., [462, 274, 9, 430]). In particular, we note that Thornburg [462] and Shoemaker *et al.* [430] report very close results at $d_c = 1.532$ and $d_c = 1.535$ respectively. Nevertheless, Thornburg reports $A = 196.407$ for the area of the critical apparent horizon, which is quite different from the value $A = 184.16$ obtained by Shoemaker *et al.*.

Here we test our finder by trying to find a common horizon at the critical separations as reported by Thornburg [462] and Shoemaker *et al.* [430]. The black holes are on the z -axis, with their centers

¹The error $\Delta A/A$ drops down to 2×10^{-5} for the case $d = 0.4$ using collocation points $(N_r, N_\theta, N_\varphi) = (33, 25, 24)$.

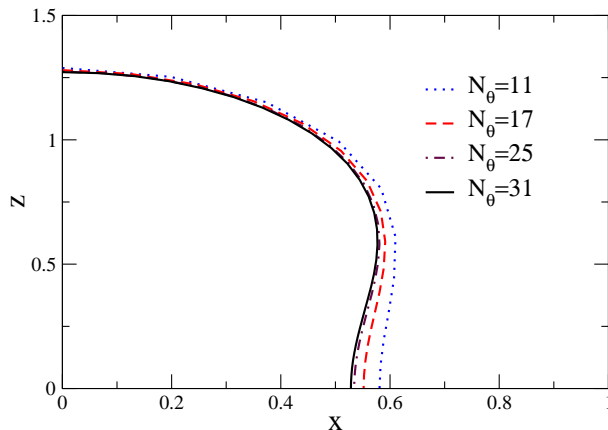


Figure 7.2: Position of the common apparent horizon on the x - z plane for Brill-Lindquist data with $d = 1.532$. The black holes are centered at $z = \pm d/2$ along the z -axis. The results obtained by four different values of N_θ are shown (with $N_r = 41$ and $N_\varphi = 1$ fixed).

at $z = \pm d/2$. In the test, we use four spectral domains to cover the spatial slice up to $r = 2$. The boundaries between the domains are $r_{12} = 0.5$, $r_{23} = 1$, and $r_{34} = 1.5$. The initial guesses are $a = b = c = 2$ in equation (7.34). We use $(N_r, N_\theta, N_\varphi) = (41, 31, 1)$ in each domain and the iteration parameter $\epsilon_h = 10^{-6}$. Our finder reports a common horizon at $d = 1.532$ (Thornburg's critical value) with the area of that horizon determined to be $A = 196.417$, which agrees to Thornburg's value to 0.005%. The maximum remaining error of the expansion function on the horizon is $\Delta\Theta_{\max} = 7 \times 10^{-4}$. The finder took 59.2 s to locate the horizon. We note that increasing ϵ_h to 10^{-4} would reduce the run time to 23.3 s, without changing the three significant figures of A . On the other hand, for the same grid setting and parameters, our finder does not find a common horizon at the critical value $d = 1.535$ reported by Shoemaker *et al.*. In general, for $d > 1.532$, we find two disjoint apparent horizons surrounding \vec{r}_1 and \vec{r}_2 by setting the coordinate origin for the apparent horizon finder (see section 7.2) separately at around the points \vec{r}_1 and \vec{r}_2 . In figure 7.2 we show the position of the common apparent horizon on the x - z plane for the case $d = 1.532$. The results obtained by four different values of N_θ (with $N_r = 41$ and $N_\varphi = 1$ fixed) are plotted together to show the convergence of the horizon.

7.6 Conclusions

In this paper we have presented a new apparent horizon finder which is based on spectral methods. Our proposed algorithm does not need to treat the $\ell = 0$ coefficient of the spherical harmonics decomposition separately as required in previous spectral apparent horizon finders [330, 274]. Hence, this leads to a faster and more robust finder based solely on spectral methods. We have made a performance comparisons with other apparent horizon finders using the Kerr-Schild data. Our finder is much faster (by orders of magnitude) than other commonly-used methods (e.g., the fast-flow and minimization algorithms). It is also as efficient as the currently fastest methods developed recently by Schnetter [406] and Thornburg [462]. We have also shown that our finder is capable of locating the horizon of a shifted Schwarzschild black hole with a large offset from the coordinate origin. This would not be possible by using the original Nakamura *et al.* spectral algorithm [330] because equation (7.15)

has no roots if the offset is too large. We have also tested our finder for a two black-hole spacetime using the Brill-Lindquist data. In particular, we have verified previous results on the critical separation at which a common horizon appears in this spacetime.

Our apparent horizon finder is implemented within the C++ library LORENE for numerical relativity [216], and is freely available. The finder should be easily adopted in spectral-method based evolution codes [73, 403, 466, 86], particularly to those using shell-like domains in spherical coordinates. Comparing to other freely available apparent horizon finders which are based on finite-differencing method (AHFINDER [9] and AHFINDERDIRECT [462]), our finder also represents another option available to finite-differencing evolution codes, with some interpolation to be implemented between the finite-difference and spectral grids as, for example, in [151].

Troisième partie

Simulations d'astres compacts

Après avoir détaillé les travaux sur la formulation des équations d'Einstein et les techniques numériques pour les résoudre, cette dernière partie donne les résultats d'intérêt astrophysique obtenus sur les modèles numériques d'astres compacts. Les observations de ces astres compacts, tels que les trous noirs ou les étoiles à neutrons, sont venues avec l'exploration de nouvelles gammes de fréquences à partir des années 1960 : en rayons X (binaires) et ondes radio (pulsars). Cependant, les concepts et les modèles qui leurs sont attachés aujourd'hui ont été développés avant : peu après la publication de la théorie de la relativité générale (1915) pour les trous noirs¹ et la découverte du neutron (1932) pour les étoiles à neutrons. C'est le champ gravitationnel extrêmement intense qui caractérise ces deux types d'objets, ce champ est quantifié par la compacité de l'astre, définie comme le rapport

$$\Xi = \frac{2GM}{Rc^2},$$

où M et R sont, respectivement, la masse et le rayon de l'astre. Par définition pour un trou noir $\Xi = 1$, alors que pour une étoile à neutrons il a été possible de mesurer $\Xi \sim 0.3$ [136], ce qui est conforme aux prédictions théoriques. Ces valeurs de Ξ montrent la nécessité de faire appel à la théorie de la relativité générale pour décrire correctement ces astres et qu'une approche purement newtonienne reste très incomplète, même au niveau qualitatif. Il en va de même si l'on cherche à modéliser la formation des astres compacts : les codes numériques simulant les effondrements gravitationnels des *supernovae* donnant naissance aux étoiles à neutrons, comme les *hypernovae* supposées former un trou noir en leur centre, risquent d'être incomplets s'ils ne résolvent pas, au moins partiellement, les équations d'Einstein. Ainsi, le travail présenté au Chap. 8 décrit un code de simulation d'effondrement gravitationnel des cœurs d'étoiles dégénérés, donnant naissance à une étoile à neutrons. Ce code, pour l'instant, n'a pas pour objectif de simuler de manière auto-consistante le phénomène de supernova, mais de prendre un modèle effectif pour l'équation d'état, qui permet d'obtenir une explosion. Le mécanisme exact conduisant à cette explosion est aujourd'hui encore un problème ouvert. Notre but est plutôt d'estimer, de la manière la plus précise possible, quel est le signal d'ondes gravitationnelles émis lors de l'explosion d'une supernova. Ainsi le code CoCoNuT [150] résout les équations d'hydrodynamique relativiste couplées au champ gravitationnel obtenu par l'approximation conformément plate (voir plus haut, le chapitre sur le formalisme contraint) des équations d'Einstein. L'originalité de ce code réside dans l'utilisation combinée de deux techniques numériques très différentes : les méthodes de capture de choc (ou « de Godunov ») pour la résolution des équations d'Euler relativistes et les méthodes spectrales pour le champ gravitationnel. Cette combinaison des deux types de méthodes numériques (appelée *Mariage des maillages*) est justifiée par le fait qu'elles possèdent des qualités complémentaires. Les méthodes spectrales sont extrêmement précises et peu coûteuses en ressources informatiques, mais ne peuvent représenter correctement des fonctions discontinues à cause du phénomène de Gibbs. Elles sont donc bien adaptées pour représenter le champ gravitationnel (qui est toujours continu), mais sont sérieusement handicapées pour la modélisation des quantités hydrodynamiques lors d'événements tels que les supernovæ où il se forme des chocs. D'un autre côté, les méthodes dites de capture de chocs sont capables de résoudre ce genre de discontinuités

¹un premier concept de « trou noir » a été introduit par Michell [317] au XVIII^e siècle

mais requièrent beaucoup de mémoire et de temps de calcul, ce qui les rend peu attrayantes pour traiter les équations du champs gravitationnel dans les problèmes complexes à deux ou trois dimensions (sans hypothèse de symétrie). Une des difficultés techniques a été le passage de l'information sur les champs physique d'une méthode numérique à l'autre ; il a fallu en effet développer des techniques d'interpolation et de filtrage performantes.

Les résultats de ce code ont été exposés dans un article commun Dimmelmeier *et al.* 2005 [151], où nous avons démontré la capacité du code à suivre parfaitement l'effondrement et la formation de l'étoiles à neutrons. Les ondes gravitationnelles sont extraites par la formule du quadrupôle, à partir de l'évolution de la distribution du fluide. Des tests ont été faits en simulant cette fois-ci l'évolution d'une étoile à neutrons en rotation, qui a été perturbée et dont on a suivi les oscillations. Les modes fondamentaux, ainsi que les premiers harmoniques ont été retrouvés avec une très bonne précision. COCONUT a été ensuite utilisé pour affiner les estimations d'ondes gravitationnelles émises en prenant en compte un équation d'état plus réaliste et un processus de déleptonisation effectif [352]. Cela a permis de ne garder qu'un seul type de formes d'ondes, contre trois auparavant, en éliminant la possibilité de rebonds multiples. Avec les améliorations apportées récemment sur la stabilité des solutions des équations elliptiques (discutées au chapitre 3) et le trouveur d'horizon apparent (Chap. 7), le code est maintenant capable de suivre aussi les effondrements d'étoiles plus massives menant à un trou noir. De multiples autres applications de ce code ont été faites depuis, si bien qu'il a fallu organiser une école au mois de novembre 2008, afin de former des thésitifs et jeunes post-doctorants venus de plusieurs pays d'Europe. Cela a aussi montré que, malgré le départ de la recherche de son principal développeur M. Dimmelmeier, le relais a été pris par de jeunes chercheurs, assurant ainsi la pérennité du projet.

Les études qui sont présentées ensuite portent essentiellement sur la structure interne des astres compacts, c'est-à-dire les propriétés de l'intérieur de ces objets jusqu'au voisinage de la surface (ou horizon pour les trous noirs), par opposition aux questions d'accrétion-éjection ou des mécanismes d'émission des pulsars. Les questions et problèmes physiques abordés peuvent être néanmoins très riches. Dans le cas des étoiles à neutrons, la question de l'équation d'état est centrale : quelle sont la composition et les propriétés de la matière froide aux densités voisines de la densité nucléaire ? Il faut ajouter à cela les propriétés du champ magnétique (Fig. III.1), la superfluidité et supraconductivité, l'écorce (élasticité), l'apparition de condensats de particules exotiques au centre, ... Tous ces points n'ont pas été étudiés dans les travaux présentés ci-après, il convient donc de garder en mémoire que les modèles sont encore trop incomplets pour être tout-à-fait réalistes et qu'il reste beaucoup de travail à effectuer pour incorporer tous les « ingrédients physiques » dans un modèle numérique cohérent. Afin d'illustrer ce point, on peut citer la quasi-impossibilité (aujourd'hui) d'effectuer des calculs exacts ou numériques en chromodynamique quantique (QCD) et d'obtenir une équation d'état fiable pour la matière froide au-delà de la densité nucléaire. Ces conditions de température et de pression n'étant pas non plus accessibles par les expériences de physique des particules, il reste la possibilité de contraindre cette équation d'état par les observations astrophysiques : beaucoup d'informations sont données par les vitesses de rotation (ou pulsation), les masses et surtout les rayons, bien que ces derniers soient très difficiles à obtenir.

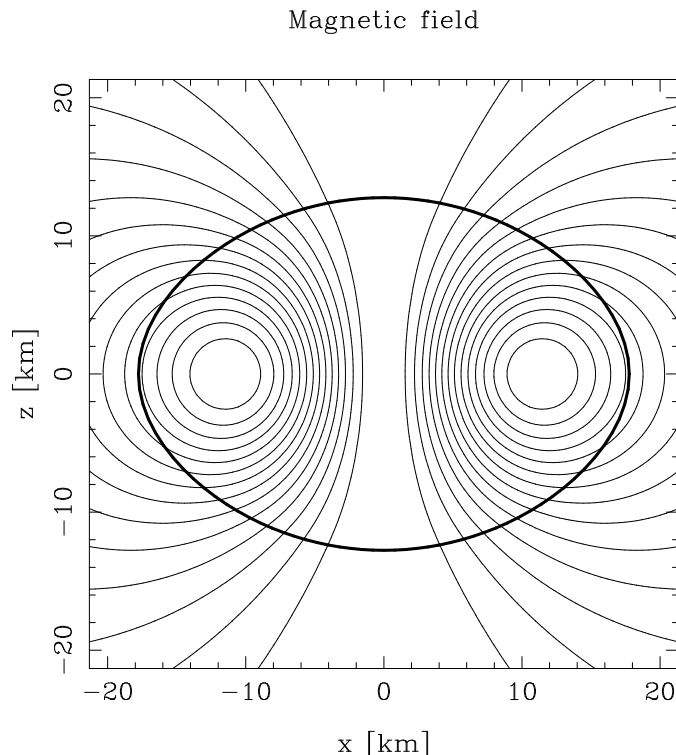


FIG. III.1 – Lignes de champ magnétique dans le plan (x, z) , pour une étoile à neutrons en rotation. La surface de l'étoile est donnée par le trait épais. D'après les modèles numériques décrits dans [64, 343].

Un travail a été réalisé avec M. Lap-Ming Lin, afin de pouvoir obtenir des conditions initiales pour le code d'effondrement COCONUT, mais aussi pour étudier les propriétés de la jauge de Dirac et du formalisme contraint en présence de matière. Dans cette optique, nous avons mis au point un programme de calcul des caractéristiques d'étoiles en rotation en relativité générale dans la jauge de Dirac et nous l'avons testé en détails. Les résultats ont été publiés dans l'article Lin & Novak 2006 [293] (Chap. 9), où nous explicitons aussi les techniques numériques. Cette approche est particulièrement bien adaptée au calcul de données initiales dans l'approximation de la 3-métrique conformément plate, puisqu'il suffit alors de mettre à zéro le tenseur h^{ij} de déviation de la 3-métrique conforme par rapport à la métrique plate. Nous avons ainsi à notre disposition les données initiales nécessaires à COCONUT, de la manière la plus correcte possible. Toujours dans le domaine des modèles d'étoiles en rotation, nous avons développé, avec MM. Reinhardt Prix et Gregory Comer, des modèles superfluides. En effet, assez vite après leur formation dans la supernova, les étoiles à neutrons se refroidissent bien en dessous de leur température de Fermi et les neutrons qui la constituent deviennent superfluides. Or, dans les modèles numériques utilisés habituellement, cette propriété n'était pas prise en compte. Dans l'article Prix *et al.* 2005 [379] (Chap. 10 ci-après), nous avons développé un cadre théorique, ainsi qu'un code numérique pour le calcul de modèles d'étoiles à neutrons en rotation, prenant en compte la superfluidité dans la théorie de la relativité générale. En particulier, les modèles font appel au formalisme à deux fluides développé par Brandon Carter, pour lequel un fluide

représente les neutrons superfluides et l'autre l'ensemble des particules chargées qui sont liées ensemble par la viscosité et le champ magnétique. L'équation d'état, bien qu'analytique, prend en compte l'interaction entre ces deux fluides, notamment à travers un terme d'entraînement, qui dépend de la vitesse relative des deux fluides. Avec ce code, nous avons trouvé l'existence de configurations dans lesquelles l'un des fluides a bien une forme aplatie le long de l'axe de rotation (ce qui est la situation intuitive) et l'autre a, en revanche, une forme allongée le long de cet axe. Un résultat intéressant du point de vue observationnel est que la limite de rotation maximale d'étoiles à deux fluides est donnée par la rotation maximale du fluide le plus externe, même si celle-ci est inférieure à celle du fluide qui n'atteint pas la surface. D'une manière générale, les propriétés superfluides des étoiles à neutrons sont invoquées pour expliquer les phénomènes observés de « glitch » des pulsars, où le signal subit une brusque accélération.

En ce qui concerne le champ magnétique dans les étoiles à neutrons et suivant l'idée du professeur Pfister de l'Université de Tübingen, une étude sur le rapport gyromagnétique (masse \times moment magnétique / charge \times moment cinétique) des objets autogravitants chargés en relativité générale a été faite avec M. Emmanuel Marcq. Nous avons ainsi numériquement montré que, dans le cadre de la relativité générale et pour des objets isolants chargés, ce rapport pouvait varier entre 1 (qui est la valeur dans le cadre de la théorie Newtonienne de la gravité) et 1.8 [343]. Il existe donc un « gap » entre cette valeur maximale et celle associée aux trous noirs de Kerr chargés, qui est 2. Cette valeur 2 est par ailleurs associée au rapport gyromagnétique des particules élémentaires en mécanique quantique. Cette étude, exposée au chapitre 11 a également permis d'implémenter dans la bibliothèque LORENE quelques outils pour la résolution des équations de Maxwell stationnaires, telles qu'elles sont décrites dans les travaux plus anciens [67, 64].

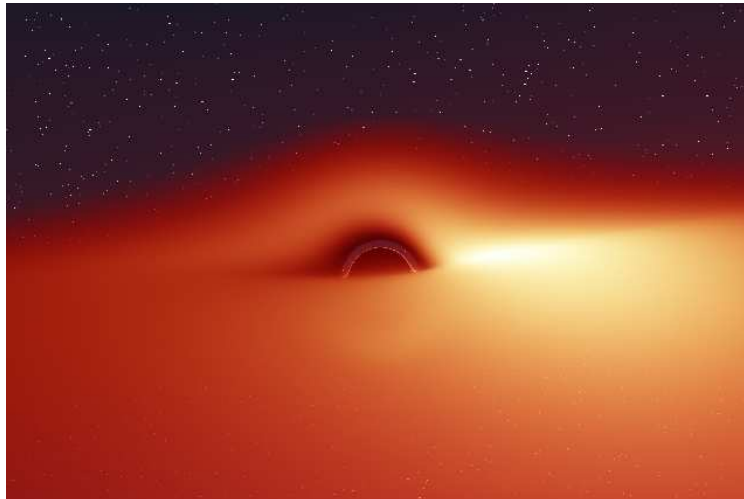


FIG. III.2 – Image simulée d'un disque d'accrétion autour d'un trou noir © Jean-Alain Marck. La courbure des rayons lumineux fait qu'il est possible de voir la partie du disque qui est « derrière » le trou noir comme étant au dessus. Des images plus récentes et plus réalistes ont été réalisées par A. Riazuelo [386].

Enfin, un autre aspect a été abordé avec un travail sur l'effondrement d'une étoile à neutrons,

de masse inférieure à la masse critique, en trou noir [338] (voir Chap. 12). Cela peut se produire si l'étoile à neutrons, récemment produite lors de la supernova, reçoit de l'énergie cinétique des couches externes du progéniteur, qui lui retombent dessus. Cette énergie cinétique peut alors aider l'étoile à neutrons à passer la « barrière de potentiel » qui la sépare d'un trou noir et former des trous noirs de faibles masses. S'il est aujourd'hui admis que les trous noirs provenant de l'évolution stellaire ont une masse supérieure à la masse maximale des étoiles à neutrons (autour de 2 masses solaires, suivant les caractéristiques mal connues de la matière nucléaire), les résultats obtenus montrent qu'ils peuvent aussi avoir une masse inférieure, suivant les conditions exactes de leur naissance au cours du phénomène de *supernova*. En plus, ces simulations numériques ont permis de montrer que ces objets suivaient également une loi d'échelle pour la masse du trou noir formé en fonction de l'énergie cinétique impulsée à l'étoile à neutrons. Ces phénomènes entrent ainsi dans une classe d'universalité étudiée par Matt Choptuik dans les années 90 appelée *effondrements critiques* [117]. L'aspect d'effondrement critique de ce travail a été ensuite amélioré, avec un code nettement plus performant, et les valeurs erronées des exposants critiques ont été récemment corrigées par Noble et Choptuik (2008) [335].

En ce qui concerne les trous noirs la théorie peut sembler moins incertaine. Il reste que ces objets se comportent souvent de manière contraire à l'intuition (Fig. III.2) et que leur modélisation numérique n'est pas aisée. En effet, dans le cadre de la relativité générale, un trou noir implique l'existence d'une singularité c'est-à-dire que tous les champs physiques divergent en ce(s) point(s). Il existe alors essentiellement deux techniques numériques pour représenter le trou noir. La première est d'appliquer une prescription analytique (généralement en $1/r$) à la partie singulière des champs au voisinage du centre du trou noir, puis d'évoluer ces champs dans un formalisme et une jauge bien adaptés ; c'est la méthode des « punctures » [87, 474]. La seconde consiste à ne pas résoudre les équations au voisinage de la singularité, et à remplacer ce domaine par des conditions au bord, quand c'est nécessaire ; c'est la méthode d'excision [14, 264]. C'est cette dernière méthode qui est utilisée dans notre groupe, à l'Observatoire de Meudon. D'une part cette approche est plus claire du point de vue mathématique [238] et d'autre part, elle permet aussi des diagnostics très précis sur les propriétés physiques du trou noir. En effet, cette technique est basée sur les concepts *locaux* d'horizon apparent et d'horizon dynamique [39, 222] (voir aussi chapitre 7). Ainsi, le travail avec M. Nicolas Vasset, qui a fini sa thèse sous ma responsabilité, sur les modèles numériques de trous noirs a donné lieu à un article Vasset *et al.* (2009) [475] (Chap. 13). Il montre en particulier que, dans le formalisme contraint et la jauge de Dirac, il n'est pas non plus nécessaire d'imposer des conditions au bord du trou noir sur la métrique conforme ($\tilde{\gamma}_{ij}$, voir section 1.2.2) dans le cas stationnaire, contrairement à ce qui avait été annoncé dans la littérature par un groupe américain [132]. C'est aussi le premier résultat numérique capable de retrouver la métrique d'un trou noir en rotation (Kerr), en ne partant que de conditions au bord données sur l'horizon. De nombreux tests ont été donnés dans cet article pour valider le fait que l'espace-temps obtenu numériquement était bien celui d'un trou noir de Kerr.

Chapitre 8

Combining spectral and shock-capturing methods : A new numerical approach for 3D relativistic core-collapse simulations

Version publiée : H. Dimmelmeier, J. Novak, J. A. Font, J. M. Ibáñez et E. Müller, Physical Review D 71, 064023 (2005).

Sommaire

8.1	Introduction	245
8.2	Physical model and equations	249
8.3	Numerical methods	254
8.4	Code tests and applications	265
8.5	Conclusions	289
8.A	Differences to previous 2D CFC simulations	290

8.1 Introduction

8.1.1 Relativistic core collapse simulations

Improving our understanding of the formation of neutron stars as a result of the gravitational collapse of the core of massive stars is a difficult endeavour involving many aspects of extreme and not very well understood physics of the supernova explosion mechanism [97]. Numerical simulations of core collapse supernova are driving progress in the field despite the limited knowledge on issues such as realistic precollapse stellar models (including rotation) or realistic equation of state, as well as numerical limitations due to Boltzmann neutrino transport, multidimensional hydrodynamics, and relativistic gravity. Axisymmetric and three-dimensional approaches based on Newtonian gravity are available since a few decades now (see e.g. [325] and references therein). These approaches, which are

constantly improving over time, have provided valuable information on important issues such as the dynamics of the collapse of a stellar core to nuclear density, the formation of a proto-neutron star, and the propagation of the shock front which ultimately is believed to eject the outer layers of the stellar progenitor. Currently, however, even the most realistic simulations of both nonrotating and rotating progenitor models do not succeed in producing explosions (see [97] and references therein).

In addition, the incorporation of full relativistic gravity in the simulations is likely to bring in well-known difficulties of numerical relativity, where the attempts are traditionally hampered by challenging mathematical, computational, and algorithmic issues as diverse as the formulation of the field equations, robustness, efficiency, and long-term stability (particularly if curvature singularities are either initially present or develop during black hole formation). As high densities and velocities are involved in combination with strong gravitational fields, gravitational collapse and neutron star formation constitute a challenging problem for general relativistic hydrodynamic simulations. The pace of the progress is, no wonder, slow; for instance, in the three-dimensional case, there is still no description of core collapse in full general relativity today, even for the simplest matter models one can conceive, where all microphysics is neglected.

In recent years, the interest in performing core collapse simulations has been further motivated by the necessity of obtaining reliable gravitational waveforms from (rotating) core collapse, one of the main targets of gravitational radiation for the present and planned interferometer detectors such as LIGO, GEO600, and VIRGO (see [194] for a review). As a result of the complexities listed above, it is not surprising that most previous studies aimed at computing the gravitational wave signature of core collapse supernovae have considered greatly simplified parameterized models [324, 175, 321, 484, 499, 383, 147, 148, 149, 192, 193, 258, 285, 423, 350]. In addition to the burst signal of gravitational waves emitted during core bounce, multidimensional simulations have also provided the signals produced by convection [327] (see also [326] for the most realistic simulations available at present), as well as those from the resulting neutrino emission [98, 327].

From the above references it becomes apparent that our understanding of core collapse and neutron star formation has advanced mainly by studies carried out employing Newtonian dynamics. The situation is now slowly changing, at least for simplified matter models where microphysics and radiation transport are not yet included, with new formulations of the Einstein field equations and of the general relativistic hydrodynamics equations. Unfortunately, the $3 + 1$ Einstein equations describing the dynamics of spacetime are a complicated set of coupled, highly nonlinear hyperbolic-elliptic equations with plenty of terms. Their formulation in a form suitable for accurate and stable numerical calculations is not unique, and constitutes one of the major fields of current research in numerical relativity (see [289, 299] and references therein). Not surprisingly, approximations of those equations have been suggested, such as the conformal flatness condition of Isenberg–Wilson–Mathews [260, 481] (CFC hereafter), who proposed to approximate the 3-metric of the $3 + 1$ decomposition by a conformally flat metric.

Using this approximation, Dimmelmeier *et al.* [147, 148, 149] presented the first relativistic simulations of the core collapse of rotating polytropes and neutron star formation in axisymmetry, providing an in-depth analysis of the dynamics of the process as well as of the gravitational wave emission. The results showed that relativistic effects may qualitatively change in some cases the dynamics of the collapse obtained in previous Newtonian simulations [321, 325]. In particular, core collapse with multiple bounces was found to be strongly suppressed when employing relativistic gravity. In most cases, compared to Newtonian simulations, the gravitational wave signals are weaker and their spectra exhibit higher average frequencies, as the newly born proto-neutron stars have stronger compactness

in the deeper relativistic gravitational potential. Therefore, telling from simulations based on rotating polytropes, the prospects for detection of gravitational wave signals from supernovae are most likely not enhanced by taking into account relativistic gravity. The gravitational wave signals computed by Dimmelmeier et al. [147, 148, 149] are within the sensitivity range of the planned laser interferometer detectors if the source is located within our Galaxy or in its local neighbourhood. A catalogue of the core collapse waveforms presented in [149] is available electronically [197]. This catalogue is currently being employed by gravitational wave data analysis groups to calibrate their search algorithms (see e.g. [372] for results concerning the VIRGO group).

More recently, Shibata and Sekiguchi [423] have presented simulations of axisymmetric core collapse of rotating polytropes to neutron stars in *full* general relativity. These authors used a conformal-traceless reformulation of the $3+1$ gravitational field equations commonly referred to in the literature by the acronym BSSN after the works of [421, 54] (but note that many of the new features of the BSSN formulation were anticipated as early as 1987 by Nakamura, Oohara, and Kojima [331]). The results obtained for initial models similar to those of [149] agree to high precision in both the dynamics of the collapse and the gravitational waveforms. This conclusion, in turn, implies that, at least for core collapse simulations to neutron stars, CFC is a very precise approximation of general relativity.

We note that in the relativistic core collapse simulations mentioned thus far [149, 423], the gravitational radiation is computed using the (Newtonian) quadrupole formalism. To the best of our knowledge the only exception to this is the work of Siebel et al. [432], where, owing to the use of the characteristic (light-cone) formulation of the Einstein equations, the gravitational radiation from axisymmetric core collapse simulations was unambiguously extracted at future null infinity without any approximation.

8.1.2 Einstein equations and spectral methods

The most common approach to numerically solve the Einstein equations is by means of finite differences (see [289] and references therein). However, it is well known that spectral methods [210, 102] are far more accurate than finite differences for smooth solutions (e.g. best for initial data without discontinuities), being particularly well suited to solve elliptic and parabolic equations. Good results can be obtained for hyperbolic equations as well, as long as no discontinuities appear in the solution. The basic principle underlying spectral methods is the representation of a given function $f(x)$ by its coefficients in a complete basis of orthonormal functions: sines and cosines (Fourier expansion) or a family of orthogonal polynomials (e.g. Chebyshev polynomials $T_i(x)$ or Legendre polynomials). In practice, of course, only a *finite* set of coefficients is used and one approximates f by the truncated series $f(x) \simeq \sum_{i=0}^n c_i T_i(x)$ of such functions. The use of spectral methods results in a very high accuracy, since the error made by this truncation decreases like e^{-n} for smooth functions (exponential convergence).

In an astrophysical context spectral methods have allowed to study subtle phenomena such as the development of physical instabilities leading to gravitational collapse [79]. In the last few years, spectral methods have been successfully employed by the *Meudon group* in a number of relativistic astrophysics scenarios [72], among them the gravitational collapse of a neutron star to a black hole, the infall phase of a tri-axial stellar core in a core collapse supernova (extracting the gravitational waves emitted in such process), the construction of equilibrium configurations of rapidly rotating neutron stars endowed with magnetic fields, or the tidal interaction of a star with a massive black hole. Their most recent work concerns the computation of the inertial modes of rotating stars [478], of quasi-equilibrium configurations of co-rotating binary black holes in general relativity [229], as well as the

evolution of pure gravitational wave spacetimes [73]. To carry out these numerical simulations the group has developed a fully object-oriented library called LORENE [216] (based on the C++ computer language) to implement spectral methods in spherical coordinates. Spectral methods are now employed in numerical relativity by other groups as well [185, 361].

8.1.3 Hydrodynamics equations and HRSC schemes

On the other hand, robust finite difference schemes to solve hyperbolic systems of conservation (and balance) laws, such as the Euler equations of fluid dynamics, are known for a long time and have been employed successfully in computational fluid dynamics (see e.g. [469] and references therein). In particular, the so-called upwind high-resolution shock-capturing schemes (HRSC schemes hereafter) have shown their advantages over other type of methods even when dealing with relativistic flows with highly ultrarelativistic fluid speeds (see e.g. [311, 176] and references therein). HRSC schemes are based on the mathematical information contained in the characteristic speeds and fields (eigenvalues and eigenvectors) of the Jacobian matrices of the system of partial differential equations. This information is used in a fundamental way to build up either exact or approximate Riemann solvers to propagate forward in time the collection of local Riemann problems contained in the initial data, once these data are discretized on a numerical grid. These schemes have a number of interesting properties: (1) The convergence to the physical solution (i.e. the unique weak solution satisfying the so-called entropy condition) is guaranteed by simply writing the scheme in conservation form, (2) the discontinuities in the solution are sharply and stably resolved, and (3) these methods attain a high order of accuracy in smooth parts of the solution.

8.1.4 Mariage des Maillages

From the above considerations, it seems a promising strategy, in the case of relativistic problems where coupled systems of elliptic (for the spacetime) and hyperbolic (for the hydrodynamics) equations must be solved, to use spectral methods for the former and HRSC schemes for the latter (where discontinuous solutions may arise). Showing the feasibility of such an approach is, in fact, the main motivation and aim of this paper. Therefore, we present and assess here the capabilities of a new, fully three-dimensional code whose distinctive features are that it combines both types of numerical schemes and implements the field equations and the hydrodynamic equations using spherical coordinates. It should be emphasized that our *Mariage des Maillages* approach is hence best suited for formulations of the Einstein equations which favor the appearance of elliptic equations against hyperbolic equations, i.e. either approximations such as CFC [260, 481] (the formulation we adopt in the simulations reported in this paper), higher-order post-Newtonian extensions [114], or *exact* formulations as recently proposed by [73, 401]. The hybrid approach put forward here has a successful precedent in the literature; using such combined methods, first results were obtained in one-dimensional core collapse in the framework of a tensor-scalar theory of gravitation [342].

We note that one of the main limitations of the previous axisymmetric core collapse simulations presented in [147, 148, 149] was the CPU time spent when solving the elliptic equations describing the gravitational field in CFC. The restriction was severe enough to prevent the practical extension of the investigation to the three-dimensional case. In that sense, spectral methods are again particularly appropriate as they provide accurate results with reasonable sampling, as compared with finite difference methods.

The three-dimensional code we present in this paper has been designed with the aim of studying general relativistic astrophysical scenarios such as rotational core collapse to neutron stars (and, eventually, to black holes), as well as pulsations and instabilities of the formed compact objects. Core collapse may involve, obviously, matter fields which are not rotationally symmetric. While during the infall phase of the collapse the deviations from axisymmetry should be rather small, for rapidly rotating neutron stars which form as a result of the collapse, or which may be spun up by accretion at later times, rotational (nonaxisymmetric) bar mode instabilities may develop, particularly in relativistic gravity and for differential rotation. In this regard, in the previous axisymmetric simulations of Dimmelmeier et al. [149], some of the most extremely rotating initial models yielded compact remnants which are above the thresholds for the development of such bar mode instabilities on secular or even dynamic time scales for Maclaurin spheroids in Newtonian gravity (which are $\beta_s \sim 0.14$ and $\beta_d \sim 0.27$, respectively, with $\beta = E_r/|E_b|$ being the ratio of rotational energy and gravitational binding energy).

Presently, only a few groups worldwide have developed finite difference, three-dimensional (Cartesian) codes capable of performing the kind of simulations we aim at, where the joint integration of the Einstein and hydrodynamics equations is required [414, 179, 181]. Further 3D codes are currently being developed by a group in the U.S. [161] and by a E.U. Research Training Network collaboration [41, 241].

8.1.5 Organization of the paper

The paper is organized as follows: In Section 8.2 we introduce the assumptions of the adopted physical model and the equations governing the dynamics of a general relativistic fluid and the gravitational field. Section 8.3 is devoted to describing algorithmic and numerical features of the code, such as the setup of both the spectral and the finite difference grids, as well as the basic ideas behind the HRSC schemes we have implemented to solve the hydrodynamics equations. In addition, a detailed comparison of the three different solvers for the metric equations and their practical applicability is given. In Section 8.4 we present a variety of tests of the numerical code, comparing the metric solver based on spectral methods to two other alternative methods using finite differences. We conclude the paper with a summary and an outlook to future applications of the code in Section 8.5. We use a spacelike signature $(-, +, +, +)$ and units in which $c = G = 1$ (unless explicitly stated otherwise). Greek indices run from 0 to 3, Latin indices from 1 to 3, and we adopt the standard convention for the summation over repeated indices.

8.2 Physical model and equations

8.2.1 General relativistic hydrodynamics

Flux-conservative hyperbolic formulation

Let ρ denote the rest-mass density of the fluid, u^μ its four-velocity, and P its pressure. The hydrodynamic evolution of a relativistic perfect fluid with rest-mass current $J^\mu = \rho u^\mu$ and energy-momentum tensor $T^{\mu\nu} = \rho h u^\mu u^\nu + P g^{\mu\nu}$ in a (dynamic) spacetime $g^{\mu\nu}$ is determined by a system of local conservation equations, which read

$$\nabla_\mu J^\mu = 0, \quad \nabla_\mu T^{\mu\nu} = 0, \quad (8.1)$$

where ∇_μ denotes the covariant derivative. The quantity h appearing in the energy-momentum tensor is the specific enthalpy, defined as $h = 1 + \epsilon + P/\rho$, where ϵ is the specific internal energy. The three-velocity of the fluid, as measured by an Eulerian observer at rest in a spacelike hypersurface Σ_t is given by

$$v^i = \frac{u^i}{\alpha u^0} + \frac{\beta^i}{\alpha}, \quad (8.2)$$

where α is the lapse function and β^i is the shift vector (see Section 8.2.2).

Following the work laid out in [46] we now introduce the following set of conserved variables in terms of the primitive (physical) hydrodynamic variables (ρ, v_i, ϵ) :

$$\begin{aligned} D &\equiv \rho W, \\ S_i &\equiv \rho h W^2 v_i, \\ \tau &\equiv \rho h W^2 - P - D. \end{aligned}$$

In the above expressions W is the Lorentz factor defined as $W = \alpha u^0$, which satisfies the relation $W = 1/\sqrt{1 - v_i v^i}$ and $v_i = \gamma_{ij} v^j$, where γ_{ij} is the 3-metric.

Using the above variables, the local conservation laws (8.1) can be written as a first-order, flux-conservative hyperbolic system of equations,

$$\frac{1}{\sqrt{-g}} \left[\frac{\partial \sqrt{\gamma} \mathbf{U}}{\partial t} + \frac{\partial \sqrt{-g} \mathbf{F}^i}{\partial x^i} \right] = \mathbf{Q}, \quad (8.3)$$

with the state vector, flux vector, and source vector given by

$$\begin{aligned} \mathbf{U} &= [D, S_j, \tau], \\ \mathbf{F}^i &= [D \hat{v}^i, S_j \hat{v}^i + \delta_j^i P, \tau \hat{v}^i + P v^i], \\ \mathbf{Q} &= \left[0, T^{\mu\nu} \left(\frac{\partial g_{\nu j}}{\partial x^\mu} - \Gamma_{\mu\nu}^\lambda g_{\lambda j} \right), \right. \\ &\quad \left. \alpha \left(T^{\mu 0} \frac{\partial \ln \alpha}{\partial x^\mu} - T^{\mu\nu} \Gamma_{\mu\nu}^0 \right) \right]. \end{aligned} \quad (8.4)$$

Here $\hat{v}^i = v^i - \beta^i/\alpha$, and $\sqrt{-g} = \alpha\sqrt{\gamma}$, with $g = \det(g_{\mu\nu})$ and $\gamma = \det(\gamma_{ij})$ being the determinant of the 4-metric and 3-metric, respectively (see Section 8.2.2). In addition, $\Gamma_{\mu\nu}^\lambda$ are the Christoffel symbols associated with $g_{\mu\nu}$.

Equation of state

The system of hydrodynamic equations (8.3) is closed by an equation of state (EoS) which relates the pressure to some thermodynamically independent quantities, e.g. $P = P(\rho, \epsilon)$. As in [148, 149, 432] we have implemented in the code a hybrid ideal gas EoS [262], which consists of a polytropic pressure contribution and a thermal pressure contribution, $P = P_p + P_{th}$. This EoS, which despite its simplicity is particularly suitable for stellar core collapse simulations, is intended to model the degeneracy pressure of the electrons and (at supranuclear densities) the pressure due to nuclear forces in the polytropic part, and the heating of the matter by shock waves in the thermal part. The hybrid EoS is constructed as follows.

For a rotating stellar core before collapse the polytropic relation between the pressure and the rest mass density,

$$P_p = K\rho^\gamma, \quad (8.5)$$

with $\gamma = \gamma_{\text{ini}} = 4/3$ and $K = 4.897 \times 10^{14}$ (in cgs units) is a fair approximation of the density and pressure stratification [325].

In order to start the gravitational collapse of a configuration initially in equilibrium, the effective adiabatic index γ is reduced from γ_{ini} to γ_1 on the initial time slice. During the infall phase of core collapse the matter is assumed to obey a polytropic EoS (8.5), which is consistent with the ideal gas EoS for a compressible inviscid fluid, $P = (\gamma - 1)\rho\epsilon$.

To approximate the stiffening of the EoS for densities larger than nuclear matter density ρ_{nuc} , we assume that the adiabatic index γ jumps from γ_1 to γ_2 at $\rho = \rho_{\text{nuc}}$. At core bounce a shock forms and propagates out, and the matter accreted through the shock is heated, i.e. its kinetic energy is dissipated into internal energy. This is reflected by a nonzero $P_{\text{th}} = \rho\epsilon_{\text{th}}(\gamma_{\text{th}} - 1)$, where $\epsilon_{\text{th}} = \epsilon - \epsilon_p$ with $\epsilon_p = P_p/[\rho(\gamma - 1)]$, in the post-shock region. We choose $\gamma_{\text{th}} = 1.5$. This choice describes a mixture of relativistic ($\gamma = 4/3$) and nonrelativistic ($\gamma = 5/3$) components of an ideal fluid.

Requiring that P and ϵ are continuous at the transition density ρ_{nuc} , one can construct an EoS for which both the total pressure P and the individual contributions P_p and P_{th} are continuous at ρ_{nuc} , and which holds during all stages of the collapse:

$$P = \frac{\gamma - \gamma_{\text{th}}}{\gamma - 1} K \rho_{\text{nuc}}^{\gamma_1 - \gamma} \rho^\gamma - \frac{(\gamma_{\text{th}} - 1)(\gamma - \gamma_1)}{(\gamma_1 - 1)(\gamma_2 - 1)} K \rho_{\text{nuc}}^{\gamma_1 - 1} \rho + (\gamma_{\text{th}} - 1)\rho\epsilon. \quad (8.6)$$

For more details about this EoS, we refer to [148, 262].

Our implementation of the hybrid EoS allows us to suppress the contribution of the thermal pressure P_{th} . In this case the EoS (8.6) analytically reduces to the polytropic relation (8.5). We use this EoS, with different values for γ and K , in the simulations of polytropic neutron star models presented below.

8.2.2 Metric equations

ADM metric equations

We adopt the ADM 3+1 formalism [35] to foliate the spacetime into a set of non-intersecting spacelike hypersurfaces. The line element reads

$$ds^2 = -\alpha^2 dt^2 + \gamma_{ij}(dx^i + \beta^i dt)(dx^j + \beta^j dt), \quad (8.7)$$

where α is the lapse function which describes the rate of advance of time along a timelike unit vector n^μ normal to a hypersurface, β^i is the spacelike shift three-vector which describes the motion of coordinates within a surface, and γ_{ij} is the spatial three-metric.

In the 3+1 formalism, the Einstein equations are split into evolution equations for the three-metric γ_{ij} and the extrinsic curvature K_{ij} , and constraint equations (the Hamiltonian and momentum

constraints) which must be fulfilled at every spacelike hypersurface:

$$\begin{aligned}
\partial_t \gamma_{ij} &= -2\alpha K_{ij} + \nabla_i \beta_j + \nabla_j \beta_i, \\
\partial_t K_{ij} &= -\nabla_i \nabla_j \alpha + \alpha (R_{ij} + K K_{ij} - 2K_{ik} K_j^k) \\
&\quad + \beta^k \nabla_k K_{ij} + K_{ik} \nabla_j \beta^k + K_{jk} \nabla_i \beta^k \\
&\quad - 8\pi \alpha \left(S_{ij} - \frac{\gamma_{ij}}{2} (S_k^k - \rho_H) \right), \\
0 &= R + K^2 - K_{ij} K^{ij} - 16\pi \rho_H, \\
0 &= \nabla_i (K^{ij} - \gamma^{ij} K) - 8\pi S^j.
\end{aligned} \tag{8.8}$$

In these equations ∇_i is the covariant derivative with respect to the three-metric γ_{ij} , R_{ij} is the corresponding Ricci tensor, R is the scalar curvature, and K is the trace of the extrinsic curvature K_{ij} . The matter fields appearing in the above equations, S_{ij} , S^j , and $\rho_H = \rho h W^2 - P$, are the spatial components of the stress-energy tensor, the three momenta, and the total energy, respectively.

The ADM equations have been repeatedly shown over the years to be intrinsically numerically unstable. Recently, there have been numerous attempts to reformulate above equations into forms better suited for numerical investigations (see [421, 54, 289, 299] and references therein). These approaches to delay or entirely suppress the excitation of constraint violating unstable modes include the BSSN reformulation of the ADM system [331, 421, 54] (see Section 8.1.2), hyperbolic reformulations (see [385] and references therein), or a new form with maximally constrained evolution [73]. In our opinion a consensus seems to be emerging currently in numerical relativity, which in general establishes that the more constraints are used in the formulation of the equations the more numerically stable the evolution is.

Conformal flatness approximation for the spatial metric

Based on the ideas of Isenberg [260] and Wilson *et al.* [481], and as it was done in the work of Dimmelmeier *et al.* [149], we approximate the general metric $g_{\mu\nu}$ by replacing the spatial three-metric γ_{ij} with the conformally flat three-metric, $\gamma_{ij} = \phi^4 \hat{\gamma}_{ij}$, where $\hat{\gamma}_{ij}$ is the flat metric ($\hat{\gamma}_{ij} = \delta_{ij}$ in Cartesian coordinates). In general, the conformal factor ϕ depends on the time and space coordinates. Therefore, at all times during a numerical simulation we assume that all off-diagonal components of the three-metric are zero, and the diagonal elements have the common factor ϕ^4 .

In CFC the following relation between the time derivative of the conformal factor and the shift vector holds:

$$\partial_t \phi = \frac{\phi}{6} \nabla_k \beta^k. \tag{8.9}$$

With this the expression for the extrinsic curvature becomes time-independent and reads

$$K_{ij} = \frac{1}{2\alpha} \left(\nabla_i \beta_j + \nabla_j \beta_i - \frac{2}{3} \gamma_{ij} \nabla_k \beta^k \right). \tag{8.10}$$

If we employ the maximal slicing condition, $K = 0$, then in the CFC approximation the ADM equations (8.8) reduce to a set of five coupled elliptic (Poisson-like) nonlinear equations for the metric

components,

$$\begin{aligned}\hat{\Delta}\phi &= -2\pi\phi^5\left(\rho hW^2 - P + \frac{K_{ij}K^{ij}}{16\pi}\right), \\ \hat{\Delta}(\alpha\phi) &= 2\pi\alpha\phi^5\left(\rho h(3W^2 - 2) + 5P + \frac{7K_{ij}K^{ij}}{16\pi}\right), \\ \hat{\Delta}\beta^i &= 16\pi\alpha\phi^4S^i + 2\phi^{10}K^{ij}\hat{\nabla}_j\left(\frac{\alpha}{\phi^6}\right) - \frac{1}{3}\hat{\nabla}^i\hat{\nabla}_k\beta^k,\end{aligned}\tag{8.11}$$

where $\hat{\nabla}_i$ and $\hat{\Delta}$ are the flat space Nabla and Laplace operators, respectively. We note that the way of writing the metric equations with a Laplace operator on the left hand side can be exploited by numerical methods specifically designed to solve such kind of equations (see Sections 8.3.4 and 8.3.4 below).

These elliptic metric equations couple to each other via their right hand sides, and in case of the three equations for the components of β^i also via the operator $\hat{\Delta}$ acting on the vector β^i . They do not contain explicit time derivatives, and thus the metric is calculated by a fully constrained approach, at the cost of neglecting some evolutionary degrees of freedom in the spacetime metric. In the astrophysical situations we plan to explore (e.g. evolution of neutron stars or core collapse of massive stars), the equations are entirely dominated by the source terms involving the hydrodynamic quantities ρ , P , and v^i , whereas the nonlinear coupling through the remaining, purely metric, source terms becomes only important for strong gravity. On each time slice the metric is hence solely determined by the instantaneous hydrodynamic state, i.e. the distribution of matter in space.

Recently, Cerdá-Durán et al. [114] have extended the above CFC system of equations (and the corresponding core collapse simulations in CFC reported in [149]) by the incorporation of additional degrees of freedom in the approximation, which render the spacetime metric exact up to the second post-Newtonian order. Despite the extension of the five original elliptic CFC metric equations for the lapse, the shift vector, and the conformal factor by additional equations, the final system of equations in the new formulation is still elliptic. Hence, the same code and numerical schemes employed in [149] and in the present work can be used. The results obtained by Cerdá-Durán et al. [114] for a representative subset of the core collapse models in [149] show only minute differences with respect to the CFC results, regarding both the collapse dynamics and the gravitational waveforms. We point out that Shibata and Sekiguchi [423] have recently considered axisymmetric core collapse of rotating polytropes to neutron stars in full general relativity (i.e. no approximations) using the 3+1 BSSN formulation of the Einstein equations. Interestingly, the results obtained for initial models similar to those of [149] agree to high precision in the dynamics of the collapse and on the gravitational waveforms, which supports the suitability and accuracy of the CFC approximation for simulations of relativistic core collapse to neutron stars (see also Section 8.4.2).

In addition, there has been a direct comparison between the CFC approximation and perturbative analytical approaches (post-Newtonian and effective-one-body), which shows a very good agreement in the determination of the innermost stable circular orbit of a system of two black holes [142].

Metric equation terms with noncompact support

In general, the right hand sides of the metric equations (8.11) contain nonlinear source terms of noncompact support. For a system with an isolated matter distribution bounded by some stellar radius r_s , the source term of each of the metric equations for a metric quantity u can be split into a “hydrodynamic” term with compact support S_h and a purely “metric” term with noncompact support

S_m . Where no matter is present, only the metric term remains:

$$\hat{\Delta}u = \begin{cases} S_h(u) + S_m(u) & \text{for } r \leq r_s, \\ S_m(u) & \text{for } r > r_s. \end{cases} \quad (8.12)$$

The source term S_m vanishes only for $K_{ij} = 0$ and thus $\beta^i = 0$, i.e. if the three-velocity vanishes and the matter is static. As a consequence of this, only a spherically symmetric static matter distribution will yield a time-independent solution to Eq. (8.12), which is equivalent to the spherically symmetric Tolman–Oppenheimer–Volkoff (TOV) solution of hydrostatic equilibrium. In this case the vacuum metric is given by the solution of a homogeneous Poisson equation, $u = k_1 + k_2/r$, the constants k_1 and k_2 being determined by boundary values e.g. at r_s .

A time-dependent spherically symmetric matter interior suffices to yield a nonstatic vacuum metric ($u = u(t)$ everywhere). However, this is not a contradiction to Birkhoff’s theorem, as it is purely a gauge effect. A transformation of the vacuum part of the metric from an isotropic to a Schwarzschild-like radial coordinate leads to the static (and not conformally flat) standard Schwarzschild vacuum spacetime.

Thus, in general, the vacuum metric solution to Eqs. (8.11) cannot be obtained analytically, and therefore (except for TOV stars) no exact boundary values can be imposed for ϕ , α , and β^i at some finite radius r . We note that this property of the metric equations is no consequence of the *approximative* character of conformal flatness, as in spherical symmetry the CFC renders the exact ADM equations (8.8), but rather results from the choice of the (isotropic) radial coordinate.

8.3 Numerical methods

8.3.1 Finite difference grid

The expressions for the hydrodynamic and metric quantities outlined in Section 8.2 are in covariant form. For a numerical implementation of these equations, however, we have to choose a suitable coordinate system adapted to the geometry of the astrophysical situations intended to be simulated with the code.

As we plan to investigate isolated systems with matter configurations not too strongly departing from spherical symmetry with a spacetime obeying asymptotic flatness, the formulation of the hydrodynamic and metric equations, Eqs. (8.3) and (8.11), and their numerical implementation are based on spherical polar coordinates (t, r, θ, φ) . This coordinate choice facilitates the use of fixed grid refinement in form of nonequidistant radial grid spacing. Additionally, in spherical coordinates the boundary conditions for the system of partial differential metric equations (8.11) are simpler to impose (at finite or infinite distance) on a spherical surface than on a cubic surface if Cartesian coordinates were used. We have found no evidence of numerical instabilities arising at the coordinate singularities at the origin ($r = 0$) or at the axis ($\theta = 0, \pi$) in all simulations performed thus far with the code (see [165, 439] for related discussions on instabilities in codes based upon spherical coordinates).

Both the discretized hydrodynamic and metric quantities are located on the Eulerian *finite difference grid* at cell centers $(r_i, \theta_j, \varphi_k)$, where i, j, k run from 1 to n_r, n_θ, n_φ , respectively. The angular grid zones in the θ - and φ -direction are each equally spaced, while the radial grid, which extends out to a finite radius r_{fd} larger than the stellar radius r_s , can be chosen to be equally or logarithmically spaced. Each cell is bounded by two interfaces in each coordinate direction. Values on ghost zone cell centers, needed to impose boundary conditions, are obtained with the symmetry conditions described

in [148]. We further assume equatorial plane symmetry in all simulations presented below (the code, however, is not restricted to this symmetry condition). Expressions containing finite differences in space on this grid are calculated with second order accuracy.

Note that the space between the surface of the star, the radius of which in general is angular dependent, and the outer boundary of the finite difference grid is filled with an artificial atmosphere (as done in codes similar to ours, see [181, 161, 41]). This atmosphere obeys the polytropic EoS (8.5), and has a very low density such that its presence does not affect the dynamics of the star [148]. As an example, we observe a slight violation of conservation of rest mass and angular momentum in simulations of axisymmetric rotational core collapse of the order of 10^{-4} . This small violation can be entirely attributed to the interaction of the stellar matter with the artificial atmosphere (see Appendix 8.A.2).

8.3.2 Spectral methods and grid

Spectral methods

Our most general metric solver is based on spectral methods (see Section 8.3.4). The basic principle of these methods has been given in Section 8.1.2. Let us now describe some details of our implementation in the case of 3D functions in spherical coordinates. The interested reader can refer to [72] for details. A function f can be decomposed as follows (ξ is linked with the radial coordinate r , as given below):

$$f(\xi, \theta, \varphi) = \sum_{k=0}^{\hat{n}_\varphi} \sum_{j=0}^{\hat{n}_\theta} \sum_{i=0}^{\hat{n}_r} c_{ijk} T_i(\xi) Y_j^k(\theta, \varphi), \quad (8.13)$$

where $Y_j^k(\theta, \varphi)$ are spherical harmonics. The angular part of the function can also be decomposed into a Fourier series, to compute angular derivatives more easily. If f is represented by its coefficients c_{ijk} , it is easy to obtain the coefficients of e.g. $\partial f / \partial r$, Δf (or the result of any linear differential operator applied to f) thanks to the properties of Chebyshev polynomials or spherical harmonics. For instance, to compute the coefficients of the radial derivative of f , we make use of the following recursion formula on Chebyshev polynomials:

$$\frac{dT_{n+1}(x)}{dx} = 2(n+1)T_n(x) + \frac{n+1}{n-1} \frac{dT_{n-1}(x)}{dx} \quad \forall n > 1. \quad (8.14)$$

A grid is still needed for two reasons: firstly, to calculate these coefficients through the computation of integrals, and secondly to evaluate non-linear operators (e.g. $\nabla f \times \nabla f$), using the values of the functions at grid points (in physical space). The spectral grid points, called collocation points are situated at $(\hat{r}_i, \hat{\theta}_j, \hat{\varphi}_k)$, where i, j, k run from 1 to $\hat{n}_r, \hat{n}_\theta, \hat{n}_\varphi$, respectively. They are the nodes of a Gauss–Lobato quadrature used to compute the integrals giving the spectral coefficients. The use of Fast Fourier Transforms (FFT) for the angular part requires equally spaced points in the angular directions, whereas a fast Chebyshev transform (also making use of FFT) requires that the radial grid points correspond, in ξ , to the zeros of $T_{\hat{n}_r}$. Note that in our simulations each of the domains contains the same number of radial and angular collocation points.

In order to be able to cover the entire space ($r \in [0, +\infty]$) and to handle coordinate singularities at the origin ($r = 0$), we use several grid *domains*:

- a nucleus spanning from $r = 0$ to r_d , where we set $r = \alpha\xi$, with $\xi \in [0, 1]$ and α being a constant (we use either only even Chebyshev polynomials $T_{2i}(\xi)$, or only odd polynomials $T_{2i+1}(\xi)$);

- an arbitrary number (including zero) of shells bounded by the inner radius r_{di} and outer radius r_{di+1} , where we set $r = \alpha_i \xi + \beta_i$ with $\xi \in [-1, 1]$ and α_i and β_i being constants depending on the shell number i ;
- a compactified external domain extending from the outer boundary of the finite difference grid at r_{fd} to radial infinity, where we set $r = 1/[\alpha_c(\xi + 1)]$, with $\xi \in [-1, 1]$ and α_c being a constant.

Furthermore, we assume that the ratio f_d between the outer boundary radii of two consecutive domains is constant, which yields the relation

$$f_d = \left(\frac{r_{fd}}{r_d} \right)^{1/(n_d-2)} \quad (8.15)$$

where n_d is the number of domains (including the nucleus and the external compactified domain). Thus a particular choice of n_d and fixing the radius of the nucleus r_d completely specifies the setup of the spectral grid:

$$\begin{aligned} r_{d1} &= r_d, \\ &\vdots \\ r_{di} &= f_d \times r_{di-1}, \\ &\vdots \\ r_{dn_d-1} &= r_{fd}, \\ r_{dn_d} &= \infty. \end{aligned} \quad (8.16)$$

The setup of the spectral grid and the associated finite difference grid for a typical stellar core collapse model is exemplified in Fig. 8.1 for $\hat{n}_r = 33$ grid points per spectral radial domain and $n_r = 200$ finite difference grid points. Particularly in the central parts of the star (upper panel) the logarithmic radial spacing of the finite difference grid is obvious. While the finite difference grid ends at the finite radius r_{fd} (with the exception of four ghost zones, which are needed for the hydrodynamic reconstruction scheme; see Section 8.3.3), the radially compactified outermost 6th domain of the spectral grid covers the entire space to radial infinity (lower panel). The finite difference grid is fixed in time, while the boundaries r_{di} of the spectral radial domains (and thus the radial collocation points) change adaptively during the evolution (for details, we refer to Section 8.4.2). Note that the radial collocation points of the spectral grid, which correspond to the roots of the Chebyshev polynomials (for the Gauss–Lobato quadrature), are concentrated towards the domain boundaries.

Generally speaking, in order to achieve a comparable accuracy in the representation of functions and their derivatives, the finite difference grid needs much more points than the spectral one. For example, when considering the representation of some function like $\exp(-x^2)$ on the interval $[0, 1]$, spectral methods using Chebyshev polynomials need ~ 30 coefficients (and grid points) to reach machine double precision (10^{-16}) for the representation of the function and 10^{-13} for the representation of its first derivative. For comparison, a third order scheme based on finite differences needs $\sim 10^5$ points to achieve the same accuracy.

Communication between grids

Passing information from the spectral grid to the finite difference grid is technically very easy. Knowing the spectral coefficients of a function, this step simply requires the evaluation of the sum (8.13) at the finite difference grid points. The drawback of this method, as it will be discussed in Section 8.4.1, is the computational time spent. In 3D this time can even be larger than the time spent by the spectral elliptic solver. Going from the finite difference grid to the spectral grid requires an actual

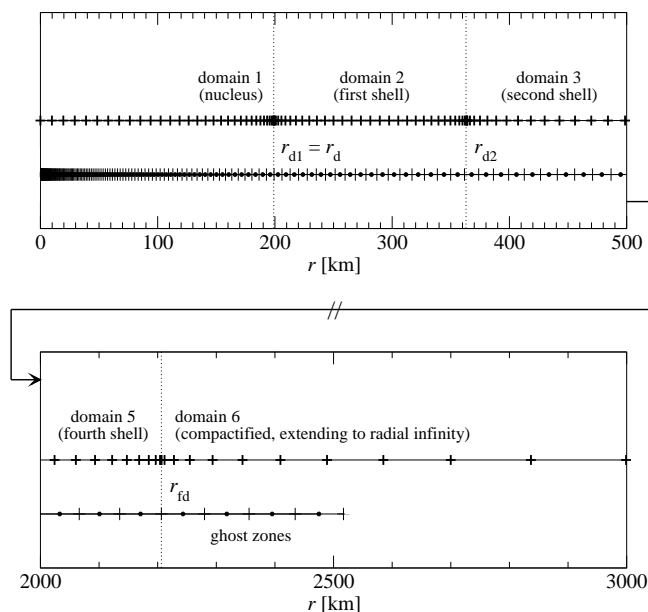


Figure 8.1: Radial setup of the initial spectral grid (collocation points are marked by plus symbols) and the time-independent finite difference grid (cell centers are marked by filled circles, separated by cell interfaces symbolized by vertical dashes) for a typical core collapse simulation. The upper panel shows the innermost 500 km containing the nucleus (ending at $r_d \approx 200$ km), the first shell, and a part of the second shell of the spectral grid. In the lower panel a part of the last regular shell (which is confined by the outer boundary of the finite difference grid at $r_{fd} \approx 2200$ km) and the beginning of the compactified domain of the spectral grid are plotted. The domain boundaries are indicated by vertical dotted lines.

interpolation, taking special care to avoid Gibbs phenomena that can appear in the spectral representation of discontinuous functions. The matter terms entering in the sources of the gravitational field equations can be discontinuous when a shock forms. Thus, it is necessary to smooth or filter out high frequencies that would otherwise spoil the spectral representation. This introduces a numerical error in the fields that should remain within the overall error of the code. The important point to notice is that an accurate description needs not be achieved in the spectral representation of the sources (the hydrodynamic quantities are well described on the finite difference grid), but in that of the gravitational field, which is always continuous, as well as its first derivatives.

Technically, we interpolate from the finite difference grid to the spectral grid using a one-dimensional algorithm and intermediate grids. We first perform an interpolation in the r -direction, then in the θ -direction and finally in the φ -direction. We can choose between piecewise linear or parabolic interpolations, and a scheme that globally minimizes the norm of the second derivative of the interpolated function [342]. The filtering of spectral coefficients is performed *a posteriori* by removing the coefficients corresponding to higher frequencies. For example, in the radial direction, this is done by canceling the c_{ijk} in Eq. (8.13) for i larger than a given threshold. In practice, best results were found when cancelling the last third of radial coefficients. This can be linked with the so-called “two-thirds rule” used for spectral computations of quadratically nonlinear equations [85]. Nevertheless, a different (higher) threshold would also give good results, in the sense that there are no high-frequency

terms rising during the metric iteration.

8.3.3 High-resolution shock-capturing schemes

As in our previous axisymmetric code [148, 149], in the present code the numerical integration of the system of hydrodynamic equations is performed using a Godunov-type scheme. Such schemes are specifically designed to solve nonlinear hyperbolic systems of conservation laws (see, e.g. [469] for general definitions and [311, 176] for specific details regarding their use in special and general relativistic hydrodynamics). In a Godunov-type method the knowledge of the characteristic structure of the equations is crucial to design a solution procedure based upon either exact or approximate Riemann solvers. These solvers, which compute at every cell-interface of the numerical grid the solution of local Riemann problems, guarantee the proper capturing of all discontinuities which may appear in the flow.

The time update of the hydrodynamic equations (8.3) from t^n to t^{n+1} is performed using a method of lines in combination with a second-order (in time) conservative Runge–Kutta scheme. The basic conservative algorithm reads:

$$\begin{aligned} U_{i,j,k}^{n+1} = U_{i,j,k}^n &- \frac{\Delta t}{\Delta r_i} \left(\widehat{F}_{i+1/2,j,k}^r - \widehat{F}_{i-1/2,j,k}^r \right) \\ &- \frac{\Delta t}{\Delta \theta} \left(\widehat{F}_{i,j+1/2,k}^\theta - \widehat{F}_{i,j-1/2,k}^\theta \right) \\ &- \frac{\Delta t}{\Delta \varphi} \left(\widehat{F}_{i,j,k+1/2}^\varphi - \widehat{F}_{i,j,k-1/2}^\varphi \right) \\ &+ \Delta t Q_{i,j,k}. \end{aligned} \quad (8.17)$$

The index n represents the time level, and the time and space discretization intervals are indicated by Δt and Δr_i , $\Delta \theta$, and $\Delta \varphi$ for the r -, θ -, and φ -direction, respectively. The numerical fluxes along the three coordinate directions, \widehat{F}^r , \widehat{F}^θ , and \widehat{F}^φ , are computed by means of Marquina’s flux formula [157]. A family of local Riemann problems is set up at every cell-interface, whose jumps are minimized with the use of a piecewise parabolic reconstruction procedure (PPM) which provides third-order accuracy in space.

We note that Godunov-type schemes have also been implemented recently in 2D and 3D Cartesian codes designed to solve the coupled system of the Einstein and hydrodynamic equations, as reported in [179, 181, 416, 41].

8.3.4 Elliptic solvers

In the following we present the three different approaches we have implemented in our code to numerically solve the system of metric equations (8.11). We compare the properties of these solvers with special focus on issues like

- radius and order of convergence,
- scaling with resolution in various coordinate directions,
- imposition of boundary conditions,
- assumptions about the radial extension of the grid,
- computational performance,

- parallelization issues, and
- extensibility from two to three spatial dimensions.

In order to formalize the metric equations we define a vector of unknowns

$$\hat{u} = u^p = (\phi, \alpha\phi, \beta^1, \beta^2, \beta^3). \quad (8.18)$$

Then the metric equations (8.11) can be written as

$$\hat{f}(\hat{u}) = f^q(u^p) = 0, \quad (8.19)$$

with $\hat{f} = f^q$ denoting the vector of the five metric equations for \hat{u} ($p, q = 1, \dots, 5$). For metric solvers 1 and 2 the metric equations are discretized at cell centers $(r_i, \theta_j, \varphi_k)$ on the finite difference grid. Correspondingly, for metric solver 3 the metric equations are evaluated at collocation points $(\hat{r}_i, \hat{\theta}_j, \hat{\varphi}_k)$ on the spectral grid. Thus, when discretized, Eq. (8.19) transforms into the following coupled nonlinear system of equations of dimension $5 \times n_r \times n_\theta \times n_\varphi$ or $5 \times \hat{n}_r \times \hat{n}_\theta \times \hat{n}_\varphi$, respectively:

$$\hat{\mathbf{f}}(\hat{\mathbf{u}}) = \hat{f}_{i,j,k}(\hat{u}_{l,m,n}) = f_{i,j,k}^q(u_{l,m,n}^p) = 0, \quad (8.20)$$

with the vector of discretized equations $\hat{\mathbf{f}} = \hat{f}_{i,j,k} = f_{i,j,k}^q$ for the unknowns $\hat{\mathbf{u}} = \hat{u}_{l,m,n} = u_{l,m,n}^p$. For this system we have to find the roots. Note that, in general, each discretized metric equation $f_{i,j,k}^q$ couples both to the other metric equations through the five unknowns (indices p), and to other (neighboring) cell locations on the grid (indices l, m, n).

All three metric solvers are based on iterative methods, where the new value for the metric $\hat{\mathbf{u}}^{s+1}$ is computed from the value at the current iteration s by adding an increment $\Delta\hat{\mathbf{u}}^s$ which is weighted with a relaxation factor f_r . The tolerance measure we use to control convergence of the iteration is the maximum increment of the solution vector on the grid the iteration is executed on, i.e.

$$\Delta\hat{u}_{\max}^s = \max(\Delta\hat{\mathbf{u}}^s) = \max(\Delta u_{i,j,k}^{p,s}). \quad (8.21)$$

Multidimensional Newton–Raphson solver (Solver 1)

Solver 1, which was already introduced in the core collapse simulations reported in [148, 149], uses a multi-dimensional Newton–Raphson iteration method to find the roots of Eq. (8.20). Thus, solving the nonlinear system is reduced to finding the solution of a linear problem of the same dimension during each iteration. The matrix \mathbf{A} defining the linear problem consists of the Jacobi matrix of $\hat{\mathbf{f}}$ and additional contributions originating from boundary and symmetry conditions (see [148] for further details). As the spatial derivatives in the metric equations (which also contain mixed derivatives of second order) are approximated by second-order central differences with a three-point stencil, \mathbf{A} has a band structure with $1 + 2d^2$ bands of blocks of size 5×5 , where d is the number of spatial dimensions of the finite difference grid. Furthermore, matrix \mathbf{A} is sparse and usually diagonally dominated.

A simple estimate already shows that the size $n \times n$ of the linear problem grows impractically large in 3D. A resolution of 100 grid points in each coordinate direction results in a square $(5 \times 10^6) \times (5 \times 10^6)$ matrix \mathbf{A} . Thus, direct (exact) inversion methods, like Gauss–Jordan elimination or exact LU decomposition, are beyond practical applicability, as these are roughly n^3 processes, where n is the dimension of the matrix. Even when exploiting the sparsity and band structure of \mathbf{A} the linear problem remains too large to be solved on present-day computers in a reasonable time by using iterative methods like successive over-relaxation (SOR) or conjugate gradient (CG) methods with appropriate preconditioning.

Because of these computational restrictions, the use of solver 1 is restricted to 2D axisymmetric configurations, where the matrix \mathbf{A} has nine bands of blocks. Even in this case, for coupled spacetime and hydrodynamic evolutions, the choice of linear solver methods is limited: The computational time spent by the metric solver should not exceed the time needed for one hydrodynamical time step by an excessive amount. We have found that a recursive block tridiagonal sweeping method [371] (for the actual numerical implementation, see [148]) yields the best performance for the linear problem. Here the three leftmost, middle, and rightmost bands are combined into three new bands of n_r blocks of size $(5 \times n_\theta) \times (5 \times n_\theta)$ and which are inverted in a forward-backward recursion along the bands using a standard LU decomposition scheme for dense matrices. Actual execution times for this method and the scaling with grid resolution are given in Section 8.4.2.

We point out that the recursion method provides us with a non-iterative linear solver, and the Newton–Raphson method exhibits in general very rapid and robust convergence. Therefore, solver 1 converges rapidly to an accurate solution of the metric equations (8.19) even for strongly gravitating, distorted configurations, irrespective of the relative strength of the “hydrodynamics” term S_h and “metric” term S_m in the metric equations (see Eq. (8.12)). Its convergence radius is sufficiently large, so that even the flat Minkowski metric can be used as an initial guess for the iteration, and the relaxation factor f_r can be set equal to 1. Note that in solver 1 every metric function is treated numerically in an equal way; in particular, the equations for each of the three vector components of the shift vector β^i are solved separately.

In its current implementation, solver 1 exhibits a particular disadvantage, which will be discussed in more detail in Section 8.4.2. As its spatial grid, on which the metric equations are discretized, is not radially compactified, there is a need for explicit boundary conditions of the metric functions \hat{u} at the outer radial boundary of the finite difference grid. This poses a severe problem, as there exists no general analytic solution for the vacuum spacetime surrounding an arbitrary rotating fluid configuration in any coordinate system. Even in spherical symmetry, our choice of isotropic coordinates yields equations with noncompact support terms, which leads to imprecise boundary conditions, as demonstrated in Section 8.2.2. Therefore, as an approximate boundary condition for an arbitrary matter configuration with gravitational mass M_g , we use the monopole field for a static TOV solution,

$$\phi = 1 + \frac{M_g}{2r}, \quad \alpha = \frac{1 - \frac{M_g}{2r}}{1 + \frac{M_g}{2r}}, \quad \beta^i = 0, \quad (8.22)$$

evaluated at r_{fd} . The influence of this approximation on the accuracy of the solution for typical compact stars is discussed in Section 8.4.2. We emphasize that the use of a noncompactified finite radial grid is not an inherent restriction of this solver method. However in the case of metric solver 1, for practical reasons we have chosen to keep the original grid setup as presented in [148], where both the metric and hydrodynamic equations are solved on the same finite difference grid.

Finally, a further drawback of solver 1 is its inefficiency regarding scalability on parallel or vector computer architectures. The recursive nature of the linear solver part of this method prevents efficient distribution of the numerical load onto multiple processors or a vector pipeline. In combination with the disadvantageous scaling behavior of the linear solver with resolution (see also Table 8.3 below), these practical constraints render any extension of solver 1 to 3D beyond feasibility.

Conventional iterative integral nonlinear Poisson solver (Solver 2)

While solver 1 makes no particular assumption about the form of the (elliptic) equations to be solved, solver 2 exploits the fact that the metric equations (8.11) can be written in the form of a system of

nonlinear coupled equations with a Laplace operator on the left hand side (8.12). A common method to solve such kind of equations is to keep the right hand side $S(\hat{u})$ fixed, solve each of the resulting decoupled linear Poisson equations, $\hat{\Delta}\hat{u}^{s+1} = S(\hat{u}^s)$, and iterate until the convergence criterion (8.21) is fulfilled.

The linear Poisson equations are transformed into integral form by using a three-dimensional Green's function,

$$\hat{u}^{s+1}(r, \theta, \varphi) = -\frac{1}{4\pi} \int r'^2 dr' \int \sin \theta' d\theta' \int d\varphi' \frac{S(\hat{u}^s(r', \theta', \varphi'))}{|\mathbf{x} - \mathbf{x}'|}, \quad (8.23)$$

where the spatial derivatives in S are approximated by central finite differences. The volume integral on the right hand side of Eq. (8.23) is numerically evaluated by expanding the denominator into a series of radial functions $f_l(r, r')$ and associated Legendre polynomials $P_l^m(\cos \theta)$, which we cut at $l = 10$. The integration in Eq. (8.23), which has to be performed at every grid point, yields a problem of numerical size $(n_r \times n_\theta \times n_\varphi)^2$. However, the problem size can be reduced to $n_r \times n_\theta \times n_\varphi$ by recursion. Thus, solver 2 scales linearly with the grid resolution in all spatial dimensions (see Section 8.4.2). However, while the numerical solution of an integral equation like Eq. (8.23) is well parallelizable, the recursive method which we employ to improve the resolution scaling performance poses a severe obstacle. In practice only the parallelization across the expansion series index l (or possibly cyclic reduction) can be used to distribute the computational workload over several processors.

An advantage of solver 2 is that it does not require the imposition of explicit boundary conditions at a finite radius due to the integral form of the equations. Demanding asymptotic flatness at spatial infinity fixes the integration constants in Eq. (8.23). However, as the metric equations contain in general source terms with noncompact support (see Section 8.2.2), the radial integration must be performed up to infinity to account for the source term contributions. As the discretization scheme used in solver 2 limits the radial integration to some finite radius r_{fd} , the metric equations are solved only approximately if the source terms with noncompact support are nonzero. The consequences of this fact are discussed in Section 8.4.2. As in the case of metric solver 1, the metric solver 2 could be used with a compactified radial coordinate as well.

One major disadvantage of solver 2 is its slow convergence rate and a small convergence radius. For simplicity, we decompose the metric vector equation for the shift vector β^i into three scalar equations for its components. If the θ -component of the shift vector does not vanish, $\beta^\theta \neq 0$, and if the spacetime is nonaxisymmetric, solver 2 does not converge at all (probably due to diverging terms like $\beta^\theta / \sin^2 \theta$ in the vector Laplace operator). Even when using a known solution obtained with another metric solver as initial guess, solver 2 fails to converge. Thus, the use of solver 2 is limited to axisymmetry. Even so, when $\beta^\theta \neq 0$, a quite small relaxation factor $f_r \approx 0.05$ is required. Furthermore, as the iteration scheme is of fix-point type, it already has a much lower convergence rate than e.g. a Newton–Raphson scheme. Both factors result in typically several hundred iterations until convergence is reached (see Section 8.4.2). For strong gravity, the small convergence radius restricts the initial guess to a metric close to the actual solution of the discretized equations.

Iterative spectral nonlinear Poisson solver (Solver 3)

The basic principles of this iterative solver are similar to the ones used for solver 2: A numerical solution of the nonlinear elliptic system of the metric differential equations is obtained by solving the associated linear Poisson equations with a fix-point iteration procedure until convergence. However, instead of

using finite difference scalar Poisson solvers, solver 3 is built from routines of the publicly available LORENE library [216] and uses spectral methods to solve scalar and vector Poisson equations [228].

Before every computation of the spacetime metric, the hydrodynamic and metric fields are interpolated from the finite difference to the spectral grid by the methods detailed in Section 8.3.2. All three-dimensional functions are decomposed into Chebyshev polynomials $T_n(r)$ and spherical harmonics $Y_l^m(\theta, \varphi)$ in each domain. When using solver 3 the metric equations (8.8) are rewritten in order to gain accuracy according to the following transformations. The scalar metric functions ϕ and α have the same type of asymptotic behavior near spatial infinity, $\phi|_{r \rightarrow \infty} \sim 1 + \Delta\phi(r)$, $\alpha|_{r \rightarrow \infty} \sim 1 + \Delta\alpha(r)$, with $\Delta\phi(r)$ and $\Delta\alpha(r)$ approaching 0 as $r \rightarrow \infty$. Therefore, to obtain a more precise numerical description of the (usually small) deviations of ϕ and α from unity, we solve the equations for the logarithm of ϕ and $\alpha\phi$, imposing that $\ln\phi$ and $\ln(\alpha\phi)$ approach zero at spatial infinity. Another important difference to the other two solvers is that the vector Poisson equation for the shift vector β^i is not decomposed into single scalar components, but instead the entire linear vector Poisson equation is solved, including the $\frac{1}{3}\hat{\nabla}^i\hat{\nabla}_k$ operator on the left hand side. Therefore, the system of metric equation to be solved reads

$$\begin{aligned}\hat{\Delta}\ln\phi &= -4\pi\phi^4\left(\rho hW^2 - P + \frac{K_{ij}K^{ij}}{16\pi}\right) \\ &\quad -\hat{\nabla}^i\ln\phi\hat{\nabla}_i\ln\phi, \\ \hat{\Delta}\ln\alpha\phi &= 2\pi\phi^4\left(\rho h(3W^2 - 2) + 5P + \frac{7K_{ij}K^{ij}}{16\pi}\right) \\ &\quad -\hat{\nabla}^i\ln\alpha\phi\hat{\nabla}_i\ln\alpha\phi, \\ \hat{\Delta}\beta^i + \frac{1}{3}\hat{\nabla}^i\hat{\nabla}_k\beta^k &= 16\pi\alpha\phi^4S^i + 2\phi^{10}K^{ij}\hat{\nabla}_j\left(\frac{\alpha}{\phi^6}\right).\end{aligned}\tag{8.24}$$

During each iteration a spectral representation of the solution of the linear scalar and vector Poisson equations associated with the above system is obtained. The Laplace operator is inverted (i.e. the linear Poisson equation is solved) in the following way: For a given pair of indices l and m of $Y_l^m(\theta, \varphi)$, the linear scalar Poisson equation reduces to an ordinary differential equation in r . The action of the differential operator

$$\frac{\partial^2}{\partial r^2} + \frac{2}{r}\frac{\partial}{\partial r} - \frac{l(l+1)}{r^2}\tag{8.25}$$

acting thus on each multipolar component (l and m) of a scalar function corresponds to a matrix multiplication in the Chebyshev coefficient space. The corresponding matrix is inverted to obtain a particular solution in each domain, which is then combined with homogeneous solutions (r^l and $1/r^l$, for a given l) to satisfy regularity and boundary conditions. The matrix has a small size (about 30×30) and can be put into a banded form, owing to the properties of the Chebyshev polynomials, which facilitates its fast inversion. For more details about this procedure, and how the vector Poisson equation is treated, the interested reader is addressed to [228]. Note also that when solving the shift vector equation, β^i is decomposed into Cartesian components defined on the spherical polar grid (see [228]).

The spatial differentials in the source terms on the right hand sides of the metric equations are approximated by second-order central differences in solvers 1 and 2, while they are obtained by spectral methods in solver 3 (see Section 8.3.2). When using ~ 30 collocation points, very high precision ($\sim 10^{-13}$) can be achieved in the evaluation of these derivatives. Another advantage of metric solver 3 is that a compactified radial coordinate $u = 1/r$ enables us to solve for the entire space, and to impose

exact boundary conditions at spatial infinity, $u = 0$. This ensures both asymptotic flatness and fully accounts for the effects of the source terms in the metric equations with noncompact support. Solver 3 uses the same fix-point iteration method as solver 2, but does not suffer from the convergence problem encountered with that solver. Due to the direct solution of the vector Poisson equation for the shift vector β^i , it converges to the correct solution in all investigated models (including highly distorted 3D matter configurations with velocity perturbations, see Section 8.4.2). Furthermore, this can be achieved with the maximum possible relaxation factor, $f_r = 1$, starting from the flat metric as initial guess.

However, the strongest reason in favor of solver 3 is its straightforward extension to 3D. As mentioned previously, both metric solvers 1 and 2 are limited to axisymmetric situations. The spectral elliptic solvers provided by the LORENE library are already intrinsically three-dimensional. Indeed, even in axisymmetry the spectral grid of solver 3 requires $\hat{n}_\varphi = 4$ grid points in the φ -direction order to correctly represent the Cartesian components of the shift vector.

There is an additional computational overhead due to the communication between the finite difference and the spectral grids. These computational costs may actually become a dominant part when calculating the metric (as will be shown in Section 8.4.1). The interpolation methods also have to be chosen carefully to obtain the desired accuracy. Furthermore, spectral methods may suffer from Gibbs phenomena if the source terms of the Poisson-like equations contain discontinuities. For the particular type of simulations we are aiming at, discontinuities are present (supernova shock front, discontinuity at the transition from the stellar matter distribution to the artificial atmosphere at the boundary of the star). This can result in high-frequency spurious oscillations of the metric solution, if too few radial domains are used, or if the boundaries of the spectral domains are not chosen properly. As mentioned before, a simple way to reduce the oscillations is to filter out part of the high-frequency spectral coefficients.

As the C++ routines of the LORENE library in the current release are optimized for neither vector nor parallel computers, solver 3 cannot yet exploit these architectures. However, we were able to improve the computational performance by coarse-grain parallelizing the routines which interpolate the metric solution in the spectral representation to the finite difference grid.

8.3.5 Extraction of gravitational waves

In a conformally flat spacetime the dynamical gravitational wave degrees of freedom are not present [148]. Therefore, in order to extract information regarding the gravitational radiation emitted in core collapse events and in rotating neutron star evolutions, we have implemented in the code the 3D generalization of the axisymmetric Newtonian quadrupole formula used in [147, 148, 149]. Note that we use spherical polar components for the tensors of the radiation field.

Whereas in axisymmetry there exists only one independent component of the quadrupole gravitational radiation field h_{ij}^{TT} in the transverse traceless gauge,

$$h_{ij}^{\text{TT}}(r, \theta) = \frac{1}{r} A_+(\theta) e_+, \quad (8.26)$$

in three dimensions we have

$$h_{ij}^{\text{TT}}(r, \theta, \varphi) = \frac{1}{r} [A_+(\theta, \varphi) e_+ + A_\times(\theta, \varphi) e_\times], \quad (8.27)$$

with the unit vectors \mathbf{e}_+ and \mathbf{e}_\times defined as

$$\mathbf{e}_+ = \mathbf{e}_\theta \otimes \mathbf{e}_\theta - \mathbf{e}_\varphi \otimes \mathbf{e}_\varphi, \quad (8.28)$$

$$\mathbf{e}_\times = \mathbf{e}_\theta \otimes \mathbf{e}_\varphi + \mathbf{e}_\varphi \otimes \mathbf{e}_\theta. \quad (8.29)$$

The amplitudes A_+ and A_\times are linear combinations of the second time derivative of some components of the quadrupole moment tensor I_{ij} , which for simplicity we evaluate at $\varphi = 0$ on the polar axis and in the equatorial plane, respectively:

$$\begin{aligned} A_+^p &= \ddot{I}_{11} - \ddot{I}_{22}, & \text{at } \theta = 0 \text{ (pole),} \\ A_\times^p &= 2\ddot{I}_{12}, \end{aligned} \quad (8.30)$$

$$\begin{aligned} A_+^e &= \ddot{I}_{33} - \ddot{I}_{22}, & \text{at } \theta = \pi/2 \text{ (equator).} \\ A_\times^e &= -2\ddot{I}_{13}, \end{aligned} \quad (8.31)$$

A direct numerical calculation of the quadrupole moment in the *standard quadrupole formulation*,

$$I_{ij} = \int dV \rho^* \left[x_i x_j - \frac{1}{3} \delta_{ij} (x_1^2 + x_2^2 + x_3^2) \right], \quad (8.32)$$

results in high frequency noise completely dominating the wave signal due to the presence of the second time derivatives in Eq. (8.31). Therefore, we make use of the time-differentiated quadrupole moment in the *first moment of momentum density formulation*,

$$\dot{I}_{ij} = \int dV \rho^* \left[v_i x_j + v_j x_i - \frac{2}{3} \delta_{ij} (v_1 x_1 + v_2 x_2 + v_3 x_3) \right], \quad (8.33)$$

and *stress formulation*,

$$\ddot{I}_{ij} = \int dV \rho^* [2v_i v_j - x_i \partial_j \Phi - x_j \partial_i \Phi], \quad (8.34)$$

of the quadrupole formula [174, 63].

In the above equations, x_i and v_i are the coordinates and velocities in Cartesian coordinates, respectively. When evaluating Eq. (8.34) numerically, we transform v_i to spherical polar coordinates. In the quadrupole moment, we use $\rho^* = \rho W \phi^6$ instead of ρ as in [147, 148, 149], as this quantity is evolved by the continuity equation (note that both quantities have the same Newtonian limit). This also allows a direct comparison with the results presented in [422], which we show in Section 8.4.2. For a discussion about the ambiguities arising from the spatial derivatives of the Newtonian potential Φ in Eq. (8.34) in a general relativistic framework and their solution (which we also employ in this work), we refer to [149].

The total energy emitted by gravitational waves can be expressed either as a time integral,

$$\begin{aligned} E_{\text{gw}} &= \frac{2}{15} \int dt \left[-\ddot{I}_{11} \ddot{I}_{22} - \ddot{I}_{11} \ddot{I}_{33} - \ddot{I}_{22} \ddot{I}_{33} \right. \\ &\quad \left. + \ddot{I}_{11}^2 + \ddot{I}_{22}^2 + \ddot{I}_{33}^2 + 3 \left(\ddot{I}_{12}^2 + \ddot{I}_{13}^2 + \ddot{I}_{23}^2 \right) \right], \end{aligned} \quad (8.35)$$

or, equivalently, as a frequency integral,

$$\begin{aligned} E_{\text{gw}} &= \frac{1}{15} \int \nu^2 d\nu \left[-\hat{I}_{11} \hat{I}_{22} - \hat{I}_{11} \hat{I}_{33} - \hat{I}_{22} \hat{I}_{33} \right. \\ &\quad \left. + \hat{I}_{11}^2 + \hat{I}_{22}^2 + \hat{I}_{33}^2 + 3 \left(\hat{I}_{12}^2 + \hat{I}_{13}^2 + \hat{I}_{23}^2 \right) \right], \end{aligned} \quad (8.36)$$

where $\hat{\hat{I}}_{ij}(\nu)$ is the Fourier transform of $\ddot{I}_{ij}(t)$. We point out that the above general expressions reduce to the following ones in axisymmetry:

$$A_+^p = 0, \quad A_\times^p = 0, \quad A_+^e = \ddot{I}, \quad A_\times^e = 0, \quad (8.37)$$

$$E_{\text{gw}} = \frac{2}{15} \int dt \ddot{I}^2 = \frac{1}{15} \int \nu^2 d\nu \hat{\hat{I}}^2, \quad (8.38)$$

with $I = I_{33} - I_{22}$ being the only nonzero independent component of the quadrupole tensor, and $\hat{\hat{I}}^2$ being the Fourier transform of \ddot{I}^2 . The quadrupole wave amplitude A_{20}^{E2} used in [499, 147, 149] is related to I according to $A_{20}^{E2} = 8\sqrt{\pi/15} \ddot{I}$.

We have tested the equivalence between the waveforms obtained by the axisymmetric code presented in [147, 148, 149] and those by the current three-dimensional code using the corresponding axisymmetric model. In all investigated cases, they agree with excellent precision.

8.4 Code tests and applications

We turn now to an assessment of the numerical code with a variety of tests and applications. We recall that we do not attempt in the present paper to investigate any realistic astrophysical scenario, which is deferred to subsequent publications. Instead, we focus here on discussing standard tests for general relativistic three-dimensional hydrodynamics code, which were all passed by our code. In particular, we show that the code exhibits long-term stability when evolving strongly gravitating systems like rotational core collapse and equilibrium configurations of (highly perturbed) rotating relativistic stars. Each separate constituent methods of the code (HRSC schemes for the hydrodynamics equations and elliptic solvers based on spectral methods for the gravitational field equations) has already been thoroughly tested and successfully applied in the past (see e.g. [176, 311, 228] and references therein). Therefore, we mainly demonstrate here that the coupled numerical schemes work together as desired.

8.4.1 Interpolation efficiency and accuracy

The interpolation procedure from the finite difference grid to the spectral grid has been described in Section 8.3.2. Among the three possible algorithms we have implemented in the code, the most efficient turned out to be the one based on a piecewise parabolic interpolation (see Table 8.1). It is as fast as the piecewise linear interpolation, and more accurate than the algorithm based on the minimization of the second derivative of the interpolated function. Table 8.1 shows, for a particular example of an interpolated test function $f_t(r, \theta, \varphi) = \exp[-r^2(1 + \sin^2 \theta \cos^2 \varphi)]$, the relative accuracy Δf_{int} (in the L_0 norm) achieved by this interpolation, as well as the CPU time spent on a Pentium IV Xeon processor at 2.2 GHz. The spectral grid consists of two domains (nucleus + shell) with $\hat{n}_r = 17$, $\hat{n}_\theta = 17$, and $\hat{n}_\varphi = 16$. The outer radius of the nucleus is located at 0.5, and the outer boundary of the shell is at 1.5 (corresponding to the radius of the finite difference grid r_{fd}).

This test demonstrates that the piecewise parabolic interpolation is indeed third-order accurate, and that the time spent scales roughly linearly with the number of points of the finite difference grid in any direction. We have made other tests which show that the interpolation accuracy is independent of \hat{n} , and that it scales in time like $\mathcal{O}(\hat{n}^3) + \mathcal{O}(n^3)$, where \hat{n} and n are the number of points used in each dimension by the spectral and the finite difference grid, respectively. The interpolation is exact, up to machine precision, for functions which can be expressed as polynomials of degree ≤ 2 with respect to all three coordinates.

Table 8.1: Execution time $t_{\text{fd} \rightarrow \text{sp}}$ and accuracy $\Delta f_{\text{fd} \rightarrow \text{sp}}$ for the interpolation of a test function $f_t(r, \theta, \varphi)$ (see text) from the finite difference grid to the spectral grid, listed for different finite difference grid resolutions $n_r \times n_\theta \times n_\varphi$ and interpolation types. The interpolation methods are piecewise linear (type 1), piecewise parabolic (type 2), and globally minimizing the norm of the second derivative of the interpolated function [342] (type 0). The spectral grid has a resolution of $\hat{n}_r = 17$, $\hat{n}_\theta = 17$, and $\hat{n}_\varphi = 16$ grid points.

$n_r \times n_\theta \times n_\varphi$	Type	$t_{\text{fd} \rightarrow \text{sp}}$ [s]	$\Delta f_{\text{fd} \rightarrow \text{sp}}$ [L_0 norm]
$400 \times 200 \times 800$	2	5.13	5.0×10^{-8}
$400 \times 200 \times 800$	1	5.12	7.0×10^{-6}
$400 \times 200 \times 800$	0	9.44	1.8×10^{-6}
$400 \times 200 \times 400$	2	2.92	3.1×10^{-7}
$400 \times 200 \times 200$	2	1.43	1.6×10^{-6}
$400 \times 200 \times 100$	2	0.77	1.7×10^{-5}
$400 \times 200 \times 10$	2	0.09	1.3×10^{-2}
$400 \times 100 \times 800$	2	2.55	3.1×10^{-7}
$400 \times 50 \times 800$	2	1.60	1.8×10^{-6}
$400 \times 5 \times 800$	2	0.32	2.0×10^{-3}
$200 \times 200 \times 800$	2	3.61	2.7×10^{-7}
$100 \times 200 \times 800$	2	1.81	2.1×10^{-6}
$50 \times 200 \times 800$	2	1.40	1.6×10^{-5}
$5 \times 200 \times 800$	2	0.99	1.4×10^{-2}

The direct spectral summation from the spectral to the finite difference grid is a very precise way of evaluating a function: For smooth functions, the relative error decreases like $\exp(-\hat{n})$ (infinite order scheme). This property is fulfilled in our code, as shown in Table 8.2 for the same test function $f_t(r, \theta, \varphi)$ and the same domain setup as for Table 8.1 (again the timings are for a Pentium IV Xeon processor at 2.2 GHz). Double precision accuracy is reached with a reasonable number of points ($\hat{n}_r = 33$, $\hat{n}_\theta = 17$, and $\hat{n}_\varphi = 64$). According to Table 8.2 the CPU cost scales linearly with the number of coefficients \hat{n} in any direction. We have also confirmed that it scales linearly with the number of finite difference grid points n in any direction. The drawback of this most straightforward procedure is that it requires $\mathcal{O}(\hat{n}^3 n^3)$ operations, which is much more expensive than the interpolation from the finite difference grid to the spectral one, and even more expensive than the iterative procedure providing the solution of system (8.24). Nevertheless, it is computationally not prohibitive since the overall accuracy of the code does not depend on \hat{n} (which can thus remain small). A way to reduce the execution time is to use a partial summation algorithm (see e.g. [85]), which needs only $\mathcal{O}(\hat{n} n^3) + \mathcal{O}(\hat{n}^2 n^2) + \mathcal{O}(\hat{n}^3 n)$ operations, at the additional cost of increased central memory requirement. Another alternative is to truncate the spectral sum, staying at an accuracy level comparable to that of finite difference differential operators.

Table 8.2: Execution time $t_{\text{sp} \rightarrow \text{fd}}$ and accuracy $\Delta f_{\text{sp} \rightarrow \text{fd}}$ for the evaluation of a test function $f_t(r, \theta, \varphi)$ (see text) on the finite difference grid from its representation in spectral coefficients, listed for different numbers of spectral grid points $\hat{n}_r \times \hat{n}_\theta \times \hat{n}_\varphi$. The finite difference grid has a resolution of $n_r = 100$, $n_\theta = 50$, and $n_\varphi = 30$ grid points.

$\hat{n}_r \times \hat{n}_\theta \times \hat{n}_\varphi$	$t_{\text{sp} \rightarrow \text{fd}}$ [s]	$\Delta f_{\text{sp} \rightarrow \text{fd}}$ [L_0 norm]
$33 \times 17 \times 64$	75.8	1.5×10^{-15}
$33 \times 17 \times 32$	38.4	5.5×10^{-9}
$33 \times 17 \times 16$	19.6	2.6×10^{-4}
$33 \times 17 \times 8$	10.3	2.8×10^{-2}
$33 \times 9 \times 64$	40.8	6.4×10^{-9}
$33 \times 5 \times 64$	23.4	3.2×10^{-4}
$17 \times 17 \times 64$	41.2	1.9×10^{-13}
$9 \times 17 \times 64$	24.6	9.2×10^{-7}
$5 \times 17 \times 64$	16.7	1.9×10^{-3}

8.4.2 Solver comparison in 2D

Convergence properties

The theoretical considerations about the convergence properties of the three implemented metric solvers (as outlined in Section 8.3.4) are checked by solving the spacetime metric for a 2D axisymmetric rotating neutron star model in equilibrium (labeled model RNS), which we have constructed with the method described in Komatsu et al. [283]. This model has a central density $\rho_c = 7.905 \times 10^{14}$ g cm $^{-3}$, obeys a polytropic EoS with $\gamma = 2$ and $K = 1.455 \times 10^5$ (in cgs units), and rotates rigidly at the mass shedding limit, which corresponds to a polar-to-equatorial axis ratio of 0.65. These model parameters are equivalent to those used for neutron star models in [178, 181].

To the initial equilibrium model we add an r - and θ -dependent density and velocity perturbation,

$$\begin{aligned}
 \rho &= \rho_{\text{ini}} \left[1 + 0.02 \sin^2 \left(\pi \frac{r}{r_s} \right) (1 + \sin^2(2\theta)) \right], \\
 v_r &= 0.05 \sin^2 \left(\pi \frac{r}{r_s} \right) (1 + \sin^2(2\theta)), \\
 v_\theta &= 0.05 \sin^2 \left(\pi \frac{r}{r_s} \right) \sin^2(2\theta), \\
 v_\varphi &= v_{\varphi \text{ ini}} + 0.05 \sin^2 \left(\pi \frac{r}{r_s} \right) (1 + \sin^2(2\theta)),
 \end{aligned} \tag{8.39}$$

where r_s is the (θ -dependent) stellar radius, and $v_r = \sqrt{v_1 v^1}$, $v_\theta = \sqrt{v_2 v^2}$, and $v_\varphi = \sqrt{v_3 v^3}$. The metric equations (Eqs. (8.11) for solvers 1 and 2, and Eqs. (8.24) in the case of solver 3) are then solved using the three implemented metric solvers. The perturbation of v_r and v_θ ensures that the

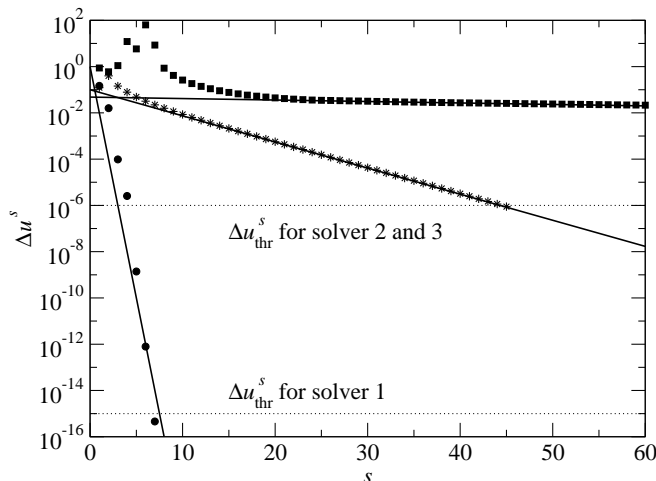


Figure 8.2: Comparison of the convergence behavior for the three metric solvers in 2D. For solver 1 (filled circles), the maximum increment $\Delta\hat{u}_{\max}^s$ per iteration s decreases to the threshold $\Delta\hat{u}_{\text{thr}}^s = 10^{-15}$ (lower horizontal dotted line) within less than 10 iterations, while solver 3 (asterisks) needs more than 40 iterations to reach its (less restrictive) threshold (upper horizontal dotted line) of 10^{-6} . The very low relaxation factor needed for solver 2 (filled squares) results in a remarkably slow convergence, requiring more than 700 iterations. The solid lines mark the approximate linear decrease of $\log \Delta\hat{u}_{\max}^s$.

metric equations yield the general case of a shift vector with three nonzero components, which cannot be obtained with an initial model in equilibrium.

We point out that by adding the perturbations specified in Eq. (8.39) and calculating the metric for these perturbed initial data, we add a small inconsistency to the initial value problem. As the Lorentz factor W in the right hand sides of the metric equations contains metric contributions (which are needed for computing the covariant velocity components), it would have to be iterated with the metric solution until convergence. However, as the perturbation amplitude is small, and as we do not evolve the perturbed initial data, we neglect this small inconsistency.

The most relevant quantity related to convergence properties of the metric solver is the maximum increment $\Delta\hat{u}_{\max}^s$ of all metric components on the grid (see Fig. 8.2). As expected solver 1 exhibits the typical quadratic decline of a Newton–Raphson solver to its threshold value $\Delta\hat{u}_{\text{thr}}^s = 10^{-15}$. As the methods implemented in solvers 2 and 3 correspond to a fix-point iteration, the decline of their metric increment is significantly slower. Therefore, for the Poisson-based solvers, we typically use a less restrictive threshold $\Delta\hat{u}_{\text{thr}}^s = 10^{-6}$. While the spectral Poisson solver 3 allows for a relaxation factor of 1 and thus for a still quite rapid convergence, the conventional Poisson solver 2 requires more than 700 iterations due to its much smaller relaxation factor imposed by the β^2 -equation.

It is worth stressing that all three solvers show rather robust convergence, if one keeps in mind that the initial guess is the flat spacetime metric. If the metric is changing dynamically during an evolution, the metric values from the previous computation can be used as new starting values, which reduces the number of iterations by about a factor of two with respect to those reported in Fig. 8.2.

Besides the convergence rate, the execution time t_m required for a single metric computation and its dependence on the grid resolution is also of paramount relevance for the practical usefulness of a solver.

Table 8.3: Metric solver execution time t_m for different finite difference grid resolutions $n_r \times n_\theta$ for the three metric solvers in 2D applied to the perturbed rotating neutron star model RNS. The ratios a_{n_r} (a_{n_θ}) between execution times for a given n_r (n_θ) and for half that resolution exhibit the behavior expected from theoretical considerations. The spectral grid has a resolution of $\hat{n}_r = 33$, $\hat{n}_\theta = 17$, and $\hat{n}_\varphi = 4$ grid points.

$n_r \times n_\theta$	Solver 1			Solver 2			Solver 3		
	t_m [s]	a_{n_r}	a_{n_θ}	t_m [s]	a_{n_r}	a_{n_θ}	t_m [s]	a_{n_r}	a_{n_θ}
50×16	1.8			2.8			20.7		
100×16	3.7	2.0		5.9	2.1		20.6	1.0	
200×16	7.4	2.0		12.9	2.2		20.8	1.0	
50×32	12.5		6.9	5.9		2.1	20.8		1.0
100×32	25.4	2.0	6.9	12.3	2.1	2.1	20.5	1.0	1.0
200×32	50.8	2.0	6.9	27.1	2.2	2.1	21.7	1.1	1.0
50×64	109.7		8.8	12.4		2.1	20.9		1.0
100×64	224.2	2.0	8.8	–			21.5	1.0	1.1
200×64	445.2	2.0	8.8	–			21.7	1.0	1.1

These times for one metric computation of the perturbed RNS stellar model on a finite difference grid with various r - and θ -resolutions on an IBM RS/6000 Power4 processor are summarized in Table 8.3. As theoretically expected, both solver 1 and 2 show a linear scaling of t_m with the number of radial grid points n_r , i.e. the ratio $r_{n_r} = t_m(n_r)/t_m(n_r/2)$ is approximately 2. While the integration method of solver 2 shows linear dependence also for the number of meridional grid zones n_θ , the inversion of the dense $n_\theta \times n_\theta$ matrices during the radial sweeps in solver 1 is roughly a n_θ^3 process. Thus, the theoretical value of $r_{n_\theta} = 8$ for that solver is well met by the results shown in Table 8.3. We note that for even larger values of n_θ , specific processor properties like cache-miss problems can even worsen the already cubic scaling of solver 1, while for $n_\theta \gtrsim 64$ solver 2 fails to converge altogether. On the other hand for solver 3 t_m is approximately independent of the number of finite difference grid points in either coordinate direction, as the number of spectral collocation points is fixed. A dependence on n_r and n_θ can only enter via the interpolation procedure between the two grids, the time for which is, however, entirely negligible in 2D.

The break even point for the three solvers corresponds roughly to a resolution of 100×32 grid points at $t_m \sim 20$ s. We emphasize that this value of t_m is *much larger* than the time needed for one hydrodynamic step at the same resolution, which is roughly $t_h \sim 0.1$ s. From the results reported in Table 8.3 it becomes evident that due to the independence of t_m on the finite difference grid resolution in the spectral metric solver 3, this method is far superior to the other two solvers for simulations requiring a large number of grid points in general, and particularly in θ -direction.

Radial fall-off of the metric components

When comparing in Section 8.3.4 the theoretical foundations of the three alternative metric solvers implemented in the code, we already raised the issue of the existence of source terms with noncompact support in the metric equations (8.11) (see Section 8.2.2). Neither the Newton–Raphson-based solver 1, which requires explicit boundary conditions at the finite radius r_{fd} (which are in general not exactly known and possibly time-dependent), nor the conventional iterative Poisson solver 2, which integrates the Poisson-like metric equations only up to the same finite radius r_{fd} , are able to fully account for the nonlinear source terms, even if the radial boundary of the finite difference grid is in the vacuum region outside the star, $r_{\text{fd}} > r_s$.

Hence, both solvers yield a numerical solution of the exact metric equations only in very few trivial cases, like e.g. the solution for the metric of a spherically symmetric static matter distribution (TOV solution), when the metric equations reduce to Poisson-like equations with compact support. However, due to the radial compactification of the spectral grid, which allows for the Poisson equations to be numerically integrated out to spacelike infinity, the spectral solver 3 can consistently handle all noncompact support source terms in the metric equations in a non-approximative way. This property holds even when the metric quantities are mapped from the spectral grid onto the finite difference grid, the latter extending only to r_{fd} . Thus, we expect that only solver 3 captures the correct radial fall-off behavior of the metric quantities outside the matter distribution.

In the following we illustrate the effects of noncompact support terms in the metric equations on the numerical solution using the three different solvers. Fig. 8.3 shows the radial equatorial profiles of the rotational shift vector component $\beta_\varphi = \sqrt{\gamma_{33}}\beta^3$ for the rapidly rotating neutron star initial model (RNS) specified in Section 8.4.2, obtained with the three alternative metric solvers. While we restrict our discussion to the particular metric quantity $\beta_{\varphi e}$ we notice that the radial fall-off behavior and the dependence on the solver method is equivalent for all other metric components.

In the upper panel of Fig. 8.3 the equatorial stellar boundary r_{se} is very close to the radial outer boundary of the finite difference grid, $r_{se} = 0.9 r_{\text{fd}}$ (both indicated by vertical dotted lines). The star and the exterior atmosphere are resolved using $n_{rs} = 90$ radial grid points for the star and $n_{ra} = 10$ radial grid points for the atmosphere (along the equator), respectively, and $n_\theta = 30$ meridional points. The spectral solver 3 uses $\hat{n}_r = 33$ radial and $\hat{n}_\theta = 17$ meridional grid points.

If the boundary value for the metric at r_{fd} is exact, solver 1 always yields the correct solution, irrespective of the source terms not having compact support. For stationary solutions like rotating neutron stars these exact values can in principle be provided by the initial data solver. However, for instance in a dynamical situation, exact values cannot be provided, and we are forced to use approximate boundary conditions, which we choose according to Eq. (8.22). As the approximate boundary value for solver 1, $\beta_\varphi(r_{\text{fd}}) = 0$, is far from the exact value, the corresponding profile of the shift vector (dashed line) strongly deviates from the correct $\beta_{\varphi e}$ obtained by the initial data solver (solid line). Note that the exact solution is given only for $r \leq r_{se}$, due to limitations of the initial solver method [283]. As shown in the lower panel of the figure, with increasing distance of the finite difference grid boundary from the stellar boundary ($r_{\text{fd}} = 2.0 r_{se}$ with $n_{rs} = n_{ra} = 90$), the approximation for $\beta_{\varphi e}(r_{\text{fd}})$ improves noticeably, and so does the matching of $\beta_{\varphi e}$ with the correct solution.

On the other hand, as the integral approach of solvers 2 and 3 requires no specific boundary conditions at a finite radius (contrary to solver 1), the numerical solution for $\beta_{\varphi e}$ agrees well with the correct solution even for an integration boundary r_{fd} close to the stellar boundary r_{se} (dashed-dotted and dotted lines in Fig. 8.3, respectively). For $r_{\text{fd}} \gg r_{se}$, when the influence of the source terms with noncompact support is increasingly picked up by the radial integral, the solutions supplied by solver 2

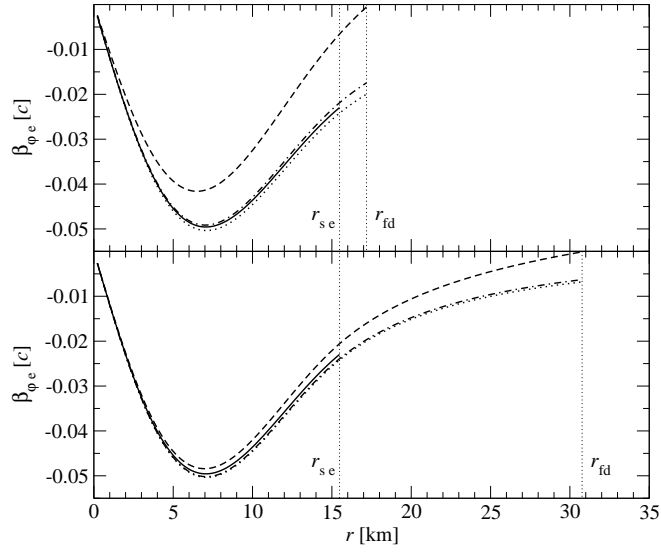


Figure 8.3: Equatorial profile of the shift vector component $\beta_{\varphi e}$ obtained by different metric solvers compared with the correct profile from the initial data solver (solid line) for the rotating neutron star model RNS. Due to its approximate boundary value, the profile from solver 1 (dashed line) shows large deviation from the correct solution, particularly for a grid boundary r_{fd} close to the stellar equatorial radius r_{se} (upper panel). As solver 2 (dashed-dotted line) needs no explicit boundary conditions, its solution matches well with the correct solution, with improving agreement as r_{fd} is at larger distance from r_{se} (lower panel). The compactified radial grid of solver 3 (dotted line) fully accounts for non-compact support terms, and thus agrees very well with the correct solution, independent of the location of r_{fd} . The radii r_{se} and r_{fd} are indicated by vertical dotted lines.

rapidly approach the correct one. The terms with noncompact support usually do not contribute strongly to the solution of the metric equations (except in cases of very strong gravity and extremely rapid contraction or rotation). Thus, solver 2 is superior to solver 1 when approximate boundary values must be used, Eq. (8.22). Solver 3, on the other hand, has the key advantage over solver 2 of using very accurate spectral methods for solving the Poisson equation over the *entire* spatial volume due to its compactified radial coordinate. Hence, irrespective of the distance of r_{fd} from r_{se} , it yields the same results on the finite difference grid, onto which the results are mapped from the spectral grid.

The (small) difference between the results for $\beta_{\varphi e}$ from solver 3 and from the initial data solver is partly due to the accuracy of the numerical schemes and the mapping between different grids, and particularly a result of the CFC approximation of the field equations employed by the evolution code (note that the initial data are generated from a numerical solution of the exact Einstein metric equations). In the case of rapidly rotating neutron star models we have found that the truncation error and the error arising from the mapping of the initial data to the evolution code is typically more than one order of magnitude smaller than the error which can be attributed to the CFC approximation, if a grid with a resolution $n_r \sim 100$, $n_\theta \sim 30$ and $\hat{n}_r = 33$, $\hat{n}_\theta = 17$ is used. For estimates of the quality of the CFC approximation in such cases, see [148] and references therein.

We again note that, in principle, the use of a compactified radial grid is not confined to the spectral solver 3. A finite difference grid extending to spatial infinity could be used for solvers 1 and 2 as well. However, in that case either the exterior atmosphere would also have to be extended to the entire grid too (generating unnecessary computations), or only the relevant portion of the grid containing the star would have to be evolved in time (creating an additional boundary). When using solver 3, there is a clearcut split between the finite difference grid and the spectral grid. Thus, the hydrodynamic quantities can be defined on a grid with an atmosphere of only small size, while the metric in the compactified domain can be computed very accurately with only few radial collocation points due to the exponential convergence of spectral methods in this smooth region. Additionally, the LORENE library provides the use of a compactified radial domain as an already implemented option at no extra cost.

Axisymmetric core collapse to a neutron star – Construction of the spectral grid domains

As all three metric solvers yield equally precise numerical solutions of the spacetime metric in 2D, they give nearly identical results when applied to simulations of rotational core collapse, as shown in Fig. 8.4. For the results presented in this figure we have chosen the stellar core collapse model labeled A3B2G4 in [149] (model SCC in the following), which rotates differentially and moderately fast, and has an initial central density $\rho_c = 10^{10} \text{ g cm}^{-3}$. The initial adiabatic index is reduced from $\gamma_i = 4/3$ to $\gamma_1 = 1.3$ during contraction, and is increased to $\gamma_2 = 2.5$ beyond supranuclear matter densities, $\rho > \rho_{\text{nuc}} = 2.0 \times 10^{14} \text{ g cm}^{-3}$. The details of the EoS for this model are given by Eq. (8.6). As the metric calculation is computationally very expensive, it is done only every 100/10/50 hydrodynamic time steps before/during/after core bounce, and extrapolated in between (for details on the satisfactory accuracy of this procedure see [148]). The number of zones used in the finite difference grid is $n_r = 200$ and $n_\theta = 30$, with logarithmic spacing in the r -direction and a central resolution of 500 m, and an equidistant spacing in the θ -direction. Again, the grid resolution of the spectral solver 3 is $\hat{n}_r = 33$ and $\hat{n}_\theta = 17$.

In the upper panel of Fig. 8.4 we plot the time evolution of the central conformal factor ϕ_c , which rises steeply when the central density increases to supranuclear densities, reaches a maximum at the time of core bounce t_b (vertical dotted line), and subsequently approaches a new equilibrium value with decreasing ringdown oscillations. This new state, which is reached asymptotically, signals the formation of a pulsating compact remnant which can be identified with the nascent proto-neutron star. Each of the three curves in this upper panel is the result of using one of the three available metric solver (see caption for details). The lower panel of the figure demonstrates that the relative differences found in the dynamical evolution of our representative core collapse model are negligibly small when using either metric solver, which proves the applicability of any of the metric solvers in 2D.

However, in such a highly dynamical situation, where the relevant radial scales vary by a factor of about 100, solver 3 requires a special treatment of the radial domain setup of the spectral grid defined in Section 8.3.2. During the infall phase of a core collapse simulation the contracting core must be sufficiently resolved by the radial grid, and thus we adjust the radius of the nucleus r_d dynamically before core bounce. (Note that this is no contradiction to the assumption $f_d = \text{const.}$ in Eq. (8.15), as f_d may change between *subsequent* metric calculations during the evolution.) Initially the value of r_d is given by half the stellar radius. As the evolution proceeds it is set equal to the radial location of the sonic point in the equatorial plane (once unambiguously detected). Alternatively r_d can be determined

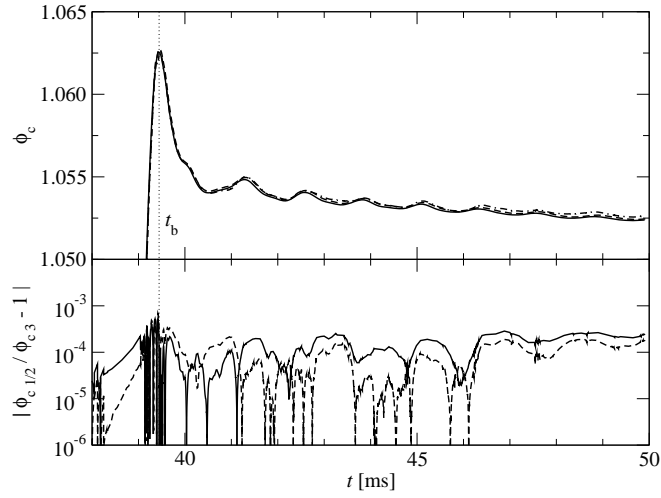


Figure 8.4: Time evolution of the central conformal factor ϕ_c (upper panel) for the core collapse model SCC, using metric solver 1 (solid line), 2 (dashed line), and 3 (dashed-dotted line), respectively. All three solvers yield similar results. The small relative differences of less than 10^{-3} in ϕ_c (lower panel) obtained with solvers 1 and 3 (solid line) and solver 2 and 3 (dashed line) prove that numerical variations of the metric from each solver are of the order of the small overall discretization error of the entire evolution code. The time of bounce t_b is indicated by the vertical dotted line.

by the radius enclosing a shell of a fixed fraction of the total rest mass of the star (typically 10%), whereby r_d moves inward during the collapse, too. In either case r_d is held fixed when some minimal radial threshold $r_{d\min}$ is crossed, which we set equal to the radius of some given radial grid point (e.g. the 40th grid point at r_{40}). This ensures that there is always a sufficient number of grid points on the finite difference grid, such that the interpolation to the spectral grid is well behaved. For $n_d = 6$ domains, both approaches yield equally accurate results, the relative difference between the values of ϕ_c being less than 10^{-4} throughout the evolution of the collapse model SCC (see lower panel of Fig. 8.5).

At least for core collapse simulations, the appropriate choice of the radial spectral domain setup parameters n_d and $r_d(t)$ is crucial, as exemplified in Fig. 8.6. The reduction of r_d with time must follow the contraction of the core to a sufficiently small radius, while $r_{d\min}$ must retain enough grid points for the nucleus. Furthermore, when splitting the spectral grid into several radial domains, well-behaved differential operators (in particular, the Poisson operator) are only obtained if, for a *shell*-type domain, the criterion of thin shell-type domains, $f_d \lesssim 2$, is fulfilled. This restriction for the ratio f_d between the outer and the inner radii originates from the requirement to keep the condition number of the matrix representing (for a given multipolar momentum l) the radial Poisson operator (8.25), which is a very fast growing function of f_d , lower than $\sim 10^3$.

In particular Fig. 8.6 shows that if r_d is not properly adjusted or if $r_{d\min}$ is too large, the central conformal factor deviates strongly from the correct value (upper panel). In addition, if the number of domains is too small while keeping the radial resolution $\hat{n}_r = 33$ fixed, the conformal factor inside the core shows large amplitude oscillations after core bounce, due to a too large value of f_d (lower panel). If $f_d \lesssim 2$ is violated because of too few domains in a collapse situation, such oscillations are

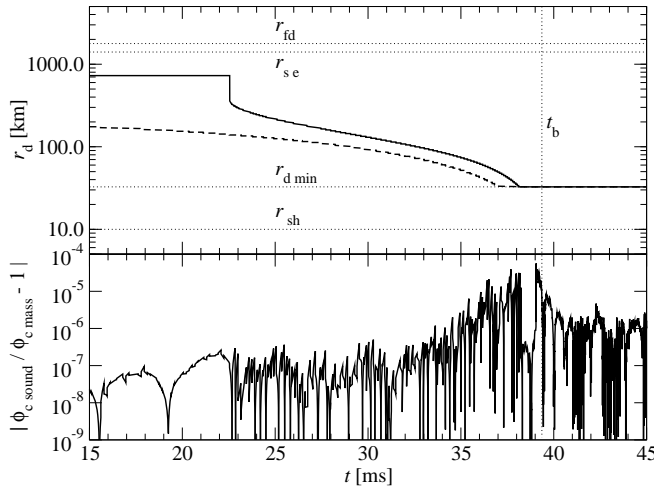


Figure 8.5: Two different methods for determining the domain radii of the spectral grid boundary. The upper panel shows the time evolution of the domain radius parameter r_d for the core collapse model SCC, where r_d is either set by the sonic point method (solid line; sonic point first detected at $t \sim 23$ ms) or by the rest mass fraction method (dashed line). The boundary of the finite difference grid r_{fd} , the stellar equatorial radius r_{se} , the minimal domain radius $r_{d\min}$ (set to r_{40}), and the approximate location of shock formation r_{sh} are indicated by horizontal dotted lines. The relative difference between the values of ϕ_c from simulations using the two methods (lower panel) is less than 10^{-4} throughout the evolution. The time of bounce t_b is indicated by the vertical dotted line.

even present if the radial resolution \hat{n}_r is increased.

On the other hand, in quasi-stationary situations with no large dynamical radial range (e.g. oscillations of neutron stars), one can safely reduce n_d from 6 to 3 and keep r_d fixed throughout the evolution. The optimal number of domains n_d is thus determined by balancing radial resolution and the requirement of thin shell-type domains against computational costs.

Axisymmetric core collapse to a neutron star – Comparison with fully general relativistic simulations

Only recently, fully general relativistic simulations of axisymmetric rotational core collapse have become available [423]. We now estimate the quality of the CFC approximation adopted in our code by simulating one of the core collapse models presented in [423] and comparing the results.

In their simulations, Shibata and Sekiguchi [423] make use of the CARTOON method [11] which reduces the dimensionality of a code based on 3D Cartesian coordinates to 2D in the case of axisymmetric configurations. Using this approach, and solving the full set of BSSN metric equations, these authors present a series of rotational core collapse models with parameters close (but not exactly equal) to the ones simulated by Dimmelmeier *et al.* [149]. As an additional difference, $\rho^* = \rho W \phi^6$ is employed by [423] in the gravitational wave extraction with the first moment of momentum density formula, while in [149] the wave extraction is performed with the stress formula using the density ρ (see Section 8.3.5 for details). Furthermore, in the simulations reported in [423], the equidistant

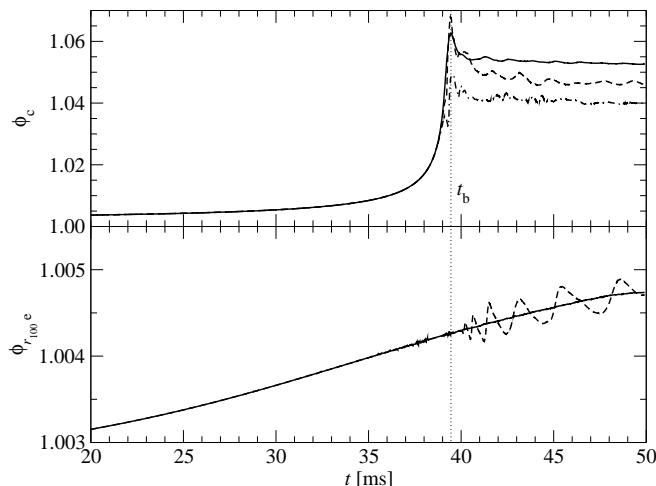


Figure 8.6: Importance of the correct spectral domain setup for highly dynamic simulations, shown for the core collapse model SCC. If the domain radius parameter is not reasonably adjusted (upper panel), e.g. r_d is held fixed at 10% of the initial stellar equatorial radius (dashed line), or if the minimal domain radius is too large, $r_{d\min} = r_{100}$ (dashed-dotted line), the central conformal factor ϕ_c deviates strongly from the correct value (solid line; c.f. Fig. 8.4). If the number of domains is too small (lower panel), e.g. $n_d = 3$ (dashed line) instead of $n_d = 6$ (solid line), the metric inside the star (here the equatorial conformal factor $\phi_{r_{100}e}$ at the 100th radial grid point) shows strong oscillations after core bounce. The time of bounce t_b is indicated by the vertical dotted line.

Cartesian finite difference grid is repeatedly remapped during the collapse, so that the grid spacing in the center increases from initially ~ 3 km to ~ 300 m during core bounce. As the outer boundary moves in accordingly, matter leaves the computational grid, resulting in a mass loss of about 3%.

In their paper, Shibata and Sekiguchi investigated a core collapse model which is identical to our model SCC (A3B2G4 in [149]) with the exception of a slightly smaller rotation length parameter $\hat{A} = A/r_{se} = 0.25$ (compared to $\hat{A} = 0.32$ in [149]) in the initial equilibrium model. They found that the evolution of this model (labeled SCC_{SS} hereafter) computed with their fully general relativistic code agrees qualitatively well with the evolution of our model SCC simulated with our CFC code. However, it produces an increased gravitational wave amplitude of about 20% at the peak during core bounce, and up to a factor 2 in the ringdown. Furthermore, the damping time of the ringdown signal of model SCC_{SS} as shown in [423] is significantly longer compared to that of model SCC presented in [149].

Shibata and Sekiguchi offer several possible explanations for this noticeable disagreement, the most plausible ones being the different functional forms of the rest mass density used in the wave extraction method, and the different formulations (stress formulation (8.34) versus first moment of momentum density formulation (8.33)). By comparing waveforms obtained from evolutions of oscillating neutron stars (as presented in [422]), both using the quadrupole formula and by directly reading off metric components, they find that the quadrupole formula underestimates the wave amplitude of model SCC_{SS} by $\sim 10\%$. Extrapolating these results they arrive at the estimate that the waveforms presented in [149] are accurate at best to within $\sim 20\%$. Shibata and Sekiguchi claim that other differences,

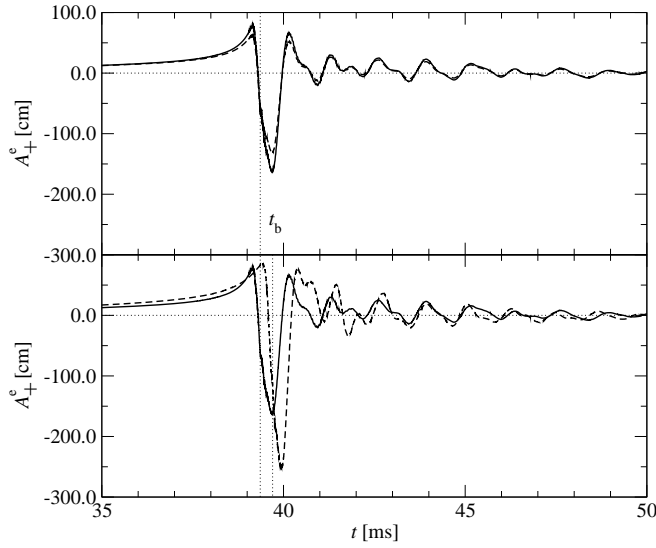


Figure 8.7: Influence of the density used in the wave extraction equations (upper panel) and of small differences in the initial model (lower panel) on the gravitational waveforms from rotational core collapse. If $\rho^* = \rho h W^2$ is used in the quadrupole formula (solid line) instead of ρ (dashed line), the wave amplitude A_+^e increases by about 20% at core bounce (upper panel). A change from model SCC (solid line) to model SCC_{SS} (dashed line), which corresponds solely to a difference in the initial configuration, results in a qualitatively different waveform, in particular during the ringdown phase (lower panel). The times of bounce t_b are indicated by the vertical dotted lines.

namely the CFC approximation versus the BSSN formulation, different grid setups, coordinate choices and slicing conditions, or the small discrepancy of \hat{A} in the initial model, have only negligible impact on the waveform.

To test this conjecture, we have simulated the evolution of model SCC with our new version of the CFC code in 2D, and extracted the wave amplitude A_+^e using the first moment of momentum density formulation (8.33) with ρ , and also alternatively substituting ρ by ρ^* . As our results show (see upper panel of Fig. 8.7), the use of ρ^* results in a small increase of A_+^e by about 20% during the bounce and the ringdown phase, limiting possible deviations due to the difference in the quadrupole formula stated in [423] to about 20%. However, the results depicted in Fig. 8.7 exclude that the doubling of A_+^e observed by [423] for the ringdown signal is due to the wave extraction method. On the contrary, comparing the waveforms for model SCC and SCC_{SS} (see lower panel of Fig. 8.7), both computed with our CFC method, shows that the strong qualitative difference found by Shibata and Sekiguchi is clearly due to the differences in the core collapse initial model, notably the small decrease of the differential rotation length scale \hat{A} in model SCC_{SS}. This gives rise to an approximately 50% higher peak value of the amplitude during bounce, and a strong increase of the post bounce wave amplitude, as also observed by Shibata and Sekiguchi (compare with Fig. 13 (b) in [423]).

Furthermore, from the evolution of the central density computed with our code (see Fig. 8.8), it is evident that model SCC_{SS} exhibits significantly stronger ringdown oscillations than model SCC with a somewhat longer damping timescale, which is also in good agreement with the results in [423] (see their Fig. 7 (b)). Clearly the small difference in the rotation length parameter \hat{A} of the initial model

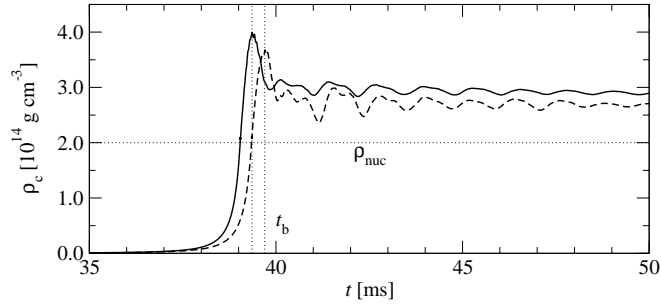


Figure 8.8: Influence of differences in the initial model on the evolution of the central density ρ_c for rotational core collapse. Changing from the collapse model SCC (solid line) to SCC_{SS} (dashed line) only slightly shifts the time of bounce t_b (indicated by the vertical dotted line), but leads to much stronger post-bounce ring down oscillations. Nuclear matter density ρ_{nuc} is indicated by the horizontal dotted line.

has a major impact on the post-bounce dynamics of the dense core, which is in turn reflected in the gravitational wave signal.

We have also simulated the evolution of models SCC and SCC_{SS} using a larger number of radial and meridional grid points ($n_r = 250$ and $n_\theta = 60$ with a central radial resolution $\Delta_{r_c} = 250$ m) as compared to the standard grid setup with $n_r = 200$, $n_\theta = 30$, and $\Delta_{r_c} = 500$ m (in either case the spectral grid resolution is $\hat{n}_r = 33$ and $\hat{n}_\theta = 17$). Neither improving the resolution of the finite difference grid nor discarding a significant mass fraction in the outer parts of the star (to mimic the mass loss introduced by the regridding method in [423]) have a significant impact on the collapse dynamics or the waveform for both initial models. When simulating the *same* collapse model, the observed small differences to Shibata and Sekiguchi’s results in e.g. the central density or the waveform are most likely due to the use of the CFC approximation for the spacetime metric employed in our code. Nevertheless, for core collapse simulations, the results obtained using either CFC or the full Einstein equations agree remarkably well.

8.4.3 Applications of the spectral solver 3 in 3D

Computation of a nonaxisymmetric spacetime metric

While the previous tests were all restricted to 2D (and thus solvers 1 and 2 could as well be used), the genuine 3D properties of the spectral metric solver 3 can be fully exploited and tested when applied to the computation of the metric for a nonaxisymmetric configuration. For this purpose we consider now the uniformly rotating neutron star initial model RNS (see Section 8.4.2) to which we add a nonaxisymmetric perturbation. This is done by generalizing the expressions in Eq. (8.39) through the multiplication of a φ -dependent term of the form $(1 + \sin^2 \varphi)$. The effect of such a perturbation on representative quantities is depicted in Fig. 8.9. The metric equations (8.24) are then integrated using solver 3. Convergence is reached after about 50 iterations (threshold value $\Delta \hat{u}_{\text{thr}}^s = 10^{-6}$), and the solution for the metric is interpolated from the spectral to the finite difference grid.

To exclude convergence to an incorrect solution and errors within the interpolation routine, we compare the left and right hand sides, lhs_u and rhs_u , of selected metric components u on the finite difference grid, in Fig. 8.10. We note that in this figure, along each of the profile directions, the two

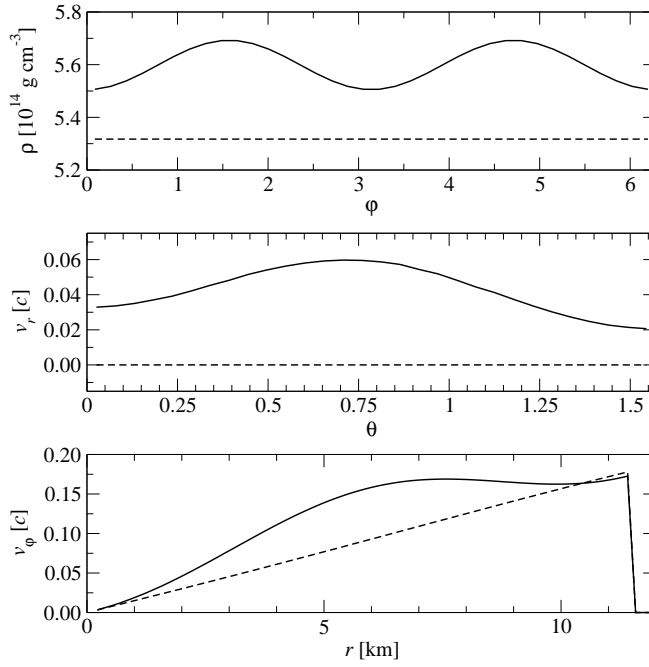


Figure 8.9: Nonaxisymmetric density and velocity perturbation of the rapidly rotating neutron star equilibrium model RNS. By applying the perturbations described in the text, the original profiles (dashed lines) of the density ρ along the azimuthal direction φ (upper panel), the radial velocity v_r along the meridional direction θ (center panel), and the rotation velocity v_φ along the radial direction r (lower panel) become strongly distorted (solid lines). The φ -dependence of ρ in the upper panel shows the nonaxisymmetric character of the perturbation.

other coordinates are kept fixed ($r = r_{50}$, $\theta = \pi/4$, and $\varphi = 0$, respectively). The left and right hand sides of the metric equations (8.24) for the conformal factor ϕ and the shift vector components β^1 and β^3 , when evaluated on the finite difference grid, match very accurately along all three coordinate directions. The largest deviations are found near the rotation axis ($\theta = 0$) for β^1 .

The accuracy of the metric calculation can be better quantified by plotting the relative difference of the left and right hand sides, $\Delta_{\text{rel } u} = |\text{lhs}_u/\text{rhs}_u - 1|$, rather than lhs_u and rhs_u alone. This is shown for the metric quantities ϕ , β^1 , and β^3 in the insets of Fig. 8.10. Along any of the plotted profiles, the spectral solver yields a solution for which the relative difference measure is better than 10^{-2} . As lhs_u and rhs_u contain second spatial derivatives of the metric, evaluated by finite differencing, this is an accurate numerical result. We note that some of the metric components are close to zero or change sign. Hence, the relative difference may become large or develop a pole at some locations, as can be seen in the insets of Fig. 8.10.

Under idealized conditions (i.e. without discontinuities in the source terms of the metric equations, no artificial atmosphere, only laminar matter flows, uniform grid spacing of the finite difference grid, and perturbations which are regular at the grid boundaries), such a test case also offers an opportunity to examine the order of convergence of the metric solver 3 on the spectral and finite difference grid, respectively. To this end we perform a metric calculation using increasingly finer resolutions on the two grids. By varying the number of spectral collocation points in all three spatial directions while keeping the number of finite difference grid points fixed (at high resolution), we observe an exponential decrease

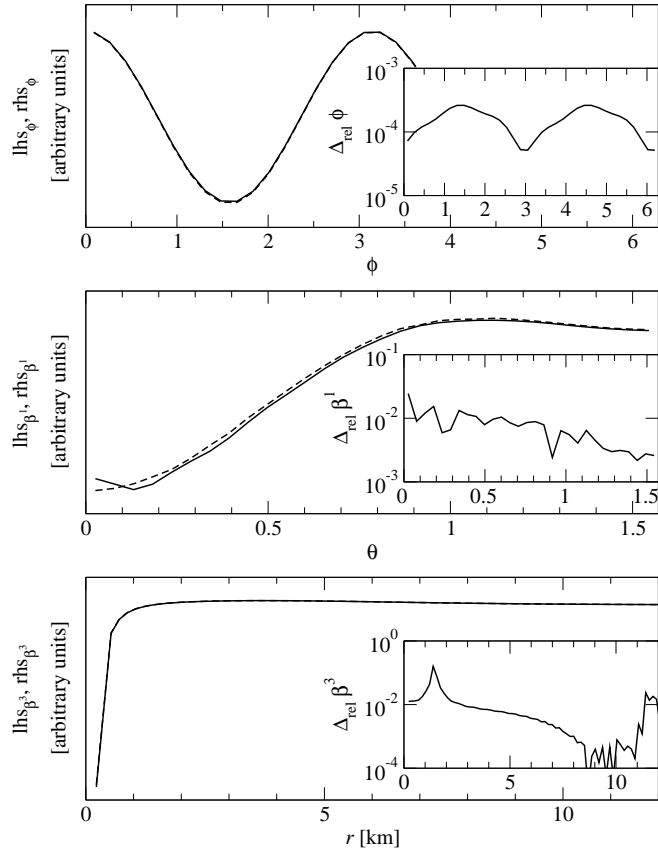


Figure 8.10: Left (solid line) and right (dashed line) hand sides (computed on the finite difference grid) of the equation for the metric components ϕ along the azimuthal direction φ (upper panel), β^1 along the meridional direction θ (center panel), and β^3 along the radial direction (lower panel). Even for strong nonaxisymmetric perturbations of the rotating neutron star model RNS, the metric solver 3 yields a highly accurate matching, such that the lines almost lie on top of one another. The insets show the relative difference $\Delta_{\text{rel}u}$ between the left and right hand sides of the equation for the same metric components. The relative differences are $\lesssim 10^{-2}$, except where they exhibit a pole.

of the relative differences $\Delta_{\text{rel}u}$ between the left and right hand sides of the equation for the various metric components u . Correspondingly, the metric solution evaluated on the finite difference grid exhibits second order convergence with grid resolution for a fixed (and high) spectral grid resolution. Furthermore, the (at least) second order accurate time integration scheme of the code in combination with the PPM reconstruction of the Riemann solver also guarantees second order convergence during time evolution. For fixed time steps we actually observe this theoretical convergence order globally and even locally (except close to the grid boundaries, where symmetry conditions and ghost zone extrapolation spoil local convergence).

In the three-dimensional case the computational load of the interpolation from the spectral grid to the finite difference grid after every metric calculation on the spectral grid becomes significant. The time spent in the interpolation between grids can, in fact, even surpass the computational costs of the

Table 8.4: Dependence of the metric solver execution time t_m on the finite difference grid resolution $n_r \times n_\theta \times n_\varphi$ and the spectral grid azimuthal resolution \hat{n}_φ using the metric solver 3 in 3D for the nonaxisymmetrically perturbed rotating neutron star model RNS. For typical finite difference grid point numbers, the ratio r_{n_φ} between execution times for a given n_φ and for half that resolution is smaller than 2, i.e. the increase of t_m is less than linear. Furthermore, when doubling both the radial *and* meridional grid zones, a sublinear increase in the corresponding ratio $r_{n_{r,\theta}} < 4$ is observed. Doubling the spectral resolution \hat{n}_φ increases t_m by $r_{\hat{n}_\varphi} \sim 2$. For comparison, the values of t_m for the corresponding axisymmetric model are given at the bottom.

$n_r \times n_\theta \times n_\varphi$	$\hat{n}_\varphi = 6$			$\hat{n}_\varphi = 12$			
	t_m [s]	r_{n_φ}	$r_{n_{r,\theta}}$	t_m [s]	r_{n_φ}	$r_{n_{r,\theta}}$	$r_{\hat{n}_\varphi}$
$100 \times 32 \times 8$	37.2			71.5			2.0
$100 \times 32 \times 16$	39.9	1.1		77.8	1.1		2.0
$100 \times 32 \times 32$	47.4	1.2		90.6	1.2		1.9
$100 \times 32 \times 64$	62.3	1.3		116.1	1.3		1.9
$200 \times 64 \times 8$	48.3		1.3	90.7		1.3	1.9
$200 \times 64 \times 16$	62.5	1.3	1.6	116.6	1.3	1.5	1.9
$200 \times 64 \times 32$	92.0	1.5	1.9	166.2	1.4	1.8	1.8
$200 \times 64 \times 64$	149.9	1.6	2.4	269.5	1.6	2.3	1.8
$n_r \times n_\theta \times n_\varphi$	$\hat{n}_\varphi = 4$						
	t_m [s]						
	$100 \times 32 \times 1$	20.5					
$200 \times 32 \times 1$	21.7						

spectral metric solution itself (see Section 8.4.1). As a consequence, the independence of the metric execution time t_m on the number of finite difference grid points found in the axisymmetric case (as shown in Table 8.3) cannot be maintained. Table 8.4 reports the summary of runtime results for a single metric computation of the above neutron star model on an IBM RS/6000 Power4 processor. These results indicate an (albeit sublinear) increase of t_m with the number of finite difference grid points. As expected, a doubling of the spectral grid resolution e.g. in the φ -direction (while keeping $\hat{n}_r = 33$ and $\hat{n}_\theta = 17$ fixed) results in a proportional increase of t_m . The runtime scaling results reported in Table 8.4 also demonstrate that the different coordinate directions contribute equally to the computational costs.

It is worth pointing out that the other two metric solvers we have available in the code fail to compute the metric for the nonaxisymmetric neutron star configuration considered in this section due to the known limitations (excessive computing time for solver 1, convergence problems for solver 2).

Stability of symmetric configurations against perturbations

An important requirement for any hydrodynamics code is the preservation of the symmetry of an initially symmetric configuration during time evolution. In a practical application this means that if

a small perturbation is added to symmetric and *stable* initial data, the perturbation amplitude must not grow in time. Due to the choice of spherical polar coordinates (r, θ, φ) , our code is particularly well suited to test the preservation of the symmetry of spherically symmetric and axisymmetric initial data. Additionally, this coordinate choice implies that when simulating axisymmetric or spherically symmetric problems, either one or two dimensions can be trivially suppressed, respectively, which results in considerable savings of computational time.

Next, we present results from the evolution of both a spherically symmetric neutron star model (labeled SNS) and the axisymmetric rapidly rotating neutron star model RNS. Model SNS has the same central density and EoS as model RNS described in Section 8.4.2. To each equilibrium model SNS and RNS we respectively add an axisymmetric (r, θ) - and a nonaxisymmetric (r, θ, φ) -dependent three-velocity perturbation of the form

$$\begin{aligned} v_r &= 0.02 \sin^2 \left(\pi \frac{r}{r_s} \right) (1 + a \sin^2(2\theta)), \\ v_\theta &= 0.02 \sin^2 \left(\pi \frac{r}{r_s} \right) a \sin^2(2\theta), \end{aligned} \tag{8.40}$$

and

$$\begin{aligned} v_r &= 0.02 \sin^2 \left(\pi \frac{r}{r_s} \right) (1 + \sin^2(2\theta)) (1 + a \sin^2 \varphi), \\ v_\theta &= 0.02 \sin^2 \left(\pi \frac{r}{r_s} \right) \sin^2(2\theta) (1 + a \sin^2 \varphi), \\ v_\varphi &= v_{\varphi \text{ ini}} + 0.02 \sin^2 \left(\pi \frac{r}{r_s} \right) (1 + \sin^2(2\theta)) (1 + a \sin^2 \varphi), \end{aligned} \tag{8.41}$$

respectively, where a is the perturbation amplitude. Model SNS is then evolved in time using the code in axisymmetric 2D mode, and model RNS using the fully 3D capabilities of the code. The metric is calculated every 100 (300) time steps in 2D (3D) and extrapolated in between. The number of finite difference grid zones is $n_r = 80$, $n_\theta = 16$, $n_\varphi = 1$ in the 2D case and $n_r = 80$, $n_\theta = 16$, $n_\varphi = 12$ in the 3D case. Correspondingly, for the spectral grid we use $\hat{n}_r = 25$, $\hat{n}_\theta = 13$, $\hat{n}_\varphi = 4$ in 2D, and $\hat{n}_r = 25$, $\hat{n}_\theta = 13$, $\hat{n}_\varphi = 6$ in 3D.

The results of the evolution of the symmetry violating perturbations in both models are depicted in Fig. 8.11. The upper panels correspond to model SNS which is evolved up to 5 ms, while the bottom panels correspond to model RNS which is only evolved up to 1 ms. The left and right panels differ by the value of the initial amplitude a of the velocity perturbation. We observe that the perturbation amplitude, measured as the relative difference Δq of an arbitrary matter or metric quantity q evaluated at two points of constant r (for model SNS) and constant r, θ (for model RNS), remains practically unchanged for many hydrodynamic time scales. Note that the spikes in Δq appearing in Fig. 8.11 are the poles associated with a vanishing q . Fig. 8.11 also shows that the amplitude of the symmetry violation Δq approximately scales with the amplitude a of the initial velocity perturbation (indicated by horizontal dotted lines).

In the course of many hydrodynamic time scales, the perturbations (which are of small amplitude, $a \ll 1$) will be finally damped due to the intrinsic numerical viscosity of the schemes implemented in the code. However, if the rotation rate β of a rotating neutron star were high enough such that $\beta \gtrsim \beta_s$ or even $\beta \gtrsim \beta_d$, perturbations of the form given by Eq. (8.41) could trigger the onset of *physically* growing modes, leading to bar mode instabilities.

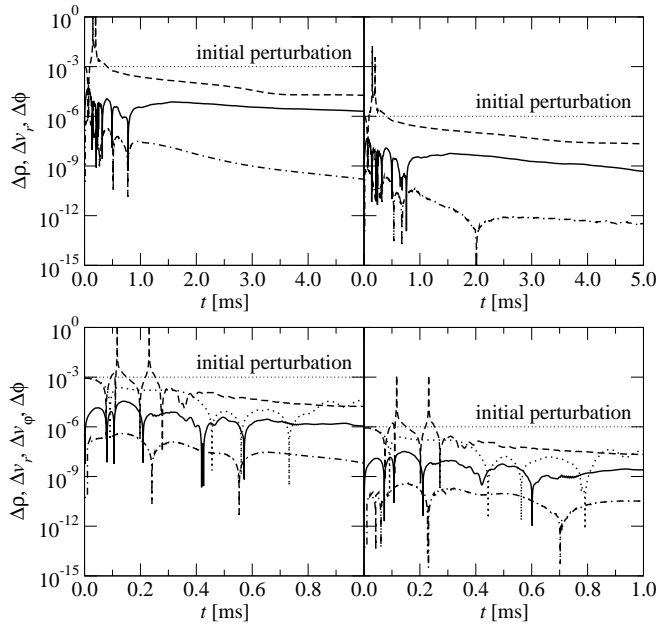


Figure 8.11: Time evolution of a symmetry violating perturbation. The upper two panels correspond to the spherically symmetric model SNS, and the lower two panels to the axisymmetric model RNS. The relative variation in density $\Delta\rho$ (solid line), radial velocity Δv_r (dashed line), rotational velocity Δv_φ (dotted line), and conformal factor $\Delta\phi$ (dashed-dotted line) show a remarkable constancy in time (note that Δv_φ is nonzero only for the rotating model RNS). The symmetry violating variation of the different fields scale with the initial perturbation amplitude (horizontal dotted lines; left panels: $a = 10^{-3}$; right panels: $a = 10^{-6}$).

Evolution of an axisymmetric uniformly rotating neutron star in 3D

The ability to handle long-term evolutions of rapidly rotating relativistic equilibrium configurations is a difficult test for any numerical code. To demonstrate the capabilities of our code to pass this stringent test we evolve the rotating neutron star initial model RNS in 3D until $t = 10$ ms, which corresponds to about 10 hydrodynamic time scales and rotation periods. The simulation is performed with a resolution for the finite difference grid of $n_r = 100$, $n_\theta = 30$, $n_\varphi = 8$, and $\hat{n}_r = 33$, $\hat{n}_\theta = 17$, $\hat{n}_\varphi = 6$ for the spectral grid. During the evolution, the metric is calculated every 100 time steps and extrapolated in between.

The preservation of the radial profile of the rotation velocity $v_{\varphi e}$ along the equator over a long evolution time is shown in Fig. 8.12. Depicted is the initial equilibrium solution (solid line) as a function of the radial coordinate (in the equatorial plane) and the final configuration (dashed line), after an evolution time of 10 ms (about 10 rotational periods). The figure shows that v_φ remains close to its initial value in the interior of the star, showing the strongest (but still small) deviations near the stellar surface (at the interface to the artificial atmosphere). This local decrease of v_φ due to interaction of stellar matter with the atmosphere and its dependence on the order of the reconstruction scheme has also been observed in other studies (see e.g. [178]).

It is important to emphasize that the accurate preservation of the rotational profile is achieved because of the use of third-order cell-reconstruction schemes for the hydrodynamics equations, such as

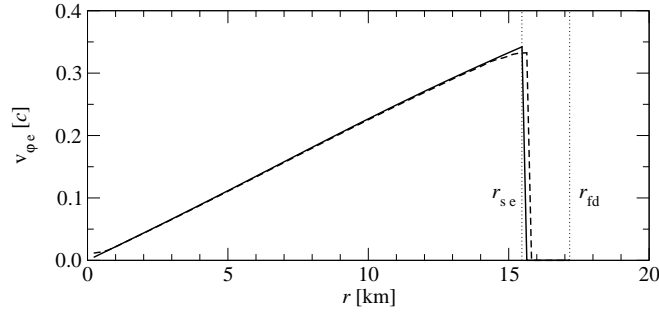


Figure 8.12: Radial profile of the equatorial rotation velocity v_{φ_e} for the unperturbed axisymmetric rapidly rotating neutron star model RNS evolved in 3D. The profile of v_{φ_e} at $t = 10$ ms (dashed line) closely reproduces the initial profile (solid line). The stellar equatorial radius r_{se} and the boundary of the finite difference grid r_{fd} are indicated by vertical dotted lines.

PPM, as first shown by [178]. Despite the comparably coarse resolution of the finite difference grid and the use of the CFC approximation for the gravitational field equations, our code captures the profile of v_{φ_e} at the stellar boundary about as accurately as codes solving the full Einstein metric equations coupled to the hydrodynamics equations [181], or codes restricted to hydrodynamic evolutions in a fixed curved spacetime (i.e. using the so-called Cowling approximation) [178].

Long-term evolutions of rotating neutron stars as the one presented here can be effectively used for extracting the oscillation frequencies of the various pulsation eigenmodes of the star. This topic has been traditionally studied using perturbation theory (see e.g. [282] and references therein). In recent years fully nonlinear hydrodynamical codes have helped to drive progress in the field. They have provided the quasi-radial mode-frequencies of rapidly rotating relativistic stars, both uniformly and differentially rotating, which is a problem still not amenable to perturbation techniques (see e.g. [178, 180, 181, 443, 152]).

In order to test our code against existing results we show next an example of the procedure to compute mode-frequencies using the model RNS. The frequencies can in principle be extracted from a Fourier transform of the time evolution of various pulsating quantities when the oscillations are triggered by numerical truncation errors. However, the results significantly improve when a perturbation of some specific parity is added to the initial equilibrium model. To excite small amplitude quasi-radial oscillations, we hence apply an $l = 0$ radial velocity perturbation to the equilibrium configuration of the form

$$v_r = a \sin^2\left(\pi \frac{r}{r_s}\right), \quad (8.42)$$

with an amplitude $a = -0.01$.

Due to this perturbation, various metric and hydrodynamic quantities exhibit very regular periodic oscillations around their equilibrium state, as shown for the radial velocity v_r in Fig. 8.13. The pulsations, which show no noticeable numerical damping during the entire duration of the simulation (10 ms), are extracted at half the stellar equatorial radius. The same oscillation pattern is obtained when instead of using the 3D code (solid line in the figure) the model is evolved using the code in axisymmetric mode (dashed line in Fig. 8.13 with finite difference grid size of $n_r = 160$, $n_\theta = 60$). The latter, axisymmetric setup is currently being used in a comprehensive parameter study of the oscillation frequencies of rotating neutron star models [152]. Note that Fig. 8.13 also demonstrates

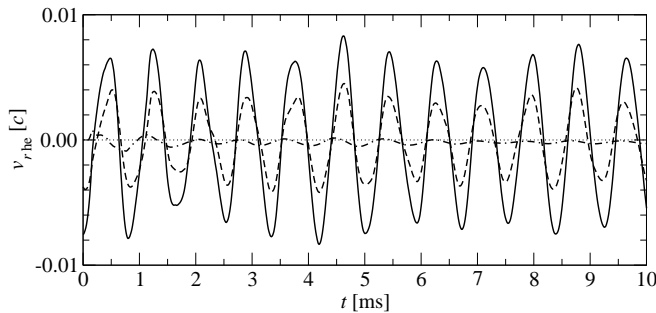


Figure 8.13: Time evolution of the radial velocity at half the stellar equatorial radius $v_{r,he}$ for the perturbed rapidly rotating neutron star model RNS. The radial velocity shows regular oscillations with neither a noticeable drift nor damping when the 3D code is used in low resolution (solid line) as well as for the 2D code with high resolution (dashed line). For comparison, the dashed-dotted line shows $v_{r,he}$ when no explicit perturbation is added. In this case the oscillations are triggered by truncation errors and (mostly) by the error resulting from using the CFC approximation in the evolution code.

that the oscillation amplitude scales linearly with the initial perturbation amplitude a (at least if $a \ll 1$), which was chosen as $a = -0.005$ in the 2D simulations. In the radial velocity, neither an offset nor a noticeable drift with time can be observed. This is in agreement with previous results using alternative formulations and different numerical codes [178, 181].

Time evolution data like the one shown in Fig. 8.13 can be used to extract the eigenmode frequencies. A Fourier transformation of different metric and hydrodynamic quantities at various locations in the star yields identical (discrete) frequencies. Table 8.5 summarizes the frequencies f_F and f_{H1} for the quasi-radial fundamental mode and its first harmonic overtone, respectively. Both frequencies obtained with the current 3D code differ only by a few percent from those computed with the code in 2D [152] or the CACTUS code, which is based on a Cartesian grid and uses the BSSN formulation for the Einstein equations [181].

Additionally, we have investigated the influence of grid resolution and finite evolution time on the accuracy of the frequency extraction. We have found that the differences in the frequencies between the 2D and 3D simulations presented in Table 8.5 can be almost entirely attributed to the twice as long evolution time of the 2D simulation (20 ms), for which the Fourier transformation renders more accurate frequencies. For practical evolution times of several tens of milliseconds and for grid resolutions better than $n_r \sim 100$ and $n_\theta \sim 30$, the extracted oscillation frequencies are almost independent of the number of grid points used.

Note also that the mode-frequencies agree well even though we have used different perturbation amplitudes a in the 3D and 2D simulations (while in the CACTUS run an $l = 0$ rest mass density perturbation with an amplitude $a = 0.02$ was used). Table 8.5 hence proves that our code is able to simulate rotating neutron stars in a fully three-dimensional context for sufficiently long time scales to successfully extract oscillation frequencies.

Evolution of a nonaxisymmetric uniformly rotating neutron star in 3D

Contrary to the small amplitude nonaxisymmetric perturbations employed in Section 8.4.3, we turn now to assess the ability of the numerical code to manage long-term stable evolutions of strongly

Table 8.5: Comparison of the oscillation frequencies of two perturbed equilibrium neutron star models SNS and RNS with different axis ratios $r_{\text{sp}}/r_{\text{se}}$ obtained with the current code (both in 2D and 3D) and with the CACTUS code [181]. The frequencies for the fundamental mode f_{F} and for the first harmonic f_{H1} computed with the current code show a relative difference with respect to the CACTUS code (in parentheses) of at most 2%. Due to the coarse spatial resolution used, the 3D code results were only calculated to 3 significant figures.

Code	SNS $r_{\text{sp}}/r_{\text{se}} = 1.00$		RNS $r_{\text{sp}}/r_{\text{se}} = 0.65$	
	f_{F} [kHz]	f_{H1} [kHz]	f_{F} [kHz]	f_{H1} [kHz]
current (3D)	1.40 (3.4)	3.95 (0.2)	1.20 (0.4)	3.68 (1.0)
current (2D)	1.463(0.9)	3.951 (0.2)	1.219(2.0)	3.659 (1.6)
CACTUS	1.450	3.958	1.195	3.717

gravitating systems with large departures from axisymmetry. This is an essential test for future astrophysical applications of the code as e.g. the numerical investigation of bar mode instabilities in rotating neutron stars.

For this purpose we construct a uniformly rotating neutron star model with the same parameters as model RNS, but with only half the central density. The finite difference grid extends out to $r_{\text{fd}} = 80$ km, with 60 equidistant radial grid points resolving the neutron star out to $r_{\text{se}} = 18.6$ km. The atmosphere is covered by 80 logarithmically spaced radial grid points. The number of angular zones used in the finite difference grid is $n_{\theta} = 24$ and $n_{\varphi} = 32$, respectively, while the spectral grid has $\hat{n}_r = 17$, $\hat{n}_{\theta} = 13$, and $\hat{n}_{\varphi} = 12$ grid points in 3 radial domains.

On top of the equilibrium neutron star model we add a strongly nonaxisymmetric (i.e. φ -dependent) perturbation of the rest-mass density

$$\rho = \rho_{\text{ini}} + a \rho_{\text{c}} \sin^2 \left[\pi \left(\frac{r}{2r_{\text{s}}} \right)^2 \right] \sin^{10} \varphi \quad \text{for } r \leq 2r_{\text{s}}, \quad (8.43)$$

with an amplitude $a = 0.1$, which yields an $l = m = 2$ bar-like structure. The rotation velocity of the uniformly rotating unperturbed neutron star is extrapolated into the areas filled with matter by the perturbation. The initial configuration with the perturbation added is shown in the left panel of Fig. 8.14.

We have chosen this particular (albeit unphysically strong) perturbation and velocity field in order to prevent both, an immediate accretion of the added matter bars on to the neutron star or an ejection. This allows us to follow the rotation of the neutron star for a time comparable to its rotation period (which is about 1 ms for the unperturbed neutron star). The density and rotation velocity plots in Fig. 8.14 after $t = 0.5$ ms (center panel) and $t = 1.0$ ms (right panel) prove this property of the chosen perturbation. These plots also demonstrate that the corotating bar structures slowly disappear. The innermost parts are being gradually accreted by the neutron star, which leads to a significant initial rise in the central density, as shown in Fig. 8.15. At later times the more massive neutron star oscillates with a period of $t_{\text{osc}} \sim 1.0$ ms around a new quasi-equilibrium state, which possesses a central density

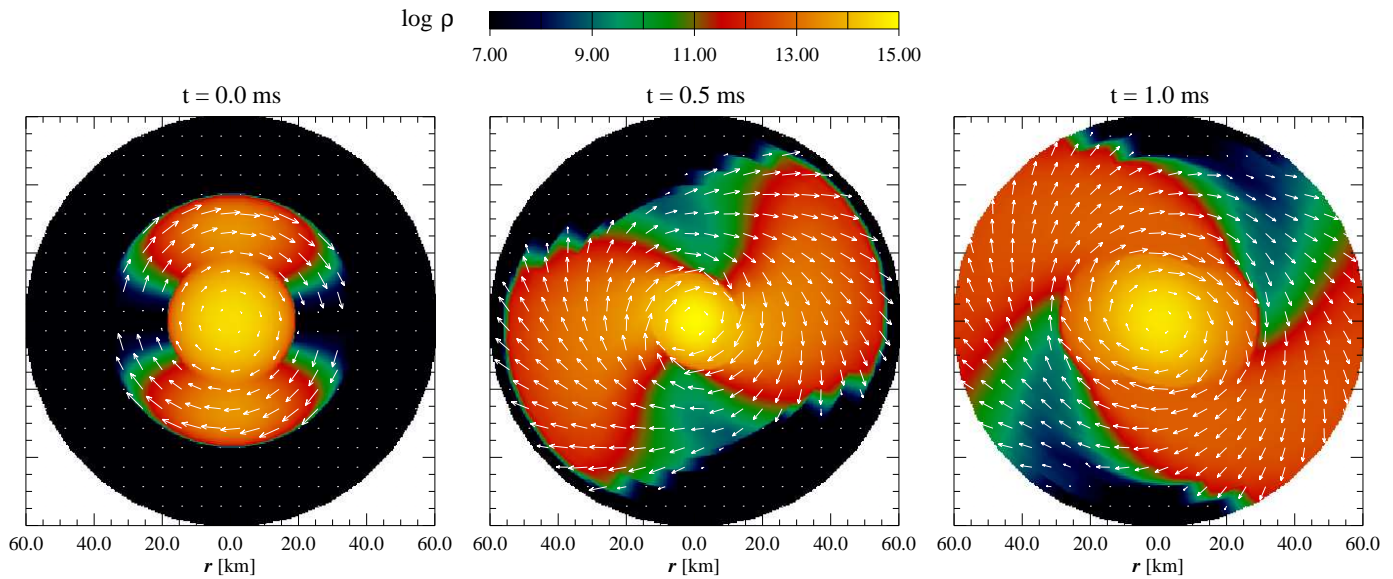


Figure 8.14: Evolution of a strongly distorted nonaxisymmetric rotating neutron star model. The color coded distribution of $\log \rho$ on the equatorial plane shows how the initial perturbation (left panel) is partly accreted by the neutron star, and partly stretched into spiral arms (center panel). After about one rotation period of the neutron star, the trailing spiral arms have grown considerably in size (right panel). The rotation velocity v_φ is indicated by white arrows. Note that the atmosphere (color coded in black) has a density of much less than 10^7 g cm^{-3} , and that only the innermost 60 km of the computational domain are shown.

of more than 50% above the initial equilibrium central density. Despite this strong interaction of the bar perturbation with the neutron star, the rotation *profile* inside the neutron star remains uniform throughout the evolution, although the rotation *velocity* nearly doubles during the oscillation maxima. This behavior is most likely due to the particular choice of a uniform rotation profile for the initial bar perturbation.

For the outer parts of the initial bar, the increasing distance from the neutron star and the sufficiently high specific angular momentum prevents their accretion onto the neutron star. Thus the matter in this region of the bar drifts to larger radii during the evolution. As on the dynamical timescales considered of one rotation period there is no efficient transport mechanism of local angular momentum by viscous effects (which act on much longer timescales), the evolution leads to the development of spiral arms which are clearly visible in the middle and right panels of Fig. 8.14. The outer parts of these arms are centrifugally expelled from the finite difference grid, crossing the outer boundary at $t \sim 0.84 \text{ ms}$. By the end of the simulation, at $t = 4 \text{ ms}$, there is neither significant backscattering of matter from the outermost boundary of the radial grid, nor there are numerical artifacts visible at the leading or trailing edges of the spiral arms. This proves that our numerical treatment of the radial boundary conditions and of the artificial low density atmosphere surrounding the star have the desired behavior.

Fig. 8.15 shows that already after an evolution time of $\sim 1 \text{ ms}$, the evolution of the spiral arms has no further significant impact in the dynamics of the neutron star, as then the slowly decaying oscillation around the final equilibrium state exhibits a rather regular ring-down pattern. Plotted in

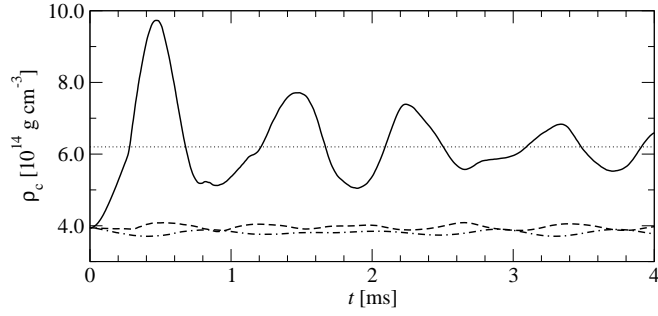


Figure 8.15: Time evolution of the central density ρ_c for distorted nonaxisymmetric rotating neutron star models. If the distortion is strong ($a = 0.1$, solid line), matter accretion from the rotating bars results in a steep initial increase of ρ_c , which slowly settles down to a new equilibrium state (indicated by the horizontal dotted line). For a small perturbation ($a = 0.01$, dashed line), the evolution of ρ_c follows very closely that of an unperturbed model (dashed-dotted line).

this figure is also the time evolution of the central density for a model with an amplitude $a = 0.01$ of the initial perturbation given by Eq. (8.43) (dashed line). In addition, the dashed-dotted line shows the corresponding time evolution of ρ_c for an unperturbed model (the small amplitude oscillations are in this case triggered by the truncation errors of the numerical schemes and by the use of the CFC approximation in the evolution code). The similarity in the behavior of ρ_c in these cases demonstrates that for perturbations with an amplitude $a \lesssim 0.01$, the dynamics of the central neutron star is virtually unaffected by the initial bar and by the spiral arms forming at later times. However, we observe that also for small values of a spiral arms develop which are stable over many rotation periods.

Apparently, strong nonaxisymmetric perturbations of the form (8.43) give rise to significant gravitational wave emission. The waveforms of the nonzero gravitational wave amplitudes A_+^e , A_+^p , and A_\times^p (as shown in the upper, center, and lower panel of Fig. 8.16, respectively) exhibit peak values of up to $\sim 15 \times 10^3$ cm for the model with a perturbation amplitude $a = 0.1$ (solid lines). In Fig. 8.16 we also present the waveforms for the model with a bar perturbation of amplitude $a = 0.01$ (dashed lines). Their amplitudes are roughly a factor 10 smaller than those of the corresponding waveforms of the model with $a = 0.1$. Thus we can infer that the gravitational radiation amplitude approximately scales with a .

We emphasize that owing to the particular form of the perturbation (8.43), the \times -mode of the gravitational radiation is zero at the equator, $A_\times^e = 0$. We also note that if instead of the nonaxisymmetric perturbation in Eq. (8.43) we use an axisymmetric one,

$$\rho = \rho_{\text{ini}} + a \rho_{c,\text{ini}} \sin^2 \left[\pi \left(\frac{r}{2r_s} \right)^2 \right] \quad \text{for } r \leq 2r_s, \quad (8.44)$$

then the \times -mode of gravitational radiation vanishes completely, and only the $+$ -mode is present (dashed-dotted line in the upper panel of Fig. 8.16). Additionally, in axisymmetry the $+$ -mode on the pole is always zero, $A_+^p = 0$.

We point out that the waveform pattern for the model with the $a = 0.1$ bar perturbation in Fig. 8.16 does not solely reflect the oscillation and ring-down structure of the central neutron star, as visible in the time evolution of ρ_c in Fig. 8.15. For instance the $+$ -mode at the equator (upper panel)

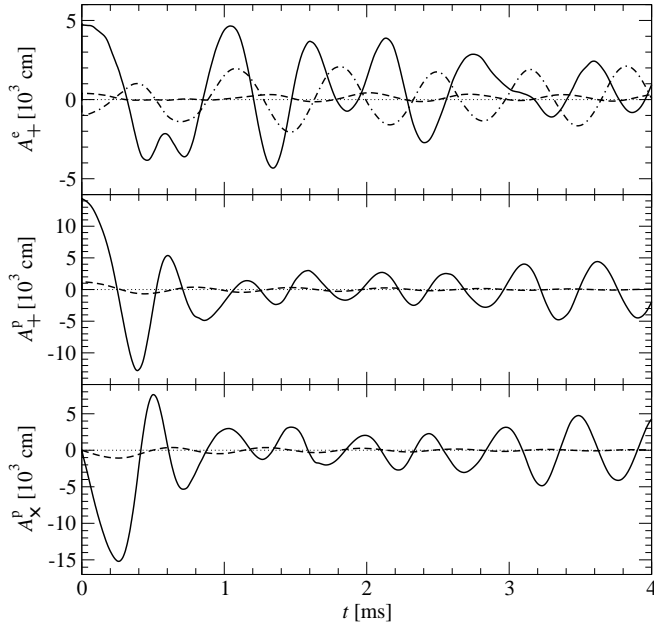


Figure 8.16: Gravitational wave signal for distorted nonaxisymmetric rotating neutron star model. If the distortion is strong ($a = 0.1$, solid lines), the nonzero gravitational wave amplitudes A_+^e (upper panel), A_+^p (center panel), and A_x^p (lower panel) reach peak values of up to $\sim 15,000$ cm. The amplitudes reduce significantly for $a = 0.01$ (dashed lines). If an axisymmetric perturbation with $a = 0.1$ is applied (dashed-dotted line), only the A_+^e gravitational wave mode is present.

decays on a much longer time scale than the corresponding ring-down time of ρ_c . On the other hand, the waveforms for the two polarizations of the radiation at the pole exhibit their peaks during the first oscillation of ρ_c and then decay rapidly (center and lower panel). However, after an evolution time of ~ 2 ms their amplitudes increase again. From this behavior we deduce that initially the waveform signal is dominated by the gravitational wave emission from the oscillating neutron star. As this contribution decays during the ring-down, the wave emission from spiral arms becomes increasingly important. As they expand into the atmosphere the radial weight arm in the quadrupole formula compensates for the relatively low density of the spiral arms, and the radiation emitted in this region becomes visible in the signal. We cannot clearly attribute the late-time increase in the waveform amplitude to the onset of a bar mode instability, because the rotation parameter β of our model clearly falls short of the approximate threshold for dynamical growth of bar modes: $\beta \sim 0.14 \ll \beta_d$. We plan to investigate this issue more thoroughly in the future.

The maximum amplitude $A \sim 15 \times 10^3$ cm of the wave signal for $a = 0.1$ corresponds to a dimensionless gravitational wave amplitude $h \sim 5 \times 10^{-19}$ at a distance of $r = 10$ kpc to the source. Thus, in this case of a strongly nonaxisymmetric artificial perturbation, the typical wave amplitudes have a value of roughly one order of magnitude above the ones of waveforms obtained from the simplified models of rotational supernova core collapse in axisymmetry by Dimmelmeier *et al.* [149]. For the waveforms plotted in Fig. 8.16 we utilize the stress formula (8.34) with ρ^* as density. The use of this formula efficiently reduces the numerical noise in the signal as compared with the first moment of momentum density formula and particularly with the standard quadrupole formula.

We consider the grid resolution used in this test simulation to be the minimal one required for obtaining reasonably converged results. By repeating the same model with different grid resolutions we are able to estimate that the waveform amplitudes are correctly computed within $\sim 30\%$ accuracy.

8.5 Conclusions

In this paper we have presented a new three-dimensional general relativistic hydrodynamics code which is primarily intended for applications of stellar core collapse to a neutron star or a black hole, as well as for studies of rapidly rotating relativistic stars which may oscillate in their quasi-normal modes of pulsation, emitting gravitational radiation, or which may be subject to nonaxisymmetric instabilities. The main novelty of this code compared to other existing numerical relativistic codes is that it *combines* very accurate state-of-the-art numerical methods specifically tailored to solve the general relativistic hydrodynamics equations on the one hand, and the gravitational field equations on the other hand. More precisely, the hydrodynamic equations, formulated in conservation form, are solved using high-resolution shock-capturing schemes based upon approximate Riemann solvers and third-order cell-reconstruction interpolation procedures, while the elliptic metric equations are solved using an iterative nonlinear solver based on spectral methods. Furthermore, the present code also departs noticeably from other three-dimensional codes in the coordinate system used in the formulation of the equations and in the discretization. In our approach both the metric and the hydrodynamics equations are formulated and solved numerically using spherical polar coordinates. In the present investigation we have adopted the so-called conformal flatness approximation of the Einstein equations, which reduces them to a set of five elliptic nonlinear equations, particularly suited for the use of spectral methods. Recently, constrained formulations of the full Einstein equations in which elliptic equations have a preeminence over hyperbolic equations have been reported, and appear to be amenable to the current code.

The main purpose of the paper has been to assess the code by demonstrating that the combination of the finite difference grid and the spectral grid, on which the hydrodynamics and metric equations are respectively solved, can be successfully accomplished. This approach, which we call *Mariage des Maillages* (French for grid wedding), results in high accuracy of the metric solver and, in practice, has allowed for fully three-dimensional applications using computationally affordable resources, along with ensuring long term numerical stability of the evolution. To facilitate the *Mariage des Maillages*, i.e. the combination of the finite difference grid for the hydrodynamic solver and the spectral grid for the metric solver, a sophisticated interpolation and grid communication scheme has been used. In addition, we have compared our novel approach to two other, finite difference based, methods to solve the metric equations, which we already employed in earlier axisymmetric investigations [148, 149].

We have presented a variety of tests in two and three dimensions, involving neutron star spacetimes and stellar core collapse. Axisymmetric simulations have also been performed to compare core collapse to neutron stars using the CFC approximation and full general relativity, for which only very recently results have become available [423]. This comparison has shown the suitability of the conformally flat approximation for such mildly relativistic scenarios. Furthermore, the code has succeeded in simulating the highly perturbed nonaxisymmetric configuration of a uniformly rotating neutron star for several dynamical times. This simulation has also been used to assess the 3D gravitational waveform extraction capabilities of the code. In summary the numerical experiments reported in the paper demonstrate the ability of the code to handle spacetimes with and without symmetries in strong gravity. In future work we plan to apply this code to simulations of stellar core collapse to neutron stars or black holes

in three dimensions, and particularly to studies of the nonlinear development of bar mode instabilities in rapidly rotating neutron stars.

APPENDIX

8.A Differences to previous 2D CFC simulations

8.A.1 Compact form of the Euler equation sources

In the axisymmetric CFC code presented in [148, 149] the source terms Q_j for the hydrodynamic momentum equations (Euler equations) were evaluated on the finite difference grid using a formulation containing time derivatives and explicit Christoffel symbols (see Equation (8.4)):

$$Q_j = T^{\mu\nu} \left(\frac{\partial g_{\nu j}}{\partial x^\mu} - \Gamma_{\mu\nu}^\lambda g_{\lambda j} \right). \quad (8.45)$$

Using the relation between the Christoffel symbols and the derivatives of the spacetime metric,

$$\Gamma_{\mu\nu}^\lambda = \frac{1}{2} g^{\lambda\delta} \left(\frac{\partial g_{\delta\nu}}{\partial x^\mu} + \frac{\partial g_{\delta\mu}}{\partial x^\nu} - \frac{\partial g_{\mu\nu}}{\partial x^\delta} \right), \quad (8.46)$$

the sources Q_j can be written in a more compact form as

$$Q_j = \frac{1}{2} T^{\mu\nu} \frac{\partial g_{\mu\nu}}{\partial x^j}. \quad (8.47)$$

In this formulation, only *spatial* derivatives of the metric are needed, and the numerical evaluation of Q_j involves significantly fewer terms, making a numerical implementation both faster and more accurate. For these reasons, we have preferred the use of Equation (8.47) to Equation (8.45) in the code presented in this paper.

8.A.2 Exact numerical conservation of the hydrodynamic equations

As emphasized in Section 5.4 in [148], the conserved hydrodynamic quantity in the system of conservation equations (8.3) is not simply the state vector \mathbf{U} but rather $\sqrt{\gamma}\mathbf{U}$ with $\sqrt{\gamma} = \phi^6 r^2 \sin\theta$. Therefore, if only the state vector \mathbf{U} is evolved, this gives rise to an additional source term $\hat{\mathbf{Q}}$ which contains time derivatives of the conformal factor ϕ . These generally time-dependent source terms result in a variation of the volume-integrated state vector with time, and thus in a violation of exact numerical rest mass and angular momentum conservation of several percent, even though the “physical” sources vanish, $\mathbf{Q} = 0$ (see Figs. 9 and 10 in Ref. [148]).

It is not possible to evolve $\sqrt{\gamma}\mathbf{U}$ in a straightforward way and then consistently solve the elliptic metric equations (8.11) on the new time slice. This is due to the fact that the sources for these equations contain the pressure P , which can only be extracted from \mathbf{U} but not from $\sqrt{\gamma}\mathbf{U}$. However, one can make use of the time evolution equation for the conformal factor, Eq. (8.9), to obtain an auxiliary value for ϕ and thus for $\sqrt{\gamma}$ on the new time slice. With this the state vector \mathbf{U} can be consistently calculated from $\sqrt{\gamma}\mathbf{U}$ after the time evolution step to the new time slice, which in turn is used in the sources of the metric equations (8.11). These are subsequently solved on the new time

slice. With the help of this reformulation of the hydrodynamic time evolution problem in the current code (in combination with the compact time-independent form for the sources in the Euler equations, Eq. (8.47)), we are able to achieve exact numerical conservation of the total rest mass and angular momentum up to machine roundoff errors, provided that there is no artificial atmosphere and no mass flow across the outer radial grid boundary.

8.A.3 Shift vector boundary conditions

The results for the evolution of the central density ρ_c and the waveform for the core collapse model SCC (A3B2G4 in [149]) presented in this paper slightly differ from those reported in the previous paper by Dimmelmeier et al. [149]. This is partly due to the improvements related to evaluating the Euler equation source terms in compact form and using exact numerical conservation in the new code, as discussed above. However, the main reason for the small discrepancy is that in the simulations in [149] a symmetric boundary condition for the shift vector component β^2 across the equatorial plane was chosen. This leads to a nonzero value for β^2 at $\theta = \pi/2$ close to and after core bounce, i.e. when meridional motions set in. As a consequence of this, the deviation is stronger for models where rotation plays a significant role in the collapse dynamics.

The physically accurate antisymmetric equatorial boundary condition for β^2 which is used in the present code, systematically yields lower post-bounce values for ρ_c in regular collapse type models compared to the simulations presented in [149], with a difference of 11% on average. For models which show multiple bounce behavior, we obtain a lower ρ_c also at core bounce.

Accordingly, the waveform amplitudes and frequencies of the gravitational radiation are altered by a small amount (-11% for $|A_{20}^{E2}|_{\max}$ and -18% for ν). Despite of these small quantitative changes, the qualitative statements related to the influence of general relativistic effects in rotational core collapse made by Dimmelmeier et al. [149] remain unaffected, even when the antisymmetric boundary condition is used. We particularly emphasize that the change in the boundary condition for β^2 plays no role when comparing our results with the fully general relativistic simulations by Shibata and Sekiguchi [423] discussed in Section 8.4.2.

We note that for all core collapse models presented in the parameter study by Dimmelmeier et al. [149], results obtained with the new boundary condition for β^2 can be found in the revised waveform catalogue [197].

Chapitre 9

Rotating star initial data for a constrained scheme in numerical relativity

Version publiée : L.-M. Lin et J. Novak, *Classical and Quantum Gravity* **23**, pp.4545-4561 (2006).

Sommaire

9.1	Introduction	293
9.2	Formulation	294
9.3	Numerical results	300
9.4	Conclusion	305
9.A	Resolution of the Poisson equations for h^{ij}	308

9.1 Introduction

In the $3 + 1$ formalism of general relativity, the Einstein equations are decomposed into a set of four constraint equations and six evolution equations [486, 55]. Solving the (elliptic-type) constraint equations at each time-step in multidimensional simulations is in general not feasible as it is computationally expensive for most numerical techniques. Hence, a free-evolution approach, i.e., solving the constraint equations only for the initial data and performing the evolutions without enforcing the constraints, is generally favoured over a fully constrained scheme (solving the constraints at each time step) in three-dimensional numerical simulations. While mathematically the constraints are preserved by the evolution equations, in practice small constraint violations due to numerical errors typically grow quickly to a significant level that make the solution unphysical and plague the simulations. Although numerous techniques to control the growth of constraint violations have been developed (e.g., [99, 296, 278, 255, 468, 202]), it is not clear yet to what extent they can control the constraint violations successfully in general.

Fully constrained-evolution scheme has been used in the past only in spherically symmetric or axisymmetric problems (e.g., [440, 117, 4, 118]). The main advantage of a fully constrained scheme is

that the constraints are fulfilled to within the discretisation errors, and the constraint-violating modes do not exist by construction. Recently, a new formulation for 3+1 numerical relativity based on a fully constrained-evolution scheme is proposed by Bonazzola *et al.* [73]. The chosen coordinate conditions (maximal slicing and Dirac gauge, see Sec. 9.2.3), together with the use of spherical components of tensor fields, reduce the ten Einstein equations to a system of five quasi-linear elliptic equations, which are solved by efficient multi-domain spectral methods, and two quasi-linear scalar wave equations [73]. The Dirac gauge is used to fix the remaining three degrees of freedom. The stability of the proposed scheme has been demonstrated for a three-dimensional pure gravitational wave spacetime [73].

In the proposed constrained scheme, the coordinates are fixed by the Dirac gauge on each hypersurface (with maximal slicing condition), including the initial one. This implies that initial data must be prepared in the same coordinate choices in order to perform dynamical evolutions. As an advantage of this gauge-fixing, stationary solutions of the Einstein equations can be computed within the same framework simply by setting the time derivative terms to zero in the equations. The aim of the present work is to construct rotating-star initial data for this new formulation of 3 + 1 numerical relativity. For this purpose, we have developed a numerical code to calculate stationary axisymmetric rotating star models based on the Dirac gauge and maximal slicing.

The purpose of this paper is to present the formulation of the problem and the tests that have been done to validate our numerical code. The numerical code can be used to provide initial rotating star models for hydrodynamics simulations in full general relativity within the new formulation. Our emphasis here is put on the comparison of the accuracy between our code and a well-established code LORENE-rotstar [67, 217, 216]. In particular, we demonstrate that our numerical code can compute rapidly rotating neutron star and strange star models to high accuracy. Unless otherwise noted, we use units such that $G = c = 1$. Latin (Greek) indices go from 1 to 3 (0 to 3).

9.2 Formulation

9.2.1 The 3 + 1 decomposition

In this section, we give a brief description of the 3+1 formulation of the Einstein equations in order to define our notations (see, e.g., [486, 55] for details). In the 3 + 1 formalism, the spacetime is foliated by a family of spacelike hypersurfaces Σ_t , labelled by the time coordinate t . Introducing a coordinate system (x^i) on each hypersurface, the line element may be written as

$$ds^2 = -N^2 dt^2 + \gamma_{ij}(dx^i + \beta^i dt)(dx^j + \beta^j dt), \quad (9.1)$$

where N is the lapse function, β^i is the shift vector, and γ_{ij} is the 3-metric induced by the spacetime metric $g_{\alpha\beta}$ onto each hypersurface Σ_t

$$\gamma_{\alpha\beta} := g_{\alpha\beta} + n_\alpha n_\beta. \quad (9.2)$$

Here $n_\alpha := -N\nabla_\alpha t$ is the unit normal to Σ_t , where ∇_α is the covariant derivative associated with the spacetime metric $g_{\alpha\beta}$. The stress-energy tensor $T^{\alpha\beta}$ is decomposed as

$$T^{\alpha\beta} = En^\alpha n^\beta + n^\alpha J^\beta + J^\alpha n^\beta + S^{\alpha\beta}, \quad (9.3)$$

where $E := T_{\alpha\beta} n^\alpha n^\beta$, $J_\alpha := -\gamma_\alpha^\mu T_{\mu\nu} n^\nu$, and $S_{\alpha\beta} := \gamma_\alpha^\mu \gamma_\beta^\nu T_{\mu\nu}$ are the energy density, momentum density, and the stress tensor, as measured by the observers of 4-velocity n^α (the so-called Eulerian observers O_e).

The evolution of the 3-metric γ_{ij} is governed by

$$\frac{\partial}{\partial t}\gamma_{ij} - \mathcal{L}_{\beta}\gamma_{ij} = -2NK_{ij}, \quad (9.4)$$

where \mathcal{L} is the Lie derivative operator and K_{ij} is the extrinsic curvature of Σ_t . The evolution equation for K_{ij} is

$$\begin{aligned} \frac{\partial}{\partial t}K_{ij} - \mathcal{L}_{\beta}K_{ij} &= -D_iD_jN + N\{R_{ij} - 2K_{ij}K^{ij} + KK_{ij} \\ &\quad + 4\pi[(S - E)\gamma_{ij} - 2S_{ij}]\}, \end{aligned} \quad (9.5)$$

where D_i is the covariant derivative associated with the 3-metric γ_{ij} , R_{ij} is the Ricci tensor associated with this 3-metric, $K := K^i_i$ is the trace of the extrinsic curvature, and $S := S^i_i$. In the 3+1 formulation, the full set of Einstein equations is equivalent to the above evolution equations, together with the Hamiltonian constraint

$$R + K^2 - K_{ij}K^{ij} = 16\pi E, \quad (9.6)$$

and the momentum constraint

$$D_jK_i^j - D_iK = 8\pi J_i, \quad (9.7)$$

where $R := R^i_i$ is the three-dimensional Ricci scalar.

9.2.2 The matter sources: uniformly rotating fluid

We assume that the matter consists of a perfect fluid with a stress-energy tensor

$$T^{\alpha\beta} = (e + P)u^\alpha u^\beta + Pg^{\alpha\beta}, \quad (9.8)$$

where u^α is the 4-velocity of the fluid; e and P are respectively the energy density and pressure, as measured by the fluid comoving observer O_f . Defining the Lorentz factor linking the two observers O_e and O_f by

$$\Gamma := -n_\alpha u^\alpha = Nu^t, \quad (9.9)$$

the energy density E in Eq. (9.3) can be written as

$$E = \Gamma^2(e + P) - P. \quad (9.10)$$

The momentum density J^i is

$$J^i = (E + P)v^i, \quad (9.11)$$

where the fluid 3-velocity v^i is related to the spatial components of the fluid 4-velocity u^i by

$$u^i = \Gamma \left(v^i - \frac{\beta^i}{N} \right). \quad (9.12)$$

Note that the Lorentz factor can be expressed as $\Gamma = (1 - v^2)^{-1/2}$, where $v := (v_i v^i)^{1/2}$ is the ‘‘physical’’ fluid speed as measured by the Eulerian observer O_e . The stress tensor S_{ij} is given by

$$S_{ij} = (E + P)v_i v_j + P\gamma_{ij}. \quad (9.13)$$

Up to this point, we have not made any assumptions on the spacetime and fluid flow. Now, we consider that the spacetime is stationary, axisymmetric, and asymptotically flat. These assumptions imply the existence of two Killing vector fields: $\vec{\zeta}$, which is timelike at spatial infinity; $\vec{\chi}$, which is spacelike everywhere and with closed orbits. Furthermore, the Killing vectors commute [107], and hence we can choose an adapted coordinate system (t, x^1, x^2, φ) , such that $\vec{\zeta} = \partial/\partial t$ and $\vec{\chi} = \partial/\partial \varphi$ are the coordinate vector fields (see also [67]). We choose the remaining two coordinates to be of spherical type (i.e., $x^1 = r$ and $x^2 = \theta$).

We also impose the so-called circularity condition on the stress-energy tensor:

$$T^\alpha_\beta \zeta^\beta = \mu \zeta^\alpha + \nu \chi^\alpha, \quad (9.14)$$

$$T^\alpha_\beta \chi^\beta = \lambda \zeta^\alpha + \sigma \chi^\alpha. \quad (9.15)$$

This condition is equivalent to the absence of meridional convective currents, and implies that the fluid 4-velocity is given by

$$\vec{u} = u^t \left(\frac{\partial}{\partial t} + \Omega \frac{\partial}{\partial \varphi} \right), \quad (9.16)$$

where $\Omega := u^\varphi/u^t$ is the fluid coordinate angular velocity, and can be interpreted as the fluid angular velocity as seen by an inertial observer at rest at infinity. A theorem of Carter [106] shows that the circularity condition implies that the line element can be written as

$$ds^2 = -N^2 dt^2 + \gamma_{\varphi\varphi} (d\varphi + \beta^\varphi dt)^2 + \gamma_{rr} dr^2 + 2\gamma_{r\theta} dr d\theta + \gamma_{\theta\theta} d\theta^2. \quad (9.17)$$

Notice that only the φ -component of the shift vector is nonzero and we have not specified the gauge choice at this point. The so-called quasi-isotropic gauge (see Sec. 9.3.3) corresponds to $\gamma_{r\theta} = 0$, $\gamma_{\theta\theta} = r^2 \gamma_{rr}$, while the Dirac gauge relates the metric components by differential equations (see Eq. (9.26)).

The equation of stationary motion follows from the projection of the conservation equation

$$\nabla_\alpha T^{\alpha\beta} = 0$$

normal to the 4-velocity u^α . In this paper, we focus on the case of uniformly rotating star (i.e., Ω is a constant). We also assume that the fluid is barotropic. In this case, the equation of stationary motion can be integrated analytically and is given by (see, e.g., [67])

$$H + \ln N - \ln \Gamma = \text{const.}, \quad (9.18)$$

where H is the log-enthalpy defined by

$$H := \int \frac{dP}{e + P}. \quad (9.19)$$

9.2.3 The metric equations

Here we summarise the full set of Einstein equations in the constrained-evolution scheme based on the Dirac gauge and maximal slicing. We refer the reader to Ref. [73] for details and derivations. First, we define a conformal metric $\tilde{\gamma}_{ij}$ by

$$\tilde{\gamma}_{ij} := \Psi^{-4} \gamma_{ij}, \quad (9.20)$$

with the conformal factor Ψ defined by

$$\Psi := \left(\frac{\det \gamma_{ij}}{\det f_{ij}} \right)^{1/12}, \quad (9.21)$$

where f_{ij} is a flat 3-metric, given by the asymptotic condition on γ_{ij} . The four constraint equations (9.6) and (9.7), together with the maximal slicing condition $K = 0$, result in two scalar equations for the lapse and conformal factor; and one vectorial elliptic equations for the shift vector.

The lapse function N is given by

$$\Delta N = \Psi^4 N \left[4\pi(E + S) + \tilde{A}_{kl} A^{kl} \right] - h^{kl} \mathcal{D}_k \mathcal{D}_l N - 2\tilde{D}_k \Phi \tilde{D}^k N, \quad (9.22)$$

where \mathcal{D}_i is the covariant derivative associated with the flat metric f_{ij} and its contravariant component is defined by $\mathcal{D}^i := f^{ij} \mathcal{D}_j$; $\Delta := f^{ij} \mathcal{D}_i \mathcal{D}_j$ is the flat-space Laplacian operator; \tilde{D}_i is the covariant derivative associated with the conformal metric $\tilde{\gamma}_{ij}$ and its contravariant component is $\tilde{D}^i := \tilde{\gamma}^{ij} \tilde{D}_j$ (with the inverse conformal metric $\tilde{\gamma}^{ij}$ defined by $\tilde{\gamma}_{ik} \tilde{\gamma}^{kj} = \delta_i^j$). The quantity Φ is defined by $\Phi := \ln \Psi$. The traceless part of the conformal extrinsic curvature A^{ij} is defined by

$$A^{ij} := \Psi^4 \left(K^{ij} - \frac{1}{3} \gamma^{ij} K \right), \quad (9.23)$$

while the tensor field \tilde{A}_{ij} is defined by

$$\tilde{A}_{ij} := \tilde{\gamma}_{ik} \tilde{\gamma}_{jl} A^{kl} = \Psi^{-4} \left(K_{ij} - \frac{1}{3} \gamma_{ij} K \right). \quad (9.24)$$

The tensor field h^{ij} on the right-hand side (RHS) of Eq. (9.22) is the deviation of the inverse conformal metric from the inverse flat metric defined by

$$h^{ij} := \tilde{\gamma}^{ij} - f^{ij}. \quad (9.25)$$

In the proposed constrained scheme, the Dirac gauge condition is given by

$$\mathcal{D}_j h^{ij} = 0. \quad (9.26)$$

Next, the conformal factor Ψ (or equivalently $Q := \Psi^2 N$) is determined from

$$\begin{aligned} \Delta Q &= -h^{kl} \mathcal{D}_k \mathcal{D}_l Q + \Psi^6 \left[N \left(4\pi S + \frac{3}{4} \tilde{A}_{kl} A^{kl} \right) \right] \\ &\quad + 2\Psi^2 \left[N \left(\frac{\tilde{R}_*}{8} + \tilde{D}_k \Phi \tilde{D}^k \Phi \right) + \tilde{D}_k \Phi \tilde{D}^k N \right], \end{aligned} \quad (9.27)$$

where the quantity \tilde{R}_* on the RHS is given by

$$\tilde{R}_* := \frac{1}{4} \tilde{\gamma}^{kl} \mathcal{D}_k h^{mn} \mathcal{D}_l \tilde{\gamma}_{mn} - \frac{1}{2} \tilde{\gamma}^{kl} \mathcal{D}_k h^{mn} \mathcal{D}_n \tilde{\gamma}_{ml}. \quad (9.28)$$

The elliptic equation for the shift vector is

$$\begin{aligned} \Delta \beta^i + \frac{1}{3} \mathcal{D}^i (\mathcal{D}_j \beta^j) &= 16\pi N \Psi^4 J^i + 2A^{ij} \mathcal{D}_j N - 12N A^{ij} \mathcal{D}_j \Phi - 2N \Delta^i_{kl} A^{kl} \\ &\quad - h^{kl} \mathcal{D}_k \mathcal{D}_l \beta^i - \frac{1}{3} h^{ik} \mathcal{D}_k \mathcal{D}_l \beta^l, \end{aligned} \quad (9.29)$$

where the tensor field Δ^k_{ij} is defined by

$$\Delta^k_{ij} := \frac{1}{2} \tilde{\gamma}^{kl} (\mathcal{D}_i \tilde{\gamma}_{lj} + \mathcal{D}_j \tilde{\gamma}_{il} - \mathcal{D}_l \tilde{\gamma}_{ij}). \quad (9.30)$$

Now we turn to the dynamical part of the Einstein equations. In the proposed constrained scheme, one solves for the tensor field h^{ij} instead of $\tilde{\gamma}^{ij}$. The evolution equation in this formulation is given by a flat-space (second-order) wave equation for h^{ij} (see Eq. (85) of Ref. [73]). As mentioned in Sec. 9.1, one advantage of using the Dirac gauge to fix the coordinates on each slice Σ_t is that stationary solutions of the Einstein equations can be computed within the same scheme, simply by setting the time-derivative terms to zeros in the equations. This is possible because of the existence of the Killing vector $\vec{\zeta} = \partial/\partial t$ as discussed in Sec. 9.2.2. This reduces the wave equation for h^{ij} to the following tensorial Poisson-like equation:

$$\begin{aligned} \Delta h^{ij} = \frac{\Psi^4}{N^2} \left\{ \mathcal{L}_\beta \mathcal{L}_\beta h^{ij} + \frac{4}{3} \mathcal{D}_k \beta^k \mathcal{L}_\beta h^{ij} + \frac{N}{\Psi^6} \mathcal{D}_k Q \left(\mathcal{D}^i h^{jk} + \mathcal{D}^j h^{ik} - \mathcal{D}^k h^{ij} \right) - 2N \mathcal{S}^{ij} \right. \\ \left. - \frac{2}{3} \mathcal{D}_k \beta^k (L\beta)^{ij} + 2(\mathcal{L}_\beta N) A^{ij} + \frac{2}{3} \left[\mathcal{L}_\beta (\mathcal{D}_k \beta^k) + \frac{2}{3} (\mathcal{D}_k \beta^k)^2 \right] h^{ij} \right. \\ \left. - \mathcal{L}_\beta (L\beta)^{ij} \right\}, \quad (9.31) \end{aligned}$$

where the notation $(L\beta)^{ij}$ stands for the conformal Killing operator associated with the flat metric acting on the shift vector β^i :

$$(L\beta)^{ij} := \mathcal{D}^i \beta^j + \mathcal{D}^j \beta^i - \frac{2}{3} \mathcal{D}_k \beta^k f^{ij}. \quad (9.32)$$

The tensor field \mathcal{S}^{ij} on the RHS of Eq. (9.31) is given by

$$\begin{aligned} \mathcal{S}^{ij} = \Psi^{-4} \left\{ N \left(\tilde{R}_*^{ij} + 8\tilde{D}^i \Phi \tilde{D}^j \Phi \right) + 4 \left(\tilde{D}^i \Phi \tilde{D}^j N + \tilde{D}^j \Phi \tilde{D}^i N \right) \right. \\ \left. - \frac{1}{3} \left[N \left(\left[\tilde{R}_* + 8\tilde{D}_k \Phi \tilde{D}^k \Phi \right] \tilde{\gamma}^{ij} \right) + 8\tilde{D}_k \Phi \tilde{D}^k N \tilde{\gamma}^{ij} \right] \right. \\ \left. + 2N \left[\tilde{\gamma}_{kl} A^{ik} A^{jl} - 4\pi \left(\Psi^4 \mathcal{S}^{ij} - \frac{1}{3} S \tilde{\gamma}^{ij} \right) \right] \right. \\ \left. - \Psi^{-6} \left[\tilde{\gamma}^{ik} \tilde{\gamma}^{jl} \mathcal{D}_k \mathcal{D}_l Q + \frac{1}{2} \left(h^{ik} \mathcal{D}_k h^{lj} + h^{kj} \mathcal{D}_k h^{il} - h^{kl} \mathcal{D}_k h^{ij} \right) \mathcal{D}_l Q \right. \right. \\ \left. \left. - \frac{1}{3} \left(\tilde{\gamma}^{kl} \mathcal{D}_k \mathcal{D}_l Q \tilde{\gamma}^{ij} \right) \right] \right\}, \quad (9.33) \end{aligned}$$

with

$$\begin{aligned} \tilde{R}_*^{ij} = \frac{1}{2} \left[h^{kl} \mathcal{D}_k \mathcal{D}_l h^{ij} - \mathcal{D}_l h^{ik} \mathcal{D}_k h^{jl} - \tilde{\gamma}_{kl} \tilde{\gamma}^{mn} \mathcal{D}_m h^{ik} \mathcal{D}_n h^{jl} \right. \\ \left. + \tilde{\gamma}_{nl} \mathcal{D}_k h^{mn} \left(\tilde{\gamma}^{ik} \mathcal{D}_m h^{jl} + \tilde{\gamma}^{jk} \mathcal{D}_m h^{il} \right) + \frac{1}{2} \tilde{\gamma}^{ik} \tilde{\gamma}^{jl} \mathcal{D}_k h^{mn} \mathcal{D}_l \tilde{\gamma}_{mn} \right]. \quad (9.34) \end{aligned}$$

Furthermore, after setting the time-derivative term of h^{ij} to zero, the conformal extrinsic curvature A^{ij} as defined in Eq. (9.23) is deduced from (see Eq. (92) of [73])

$$A^{ij} = \frac{1}{2N} \left[(L\beta)^{ij} - \mathcal{L}_\beta h^{ij} - \frac{2}{3} \mathcal{D}_k \beta^k h^{ij} \right]. \quad (9.35)$$

In summary, to calculate stationary axisymmetric uniformly rotating star models in the framework of the constrained scheme [73] based on the Dirac gauge and maximal slicing, one needs to solve for two scalar elliptic equations (9.22) and (9.27) respectively for N and Ψ , a vectorial Poisson-like equation (9.29) for β^i , and a tensorial elliptic equation (9.31) for h^{ij} , together with the first integral of motion Eq. (9.18) for the matter. The numerical procedure on how to solve this system of equations is described in Sec. 9.3.1.

9.2.4 Global quantities

We list here various global quantities relevant to axisymmetric rotating-star spacetimes. These gauge invariant quantities are useful to estimate the accuracy of our numerical code as they provide a direct comparison between our code and a different code, which uses a different gauge condition, as presented in Sec. 9.3.3.

Given a baryon current nu^α , where n is the number density in the fluid frame, the baryon mass of the star is expressed as

$$M_b = m_B \int [-n_\alpha (nu^\alpha)] dV = m_B \int \Gamma n dV, \quad (9.36)$$

where m_B is the baryon rest mass, $dV = \sqrt{\gamma} d^3x$ is the proper 3-volume element (with γ being the determinant of the 3-metric), and we have used Eq. (9.9) in the second equality. As we follow Ref. [73] to expand all tensor fields onto the spherical basis $(e_{\hat{i}}) = (\frac{\partial}{\partial r}, \frac{1}{r} \frac{\partial}{\partial \theta}, \frac{1}{r \sin \theta} \frac{\partial}{\partial \varphi})$, which is orthonormal with respect to the flat metric, the proper volume element is written explicitly as $dV = \sqrt{\hat{\gamma}} r^2 \sin \theta dr d\theta d\varphi$. Notice that we denote by $\hat{\gamma}$ the determinant of the 3-metric expanded onto the basis $(e_{\hat{i}})$. Here and afterward we denote by $(\hat{r}, \hat{\theta}, \hat{\varphi})$ indices of specific components on the orthonormal basis $(e_{\hat{i}})$.

The gravitational mass M_g is given by the Komar integral (see Eq. (11.2.10) of [479])

$$M_g = 2 \int \left(T_{\alpha\beta} - \frac{1}{2} T^\lambda{}_\lambda g_{\alpha\beta} \right) n^\alpha \zeta^\beta dV, \quad (9.37)$$

where ζ^α is the timelike Killing vector discussed in Sec. 9.2.2. Explicitly, we have

$$M_g = \int \left[N(E + S) - 2J_{\hat{\varphi}} \beta^{\hat{\varphi}} \right] dV, \quad (9.38)$$

The total angular momentum J is given by (see Problem 6 of [479])

$$J = - \int T_{\alpha\beta} n^\alpha \chi^\beta dV = \int J_{\hat{\varphi}} r \sin \theta dV, \quad (9.39)$$

where χ^α is the axial Killing vector of the spacetime. The rotational kinetic energy for a uniformly rotating star is $T = \frac{1}{2} \Omega J$. The gravitational potential energy is

$$W = M_p + T - M_g, \quad (9.40)$$

where M_p is the proper mass of the star defined by

$$M_p = \int [-n_\alpha (eu^\alpha)] dV = \int \Gamma e dV. \quad (9.41)$$

Note that W is defined to be positive.

Furthermore, two relativistic virial identities (the so-called GRV2 and GRV3) have been proved to be useful for checking the consistency and accuracy of numerical solutions of rotating relativistic star models. The three-dimensional virial identity GRV3 [220] is a relativistic generalisation of the Newtonian virial identity, valid for any stationary and asymptotically flat spacetime. The two-dimensional virial identity GRV2 [76] is valid for any asymptotically flat spacetime (without any symmetry assumption). The two virial identities are integral relations between the matter and metric fields (see [220, 76] for expressions). In practice, we define the quantities $GRV2 := |1 - \lambda_2|$ and $GRV3 := |1 - \lambda_3|$ as the error indicators for the virial identities, where λ_2 and λ_3 are defined via the integral relations, such that exact solutions of the Einstein equations satisfy $GRV2 = GRV3 = 0$ (see [344]). Note that these identities are not imposed during the numerical calculation, and hence are useful indicators for checking the accuracy of numerical results.

9.3 Numerical results

9.3.1 Numerical procedure

To calculate stationary axisymmetric rotating stars within the Dirac gauge and maximal slicing, we solve the nonlinear elliptic equations described in Sec. 9.2.3 iteratively by means of multi-domain spectral methods [69, 72] in spherical coordinates. The code is constructed upon the LORENE C++ library [216]. We use three spherical numerical domains to cover the whole hypersurface Σ_t . Specifically, we use one domain to cover the whole star and one domain for the space around the star (typically to about twice the stellar radius). The last domain covers the space out to spatial infinity by means of a compactification $u = 1/r$ [67].

In each domain, we use N_θ collocation points in the polar direction and $N_\varphi = 1$ point in the azimuthal direction for the spectral method. For the radial direction, we can choose to have different numbers of collocation points in different domains. In Sec. 9.3.3, we use the notation $N_r = (N_{r1}, N_{r2}, N_{r3})$, where N_{r1} denotes the number of points in the first domain etc, to specify the grid structure in the radial direction.

The numerical iteration procedure is briefly described here. For a given equation of state, we choose Ω and the central value of the log-enthalpy H (see Eq. (9.19)) as the physical parameters that specify the rotating star model. First we start with an initial guess by setting all the metric quantities to their flat spacetime values, together with a spherically symmetric distribution for the matter sources. The iteration procedure begins by solving Eqs. (9.22) and (9.29) respectively for the corresponding lapse and shift. Thus, we obtain the only nonzero component of the 3-velocity $v^{\hat{\varphi}} = (\Omega r \sin \theta + \beta^{\hat{\varphi}})/N$ (see Eq. (9.12)), and hence the Lorentz factor Γ . Next we use the first integral of motion (Eq. (9.18)) to obtain H , from which we deduce the pressure P and the energy density e through the EOS. Finally, we solve Eqs. (9.27) and (9.31) respectively for Q and h^{ij} . The iteration procedure continues until the relative difference in H throughout the whole star between two consecutive steps is smaller than some prescribed value.

The resolutions of the scalar Poisson equations for N and Q , and the vectorial elliptic equation for β^i have been described in details in [228]. The technique for solving the tensorial Poisson equation (9.31) is described in 9.A.

9.3.2 Equation of state

In Sec. 9.3.3, we present various tests that have been done to validate our numerical code. For this purpose, we use a polytropic EOS in the following form to construct rotating neutron star models:

$$P = \kappa n^\gamma, \quad (9.42)$$

where κ and γ are constants. The number density n is related to the energy density e by

$$e = m_B n + \frac{\kappa}{\gamma - 1} n^\gamma, \quad (9.43)$$

where the baryon mass $m_B = 1.66 \times 10^{-24}$ g. In particular, we take $\gamma = 2$ and $\kappa = 0.03 \rho_{\text{nuc}} c^2 / n_{\text{nuc}}^2$, where $\rho_{\text{nuc}} = 1.66 \times 10^{14}$ g cm $^{-3}$ and $n_{\text{nuc}} = 0.1$ fm $^{-3}$. For this EOS, the log-enthalpy is given analytically by

$$H = \ln \left[1 + \frac{\kappa \gamma}{m_B (\gamma - 1)} n^{\gamma-1} \right]. \quad (9.44)$$

We also use the simplest MIT bag model EOS, with noninteracting massless quarks, to construct rapidly rotating strange stars. The EOS is given in the following form (see, e.g., [217])

$$\begin{aligned} P &= \frac{1}{3} a n^{4/3} - B, \\ e &= a n^{4/3} + B, \end{aligned} \quad (9.45)$$

where B is the MIT bag constant and the parameter $a = 9\pi^{2/3} \hbar c / 4 = 952.371$ MeV fm. We choose $B = 60$ MeV fm $^{-3}$ in this work. The stellar surface is characterised by the properties of strange matter at zero pressure: the number density $n_0 = 0.28665$ fm $^{-3}$ and the mass density $\rho_0 = 4.2785 \times 10^{14}$ g cm $^{-3}$. The log-enthalpy is related to n simply by $H = \ln(n/n_0)^{1/3}$. The MIT bag model EOS is useful to test our numerical code in the highly relativistic regime, since strange stars can reach higher compactness ratios and rotation rates than ordinary neutron stars.

9.3.3 Tests of the numerical code

To test our numerical code, we start with a non-rotating star modelled by the polytropic EOS described in Sec. 9.3.2. The central value of the log-enthalpy is $H_0 = 0.2308$ (or equivalently the energy density $e_0 = 4.889 \rho_{\text{nuc}} c^2$) and the baryon mass of the star is $M_b = 1.6 M_\odot$. The star has a gravitational mass $M_g = 1.4866 M_\odot$ and a compactness ratio $M_g/R = 0.147$, where R is the circumferential radius. In the numerical calculations, we use a parameter ϵ_H (typically set to be 10^{-10} or smaller) to control the iteration procedure and the precision of the numerical models: the iteration (see Sec. 9.3.1) is stopped if the relative difference in H throughout the whole star between two consecutive steps is smaller than ϵ_H . In Fig. 9.1, we show the convergence of the relative difference in H towards zero with the number of iterations using radial collocation points $N_r = (33, 33, 17)$. We see that a precision of 10^{-15} is achieved for the numerical result within 40 iteration steps. After that, the accuracy is limited by the round-off errors. The solution also satisfies the virial identities to the level of 10^{-15} .

Next, we test the convergence property of the numerical code with respect to increasing number of radial collocation points using the same model. In particular, we vary the number of points in the first numerical domain (i.e., inside the star), while keeping the points in the other two domains fixed

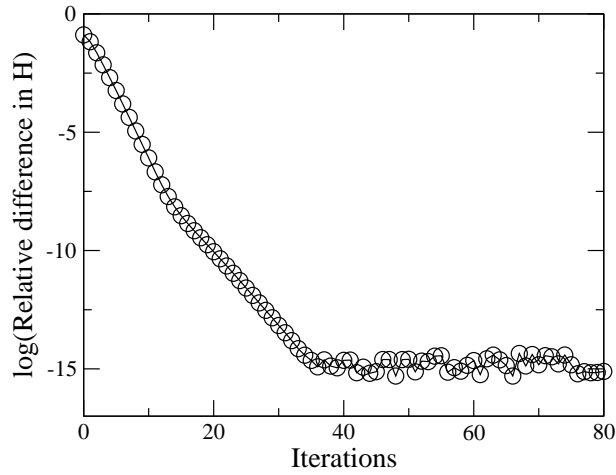


Figure 9.1: Convergence towards zero of the relative difference in H throughout the star between two consecutive steps for a non-rotating polytropic star model (see text).

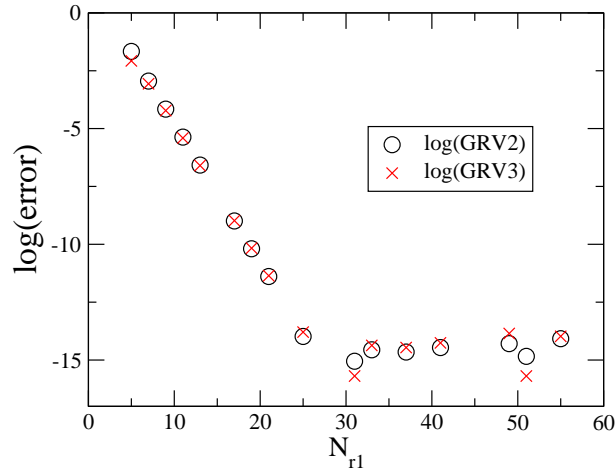


Figure 9.2: Convergence towards zero of $GRV2$ and $GRV3$ with the number of collocation points N_{r1} inside the star for the same model as shown in Fig. 9.1.

to $N_{r2} = 33$ and $N_{r3} = 17$, and we choose $\epsilon_H = 10^{-15}$ in this test. In Fig. 9.2, we plot $\log(GRV2)$ and $\log(GRV3)$ together against the number of points N_{r1} in the first domain. It is seen clearly that both $GRV2$ and $GRV3$ converge exponentially towards zero with the number of points, as expected for spectral methods. The accuracy is limited by the round-off errors for $N_{r1} > 30$.

Starting from the above non-rotating polytropic model, we then construct a sequence of increasing uniformly rotating configurations at fixed baryon mass $M_b = 1.6M_\odot$, up to the mass-shedding limit. The accuracy of the numerical models are estimated by comparing the results to those obtained by a separated code LORENE-rotstar [67, 217], which uses the so-called quasi-isotropic gauge to construct rotating relativistic stars. LORENE-rotstar is a well-established code which has been tested extensively and compared with a few different numerical codes [344]. A comparison of some of the gauge invariant quantities for the sequence between our code and LORENE-rotstar is given in Table 9.1.

Table 9.1: Comparison between our numerical code based on the Dirac gauge (first row for each given frequency) and a well-established code LORENE-rotstar (second row), which uses a quasi-isotropic gauge for the coordinates, for a sequence of $\gamma = 2$ polytropic neutron star models with fixed baryon mass $M_b = 1.6M_\odot$. Listed are the rotation frequency f , gravitational mass M_g , total angular momentum parameter J/M_g^2 , ratio of the rotational kinetic energy to the potential energy T/W , equatorial circumferential radius R_{eq} , and errors indicators in the virial identities $GRV2$ and $GRV3$.

f (Hz)	$M_g(M_\odot)$	J/M_g^2	T/W	R_{eq} (km)	$GRV2$	$GRV3$
0	1.486610961	0	0	14.91222928	7e-9	2e-9
	1.486610965	0	0	14.91222929	9e-9	1e-9
100	1.486837016	0.066036124	0.00107222950	14.9609161	3e-9	3e-8
	1.486837013	0.066036126	0.00107222954	14.9609165	3e-8	5e-8
200	1.487539907	0.13421663	0.004395974	15.113935	2e-7	5e-7
	1.487539902	0.13421665	0.004395975	15.113937	3e-7	7e-7
300	1.4888008	0.2072617	0.010340091	15.395905	3e-7	6e-7
	1.4888007	0.2072618	0.010340095	15.395908	2e-8	6e-7
400	1.49080352	0.289551	0.01973704	15.865576	1e-6	3e-6
	1.49080359	0.289550	0.01973701	15.865574	7e-7	4e-6
500	1.493991	0.390430	0.0345952	16.67896	4e-6	8e-6
	1.493990	0.390432	0.0345954	16.67900	6e-6	1e-5
550	1.4964095	0.455303	0.0457202	17.35894	2e-5	2e-5
	1.4964092	0.455307	0.0457206	17.35898	1e-5	2e-5
600	1.500054	0.54397	0.062368	18.5382	5e-6	2e-6
	1.500055	0.54398	0.062369	18.5383	3e-6	3e-6
640 $\approx f_k$	1.506928	0.695855	0.0929183	22.1467	2e-5	5e-5
	1.506929	0.695857	0.0929188	22.1469	1e-5	6e-5

The parameters used to obtain the numerical results are $N_r = (33, 17, 17)$, $N_\theta = 17$, and $\epsilon_H = 10^{-10}$ for both codes. In the table, for each value of the rotation frequency f , we display the results obtained from our numerical code based on the Dirac gauge in the first row. Below this are the results obtained from LORENE-rotstar. Table 9.1 shows that the two sets of results agree to high accuracy. In particular, the overall discrepancy between the two different codes is consistent with the errors in the virial identities, which increase with the rotation frequency. Note that the errors in the virial identities for the non-rotating configuration listed in the table is about 10^{-9} instead of 10^{-15} as shown in Fig. 9.2. This is due to our choice of using $\epsilon_H = 10^{-10}$ in this test.

We note, however, that the numerical error no longer decreases exponentially with the number of grid points as in the non-rotating case, but as a power-law (see Fig. 9.3), due to the discontinuities in the derivative of the matter fields at the stellar surface. The non-rotating model is free from any such phenomenon because the stellar surface is at the boundary between two spherical numerical domains.

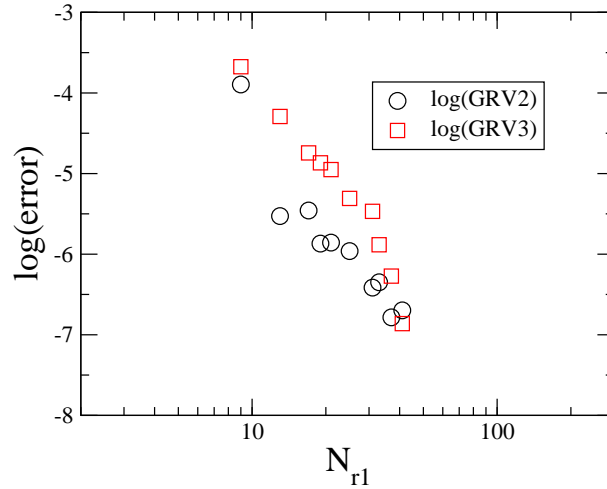


Figure 9.3: Convergence behaviours of *GRV2* and *GRV3* for the $f = 400$ Hz rotating star model listed in Table 9.1. Note that the plot is in log-log scale. The best-fit to the data points shows that *GRV2* (*GRV3*) decreases as $N_{r1}^{-4.3}$ ($N_{r1}^{-3.9}$).

For rotating models, because of the flattening of the stars, the stellar surface no longer coincides with the boundary of the domains, and hence the spectral method loses its exponential-convergence property. Such difficulty associated with rotating stars can be handled by the adaptation of the numerical domains to the stellar surface as developed in [69]. We plan to improve our numerical code by implementing this surface-adaptation technique in the near future¹. Nevertheless, even without a surface-adaptation technique, Table 9.1 shows that both numerical codes still agree to high accuracy and achieve a precision of 10^{-5} for a configuration rotating near the mass-shedding limit (i.e., the $f = 640 \approx f_k$ Hz configuration in Table 9.1, where f_k is the Kepler frequency). To visualise the gravitational field generated by a rotating star, we plot in Figs. 9.4-9.7 the non-vanishing components for the metric field h^{ij} (namely, $h^{\hat{r}\hat{r}}$, $h^{\hat{r}\hat{\theta}}$, $h^{\hat{\theta}\hat{\theta}}$, and $h^{\hat{\varphi}\hat{\varphi}}$) for the rotating star model with $f = 640$ Hz. In these figures, we show the iso-contours of the fields in the meridional plane, where solid (dashed) lines indicate positive (negative) values of the fields. The thick solid lines represent the stellar surface. Finally, the dot-dashed circles represent the boundary between the first two spherical numerical domains. The figures show clearly that the gravitational field is dominated by the quadrupole moment.

To further calibrate our numerical code against LORENE-rotstar, we now compare the two codes using a very relativistic and rapidly rotating strange star model. The matter is described by the MIT bag model as described in Sec. 9.3.2. This configuration, shown in Fig. 9.8, has a baryon mass $M_b = 2.2M_\odot$ and compactness ratio $M_g/R_{eq} = 0.204$ (with the gravitational mass $M_g = 1.719M_\odot$ and the circumferential equatorial radius $R_{eq} = 12.425$ km). The rotation frequency is $f = 1000$ Hz. In Table 9.2, we show the values of various physical quantities obtained from both numerical codes, together with the relative difference between them. As in the case of the polytropic EOS model, the discrepancy of the two numerical codes is consistent with the errors in *GRV2* and *GRV3*. Note also that, even with a strong density discontinuity at the strange star surface, our numerical model still

¹Such numerical technique is already available in LORENE-rotstar as described in [217]. However, in order to compare to our numerical code, the results obtained from LORENE-rotstar as listed in Table 9.1 are based on fixed spherical numerical domains.

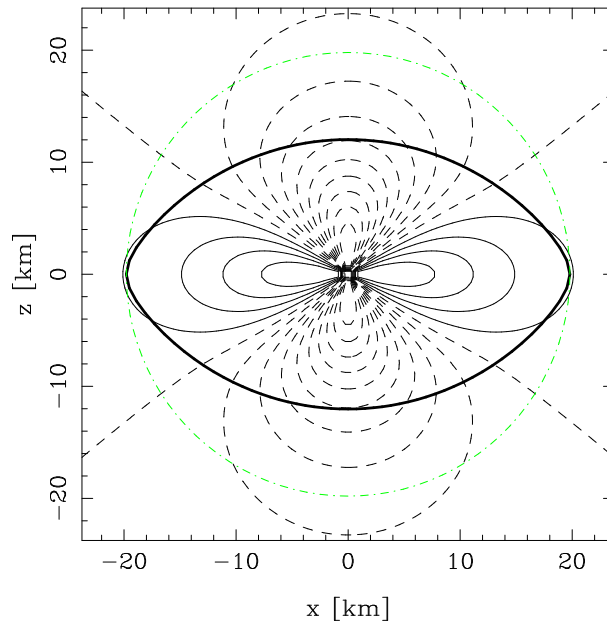


Figure 9.4: Iso-contours of the metric component $h^{\hat{r}\hat{r}}$ in the meridional plane for the $f = 640$ Hz rotating polytropic model given in Table 9.1. The solid (dashed) lines indicate positive (negative) values of the field. The thick solid line represents the stellar surface. The dot-dashed circle is the boundary between the first two spherical numerical domains.

achieves a precision of 10^{-3} .

9.4 Conclusion

In this paper we have developed a computer code (LORENE-rotstar_dirac) to construct relativistic rotating stars within the framework of a new constrained-evolution formulation of the $3 + 1$ Einstein equations based on the Dirac gauge and maximal slicing [73]. As the Dirac gauge fixes the spatial coordinates on each time slices, including the initial one, this formulation can be used to compute stationary solutions of the Einstein equations simply by setting the time derivative terms in various equations to zeros. The system reduces to two scalar elliptic equations for the lapse function N and conformal factor Ψ (equivalently for $Q := \Psi^2 N$), a vectorial elliptic equation for the shift vector β^i , and a tensorial elliptic equation for a tensor field h^{ij} . We couple this system of equations to the first integral of motion for the matter, and solve the equations iteratively using multi-domain spectral method.

We have demonstrated that this formulation can be used to compute stationary rotating equilibrium configurations to high accuracy. In particular, we used the polytropic EOS and MIT bag model to calculate rotating neutron star and strange star models respectively. We compared our code to a well-established code LORENE-rotstar, which uses a quasi-isotropic gauge to fix the coordinates, and found that the global quantities of the numerical models obtained from the two codes agree to high accuracy. The discrepancy between the two codes is consistent to the errors in the virial identities.

Finally, we remark that the proposed constrained-evolution scheme [73] is particular well suited to

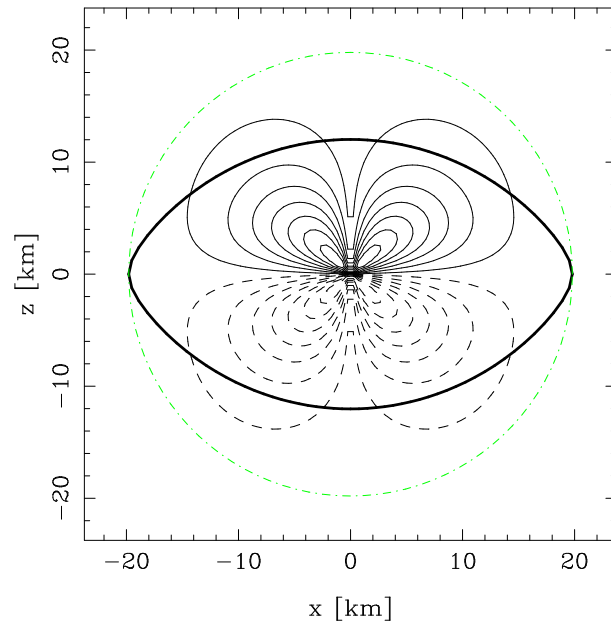


Figure 9.5: Same as Fig. 9.4 but for the component $h^{\hat{r}\hat{\theta}}$.

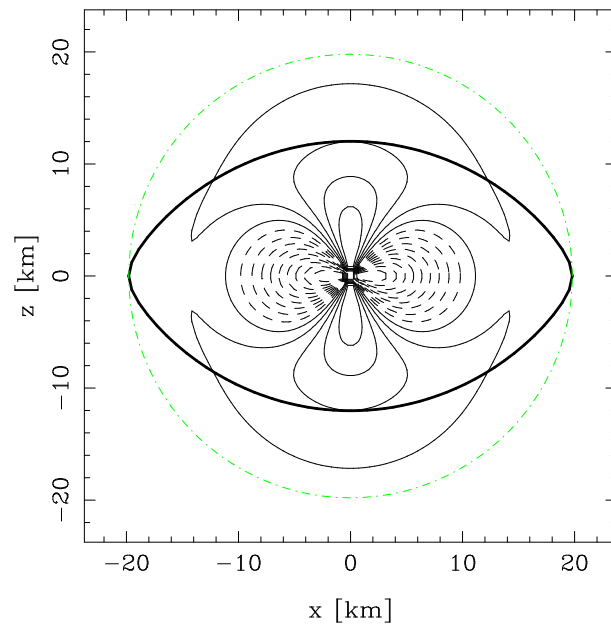


Figure 9.6: Same as Fig. 9.4 but for the component $h^{\hat{\theta}\hat{\theta}}$.

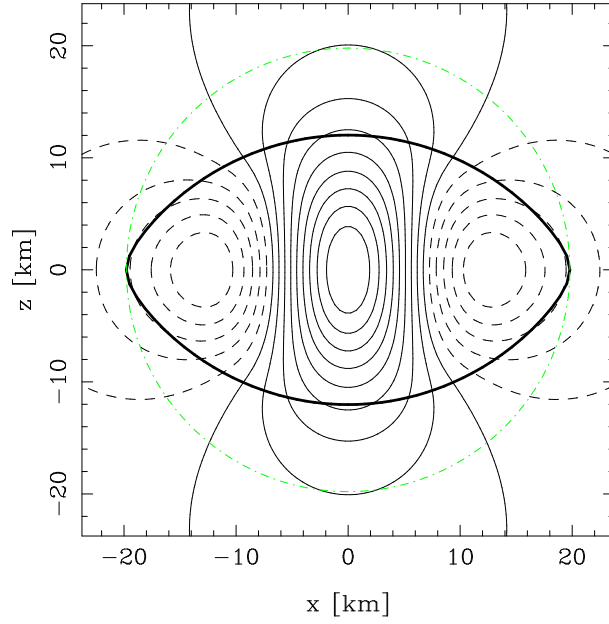


Figure 9.7: Same as Fig. 9.7 but for the component $h^{\hat{\phi}\hat{\phi}}$.

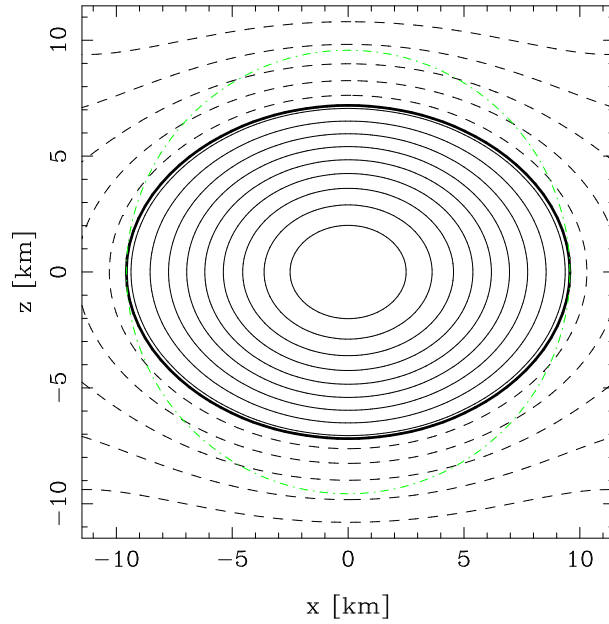


Figure 9.8: Meridional plane cross section of a rapidly rotating strange star. The star has a baryon mass $M_b = 2.3M_\odot$, gravitational mass $M_g = 1.787M_\odot$, and rotation frequency $f = 1000$ Hz. The lines are iso-contours of the log-enthalpy H . The thick solid line represents the stellar surface. Outside the star, H is defined by the first integral of motion Eq. (9.18).

Table 9.2: Comparison between our numerical code (LORENE-rotstar_dirac) and LORENE-rotstar for a rapidly rotating strange star model. The star has a baryon mass $M_b = 2.2M_\odot$, gravitational mass $M_g = 1.719M_\odot$, and rotation frequency $f = 1000$ Hz.

	rotstar_dirac	rotstar	rel. diff.
$M_g(M_\odot)$	1.7194	1.7198	2e-4
J/M_g^2	0.5940	0.5945	8e-4
T/W	0.0888	0.0890	2e-3
R_{eq} (km)	12.425	12.433	7e-4
$GRV2$	7e-4	2e-4	
$GRV3$	1e-3	6e-4	

the conformally-flat relativistic hydrodynamics code, with a metric solver based on spectral methods and spherical coordinates, developed by Dimmelmeyer *et al.* in the so-called *Marriage des Maillages* (MDM) project [151]. The numerical code that we described in this paper can be used to generate rotating-star initial data for hydrodynamics simulations in full general relativity within the new constrained-evolution scheme [73] for the MDM project.

APPENDIX

9.A Resolution of the Poisson equations for h^{ij}

Here we describe the numerical strategy used to solve the tensorial Poisson equation (9.31), imposing that the solution h^{ij} satisfies the gauge condition (9.26) and be such that the conformal metric has a unitary determinant:

$$\det(\tilde{\gamma}^{\hat{i}\hat{j}} = f^{\hat{i}\hat{j}} + h^{\hat{i}\hat{j}}) = 1. \quad (9.46)$$

Note that this relation follows directly from the definition of the conformal factor in the proposed constrained scheme (see Eqs. (9.20) and (9.21)), together with the condition $\det f_{\hat{i}\hat{j}} = 1$ in the orthonormal basis ($e_{\hat{i}}$) (see Sec. 9.2.4). In Ref. [73], one would solve two (scalar) Poisson equations: for $h^{\hat{r}\hat{r}}$ and the potential μ (see Eq. (9.53)); the other four components are deduced from the three gauge conditions and the non-linear relation (9.46) through an iteration. The drawback of this method is that some components of h^{ij} are calculated as second radial derivatives of $h^{\hat{r}\hat{r}}$ and μ . Since the source of Eq. (9.31) contains second-order radial derivatives of h^{ij} , one needs to calculate fourth-order radial derivatives of $h^{\hat{r}\hat{r}}$ and μ , which are solutions of scalar-like Poisson equations with matter terms on the RHS. In the case of neutron stars, it is quite often that radial density profiles have a discontinuous derivative at the surface of the star. Therefore, $h^{\hat{r}\hat{r}}$ and μ admit discontinuous third-order radial derivatives and their fourth-order derivatives cannot be represented at all by means of spectral methods. A solution could be to use adaptive mapping: the boundary between two spectral domains coincides with the (non-spherical) surface of the star (see [69]). Still, the evaluation of a fourth-order

radial derivative introduces too much numerical noise, even using spectral methods. We have therefore chosen to use a different approach, detailed hereafter.

Instead of using directly all the spherical components of the tensor h^{ij} , we use only the $\hat{r}\hat{r}$ -component, the trace $h = f_{ij}h^{ij}$ and the four potentials η , μ , W and X defined as follow, in the orthonormal basis (e_i):

$$h^{\hat{r}\hat{\theta}} = \frac{1}{r} \left(\frac{\partial \eta}{\partial \theta} - \frac{1}{\sin \theta} \frac{\partial \mu}{\partial \varphi} \right), \quad (9.47)$$

$$h^{\hat{r}\hat{\varphi}} = \frac{1}{r} \left(\frac{1}{\sin \theta} \frac{\partial \eta}{\partial \varphi} + \frac{\partial \mu}{\partial \theta} \right), \quad (9.48)$$

and

$$P = \frac{\partial^2 W}{\partial \theta^2} - \frac{1}{\tan \theta} \frac{\partial W}{\partial \theta} - \frac{1}{\sin^2 \theta} \frac{\partial^2 W}{\partial \varphi^2} - 2 \frac{\partial}{\partial \theta} \left(\frac{1}{\sin \theta} \frac{\partial X}{\partial \varphi} \right), \quad (9.49)$$

$$h^{\hat{\theta}\hat{\varphi}} = \frac{\partial^2 X}{\partial \theta^2} - \frac{1}{\tan \theta} \frac{\partial X}{\partial \theta} - \frac{1}{\sin^2 \theta} \frac{\partial^2 X}{\partial \varphi^2} + 2 \frac{\partial}{\partial \theta} \left(\frac{1}{\sin \theta} \frac{\partial W}{\partial \varphi} \right); \quad (9.50)$$

with $P = (h^{\hat{\theta}\hat{\theta}} - h^{\hat{\varphi}\hat{\varphi}})/2$. These equations can be inverted to compute the potentials in terms of the angular part of the Laplace operator

$$\Delta_{\theta\varphi} = \frac{\partial^2}{\partial \theta^2} + \frac{1}{\tan \theta} \frac{\partial}{\partial \theta} + \frac{1}{\sin^2 \theta} \frac{\partial^2}{\partial \varphi^2}, \quad (9.51)$$

giving

$$\Delta_{\theta\varphi} \eta = r \left(\frac{\partial h^{\hat{r}\hat{\theta}}}{\partial \theta} + \frac{h^{\hat{r}\hat{\theta}}}{\tan \theta} + \frac{1}{\sin \theta} \frac{\partial h^{\hat{r}\hat{\varphi}}}{\partial \varphi} \right), \quad (9.52)$$

$$\Delta_{\theta\varphi} \mu = r \left(\frac{\partial h^{\hat{r}\hat{\varphi}}}{\partial \theta} + \frac{h^{\hat{r}\hat{\varphi}}}{\tan \theta} - \frac{1}{\sin \theta} \frac{\partial h^{\hat{r}\hat{\theta}}}{\partial \varphi} \right), \quad (9.53)$$

$$\begin{aligned} \Delta_{\theta\varphi} (\Delta_{\theta\varphi} + 2) W &= \frac{\partial^2 P}{\partial \theta^2} + \frac{3}{\tan \theta} \frac{\partial P}{\partial \theta} - \frac{1}{\sin^2 \theta} \frac{\partial^2 P}{\partial \varphi^2} - 2P \\ &\quad + \frac{2}{\sin \theta} \frac{\partial}{\partial \varphi} \left(\frac{\partial h^{\hat{\theta}\hat{\varphi}}}{\partial \theta} + \frac{h^{\hat{\theta}\hat{\varphi}}}{\tan \theta} \right), \end{aligned} \quad (9.54)$$

$$\begin{aligned} \Delta_{\theta\varphi} (\Delta_{\theta\varphi} + 2) X &= \frac{\partial^2 h^{\hat{\theta}\hat{\varphi}}}{\partial \theta^2} + \frac{3}{\tan \theta} \frac{\partial h^{\hat{\theta}\hat{\varphi}}}{\partial \theta} - \frac{1}{\sin^2 \theta} \frac{\partial^2 h^{\hat{\theta}\hat{\varphi}}}{\partial \varphi^2} - 2h^{\hat{\theta}\hat{\varphi}} \\ &\quad - \frac{2}{\sin \theta} \frac{\partial}{\partial \varphi} \left(\frac{\partial P}{\partial \theta} + \frac{P}{\tan \theta} \right). \end{aligned} \quad (9.55)$$

These quantities η, μ, W, X are interesting for, at least, two reasons: first they can be expanded onto a basis of scalar spherical harmonics $Y_\ell^m(\theta, \varphi)$, which are often used in the framework of spectral methods, for they are eigenfunctions of the angular Laplace operator (9.51). Furthermore, the three

gauge conditions (9.26) can be reformulated in terms of these potentials:

$$\frac{\partial h^{\hat{r}\hat{r}}}{\partial r} + \frac{3h^{\hat{r}\hat{r}}}{r} + \frac{1}{r^2} \Delta_{\theta\varphi} \eta - \frac{h}{r} = 0, \quad (9.56)$$

$$\frac{\partial \eta}{\partial r} + \frac{2\eta}{r} + (\Delta_{\theta\varphi} + 2) W + \frac{1}{2} (h - h^{\hat{r}\hat{r}}) = 0, \quad (9.57)$$

$$\frac{\partial \mu}{\partial r} + \frac{2\mu}{r} + (\Delta_{\theta\varphi} + 2) X = 0. \quad (9.58)$$

When decomposing the fields on a basis of spherical harmonics, these relations reduce to a system of ordinary differential equations with respect to r , which is solved by spectral methods in a similar way to the Poisson equation [228].

The numerical algorithm is then:

1. transform the source term of Eq. (9.31) to the Cartesian basis,
2. solve the resulting six decoupled scalar Poisson equations for h^{ij} ,
3. transform h^{ij} back to the spherical basis and compute the potentials W and X ,
4. do an iteration on h , first solving the system (9.56)-(9.58) with h, W and X as sources and then calculating the new value of h from the non-linear equation (9.46).

Since the system is overdetermined (four additional relations to satisfy), the integrability condition is that the source of the tensor Poisson equation (9.31) be divergence-free. We do not impose this condition during the main iteration of the code, since this is not true for intermediate solutions of the metric and matter fields. We only check that this is satisfied, up to the accuracy of the code, at the end of the iteration, and we have found that this was true at the error level given by the virial identities (see Sec. 9.2.4). The potentials W and X have been chosen among the six degrees of freedom of h^{ij} because none of their radial derivatives appear in the gauge conditions (9.56)-(9.58), hence, we do not calculate any radial derivative of these quantities to get the other components of h^{ij} . Another reason for this choice is that, when considering a more general case of dynamically evolving spacetime, these two potentials are asymptotically related to the two gravitational wave polarisation modes: $P \rightarrow h_+$ and $h^{\theta\varphi} \rightarrow h_\times$ in our asymptotically transverse-traceless gauge¹. Note that in our case of stationary and axisymmetric spacetime, we have $\mu = X = 0$, which simplifies the resolution.

¹The condition (9.46) implies that $h = 0$ to the linear order

Chapitre 10

Relativistic numerical models for stationary superfluid neutron stars

*Version publiée : R. Prix, J. Novak et G. L. Comer, Phys. Rev. D **71**, 043005 (2005).*

Sommaire

10.1 Introduction	311
10.2 Canonical Two–Fluid Hydrodynamics	313
10.3 Stationary axisymmetric configurations	316
10.4 Numerical procedure	320
10.5 Tests of the numerical code	323
10.6 Numerical Results	328
10.7 Conclusions	332
10.A The Newtonian analytic slow-rotation solution	334

10.1 Introduction

The aim of this work is to calculate fully relativistic stationary models of superfluid neutrons stars including all non-dissipative couplings between the two fluids induced by the equation of state (EOS), in particular the entrainment effect. In addition to studying the stationary properties of relativistic superfluid neutron stars, these models can serve as the unperturbed initial state in a dynamical study of neutron star oscillations, neutron star collapse to a black hole, or as a starting point in studying pulsar glitch-models.

Neutron stars are fascinating astrophysical objects: on one hand they represent a formidable “laboratory” of fundamental physics, as the composition and equation of state of their inner core still lies beyond the reach of experimental and theoretical physics. On the other hand, the advent of increasingly sensitive gravitational wave detectors promises to open a new observational window on neutron stars, which will allow us to gain new insights into these still rather poorly understood objects. Gravitational wave astronomy could represent the first opportunity to observe neutron star oscillations, providing a new view on their inner dynamics. Considering the success of classical terrestrial seismol-

ogy and astero-seismology of the sun and of main-sequence stars, one could expect this to result in substantial progress in our understanding of the dynamics and composition of neutron stars.

Additionally, observing quasi-permanent quadrupolar deformations (“mountains”) on neutron stars via gravitational waves¹ will give valuable complementary information about their rotational behavior, which is currently only observable via their electromagnetic pulses.

Most theoretical studies of neutron star dynamics have relied on rather simplistic single-fluid models. In this work we attempt a more realistic description of neutron stars by taking their superfluidity into account via the use of a two-fluid model. Neutrons and protons in neutron stars are predicted to be superfluid (e.g. see [45, 433]), and this feature forms a fundamental ingredient in the current (albeit rudimentary) understanding of the glitch phenomenon observed in pulsars (e.g. see [301, 111, 20]). Due to the superfluidity and therefore lack of viscosity of the neutrons in the crust and in the outer core, they can flow freely through the other components. The remaining constituents (i.e. crust-nuclei, electrons, muons and protons) are assumed to be “locked” together on short timescales by viscosity and the magnetic field. Thereby they form another fluid, which in the following will be referred to as “protons” for simplicity. These assumptions characterize the so-called two-fluid model of neutron stars. These two fluids are strongly coupled by the strong nuclear force acting between protons and neutrons, and therefore a hydrodynamic two-fluid framework incorporating these couplings is required for their description. This framework will be presented in the next section. Recently it was pointed out that such a two-fluid system can be subject to a two-stream instability if the relative velocity of the two fluids is above a critical velocity [21]. This could therefore be relevant in neutron stars and might be related to the glitch phenomenon [20], which provides another motivation for studying the properties of such two-fluid systems.

In this paper we study the stationary structure of such two-fluid models, in which the two fluids are restricted to uniform rotation around a common axis, but allowing for two different rotation rates. This neutron star model was first studied quantitatively by [376] in the Newtonian context using a generalized Chandrasekhar-Milne slow-rotation approximation, and neglecting the direct interactions between the two fluids. [22] used Hartle’s variant of the slow-rotation approximation to study this model in general relativity. [377] further extended the Newtonian study to fully include all (non-dissipative) couplings via entrainment and the nuclear “symmetry-energy”, and they found an analytic solution for a subclass of two-fluid equations of state (which generalizes the $P \propto \rho^2$ -type polytropes). More recently, [488] have devised an alternative approach in the Newtonian case, by treating only the relative rotation between the two fluids as small, while allowing for fast rotation of the neutron star as a whole. Furthermore, [124] has recently used the relativistic slow-rotation approximation to study the properties of the first available fully relativistic two-fluid EOS incorporating entrainment, which was derived by [125].

Here we present a generally relativistic numerical code for solving the full two-fluid model without approximations. A preliminary progress-report on the development of this code, and some early results were presented in [378].

While our model and code allow in principle for any given two-fluid equation of state (EOS), for the sake of simplicity and a better numerical convergence we restrict ourselves in this paper to the use of a (rather general) class of two-fluid “polytropes”. This choice is also motivated by the lack of a useful two-fluid neutron star equation of state in the literature, especially concerning the aspect of entrainment. Even though [125] have a fully relativistic model that includes entrainment, it has not yet been developed to the point that it will produce a tabular equation of state that could be used in

¹Note that this search has already begun, see [1] for a discussion and first results

our code. We expect the qualitative features of our model to be well represented by the analytic EOS used in this work.

The plan of this paper is as follows: In section 10.2 we introduce the formalism and notation of covariant two-fluid hydrodynamics. In section 10.3 we discuss the specialization to an axisymmetric and stationary system, and we introduce the 3 + 1 framework for Einstein’s equations. In section 10.4 we describe the numerical procedure for solving the resulting elliptical system of equations. The tests performed on the numerical code are discussed in section 10.5, and our numerical results are presented in section 10.6. A discussion of this work is given in section 10.7. In appendix 10.A we derive a new analytic Newtonian slow-rotation solution, which is used for extensive comparisons of our numerical results.

10.2 Canonical Two–Fluid Hydrodynamics

The general relativistic framework for describing a coupled two-fluid system has been developed by Carter, Langlois and coworkers [110, 126, 112, 287], based on an elegant variational principle. The same relativistic two-fluid model was used by [22] in their slow-rotation description of superfluid neutron stars.

We consider a system consisting of two fluids, namely neutrons and “protons”, which we label by n and p respectively. The kinematics of the two fluids is described by the two conserved particle 4-currents n_n^α and n_p^α , i.e.

$$\nabla_\alpha n_n^\alpha = 0, \quad \text{and} \quad \nabla_\alpha n_p^\alpha = 0. \quad (10.1)$$

The dynamics of the system is governed by a Lagrangian density of the form $\Lambda(n_n^\alpha, n_p^\alpha)$. Due to the requirement of covariance, the scalar density Λ can only depend on scalars, and we can form exactly three independent scalar combinations out of n_n^α and n_p^α , for example

$$\begin{aligned} n_n^2 &\equiv -\frac{1}{c^2} g_{\alpha\beta} n_n^\alpha n_n^\beta, \\ n_p^2 &\equiv -\frac{1}{c^2} g_{\alpha\beta} n_p^\alpha n_p^\beta, \\ x^2 &\equiv -\frac{1}{c^2} g_{\alpha\beta} n_n^\alpha n_p^\beta, \end{aligned} \quad (10.2)$$

where $g_{\alpha\beta}$ is the spacetime metric, so the Lagrangian density can be written as

$$\Lambda(n_n^\alpha, n_p^\alpha) = -\mathcal{E}(n_n^2, n_p^2, x^2), \quad (10.3)$$

where \mathcal{E} is a thermodynamic potential representing the total energy density of the two-fluid system, or “equation of state”. Introducing the 4-velocities u_n^α , u_p^α of the two fluids, which satisfy the normalization conditions

$$g_{\alpha\beta} u_n^\alpha u_n^\beta = -c^2, \quad \text{and} \quad g_{\alpha\beta} u_p^\alpha u_p^\beta = -c^2, \quad (10.4)$$

the particle 4-currents can be written as

$$n_n^\alpha = n_n u_n^\alpha, \quad \text{and} \quad n_p^\alpha = n_p u_p^\alpha, \quad (10.5)$$

in terms of the neutron- and proton densities n_n and n_p respectively. Variation of the Lagrangian density (10.3) with respect to the particle currents n_n^α and n_p^α defines the conjugate momenta p_α^n and p_α^p , namely

$$d\Lambda = p_\alpha^n dn_n^\alpha + p_\alpha^p dn_p^\alpha. \quad (10.6)$$

Due to the covariance constraint (10.3) we can further express the conjugate momenta in terms of the currents as

$$\begin{aligned} p_\alpha^n &= \mathcal{K}^{nn} n_{n\alpha} + \mathcal{K}^{np} n_{p\alpha}, \\ p_\alpha^p &= \mathcal{K}^{pn} n_{n\alpha} + \mathcal{K}^{pp} n_{p\alpha}, \end{aligned} \quad (10.7)$$

where the symmetric “entrainment matrix” \mathcal{K}^{XY} is given by the partial derivatives of $\mathcal{E}(n_n^2, n_p^2, x^2)$, namely¹

$$\mathcal{K}^{nn} = \frac{2}{c^2} \frac{\partial \mathcal{E}}{\partial n_n^2}, \quad \mathcal{K}^{pp} = \frac{2}{c^2} \frac{\partial \mathcal{E}}{\partial n_p^2}, \quad \mathcal{K}^{np} = \frac{1}{c^2} \frac{\partial \mathcal{E}}{\partial x^2}. \quad (10.8)$$

The equations of motion for the two fluids can be obtained from an elegant variational principle developed by [109]. In the absence of direct dissipative forces acting between the two fluids (e.g. see [287]), the equations of motion can be expressed as²

$$n_n^\alpha \nabla_{[\alpha} p_{\beta]}^n = 0, \quad \text{and} \quad n_p^\alpha \nabla_{[\alpha} p_{\beta]}^p = 0. \quad (10.9)$$

The energy–momentum tensor $T^{\alpha\beta}$ of the two–fluid system, which is equally derived from the variational principle, has the form

$$T^\alpha{}_\beta = n_n^\alpha p_\beta^n + n_p^\alpha p_\beta^p + \Psi g_\beta^\alpha. \quad (10.10)$$

If the equations of motion (10.1) and (10.9) are satisfied, the stress-energy tensor automatically satisfies $\nabla_\alpha T^{\alpha\beta} = 0$, which is a Noether-type identity of the variational principle. The generalised pressure Ψ of the two–fluid system is defined by the thermodynamical identity

$$\mathcal{E} + \Psi = -n_n^\alpha p_\alpha^n - n_p^\alpha p_\alpha^p, \quad (10.11)$$

which can be considered as the Legendre-transform of Λ . Using the entrainment relation (10.7), we can rewrite this as

$$\frac{\mathcal{E} + \Psi}{c^2} = \mathcal{K}^{nn} n_n^2 + 2\mathcal{K}^{np} x^2 + \mathcal{K}^{pp} n_p^2. \quad (10.12)$$

Instead of x^2 defined in (10.2), we will use a physically more intuitive quantity as the third independent scalar, namely the “relative speed” Δ . We define the relative speed Δ as the norm of the neutron velocity u_n^α as seen in the frame of the protons u_p^α , and vice versa. The corresponding relative Lorentz factor Γ_Δ is therefore given by

$$\Gamma_\Delta = -\frac{1}{c^2} u_n^\alpha u_p^\beta g_{\alpha\beta} = \frac{x^2}{n_n n_p} = \left(1 - \frac{\Delta^2}{c^2}\right)^{-1/2}, \quad (10.13)$$

¹The corresponding notation in [22] is $n_n^\alpha \rightarrow n^\alpha$, $n_p^\alpha \rightarrow p^\alpha$, $u_n^\alpha \rightarrow u^\alpha$, $u_p^\alpha \rightarrow v^\alpha$, $\mathcal{K}^{np} \rightarrow \mathcal{A}$, $\mathcal{K}^{nn} \rightarrow \mathcal{B}$, and $\mathcal{K}^{pp} \rightarrow \mathcal{C}$.

²the square brackets denote averaged index antisymmetrization, i.e. $2v_{[a,b]} = v_{ab} - v_{ba}$.

and the relative speed Δ is expressible in terms of x as

$$\Delta^2 = c^2 \left[1 - \left(\frac{n_n n_p}{x^2} \right)^2 \right]. \quad (10.14)$$

In the case of comoving fluids (i.e. $u_n^\alpha = u_p^\alpha$), we see from (10.2) that $x^2 = n_n n_p$, and so $\Delta = 0$ as expected.

We can now equivalently consider the equation of state \mathcal{E} as a function of the form $\mathcal{E}(n_n, n_p, \Delta^2)$, for which the first law of thermodynamics reads as

$$d\mathcal{E} = \mu^n dn_n + \mu^p dn_p + \alpha d\Delta^2, \quad (10.15)$$

closely analogous to the Newtonian formulation [377]. The conjugate quantities defined in this equation are the entrainment α and the neutron- and proton chemical potentials μ^n and μ^p (sometimes also referred to as specific enthalpies, which is equivalent in the zero-temperature case). It is often useful to characterize the entrainment by the dimensionless entrainment numbers ε_X , which we define as

$$\varepsilon_X \equiv \frac{2\alpha}{m^X n_X}, \quad (10.16)$$

where m^X is the particle rest-mass of the respective fluid, and the fluid-index is $X = n, p$ (no summation over X).

The conjugate variables of (10.15) can be expressed in terms of the kinematic scalars and the entrainment matrix \mathcal{K}^{XY} as

$$\begin{aligned} \mu^n &= \frac{c^2}{n_n} (\mathcal{K}^{nn} n_n^2 + \mathcal{K}^{np} x^2) = -u_n^\alpha p_\alpha^n, \\ \mu^p &= \frac{c^2}{n_p} (\mathcal{K}^{pp} n_p^2 + \mathcal{K}^{np} x^2) = -u_p^\alpha p_\alpha^p, \\ \alpha &= \frac{1}{2} \mathcal{K}^{np} n_n n_p \Gamma_\Delta^3. \end{aligned} \quad (10.17)$$

Using (10.14), the inverse relations can be obtained as

$$\begin{aligned} \mathcal{K}^{nn} &= \frac{\mu^n}{n_n c^2} - \frac{2\alpha}{n_n^2 \Gamma_\Delta^2} \\ \mathcal{K}^{pp} &= \frac{\mu^p}{n_p c^2} - \frac{2\alpha}{n_p^2 \Gamma_\Delta^2} \\ \mathcal{K}^{np} &= \frac{2\alpha}{n_n n_p \Gamma_\Delta^3}, \end{aligned} \quad (10.18)$$

which reduces exactly to the corresponding relations in the Newtonian limit [377], where $\Gamma_\Delta \rightarrow 1$ and $\mu^X \rightarrow m^X c^2 + \hat{\mu}^X$. In terms of these quantities, the generalised pressure Ψ (10.11) can also be written as

$$\Psi = -\mathcal{E} + n_n \mu^n + n_p \mu^p. \quad (10.19)$$

10.3 Stationary axisymmetric configurations

10.3.1 The metric

Here and in the following we choose units such that $G = c = 1$ for simplicity. We consider spacetimes that are stationary, axisymmetric, and asymptotically flat. The symmetries of stationarity and axisymmetry are associated with the existence of two Killing vector fields, one timelike at spatial infinity, t^α , and one spacelike everywhere and with closed orbits, φ^α .

It was shown by [107] that under these assumptions the Killing vectors commute, and one can choose an adapted coordinate system (t, x^1, x^2, φ) , such that $t^\alpha \partial_\alpha = \partial/\partial t$ and $\varphi^\alpha \partial_\alpha = \partial/\partial \varphi$, ie.

$$t^\alpha = (1, 0, 0, 0), \quad \text{and} \quad \varphi^\alpha = (0, 0, 0, 1). \quad (10.20)$$

We choose the remaining two coordinates to be of spherical type, ie. $x^1 = r$, $x^2 = \theta$, and following [217], we fix the gauge to be of maximal-slicing quasi-isotropic type (MSQI), for which the line element reads as

$$ds^2 = g_{\alpha\beta} dx^\alpha dx^\beta = -(N^2 - N_\varphi N^\varphi) dt^2 - 2N_\varphi d\varphi dt + A^2 (dr^2 + r^2 d\theta^2) + B^2 r^2 \sin^2 \theta d\varphi^2, \quad (10.21)$$

where the functions N , N^φ , A and B depend on r and θ only, and $N_\varphi \equiv g_{\varphi\varphi} N^\varphi$.

10.3.2 Fluid dynamics

We assume the flow of the two fluids to be purely *axial* (i.e. no convective meridional currents), so we can write the unit 4-velocities of the two fluids as

$$u_n^\alpha = u_n^t \zeta_n^\alpha \quad \text{and} \quad u_p^\alpha = u_p^t \zeta_p^\alpha, \quad (10.22)$$

where the helical vectors ζ_n^α and ζ_p^α are expressible in terms of the Killing vectors as

$$\zeta_n^\alpha = t^\alpha + \Omega_n \varphi^\alpha, \quad \text{and} \quad \zeta_p^\alpha = t^\alpha + \Omega_p \varphi^\alpha, \quad (10.23)$$

and the two rotation rates Ω_n and Ω_p are scalar functions which can only depend on r and θ .

Using Cartan's formula for the Lie derivative of a 1-form p_β with respect to a vector-field ξ^α , namely

$$\mathcal{L}_\xi p_\alpha = 2\xi^\beta \nabla_{[\beta} p_{\alpha]} + \nabla_\alpha (\xi^\beta p_\beta), \quad (10.24)$$

we can rewrite the equations of motion (10.9) as

$$\mathcal{L}_{\zeta_X} p_\alpha^X - \nabla_\alpha (\zeta_X^\beta p_\beta^X) = 0. \quad (10.25)$$

Linearity of the Lie derivative together with (10.23) and (10.24) allows us to rewrite this as

$$\mathcal{L}_t p_\alpha^X + \Omega_X \mathcal{L}_\varphi p_\alpha^X + \varphi^\beta p_\beta^X \nabla_\alpha \Omega_X - \nabla_\alpha (\zeta_X^\beta p_\beta^X) = 0. \quad (10.26)$$

Stationarity and axisymmetry imply that the first two terms vanish, and so the equations of motion for neutrons and protons are reduced to

$$p_\varphi^n \nabla_\alpha \Omega_n = \nabla_\alpha (\zeta_n^\beta p_\beta^n), \quad p_\varphi^p \nabla_\alpha \Omega_p = \nabla_\alpha (\zeta_p^\beta p_\beta^p). \quad (10.27)$$

In the general case of differential rotation, the integrability condition of these equations are therefore

$$p_\varphi^n = p_\varphi^n(\Omega_n), \quad \text{and} \quad p_\varphi^p = p_\varphi^p(\Omega_p), \quad (10.28)$$

and the first integrals of motion are obtained as

$$p_t^n + \Omega_n p_\varphi^n - \int^{\Omega_n} p_\varphi^n(\Omega') d\Omega' = \text{const}^n, \quad (10.29)$$

$$p_t^p + \Omega_p p_\varphi^p - \int^{\Omega_p} p_\varphi^p(\Omega') d\Omega' = \text{const}^p. \quad (10.30)$$

In the special case of *uniform rotation*, ie. $\nabla_\alpha \Omega_X = 0$, these first integrals reduce to

$$p_t^n + \Omega_n p_\varphi^n = \text{const}^n, \quad \text{and} \quad p_t^p + \Omega_p p_\varphi^p = \text{const}^p, \quad (10.31)$$

which are equivalent to the expressions obtained by [22]. We can further express these first integrals in terms of the chemical potentials μ^n, μ^p of (10.17), namely

$$p_t^n + \Omega_n p_\varphi^n = \zeta_n^\alpha p_\alpha^n = -\frac{1}{u_n^t} \mu^n = \text{const}^n, \quad (10.32)$$

$$p_t^p + \Omega_p p_\varphi^p = \zeta_p^\alpha p_\alpha^p = -\frac{1}{u_p^t} \mu^p = \text{const}^p. \quad (10.33)$$

10.3.3 The 3 + 1 decomposition

We introduce the vector \mathbf{n}^α as the unit normal to the spacelike hypersurfaces Σ_t defined by $t = \text{const.}$, namely

$$\mathbf{n}_\alpha \equiv -N \nabla_\alpha t, \quad (10.34)$$

which defines the so-called *Eulerian observers* \mathcal{O}_0 following [435]. The induced metric $h_{\alpha\beta}$ on the spacelike hypersurfaces Σ_t is given by the projection

$$h_{\alpha\beta} \equiv g_{\alpha\beta} + \mathbf{n}_\alpha \mathbf{n}_\beta. \quad (10.35)$$

The corresponding 3 + 1 decomposition of the energy–momentum tensor $T^{\alpha\beta}$ reads as¹

$$T^{\alpha\beta} = S^{\alpha\beta} + 2\mathbf{n}^{(\alpha} J^{\beta)} + E \mathbf{n}^\alpha \mathbf{n}^\beta, \quad (10.36)$$

where

$$E = \mathbf{n}^\alpha T_{\alpha\beta} \mathbf{n}^\beta, \quad J_\alpha = -h_\alpha^\gamma T_{\gamma\beta} \mathbf{n}^\beta, \quad S_{\alpha\beta} = h_\alpha^\gamma T_{\gamma\nu} h_\beta^\nu, \quad (10.37)$$

which can be interpreted as the energy, momentum and stress tensor as measured by the Eulerian observers. In the MSQI gauge (10.21), we can explicitly express these quantities as

$$E = N^2 T^{tt}, \quad J_i = N T_i^t, \quad S_j^i = T_j^i - N^i T_j^t. \quad (10.38)$$

¹Round brackets denote symmetrization, i.e. $2v_{(a,b)} = v_{ab} + v_{ba}$.

The Einstein equations in this formulation result in a set of four elliptic equations for the metric potentials (see [67] and [217] for details), namely

$$\Delta_3 \nu = 4\pi A^2 (E + S_i^i) + A^2 K_{ij} K^{ij} - \partial \nu \partial (\nu + \beta), \quad (10.39)$$

$$\tilde{\Delta}_3 \tilde{N}^\varphi = -16\pi N A^2 \tilde{J}^\varphi - r \sin \theta \partial N^\varphi \partial (3\beta - \nu), \quad (10.40)$$

$$\Delta_2 [(NB - 1)r \sin \theta] = 8\pi N A^2 B r \sin \theta (S_r^r + S_\theta^\theta), \quad (10.41)$$

$$\Delta_2 (\nu + \alpha) = 8\pi A^2 S_\varphi^\varphi + \frac{3}{2} A^2 K_{ij} K^{ij} - (\partial \nu)^2, \quad (10.42)$$

where we defined $\tilde{N}^\varphi \equiv r \sin \theta N^\varphi$ and $\tilde{J}^\varphi \equiv r \sin \theta J^\varphi$. Δ_3 and Δ_2 are the flat three- and two-dimensional Laplace operators, whereas $\tilde{\Delta}_3 = \Delta_3 - (r^2 \sin^2 \theta)^{-1}$. We further used the notation

$$\nu \equiv \ln N, \quad \alpha \equiv \ln A, \quad \beta \equiv \ln B, \quad (10.43)$$

and we define $\partial \alpha \partial \beta$ as the flat-space scalar product of two gradients, i.e.

$$\partial \alpha \partial \beta \equiv \partial_r \alpha \partial_r \beta + \frac{1}{r^2} \partial_\theta \alpha \partial_\theta \beta. \quad (10.44)$$

The only non-zero components of the extrinsic curvature K_{ij} in our spherical coordinate basis are given by

$$K_{r\varphi} = -\frac{g_{\varphi\varphi}}{2N} \partial_r N^\varphi, \quad K_{\theta\varphi} = -\frac{g_{\varphi\varphi}}{2N} \partial_\theta N^\varphi. \quad (10.45)$$

We note that the gravitational mass \mathcal{M} , which is defined as the (negative) coefficient of the term $1/r$ in an asymptotic expansion of the ‘‘gravitational potential’’ $\log N$, can be expressed explicitly (see [67]) as

$$\mathcal{M} = \int A^2 B \left[N(E + S_i^i) + 2B^2 \tilde{N}^\varphi \tilde{J}^\varphi \right] r^2 \sin \theta dr d\theta d\varphi, \quad (10.46)$$

Here and in the following we will use \mathcal{M} to denote the gravitational mass, while M will stand for the baryon mass. The total angular momentum \mathcal{J} is given by

$$\mathcal{J} = \int \left[A^2 B^3 r \sin \theta \tilde{J}^\varphi \right] r^2 \sin \theta dr d\theta d\varphi. \quad (10.47)$$

The 2D- and 3D virial identities, which have been derived by Bonazzola and Gourgoulhon [220, 76], can serve as a useful check of consistency and precision of the numerical results. The 2D virial identity (referred to as GRV2), which derives from the Poisson-equation (10.42), has the form

$$\int \left[8\pi A^2 S_\varphi^\varphi + \frac{3}{2} A^2 K_{ij} K^{ij} - (\partial \nu)^2 \right] r dr d\theta = 0, \quad (10.48)$$

while the 3D virial identity (GRV3), which reduces to the usual virial theorem in the Newtonian limit, can be written as

$$\int 4\pi A^2 B S_i^i dV + \int B \left[\frac{3}{4} A^2 K_{ij} K^{ij} - (\partial \nu)^2 + \frac{1}{2} \partial \alpha \partial \beta \right] dV + \int \frac{1}{2r} \left(B - \frac{A^2}{B} \right)$$

$$\times \left[\partial_r (\alpha - \beta/2) + \frac{1}{r \tan \theta} \partial_\theta (\alpha - \beta/2) \right] = 0. \quad (10.49)$$

Both of these virial theorems (10.48) and (10.49) can be written as the sum of an integral over a “material” term I_{mat} (the first term in (10.48) and (10.49) respectively), and an integral over pure field-quantities I_{fields} (the remaining terms). Therefore it will be convenient to consider the following dimensionless quantity to numerically characterize the respective virial violations:

$$GRV \equiv \frac{I_{\text{mat}} + I_{\text{fields}}}{I_{\text{mat}}}. \quad (10.50)$$

10.3.4 The matter sources

Let us write Γ_n and Γ_p for the two Lorentz factors linking the Eulerian observers \mathcal{O}_0 to the comoving fluid observers \mathcal{O}_n (defined by u_n^α) and \mathcal{O}_p (defined by u_p^α), namely

$$\Gamma_n \equiv -\mathbf{n}_\alpha u_n^\alpha = Nu_n^t, \quad \text{and} \quad \Gamma_p \equiv -\mathbf{n}_\alpha u_p^\alpha = Nu_p^t. \quad (10.51)$$

The “physical” fluid velocities U_n and U_p of the two fluids¹ in the φ direction, as measured by \mathcal{O}_0 , are given by

$$U_n = \frac{1}{\Gamma_n} \hat{\varphi}_\alpha u_n^\alpha, \quad \text{and} \quad U_p = \frac{1}{\Gamma_p} \hat{\varphi}_\alpha u_p^\alpha, \quad (10.52)$$

where $\hat{\varphi}^\alpha$ is the *spatial* unit vector in the φ direction, ie.

$$\hat{\varphi}^\alpha = \frac{1}{\sqrt{g_{\varphi\varphi}}} \varphi^\alpha, \quad \text{such that} \quad h_{\alpha\beta} \hat{\varphi}^\alpha \hat{\varphi}^\beta = 1. \quad (10.53)$$

Using (10.22) and (10.51), we obtain

$$U_n = \frac{\sqrt{g_{\varphi\varphi}}}{N} (\Omega_n - N^\varphi), \quad U_p = \frac{\sqrt{g_{\varphi\varphi}}}{N} (\Omega_p - N^\varphi), \quad (10.54)$$

and the Lorentz factors can be expressed equivalently as

$$\Gamma_n = (1 - U_n^2)^{-1/2}, \quad \text{and} \quad \Gamma_p = (1 - U_p^2)^{-1/2}. \quad (10.55)$$

The “crossed” scalar x^2 , defined in (10.2), can be expressed in terms of the respective scalar particle densities n_n, n_p and the 3-velocities U_n and U_p , as

$$x^2 = n_n n_p \frac{1 - U_n U_p}{\sqrt{(1 - U_n^2)(1 - U_p^2)}}, \quad (10.56)$$

and using (10.14), we can write the relative velocity Δ as

$$\Delta^2 = \frac{(U_n - U_p)^2}{(1 - U_n U_p)^2}. \quad (10.57)$$

Using expressions (10.32),(10.33) and (10.51), the first integrals can be cast into the form

$$\frac{N}{\Gamma_n} \mu^n = \text{const}^n, \quad \text{and} \quad \frac{N}{\Gamma_p} \mu^p = \text{const}^p. \quad (10.58)$$

¹In [22] these were denoted $-\omega_n$ and $-\omega_p$ respectively.

In closer analogy with [67, 217], we can alternatively write these first integrals as

$$H_n + \nu - \ln \Gamma_n = C_n, \quad (10.59)$$

$$H_p + \nu - \ln \Gamma_p = C_p, \quad (10.60)$$

where we introduced the abbreviations

$$H_n \equiv \ln(\mu_n/m^n), \quad \text{and} \quad H_p \equiv \ln(\mu_p/m^p). \quad (10.61)$$

The components of the 3 + 1 decomposition (10.36) of the energy–momentum tensor (10.10) are explicitly found as

$$E = -\Psi + (\Gamma_n^2 \mathcal{K}^{nn} n_n^2 + \Gamma_p^2 \mathcal{K}^{pp} n_p^2 + 2\Gamma_n \Gamma_p \mathcal{K}^{np} n_n n_p), \quad (10.62)$$

$$\sqrt{g_{\varphi\varphi}} J^\varphi = \Gamma_n^2 \mathcal{K}^{nn} n_n^2 U_n + \Gamma_p^2 \mathcal{K}^{pp} n_p^2 U_p + \Gamma_n \Gamma_p \mathcal{K}^{np} n_n n_p (U_n + U_p), \quad (10.63)$$

$$S_r^r = S_\theta^\theta = \Psi, \quad (10.64)$$

$$S_\varphi^\varphi = \Psi + (\Gamma_n^2 \mathcal{K}^{nn} n_n^2 U_n^2 + \Gamma_p^2 \mathcal{K}^{pp} n_p^2 U_p^2 + 2\Gamma_n \Gamma_p \mathcal{K}^{np} n_n n_p U_n U_p), \quad (10.65)$$

One can check the consistency of this result with the single fluid case of [67], considering the special case of both fluids moving together.

10.4 Numerical procedure

10.4.1 Iteration scheme

The numerical solution of the stationary axisymmetric configurations described in the previous sections proceeds in a very similar manner to the single-fluid case, which is described in more detail in [67, 217]. The central iteration scheme is nearly identical:

Initialization: Start from a simple “guess” for a spherically symmetric matter distribution $n_n^{(0)}$ and $n_p^{(0)}$ of the two fluids, and use a flat metric.

Step 1: Calculate the matter source-terms E , J^φ and \mathcal{S}_j^i from (10.62)–(10.65).

Step 2: Solve the equations (10.39)–(10.42) for the corresponding metric using the pseudo-spectral elliptic solver in LORENE, the numerical relativity package used here[216].

Step 3: Use the first integrals (10.58) to obtain the chemical potentials μ^n and μ^p .

Step 4: Calculate the new density fields n_n and n_p by inverting the relations (10.17) for the given equation of state.

Step 5: Continue at Step 1 until the desired convergence is achieved.

In general we are using three spherical-type numerical domains to cover the hypersurface Σ_t : the innermost domain covers the whole star. An intermediate domain is used for the vicinity of the star to about twice the stellar radius, and an outer domain covers the space out to infinity, using a compactification of the type $u = 1/r$ (see [67] for details). For the inner domain we have the choice of either using a simple spherical grid containing the whole star, or we can use an adaptive-grid algorithm, in order to adapt the domain-boundary to the stellar surface. Contrary to the single-fluid case (e.g. see [217]), however, the adaptive-grid approach is much less effective in increasing precision and convergence. The reason for this is simply that only one of the two fluid-surfaces can be matched up with a domain boundary, and therefore the (weak) Gibbs phenomenon due to the inner fluid surface (representing at least a discontinuity in the derivative) is not completely avoidable.

Another important difference in the case of two-fluids compared to single-fluid stars is the way we determine the location of the fluid surfaces. In a single fluid star, the surface can always be found by the vanishing of the pressure, which usually translates into a simple condition in terms of the vanishing of the chemical potential μ . In the two-fluid case, however, this is not generally possible (especially for the “inner” fluid), due to the coupling of the fluids. Therefore we need to define the fluid surfaces directly in terms of the vanishing of the respective density fields. Contrary to the chemical potential, the density can have a vanishing or diverging gradient at the surface, and a precise determination of the surface can therefore be numerically difficult.¹

A related numerical problem specific to two-fluid configurations appears when the surfaces of the two fluids are very close to each other. In this case, the 1-fluid region in between the two surfaces will be poorly resolved by the grid covering the star, and therefore the determination of the outer surface will have a low numerical precision. As will be seen later, this problem can be cured to some extent by adding another domain, which covers just a thin shell below and up to the outer fluid surface. In this case one observes a drastic improvement in the precision of finding the outer surface, which can be quantified by comparison with the analytic slow-rotation solution.

We note that this numerical code can be used equally well for Newtonian configurations, simply by replacing the matter-sources by their Newtonian limits, and forcing the spatial metric to be flat. The central iteration scheme remains unchanged, and we can relate the lapse N to the Newtonian gravitational potential, namely by the relation $\nu = \ln N = \Phi/c^2$, where Φ is the Newtonian gravitational potential. The Newtonian limit of the matter source-term in Eq. (10.39) is

$$\frac{E + S_i^i}{c^2} = \rho + \mathcal{O}(c^{-2}), \quad (10.66)$$

where ρ is the total (rest-)mass-density, so that this component of the Einstein equations reduces to the Newtonian Poisson equation, while the remaining Einstein equations (10.40)–(10.42) become trivial in this limit. In a similar manner, the first integrals are seen to reduce exactly to their Newtonian counterparts [377].

The parameters of the numerical scheme that will be used for the rest of the paper are the following: the required convergence of the iteration scheme is 10^{-10} , and we use 17 points in the θ direction, and 33 grid-points in the radial direction in the innermost domain (containing the star), 33 radial points in the intermediate domain and 17 radial points in the compactified outer domain.

¹We note that [488] chose to avoid this difficulty by *defining* the “fluid surfaces” by the vanishing of the respective chemical potentials. These “surfaces”, however, do generally *not* coincide with the surfaces of vanishing density (contrary to the single-fluid case), as can be seen from (10.17).

10.4.2 The polytropic 2-fluid equation of state

The numerical scheme described in the previous section can be used for any invertible 2-fluid equation of state (EOS). The current implementation of our code, however, only covers a “polytropic” subclass of 2-fluid EOS, which generalizes the types of EOS used in previous studies, e.g. [380, 377, 22, 488], and which has the general form

$$\begin{aligned} \mathcal{E} = & (m_n n_n + m_p n_p) c^2 + \frac{1}{2} \kappa_n n^{\gamma_1} + \frac{1}{2} \kappa_p n_p^{\gamma_2} \\ & + \kappa_{np} n_n^{\gamma_3} n_p^{\gamma_4} + \kappa_\Delta n_n^{\gamma_5} n_p^{\gamma_6} \Delta^2. \end{aligned} \quad (10.67)$$

As discussed in the introduction, we expect this polytropic EOS-class to be quite general, and to allow one to study the qualitative features of a broad range of different superfluid neutron star models. For example, general features of the Kepler limit (cf. Fig. 10.5) are seen to be in qualitative agreement with the mean field results of [124].

The two fluids in (10.67) are coupled via a “symmetry energy”-type term proportional to κ_{np} and an entrainment term proportional to $\kappa_\Delta \Delta^2$. The resulting expressions for the chemical potentials and the entrainment α are directly obtainable from (10.15).

In general this class of 2-fluid EOS requires a numerical inversion in the iteration scheme described in section 10.4.1, in order to obtain the densities n_n, n_p from the chemical potentials μ^n, μ^p at a given relative speed Δ . For testing purposes and for comparison to the Newtonian and relativistic slow-rotation results, we will in the following be mostly interested in a further subclass of the above EOS, namely the special 2-fluid polytropes described by

$$\mathcal{E} = \frac{1}{2} \kappa_n n_n^2 + \frac{1}{2} \kappa_p n_p^2 + \kappa_{np} n_n n_p + \kappa_\Delta n_n n_p \Delta^2, \quad (10.68)$$

which are a 2-fluid generalization of the 1-fluid polytrope $P \propto n^2$. This special EOS class still exhibits all the coupling-types (entrainment + symmetry energy) of the general EOS, but allows an analytic inversion, namely

$$\mu^n - m_n c^2 = \kappa_n n_n + (\kappa_{np} + \kappa_\Delta \Delta^2) n_p, \quad (10.69)$$

$$\mu^p - m_p c^2 = \kappa_p n_p + (\kappa_{np} + \kappa_\Delta \Delta^2) n_n, \quad (10.70)$$

and the entrainment is found as

$$\alpha = \kappa_\Delta n_n n_p. \quad (10.71)$$

The generalized pressure Ψ in (10.19) is expressible as

$$\Psi = \frac{1}{2} \kappa_n n^2 + \frac{1}{2} \kappa_p n_p^2 + \kappa_{np} n_n n_p + \kappa_\Delta n_n n_p \Delta^2. \quad (10.72)$$

Contrary to the two-fluid EOS used in the Newtonian slow-rotation study [377], which exhibits the somewhat unphysical feature of constant entrainment numbers, as discussed in appendix 10.A, this EOS results in a much more physical behavior of the entrainment. Namely, using (10.16), we find

$$\varepsilon_n = \frac{2\kappa_\Delta}{m^n} n_p, \quad \text{and} \quad \varepsilon_p = \frac{2\kappa_\Delta}{m^p} n_n, \quad (10.73)$$

which ensures that the entrainment effect automatically vanishes when one of the two fluid-densities goes to zero. Such a linear behavior of entrainment also happens to be in quite good qualitative agreement with the theoretical predictions of nuclear physics, e.g. see¹ [116, 433, 45]

Using the method developed in [377] for the EOS (10.68), we can find an analytic solution in the Newtonian slow-rotation approach, which is presented in appendix 10.A. This allows us to run extensive tests by comparing our numerical code to the analytic solution in the Newtonian case. The results of this comparison are presented in section 10.5.3.

10.5 Tests of the numerical code

10.5.1 Comparison to 1-fluid results

As a first consistency check we use the two-fluid code for strictly co-rotating configurations with a common outer surface, and compare the results to those of the well-tested single-fluid code [67, 217]. For this purpose we study a stellar sequence of fixed central density and vary the rotation rate. We define the “natural scale” of the rotation-rate as

$$\Omega_0 \equiv \sqrt{4\pi G \rho(0)}, \quad (10.74)$$

where $\rho(0)$ is the central rest-mass density, i.e. $\rho(0) = m^n n_n(0) + m^p n_p(0)$. The Kepler rotation rate Ω_K is typically found at about $\Omega_K \sim 0.1 \Omega_0$ for the configurations considered here. The results of the comparison with the single-fluid case are shown in Fig. 10.1. Here we plot the relative differences, defined as

$$\Delta Q \equiv \frac{|Q^{2f} - Q^{1f}|}{Q^{1f}}, \quad (10.75)$$

of a global quantity Q in the two-fluid case (Q^{2f}) and in the single-fluid case (Q^{1f}). The first column, figures 10.1 (a) and (c), shows the comparison of 1-fluid and 2-fluid results using a *fixed* spherical grid for the inner domain in the two-fluid case. The single-fluid code on the other hand always uses an adaptive grid for the stellar surface. We notice that toward higher rotation rates the relative errors increase. These errors can be entirely ascribed to the lack of grid adaption in the two-fluid case: by using an adaptive grid for the inner domain also in the two-fluid case, we find a consistent agreement of better than 10^{-9} , as can be seen in the second column in figure 10.1 (b) and (d). We note, however, that this improvement of using an adaptive grid is restricted to cases where the two-fluids share a common outer surface, while it is of much less use in the general two-fluid case as mentioned earlier. We can therefore conclude that the two-fluid code reproduces results consistent with the single-fluid code in cases where the two fluids co-rotate.

10.5.2 Virial theorem violation

In the next step we consider the more general case where the two fluids have different rotation rates. We fix the relative rotation rate, defined as

$$\mathcal{R} \equiv \frac{\Omega_n - \Omega_p}{\Omega_p}, \quad (10.76)$$

¹These references give the neutron and proton effective masses m^{X*} , which are related to the entrainment via $\varepsilon_X = (m^X - m^{X*})/m^X$, see [377] for details.

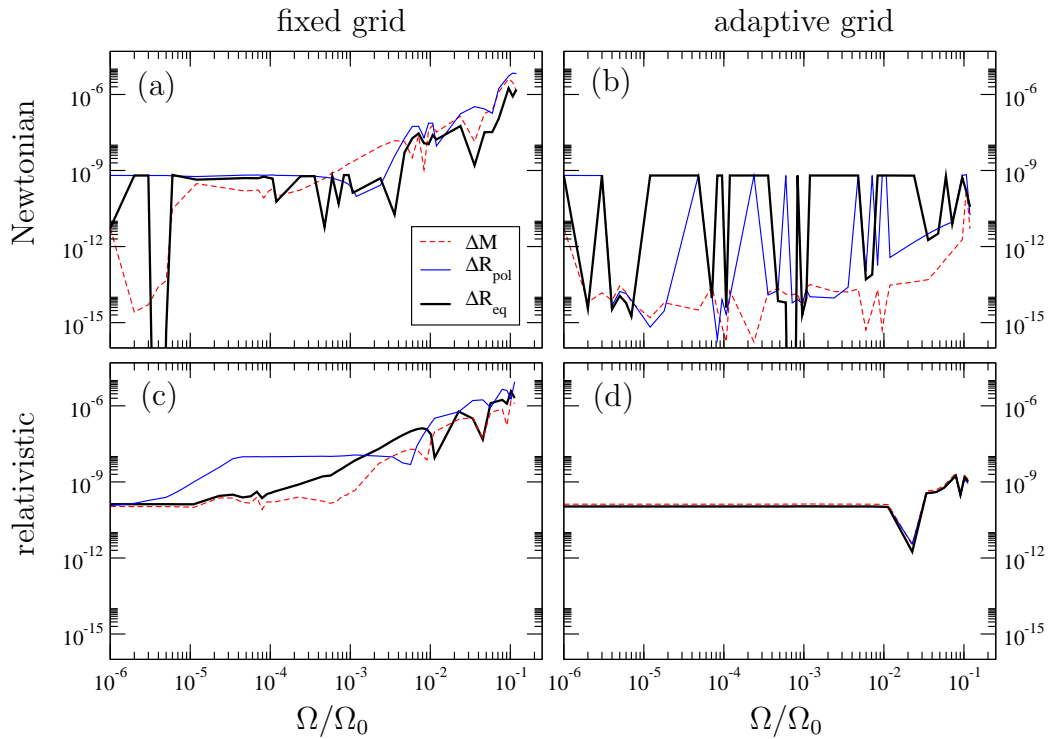


Figure 10.1: Relative differences ΔQ in the total baryon mass M , and the equatorial and polar radii R_{eq} and R_{pol} . The first row is the Newtonian case, while the second row shows the relativistic results. In the first column, the two-fluid code used a fixed spherical inner domain, while in the second column the inner domain-grid is adapted to the stellar surface (which is the default in the single-fluid case).

to be $\mathcal{R} = 1.51$ and vary Ω_n . As mentioned before, in these general situations the use of an adaptive grid does not substantially improve the precision and has therefore been omitted. We consider the

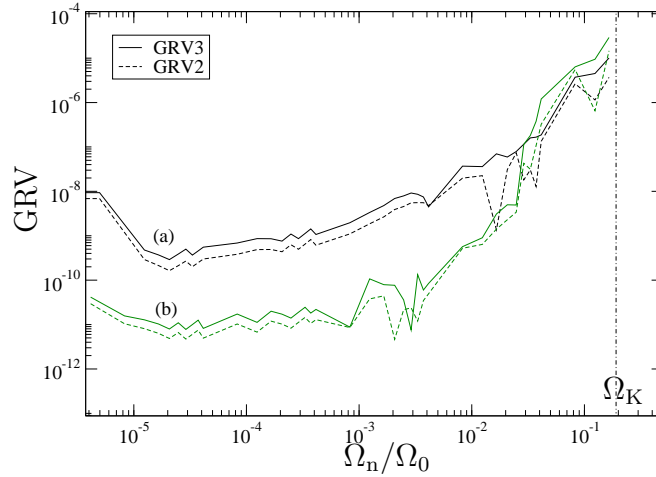


Figure 10.2: GRV2 and GRV3 for (a) 1 domain and (b) 2 domains covering the star. Only the Newtonian case is shown, as the relativistic results are very similar.

internal consistency check provided by the virial identities GRV2 and GRV3 defined in (10.50), the result of which is shown in Fig. 10.2. We note that in the case (a), where one inner domain is used to cover the star, even at low rotation rates the result falls somewhat short of the convergence-goal of 10^{-10} , which we required in the iteration scheme. This lack of precision at small rotation rates can be understood as follows: due to the difference in rotation rates, the two fluids do not share a common outer surface, and there will necessarily be a 1-fluid region close to the outer surface. However, this 1-fluid region will be very thin compared to the dimensions of the star, and will therefore be poorly resolved in terms of the numerical grid. We can improve this by choosing a second domain to cover just a thin layer (of about 1% of the radius) below the outer surface, resolved by some 33 radial grid-points. The effect of this “trick” is rather impressive and can be seen in the in Fig. 10.2 (b). While this gain in precision is not very important by itself, it underlines the consistency of the results and shows that the source of these errors is understood. The decrease in precision when approaching the Kepler rotation can be ascribed to the appearance of singularities on the equator (see Fig. 10.5) corresponding to the mass-shedding limit, and therefore the presence of the Gibbs phenomenon. Nevertheless, one should note that this phenomenon happens also in the one-fluid case, the precision of the code at the Kepler limit being of the same order as here [217].

10.5.3 Comparison to Newtonian slow-rotation results

We can use the analytic Newtonian solution of the slow-rotation approximation (derived in appendix 10.A) for a systematic comparison with the numerical code run in “Newtonian mode”. As described in section 10.4.1, the majority of the Newtonian code is shared by the relativistic one, so that these tests nevertheless provide a useful validation of the overall numerical code.

We denote the numerical solution of a quantity as $Q_L(\Omega_X)$, and the analytic slow-rotation solution

as $Q_{\text{sr}}(\Omega_X)$, and we define the relative difference as

$$\diamond Q \equiv \frac{Q_{\text{L}} - Q_{\text{sr}}}{Q^{(0)}}. \quad (10.77)$$

At fixed relative rotation rate \mathcal{R} , the slow-rotation solution can be written as

$$Q_{\text{sr}}(\Omega_{\text{n}}) = Q^{(0)} + Q^{(2)} \Omega_{\text{n}}^2. \quad (10.78)$$

Ideally we would like to compare only up to the Ω^2 component of the numerical solution, but obviously we do not know its Taylor-expansion in orders of Ω . Nevertheless the numerical solution can generally be written as

$$Q_{\text{L}}(\Omega_{\text{n}}) = Q_{\text{L}}^{(0)} + Q_{\text{L}}^{(2)} \Omega_{\text{n}}^2 + Q_{\text{L}}^{(4)} \Omega_{\text{n}}^4 + \dots, \quad (10.79)$$

so that the relative difference (10.77) can be expanded as

$$\diamond Q = \frac{Q_{\text{L}}^{(0)} - Q^{(0)}}{Q^{(0)}} + \frac{Q_{\text{L}}^{(2)} - Q^{(2)}}{Q^{(0)}} \Omega_{\text{n}}^2 + \frac{Q_{\text{L}}^{(4)}}{Q^{(0)}} \Omega_{\text{n}}^4 + \dots \quad (10.80)$$

If the numerical solution agreed perfectly with the analytic solution (up to order Ω^2), the first two terms would be zero, and the leading order of the difference would be Ω_{n}^4 . In practice, however, there will be contributions on all orders, and we will try to quantify these respective errors. If in some region of Ω_{n} , one of these terms dominates in the series, then a log-log plot of $\diamond Q(\Omega_{\text{n}})$ in this region would look like

$$y = \log(a \Omega_{\text{n}}^m) = \log a + m \log \Omega_{\text{n}}, \quad (10.81)$$

i.e. a straight line with steepness m and an offset $\log a$. Conversely, if the log-log plot of $\diamond Q$ contains sections of straight lines, we can infer the leading power of Ω_{n} and its coefficient.

The results of these comparisons are shown in figure 10.3. The neutron-star model used here is characterized by the following choice of EOS-parameters:

$$\kappa_{\text{n}} = 0.02, \quad \kappa_{\text{p}} = 0.12, \quad \kappa_{\text{np}} = 0.01, \quad \kappa_{\Delta} = 0.02, \quad (10.82)$$

and the (fixed) central chemical potentials

$$\mu^{\text{n}}(0) = \mu^{\text{p}}(0) = 0.2 m_{\text{b}} c^2, \quad (10.83)$$

where $m_{\text{b}} = 1.66 \times 10^{-27}$ kg is the baryon mass and c is the speed of light. The resulting neutron-star model in the static case has a total mass of $M = 1.50 M_{\odot}$ (where M_{\odot} is the solar mass), a radius of $R = 11.1$ km, a central baryon number density $n(0) = 1.04 \text{ fm}^{-3}$, proton fraction $x_{\text{p}} \equiv n_{\text{p}}/n = 0.083$ and an entrainment value of $\varepsilon_{\text{p}}(0) = 0.38$ (defined in (10.16)). We note that in the Newtonian case there is no distinction between the gravitational mass \mathcal{M} and the baryon mass M .

In Fig. 10.3 we show the relative differences $\diamond Q$ for the radii R_{n} and R_{p} at the equator. We also plotted the straight lines corresponding to a pure Ω^4 and Ω^2 behavior, in order to facilitate the interpretation of these results.

In the first figure 10.3 (a) we see that for small rotation rates ($\Omega_{\text{n}}/\Omega_0 < 10^{-3}$) the error in the equatorial proton radius $R_{\text{p}}(\text{eq})$ reaches a ‘‘plateau’’ at about $\sim 10^{-9}$, which corresponds to numerical errors and the finite convergence-condition of the iteration scheme, while for higher rotation rates, the quartic error starts to dominate. The same behavior is observed for the other global quantities, e.g. M_{n}

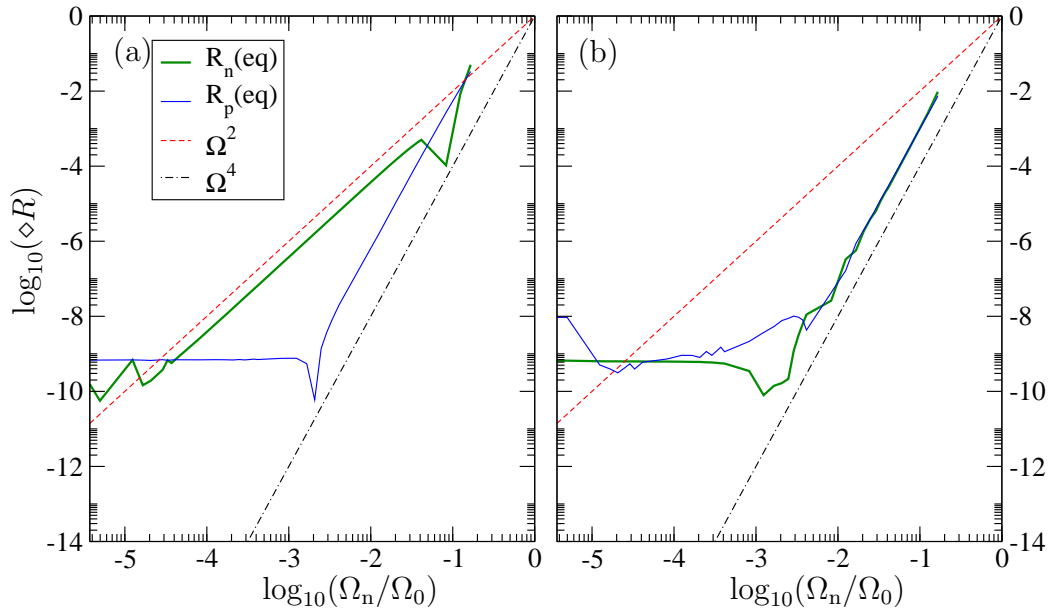


Figure 10.3: Relative difference $\diamond Q(\Omega_n)$ between the numerical code in “Newtonian mode” and the slow-rotation analytic solution of appendix 10.A, for the equatorial radii R_n and R_p . In (a) we used the normal “physical” EOS-inversion, while (b) shows the results for a “slow-rotation style” EOS inversion.

and M_p and $R(\text{pol})$), which have therefore been omitted in this plot. However, the neutron equatorial radius $R_n(\text{eq})$ (which is the outer radius) displays a consistent *quadratic* error of order unity! The reason for this apparent discrepancy is rather subtle, and stems from the somewhat different nature of the slow-rotation approach and the fully numerical solution. In the numerical code, when one of the two fluid-densities vanishes, we switch from the 2-fluid EOS (10.67) to the corresponding 1-fluid EOS *before* we do the inversion $\mu^X \rightarrow n_Y$ in the numerical procedure (cf. section 10.4.1), which is the correct “physical” way to do this. In the slow-rotation approach, however, the rotation rates are treated as infinitesimal, and there is actually no finite 1-fluid region. Therefore the EOS is always used in the form (10.67), which will be seen in the following to account for the difference in $R_n(\text{eq})$. In order to test this explanation, we have also implemented a “slow-rotation style” EOS-inversion in the code, in which we *do not* switch to a 1-fluid EOS when one of the two fluids vanishes. The result of this is shown in figure 10.3 (b). We see that the discrepancy of the outer radius has completely disappeared. However, this only served as a test of consistency, and this rather unphysical method of EOS-inversion will not be used in the following.

10.5.4 Comparison to relativistic slow-rotation results

Finally, we compare our results in the fully relativistic case to the results obtained by using a code developed by [22], which is based on the relativistic slow-rotation approximation.

In the relativistic case the physical “radius” will generally be different from the coordinate-radius, and can be defined in various non-equivalent ways (e.g. circumferential radius, proper radius). For an unambiguous comparison we define the “radius” R as the proper distance of the surface from the

center of the star, along a line of constant θ and φ (the definition of which is equivalent in both cases), i.e.

$$R \equiv \int_0^{R_0} dl = \int_0^{R_0} A(r) dr, \quad (10.84)$$

where R_0 is the coordinate-radius of the surface. Another quantity specific to the relativistic case is the shift-vector $N^i = (0, 0, N^\varphi)$, and we will consider its 3-norm, i.e.

$$\|N^i\| \equiv \sqrt{g_{ij}N^iN^j} = N^\varphi \sqrt{g_{\varphi\varphi}}, \quad (10.85)$$

which is independent of the coordinate-system chosen on the spacelike hypersurface.

The stellar model used in this comparison is defined by the EOS parameters

$$\kappa_n = 0.04, \quad \kappa_p = 0.24, \quad \kappa_{np} = 0.02, \quad \kappa_\Delta = 0.02, \quad (10.86)$$

and the central chemical potentials are $\mu^n(0) = \mu^p(0) = 0.2 m_b c^2$. The configurations obtained have the following (fixed) central values: the central baryon density is $n(0) = 0.5776 \text{ fm}^{-3}$, which corresponds to 3.61 times nuclear density ($n_{\text{nucl}} = 0.16 \text{ fm}^{-3}$). The central proton entrainment is $\varepsilon_p(0) = 0.212$, and the proton fraction is found as $x_p(0) = 0.083$. We fix the relative rotation to $\mathcal{R} = 0.5$, i.e. the neutron superfluid is rotating 50% faster than the proton-electron fluid. In Table 10.1

$\Omega_n/2\pi$	0 Hz	100 Hz	500 Hz
$M_n [M_\odot]$	1.0978 (-0.02%)	1.0998 (-0.1%)	1.1509 (-2%)
$M_p [M_\odot]$	0.0998 (-0.02%)	0.0997 (-0.1%)	0.0959 (-2%)
$\mathcal{M} [M_\odot]$	1.1194 (-0.02%)	1.1210 (-0.04%)	1.1644 (0.04%)
$R_n^{\text{eq}} [\text{km}]$	13.545 (-0.01%)	13.570 (0.2%)	14.260 (5%)
$R_n^{\text{pol}} [\text{km}]$	13.545 (-0.01%)	13.527 (-0.1%)	13.103 (-3%)
$R_p^{\text{eq}} [\text{km}]$	13.545 (-0.01%)	13.534 (-0.1%)	13.302 (-2%)
$R_p^{\text{pol}} [\text{km}]$	13.545 (-0.01%)	13.527 (-0.1%)	13.103 (-3%)
$N(0)$	0.700102 (1e-4%)	0.69983 (2e-3%)	0.69267(-0.04%)
$\ N^i\ (\text{eq})$	0	0.00206 (0.1%)	0.01072 (3%)

Table 10.1: Numerical results Q_L and (in parentheses) relative differences $(Q_L - Q_{\text{sr}})/Q_L \times 100\%$ to the relativistic slow-rotation results Q_{sr} .

we show the results of the comparison to the relativistic slow-rotation code. We observe that generally the agreement is quite good, and (as expected) gets worse with higher rotation rates. However, we note that this slow-rotation code imposes an additional constraint on the radii, namely the two fluids are forced to share a common outer surface. Therefore part of the disagreement observed here does not actually stem from the slow-rotation approximation or numerical differences, but from the somewhat different assumptions in the model. Given these differences, the agreement seems very good.

10.6 Numerical Results

The existence of configurations with one fluid-surface having a prolate shape was found initially using the Newtonian analytic solution[377] in the slow-rotation approximation. While this might not be

very astrophysically realistic, it is still interesting to study this particularity of an interacting two-fluid system. We can confirm the existence of such configurations in the fully relativistic treatment, as reported earlier by us[378]. In order to show this, we choose the polytropic EOS parameters $\kappa_n = 0.016$, $\kappa_p = 0.16$, $\kappa_{np} = 0.008$, and $\kappa_\Delta = 0.03$, with the central chemical potentials $\mu^n(0) = 0.2m_b c^2$ and $\mu_p(0) = 0.198m_b c^2$. This corresponds to a central proton fraction of $x_p(0) = 0.05$ and a central proton-entrainment number of $\varepsilon_p(0) = 0.80$. In figure 10.4 we show the resulting configuration with

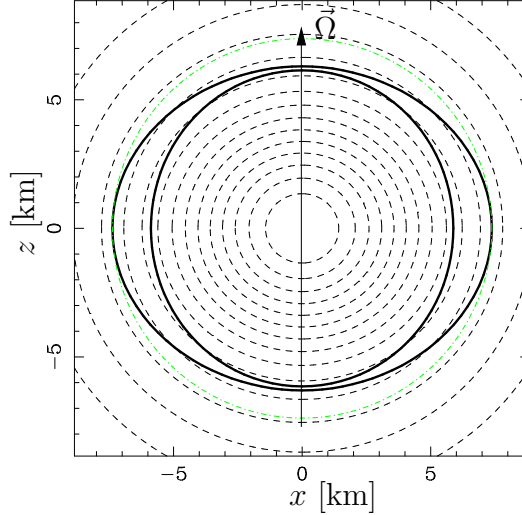


Figure 10.4: Meridional cross-section of an oblate-prolate two-fluid configuration. The dotted lines represent lines of constant “gravitational potential” N , while the thick lines are the respective surfaces of the neutron- and proton fluids.

the two fluids counter-rotating at $\Omega_n/2\pi = 1000$ Hz and $\Omega_p/2\pi = -100$ Hz. We define the ellipticity of fluid X as

$$\epsilon_X \equiv \frac{R_X(\text{eq}) - R_X(\text{pol})}{R_X(\text{eq})}, \tag{10.87}$$

in terms of the proper radii R of (10.84). Using this definition, this configuration is found to have $\epsilon_n = 0.137$, and $\epsilon_p = -0.037$, so the proton fluid has a prolate shape despite the fact that it is rotating. This is made possible by the effective interaction potential created by the neutron-fluid, which “squeezes” the proton-fluid, and overcomes the centrifugal potential.

EOS	κ_n	κ_p	κ_{np}	κ_Δ
I	0.05	0.5	0.025	0.02
II	0.05	0.5	0.0	0.0
III	0.05	0.5	-0.025	0.02

Table 10.2: Polytropic parameters defining EOS-models I, II, and III

To simplify the presentation of results, we focus in the following on three EOS-models, defined in table 10.2, which differ only by their interaction-terms. The EOS-models I and III differ by the sign of the “symmetry-interaction” term κ_{np} , which corresponds to a value of the canonical “symmetry-energy

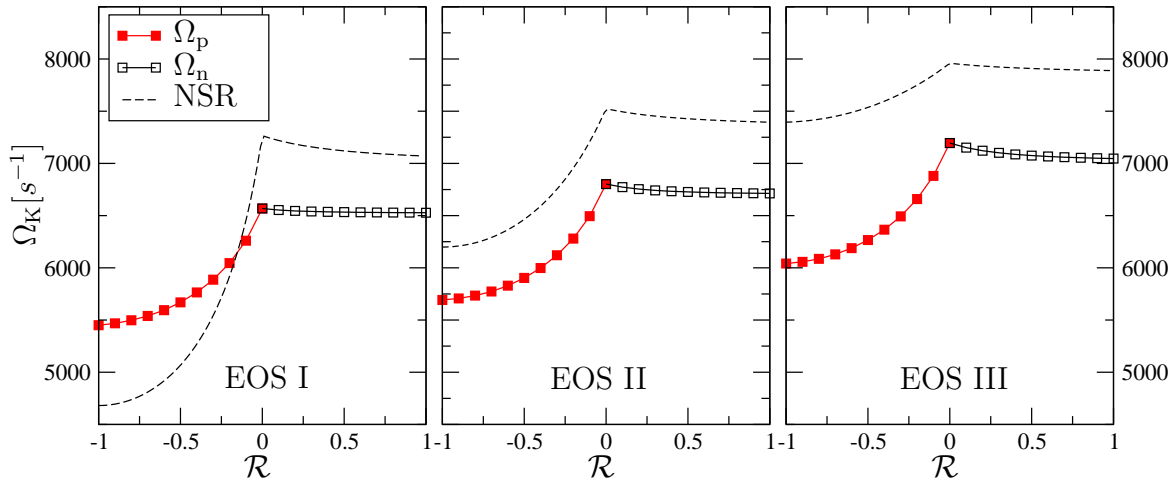


Figure 10.5: Kepler limit Ω_K (of the faster fluid) as a function of relative rotation \mathcal{R} for EOS-models I, II and III. The dashed line (NSR) represents the result from the analytic Newtonian slow-rotation solution (cf. Appendix 10.A)

term” σ , introduced in [377], of $\sigma = -0.5$ for EOS I and $\sigma = 0.5$ for EOS III. EOS II represents two fluids without local interactions. If not otherwise stated, we choose the central chemical potentials to be $\mu_n = \mu_p = 0.3 m_b c^2$. In the static case we obtain the results shown in Table 10.3 for these three EOS-models. We note that all three static configurations are on the stable branch of the mass-density relation, which can be seen explicitly in Fig. 10.7 for the case of EOS-model I. We note that when

	EOS I	EOS II	EOS III
n_c [fm^{-3}]	0.7177	0.7697	0.8612
$\varepsilon_p(0)$	0.273	0.0	0.301
$x_p(0)$	0.05	0.09	0.125
M [M_\odot]	1.586	1.532	1.448
\mathcal{M} [M_\odot]	1.460	1.409	1.332
R [km]	14.37	13.88	13.12

Table 10.3: Results for the central baryon number density n_c , entrainment ε_p , proton fraction x_p , total baryon mass M and gravitational mass \mathcal{M} and the proper radius R for EOS-models I, II and III in the static case.

considering rotation, the individual fluid radii will obviously change, but also the masses, because in the following we only consider stellar sequences of fixed central density.

Next we consider these stellar models rotating at their maximum rotation rate Ω_K (called Kepler limit) for a given relative rotation \mathcal{R} , which is shown in Fig. 10.5. The convention in this figure is to always plot as Ω_K the rotation rate of the faster fluid (which in this case also happens to be the outer fluid), i.e. the protons for $\mathcal{R} < 0$ and the neutrons for $\mathcal{R} > 0$. The rotation rate of the slower fluid is trivially determined by Ω_K and \mathcal{R} . Also shown (dashed line) is the result from the Newtonian slow-rotation solution (10.129). This is seen to overestimate the Kepler rate typically by about 15%, except for the case of EOS I, where it can even underestimate the Kepler limit for $\mathcal{R} < 0$. We see

that in the fixed central-density sequences considered here, the local maximum of the Kepler rate is always attained for the co-rotating configuration (i.e. $\mathcal{R} = 0$), which contrasts with the case of fixed mass-sequences considered in the Newtonian study [377]. A similar feature of Kepler decreasing as \mathcal{R} decreases through zero can be seen in the mean-field results of [124].

In the Fig. 10.6, we show the fluid surfaces of the two fluids rotating at the Kepler-rate for two different relative rotation rates, $\mathcal{R} = 0.1$ and $\mathcal{R} = 0.01$ respectively. We see the characteristic “cusp” appearing at the equator of the outer fluid, which indicates the onset of mass-shedding if the rotation rate were to be increased any further. Because we fixed the central densities of these configurations to be equal to the static case, it can be seen from Fig. 10.7 that both of these configurations belong to the so-called “supramassive” class, i.e. they do not have a corresponding stable non-rotating configuration of equal baryon-mass.

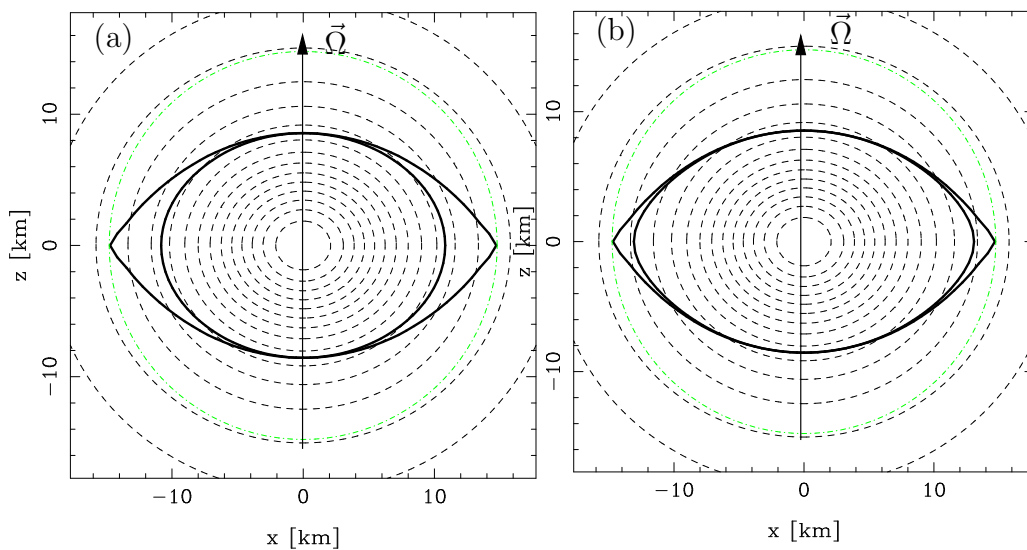


Figure 10.6: Kepler configurations for EOS-model I. Figure (a) shows the configuration rotating with a relative rotation rate of $\mathcal{R} = 0.1$, while in (b) the relative rotation rate is $\mathcal{R} = 0.01$.

Fig. 10.7 shows the mass-density diagram for the static configuration of EOS I and for three different relative rotation-rates at the Kepler-limit. The configurations to the right of the maximum are on the so-called “unstable branch”, because they will be subject to unstable modes resulting in collapse under small perturbations. The configurations above the dotted line correspond to stars on the unstable-branch of the static curve. They have no stable non-rotating counter-part, even if they are on the stable branch of the mass-curve of the rotating case, and they are therefore called “supramassive stars”. These configurations are stabilized by rotation and would collapse if slowed down below a certain critical rotation rate.

So far we have mostly considered stars with chemical equilibrium at the center, i.e. $\mu_n = \mu_p$. Incidentally, for the EOS-class considered here, the resulting static configurations share a common outer surface in this case. However, global chemical equilibrium is generally not possible for configurations with the two fluids rotating at different rates, which was shown by [22] and [377]. In order to model more “realistic” configurations, in which the proton-fluid mimics a neutron-star “crust” (albeit without any solidity) by extending further outside than the neutrons, we can easily achieve this by choosing different central densities (i.e. chemical potentials). For example, using EOS II and setting

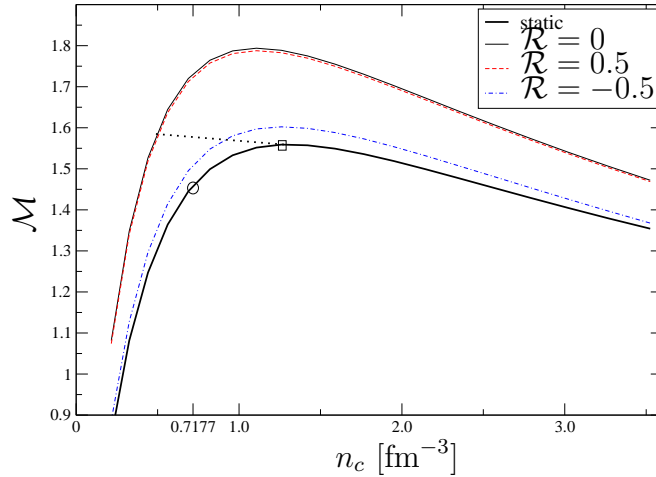


Figure 10.7: Gravitational mass \mathcal{M} as a function of the central baryon number density n_c for EOS-model I with a fixed central proton fraction of $x_p = 0.05$. The four curves correspond to the non-rotating ('static') case, the co-rotating Kepler-configuration ($\mathcal{R} = 0$), and two Kepler-configurations at relative rotation rates of $\mathcal{R} = 0.5$ and $\mathcal{R} = -0.5$ respectively. The small circle indicates the static configuration with central chemical potentials of $\mu_n = \mu_p = 0.3 m_b c^2$. The box indicates the maximum-mass configuration for the static case. The dotted line represents the constant baryon-mass sequence connecting to the static maximum-mass configuration. Configurations above this line have no stable non-rotating counterpart and are called "supramassive" stars.

$\mu_n = 0.228 m_b c^2$ and $\mu_p = 0.220 m_b c^2$, we obtain the configuration shown in Fig. 10.8. For this figure we have chosen the rotation rate of the fastest known millisecond pulsar, which has a period of $P \sim 1.56$ ms.

On the other hand, a similar configuration with $\mu_n = 0.28 m_b c^2$ and $\mu_p = 0.3 m_b c^2$ rotating at the Kepler-limit for a relative rotation rate of $\mathcal{R} = 0.01$ is displayed in Fig. 10.9. As can be seen by the cusp-formation, the Kepler-limit is determined by the *outer* fluid, i.e. the protons in this case, despite the fact that they are rotating *more slowly* than the neutrons. This is different to the case depicted in Fig. 10.5, in which the faster fluid also always happens to be the outer fluid, which is a particularity of this EOS-class and the choice of central chemical equilibrium $\mu_n = \mu_p$ (cf. [377]).

10.7 Conclusions

We have developed a theoretical framework and a numerical code for computing stationary, fully relativistic superfluid neutron star models.

Using this code we have reconfirmed the existence of oblate-prolate shaped two-fluid configurations, previously shown in [377, 378]. We have studied the dependency of the Kepler rate of a two-fluid star on the relative rotation rate \mathcal{R} . We have compared this to the Kepler-rate predicted by a Newtonian slow-rotation approximation, which is found to typically overestimate the Kepler-rate by about 25%, while it can also underestimate it for $R \neq 0$, as seen in the case of EOS I and $\mathcal{R} \lesssim -0.25$ (cf. Fig. 10.5).

The relative rotation rate can also have a large influence (at fixed central density) on the mass-

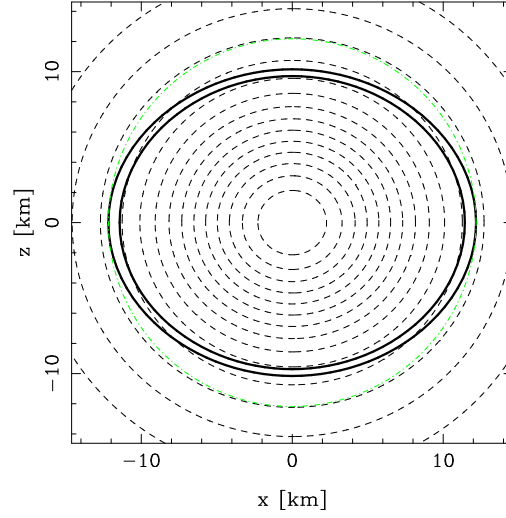


Figure 10.8: Configuration with protons rotating at the speed of the fastest known millisecond pulsar, $\Omega_p/2\pi = 641$ Hz, and $\Omega_n/2\pi = 645$ Hz. The protons are extending further outside than the neutrons. The physical parameters are $\mu_n = 0.228 m_b c^2$ and $\mu_p = 0.220 m_b c^2$, resulting in central baryon number density $n_c = 0.561 \text{ fm}^{-3}$, proton fraction $x_p = 0.09$ and a gravitational mass of $\mathcal{M} = 1.39 M_\odot$.

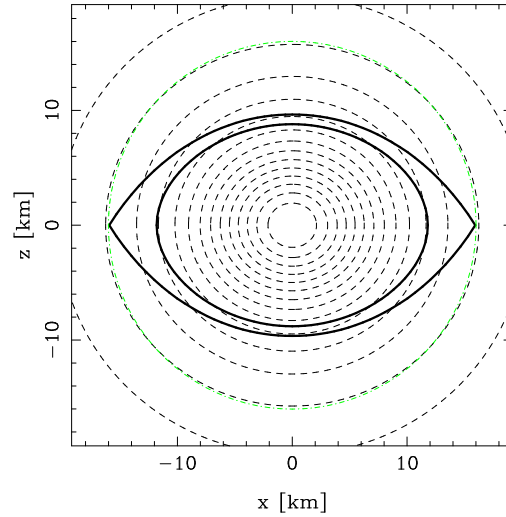


Figure 10.9: Kepler configuration at $\mathcal{R} = 0.01$ for $\mu_n = 0.28 m_b c^2$ and $\mu_p = 0.3 m_b c^2$, resulting in central baryon number density $n_c = 0.716 \text{ fm}^{-3}$, proton fraction $x_p = 0.09$ and a gravitational mass of $\mathcal{M} = 1.57 M_\odot$. The protons extend to the outer surface. The maximal rotation rates are found as $\Omega_n/2\pi = 924.5$ Hz and $\Omega_p/2\pi = 915.3$ Hz.

density relation, as shown in Fig. 10.7.

Another interesting aspect of this model is that we are not restricted to configurations which are in chemical equilibrium at the center. Choosing the central chemical potentials to be different allows one to emulate a neutron star “crust” (albeit a fluid one), as one fluid will now extend further outwards than the other, as can be seen in Fig. 10.8 and Fig. 10.9. One interesting observation from such configurations is that the Kepler-limit will be determined by the outer fluid (forming a cusp), while this can actually be rotating *slower* than the inner fluid.

We currently use a (quite general) EOS class of two-fluid polytropes, but this can be extended straightforwardly to more “realistic” nuclear-physics equations of state. In particular it might be interesting in the next step to use the first relativistic two-fluid EOS incorporating entrainment by [125]. Furthermore it would be important to add the presence of a solid crust and to allow for differential rotation in the superfluid neutrons. The astrophysically most interesting future extension of this work would probably consist in studying the oscillation modes of such models, which would be directly related to the emission of gravitational waves. In these non-stationary situations, however, dissipative mechanisms like viscosity and mutual friction would also start to play a role and should be included in the model.

APPENDIX

10.A The Newtonian analytic slow-rotation solution

A method for solving the stationary 2-fluid configuration in the Newtonian slow-rotation approximation was initially developed in [376], and was completed to include all EOS-interactions in [377] (in the following referred to as Paper I). Using this method, an analytic solution was found in Paper I for equations of state of the form $\mathcal{E} = \frac{1}{2}\kappa_n n_n^2 + \frac{1}{2}\kappa_p n_p^2 + \kappa_{np} n_n n_p + \beta^p n_p \Delta^2$. While this solution was very useful to study the qualitative properties of an interacting 2-fluid system, it is unfortunately not very suitable for comparison to the numerical solution presented in this paper. The reason for this lies in the somewhat unphysical behavior of entrainment in this model. Namely, the entrainment numbers (10.16) are found as $\varepsilon_p = 2\beta/m$, and $\varepsilon_n = 2x_p\beta/(m(1-x_p))$, where $x_p \equiv n_p/n$ is the proton fraction, which is constant for this EOS (cf. Paper I). Therefore the entrainment numbers are constant, independently of the densities, and so the entrainment effect would still be present in a 1-fluid region. This unphysical behavior did not pose a problem in the slow-rotation approximation, which consists of an expansion around a static chemical-equilibrium configuration: the two fluids share a common surface in the unperturbed state, and the rotation will only induce infinitesimal displacements of the fluids. In this framework there are therefore no finite 1-fluid regions. However, in a numerical code allowing for arbitrary rotations and deviations from chemical equilibrium, such an entrainment model would be problematic. The EOS-class (10.68) used in this work is therefore preferable on both physical and numerical grounds.

Fortunately, an analytic solution can also be found for this physically preferable EOS using the slow-rotation approach developed in Paper I. This solution is very valuable for quantitative comparisons with our numerical results, which have been presented in section 10.5.3. In this section we derive this new analytic solution, skipping some of the more technical steps, which have been explained in more detail already in Paper I.

Because of axisymmetry, the rotating solution only depends on the spherical coordinates r and

θ , while the static configuration is assumed to be spherically symmetric. The 2-fluid slow-rotation approximation proceeds by expanding any local stellar quantity Q as follows:

$$Q(r, \theta; \Omega_X) = Q^{(0)}(r) + \Omega_X Q^{XY}(r, \theta) \Omega_Y + \mathcal{O}(\Omega^4), \quad (10.88)$$

where here and in the following we automatically sum over repeated constituent indices $X = n, p$. We can separate the variables r and θ by expanding in Legendre Polynomials, i.e. $Q^{XY}(r, \theta) = \sum_l Q_l^{XY}(r) P_l(\cos \theta)$, and it can be shown that only the components $l = 0, 2$ will be nonzero in the solution. The solution is therefore fully determined by two ordinary differential equations for the components $\Phi_0^{XY}(r)$ and $\Phi_2^{XY}(r)$ of the perturbation of the gravitational potential. The information about the EOS enters via the following two “structure functions”, defined as

$$\mathcal{S}_{XY} \equiv \left(\frac{\partial^2 \mathcal{E}}{\partial n_X \partial n_Y} \Big|_0 \right)^{-1}, \quad \beta^X \equiv \frac{\partial^2 \mathcal{E}}{\partial n_X \partial \Delta^2} \Big|_0, \quad (10.89)$$

where $|_0$ denotes the derivatives to be evaluated at the static configuration. For the EOS (10.68), we find

$$\mathcal{S}_{XY} = \frac{1}{\mathcal{K}} \begin{pmatrix} \kappa_p & -\kappa_{np} \\ -\kappa_{np} & \kappa_n \end{pmatrix}, \quad (10.90)$$

where $\mathcal{K} \equiv \kappa_p \kappa_n - \kappa_{np}^2$, and

$$\beta^X(r) = \kappa_\Delta M^{XY} n_Y^{(0)}(r), \quad (10.91)$$

with the constant matrix M^{XY} defined as

$$M^{XY} \equiv \begin{pmatrix} 0 & 1 \\ 1 & 0 \end{pmatrix}. \quad (10.92)$$

We further introduce the “derived” structure functions,

$$k_A \equiv \mathcal{S}_{AB} m^B, \quad \text{and} \quad k \equiv m^A k_A, \quad (10.93)$$

which are constant for this EOS. The matrices E_A^{XY} , defined as

$$E_A^{XY}(r) \equiv \frac{1}{3} \mathcal{S}_{AB} (\delta^{B,XY} - 2\beta^B(r) \Delta^{XY}), \quad (10.94)$$

are now functions of r , contrary to the EOS treated in Paper I, in which they were constant. The constant auxiliary matrices $\delta^{A,XY}$ and Δ^{XY} are defined as

$$\delta^{n,XY} \equiv \begin{pmatrix} m^n & 0 \\ 0 & 0 \end{pmatrix}, \quad \delta^{p,XY} \equiv \begin{pmatrix} 0 & 0 \\ 0 & m^p \end{pmatrix}, \quad (10.95)$$

$$\Delta^{XY} \equiv \begin{pmatrix} 1 & -1 \\ -1 & 1 \end{pmatrix}. \quad (10.96)$$

The *static* background solution only depends on \mathcal{S}_{XY} , and is identical to the one found in Paper I. Namely, in “natural units” defined by $\rho^{(0)}(0) = 1$ and $R = 1$, this static solution can be written as

$$\rho^{(0)}(r) = \frac{\sin(r\sqrt{k})}{r\sqrt{k}}. \quad (10.97)$$

In these units it must be true that $\rho^{(0)}(1) = 0$, which leads to the condition $k = m^A k_A = \pi^2$. This relation can be used to rescale the EOS parameters κ_n , κ_p and κ_{np} to natural units. The respective particle number densities $n_A^{(0)}(r)$ are expressible as

$$n_A^{(0)}(r) = \frac{k_A}{\pi^2} \rho^{(0)}(r). \quad (10.98)$$

Substituting this into (10.94), we can write

$$E_A^{XY}(r) = \tilde{E}_A^{XY} - \hat{E}_A^{XY} \rho^{(0)}(r), \quad (10.99)$$

in terms of the two constant matrices

$$\begin{aligned} \tilde{E}_A^{XY} &\equiv \frac{1}{3} \mathcal{S}_{AB} \delta^{B,XY}, \\ \hat{E}_A^{XY} &\equiv \frac{2}{3\rho^{(0)}} \mathcal{S}_{AB} \beta^B \Delta^{XY}, \end{aligned} \quad (10.100)$$

and for $E^{XY} \equiv m^A E_A^{XY}$, we write in an analogous manner

$$E^{XY} = \tilde{E}^{XY} - \hat{E}^{XY} \rho^{(0)}(r), \quad (10.101)$$

with

$$\begin{aligned} \tilde{E}^{XY} &= \frac{1}{3} k_B \delta^{B,XY}, \\ \hat{E}^{XY} &= \frac{4\kappa_\Delta}{3\pi^2} k_n k_p \Delta^{XY}. \end{aligned} \quad (10.102)$$

We can now write the differential equations determining the solution for the given EOS, namely

$$\mathcal{D}_0 \Phi_0^{XY} + \pi^2 \Phi_0^{XY} = \mathcal{C}^{XY} + r^2 \tilde{E}^{XY} - r^2 \rho^{(0)} \hat{E}^{XY}, \quad (10.103)$$

$$\mathcal{D}_2 \Phi_2^{XY} + \pi^2 \Phi_2^{XY} = -r^2 \tilde{E}^{XY} + r^2 \rho^{(0)} \hat{E}^{XY}, \quad (10.104)$$

where the differential operator \mathcal{D}_l is defined as

$$\mathcal{D}_l \equiv \frac{d^2}{dr^2} + \frac{2}{r} \frac{d}{dr} - \frac{l(l+1)}{r^2}. \quad (10.105)$$

We note that the only difference of this EOS to the one studied in Paper I concerns the entrainment $\beta^X(r)$. We can therefore formally recover the results from Paper I in the limit $\kappa_\Delta \rightarrow 0$, which corresponds to $\hat{E}^{XY} \rightarrow 0$ and $\tilde{E}_A^{XY} \rightarrow 0$. The constant matrix \mathcal{C}^{XY} is determined by the choice of stellar sequence, e.g. either characterized by fixed central densities (FCD) or fixed masses (FM). The solution to the above equations also determines the density distribution of the two-fluid star, namely via the relations

$$n_{A,0}^{XY}(r) = \mathcal{S}_{AB} \mathcal{C}^{B,XY} + r^2 E_A^{XY} - k_A \Phi_0^{XY}, \quad (10.106)$$

$$n_{A,2}^{XY}(r) = -r^2 E_A^{XY} - k_A \Phi_2^{XY}, \quad (10.107)$$

where the constants $\mathcal{C}^{A,XY}$ are also determined by the choice of stellar sequence, and they satisfy the relation $\mathcal{C}^{XY} = k_A \mathcal{C}^{A,XY}$. The complete slow-rotation solution for the density distribution of the two fluids can be written as

$$n_A(r, \theta) = n_A^{(0)}(r) + \Omega_X (n_{A,0}^{XY} + n_{A,2}^{XY} P_2(\cos \theta)) \Omega_Y. \quad (10.108)$$

The general (regular) solution of equations (10.103) and (10.104) can be found explicitly as

$$\begin{aligned} \Phi_0^{XY}(r) &= \mathcal{A}_0^{XY} \frac{J_{1/2}(r\pi)}{\sqrt{r}} + \frac{\tilde{E}^{XY}}{\pi^2} \left(r^2 - \frac{6}{\pi^2} \right) + \frac{\mathcal{C}^{XY}}{\pi^2} \\ &\quad - \frac{\hat{E}^{XY}}{12\pi^4} \{ 3r\pi \sin r\pi + (3 - 2\pi^2 r^2) \cos r\pi \}, \end{aligned} \quad (10.109)$$

$$\begin{aligned} \Phi_2^{XY}(r) &= \mathcal{A}_2^{XY} \frac{J_{5/2}(r\pi)}{\sqrt{r}} - \frac{\tilde{E}^{XY}}{\pi^2} r^2 \\ &\quad - \frac{\hat{E}^{XY}}{12\pi^7 r^3} \{ (45 + 2\pi^4 r^4) r\pi \cos r\pi \\ &\quad \quad + 15(r^2 \pi^2 - 3) \sin r\pi \}, \end{aligned} \quad (10.110)$$

where \mathcal{A}_0^{XY} and \mathcal{A}_2^{XY} are constants of integration, and $J_n(x)$ are the standard Bessel functions. One can verify the asymptotic behavior $\Phi_2^{XY} \sim r^2$ as $r \rightarrow 0$, which is required for regularity. In addition to the regularity requirements at the center, the solution must satisfy the following boundary condition at the surface ($r = 1$):

$$\Phi_l^{XY'}(1) + l(l+1)\Phi_l^{XY}(1) = 0. \quad (10.111)$$

These boundary conditions result in the following relations for the integration constants \mathcal{A}_0^{XY} and \mathcal{A}_2^{XY} :

$$\begin{aligned} 4\pi^4 \sqrt{2} \mathcal{A}_0^{XY} &= 12(\pi^2 - 2)\tilde{E}^{XY} + (1 - \pi^2)\hat{E}^{XY} \\ &\quad + 4\pi^2 \mathcal{C}^{XY}, \end{aligned} \quad (10.112)$$

$$\sqrt{2} \mathcal{A}_2^{XY} = \frac{5}{\pi^2} \tilde{E}^{XY} - \frac{5}{\pi^4} (3 + 2\pi^2) \hat{E}^{XY}, \quad (10.113)$$

Fixed central density (FCD) sequence

The FCD-sequence is the most directly comparable to the numerical results discussed in this paper. This sequence is defined by the condition $n_{A,0}^{XY}(0) = 0$, and in this case the remaining constant of integration can be determined as

$$\mathcal{C}_{\text{FCD}}^{XY} = -3 \left(1 - \frac{4}{\pi^2} \right) \tilde{E}^{XY} + \frac{1}{4} \hat{E}^{XY}, \quad (10.114)$$

and we also have the relation

$$\mathcal{S}_{AB} \mathcal{C}_{\text{FCD}}^{B,XY} = \frac{k_A}{\pi^2} \mathcal{C}_{\text{FCD}}^{XY}. \quad (10.115)$$

Putting all the pieces together, we arrive at the following explicit solution for the density perturbations of the FCD sequence:

$$\begin{aligned} n_{A,0,\text{FCD}}^{XY} &= -\frac{6k_A \tilde{E}^{XY}}{\pi^4} \left(\frac{\sin r\pi}{r\pi} + \frac{r^2 \pi^2}{6} - 1 \right) + \tilde{E}_A^{XY} r^2 \\ &\quad - \frac{k_A \hat{E}^{XY}}{4\pi^4} \left((1 - r^2 \pi^2) \frac{\sin r\pi}{r\pi} - (1 - \frac{2}{3} r^2 \pi^2) \cos r\pi \right) \\ &\quad - \frac{\hat{E}_A^{XY}}{\pi^2} r\pi \sin r\pi, \end{aligned} \quad (10.116)$$

$$\begin{aligned}
n_{A,2}^{XY}(r) &= \frac{k_A \tilde{E}^{XY}}{\pi^2} \left(r^2 - \frac{5}{\sqrt{2}} \frac{J_{5/2}(r\pi)}{\sqrt{r}} \right) - \tilde{E}_A^{XY} r^2 \\
&+ \frac{5}{6} \frac{k_A \hat{E}^{XY}}{\pi^5 r^3} \left\{ \left(\frac{\pi^2}{5} r^4 - 3 \right) r\pi \cos r\pi - (r^2 \pi^2 - 3) \sin r\pi \right\} \\
&+ \frac{\hat{E}_A^{XY}}{\pi^2} r\pi \sin r\pi, \tag{10.117}
\end{aligned}$$

in terms of the constant “structure matrices” \tilde{E} and \hat{E} defined in Eqs. (10.100) and (10.102).

Fixed-mass (FM) stellar sequence

Although in this paper we only made use of the FCD-solution, for completeness we will also give the solution corresponding to a fixed-mass sequence, which might be physically more interesting. The difference to the FCD-solution only concerns the $l = 0$ component, while $n_{A,2}^{XY}$ is the same in both cases. As discussed in Paper I, the FM-sequence is characterized by the conditions

$$\int_0^1 r^2 n_{A,0,\text{FM}}^{XY}(r) dr = 0, \tag{10.118}$$

which lead to the following condition for the potential

$$\Phi_{0,\text{FM}}^{XY}(1) = 0. \tag{10.119}$$

This results in the integration constant

$$c_{\text{FM}}^{XY} = \left(\frac{6}{\pi^2} - 1 \right) \tilde{E}^{XY} + \left(\frac{1}{6} - \frac{1}{4\pi^2} \right) \hat{E}^{XY}, \tag{10.120}$$

while we can similarly determine $\mathcal{S}_{AB} \mathcal{C}^{B,XY}$ from (10.118). Inserting this into (10.109) we get

$$\begin{aligned}
\Phi_{0,\text{FM}}^{XY}(r) &= \frac{\tilde{E}^{XY}}{\pi^2} \left(r^2 - 1 + \sqrt{2} \frac{J_{1/2}(r\pi)}{\sqrt{r}} \right) \\
&+ \frac{\hat{E}^{XY}}{12\pi^4} \left(2\pi^2 - 3 + (2\pi^2 r^2 - 3) \cos r\pi \right. \\
&\quad \left. - (1 + 3r^2) \frac{\pi^2}{\sqrt{2}} \frac{J_{1/2}(r\pi)}{\sqrt{r}} \right). \tag{10.121}
\end{aligned}$$

The $l = 0$ density coefficient is therefore found by using (10.106):

$$\begin{aligned}
n_{A,0,\text{FM}}^{XY} &= \frac{k_A \tilde{E}^{XY}}{5\pi^4} \left(30 + 3\pi^2 - 5r^2 \pi^2 - \frac{10\pi}{r} \sin r\pi \right) \\
&+ \tilde{E}_A^{XY} \left(r^2 - \frac{3}{5} \right) + \frac{\hat{E}_A^{XY}}{\pi^2} \left(3 \left(1 - \frac{6}{\pi^2} \right) - r\pi \sin r\pi \right) \\
&- \frac{k_A \hat{E}^{XY}}{12\pi^4} \left(36 \left(1 - \frac{6}{\pi^2} \right) - (3 - 2r^2 \pi^2) \cos r\pi \right. \\
&\quad \left. - (1 + 3r^2) \frac{\pi}{r} \sin r\pi \right), \tag{10.122}
\end{aligned}$$

which completes the analytic solution in the FM case.

Calculating the Kepler-limit

We briefly review the method of calculating the Kepler-limit using the slow-rotation solution presented above. The result of this calculation was used for the Newtonian slow-rotation Kepler-limit presented in Fig. 10.5. As derived in Paper I, the Kepler-rate to order Ω^2 for each of the two fluids can be expressed as the solution of the equation

$$\Omega_A^2 = \Omega_{(0)}^2 + \Omega_X \delta q_A^{XY} \Omega_Y + \mathcal{O}(\Omega^4), \quad (10.123)$$

where the zeroth-order expression is

$$\Omega_{(0)}^2 = \Phi^{(0)'}(1), \quad (10.124)$$

and the second-order correction terms reads as

$$\delta q_A^{XY} = \left[-\frac{3}{k_A} \left(n_{A,0}^{XY} - \frac{1}{2} n_{A,2}^{XY} \right) + \Phi_0^{XY'} - \frac{1}{2} \Phi_2^{XY'} \right]_{r=1}. \quad (10.125)$$

For the EOS-class considered here, we find

$$\Omega_{(0)}^2 = \frac{4}{\pi} G \rho(0), \quad (10.126)$$

$$\begin{aligned} \delta q_{A,\text{FCD}}^{XY} &= -\frac{9\tilde{E}_A^{XY}}{2k_A} + \frac{\hat{E}^{XY}}{12\pi^4} (6 - 7\pi^2) \\ &\quad + \frac{\hat{E}^{XY}}{\pi^4} (5\pi^2 - 24), \end{aligned} \quad (10.127)$$

$$\begin{aligned} \delta q_{A,\text{FM}}^{XY} &= \frac{6}{\pi^2} \left(\frac{1}{5} - \frac{3}{\pi^2} \right) \tilde{E}^{XY} - \frac{9\hat{E}_A^{XY}}{k_A \pi^4} (\pi^2 - 6) \\ &\quad - \frac{\hat{E}^{XY}}{4\pi^6} (216 - 39\pi^2 + 2\pi^4) - \frac{27}{10k_A} \tilde{E}_A^{XY}. \end{aligned} \quad (10.128)$$

For each fluid A , we find the Kepler-limit $\Omega_{K,A}(\Omega_B)$ (where $B \neq A$) by solving the quadratic equation (10.123). The Kepler-limit is then interpreted as the corresponding solution for the *faster* fluid, which in this case corresponds to the outer fluid, i.e. we have

$$\Omega_K = \begin{cases} \Omega_{K,n}(\mathcal{R}), & \text{for } \mathcal{R} > 0, \\ \Omega_{K,p}(\mathcal{R}), & \text{for } \mathcal{R} < 0. \end{cases} \quad (10.129)$$

Chapitre 11

The gyromagnetic ratio of rapidly rotating compact stars in general relativity

Version publiée : J. Novak et E. Marcq, Classical and Quantum Gravity 20, pp.3051-3060 (2003).

Sommaire

11.1 Introduction	341
11.2 Model and assumptions	342
11.3 Numerical studies	344
11.4 Conclusions	351

11.1 Introduction

For steadily rotating, charged massive bodies, the gyromagnetic factor g is defined as the ratio

$$g = \frac{2MM}{QJ}; \tag{11.1}$$

where M is the mass, Q the total charge and J the angular momentum of the system. \mathcal{M} is the magnetic moment of the system, linked with the motion of the charges that are accounting for Q . With such a definition, in classical electrodynamics a rotating charged particle has a gyromagnetic factor equal to 1. The same is thus true for any system in classical electrodynamics, with a constant ratio of charge and mass density. On the other hand, within general relativity, the gyromagnetic ratio for all charged and rotating black holes is $g = 2$. Many points concerning the gyromagnetic ratio for isolated systems within classical electrodynamics, quantum theory and general relativity have been studied by Pfister and King [367]. The question we try to address here is the following one. How does the gyromagnetic factor behave for “intermediate” objects in general relativity, that possess a gravitational field weaker than that of black holes, but in which strong field effects are not negligible?

The aim of this paper is to try to answer this question by numerically studying the g -factor of rotating and charged relativistic compact stars, within the framework of general relativity. We use a

self-consistent physical model, in which matter is supposed to be a charged (insulator type) perfect fluid; axisymmetric and in stationary rotation. As it will be shown later, the only limitation shall be on neglecting the electromagnetic forces acting on hydrodynamic equilibrium, making our study a “low charge” approximate one; but we take into account the electromagnetic field contribution to the total energy-momentum tensor. The variation of the gyromagnetic ratio as a function of the number of particles in the system, or as a function of the rotation frequency will also be discussed. Details of the physical model are presented in section 11.2, section 11.3 is then giving results of the numerical study for two equations of state, which determine local properties of matter, and making comparison with previous works. Finally, section 11.4 summarises results and gives some concluding remarks.

11.2 Model and assumptions

We here give the most important assumptions made in our study; complete details of the formalism and the way numerical stars are computed can be found in Bonazzola *et al.* [67] and in Bocquet *et al.* [64] for the magnetised configurations.

11.2.1 Stationary and axisymmetric spacetime

We want to solve the coupled Einstein-Maxwell equations to get general relativistic magnetised models of stationary rotating bodies. We make the assumption that the spacetime is also stationary (asymptotically timelike Killing vector field), axisymmetric (spacelike Killing vector field which vanishes on a timelike 2-surface, *axis of symmetry* and whose orbits are closed curves) and asymptotically flat. In addition, we suppose that the source of the gravitational field satisfies the *circularity condition*, equivalent to the absence of meridional convective currents and only *poloidal* magnetic field is allowed. We then use MSQI (Maximal Slicing - Quasi Isotropic, see [67]) coordinates (t, r, θ, φ) , in which the metric tensor takes the form

$$ds^2 = g_{\mu\nu} dx^\mu dx^\nu = -N^2 dt^2 + B^2 r^2 \sin^2 \theta (d\varphi - \beta^\varphi dt)^2 + A^2 (dr^2 + r^2 d\theta^2), \quad (11.2)$$

where N, β^φ, A and B are four functions of (r, θ) .

With our hypothesis, the electromagnetic field tensor $F_{\alpha\beta}$ must be derived from a potential 1-form with the following components

$$A_\alpha = (A_t, 0, 0, A_\varphi). \quad (11.3)$$

The Einstein-Maxwell equations result in a set of six coupled non-linear elliptic equations for the four metric and the two electromagnetic potentials (see [67] and [64]). The right-hand side of this system also involves matter terms (density and charge currents), which will be discussed in next section.

11.2.2 Fluid properties

The matter is supposed to consist of a perfect fluid, so there exists a privileged vector field: the 4-velocity u^α . The energy-momentum tensor takes its usual form

$$T^{\mu\nu} = (e + p)u^\mu u^\nu + pg^{\mu\nu} + T_{\text{EM}}^{\mu\nu}, \quad (11.4)$$

where p is the fluid pressure and e the energy density measured in the fluid frame.

$$T_{\text{EM}}^{\mu\nu} = 1/4\pi \left(F^{\mu\alpha} F_\alpha^\nu - 1/4 F_{\alpha\beta} F^{\alpha\beta} g^{\mu\nu} \right)$$

is the electromagnetic contribution to the energy-momentum tensor. Following [67], we note $\Omega = u^\varphi/u^t$ and define Γ as the Lorentz factor linking the fluid comoving observer and the locally non-rotating one. We make the assumption that the matter is rigidly rotating ($\Omega = \text{constant}$) and that the equation of state (EOS) is a one parameter EOS (ignoring the influence of temperature): $e = e(n_B)$ and $p = p(n_B)$, with n_B being the proper baryon density.

The momentum-energy conservation gives an equation of stationary motion for the fluid, which can be written as a first integral of motion (the electromagnetic contribution to the energy-momentum tensor is not considered yet), see [67]

$$\ln \frac{e+p}{n_B} + \ln N - \ln \Gamma = \text{constant}. \quad (11.5)$$

We turn now to the electromagnetic part; in order to have a complete charged body, with a constant ratio of charge and mass density (see [367]), we suppose, contrary to [64] or [105], that our system consists of an insulator, so that currents originate only from macroscopic charge movement. The 4-current is thus proportional to $j^\mu \sim u^\mu/\Gamma$ implying that $j^\varphi = \Omega j^t$. Taking then electromagnetic force term $f_i = F_{i\sigma}j^\sigma/(e+p)$ into account, the momentum-energy conservation reads

$$\partial_i \left(\ln \frac{e+p}{n_B} + \ln N - \ln \Gamma \right) + \frac{1}{e+p} j^t \partial_i (\Omega A_\varphi - A_t) = 0. \quad (11.6)$$

The integrability condition of this equation is that the last term is a gradient, so that there exists a function $M(r, \theta)$ such that $j^t \partial_i (\Omega A_\varphi - A_t) = (e+p) \partial_i M$. Following the same arguments as in [67], there must exist a regular function m , such that

$$j^t = (e+p)m (\Omega A_\varphi - A_t), \quad \text{with} \quad M(r, \theta) = \int_0^{\Omega A_\varphi(r, \theta) - A_t(r, \theta)} m(x) dx. \quad (11.7)$$

But, this gives too large a freedom for the distribution of charged particles inside the star. In particular, the charge density j^t is independent of the baryon density n_B , and the g -factor can, in principle, take any value. It is also irrelevant to compare the g -factor obtained in this way, with its value 1 in classical electrodynamics, where it is supposed that charge currents are directly proportional to mass currents and charge density to mass density [367]. So we replace (11.7) by

$$j^t = \chi n_B, \quad \text{and} \quad M = 0, \quad (11.8)$$

χ being the constant ratio between the charge and particle densities, it is an input parameter (together with the central density and the angular velocity) that controls the total charge of the system. It means that we do not integrate exactly momentum-energy conservation equation (11.6), since we neglect the electromagnetic forces. It will be shown in section 11.3 that this assumption is valid for low total charges, where the electromagnetic forces are indeed negligible, when compared to pressure, gravitational and centrifugal forces.

11.2.3 Accuracy indicators

To solve the six elliptical Poisson-like equations described in section 11.2.1, we use *spectral methods* as described by Grandclément *et al.* [228]. The complete numerical procedure is presented in [64] as well as many tests of the numerical code. Let us here emphasise that for our computations of spacetimes, we

have very reliable and independent tests through the virial identities GRV2 (Bonazzola [65], Bonazzola and Gourgoulhon [76]) and GRV3 (Gourgoulhon and Bonazzola [220]), this latter being a relativistic generalisation of the classical virial theorem. GRV2 and GRV3 are integral identities which must be satisfied by any solution of the Einstein-Maxwell equations we solve here, and are not imposed during the numerical procedure. They are very sensitive to any physical inaccuracy in the model, including eventual problems in the equation of state. In the following, when presenting accuracy of numerical results, we will refer to the accuracy by which the numerical solution satisfies these virial identities. With the exception of results shown in figure 11.1, where error bars are displayed, we only show results with better relative accuracy than 10^{-5} .

As presented by Bonazzola *et al.* [67], a key point of the numerical method is to be able to integrate Einstein-Maxwell equations up to spatial infinity, using a change of variable of the type $u = 1/r$ outside the star. This allows us to impose exact boundary conditions at $r \rightarrow \infty$, and to compute global quantities from asymptotic behaviour of the fields or integrals over the whole space. We can therefore compute values of the total gravitational mass M and the total angular momentum J , from the gravitational field $g_{\mu\nu}$; the total charge Q and the magnetic moment \mathcal{M} from the electromagnetic potential A_μ . Another global quantity characterising the star is the *circumferential radius* R_{circ} , defined as star's equatorial circumference (measured by the metric (11.2)) divided by 2π

$$R_{\text{circ}} = B\left(R, \frac{\pi}{2}\right) R, \quad (11.9)$$

where R is the coordinate equatorial radius. Finally, we shall use the total baryon number of the star and its baryon mass M_{B} .

11.3 Numerical studies

To calculate the g -factor of a given model, in addition to the choice of a particular equation of state, one has to set the three following parameters: the central density $n_{\text{B}}(r=0)$ (or, equivalently, the central log-enthalpy $\ln(e+p)/n_{\text{B}}|_{r=0}$), the angular velocity Ω and the ratio between mass and charge densities χ (11.8).

11.3.1 Polytropes

In this part we choose the EOS to be a polytropic one, of the form (6.40) of reference [67]: $p = \kappa n_{\text{B}}^\gamma$. We took $\gamma = 2$ and $\kappa = 0.07 \rho_{\text{nuc}} c^2 / n_{\text{nuc}}^2$, where nuclear density $\rho_{\text{nuc}} = 1.66 \times 10^{17} \text{kg/m}^3$ and $n_{\text{nuc}} = 0.1 \text{fm}^{-3}$. We first want to test the validity of our assumption neglecting electromagnetic forces in the equilibrium of the fluid. We computed a sequence of configurations increasing the total charge, at fixed angular velocity $\Omega = 200 \text{ Hz}$ and fixed number of baryons (equivalent to 1.6 solar mass). Results for the g -factor (11.1) as a function of the dimensionless ratio Q/M are displayed in figure 11.1, together with the errors given by the virial identities (see section 11.2.3). For $Q/M \lesssim 0.01$, g is constant at 10^{-5} accuracy. For $Q/M \gtrsim 0.01$, g starts to vary, but this variation remains within error bars, that become very important as $Q/M \rightarrow 1$. This indicates that the fact that we are neglecting electromagnetic forces in the equilibrium of the star induces an error that is lower than the numerical one, as long as $Q/M \lesssim 0.01$. It may be seen as a “low charge” approximation for our model and, *within this approximation*, we have checked with different equations of state (other polytropes, incompressible fluid EOS, strange matter EOS) that the g -factor would not depend on the charge. Let us say here

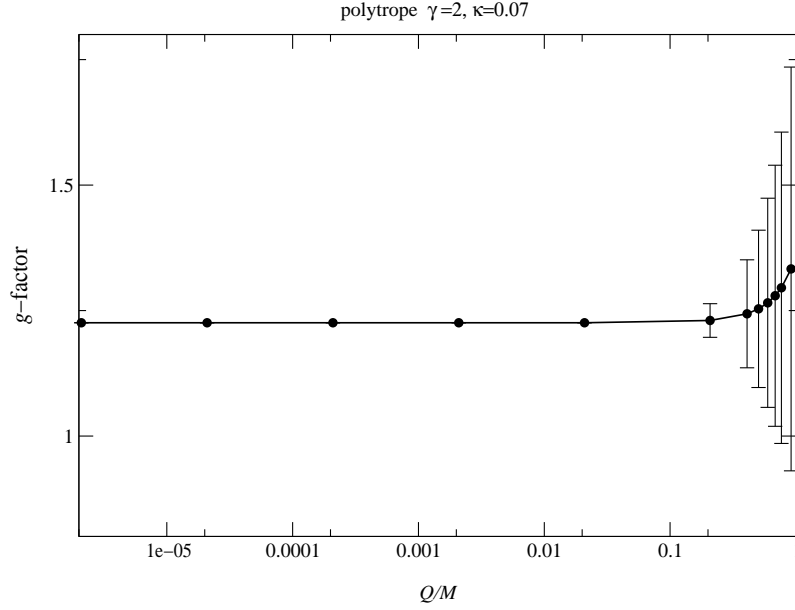


Figure 11.1: Variation of the g -factor as a function of the dimensionless ratio (total charge) / (gravitational mass), for a polytrope. Angular velocity Ω and baryon mass M_B are constant, being respectively equal to 200 Hz and $1.6M_\odot$. Error bars are given by the GRV2 test.

that, although we are neglecting electromagnetic forces in the fluid equilibrium, we are taking the electromagnetic field into account in the sources of Einstein equations.

The regime for which $Q/M > 1$ does not seem realistic for a perfect fluid. Indeed, the repulsive Coulomb force acting on charged particles becomes comparable to the gravitational force and pressure. Therefore, there may not exist any stationary configuration for Q/M too larger than 1: the electrostatic force would overcome the gravitational one and disperse particles. Moreover, Mustafa *et al.* [328] have shown that, in the case of a slowly rotating charged shell, when $Q/M > 1$ there is no upper or lower bound on the value of the g -factor. Finally, in order to find an acceptable stationary solution for $0.01 \lesssim Q/M < 1$, one would have to satisfy both equations (11.7) and $j^t = \chi n_B$. These are, in general, incompatible for a constant angular velocity Ω and one would have to allow for differential rotation of the fluid. This has not been done in our study and it would certainly be an improvement of our work. In the following, we will stay at $Q/M = 10^{-3}$ and will consider that g is independent of the total charge, in the low charge regime.

Now, we look at the variation of g , when the number of particles (the baryon mass M_B) of the rotating polytrope is changed. Results for the g -factor are displayed in figure 11.2 (solid line), together with the value of the lapse N at the centre of the star (dashed line). The parameter varying along both curves is the central density and we retrieve the well-known result of the existence of a maximal mass for those stars. Thus, the higher branch of each curve corresponds to unstable configurations. The Newtonian limit $g = 1$ is recovered at low baryon masses, corresponding to weak gravitational field ($N_c \rightarrow 1$). In more relativistic regime, the g -factor follows roughly the variation of the central lapse, never reaching the value of 2 (corresponding to $N_c = 0$), which corresponds to a charged black

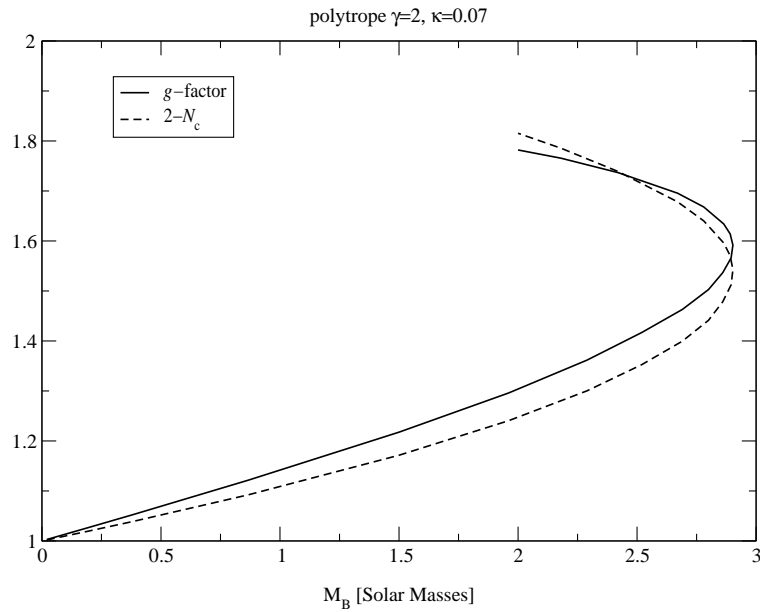


Figure 11.2: Variation of the g -factor and of the central lapse $N_c = N(r = 0)$, as a function of baryon mass, for a polytrope. Angular velocity $\Omega = 10$ Hz is kept constant.

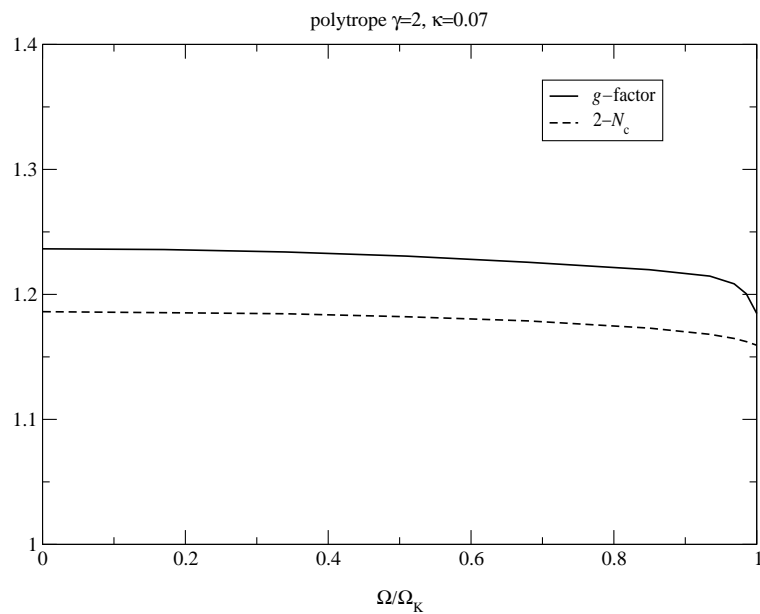


Figure 11.3: Variation of the g -factor and of the central lapse $N_c = N(r = 0)$, as a function of the angular velocity, for a polytrope. The baryon mass $M_B = 1.6M_\odot$ is kept constant.

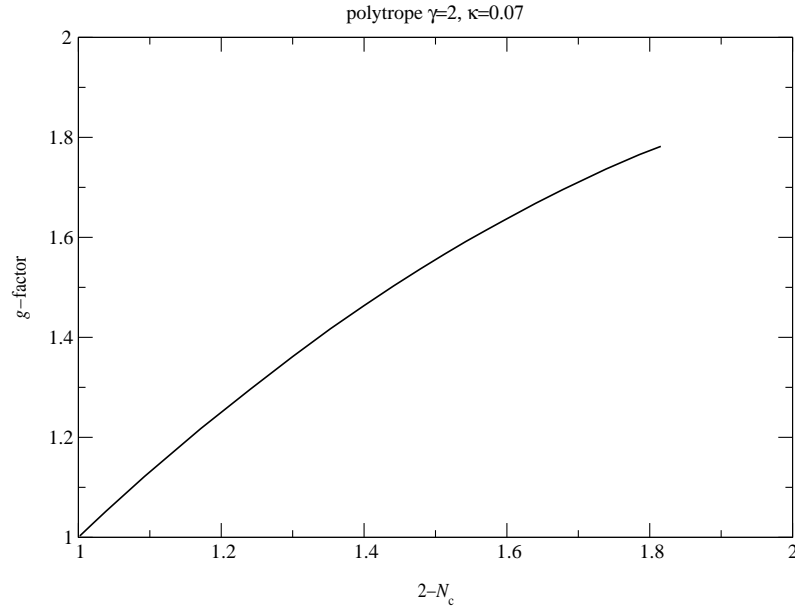


Figure 11.4: Variation of the g -factor as a function of the central lapse $N_c = N(r = 0)$, for a polytrope. The angular velocity $\Omega = 10$ Hz is kept constant.

hole. The maximal value that could be reached (for an *unstable* configuration) was $g = 1.8$, if only *stable* solutions are considered, then one has $g \leq 1.6$.

The third parameter whose influence we want to study is the angular velocity Ω . Therefore, at fixed number of particles in the star, and fixed total charge, we varied Ω from (almost) 0 to the maximal value, called *Keplerian frequency* (Ω_K), where the centrifugal force at the equator compensate the gravitational attraction (shedding limit). The variation of the g -factor as a function of Ω/Ω_K , as well as that of a linear combination of the central lapse $2 - N_c$ are displayed in figure 11.3. Both quantities show the same type of behaviour: they are decreasing functions, mainly near $\Omega \sim \Omega_K$, but the overall change is relatively small, when compared to that of figure 11.2. We have explored here high angular velocities, without any “slow-rotation” assumption, but the influence of these high velocities seems rather small. We have checked at different masses, always obtaining the same kind of result. Here again, we see that $2 - N_c$ and g follow the same type of evolution, when varying Ω . We therefore have plotted the g -factor, as a function of $2 - N_c$ as shown in figure 11.4, when varying the central value of the density $n_B(r = 0)$, like in figure 11.2. Contrary to that figure, there is no sign of the maximal mass point, the g -factor being directly dependent on the strength of the gravitational field at the centre of the star. It seems that the gyromagnetic factor (11.1) might be another indicator of the strength of the gravitational field in self-gravitating objects: when gravity is weak (well described by Newtonian theory), we have $g \sim 1$; when the star is very compact (even unstable) g takes its highest values. Finally, for a black hole, where gravity dominates over other forces, we have $g = 2$.

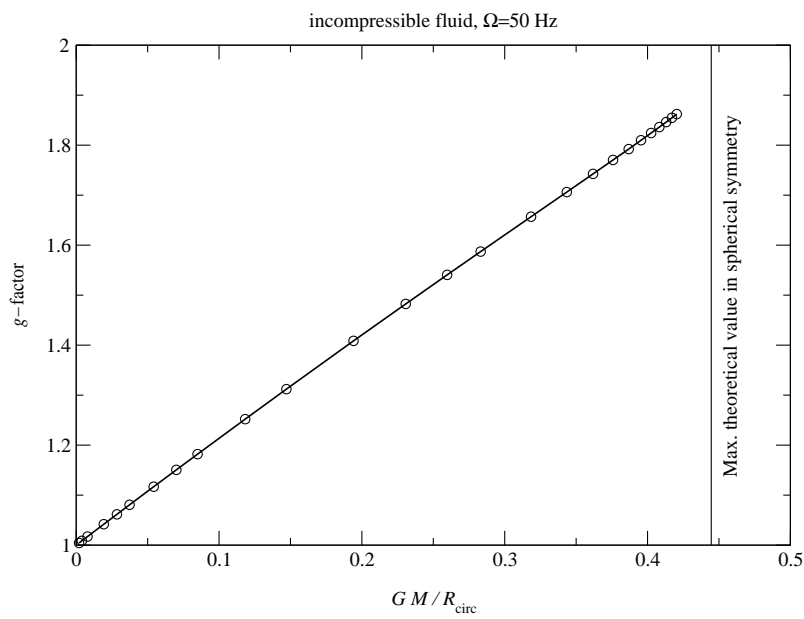


Figure 11.5: Variation of the g -factor as a function of the compaction parameter $\mathcal{C} = M/R_{\text{circ}}$, at constant angular velocity $\Omega = 50$ Hz, for an incompressible fluid. Circles show the model that have been computed. The vertical line at $\mathcal{C} = 4/9$ corresponds to the maximal value of the compaction parameter for spherically symmetric stars (see [94]).

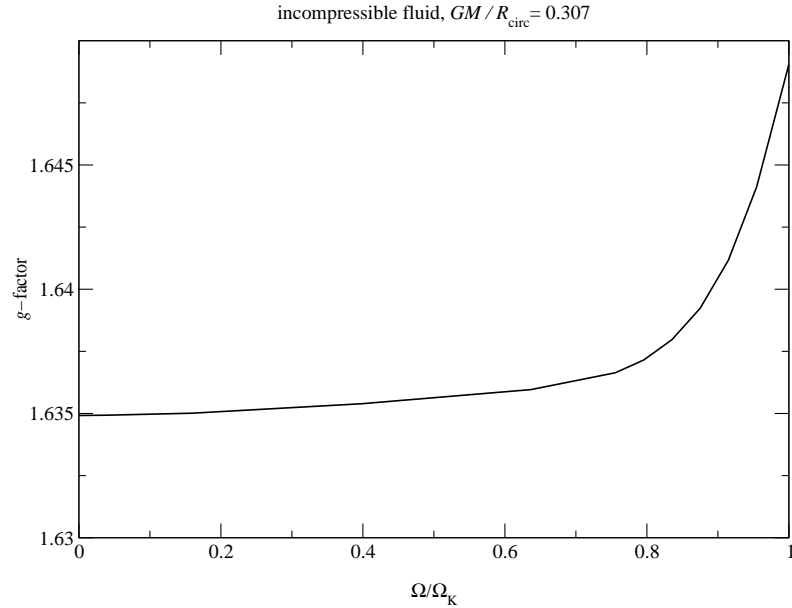


Figure 11.6: Variation of the g -factor as a function of the angular velocity, at constant compaction parameter $\mathcal{C} = M/R_{\text{circ}} = 0.307$ for an incompressible fluid.

11.3.2 Constant density models

In order to study the dependence of the results of the previous section on the particular EOS, we first changed the values of γ and κ . The results obtained were qualitatively the same as in previous section. Quantitatively, the trend described at the end of previous section (figure 11.4 and the following discussion), indicating that the g -factor be linked with the strength of the gravitational field in the star was retrieved. We found that the more compact the star, the higher the gyromagnetic factor. We checked this result with several other equations of state, described in Salgado *et al.* [399], as well as with the “strange quark matter” model (see Gourgoulhon *et al.* [217]), which is giving very compact objects. Still, none of these EOS allowed for a stable configuration with $g \gtrsim 1.8$.

Finally, we present here the limiting case of an incompressible fluid: the EOS is such that n_{B} and e are constant throughout the star. Using this EOS in spherical symmetry, it can be shown (see, [94]) that it gives an upper limit on the gravitational redshift at the surface of the star, when comparing with other EOS. We here introduce a new dimensionless quantity called compaction parameter

$$\mathcal{C} = \frac{M}{R_{\text{circ}}}, \quad (11.10)$$

with R_{circ} being defined by formula (11.9). In Newtonian theory, this is the gravitational potential at the surface of the star and $\mathcal{C} \ll 1$. On the other hand, for a Schwarzschild black hole $\mathcal{C} = 0.5$ and, for relativistic stars $0 \leq \mathcal{C} \leq 4/9$ (as derived by Buchdahl [94]). When considering charged objects the maximal value is slightly increased, as shown in Mak *et al.* [307]. In figure 11.5, we display the dependence of the gyromagnetic factor on this compaction parameter. As expected from previous results, we find that g goes to 1, when \mathcal{C} becomes very small (Newtonian limit). We could

not reach the maximal theoretical value of the compaction parameter for spherical stars ($4/9$), due to the rotation and, perhaps, to the numerical algorithm (we look for a solution by iteration, starting with a flat metric). Nevertheless, we were able to get rather close to this limiting value, reaching the highest gyromagnetic factors for self-gravitating fluids, with $g \sim 1.86$. The striking feature is that the g -factor seems to be directly proportional to the compaction parameter \mathcal{C} and, if one extrapolates the line to the maximal value of \mathcal{C} , one finds that the maximal value for the g -factor would be about 1.9, and certainly well below 2. Using only low charge objects, this value of 2 is linked with the collapse limit that cannot be reached with our stationary models.

It is now worth returning to the dependence of g on the angular velocity Ω . If we fix the value of \mathcal{C} for the star, how does then gyromagnetic factor vary as a function of Ω ? The answer is displayed in figure 11.6, still in the case of an incompressible fluid. We see that the dependence is very small, only about one percent of variation between the non-rotating limit and the shedding one. Results shown in figure 11.3 can have a new interpretation: when Ω is increased, \mathcal{C} decreases because of centrifugal forces that go against gravity and therefore make R_{circ} increase. Gravitational potential at the surface of the star decreases because of the rotation, the same being true for the gravitational field N at the centre. The gyromagnetic factor indicates that, at high angular velocities, the star is less gravitationally bound. Comparing different models, equally bound, but with different rotation rates (figure 11.6), we see that the effect of rotation is small, and must act on the increase of g through the addition of kinetic energy that contributes to the source terms of Einstein equations.

11.3.3 Comparison with previous works

There have been some studies of the gyromagnetic factor in general relativity, but none of them has considered physically consistent matter models. Much of interesting work has been done for slowly rotating charged shells, starting with that of Cohen *et al.* [123]. The study that may be most closely related to ours is that by Pfister and King [366], where the authors calculate explicitly the gyromagnetic factor of a charged mass shell in slow rotation approximation. The shell is infinitely thin and the authors match two exact solutions of the Einstein equations in vacuum across it. The properties of the energy-momentum tensor are then deduced from the matching of both metrics. The advantage of their solutions is that they were able to explore regimes with a very high charge and compaction parameter. Unfortunately, it is difficult to compare quantitatively their results with ours since one knows very little about the properties of shell matter which, apart from energy conditions, are not constrained. One might suppose that, in general, these shells are not behaving like perfect fluids. Qualitatively, both studies agree: for $Q/M \ll 1$ and taking into account energy conditions, Pfister and King find that g varies between ~ 1 , for a low compaction parameter, and 2 in the collapse limit. With a similar kind of problem, Mustafa *et al.* [328] found that g could reach values very close to 2, for the charge-to-mass ratio less than unity and for the shell radius approaching the event horizon value.

Garfinkle and Traschen [201] have calculated the g -factor of a rotating massive loop of charged matter in the presence of a static charged black hole. They have found that, for large radii of the loop, g tended to 1, whereas they found $g \rightarrow 2$ for the radius approaching the horizon. We retrieve (again qualitatively) the same results for our self-gravitating and three-dimensional objects: a loop at spatial infinity might be seen as undergoing a weak gravitational field, just like self-gravitating body with a low compaction parameter. Let us also mention here the very interesting work by Katz *et al.*,

who calculated the gyromagnetic ratio¹ in a conformastationary metric [272]. These axially symmetric metrics can be seen as the external metrics for disc sources, made of charged dust. They show that in those discs, hoop tensions are always necessary to balance the centrifugal forces induced by the motion of the rotating dust. The model therefore correspond to non-perfect fluid, and they find $g = 2$ (with our definition) for these metrics.

11.4 Conclusions

We have studied the dependence of the gyromagnetic ratio (11.1) of self-gravitating rotating fluids on their mass (number of particles), angular velocity and equation of state. We have used a physical model in which we make the assumption that the fluid is an insulator in uniform rotation, and we have neglected the electromagnetic forces acting on the equilibrium of the fluid (low charge approximation). These models have been solved numerically, with a code giving the solution in all space, which enabled us to get the value of g with a high accuracy (better than 10^{-5}) given by independent tests. We find that, with such “stars”, g can never reach the value 2, characteristic of a charged rotating black hole. The maximal value that can be achieved in our study is lower than 1.9. This gap may be linked with the fact that we have neglected electromagnetic forces on hydrodynamic equilibrium and our study has therefore been restricted to low charge-to-mass ratios. But it might also be a result of that stationary relativistic stars, made of perfect fluid, cannot reach values of the compaction parameter M/R close to $1/2$. In that sense, the g -factor is a good indicator of the strength of the gravitational field in an insulating perfect fluid, but is little dependent on the angular velocity of the star. In our study, the value $g = 2$ seems linked only with the black hole solution but, from other works, [123], [366] and [328], one can see that this may depend on the total charge of the system. An important improvement of our work would be to allow for any charge of the system, that is compatible with the stationarity assumption and therefore allow for differential rotation, which may open new possibilities.

¹there is a factor 2 difference between their definition of g and our (11.1)

Chapitre 12

Velocity-induced collapses of stable neutron stars

Version publiée : J. Novak, *Astronomy and Astrophysics* **376**, pp.606-613 (2001).

Sommaire

12.1 Introduction	353
12.2 Evolution of spherically symmetric neutron stars	354
12.3 Dynamical scenarios	357
12.4 Numerical results	359
12.5 Summary and conclusions	363

12.1 Introduction

In the early eighties [410] addressed the question of formation of black holes in astrophysical collapses. Among other, they asked the (theoretical) question of the minimum mass of a black hole formed by the adiabatic collapse of a stellar core and “In particular, can the effective mass-energy potential barrier associated with equilibrium configurations be penetrated by low-mass cores with substantial inward, radial kinetic energy?”. In astrophysical scenarios, black holes can also form from accretion-induced collapses of neutron star, if the neutron star is part of a binary system or during a *supernova* event, when part of the envelop fails to reach escape velocity and falls back onto the new born neutron star. Therefore, one can also ask the question: how much of inward kinetic energy has to be put to a neutron star to make it collapse to a black hole? Can a neutron star always collapse to a black hole, provided that it gets enough kinetic energy?

If one looks at *static* neutron star models, these are stable against perturbations if their masses are lower than some maximal mass and the density is also lower than the “critical” density corresponding to this maximal mass (they are located on the so-called *stable branch*). They can collapse to form a black hole when the central density is higher than the critical one (see e.g. [211]). The question is then whether *stable* neutron stars (i.e. with lower density and mass than the critical ones) can be “pushed”, with a certain amount of inward kinetic energy, to form a black hole, and what is the minimal mass of the formed black hole and/or progenitor? The problem of the minimal mass of a black hole has been

solved, first from a more mathematical point of view, by [117], who discovered the “critical collapse” phenomena in General Relativity (see also Sec. 12.4.1 for a discussion). Still, the problem of a stellar core/neutron star with inward kinetic energy have never been completely studied; to our knowledge, only a partial study was done by [212]. The aim of this paper is to numerically follow the collapse of stable neutron stars, with inward velocity profile, and determine the initial conditions necessary to obtain a black hole as result of the collapse; the purpose is also to allow for a realistic equation of state (EOS), to study dependence on the EOS, as well as on the initial velocity profile, giving kinetic energy. Therefore, emphasis shall be put on neutron star properties in General Relativity and the question of the physical mechanism giving this kinetic energy will not be addressed.

The complete model in General Relativity is described in Sec. 12.2, including the system of partial derivative equations (12.2.1), the two EOS used (12.2.2), and the procedure for obtaining initial numerical models (12.2.3). Time evolution is studied in Sec. 12.3, where two different possible evolutions for neutron stars are given (12.3.1 and 12.3.2). Numerical results are displayed in Sec. 12.4: together with a link with the “critical collapse” paradigm (12.4.1), properties of initial data (12.4.2) and dependence on the parameters (12.4.3) are discussed. Finally, Sec. 12.5 summarizes the results and gives some concluding remarks.

12.2 Evolution of spherically symmetric neutron stars

12.2.1 Field and Matter equations

The equations for the evolution of the matter and gravitational fields are derived from the Einstein equations using the simplifying assumption of spherical symmetry. Space-time is foliated into spacelike hypersurfaces Σ_t and equations are written in terms of the classical 3+1 formalism of General Relativity (see e.g. [35]). The real parameter t is called the *coordinate time* and it can be shown that, making the choice of *polar time slicing* and *radial gauge*, in spherical symmetry the metric can be expressed in the form (generalization of the Schwarzschild metric, see also [211]):

$$g_{\mu\nu}dx^\mu dx^\nu = -N^2(r,t)dt^2 + A^2(r,t)dr^2 + r^2(d\theta^2 + \sin^2\theta d\phi^2), \quad (12.1)$$

where $N(r,t)$ is called the *lapse function*. The two functions N and A will often be replaced by $\nu(r,t)$ and $m(r,t)$, defined as¹:

$$\nu = \ln(N) \text{ and } A = \left(1 - \frac{2m}{r}\right)^{-1/2}. \quad (12.2)$$

The 4-velocity of the fluid is denoted v^μ , the fluid radial *coordinate* velocity being thus:

$$\frac{dr}{dt} = \frac{v^r}{v^0};$$

and the “physical” fluid radial velocity U , as measured locally by the hypersurfaces observer is defined by:

$$U = \frac{A}{N} \frac{dr}{dt}. \quad (12.3)$$

¹We use geometrized units in which the speed of light c and Newton’s gravitational constant G are equal to unity

Following [393], the stress-energy tensor was taken to be that of a perfect fluid; so hydrodynamical equations in General Relativity ($\nabla_\mu T_\nu^\mu = 0$) have been written in the form of a system of conservation laws

$$\frac{\partial \vec{u}}{\partial t} + \frac{1}{r^2} \frac{\partial}{\partial r} \left[r^2 \frac{N}{A} \vec{f}(\vec{u}) \right] = \vec{s}(\vec{u}), \quad (12.4)$$

where $\vec{u} = \{D, \mu, \tau\}$ is the vector of evolved quantities, $\vec{f}(\vec{u})$ the vector of fluxes and $\vec{s}(\vec{u})$ the vector of sources (for details see [393]). The evolved quantities are defined from hydrodynamical variables, baryon and total energy densities in the fluid frame (n_B and e) by:

$$\begin{aligned} D &= A\Gamma n_B, \\ \mu &= (E + p)U, \\ \tau &= E - D, \end{aligned} \quad (12.5)$$

where p is the fluid pressure given by the EOS (see 12.2.2), $\Gamma = (1 - U^2)^{-1/2}$ is the Lorentz factor of the fluid, and $E = \Gamma^2(e + p) - p$.

The gravitational field equations in radial gauge, polar slicing and spherical symmetry reduce to two equations (with no time evolution of the gravitational field):

$$\frac{\partial m}{\partial r} = 4\pi r^2 E, \quad (12.6)$$

$$\frac{\partial \nu}{\partial r} = A^2 \left(\frac{m}{r^2} + 4\pi r(p + (E + p)U^2) \right). \quad (12.7)$$

The system therefore consists of three evolution equations for the hydrodynamical variables (Eqs. 12.4) and two constraint equations for the gravitational field (Eqs. (12.6)–(12.7)). Finally, an equation of state $p(n_B, e)$ closes the system.

12.2.2 Equation of state

In this work two different EOS for nuclear matter have been used, to describe microscopic properties of neutron stars. Apart from the initial condition models, which were calculated with an equation of state $p(n_B)$ for cold, catalyzed matter, the used equations of state were of the form $p(n_B, e)$. The first EOS used is the well-known ideal gas model:

$$p = (\gamma - 1)(e - m_B n_B) \quad (12.8)$$

where $m_B = 1.66 \times 10^{-27}$ kg is the baryon mass and γ is the index. We chose $\gamma = 2$ which may mimic relatively well the properties of neutron star matter but always keeps a sound speed lower than c (causal EOS). This EOS has been used not only because it is very convenient from a numerical point of view, but also because it allows for the calibration and test of the code. For obtaining initial conditions, the following expression has been used

$$p(n_B) = K n_0 m_B \left(\frac{n_B}{n_0} \right)^\gamma; \quad (12.9)$$

with $K = 0.1$ (as in the study of rotating neutron star models by [399]) and

$$n_0 = 0.1 \text{ fm}^{-3}. \quad (12.10)$$

To get a more realistic EOS for nuclear matter interactions, we used the EOS described in [369]. It is a relativistic field theory model supplemented by nonlinear scalar self interactions. Nucleons (n, p) interact via the exchange of σ -, ω - and ρ -mesons. The contribution from leptons is given by its non-interacting form, since their interactions give negligible contributions. Moreover, the star being at chemical equilibrium with respect to the weak processes, the neutrino chemical potentials are zero. However, as a difference from [369], kaon interactions are not considered in this work. The EOS was tabulated and, during the time integration, the interpolation has been done using bi-cubic splines. This may not be as precise as the method presented by [447] (using bi-*quintic* interpolation), but thermodynamical consistency is still preserved. At low densities, this EOS has been smoothly joined with a polytrope. As far as initial conditions are concerned, the same model has been used, but the temperature has been set to zero.

12.2.3 Initial Conditions

To get initial numerical conditions, we first obtained stable spherical neutron star models and then, to add a velocity profile. A *stable* neutron star is defined by the fact that its central density is lower than the critical one (n_B^{crit}), defined by (M_g being the total gravitational mass of the star and $n_B^c = n_B(r=0)$):

$$\left. \frac{dM_g}{dn_B^c} \right|_{n_B^c = n_B^{\text{crit}}} = 0. \quad (12.11)$$

The stable model is easily computed, integrating the well known Tolman-Oppenheimer-Volkoff (TOV) system, which is the static (all $\partial/\partial t$ terms and U are set to zero) limit of momentum evolution equation in system (12.4), plus the equations for gravitational fields Eqs. (12.6)–(12.7). For the polytropic equation of state ($\gamma = 2, K = 0.1$), one has $n_B^{\text{crit}} = 3.18 n_0$ and the maximal stable mass is $M_g = 3.16 M_\odot$. For the tabulated EOS of [369] (see previous section), one has $n_B^{\text{crit}} = 10.5 n_0$ and the maximal stable mass is $M_g = 2.08 M_\odot$. The rather high value for maximal mass for the $\gamma = 2$ polytropic EOS is linked to an also high value chosen for K . Thus mass scales between both EOS used in this work were different. However for polytropes of the form (12.9) with $\gamma = 1 + 1/n$, the constant $K^{n/2}$ has units of length in geometrized units. Following [130], one can use this constant to set the fundamental length scale of the system. Defining dimensionless quantities as in [130] ($\bar{t} = K^{-n/2} t$, $\bar{p} = K^n p$, $\bar{n}_B = K^n n_B$, ...), one can see that in our case all masses (even in dynamical evolution) scale like $K^{0.5}$.

Once the density and gravitational fields are computed, the inward velocity profile is added in the r.h.s. of gravitational field equations (12.6)–(12.7). The metric coefficients are then relaxed in order to take into account the contribution from the kinetic energy in the total gravitational mass. Therefore, initial conditions are consistent with the gravitational field equations. The considered profiles were of the form

$$U(r) = \frac{A(r)}{N(r)} V \left(\frac{r}{R_{\text{surface}}} \right),$$

where $V(x)$ has one of these forms ($x = r/R_{\text{surface}}$):

$$V(x) = \frac{V_{\text{amp}}}{2} (x^3 - 3x) \quad (12.12)$$

$$V(x) = \frac{27V_{\text{amp}}}{10\sqrt{5}} \left(x^3 - \frac{5x}{3} \right) \quad (12.13)$$

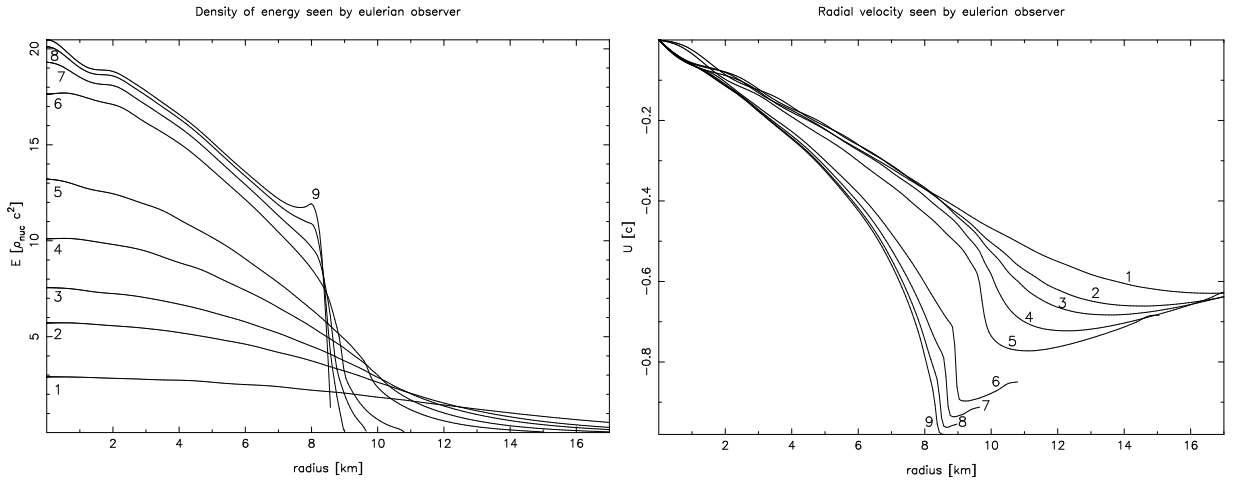


Figure 12.1: Snapshots of eulerian energy density E and radial velocity profiles U , for a $2.74 M_{\odot}$ neutron star described by a $\gamma = 2$ polytropic EOS, with an initial velocity profile of type (12.13), and a starting minimal value of the velocity of $-U_{\min} = -0.6c$. Labels correspond to the following times: $t_1 = 0.054$ ms, $t_2 = 0.088$ ms, $t_3 = 0.104$ ms, $t_4 = 0.126$ ms, $t_5 = 0.149$ ms, $t_6 = 0.202$ ms, $t_7 = 0.225$ ms, $t_8 = 0.248$ ms and $t_9 = 0.271$ ms. All profiles have been cut at the surface of the star, defined by the surface density of the initial configuration.

(V_{amp} is the parameter defining the amplitude of the profile).

Both are such that the minimal value in $[0,1]$ is $-V_{\text{amp}}$, but (12.12) verifies $V'(1) = 0$ and (12.13) has a null divergence at the surface. These profiles correspond to what is usually observed in collapses of neutron stars (see e.g. [211]) or in the formation of neutron stars (see e.g. [393]). The initial minimal value of the velocity $U(r)$ in the interior of the star ($r \in [0, R_{\text{surface}}]$) is noted $-U_{\min}$. It shall also be called the initial velocity profile amplitude.

12.3 Dynamical scenarios

Numerical time integration has been done using High Resolution Shock-Capturing schemes (HRSC, see [46]) for the hydrodynamical system (12.4). The metric constraint equations (12.6)–(12.7) were integrated using standard finite-differences methods. The need of using numerical methods able to handle shocks comes from the fact that strong discontinuities can form (see Sec. (12.3.2)), as it has first been observed by [212]. Unfortunately, this last study has been limited by the use of *spectral methods*, unable to handle shocks.

12.3.1 Direct collapse

For a stable star close to the maximal mass, but with an inward velocity profile, there may be two final issues. If the velocity is relatively small in amplitude, the star enters an (theoretically) infinite series of oscillations, for no viscous nor radiative damping is present. With higher velocity, a collapse to a black hole occurs “normally”, almost like for an unstable neutron star configuration (as in e.g. [211]). Figure 12.1 shows energy (E) and velocity profiles at different moments of the collapse of such a neutron star. It corresponds to an initial configuration of $2.74 M_{\odot}$, where the initial velocity profile is of the

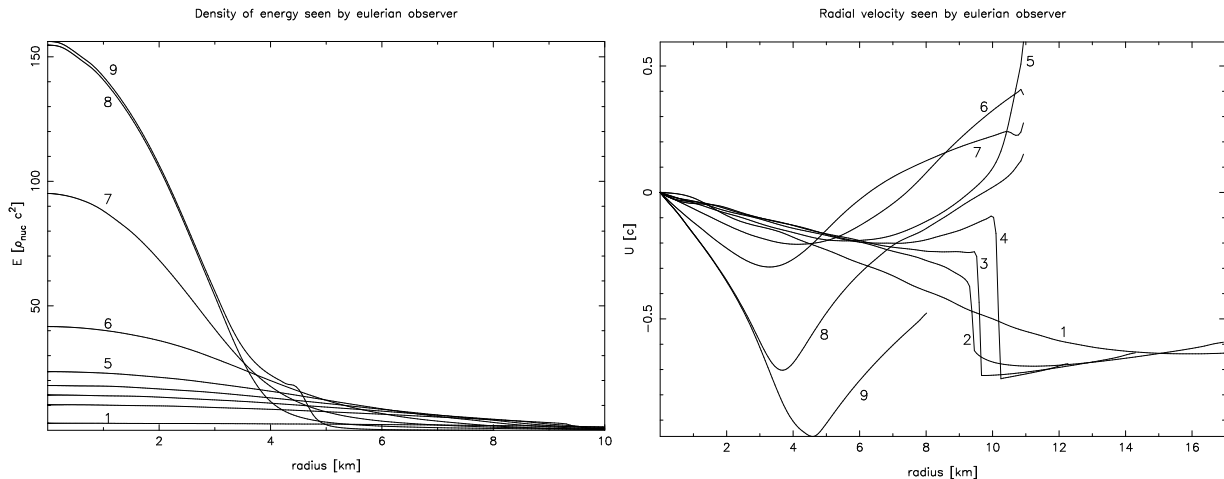


Figure 12.2: Eulerian energy density and radial velocity profiles, for a polytropic $\gamma = 2$ $1.91 M_{\odot}$ neutron star collapse, with an initial velocity profile of type (12.13), and a starting minimal value of the velocity of $-0.62c$. The displayed profiles correspond to the following times: $t_1 = 0.064$ ms, $t_2 = 0.123$ ms, $t_3 = 0.143$ ms, $t_4 = 0.16$ ms, $t_5 = 0.178$ ms, $t_6 = 0.216$ ms, $t_7 = 0.265$ ms, $t_8 = 0.348$ ms and $t_9 = 0.477$ ms. All profiles have been cut at the surface of the star, defined by the surface density of the initial configuration.

type (12.13), with $V_{\text{amp}} = 0.4c$, which gives an initial minimal radial velocity of $-U_{\text{min}} = -0.6c$. This collapse has been followed up to $t = 0.48$ ms, when then central value of the lapse became 5.13×10^{-5} , with a radial velocity at the outer edge of $-0.99c$. Due to the choice of polar slicing which avoids the appearance of singularities, the horizon of a black hole cannot be numerically described. However, the final state is a black hole, but from the “frozen star” viewpoint, with a collapse of the lapse. These criteria have been used in Sec. 12.4 to determine whether the result of the collapse was a black hole or not, namely a central value of the lapse $N(r = 0) < 10^{-4}$ with an ingoing radial velocity. If both of these conditions are fulfilled, it seems unlikely that the collapse lead to anything else than a black hole.

Still, a difference from [211] in the dynamical evolution can be seen in Fig. 12.1: a strong gradient appears in the velocity profile around $r = 9$ km, even quite before the “frozen star” regime (where the metric potentials A and N also exhibit strong gradients). This had already been observed by [212], where it limited the study. It is shown in Sec. 12.3.2 that, with higher initial velocities, a shock can form and part of the infalling matter can be ejected. In the present “direct collapse” regime all the matter ends in the black hole so that the mass of the resulting object is that of the initial neutron star. In Sec. 12.4, this has been used to distinguish between both possible types of collapses.

12.3.2 Shock and bounce

For some initial velocities, the “strong gradient” of previous section turns into a shock, and part of the infalling material is ejected. This can be seen on Fig. 12.2 where energy density and radial velocity profiles are displayed, for an initial neutron star of $1.91 M_{\odot}$ (the mass is lower than that of Fig. 12.1 due to a lower initial central baryon density). The shock appears around $t = t_3$, $r = 10$ km and then moves out of the numerical grid (t_4) due to the accumulation of matter still falling at $r > 10$

km. The velocity on the left side of the discontinuity grows and reaches positive values. Later during the collapse, one can see that part of the falling matter starts moving outward and reaches escape velocity from the central object t_5 . This of course reduces the possibility of forming a black hole, since matter is spatially less concentrated. Still, the dynamics of the central region (where the velocity is still inward) can proceed to a black hole, which shall then accrete matter which has not reached escape velocity. This has been observed in the collapse displayed on Figs. 12.2 where, at the end of the computation ($t = 0.63$ ms), the central lapse was $N(r = 0) = 1.18 \times 10^{-9}$ and the velocity on the edge of the “frozen star” equal to $-0.999 c$. The central region would collapse “directly”, as described before in Sec. 12.3.1. The final mass of the black hole was $1.61 M_\odot$ (and the areal radius in RGPS coordinates equal to 4.77 km), which shows that almost 16% of the initial matter of the neutron star has been ejected.

12.4 Numerical results

The dynamical fate of neutron stars with initial velocity are now studied, keeping in mind the different scenarios described in previous section and varying the mass of the progenitor, as well as the amplitude of the initial velocity profile. This exploration of the parameter space shows the possibility of formation of very low mass black holes, which can be seen as a feature of the “critical collapse” phenomena.

12.4.1 Link with critical collapses

The critical collapse phenomenon (for an interesting review see [234]) was discovered in the early 90s by [117], who was numerically studying the gravitational collapse of spherically symmetric massless scalar field. Depending on some parameter of the initial conditions (which is generically noted p), the final result of the collapse would be a black hole (p large) or the dispersion of the field (p small). He discovered that, when fine-tuning this parameter, he could get black holes of arbitrarily small masses. Moreover, the relation giving the mass of the resulting black hole, close to p_* the minimal value to form a black hole, appeared to be universal in the form:

$$M_{BH} \simeq C(p - p_*)^\alpha, \quad (12.14)$$

where C is a constant and α is called the *critical exponent*. The space-time obtained with $p = p_*$ shows the very interesting geometrical property of *self-similarity*.

There have been many works on critical collapses since this pioneering one and, in particular, the study concerning perfect fluids by [334] is of particular interest for our study. It is shown that perfect fluid collapses, in ultra-relativistic regime, also exhibit “critical” behavior. Our work can easily be connected to this one, if one considers, at fixed central density of the initial neutron star, the parameter p to be e.g. the parameter V_{amp} or the amplitude of the initial velocity profile U_{min} . One can then see that, by fine-tuning the parameter V_{amp} (U_{min} being a monotonic and continuous function of V_{amp}) of (12.12) or (12.13), one could get black holes of arbitrarily small masses, as a result of the velocity-induced collapse. We have not investigated the domain of very small black hole masses, for our code was not designed for it. Still, starting with a $1.16M_\odot$ neutron star and an initial velocity profile given by (12.13) (and $V_{\text{amp}} = 0.79732$), the result of the evolution was a $3.7 \times 10^{-2}M_\odot$ black hole. This corresponds to the lowest black hole mass range (about $10^{-2}M_\odot$) obtained with our code. In order to test the code against the relation (12.14), the central density of the initial configuration has been kept constant, and only the parameter V_{amp} of (12.13) has been varied (and thus U_{min}).

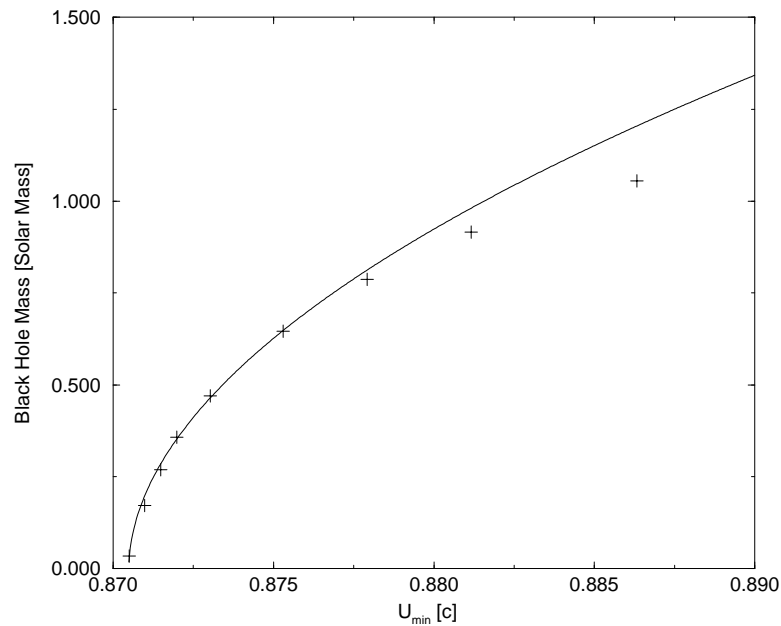


Figure 12.3: Masses of the black holes (+) formed through velocity-induced collapses, for a polytropic EOS and with an initial velocity profile of type (12.13). The initial central density is $0.1n_0$ (see Sec. 12.2.2) for all the runs. These masses have been fitted by a formula of type (12.14) (solid line).

The results displayed on Fig. 12.3 correspond to the masses of black holes resulting from collapses, if the central density of the initial configurations is held fixed to $0.1n_0$. These masses are drawn (crosses) as a function of the minimal value of the velocity U inside the neutron star. The relation (12.14) is verified, at least for “small” masses and the best fit (shown on the figure in solid line) corresponds to $\alpha = 0.52$, $C = 10.4M_\odot$ and $p_* = 0.8705c$ ($U_{\min} = p$). These values have shown to depend on the particular central density used for the initial configurations. The fit is poor for large masses and, in particular, the relation (12.14) breaks down completely near the maximal mass for stable static neutron stars (when central density reaches n_B^{crit}). The mass scaling exponent $\alpha = 0.52$ differs from the result obtained by [334] ($\alpha = 1$) who used an ultrarelativistic EOS with $\gamma = 2$. Although the result from [334] is rather universal, the study here starts from very different initial conditions (neutron star/exponential distribution of matter in their case). In particular, here, the maximal mass for stable neutron stars gives a *mass limit* to the problem. Another difference is that the parameter used to get the relation (12.14) is the amplitude of a velocity profile, which has not been studied by [334]. Finally, it has to be stressed out that the family of initial conditions used for this study depends on *two* parameters (velocity amplitude and central density), the work of [334] assumed only a one-parameter family of initial data. The role played by the central density as a parameter is not that of a “critical” one: if one considers the family of initial data given by static neutron stars (without any velocity profile) of increasing central densities, then the value n_B^{crit} defined by (12.11) would seem to be the same as p_* in controlling the formation of a black hole, but there is no critical behavior at this point. Still it is interesting to note that the mass scaling relation is valid for velocity induced neutron star collapses, at least in the limit of low masses (and therefore relatively low central densities).

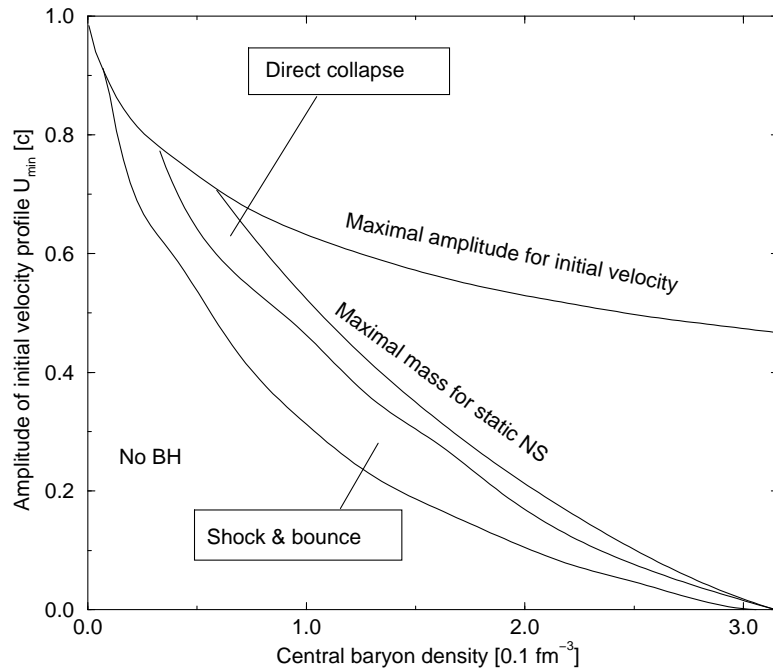


Figure 12.4: Parts of the parameter space plane (n_B^c , U_{\min}) defining the fate of a neutron star with a polytropic EOS ($\gamma = 2$) and an initial velocity profile defined by (12.13).

12.4.2 Masses of progenitors - Initial velocities

Once the EOS and type of velocity profile are chosen, a neutron star model serving as initial condition for velocity-induced collapse is completely specified by two parameters: the central baryonic density n_B^c and the parameter V_{amp} or, equivalently, the neutron star gravitational mass and the amplitude of the initial velocity profile U_{\min} . For each point (n_B^c, U_{\min}) in this parameter space the question of knowing whether the corresponding neutron star would collapse to a black hole have been addressed. First, it has been found that there exists a maximal value for U_{\min} , for which an initial model of neutron star could be computed. For higher velocities, it appeared to be numerically impossible to compute the metric coefficients taking into account this large amount of kinetic energy: the relaxation would fail to converge, leading to velocity $U > c$. This may come from the way these initial conditions are set: the addition of a velocity profile to a static model does not give a well defined result. Matter is not at equilibrium, whereas the metric potentials are static. Therefore an improvement of this study would be to consider more realistic initial conditions (as for example in [244]), where the velocity profile is not set *ad hoc* but comes from a dynamical interaction.

This maximal value of U_{\min} depends on the central density of the neutron star, as displayed on Fig. 12.4; one can see that for central densities going to zero (and therefore also masses), this maximal value goes to one. This figure also shows the various fates of a neutron star in the (n_B^c, U_{\min}) plane, for the ($\gamma = 2$) polytropic EOS of Sec. 12.2.2 and an initial velocity profile of type (12.13). Curves are described from top-right to bottom-left part of the figure. A neutron star set to a point of this parameter space can become a black hole or not. Still, some region is not really interesting to study. The second curve to be displayed selects neutron stars with a mass lower than the maximal one, as defined in Sec. 12.2.3. Studying collapses for neutron stars with higher masses is not relevant since

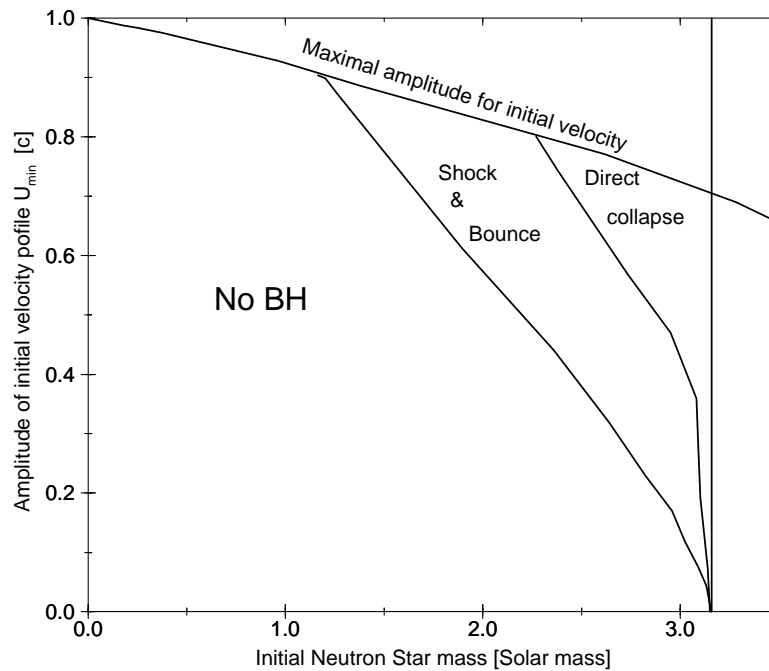


Figure 12.5: Parts of the parameter space plane (n_B^c , M_g) defining the fate of a neutron star with a polytropic EOS ($\gamma = 2$) and an initial velocity profile defined by (12.13).

one knows that in that case the neutron star shall end as a black hole; the additional velocity profile of the neutron star only gives kinetic energy so that the total mass of the star become larger than the maximal one for stars at rest. It was then observed that this collapse generally proceeds “directly”, i.e. no shock is present. One more curve gives the limit between the direct collapse domain and the part of the parameter space for which the star undergoes a shock and bounce, as described in Sec. 12.3.2. Finally, if the parameters of the initial neutron star model are below the last curve, the black hole does not form, the matter being ejected to infinity. The same regions are displayed in the (M_g, U_{\min}) plane, on Fig. 12.5. In particular, one can see that there exists a minimal mass for the initial neutron star, to form a black hole. This mass is, in the case of a polytrope $\gamma = 2$ and an initial velocity profile (12.13):

$$M_{\min} = 1.164M_{\odot}. \quad (12.15)$$

This figure also shows the minimal neutron star mass for which direct collapse (i.e. no ejection of matter) can occur, it found to be $2.276 M_{\odot}$.

12.4.3 Dependence on EOS and velocity profiles

Although the velocity profile (12.13) is supposed to occur in most of physical scenarios of gravitational collapse of compact stars, one has to check the dependence of results of previous sections on a change of this velocity profile. Therefore the study of Sec. 12.4.2 has been undertaken with the initial velocity profile for neutron stars being given by (12.12). For initial configurations, one can see that this change in the velocity profile induces, for given values of n_B^c and U_{\min} , a change in the distribution of kinetic energy in the star and thus a change in the total gravitational mass M_g , with respect to the velocity

distribution given by (12.13). Still, qualitative results concerning collapses were retrieved: direct collapse or bounce as dynamical scenarios and formation of low-mass black hole by fine-tuning the parameter U_{\min} . The scaling relation (12.14) has been studied for a fixed central density (chosen to be $0.1n_0$ as in Sec. 12.4.1) and the best fit of results gives the relation:

$$M_{BH} \simeq 6.98 \times (U_{\min} - 0.8991)^{0.52} M_{\odot},$$

for which the exponent ($\alpha = 0.52$) is the same as that obtained using velocity profile (12.13). The two other coefficients (noted C and p_* in Sec. 12.4.1) are different for the reasons stated above, concerning the difference in kinetic energy distribution. The borders of different regions of Fig. 12.5 also slightly change, nevertheless we get as minimal mass for the initial neutron star to form a black hole for a $\gamma = 2$ polytrope and an initial velocity profile (12.12):

$$M_{\min} = 1.155 M_{\odot}. \quad (12.16)$$

This is less than 1% different from the minimal mass for velocity profile (12.13), that is within global numerical error. One then may suppose that this quantity is little dependent on the particular type of velocity profile chosen.

The second global “parameter” one would like to change is the EOS for nuclear matter, since a rather important uncertainty exists on properties of neutron star matter. In particular, the $\gamma = 2$ polytrope used in this study had the advantage of rapid computation as well as numerical stability, combined with a rather good description of neutron matter properties. But if one wants to go further, it is then necessary to use a more realistic EOS, as for example the one described in Sec. 12.2.2. As stated in that section, maximal mass for static neutron stars is found to be $M_g^{\text{crit}} = 2.08 M_{\odot}$, for a corresponding central density of $n_B^c = 10.5n_0$. Therefore, results from computations using this second EOS would show lower masses and higher central densities than those using the analytical EOS. The parameter space (n_B^c, U_{\min}) has been studied, using the velocity profile given by (12.13). As for the $\gamma = 2$ polytrope, neutron stars with realistic EOS would collapse to form a black hole, provided that the amplitude of the velocity profile be large enough. This collapse could occur directly, as in the case of *unstable* neutron stars or with the bounce of a part of the matter, which would be ejected, allowing only for the central region to form a black hole. The mass scaling relation is recovered, for relatively small initial central densities; for example, with $n_B^c = 1.5n_0$, the following relation is found:

$$M_{BH} \simeq 5.79 \times (U_{\min} - 0.7519)^{0.71} M_{\odot},$$

which has been tested for black holes in the mass range $5 \times 10^{-3} - 0.7 M_{\odot}$. The global topology of regions described in figures 12.4 and 12.5 is kept and the minimal mass for a neutron star (with matter described by this realistic EOS) to form a black hole is found to be

$$M_{\min} = 0.36 M_{\odot}. \quad (12.17)$$

During the collapses leading to very low-mass black holes (a few $10^{-2} M_{\odot}$), the central regions of the star would reach very high densities and it has been checked that sound velocity had never become higher than c .

12.5 Summary and conclusions

With an important amount of inward kinetic energy, stable neutron stars may collapse to a black hole, overcoming the potential barrier which separates both types of objects. However, there seem to exist

an absolute lower mass limit, depending on the particular equation of state used to describe neutron star matter properties, below which neutron stars cannot pass this barrier. This lower-limit mass has been found to be $\simeq 1.16M_{\odot}$ for a $\gamma = 2$ polytropic EOS, and $\simeq 0.36M_{\odot}$ for a more realistic model of nuclear matter. It seems also that these values are independent from the particular initial velocity profile added to static neutron star models. But, as it has been noted in Sec. 12.2.3, for the polytropic EOS, like all masses this lower-limit mass scales like $K^{0.5}$.

For both studied EOS, in the case when the star collapses to a black hole it may either proceed directly, as if it were an *unstable* neutron star, all the matter ending in the black hole; or there may appear a shock and bounce, ejecting a part of the matter to infinity, so that only a fraction of the initial neutron star forms a black hole. With such a mechanism, the resulting black hole mass can be arbitrarily small if one is fine-tuning the amount of kinetic energy added to the initial neutron star. This result is in accordance with works by [117] on critical collapses, more precisely the mass-scaling relation (12.14) also applies here, at least for black hole masses not too close to the neutron star critical mass. The mass scaling exponent α found for the polytropic EOS is rather different from that found, with quite different initial conditions, by [334] for ultrarelativistic $\gamma = 2$ EOS.

Nevertheless, the velocity necessary to achieve the collapse to a black hole of a typical $1.4M_{\odot}$ neutron star is enormous (see Fig. 12.5). Even in the case of a smaller K , leading to a smaller maximal mass (see Sec. 12.2.3), this velocity always remains larger than $0.1c$. It is therefore difficult to imagine any physical process which could inject such an amount of kinetic energy to a neutron star. Tidal (anisotropic) effects when the neutron star is in a binary system with another compact object may result in the destruction of the star (compressed to a “pancake”, as ordinary stars passing near a black hole in [308]) or in its oscillations. It has been argued (e.g. by [312]) that in a binary neutron star system, tidal effects could induce such a compression (i.e. increase of central density) that the stars could collapse to black holes before their merging. This is very difficult to achieve, since in our calculations it happened that during the collapse the central density could reach a value substantially higher than the critical density n_B^{crit} (in some cases several times n_B^{crit}), whereas the star would not end in a black hole, but would rather be dispersed or enter an infinite series of oscillations. Even in the case of the neutron star instability transition in tensor-scalar theory (see [337]), the velocity is never larger than a few percents of c , therefore quite far from values displayed on Fig. 12.5. Finally, let us mention the recent interesting work by [244] who studied the critical collapses of *boson* stars, where the interaction with a massless real scalar field can result in a significant transfer of energy from the field to the star, allowing for the collapse to a black hole of stable configurations. In the case of neutron stars the interaction with a gravitational wave seems unlikely to transfer enough energy to lead to the collapse to a black hole.

Chapitre 13

Excised black hole spacetimes : quasilocal horizon formalism applied to the Kerr example

Version publiée : N. Vasset, J. Novak et J. L. Jaramillo, *Phys. Rev. D* **79**, 124010 (2009).

Sommaire

13.1 Introduction	365
13.2 Isolated horizons as a local description of black hole regions	367
13.3 A fully constrained formalism for Einstein equations	368
13.4 Boundary conditions and resolution of the FCF system	372
13.5 Numerical results and tests	377
13.6 Discussion	383
13.7 Conclusion	384
13.A Tensor spectral quantities adapted to the Dirac Gauge	385
13.B Recovery of h^{ij} from A and \tilde{B}	387

13.1 Introduction

Trying to accurately describe black holes solutions as evolving physical objects in numerical simulations is of direct interest in astrophysics. Numerical simulations have made a great leap forward in the past few years, mainly with the first stable simulations of black hole mergers in full general relativity by Pretorius [374], Campanelli et al. [101], Baker et al. [44], and a few other groups (see [375] for a review). Several of these simulations model black holes in their equations by punctures. These punctures basically change the topology of spacetime to handle evolution of singular objects (see [87] for the first proposal of this method).

Notable exceptions to this are references [374, 183, 448, 438], that use an excision approach for black hole evolution: the simulations only evolve the spacetime outside two-spheres that are supposed to encircle the black hole singularities.

In the same spirit, we are here trying to describe black holes as physical objects characterized by their horizons. Defining the physical laws for event horizons of black holes has been notably done by [243], [141] and [465] in a so-called *membrane paradigm*. The aim was to describe them as fluid-like two-membranes with physical properties. However, applying evolution laws to event horizons is problematic due to their teleological (non causal) behavior (see for example [82] for a description of the phenomenon). Being defined as a global property of spacetime, a local notion of causality actually does not apply to event horizons.

Alternative local characterizations have been formulated in the past 15 years by [245], [36] and [38]. They are based on the concept of trapped surfaces, dating back to Penrose’s singularity theorem [356]. Defined locally, those objects behave in a causal way in a general dynamical context, with local evolution laws following from the projection of Einstein equations, e.g the Navier-Stokes [213] “fluid bubble” analogy or the area evolution law in [223]. For this work we shall use local characterizations for isolated horizons, prescribing the physics of non-evolving black hole horizons.

Following the prescriptions of [129], [264], [222] and pursuing the numerical explorations of [133, 113] and [265] among others, we try to numerically implement those objects as boundary conditions imposed on the (3+1) form of Einstein equations, in a three-slice excised by a two-surface (single black hole case). This is done here using the fully constrained formalism (FCF) of [73] (see also [135]), with maximal slicing and Dirac gauge, based on the (3+1) formalism, and with spectral methods-based numerical resolution using the LORENE library [216]. An important point here is that we drop out the usual conformal flatness hypothesis and solve for the conformal geometry, so that we can exactly recover a slice of a stationary rotating vacuum spacetime.

Contrary to free evolution schemes, which are the most used prescription for (3+1) simulations in numerical relativity, an important feature of constrained schemes is the necessity to solve constraints on each three-slice, in the form of elliptic equations. These equations generally need additional conditions to be imposed on grid boundaries, following reasonable geometrical and physical prescriptions. Our approach particularly requires a specific handling of boundary conditions for the two dynamical gravitational degrees of freedom. This is a crucial point of our calculation; we will justify and apply here a no-boundary treatment for these quantities.

The paper is organized as follows: we first review in Sec. 13.2 fundamental geometrical properties associated with isolated horizons in general relativity. In Sec. 13.3, we quickly give the basic features of the fully constrained formalism and the methods we use to treat the conformal part. Sec. 13.4 discusses implementation of boundary conditions for the system of equations, and specifically discusses the conformal metric part. Sec. 13.5 gives the numerical results obtained, and confronts them to a battery of tests characterizing the physics of the solutions. A discussion follows in Sec. 13.6, in regard of previous works concerning the computation of the conformal part in the black hole initial data problem. We also raise the question of applicability of this scheme to other more general astrophysical cases.

Throughout all this paper, Greek letters will denote indices spanning from 0 to 3, Latin indices from k to m shall denote indices from $\{1, 2, 3\}$, and indices from a to c have the range of $\{2, 3\}$. All formulae and values are given in geometrical units ($G = c = 1$). We also use the Einstein summation convention.

13.2 Isolated horizons as a local description of black hole regions

13.2.1 Trapped surfaces and expansion

The concept of a trapped surface in a Lorentzian frame has been first defined by Penrose in 1965 [356] in connection with the singularity theorems. It relies on the notion of expansion of the light rays emitted from a surface, that we explain here. We start by a closed spacelike two-surface \mathcal{S} embedded in spacetime, topologically related to a two-sphere. We assign to it a two-metric q_{ab} induced by the ambient four-metric $g_{\mu\nu}$, and its associated area form $\epsilon_{ab}^{\mathcal{S}}$. Two future null directions orthogonal to \mathcal{S} are associated with this surface. Representative vector fields are denoted ℓ^μ and k^μ , being respectively oriented outwards and inwards. We can for example assume that our spacetime is asymptotically flat, so the orientation can be defined without ambiguity.

The expansion θ_ℓ of \mathcal{S} along ℓ^μ is the area rate of change along this vector: $\mathcal{L}_\ell \epsilon_{ab}^{\mathcal{S}} = \theta_\ell \epsilon_{ab}^{\mathcal{S}}$. \mathcal{L} is the Lie derivative, here along the vector ℓ^μ . Same definition goes for the vector field k^μ . For a two-sphere embedded in a Minkowski spacetime (flat metric), we have typically $\theta_k < 0$ and $\theta_\ell > 0$. \mathcal{S} is said to be a trapped surface if both expansions are negative or zero: $\theta_\ell \leq 0$, $\theta_k \leq 0$. This clearly characterizes strong local curvature. A marginally (outer) trapped surface will be characterized by $\theta_\ell = 0$ and $\theta_k \leq 0$. Two theorems make the connection between those objects and black holes: provided the weak energy condition holds, the singularity theorem of Penrose [356] ensures that a spacetime containing a trapped surface necessarily contains a singularity in its future. Following this result, provided the cosmic censorship holds, another result by Hawking and Ellis [242] conveys that a spacetime containing a trapped surface necessarily contains a black hole region enclosing this surface.

Marginally outer trapped surfaces (MOTS) are intended as models for the black hole boundary (see [409] for a discussion of its relation with the boundary of the black hole trapped region). Local horizons (trapping horizons for [245], isolated and dynamical horizons in [36], [38]) are defined as three-dimensional tubes “sliced” by MOTS, with additional geometrical properties. The isolated horizon case is detailed below; for a review, see [39].

In vacuum stationary spacetimes, all horizons are at the same location, which is also the location of the event and apparent horizons (constructed with outermost MOTSs). In the more general case, and assuming cosmic censorship, local horizons are always situated inside the event horizon in general relativity.

13.2.2 Isolated horizons

The notion of isolated horizon is aimed at describing stationary black holes. It is based on the notion of non-expanding horizons, and defined as a three-dimensional tube \mathcal{H} foliated by MOTS, and with a null vector field ℓ^μ as generator. The three-metric induced on the tube has then a signature $(0, +, +)$.

We also define a (3+1) spatial slicing for our spacetime, and \mathcal{S} a two-slice of our isolated horizon at a certain value of the time parameter t . The spacelike two-metric on \mathcal{S} is denoted q_{ab} .

The shear tensor σ_{ab} on the two-surface is defined along ℓ^μ as

$$\sigma_{ab} = \frac{1}{2} [\mathcal{L}_\ell q_{ab} - \theta_\ell q_{ab}]. \quad (13.1)$$

Using the fact that $\theta_\ell = 0$ and the dominant energy condition, the Raychaudhuri equation for null tubes [222] ensures that both the shear along ℓ^μ and the energy-momentum tensor projected on ℓ^μ ,

and evaluated on the surface must vanish: $\sigma_{ab} = 0$ and $T_{ab}\ell^a\ell^b = 0$. These are additional properties constraining the geometry of the horizon.

An isolated horizon is also required to be such that the extrinsic geometry of the tube is not evolving along the null generators: $[\mathcal{L}_{(\ell)}, D_i^{\mathcal{H}}] = 0$, where $D_i^{\mathcal{H}}$ is the connection on the tube induced from the ambient spacetime connection. If this last condition is dropped, we only retrieve a non-expanding horizon (linked to the notion of “perfect horizon” [237]).

The isolated horizon formalism has already been studied extensively in numerics, as a diagnosis for simulations involving black holes, where marginally trapped surfaces are found *a posteriori* with numerical tools called apparent horizon finders (See for example [463], [294], [231], [462]). Let us note that very often, apparent horizon finders actually locate MOTS on the three-slice considered (not necessarily outermost ones). A thorough study of geometrical properties of isolated horizons located *a posteriori* can be found in [159].

In the present paper we employ isolated horizons as an *a priori* ingredient in the numerical construction of Cauchy initial data for black hole spacetimes. More precisely, we impose conditions on the excised surface characterizing it as the slice of a non-expanding horizon (see below). This approach to the modeling a black hole horizon in instantaneous equilibrium has been investigated in [129, 133, 113, 264, 140, 222, 265], where a prescription for the conformal metric is assumed. The main feature of this work is the inclusion of the conformal metric in the discussion, not through analytical prescriptions, but indeed by numerical calculation. This problem has also been recently addressed in [132]. In Sec. 13.4 we tackle the description of our special treatment of the conformal metric on the excised boundary and compare with previous results, in particular through the numerical recovery of excised Kerr initial data.

13.3 A fully constrained formalism for Einstein equations

All the following is a summary of the physical and technical assumptions set in [73]. For a review of (3+1) formalism in numerical relativity, the reader is referred to [486], or more recent reviews like [214] and [7].

13.3.1 Notations and (3+1) decomposition

We consider an asymptotically flat, globally hyperbolic four-dimensional manifold \mathcal{M} , associated with a metric $g_{\mu\nu}$ of Lorentzian signature $(-, +, +, +)$. We define on \mathcal{M} a slicing by spacelike hypersurfaces Σ_t , labeled by a timelike scalar field t ; in this way, the four-metric can be written in its usual (3+1) form:

$$g_{\mu\nu}dx^\mu dx^\nu = -N^2 dt^2 + \gamma_{ij}(dx^i + \beta^i dt)(dx^j + \beta^j dt), \quad (13.2)$$

here N and β^i are the usual lapse scalar field and shift vector field. γ^{ij} is the spacelike three-metric induced on Σ_t .

We also define the second fundamental form of Σ_t , or extrinsic curvature tensor, as:

$$K_{\mu\nu} = -\frac{1}{2}\mathcal{L}_n\gamma_{\mu\nu}, \quad (13.3)$$

with n^μ the future-directed vector field normal to Σ_t . Writing the vacuum Einstein equations with this formalism, one comes up with the classical (3+1) vacuum Einstein equations system (see for example

[35]):

$$R + K^2 - K_{ij}K^{ij} = 0, \quad (13.4)$$

$$D_j K_i^j - D_i K = 0, \quad (13.5)$$

$$\begin{aligned} \frac{\partial}{\partial t} K_{ij} - \mathcal{L}_\beta K_{ij} = \\ -D_i D_j N + N \left\{ R_{ij} - 2K_{ik}K_j^k + K K_{ij} \right\}, \end{aligned} \quad (13.6)$$

D_i and R_{ij} being, respectively, the connection and the Ricci tensor associated with the three-metric γ_{ij} . Quantities without indices represent tensorial traces. These equations are referred to respectively as the Hamiltonian constraint, momentum constraint and evolution equations.

13.3.2 Conformal decomposition, maximal slicing and Dirac gauge

Now we must choose a set of variables and a gauge, to get a partial differential equations system that we solve numerically. The first ingredient in the formalism presented in [73] is the conformal decomposition of the three-metric [291]. We define on each slice Σ_t an extra metric noted f_{ij} , that will have a vanishing Riemann tensor (flat metric) and will be time independent. The existence of such a metric in a neighborhood of spatial infinity is ensured by our sub-manifold being asymptotically flat. The associated flat connection is noted \mathcal{D}_i . We introduce in Σ_t a conformal metric such that its determinant coincides with that of f_{ij} , as:

$$\tilde{\gamma}_{ij} = \psi^{-4} \gamma_{ij}; \quad \psi = \left(\frac{\det(\gamma)}{\det(f)} \right)^{\frac{1}{12}}. \quad (13.7)$$

The tensor field h^{ij} we use to encode the conformal degrees of freedom is the deviation of the conformal metric from the flat one:

$$\tilde{\gamma}^{ij} = f^{ij} + h^{ij}. \quad (13.8)$$

We also define in our equation sources the following conformal traceless extrinsic curvature:

$$\hat{A}^{ij} = \psi^{10} \left(K^{ij} - \frac{1}{3} K \gamma^{ij} \right); \quad (13.9)$$

We choose for a gauge the generalized Dirac gauge for the conformal metric:

$$\mathcal{D}_k \tilde{\gamma}^{ki} = \mathcal{D}_k h^{ki} = 0, \quad (13.10)$$

and we add to this prescription the maximal slicing condition, i.e the vanishing of the trace in the extrinsic curvature: $K = 0$. Therefore, \hat{A}^{ij} contains all the information about extrinsic geometry.

Under those conditions, we can rewrite the (3+1) Einstein equations in what we shall call the FCF system:

$$\Delta \psi = \mathcal{S}_\psi(N, \psi, \beta^i, \hat{A}^{ij}, h^{ij}), \quad (13.11)$$

$$\Delta(N\psi) = \mathcal{S}_{(N\psi)}(N, \psi, \beta^i, \hat{A}^{ij}, h^{ij}), \quad (13.12)$$

$$\Delta \beta^i + \frac{1}{3} \mathcal{D}^i \mathcal{D}_j \beta^j = \mathcal{S}_\beta^i(N, \psi, \beta^i, \hat{A}^{ij}, h^{ij}), \quad (13.13)$$

$$\begin{aligned} \frac{\partial^2 h^{ij}}{\partial t^2} - \frac{N^2}{\psi^4} \Delta h^{ij} - 2\mathcal{L}_\beta \frac{\partial h^{ij}}{\partial t} + \mathcal{L}_\beta \mathcal{L}_\beta h^{ij} = \\ \mathcal{S}_{h^{ij}}^{ij}(N, \psi, \beta^i, \hat{A}^{ij}, h^{ij}). \end{aligned} \quad (13.14)$$

Δ is the usual scalar flat laplacian (which expression from a spectral point of view is recalled in the Appendix 13.A). The actual sources $\mathcal{S}...$, in general non-linear in the variables and time-dependent, can be retrieved by the reader from [73].

We must supplement this system with the kinematical relation between the three-metric and extrinsic curvature of the slice, deduced from (13.3) and (13.9) (see equation (92) of [73]). This fully constrained scheme is strictly equivalent to the one presented in [73]. A slightly different version has been presented recently in [135], focusing on non-uniqueness issues. Although the scheme in [135] would probably pose no additional difficulty in the present setting (except maybe some more boundary conditions to prescribe to additional variables), there has been no significant indication of problems involving non-uniqueness of solutions in our study, that suggested modifications of the original formalism.

Here we choose as variables the quantities $N\psi$, ψ , β^i and h^{ij} . We especially come up with three elliptic equations, two scalar and one vectorial. Those are derived directly from the Hamiltonian and momentum constraints of the (3+1) system, together with the trace part of the dynamical equations. In an evolution scheme, these will be the conditions enforced at each value of time t . We do this for one particular slice.

We are then left in general with a second-order tensorial hyperbolic equation (13.14) dealing with the variable h^{ij} , that is obtained by the geometrical relation between γ_{ij} and K_{ij} , and the dynamical part of Einstein equations.

The goal here is to simulate as accurately as possible stationary spacetimes containing one black hole, represented by an isolated horizon. In this respect, we shall assume a coordinate system that is adapted to stationarity. This will mean that a stationary timelike Killing vector field will be identified with our time evolution vector field $(\frac{\partial}{\partial t})^i$. Using this prescription, all the time derivatives in our equations vanish, so that our sources and operators simplify somewhat. We come up in particular for the tensorial equation with an elliptic-like operator acting on h^{ij} :

$$\Delta h^{ij} - \frac{\psi^4}{N^2} \mathcal{L}_\beta \mathcal{L}_\beta h^{ij} = \mathcal{S}_2^{ij}(h^{ij}, N, \psi, \beta, A^{ij}). \quad (13.15)$$

Our problem is then totally equivalent to an actual initial data problem, where quantities have to be determined on a three-slice by elliptic equations, before evolving them. The main difference with classical initial data schemes like the conformal transverse traceless (CTT), the extended conformal thin sandwich (XCTS) scheme or the conformal flat curvature (CFC) system, is an additional elliptic equation for the conformal geometry of the three-slice. Up to now, a vast majority of initial data computations have been done using an *ad hoc* prescription for the conformal geometry. The most common one is the conformally flat approach, where $\tilde{\gamma}_{ij}$ is simply approximated to be the 3D flat metric. This has been done in numerous computations, and this type of initial data is the most frequently used for black hole evolution simulations. However, though this conformally flat approximation turns out to be well-behaved in most cases, we know that it is a strong limitation when trying to compute stationary black hole spacetimes: it has been proven that the rotating Kerr-Newman spacetime does not admit any conformally flat slice (see [473, 196]).

Other prescriptions for the conformal geometry include data suggested by the post-Newtonian formalism [114], or superposition of additional gravitational wave content (see [90]). Let us mention the work of [471] for neutron-star binary initial data, which also computes the conformal geometry using a prescription in [419], that considers as well the dynamical Einstein equations for the conformal variables. Finally, the exact scheme we have explicated above has been applied by one of the authors in the case of a single rotating neutron star in equilibrium [293]. It has led to the computation of

strictly stationary initial data, that can be directly extended into future and past time directions. This is exactly what we are trying to do here in the black hole case.

13.3.3 Resolution of conformal metric part

Apart from the boundary condition problem (that we discuss in Sec. 13.4), our approach for the resolution of the tensorial equation presents some peculiarities that we explain here.

The system of equations is composed of equation (13.15) and the gauge condition:

$$\mathcal{D}_i h^{ij} = 0, \quad (13.16)$$

that we supplement with a condition on the determinant of $\tilde{\gamma}^{ij}$, following from our definition of the conformal factor:

$$\det(\tilde{\gamma}^{ij}) = \det(h^{ij} + f^{ij}) = 1. \quad (13.17)$$

We are left with a tensorial equation for a symmetric tensor with four constraints: the system has two degrees of freedom. We now try to make them explicit and solve for the related variables. Any second-rank symmetric tensor h^{ij} can be decomposed in the following way into a divergence free part, and a symmetrized gradient part:

$$h^{ij} = \mathcal{D}^i W^j + \mathcal{D}^j W^i + h_T^{ij}, \quad (13.18)$$

with $\mathcal{D}_i h_T^{ij} = 0$. We shall use here variables associated only with the divergence-free part h_T^{ij} , meaning that the gauge component (gradient part) of the tensor considered has no influence on them. We choose to encode the information in h_T^{ij} in the two scalar spectral potentials A and \tilde{B} presented in [134], and whose definitions are quickly recalled in the Appendix 13.A. (A more extensive study shall be performed in [340]).

What is remarkable about quantities A and \tilde{B} is that they can actually be decomposed into scalar spherical harmonics, and that the tensorial Poisson equation $\Delta h^{ij} = S^{ij}$ decouples into scalar elliptic equations A and \tilde{B} (see the Appendix 13.A). This is not exactly the case for the nonlinear modified elliptic operator (13.16); however, in our numerical scheme, we just slightly modify the sources of the equation at each iteration so that we can write:

$$\Delta A - \frac{\psi^4}{N^2} \mathcal{L}_\beta \mathcal{L}_\beta A = A_S(h^{ij}, N, \psi, \beta, A^{ij}), \quad (13.19)$$

$$\tilde{\Delta} \tilde{B} - \frac{\psi^4}{N^2} \mathcal{L}_\beta \mathcal{L}_\beta \tilde{B} = \tilde{B}_S(h^{ij}, N, \psi, \beta, A^{ij}), \quad (13.20)$$

the elliptic operator $\tilde{\Delta}$ being defined in the Appendix 13.A. We keep the Lie derivative notation for scalar fields, to show that this is directly related to the operator in Eq. (13.15); of course, in the scalar case, this operator simply reduces to $\mathcal{L}_\beta A = \beta^i \mathcal{D}_i A$. During the iteration of the resolution algorithm, the sources of the equations are updated so that they stay coherent with the original equation in h^{ij} . Equations (13.19) and (13.20) are the two elliptic equations that we solve at each iteration.

Specifically, at each step, we proceed as follows: once the scalars A and \tilde{B} are determined by the resolution of (13.19) and (13.20), the Dirac gauge and unit determinant conditions allow us to totally reconstruct a divergence-free tensor, as the expected solution of our tensorial equation. This is done by inverting two differential systems ((13.66) and (13.67) of the Appendix 13.B), that express the Dirac gauge conditions and definitions of the scalars A and \tilde{B} in function of the tensor components.

Those differential systems involve scalars, which are components of h^{ij} in a tensor spherical harmonics basis (see the Appendix 13.A, and Sec. V of [134]).

The differential systems require three boundary conditions on the excised surface, to be inverted; we discuss them in Sec. 13.4, in a detailed description of the scheme. In addition, we fix the trace of our tensor with respect to the flat metric, so that the calculated determinant at this step is one. This reduces to an algebraic nonlinear condition for the tensor components. Finally, we update our sources for the next step. We note here that the resolution for the variable \tilde{C} introduced in the appendix is not necessary in this scheme: for a divergence-free tensor, \tilde{C} is unambiguously determined by the knowledge of \tilde{B} and the trace.

With this tensorial scheme, the gauge is necessarily enforced by construction, so no gauge-violating mode can occur. This is in the same spirit as the global fully constrained formalism (equations (13.11-13.13)) for our equation system, that forbids *a priori* all constraint-violating modes. We also emphasize the fact that, in the general case and with an arbitrary source for (13.15), we do not recover an actual solution of the equation by reconstructing our tensor this way. This is only true if the elliptic equation admits a solution that actually satisfies the Dirac gauge and the determinant condition. We can see it as an integrability condition for our equation, that is for example not generically true during an iteration. However, since in our case we are looking for stationary axisymmetric data for a single black hole, we know that our entire system does admit a solution: it is the Kerr-Newman spacetime in Dirac gauge. As a consequence, if our scheme converges, we know that the tensor field h^{ij} we obtain shall satisfy the dynamical Einstein equations, thus equation (13.16).

The missing ingredient for solving all our system of equations in an excised spacetime is the setting of boundary conditions for our partial differential equations, following part of the geometrical prescriptions of the isolated horizon formalism, namely non-expanding horizon boundary conditions.

13.4 Boundary conditions and resolution of the FCF system

13.4.1 Boundary conditions for the constraint equations

Besides the prescription of asymptotic flatness at infinity and the bulk stationarity prescription, all the physics of our system will be contained in the boundary conditions we shall put on our excised surface. This section follows largely the prescriptions of [222].

We consider our excised two-surface to be a slice of a non-expanding horizon, i.e. a MOTS with vanishing outgoing shear. Following Sec. 13.2, this translates into several geometrical prescriptions, namely the vanishing of the outgoing expansion and the shear two-tensor: $\theta_\ell = 0$ and $\sigma_{ab} = 0$.

Being an instantaneous non-expanding horizon, the evolution of the excision surface will be a null tube. Since we are adapting our coordinates to stationarity, another important condition on the excised boundary consists in prescribing the time evolution vector field of our coordinates to be tangent to the null tube. Thus, we are ensured that our horizon location stays instantaneously fixed during an evolution. Those prescriptions on the horizon will suffice to give four boundary conditions for the constraint equations (one is scalar and the other vectorial), as we see below.

We certainly have freedom to prescribe the coordinate location of our excision surface in our coordinate system. For simplicity, we choose the surface to be a coordinate sphere, fixed at a radius $r_{\mathcal{H}}$. We shall denote by s^i the unit outer spacelike normal to the surface, that will be tangent to the

three-slice Σ_t . The shift vector is then decomposed into two orthogonal parts adapted to the geometry of the horizon: $\beta^i = bs^i - V^i$.

The vanishing of the expansion can be expressed as a condition for the conformal factor on the horizon:

$$4\tilde{s}^i \tilde{D}_i \ln(\psi) + \tilde{D}_i \tilde{s}^i + \psi^{-2} K_{ij} \tilde{s}^i \tilde{s}^j = 0, \quad (13.21)$$

where we have used the conformal rescaling $\tilde{s}^i = \psi^2 s^i$, and the notation \tilde{D}_i for the connection associated with the conformal three-metric. Multiplying (13.21) by ψ , it can be seen as a non-linear Robin condition for the quantity ψ . The requirement for the time evolution vector field on the horizon to be tangent to the null tube provides the equality $b = N$. This is a natural way to fix the component of the shift normal to the two-sphere. We must also fix V^i , the part of the shift tangent to the two-sphere. For this we make use of the vanishing of the symmetric shear tensor σ_{ab} . It can be shown ([133] and [222]) that the vanishing of the shear is equivalent to the following equation for V^i :

$$q_{bc} {}^2D_a V^c + q_{ac} {}^2D_b V^c - q_{ab} {}^2D_c V^c = 0. \quad (13.22)$$

Here 2D is the connection associated with q_{ab} on the surface. This means that V^i is a conformal Killing symmetry for the two-sphere (in particular, quantities in (13.22) can be substituted by *tilded* conformal ones). Defining coordinates (θ, φ) on our two-sphere, we prescribe V^i as:

$$V^i = \Omega \left(\frac{\partial}{\partial \varphi} \right)^i, \quad (13.23)$$

and we shall verify *a posteriori* that this is a (conformal) axial symmetry. The constant Ω will be called the rotation rate of the horizon, φ being the azimuthal coordinate. In the case of the Kerr spacetime, there is an analytical relation between the areal radius of the apparent horizon, the (reduced) angular momentum parameter $\frac{a}{M}$, and Ω . From a more general point of view, different values for Ω will likely affect directly the angular momentum. In the general case, we define a parameter a for the angular momentum associated with the entire spacetime, from the dimensionless relation:

$$\frac{a}{M_{ADM}} = \frac{J_K}{M_{ADM}^2} \quad (13.24)$$

with M_{ADM} the ADM mass of the 3-slice, and J_K the Komar angular momentum of the 3-slice at infinity; the latter is tentatively defined with the (presumably) Killing vector $\left(\frac{\partial}{\partial \varphi} \right)^i$ (see Equations (7.14) and (7.104) in [214] for explicit expressions for M_{ADM} and J_K). Note that we do not impose any Killing symmetry, except on the horizon: we know however, by the black hole rigidity theorem [242], that an accurate resolution of Einstein equations would impose this vector to be so. We discuss the dependence between all those quantities in Sec. 13.5.

Once we have set boundary conditions for the conformal factor and the three components of the shift vector, we must still fix the lapse function on the horizon. Different prescriptions have been considered in the literature (e.g. [129, 133, 113, 264, 265, 222]). In the spirit of the effective approach in [133, 113], we arbitrarily impose the value of the lapse to be a constant $N_{\mathcal{H}}$ on the excised sphere.

As mentioned before, previous boundary conditions define with no ambiguity our excised surface to be a slice of a non-expanding horizon. Moreover, our choice for the lapse, the horizon location and the conformal Killing symmetry on the horizon fixes coordinates on the two-sphere. Only the conformal two-geometry of the excised sphere remains to be fixed. This is done in relation with the resolution scheme for the h^{ij} equation.

13.4.2 Boundary conditions for the h^{ij} equation

We recall that, with the approach developed in Sec. 13.3, the resolution of our tensorial problem in Dirac gauge reduces to two elliptic-like scalar equations, to be solved on a three-slice excised by a two-sphere: we should normally provide two additional boundary conditions for those equations.

A result by [268] shows that in the full evolution case for this tensorial equation (equation (13.14)) and in a Dirac-like gauge, the characteristics of the equation are not entering the resolution domain when the spacetime is excised by a null or spacelike marginally trapped tube. This means that in the evolution case, once the initial data are set, there is no boundary condition whatsoever to prescribe to the hyperbolic equation.

The problem is of course different here, where we are left with an elliptic equation instead of a hyperbolic one. However, a simple analysis will hint that in our particular single horizon case, there will not be any inner boundary condition to be prescribed on our data.

Let us examine the case of the elliptic equation in A , that we recall here:

$$\Delta A - \frac{\psi^4}{N^2} \mathcal{L}_\beta \mathcal{L}_\beta A = A_S(h^{ij}, N, \psi, \beta, \hat{A}^{ij}). \quad (13.25)$$

We will try and exhibit a simplified linear operator acting on the variable A , that will contain the most relevant terms. The double Lie derivative operator acting on A can be separated in:

$$\frac{\psi^4}{N^2} \mathcal{L}_\beta \mathcal{L}_\beta A = \frac{\psi^4}{N^2} (\beta^r)^2 \partial_r^2 A + \frac{\psi^4}{N^2} (\mathcal{L}_\beta \mathcal{L}_\beta A)^*; \quad (13.26)$$

the second term contains all the remaining components of the double Lie derivative.

At this point, and with a fixed system of spherical coordinates, we are allowed to make a decomposition into spherical harmonics for all the scalar variables. We write in this respect:

$$A = \sum_{(l,m)} A_{lm} Y_{lm}(\theta, \varphi), \quad (13.27)$$

where Y_{lm} are the spherical harmonics of order (l, m) , defined as eigenfunctions of the angular Laplace operator: $\Delta_{\theta\varphi} Y_{lm} = -l(l+1)Y_{lm}$.

We now point out the fact that, due to our coordinate choice, we have $(\beta^r)_{(l=0)} = (\frac{N}{\psi^2})_{(l=0)}$ on the horizon. We can use a second-order Taylor expansion to write the $l=0$ part of the factor in front of the first term of (13.26), close to our surface coordinate radius $r_{\mathcal{H}}$:

$$\left[\frac{\psi^4}{N^2} (\beta^r)^2 \right]_{(l=0)} \partial_r^2 A = [1 + \alpha(r - r_{\mathcal{H}}) + \delta(r - r_{\mathcal{H}})^2 + \mathcal{O}(r - r_{\mathcal{H}})^3] \partial_r^2 A, \quad (13.28)$$

where α and δ are two real numbers that can be directly computed during one iteration, from the values of N , ψ and β^r at the excised surface. Our global equation can be rewritten for each spherical harmonic l as:

$$\begin{aligned} [-\alpha(r - r_{\mathcal{H}}) - \delta(r - r_{\mathcal{H}})^2] \frac{\partial^2}{\partial r^2} A_{lm} + \frac{2}{r} \frac{\partial}{\partial r} A_{lm} \\ - \frac{l(l+1)}{r^2} A_{lm} = A_S + \frac{\psi^4}{N^2} (\mathcal{L}_\beta \mathcal{L}_\beta A)_{lm}^{**}, \end{aligned} \quad (13.29)$$

where we only keep on the left-hand side the terms given in (13.28), and put the rest (denoted with **) with the source. The latter contains the remaining components of the double Lie derivative, and involves either terms that are not second-order in the radial derivative, or that are multiplied by the higher harmonics of $\frac{\psi^4}{N^2}(\beta^r)^2$ (supposedly smaller than the main term, explicitly developed in (13.29)). Thus, we have isolated a linear operator $\mathcal{Q}_{\alpha\delta}$, depending on two real numbers α and δ :

$$\begin{aligned} \mathcal{Q}_{\alpha\delta} &= \left[-\alpha(r - r_{\mathcal{H}}) - \delta(r - r_{\mathcal{H}})^2 \right] \frac{\partial^2}{\partial r^2} \\ &+ \frac{2}{r} \frac{\partial}{\partial r} - \frac{l(l+1)}{r^2} I, \end{aligned} \quad (13.30)$$

other contributions being taken as source terms. This operator is different from the ordinary Laplace operator by the factor in front of the second order differential term, which vanishes on the excision boundary. It can be shown that the space of analytic solutions on \mathbb{R}^3 minus the excised horizon belonging to the kernel of $\mathcal{Q}_{\alpha\delta}$ is generally of dimension one. This is in contrast with the case of the Laplace equation, where it is of dimension two. In practice, this will mean that for a numerical resolution of an equation $\mathcal{Q}_{\alpha\delta}f = S_f$, there is only one boundary condition to fix for the unknown, mainly the behavior at infinity. No additional information is needed at the excised boundary for the *effective* operators (13.30). Operators of this kind are known in the mathematical literature as elliptic operators with weak singularities [236].

The very same scheme can be applied to the equation (13.20) for \tilde{B} , the only difference being that the original Laplace operator is replaced by a slightly modified one (see the Appendix 13.A).

As explained in Sec.13.3.3, after solving for the two main equations (13.29) and its equivalent in \tilde{B} , the inversion of the gauge differential systems (13.66-13.67) (explicited in the appendix 13.B) for the reconstruction of h^{ij} requires three extra boundary conditions, in addition to the vanishing of all quantities at infinity. We obtain them as compatibility conditions based on the original elliptic tensorial equation (13.15): we express three decoupled elliptic scalar equations for three components of h^{ij} in the spin-weighted tensor spherical harmonics basis, denoted h^{rr} , η and μ , which are directly related to the usual tensorial components of h^{ij} and defined in Appendix 13.A. From the tensor equation (13.15), we deduce:

$$\Delta\mu + \frac{2}{r} \frac{\partial\mu}{\partial r} + \frac{2\mu}{r^2} - \frac{\psi^4}{N^2} (\mathcal{L}_\beta \mathcal{L}_\beta h^{ij})^\mu = (S_2^{ij})^\mu \quad (13.31)$$

$$\Delta\eta + \frac{2}{r} \frac{\partial\eta}{\partial r} + \frac{2\eta}{r^2} + \frac{2h^{rr}}{r^2} - \frac{\psi^4}{N^2} (\mathcal{L}_\beta \mathcal{L}_\beta h^{ij})^\eta = (S_2^{ij})^\eta \quad (13.32)$$

$$\begin{aligned} \Delta h^{rr} - \frac{6h^{rr}}{r^2} - \frac{4}{r^2} \Delta_{\theta\varphi} \eta + \frac{2h}{r^2} - \frac{\psi^4}{N^2} (\mathcal{L}_\beta \mathcal{L}_\beta h^{ij})^{rr} \\ = S_2^{rr}, \end{aligned} \quad (13.33)$$

where (μ, η, rr) superscripts indicate the corresponding components of h^{ij} in the tensor spherical harmonics basis (see Appendix 13.A). As for the equation involving A , we can rewrite the above equations by extracting the weakly singular operator $\mathcal{Q}_{\alpha\delta}$ acting on the principal variable, the other contributions being put on the right-hand side of the equations. For example, the equation in μ can be rewritten the following way:

$$\mathcal{Q}_{\alpha\delta}(\mu) + \frac{2}{r} \frac{\partial\mu}{\partial r} + \frac{2\mu}{r^2} = (S_2^{ij})^\mu + \frac{\psi^4}{N^2} (\mathcal{L}_\beta \mathcal{L}_\beta h^{ij})^{\mu(**)}, \quad (13.34)$$

with the Lie derivative term containing all the left-hand-side contributions of equation (13.31) not taken into account. We do not need to invert this equation: however, as the leading order term in $\mathcal{Q}_{\alpha\delta}$ vanishes at the horizon ($r_{\mathcal{H}} = 1$), we can accordingly write a Robin-like boundary condition for the μ quantity:

$$\frac{4}{r} \frac{\partial \mu}{\partial r} + \frac{(\Delta_{\theta\varphi} + 2)}{r^2} \mu = \left(S_2^{ij}\right)^\mu + \frac{\psi^4}{N^2} (\mathcal{L}_\beta \mathcal{L}_\beta h^{ij})^{\mu(**)}. \quad (13.35)$$

This will be used as a boundary condition for the gauge system (13.66), the source terms being computed with quantities from the previous iteration. Using the same method, we can write very similar expressions (that we do not explicitly give here) for the fields h^{rr} and η , to be used as Robin boundary conditions applied to the gauge differential system (13.67). The three boundary conditions are sufficient to invert the two gauge systems (13.66-13.67) [340], and reconstruct the whole h^{ij} tensor from the tensor spherical harmonics components (see the Appendix 13.B and [340] for details).

To summarize, the method employed for the resolution of the whole h^{ij} system is iterative and can be decomposed for each step in the following way (more technical details are provided in the Appendices):

1. After calculating the source \mathcal{S}_2^{ij} from equation (13.15), we deduce the right hand side of the equation (13.29) for A , using values from the previous iteration. The same is done for the quantity \tilde{B} and its corresponding source terms.
2. We invert equations (13.29) and its equivalent for \tilde{B} , only by imposing that the fields are vanishing at infinity.
3. We compute the value of the trace from equation (13.17) (a more explicit expression can be found in equation (169) of [73]). This allows us to write the two differential systems (Dirac gauge systems) mentioned in Sec. 13.3.3 and expressed in Appendix 13.B, involving the spherical harmonics components of h^{ij} (scalar quantities).
4. We invert these two gauge differential systems using three boundary conditions similar to Eq. (13.35), for the three scalar spherical harmonics components h^{rr} , η and μ . As those are compatibility conditions expressing information already contained in Eq. (13.15), we provide in this way no additional physical information to reconstruct h^{ij} . This gives us the spherical harmonics components of h^{ij} .
5. We reconstruct the whole tensor h^{ij} from the spherical harmonics components.

We have not proven here that no boundary condition has to be put generically for the resolution of the two scalar equations involving A and \tilde{B} in the tensorial system. However, if we implement numerically the resolution by the inversion of the operator $\mathcal{Q}_{\alpha\delta}$ at each iteration, we will not have to impose any boundary condition, but only informations coming from the Einstein equations. Moreover, a convergence of the entire h^{ij} system would support the coherence of the reasoning, and hint that there is, in our case, a deeper physical motive preventing the prescription of additional information on the horizon. The results in Sec. 13.5 show this is the case.

13.5 Numerical results and tests

13.5.1 Setting of the algorithm

All the numerical and mathematical tools we use here are available in the open numerical relativity library LORENE [216]. Our simulation is made on a 3D spherical grid, using spherical harmonics decomposition for the angular part and multidomain tau spectral methods (see [230] for a review). The mapping consists in four shells and an outer compactified domain, so that infinity is part of our grid and we have no outer boundary condition to put at a finite radius. Our grid size is typically $N_r \times N_\theta \times N_\varphi = 33 \times 17 \times 1$. We also have checked our code by setting $N_\varphi = 4$, to verify that no deviation from axisymmetry occurred. Our innermost shell has a boundary at the radius $r_{\mathcal{H}}$, which will be the imposed location of a MOTS, and will be used as the unit of length in all the results presented here. We impose the values of all the fields to be equivalent at infinity to those of a flat three-space. Finally, trying to get stationary data, we prescribe our coordinates to be adapted to this stationarity, so that all the time derivatives in the Einstein (3+1) system are set to zero. However, even if we expect to get axisymmetric data (the only vacuum stationary solution for a black hole being the Kerr solution), we are always able to solve our equations in three dimensions.

We proceed with our scheme in the following way: during one iteration, all the variables are updated immediately after they have been calculated, so that the sources for the next equations are modified. The tensorial equation for h^{ij} is the last solved in a particular iteration, and we obtain at each step a local convergence for the whole tensorial system (including the determinant condition), before we proceed to the update of all quantities, and to the next iteration.

We impose on the sphere of radius $r_{\mathcal{H}}$ the conditions of zero expansion (13.21) and shear (13.22), via respectively a Robin condition on the quantity ψ and a Dirichlet condition on the partial shift V^i . We also impose the horizon-tracking coordinate condition on the radial shift component b . Having set the shape and the location of the surface in our coordinates, we are only left with two free parameters, which are the boundary value of the lapse function and the rotation rate Ω . As we said, the lapse function, which is merely a slicing gauge choice, is fixed to a constant value $0 \leq N_{\mathcal{H}} \leq 1$ on the horizon. We generate two sets of data on our three-slice, spanning the rotation rate from zero (Schwarzschild solution) to a value of about 0.22, where our code no longer converges. One set will give the solution for the whole differential system (the non-conformally flat (NCF) data, supposed to converge to the rotating Kerr solution), while the other will compute conformally flat (CF) data, by putting $h_{ij} = 0$. From a spacetime point of view, the CF data can also be seen as a computation of black hole spacetime using the so-called Isenberg-Wilson-Mathews approximation to general relativity [260], [482].

13.5.2 Numerical features of the code

Figure 13.1 presents, on the one hand, the absolute accuracy obtained for the Einstein constraints (in the form expressed in [486]) in the NCF case. Regarding fulfillment of the Einstein dynamical equation, Figure 13.1 also shows the accuracy of the NCF fully stationary solution, as well as its violation in the conformally flat case. We see the expected improvement for precision of resolution of dynamical equations in the full NCF case. Let us note that a verification of the gauge conditions is not even necessary, as it is fulfilled by construction (we only solve for variables satisfying the gauge). This is one of the strengths of our algorithm.

A non-trivial issue of our computation is the link between the two physical characteristics of the system (the mass and angular momentum of the data) and the two input quantities supposed to fix

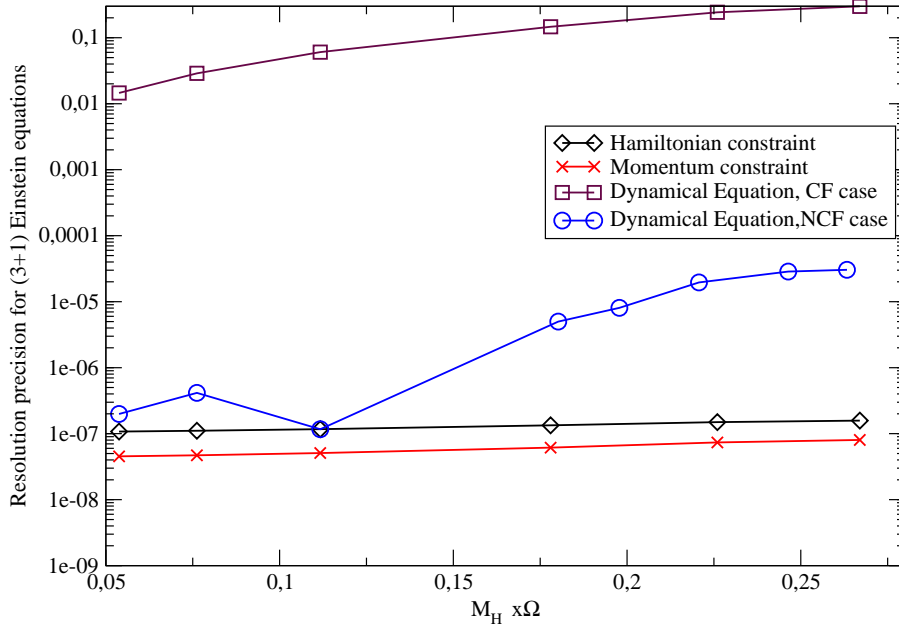


Figure 13.1: Accuracy for Einstein equations resolution (in the original (3+1) version of [486]) as a function of dimensionless parameter $M_{\mathcal{H}}\Omega$ (see section 13.5.3 for a definition of $M_{\mathcal{H}}$). Data are absolute maximum error values for both constraint equations, and dynamical equations in both cases. Data are taken with $N_r = 33$, $N_\theta = 17$, $N_\varphi = 1$. Lapse on the horizon is $N_{\mathcal{H}} = 0.55$.

them, namely the boundary value for the lapse and the rotation rate Ω on the horizon. We choose here in our sequence to fix the value of the horizon coordinate radius, removing it from the list of variables. Results are shown in figure 13.2. The value of the lapse being also fixed, we observe that an increase in Ω not only affects the angular momentum, but also the ADM mass of the spacetime. Moreover, fixing the rotation rate does not amount to the prescription of the angular momentum to an *a priori* given value. A decrease in the value of $N_{\mathcal{H}}$ on the horizon results also in an increase in $\frac{a}{M}$ (defined in section 13.4.1). This stems from the fact that our choice for the slicing directly influences in this approach the physical parameters (e.g the areal radius) of the solution obtained. We note also that for a fixed value of $N_{\mathcal{H}}$, the correspondence between Ω and $\frac{a}{M}$ is slightly different in the conformally flat case and in the NCF case. With our algorithm, a larger value of the lapse gives a slightly better convergence of the code for high rotation rates of the black hole (until $N_{\mathcal{H}} = 0.8$ approximatively). For each lapse the code stops converging at a certain value of the rotation rate. We do not yet know whether this is a problem of our algorithm to be improved, or if this has deeper physical reasons: constant values for the lapse and the rotation rate might not be “good” variables for the Kerr black hole in Dirac gauge, once we reach high rotation rates. The only conclusion we can draw from this is that there is a non trivial correspondence between our “effective parameters” $N_{\mathcal{H}}$ and Ω , and the physical ones, namely the ADM mass and Komar angular momentum. This correspondence is likely to be one to one for values of $\frac{a}{M}$ below a certain threshold of about 0.85. Reaching higher values for $\frac{a}{M}$ is left to future numerical investigations.

Let us mention again the remark made by [133] about the boundary condition for the lapse in the XCTS scheme. Although it is necessary to fix the slicing of the spacetime by an arbitrary boundary

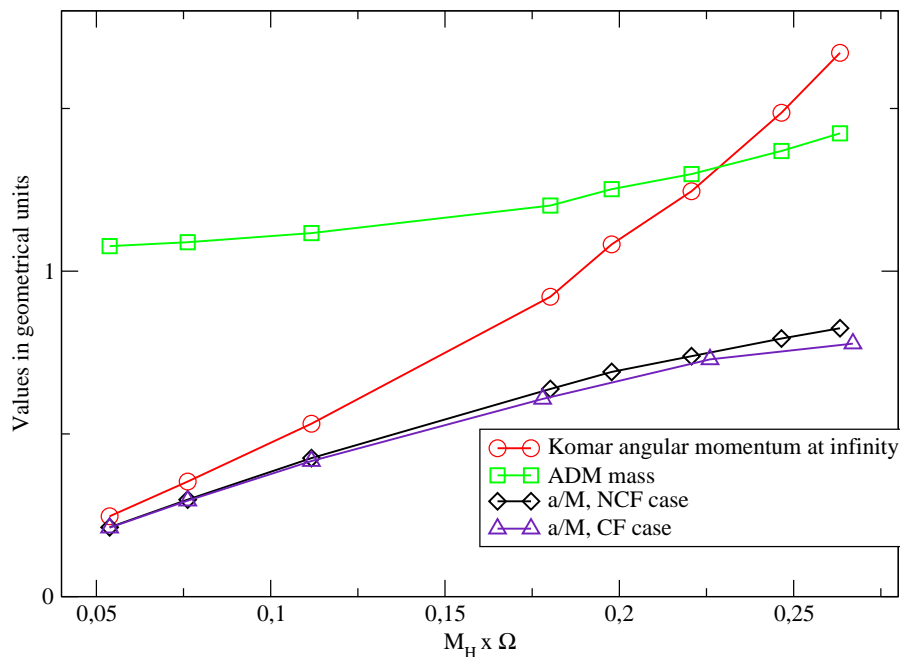


Figure 13.2: Dependence on the parameter $M_H \Omega$ of the ADM mass, the Komar angular momentum at infinity J_K and the angular momentum parameter $\frac{a}{M}$ (both defined in section 13.4.1) for both cases. The value of the lapse on the horizon is here fixed at $N_H = 0.55$.

condition on the lapse, we have the freedom to decide what kind of condition to impose. The authors in [133] suggest that an arbitrary condition of Neumann or Robin type would be preferable, because it is more flexible in view of a numerical algorithm. In particular, not fixing a value for the lapse on the horizon, but rather giving a first order prescription, allows the data to “adapt” to potentially high tidal distortions. However, having also tried to impose Neumann conditions for the lapse in our configurations, we do not see any clear improvement in the robustness of the algorithm. This is why we still keep a Dirichlet boundary condition as the simplest prescription.

13.5.3 Physical and geometrical tests for stationarity

One of the tests of stationarity to be made can be the comparison between the ADM mass and the Komar mass at infinity, defined with the (presumably) Killing vector $(\frac{\partial}{\partial t})^i$ (equation (7.91) of [214]). The results of this test are displayed in figure 13.3. The comparison between the ADM mass and the Komar mass is actually directly linked to the Virial theorem of general relativity put forth by [220]. The concordance between those masses is equivalent to the vanishing of the Virial integral, and has been also used as a stationarity marker by [219].

We have also computed in both NCF and CF cases an estimate of the amount of gravitational radiation contained outside the black hole in the 3-slice. Following the prescriptions of [36], we calculate the difference between the ADM mass and what could be called the isolated horizon mass, defined in geometrical units by:

$$M_H = \frac{\sqrt{R_H^4 + 4J_H^2}}{2R_H}. \quad (13.36)$$

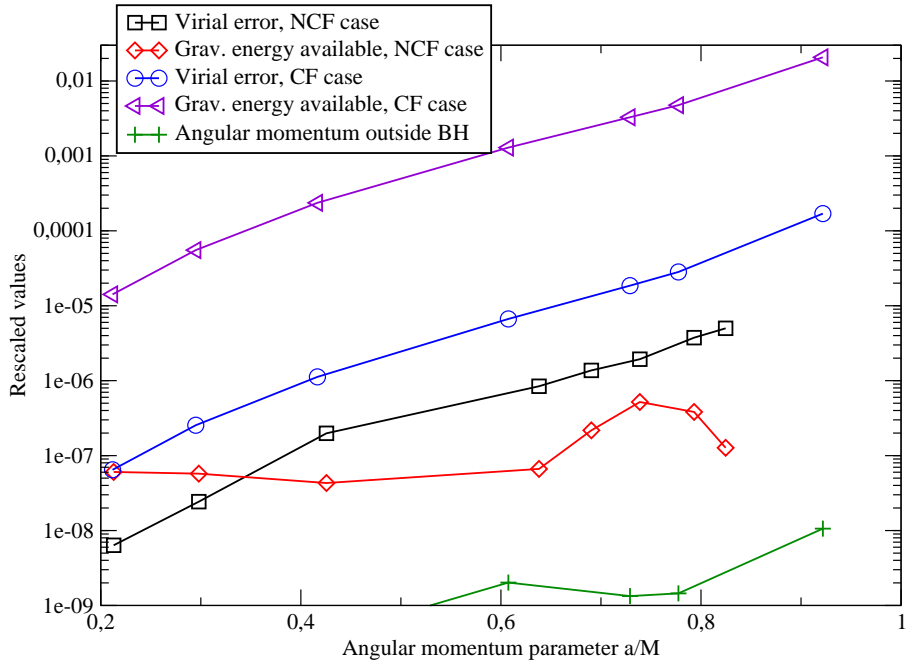


Figure 13.3: Different diagnostics for stationarity in both cases, comparing physical quantities at the horizon and at infinity. The virial error computes the difference between ADM and Komar masses at infinity, rescaled with the ADM mass, and using asymptotic behaviors of the lapse and conformal factor. The radiation energy content outside the black hole (resp. outer angular momentum content) is the absolute difference between the horizon mass $M_{\mathcal{H}}$ (resp. angular momentum on the horizon $J_{\mathcal{H}}$) and the ADM mass M_{ADM} (resp. Komar angular momentum at infinity J_K), rescaled with the ADM mass (resp. Komar angular momentum at infinity).

where $R_{\mathcal{H}}$ is the areal radius of \mathcal{H} . $M_{\mathcal{H}}$ is nothing but the formula for the Christodoulou mass [122] calculated from the Komar angular momentum $J_{\mathcal{H}}$ on the horizon (defined with the same supposed Killing symmetry as J_K). If we have an isolated horizon extending to future infinity, the difference between M_{ADM} and $M_{\mathcal{H}}$ gives exactly the radiation energy emitted at future null infinity for the data [36]. In non-stationary cases (for example binary systems), this is an appropriate estimate of the radiation content at an initial given time.

Results for comparison between the two cases studied here are shown in figure 13.3. Although the gravitational energy available for NCF spacetimes is contained under 10^{-7} whatever the rotation rate might be, in the CF case, the increase in energy with $\frac{a}{M}$ is patent. This measure of energy available with respect to $\frac{a}{M}$ gives us a way of approximating *a priori* the amount of what is usually called “junk” gravitational radiation, that could be emitted on a spacetime evolution with conformally flat initial data.

In the same spirit, we have also computed the accuracy in the verification of a Penrose-like inequality for axisymmetric data, that can be written as:

$$\epsilon_A = \frac{\mathcal{A}}{8\pi(M_{ADM}^2 + \sqrt{M_{ADM}^4 - J_K^2})} \leq 1, \quad (13.37)$$

where \mathcal{A} is the minimal area of a surface containing the horizon, J_K is the Komar angular momentum at infinity and M_{ADM} is the ADM mass at infinity. Being a little more stringent than the actual Penrose inequality, it has been first proposed by [242] for axisymmetric spacetimes. This inequality is supposed to be verified for all axisymmetric data containing an apparent horizon, and to be an equality only for actual Kerr data (this is referred to in [266] as *Dain's rigidity conjecture* [139]). The results are presented in figure 13.4. We observe that, if the equality is very well verified in the actual Kerr case, this is definitely not true for CF data, even for reasonable values of $\frac{a}{M}$. In [266] (cf. [267] for a general context), it has been proposed that this quantity ϵ_A (*Dain's number*) should be understood as a strong diagnosis tool for distinguishing between Kerr horizons and other isolated or dynamical horizons. This numerical observation shows strong support in favor of this claim, pulling apart actual Kerr data and reasonable approximations of these data. Let us also point out the virtual costlessness of this tool, as we only have to rely on a single real value.

We also note that, when computing the rescaled difference of Komar angular momentum between the horizon and infinity $\frac{J_K - J_{\mathcal{H}}}{J_K}$, we come up in all cases with a difference at the level of numerical precision for resolution (see figure 13.3). This is of course coherent with the fact that gravitational waves cannot carry any angular momentum in axisymmetric spacetimes. This result ensures us the equivalence in practice between the estimation of radiation exterior to the horizon and the verification of Penrose inequality via Dain's number.

13.5.4 Multipolar analysis

To be much more complete about the geometry of the constructed horizons, one could rely on the source multipole decomposition of the two-surface lying on our three-slice. This feature has first been presented by [37], based on an analogy with electromagnetism, and first studied in [407] in the case of dynamical horizons. We here implement the computation of multipole moments in the isolated horizon case, which is the strict situation where they have been defined in [37].

A prerequisite is the existence of a preferred divergence-free vector field φ^a on the sphere, from which the angular momentum of the horizon is defined (the divergence-free condition on φ^a ensures that all definitions will be gauge-independent). As mentioned above, our chosen vector field will be the one associated with the azimuthal coordinate, namely $\left(\frac{\partial}{\partial\varphi}\right)^i$.

Another important feature is the construction of a preferred coordinate system, so that the Legendre polynomials associated with spherical harmonics will possess the right orthonormality properties; as expressed in the implementation of [407], this reduces to finding a set of coordinates (ζ, φ) where the metric on the two-surface can be written as:

$$q_{ab}^{\mathcal{H}} = R_{\mathcal{H}}^2 (f(\zeta)^{-1} D_a \zeta D_b \zeta + f(\zeta) D_a \varphi D_b \varphi), \quad (13.38)$$

with $R_{\mathcal{H}}$ the areal radius of the sphere and $f(\zeta)$ determined in terms of the two-dimensional Ricci scalar and the norm of φ^a [37]. In the axisymmetric case studied here for the horizon, the integral curves for the coordinate φ are already defined by the orbits of the vector field $\left(\frac{\partial}{\partial\varphi}\right)^i$. The coordinate ζ is defined by

$$D_a \zeta = \frac{1}{R_{\mathcal{H}}^2} \epsilon_{ba} \varphi^b. \quad (13.39)$$

An appropriate normalization should be added, that ensures that $\oint_{\mathcal{H}} \zeta d^2V = 0$. In the Kerr case, those coordinates turn out to correspond with the Boyer-Lindquist coordinates, with $\zeta = \cos\theta$ in spherical coordinates [407].

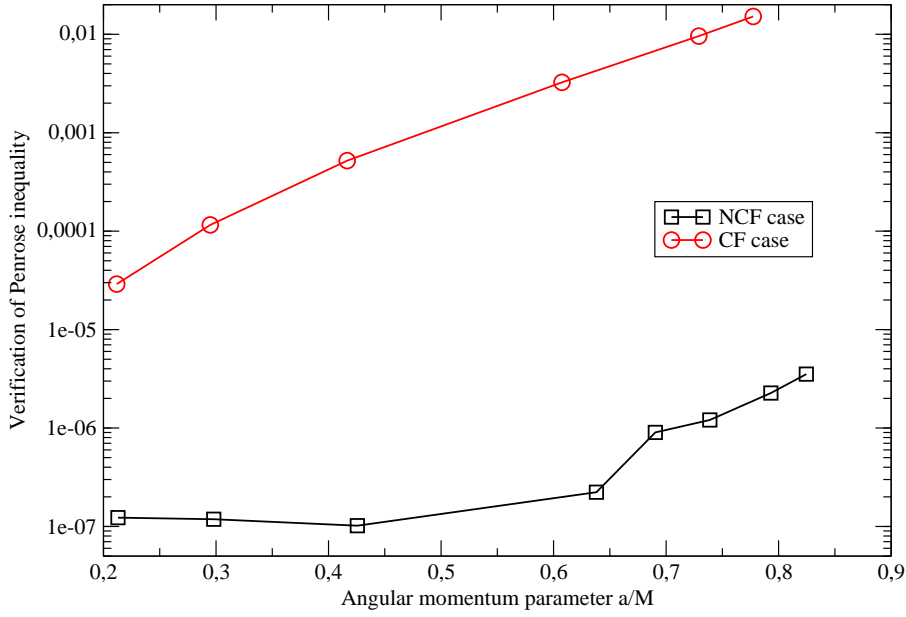


Figure 13.4: Value of $1 - \epsilon_A$ for both data sets.

The mass and angular momentum multipoles of order n are then defined, by analogy with electromagnetism [37]:

$$M_n = \frac{R_{\mathcal{H}}^n M_{\mathcal{H}}}{8\pi} \oint_{\mathcal{S}} \{\mathcal{R}P_n(\zeta)\} d^2V, \quad (13.40)$$

$$J_n = \frac{R_{\mathcal{H}}^{n-1}}{8\pi} \oint_{\mathcal{S}} P'_n(\zeta) K_{ab} s^a \varphi^b d^2V. \quad (13.41)$$

With this definition and using the Gauss-Bonnet theorem it is trivial to see that $M_0 = M_{\mathcal{H}}$ and $J_1 = J_K$, the Komar angular momentum on the horizon.

We should emphasize that these multipoles, except for M_0 and J_1 , are in general different from the field gravitational multipoles that can be defined at infinity. However, the authors in [37] have pointed out that the knowledge of all the multipoles of an isolated horizon allows to reconstruct the whole horizon, and also the spacetime in a vicinity of this horizon. The multipoles then discriminate exactly every isolated horizon, and the spacetime at its vicinity. Figure 13.5 shows the capacity of telling apart the horizon of a CF axisymmetric slice and the one of a NCF slice, in Dirac gauge. Data are also compared with an analytic Kerr solution in Kerr-Schild coordinates. Apart from the accuracy obtained for our NCF data (and a further confirmation that we indeed have obtained the actual Kerr spacetime), we see the clear distinction made by this computation between the Kerr horizon and a conformal approximation of it. Together with Dain's number, this study has proven that those two tools are very well-suited to study isolated horizon properties, and the distance between data obtained from, say an evolution scheme, and the eventual equilibrium black hole data it is supposed to reach. Ultimate tests on the characterization of the obtained data as slices of Kerr could be achieved by implementing the schemes proposed in [198, 173].

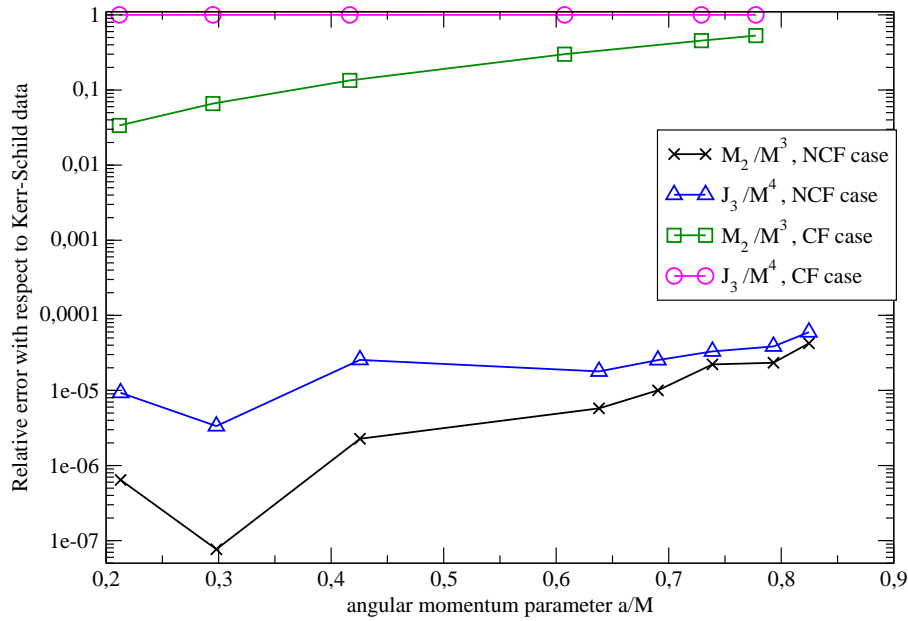


Figure 13.5: Computations of the rescaled second-order mass multipole ($\frac{M_2}{M^3}$) and the rescaled third-order angular multipole ($\frac{J_3}{M^4}$). Relative differences with respect to values for a Kerr-Schild analytical horizon are displayed.

13.6 Discussion

The data we get with our simulations are interesting at several levels. They allow to make a direct comparison between the conformally flat approximation and the exact solution for axisymmetric spacetimes containing a black hole, that are both calculated *a priori* and in the same gauge. As we have seen in Sec. 13.5, this gives us insight about the geometric features of the exact solution; we can single important issues concerning for example the intrinsic geometry of the horizon, via multipoles and the Penrose inequalities. Numerical tools are in this respect implemented and their efficiency tested.

At a more theoretical level, the method we used to get those data is a little bit heterodox: providing standard non-expanding horizon conditions for (3+1) variables such as β^i , ψ and $N\psi$, we choose in addition not to prescribe any further geometrical information for the conformal part, symbolized here by the tensorial field h^{ij} . This has been motivated by the fact that, given the tensorial equation corresponding to h^{ij} in our formalism, it appears that we most likely *cannot* prescribe anything else in the studied setting. By numerical transformation of the operator acting on h^{ij} we ensured that at every iteration step no boundary condition was required. The fact that our system of Einstein equations written this way converges to the required Kerr solution shows that indeed, no additional information was needed in the single horizon case. To be more precise, our method suggests that in this case, the conformal geometry of the MOTS is directly encoded in the Einstein equations, when written with an equilibrium ansatz: we directly use these equations to justify a no-boundary treatment.

In the light of this numerical study, we can make a parallel with the proposition made in [132]. In that paper, the authors suggested, after a gauge dependence analysis for $\tilde{\gamma}^{ij}$ on the horizon, that a prescription could be made for the conformal geometry on the horizon. In this respect, they justify,

for the projection of the three-metric on the two-surface, the following choice:

$$q_{ab} = \omega^2 f_{ab}, \quad (13.42)$$

with f_{ab} the usual diagonal round metric for a two-sphere in spherical coordinates adapted to the horizon. This choice should not affect the physics of the three-slice, and suffices to recover the solution for Einstein dynamical equation with a slice of a spacetime containing an isolated horizon. Their study is made in a differential gauge generalizing the Dirac gauge we are using, namely $\mathcal{D}_i \tilde{\gamma}^{ij} = V^i$, with V^i a regular vector field on the three-slice. Our case corresponds to $V^i = 0$, which is precisely the one treated in detail in [132].

When comparing to our data, we find that the projection of our three-metric on the two-surface is not conformally related to the flat metric in adapted spherical coordinates. This means that in our particular case, and in regard of the particular no-boundary argument we use, a boundary condition of the same type as (13.42) is probably inconsistent with our data, and is likely a choice that we do not have the freedom to make (note however that geometric conditions in [263] making full use of the isolated horizon structure are indeed compatible with the present results, i.e. they are identically satisfied in the present Kerr case, whose horizon is indeed an isolated horizon). Unfortunately, the authors in [132] did not present any numerical results to support their claims, that we could have compared with ours.

We insist here on an important caveat for our argumentation: assumptions can only be justified in the very particular case we are studying here, which is the axisymmetric vacuum spacetime. This spacetime has very specific and non-trivial properties, all related to the uniqueness theorem of Carter [108]. Although the reasoning we have made on Sec. 13.3 for the operator could apply in other isolated horizon studies, we are not certain that our algorithm would globally converge when applied to a more general case (e.g. a black-hole binary system); a failure of this behavior would probably mean that an additional information about the conformal two-geometry has to be given to the system. Geometric fully isolated horizon boundary conditions proposed in [263] could then be enforced (note that geometric inner boundary conditions in [263] are not necessarily tied to the particular analytic setting here discussed and, more generally, they would also apply in schemes not enforcing the coordinate adaptation to stationarity at the horizon, $b = N_{\mathcal{H}}$, crucial for the singular nature of operators (13.30)).

Finally, let us point out the fact that we made those simulations by prescribing only the geometry of the horizon, and the geometry of spacetime at infinity. No assumption has been made for axisymmetry in the three-slice (computations can easily be made in the full 3D case and give the same results). Prescribing a vanishing expansion and a conformal Killing symmetry on a horizon, together with asymptotically flat hypothesis, our code converges to the only solution of the Kerr spacetime. Without claiming any rigorous demonstration here, this numerical result is most likely a support to the well known black hole rigidity theorem [242], where the same hypotheses lead to a uniqueness theorem involving the Kerr solution as the only one with no electromagnetic field.

13.7 Conclusion

We have used the prescription for a fully constrained scheme of (3+1) Einstein equations in generalized Dirac gauge [73, 135] to retrieve stationary axisymmetric black hole spacetime, and compared it with the analytical solution of Kerr type. An advanced handling of the conformal geometry of our three-slice allowed us to reach actual stationarity with good resolution precision for our scheme. Although we used standard quasi-equilibrium conditions concerning boundary values for other metric fields in

the excised horizon, we found that the conformal geometry on the horizon required no prescription whatsoever in the single horizon case. This is in contrast with suggestions available in the literature [132], and probably suggests an underlying physical feature of the horizon geometry (maybe related to uniqueness of the Kerr solution). To our knowledge, it is the first time the conformal part is numerically computed in a black hole spacetime using only a prescription on the stationarity of spacetime (and without resorting to additional symmetries). The application of this feature to the more general initial data problem is evident: in the same spirit as the work done in [471] for neutron-star binaries, using it for the black-hole binary system could lead to significant improvement in the available initial data for evolution codes. Further numerical work will clarify this issue.

We have implemented and used in our study numerical tools aimed at characterizing the geometry and physical properties related to horizons embedded in spacetime; those tools, among which a complete multipole analysis for two-surfaces as gravitational sources, have proven very accurate for diagnostics involving the horizon geometry and physical features. They will be more thoroughly presented, and tested in more general cases, in an upcoming work.

APPENDIX

13.A Tensor spectral quantities adapted to the Dirac Gauge

We here give the definition of the three spectral quantities introduced in Sec. 13.3.3, that describe the divergence-free degrees of freedom (with respect to the Dirac gauge) associated with a rank two symmetric tensor. The reader is also invited to go to [134] or [340] where more detailed calculations are provided.

We first define a set of spin-weighted tensor spherical harmonics components for a symmetric rank-2 tensor, directly linked to the tensor spherical harmonics as introduced by Mathews and Zerilli [313, 498]. We shall give the expression for these components of the tensor h^{ij} using the classical spherical coordinate basis, which is used in practice in our computations. With the notation $P = h^{\theta\theta} + h^{\varphi\varphi}$, the six pure spherical harmonics components of h^{ij} are defined as :

$$\Delta_{\theta\varphi}\eta = \frac{\partial h^{r\theta}}{\partial\theta} + \frac{h^{r\theta}}{\tan\theta} + \frac{1}{\sin\theta} \frac{\partial h^{r\varphi}}{\partial\varphi}, \quad (13.43)$$

$$\Delta_{\theta\varphi}\mu = \frac{\partial h^{r\varphi}}{\partial\theta} + \frac{h^{r\varphi}}{\tan\theta} - \frac{1}{\sin\theta} \frac{\partial h^{r\theta}}{\partial\varphi}, \quad (13.44)$$

$$\begin{aligned} \Delta_{\theta\varphi}(\Delta_{\theta\varphi} + 2)\mathcal{W} &= \frac{\partial^2 P}{\partial\theta^2} + \frac{3}{\tan\theta} \frac{\partial P}{\partial\theta} - \frac{1}{\sin^2\theta} \frac{\partial^2 P}{\partial\varphi^2} \\ &\quad - 2P + \frac{2}{\sin\theta} \frac{\partial}{\partial\varphi} \left(\frac{\partial h^{\theta\varphi}}{\partial\theta} + \frac{h^{\theta\varphi}}{\tan\theta} \right), \end{aligned} \quad (13.45)$$

$$\begin{aligned} \Delta_{\theta\varphi}(\Delta_{\theta\varphi} + 2)\mathcal{X} &= \frac{\partial^2 h^{\theta\varphi}}{\partial\theta^2} + \frac{3}{\tan\theta} \frac{\partial h^{\theta\varphi}}{\partial\theta} - \frac{1}{\sin^2\theta} \frac{\partial^2 h^{\theta\varphi}}{\partial\varphi^2} \\ &\quad - 2h^{\theta\varphi} - \frac{2}{\sin\theta} \frac{\partial}{\partial\varphi} \left(\frac{\partial P}{\partial\theta} + \frac{P}{\tan\theta} \right), \end{aligned} \quad (13.46)$$

the fifth and sixth scalar fields being simply the tensor trace h with respect to the flat metric and

the h^{rr} spherical component. Let us note that these relations are more tractable when using a scalar spherical harmonics decomposition (introduced in Sec. 13.4.2) for all fields. Indeed, an angular Laplace operator acting on a field reduces then to a simple algebraic operation on every spherical harmonics component. Inverse relations can also be computed to retrieve the classical components of h^{ij} from spherical harmonics quantities.

We now derive the main variables related to our study: with the divergence-free decomposition $h^{ij} = \mathcal{D}^i V^j + \mathcal{D}^j V^i + h_T^{ij}$, and $\mathcal{D}_i h_T^{ij} = 0$, a choice for three quantities defined from h^{ij} and verifying:

$$h_T^{ij} = 0 \Rightarrow A = B = C = 0, \quad (13.47)$$

can be expressed as the following scalar fields (see [340]):

$$A = \frac{\partial \mathcal{X}}{\partial r} - \frac{\mu}{r}, \quad (13.48)$$

$$B = \frac{\partial \mathcal{W}}{\partial r} - \frac{\Delta_{\theta\varphi} \mathcal{W}}{2r} - \frac{\eta}{r} + \frac{h - h^{rr}}{4r}, \quad (13.49)$$

$$C = \frac{\partial(h - h^{rr})}{\partial r} - \frac{3h^{rr}}{r} + \frac{h}{r} - 2\Delta_{\theta\varphi} \left(\frac{\partial \mathcal{W}}{\partial r} + \frac{\mathcal{W}}{r} \right) \quad (13.50)$$

These quantities can also be decomposed onto a scalar spherical harmonics basis. The equivalence in (13.47) is achieved up to boundary conditions.

To show how the quantities A , B and C behave with respect to the Laplace operator, we shall suppose in the following that the tensor h^{ij} is the solution of a Poisson equation of the type $\Delta h^{ij} = S^{ij}$. We can deduce a scalar elliptic system verified by A , B and C as:

$$\Delta A = A_S \quad (13.51)$$

$$\Delta B - \frac{C}{2r^2} = B_S \quad (13.52)$$

$$\Delta C + \frac{2C}{r^2} + \frac{8\Delta_{\theta\varphi} B}{r^2} = C_S, \quad (13.53)$$

Where A_S , B_S and C_S are the corresponding quantities associated with the source S^{ij} . A simple way of decoupling the last two elliptic equations is to define the variables $\tilde{B} = \sum_{l,m} \tilde{B}^{lm} Y_{lm}$ and $\tilde{C} = \sum_{l,m} \tilde{C}^{lm} Y_{lm}$ with:

$$\tilde{B}^{lm} = B^{lm} + \frac{C^{lm}}{2(l+1)}, \quad (13.54)$$

$$\tilde{C}^{lm} = C^{lm} - 4lB^{lm}. \quad (13.55)$$

Thus, we can write an equivalent system for (13.51,13.52,13.53) as:

$$\Delta A = A_S, \quad (13.56)$$

$$\tilde{\Delta} \tilde{B} = \tilde{B}_S, \quad (13.57)$$

$$\Delta^* \tilde{C} = \tilde{C}_S, \quad (13.58)$$

With the following elliptic operators defined for each spherical harmonic index l :

$$\Delta = \frac{\partial^2}{\partial r^2} + \frac{2}{r} \frac{\partial}{\partial r} - \frac{l(l+1)}{r^2} I \quad (13.59)$$

$$\tilde{\Delta} = \Delta + \frac{2l}{r^2} I, \quad (13.60)$$

$$\Delta^* = \Delta - \frac{2(l+1)}{r^2} I. \quad (13.61)$$

I is the identity operator. A , \tilde{B} and \tilde{C} are then defined as three scalar fields characterizing only the divergence-free part of a symmetric rank two tensor h^{ij} , and giving a system of three decoupled scalar elliptic equations in the Poisson problem for this tensor. Hence they are very well suited to the study of a tensorial elliptic problem in Dirac gauge. Let us finally note that the quantities \tilde{B} and \tilde{C} are directly related to each other by the trace of the considered tensor [340]: If we know *a priori* the value of the trace for h^{ij} , then the knowledge of \tilde{B} suffices to recover \tilde{C} with no additional information (the converse being equally true).

13.B Recovery of h^{ij} from A and \tilde{B}

In this section, we come up with technical details for resolution of the gauge differential system introduced in Sec. 13.3.3, to reconstruct the tensor h^{ij} from the quantities A and \tilde{B} .

We begin by expressing components of the vector field representing the divergence of h^{ij} :

$$H^i = \mathcal{D}_i h^{ij}, \quad (13.62)$$

with the Dirac gauge for $H^i = 0$. Adopting the vector spherical harmonics decomposition suggested in [73], the three spherical harmonics components of H^i are expressed, in function of the spherical harmonics components of h^{ij} (see Appendix 13.A), as:

$$H^r = \frac{\partial h^{rr}}{\partial r} + \frac{3h^{rr}}{r} + \frac{1}{r} (\Delta_{\theta\varphi} \eta - h), \quad (13.63)$$

$$H^\eta = \Delta_{\theta\varphi} \left[\frac{\partial \eta}{\partial r} + \frac{3\eta}{r} + \frac{1}{r} \left((\Delta_{\theta\varphi} + 2) \mathcal{W} + \frac{h - h^{rr}}{2} \right) \right], \quad (13.64)$$

$$H^\mu = \Delta_{\theta\varphi} \left[\frac{\partial \mu}{\partial r} + \frac{3\mu}{r} + \frac{1}{r} (\Delta_{\theta\varphi} + 2) \mathcal{X} \right]. \quad (13.65)$$

Those three expressions, alongside with definitions of the quantities A and \tilde{B} , will allow to express two decoupled differential systems. The first one, involving the spherical harmonics components μ and \mathcal{X} , combines the expression for the scalar field A , as well as the fact that H^μ vanishes under the Dirac gauge :

$$\begin{cases} \frac{\partial \mathcal{X}}{\partial r} - \frac{\mu}{r} = A, \\ \frac{\partial \mu}{\partial r} + \frac{3\mu}{r} + \frac{1}{r} (\Delta_{\theta\varphi} + 2) \mathcal{X} = 0. \end{cases} \quad (13.66)$$

The second system is composed of the definition of \tilde{B} for each of its spherical harmonic component

\tilde{B}^{lm} , as well as the vanishing of H^r and H^η (again, due to Dirac gauge):

$$\begin{cases} \tilde{B}^{lm} = B^{lm} + \frac{C^{lm}}{2(l+1)}, \\ \frac{\partial h^{rr}}{\partial r} + \frac{3h^{rr}}{r} + \frac{1}{r} (\Delta_{\theta\varphi}\eta - h) = 0, \\ \frac{\partial \eta}{\partial r} + \frac{3\eta}{r} + \frac{1}{r} \left((\Delta_{\theta\varphi} + 2) \mathcal{W} + \frac{h - h^{rr}}{2} \right) = 0. \end{cases} \quad (13.67)$$

with the expressions (13.49, 13.50) of B and C as functions of the spherical harmonics components of h^{ij} . In this system, the trace is given *a priori*, so that only three spherical harmonics components are considered as unknowns.

We refer to the analysis of [340] to affirm that, when solving our equations in \mathbb{R}^3 minus an excised inner sphere, one boundary condition has to be provided at the surface for the system (13.66), and two for the system (13.67). As pointed out in Sec.13.4.2, these conditions are retrieved as compatibility conditions based on the original elliptic tensorial equation. Overall, we are able to invert the two Dirac differential systems, and retrieve all the spherical harmonics components of h^{ij} from the sole knowledge of A , \tilde{B} and the trace h .

Conclusions

Ce manuscrit détaille en trois parties les travaux de recherche que j'ai effectués dans de nombreuses collaborations depuis 2001. L'objectif global a été d'être capable de modéliser sur ordinateur les objets complexes que sont les astres compacts, en tant que sources d'ondes gravitationnelles, mais aussi pour l'étude de ces objets eux-mêmes et de la physique dans des conditions extrêmes. Le développement d'un formalisme contraint de la relativité générale (partie I) a été une étape très importante en vue de la mise au point de modèles numériques tridimensionnels en champ gravitationnel fort. Le formalisme présenté ici est intéressant en ce qu'il assure la résolution des équations de contraintes et évite ainsi l'augmentation des erreurs sur le calcul du champ gravitationnel relativiste. Le problème d'unicité du système d'équations aux dérivées partielles elliptiques associé a, dans un premier temps, empêché des simulations s'approchant du trou noir. Nous avons réussi à trouver une amélioration du formalisme contraint, qui permet de suivre les effondrements gravitationnels jusqu'à la formation de l'horizon du trou noir, et suffisamment au-delà pour pouvoir étudier les propriétés du trou noir nouvellement formé. Ainsi, ce nouveau formalisme contraint semble être aujourd'hui suffisamment au point pour des simulations complexes.

Les techniques numériques utilisées pour résoudre ces équations aux dérivées partielles sont, depuis des années dans notre groupe à Meudon, les méthodes spectrales. Une des spécificités du groupe, même par rapport à d'autres personnes qui utilisent les méthodes spectrales en physique, est certainement d'être capable de gérer en trois dimensions la singularité liée aux coordonnées sphériques au centre de la grille ($r = 0$). Dans le cadre de la relativité numérique, ce sont les fondateurs du groupe, S. Bonazzola et J.-A. Marck qui ont introduit l'utilisation de ces méthodes dès les années 80. C'est sans doute la raison pour laquelle il nous a été demandé d'écrire un article de revue sur l'utilisation de ces méthodes en relativité numérique. Même si elles sont aujourd'hui bien comprises, un certain nombre d'outils importants ont dû être développés, comme la technique pour la résolution de l'équation d'onde tensorielle avec contrainte de divergence nulle ou le trouveur d'horizon apparent. La première est absolument nécessaire pour intégrer proprement la partie hyperbolique des équations du formalisme contraint, en respectant la jauge, et la seconde afin de pouvoir diagnostiquer l'apparition ou la fusion de trous noirs dans les simulations.

Les modèles d'astres compacts et de leurs évolutions présentés ici sont bien entendu encore trop incomplets. En premier lieu, les simulations de supernovae gravitationnelles présentées ici sont très encourageantes en ce qui concerne l'hydrodynamique et le champ gravitationnel, mais les détails de la « microphysique » (équation d'état, transport des neutrinos,...) sont

beaucoup trop pauvres. Même si plusieurs points de la structure des étoiles à neutrons ont été présentés comme la superfluidité ou le champ magnétique, il reste souvent à améliorer le modèle physique (par exemple, avoir une équation d'état réaliste pour ce qui est de l'entraînement entre le superfluide et le fluide normal) et surtout à combiner ces différents points pour construire le modèle le plus complet possible. Ainsi, même s'il est encourageant de pouvoir retrouver la solution complète d'un trou noir en rotation à partir de conditions aux bords, il faut très vite construire des modèles dynamiques en présence de matière, voire de champ magnétique. Les résultats présentés dans cette partie III montrent que les modèles numériques sont capables de suivre des phénomènes violents, comme les effondrements gravitationnels d'une étoile à neutrons en trou noir, mais les simulations aujourd'hui doivent être beaucoup plus précises et donc prendre en compte les modèles de matière les plus complets.

Cette amélioration des modèles est bien entendu stimulée d'abord par l'amélioration des observations à notre disposition. Les données collectées par les télescopes à hautes énergies comme HESS, Fermi ou INTEGRAL exigent des modèles plus complets, afin également d'être capable d'expliquer des observations plus variées ou à plusieurs longueurs d'ondes. Les instruments de prochaine génération, tel CTA, ou surtout les nouveaux projets de détecteurs d'ondes gravitationnelles requerront une souplesse encore plus grande. La question commence aussi à se poser du temps nécessaire à l'élaboration d'un modèle numérique : s'il faut explorer un vaste espace des paramètres inconnus afin d'ajuster le modèle aux observations, il faut que le programme numérique tourne suffisamment vite. Là encore, les méthodes spectrales apportent un avantage certain, que l'on peut combiner avec l'accroissement de la vitesse des calculateurs.

Cependant, il ne s'agit pas ici de simplement se reposer sur la puissance constamment croissante des ordinateurs pour espérer avoir des modèles numériques de plus en plus précis. En effet, le fait d'ajouter des « ingrédients physiques » introduit souvent de nouvelles instabilités ou bruits numériques. Par exemple, les tentatives récentes de simuler l'hydrodynamique relativiste à deux fluides s'est heurtée à l'instabilité à deux courants [17], qui est connue dans le domaine (elle est une des explications possibles au phénomène de glitch des pulsars) mais qui ici, faute d'équation d'état suffisamment réaliste, n'a pas de mécanisme de saturation. De manière plus évidente encore, la détermination d'une équation d'état réaliste pour la matière au-delà de la densité nucléaire doit nécessairement passer par des modèles approchés de physique nucléaire, car les équations fondamentales du problème sont celles de la chromodynamique quantique, et rendent le problème complet impossible à résoudre numériquement.

Perspectives

Interaction d'un trou noir avec son environnement

Une première suite logique aux travaux présentés ci-dessus est la modélisation de l'évolution temporelle d'un trou noir, avec l'aide du formalisme d'« horizon dynamique » développé par E.ourgoulhon et J. L. Jaramillo [223]. Ce travail sera naturellement entrepris en collaboration avec N. Vasset (LUTH) et consistera en l'implémentation et les tests numériques de ce formalisme pour l'évolution d'un trou noir interagissant avec de la matière ou avec du rayonnement gravitationnel. Plusieurs questions peuvent être étudiées : dans le cadre des données initiales « conformément plates » (voir section 13.3) contenant un trou noir en rotation, quel est le contenu en ondes gravitationnelles ? Comment accélérer un trou noir en rotation (par exemple *via* un disque d'accrétion) pour le faire tourner à son taux maximum ? Un autre point qui sera abordé est la possibilité de prendre en compte l'apparition d'un trou noir dans la simulation lors d'un effondrement gravitationnel. En effet, l'utilisation d'une jauge évitant les singularités (de type « feuilletage maximal », voir section 1.4) permet de ne pas avoir de singularité dans le domaine de calcul alors que l'horizon apparent est déjà formé (voir figure 3.3), mais introduit néanmoins de très forts gradients sur les champs métriques qui, à court terme, déstabilisent le code numérique. Si l'on veut alors continuer la simulation en présence du trou noir, une solution est de retirer du domaine de calcul un volume situé à l'intérieur de l'horizon apparent et de procéder ensuite comme pour la technique de l'excision (voir introduction de la partie III), c'est-à-dire ne pas résoudre les équations d'Einstein sur un voisinage de la singularité centrale, mais les remplacer par des conditions au bord.

Étude dynamique de binaires compactes spirallantes

Pendant de nombreuses années, l'objectif principal de la plupart des groupes de relativité numérique a été la simulation de l'évolution de binaires d'astres compacts, car il s'agit là des principales sources attendues de rayonnement gravitationnel. Dans ce contexte, le « groupe de Meudon » s'est spécialisé dans le calcul des données initiales de ces binaires [71, 229, 226]. Ces données sont aujourd'hui utilisées comme point de départ pour de nombreux codes d'évolution de binaires : par exemple à l'Albert Einstein Institut (Potsdam) [42], ou à Louisiana State University (Bâton Rouge) [353]. La mise au point d'un code d'évolution des binaires en relativité générale au sein du groupe de Meudon est ainsi une direction évidente pour la suite des recherches, à partir du code résolvant les équations d'Einstein dans le vide qui est disponible

actuellement [73, 135, 216]. Il sera certainement très intéressant de posséder un tel outil en France, qui permettrait de contrôler toute la simulation : données initiales et évolution. Cependant, de nombreux groupes à travers le monde (essentiellement aux États-Unis, mais aussi en Allemagne et au Japon) possèdent déjà de tels codes numériques et ont beaucoup étudié le problème de l'évolution de binaires d'astres compacts.

La question peut se poser alors sur l'intérêt de développer encore un autre code en vue de résoudre les équations d'Einstein pour ce problème. Il y a plusieurs bonnes raisons à cela. D'abord, la majorité des groupes utilise plus ou moins les mêmes outils et formulation du problème des binaires : formalisme libre de type BSSN [54, 421], approche des « ponctions » [474] avec les jauges adaptées (« $1+\log$ » et « gamma-driver ») et codes AMR basés sur la plate-forme Cactus [15] et une grille cartésienne. L'extension de nos outils de simulation au cas des binaires spirallantes permettrait d'avoir un modèle numérique réellement différent avec un formalisme contraint, la jauge de Dirac [73] et un code basé sur les méthodes spectrales en coordonnées sphériques, voire bi-sphériques [227]. Ainsi, la mise au point d'un code pour la simulation de binaires d'astres compacts est une direction naturelle de poursuite des travaux de recherche.

Effondrements gravitationnels

Il faut cependant considérer une autre direction qui se développe assez vite en ce moment : la prise en compte de modèles physiques plus réalistes. En effet la communauté de relativité numérique n'a jusqu'à récemment considéré que des modèles de matière assez simples pour décrire les étoiles à neutrons ou les effondrements gravitationnels : équations d'état de type polytrophe ($p = \kappa\rho^\gamma$) ou fluide parfait ($p = (\Gamma - 1)\rho\epsilon$). Ce n'était évidemment pas à cause d'une méconnaissance des propriétés de la matière dense, mais cela venait du fait qu'il y avait déjà beaucoup de difficultés à résoudre correctement les équations du champ gravitationnel. Les travaux se sont donc longtemps concentrés sur les équations d'Einstein en simplifiant au maximum les autres points. Aujourd'hui, cette communauté de relativité numérique a commencé à se rapprocher des physiciens nucléaires, ainsi que des physiciens des particules, et de nombreuses collaborations ont été initiées afin d'améliorer la « microphysique » des modèles d'astres compacts.

Avec le développement du code tridimensionnel CoCoNuT [150] pour suivre les effondrements gravitationnels des cœurs d'étoiles dégénérés (voir le chapitre 8), notre groupe dispose d'un bon outil qu'il s'agit aussi de compléter en y incorporant une équation d'état réaliste basée sur des calculs de physique nucléaire, ainsi que la prise en compte de la déleptonisation ayant lieu au cours de l'effondrement par capture électronique. Ce dernier point requiert à long terme l'implémentation et la résolution de l'équation de Boltzmann pour le transport des neutrinos, ce qui est très complexe et extrêmement coûteux en temps de calcul. Malgré ces difficultés, avec Pablo Cerdá-Durán (Institut Max Planck pour l'astrophysique à Garching, Allemagne), Isabel Cordero-Carrión (Université de Valencia, Espagne) et Micaela Oertel (LUTH), nous avons entrepris d'enrichir le code CoCoNuT pour arriver à des simulations plus réalistes des phénomènes de supernovae. Il ne s'agit pas de chercher à se comparer directement avec les grands groupes qui effectuent ce genre de simulations (autour de T. Janka à Garching, A. Burrows à Princeton,

A. Mezzacappa à Oak Ridge, ...), mais de disposer d'un outil pour tester de nouvelles hypothèses apparaissant dans le domaine. À titre d'illustration, on peut citer la prise en compte des effets de température sur la capture électronique [172] ou la possibilité d'une transition de phase vers de la matière de quarks au moment de la formation de la proto-étoile à neutrons, ce qui impliquerait un second choc et un second signal en neutrinos [396]. Dans de tels cas, il est très important d'avoir à disposition un code qui puisse prendre en compte au moins l'hydrodynamique et la gravitation relativiste, ainsi que la rotation, mais qui soit relativement rapide à l'exécution, afin de pouvoir tester l'effet de ces idées venant de la physique des particules.

En conclusion, en plus de l'étude de l'effet de la matière sur un trou noir et du développement d'un code pour la simulation de l'évolution de deux astres compacts sous l'effet de l'émission d'ondes gravitationnelles, il me semble très important de développer la simulation des effondrements gravitationnels stellaires. Il s'agit là d'un thème de recherches qui n'existe quasiment pas en France, mais pour lequel de nombreuses compétences sont présentes : théorie sur les instabilités hydrodynamiques (Th. Foglizzo, CEA/Saclay), physique nucléaire (J. Margueron, IPN/Orsay et M. Oertel, LUTH), transport des neutrinos (P. Blottiau, CEA/Bruyères et S. Bonazzola, LUTH) et gravitation / astres compacts (S. Bonazzola, E.ourgoulhon, ... LUTH). À cela, vient s'ajouter l'expertise sur les simulations de trous noirs décrites plus haut, qui est en train d'être étendue en vue de l'étude des interactions entre un trou noir et son environnement, et qui sera des plus intéressantes pour les simulations d'effondrements d'étoiles très massives donnant des trous noirs (« hypernovae »), pour lesquelles la question de l'équation d'état a très peu été étudiée.

Liste des publications

Reuves à comité de lecture

1. J. Novak, J.-L. Cornou, N. Vasset : *A spectral method for the wave equation of divergence-free vectors and symmetric tensors inside a sphere*
Journal of Computational Physics, **229**, 399-414 (2010) [preprint : arXiv:0905.2048]
2. N. Vasset, J. Novak, J.L. Jaramillo : *Excised black hole spacetimes : quasi-local horizon formalism applied to the Kerr example*
Physical Review D, **79**, 124010 (2009) [preprint : arXiv:0901.2052]
3. I. Cordero-Carrión, P. Cerdá-Durán, H. Dimmelmeier, J.L. Jaramillo, J. Novak, E. Gourgoulhon : *An improved constrained scheme for the Einstein equations : an approach to the uniqueness issue*
Physical Review D, **79**, 024017 (2009) [preprint : arXiv:0809.2325]
4. P. Grandclément, J. Novak : *Spectral Methods for Numerical Relativity*,
Living Reviews in Relativity **12**, 1 (2009) [preprint : arXiv :0706.2286]
5. I. Cordero-Carrión, J.M. Ibáñez, E. Gourgoulhon, J.L. Jaramillo, J. Novak : *Mathematical Issues in a Fully-Constrained Formulation of Einstein Equations*, *Physical Review D*, **77**, 084007 (2008) [preprint : arXiv :0802.3018]
6. S. Bonazzola, J.L. Jaramillo, J. Novak : *A fast stroboscopic spectral method for rotating systems in numerical relativity*
Classical and Quantum Gravity **24**, 4037-4051 (2007) [preprint : gr-qc/0703118]
7. L.-M. Lin, J. Novak : *A new spectral apparent horizon finder for 3D numerical relativity*,
Classical and Quantum Gravity **24**, 2665-2676 (2007) [preprint : gr-qc/0702038]
8. L.-M. Lin, J. Novak : *Rotating star initial data for a constrained scheme in numerical relativity*
Classical and Quantum Gravity **23**, 4545-4561 (2006) [preprint : gr-qc/0603048]
9. H. Dimmelmeier, J. Novak, J.A. Font, J.M. Ibáñez, E. Müller : *Combining spectral and shock-capturing methods : A new numerical approach for 3D relativistic core collapse simulations*
Physical Review D, **71**, 064023 (2005) [preprint : astro-ph/0407174]
10. R. Prix, J. Novak, G. Comer : *Relativistic numerical models for stationary superfluid neutron stars*
Physical Review D, **71**, 043005 (2005) [preprint : astro-ph/0410023]

11. S. Bonazzola, E. Gourgoulhon, P. Grandclément, J. Novak : *A constrained scheme for Einstein equations based on Dirac gauge and spherical coordinates*
Physical Review D, **70**, 104007 (2004) [preprint : gr-qc/0307082]
12. J. Novak, S. Bonazzola : *Absorbing boundary conditions for simulation of gravitational waves with spectral methods in spherical coordinates*
Journal of Computational Physics, **197**, 186-196 (2004) [preprint : gr-qc/0203102]
13. J. Novak, E. Marq : *Gyromagnetic ratio of rapidly rotating compact stars in general relativity*
Classical and Quantum Gravity, **20**, 3051-3060 (2003) [preprint : gr-qc/0306010]
14. J. Novak : *Velocity-induced collapses of stable neutron stars*
Astronomy and Astrophysics, **376**, 606-613 (2001). [preprint : gr-qc/0107045]
15. J. Novak, J.M. Ibáñez : *Gravitational waves from the collapse and bounce of a stellar core in tensor-scalar gravity*
Astrophysical Journal **533**, 392-405 (2000). [preprint : astro-ph/9911298]
16. J. Novak : *Neutron star transition to strong-scalar-field state in tensor-scalar gravity*
Physical Review D **58**, 064019 (1998) [preprint : gr-qc/9806022]
17. J. Novak : *Spherical neutron star collapse toward a black hole in a tensor-scalar theory of gravity*
Physical Review D **57**, 4789-4801 (1998) [preprint : gr-qc/9707041]
18. M. Bocquet, S. Bonazzola, E. Gourgoulhon, J. Novak : *Rotating neutron star models with a magnetic field*
Astronomy and Astrophysics, **301**, 757-775 (1995) [preprint : gr-qc/9503044]

Actes d'écoles et de colloques

1. J. Novak : *Neutron stars and pulsars : An introduction to models and observations*, in *European Physical Journal : Special Topics* **156** *Les Houches School on exotic nuclei, Les Houches, France, mai 2007*, p.151-168 (2008).
2. J. Novak, H. Dimmelmeier, J.A. Font : *A combined spectral/Godunov code for the simulation of gravitational waves from stellar supernova core collapse*, in *Astronomical Society of the Pacific Conference Series*, **85** *ASTRONUM-2007 – the 2nd International Conference on Numerical Modeling of Space Plasma Flows, Paris juin 2007*, p. 127-132 (2008).
3. L.-M. Lin, J. Novak : *Rotating relativistic stars in the Dirac gauge and maximal slicing*. in *AIP Conference Proceedings* **861**, *ALBERT EINSTEIN CENTURY INTERNATIONAL CONFERENCE, Paris, France, juillet 2005*, p. 678-681, (2006).
4. J. Novak, E. Gourgoulhon, P. Grandclément and L.-M. Lin : *Numerical Relativity with LORENE : the study of gravitational wave sources*. in *Société Française d'Astronomie et d'Astrophysique : Scientific Highlights 2005, Proc. Semaine de l'Astrophysique Française (Strasbourg, France, juin 2005)*, Eds. F. Casoli,

- T.Contini, J.M. Hameury, L. Pagani, p. 739-742
EDP Sciences, (Les Ulis) (2005).
5. J. Novak, H. Dimmelmeier and J.A. Font : *Mariage des maillages : A new 3D general relativistic hydro code for simulation of gravitational waves from core- collapses.*
in *Société Française d'Astronomie et d'Astrophysique : Scientific Highlights 2004, Proc. Semaine de l'Astrophysique Française (Paris, France, juin 2004)*, Eds. F. Combes, D. Barret, T. Contini, F. Meynadier, L. Pagani, p.377-380
EDP Sciences, (Les Ulis) (2004).
 6. R. Prix, J. Novak, G. L. Comer : *Stationary structure of superfluid neutron star models*
in *Conference proceedings for the 26th Spanish Relativity Meeting (ERE 2002)*.
[preprint : gr-qc/0211105]
 7. E.ourgoulhon, J. Novak : *Covariant conformal decomposition of Einstein equations*
in *Proceedings of Journées Relativistes 2001* (Dublin, 6-8 septembre 2001), Eds. C. Barabès & P.A. Hogan
International Journal of Modern Physics A **17**, 2762 (2002)
 8. J. Novak : *Numerical Relativity CM1-a and CM1-b sessions*
in *Proceedings of the Ninth Marcel Grossman Meeting On General Relativity*, Eds. R. Jantzen, V. Gurzadyan & R. Ruffini
World Scientific, Singapore 2002. [preprint : gr-qc/0102015]
 9. J. Novak : *Monopolar gravitational wave signal from the collapse of a stellar core to a neutron star*
in *Proceedings of 19th Texas Symposium on Relativistic Astrophysics and Cosmology (Paris, France, 14-18 décembre 1998)* (CD-ROM version), Eds. E. Aubourg, T. Montmerle, J. Paul & P. Peter
CEA/DAPNIA (Gif sur Yvette) (2000)

Ouvrages de vulgarisation

1. J. Novak : *Les ondes gravitationnelles : où en est-on aujourd'hui ?*
L'Astronomie **122**, 10-17 (2008)
2. J. Novak : *Les étoiles à neutrons*
Pour la Science **311**, 32-37 (2003)

Autres

1. H. Dimmelmeier, P. Cerdá-Durán, I. Cordero-Carrión, J. Novak : *CoCoNuT : Core-Collapse using Nu(new) Technologies*
(2004–2009) <http://www.mpa-garching.mpg.de/hydro/COCONUT/intro.php>.
2. E.ourgoulhon, P. Grandclément, J.-A. Marck, J. Novak : *LORENE : Langage Objet pour la RElativité Numérique*
(1997–2009) <http://www.lorene.obspm.fr>.

3. J. Novak : *Étude numérique de sources de rayonnement gravitationnel en théorie tenseur-scalaire de la gravité*
thèse de doctorat, Université Paris 7 (1998)

Bibliographie

- [1] Abbott, B., Abbott, R., Adhikari, R., Ageev, A. *et al.*, (2004), *Setting upper limits on the strength of periodic gravitational waves from PSR J1939+2134 using the first science data from the GEO 600 and LIGO detectors*, Phys. Rev. D **69**, 082004, 1–16, LIGO Scientific Collaboration.
- [2] Abbott, B. P., Abbott, R., Adhikari, R., Ajith, P. *et al.*, (2009), *LIGO : the Laser Interferometer Gravitational-Wave Observatory*, Rep. Prog. Phys. **72**, 076901, LIGO Scientific Collaboration.
- [3] Abdikamalov, E. B., Dimmelmeier, H., Rezzolla, L. et Miller, J. C., (2009), *Relativistic simulations of the phase-transition-induced collapse of neutron stars*, Mon. Not. of the Royal Astron. Soc. **392**, 52–76.
- [4] Abrahams, A. M., Cook, G. B., Shapiro, S. L. et Teukolsky, S. A., (1994), *Solving Einstein's equations for rotating spacetimes : Evolution of relativistic star clusters*, Phys. Rev. D **49**, 5153–5164.
- [5] Acernese, F., Alshourbagy, M., Amico, P., Antonucci, F. *et al.*, (2008), *VIRGO : a large interferometer for gravitational wave detection started its first scientific run*, J. Phys. Conf. Ser. **120**, 032007.
- [6] Aladl, U. E., Deakin, A. S. et Rasmussen, H., (2002), *Nonreflecting boundary condition for the wave equation*, J. Comput. Appl. Math. **138**, 309.
- [7] Alcubierre, M., (2008), *Introduction to 3+1 numerical relativity*, International series of monographs on physics, Oxford University Press, Oxford.
- [8] Alcubierre, M., Brügmann, B., Miller, M. et Suen, W.-M., (1999), *Conformal hyperbolic formulation of the Einstein equations*, Phys. Rev. D **60**, 064017, 1–4.
- [9] Alcubierre, M., Brandt, S., Brügmann, B., Gundlach, C., Massó, J., Seidel, E. et Walker, P., (2000), *Test-beds and applications for apparent horizon finders in numerical relativity*, Class. Quantum Grav. **17**, 2159–2190.
- [10] Alcubierre, M., Allen, G., Brügmann, B., Seidel, E. et Suen, W.-M., (2000), *Towards an understanding of the stability properties of the 3+1 evolution equations in general relativity*, Phys. Rev. D **62**, 124011, 1–15.
- [11] Alcubierre, M., Brügmann, B., Holz, D., Takahashi, R., Brandt, S., Seidel, E., Thornburg, J. et Ashtekar, A., (2001), *Symmetry Without Symmetry*, Int. J. Mod. Phys. D **10**, 273–289.

- [12] Alcubierre, M., Brügmann, B., Diener, P., Koppitz, M., Pollney, D., Seidel, E. et Takahashi, R., (2003), *Gauge conditions for long-term numerical black hole evolutions without excision*, Phys. Rev. D **67**, 084023, 1–18.
- [13] Alcubierre, M., Allen, G., Bona, C., Fiske, D. *et al.*, (2004), *Towards standard testbeds for numerical relativity*, Class. Quantum Grav. **21**, 589–613.
- [14] Alcubierre, M. et Brügmann, B., (2001), *Simple excision of a black hole in 3+1 numerical relativity*, Phys. Rev. D **63**, 104006, 1–6.
- [15] Allen, G., El-Khamra, Y., Goodale, T., Radke, T., Rideout, D., Schnetter, E., Tao, J. et Caraba, E., (2000-2009), *The Cactus Code*, <http://www.cactuscode.org>.
- [16] Amsterdamski, P., Bulik, T., Gondek-Rosińska, D. et Kluźniak, W., (2002), *Marginally stable orbits around Maclaurin spheroids and low-mass quark stars*, Astron. Astrophys. **381**, L21–L24.
- [17] Anderson, L. et Moncrief, V., (2003), *Elliptic-Hyperbolic Systems and the Einstein Equations*, Ann. Henri Poincaré **4**, 1–34.
- [18] Anderson, M., Hirschmann, E. W., Lehner, L., Liebling, S. L., Motl, P. M., Neilsen, D., Palenzuela, C. et Tohline, J. E., (2008), *Simulating binary neutron stars : Dynamics and gravitational waves*, Phys. Rev. D **77**, 024006, 1–14.
- [19] Anderson, M. et Matzner, R. A., (2005), *Extended Lifetime in Computational Evolution of Isolated Black Holes*, Found. Phys. **35**, 1477–1495.
- [20] Andersson, N., Comer, G. L. et Prix, R., (2003), *Are Pulsar Glitches Triggered by a Superfluid Two-Stream Instability ?*, Phys. Rev. Lett. **90**, 091101.
- [21] Andersson, N., Comer, G. L. et Prix, R., (2004), *The superfluid two-stream instability*, Mon. Not. of the Royal Astron. Soc. **354**, 101–110.
- [22] Andersson, N. et Comer, G. L., (2001), *Slowly rotating general relativistic superfluid neutron stars*, Classical and Quantum Gravity **18**, 969–1002.
- [23] Andersson, N. et Comer, G. L., (2007), *Relativistic Fluid Dynamics : Physics for Many Different Scales*, Living Rev. Relativity **10**, lrr-2007-1, 1.
- [24] Anile, A. M., (1989), *Relativistic fluids and magneto-fluids*, Cambridge University Press, Cambridge.
- [25] Anninos, P., Bernstein, D., Brandt, S., Libson, J., Massó, J., Seidel, E., Smarr, L., Suen, W.-M. et Walker, P., (1995), *Dynamics of Apparent and Event Horizons*, Phys. Rev. Lett. **74**, 630–633.
- [26] Anninos, P., Camarda, K., Libson, J., Massó, J., Seidel, E. et Suen, W.-M., (1998), *Finding apparent horizons in dynamic 3D numerical spacetimes*, Phys. Rev. D **58**, 024003, 1–12.
- [27] Ansorg, M., (2005), *Double-domain spectral method for black hole excision data*, Phys. Rev. D **72**, 024018, 1–10.

-
- [28] Ansorg, M., (2007), *A multi-domain spectral method for initial data of arbitrary binaries in general relativity*, Class. Quantum Grav. **24**, 1.
- [29] Ansorg, M., Kleinwächter, A. et Meinel, R., (2002), *Highly accurate calculation of rotating neutron stars*, Astron. Astrophys. **381**, L49–L52.
- [30] Ansorg, M., Kleinwächter, A. et Meinel, R., (2003), *Highly accurate calculation of rotating neutron stars : Detailed description of the numerical methods*, Astron. Astrophys. **405**, 711–721.
- [31] Ansorg, M., Kleinwächter, A. et Meinel, R., (2003), *Relativistic Dyson Rings and Their Black Hole Limit*, Astrophys. J. Lett. **582**, L87–L90.
- [32] Ansorg, M., Kleinwächter, A. et Meinel, R., (2003), *Uniformly rotating axisymmetric fluid configurations bifurcating from highly flattened Maclaurin spheroids*, Mon. Not. R. Astron. Soc. **339**, 515–523.
- [33] Ansorg, M., Brüggmann, B. et Tichy, W., (2004), *Single-domain spectral method for black hole puncture data*, Phys. Rev. D **70**, 064011, 1–13.
- [34] Ansorg, M. et Petroff, D., (2005), *Black holes surrounded by uniformly rotating rings*, Phys. Rev. D **72**, 024019, 1–12.
- [35] Arnowitt, R., Deser, S. et Misner, C. W., (1962), dans *Gravitation : An introduction to current research*, éd. Witten, L., pp. 227–265, Wiley, New York.
- [36] Ashtekar, A., Beetle, C. et Fairhurst, S., (1999), *Isolated horizons : a generalization of black hole mechanics*, Class. Quantum Grav. **16**, L1–L7.
- [37] Ashtekar, A., Engle, J., Pawłowski, T. et Van Den Broeck, C., (2004), *Multipole moments of isolated horizons*, Class. Quantum Grav. **21**, 2549–2570.
- [38] Ashtekar, A. et Krishnan, B., (2003), *Dynamical horizons and their properties*, Phys. Rev. D **68**, 104030, 1–25.
- [39] Ashtekar, A. et Krishnan, B., (2004), *Isolated and Dynamical Horizons and Their Applications*, Living Rev. Relativity **7**, lrr-2004-10, 10.
- [40] Babiuc, M., Szilágyi, B., Hawke, I. et Zlochower, Y., (2005), *Gravitational wave extraction based on Cauchy-characteristic extraction and characteristic evolution*, Class. Quantum Grav. **22**, 5089–5107.
- [41] Baiotti, L., Hawke, I., Montero, P. J., Löffler, F., Rezzolla, L., Stergioulas, N., Font, J. A. et Seidel, E., (2005), *Three-dimensional relativistic simulations of rotating neutron-star collapse to a Kerr black hole*, Phys. Rev. D **71**, 024035, 1–30.
- [42] Baiotti, L., Giacomazzo, B. et Rezzolla, L., (2008), *Accurate evolutions of inspiralling neutron-star binaries : Prompt and delayed collapse to a black hole*, Phys. Rev. D **78**, 084033, 1–37.
- [43] Baiotti, L. et Rezzolla, L., (2006), *Challenging the Paradigm of Singularity Excision in Gravitational Collapse*, Phys. Rev. Lett. **97**, 141101.

- [44] Baker, J. G., Centrella, J., Choi, D.-I., Koppitz, M. et van Meter, J., (2006), *Gravitational-Wave Extraction from an Inspiral Configuration of Merging Black Holes*, Phys. Rev. Lett. **96**, 111102.
- [45] Baldo, M., Cugnon, J., Lejeune, A. et Lombardo, U., (1992), *Proton and neutron superfluidity in neutron star matter*, Nucl. Phys. A **536**, 349–365.
- [46] Banyuls, F., Font, J. A., Ibáñez, J. M., Martí, J. M. A. et Miralles, J. A., (1997), *Numerical {3+1} General Relativistic Hydrodynamics : A Local Characteristic Approach*, Astrophys. J. **476**, 221–231.
- [47] Bardeen, J. M. et Piran, T., (1983), *General relativistic rotating axisymmetric systems : coordinates and equations*, Phys. Rep. **96**, 205–250.
- [48] Bartnik, R., (1997), *Einstein equations in the null quasispherical gauge*, Class. Quantum Grav. **14**, 2185–2194.
- [49] Bartnik, R. et Norton, A. H., (2000), *Numerical Methods for the Einstein Equations in Null Quasi-Spherical Coordinates*, SIAM J. Sci. Comput. **22**, 917–950.
- [50] Baumgarte, T. W., (2000), *Innermost stable circular orbit of binary black holes*, Phys. Rev. D **62**, 024018, 1–8.
- [51] Baumgarte, T. W., Cook, G. B., Scheel, M. A., Shapiro, S. L. et Teukolsky, S. A., (1996), *Implementing an apparent-horizon finder in three dimensions*, Phys. Rev. D **54**, 4849–4857.
- [52] Baumgarte, T. W., Cook, G. B., Scheel, M. A., Shapiro, S. L. et Teukolsky, S. A., (1998), *General relativistic models of binary neutron stars in quasiequilibrium*, Phys. Rev. D **57**, 7299–7311.
- [53] Baumgarte, T. W., O’Murchadha, N. et Pfeiffer, H. P., (2007), *Einstein constraints : Uniqueness and nonuniqueness in the conformal thin sandwich approach*, Phys. Rev. D **75**, 044009, 1–9.
- [54] Baumgarte, T. W. et Shapiro, S. L., (1999), *Numerical integration of Einstein’s field equations*, Phys. Rev. D **59**, 024007, 1–7.
- [55] Baumgarte, T. W. et Shapiro, S. L., (2003), *Numerical relativity and compact binaries*, Phys. Rep. **376**, 41–131.
- [56] Bayliss, A. et Turkel, E., (1980), *Radiation boundary conditions for wave-like equations*, Comm. Pure Appl. Math. **33**, 707.
- [57] Bejger, M., Gondek-Rosińska, D., Gourgoulhon, E., Haensel, P., Taniguchi, K. et Zdunik, J. L., (2005), *Impact of the nuclear equation of state on the last orbits of binary neutron stars*, Astron. Astrophys. **431**, 297–306.
- [58] Bejger, M., Haensel, P. et Zdunik, J. L., (2007), *Rotation at 1122 Hz and the neutron star structure*, Astron. Astrophys. **464**, L49–L52.
- [59] Belczynski, K., Kalogera, V. et Bulik, T., (2002), *A Comprehensive Study of Binary Compact Objects as Gravitational Wave Sources : Evolutionary Channels, Rates, and Physical Properties*, Astrophys. J. **572**, 407–431.

- [60] Ben Belgacem, F. et Bernardi, C., (1999), *Spectral Element Discretization of the Maxwell Equations*, Math. Comput. **68**, 1497–1520.
- [61] Bičák, J., (2006), dans *Encyclopedia of Mathematical Physics*, éd. Françoise, J.-P., Naber, G. L. et Tsou, S. T., tome 2, pp. 165–173, Elsevier, Amsterdam.
- [62] Blanchet, L., (2006), *Gravitational Radiation from Post-Newtonian Sources and Inspiralling Compact Binaries*, Living Rev. Relativity **9**, lrr-2006-4, 4.
- [63] Blanchet, L., Damour, T. et Schäfer, G., (1990), *Post-Newtonian hydrodynamics and post-Newtonian gravitational wave generation for numerical relativity*, Mon. Not. of the Royal Astron. Soc. **242**, 289–305.
- [64] Bocquet, M., Bonazzola, S., Gourgoulhon, E. et Novak, J., (1995), *Rotating neutron star models with a magnetic field*, Astron. Astrophys. **301**, 757–775.
- [65] Bonazzola, S., (1973), *The Virial Theorem in General Relativity*, Astrophys. J. **182**, 335–340.
- [66] Bonazzola, S., (1985), dans *Non-thermal and very high temperature phenomena in X-ray astronomy*, éd. Perola, G. C. et Salvati, M., pp. 55–75, Rome, Università “La Sapienza”.
- [67] Bonazzola, S., Gourgoulhon, E., Salgado, M. et Marck, J.-A., (1993), *Axisymmetric rotating relativistic bodies : A new numerical approach for ‘exact’ solutions*, Astron. Astrophys. **278**, 421–443.
- [68] Bonazzola, S., Frieben, J. et Gourgoulhon, E., (1996), *Spontaneous Symmetry Breaking of Rapidly Rotating Stars in General Relativity*, Astrophys. J. **460**, 379–389.
- [69] Bonazzola, S., Gourgoulhon, E. et Marck, J.-A., (1998), *Numerical approach for high precision 3D relativistic star models*, Phys. Rev. D **58**, 104020, 1–14.
- [70] Bonazzola, S., Frieben, J. et Gourgoulhon, E., (1998), *Spontaneous symmetry breaking of rapidly rotating stars in general relativity : influence of the 3D-shift vector*, Astron. Astrophys. **331**, 280–290.
- [71] Bonazzola, S., Gourgoulhon, E. et Marck, J.-A., (1999), *Numerical Models of Irrotational Binary Neutron Stars in General Relativity*, Phys. Rev. Lett. **82**, 892–895.
- [72] Bonazzola, S., Gourgoulhon, E. et Marck, J.-A., (1999), *Spectral methods in general relativistic astrophysics*, J. Comput. Appl. Math. **109**, 433–473.
- [73] Bonazzola, S., Gourgoulhon, E., Grandclément, P. et Novak, J., (2004), *Constrained scheme for the Einstein equations based on the Dirac gauge and spherical coordinates*, Phys. Rev. D **70**, 104007, 1–24.
- [74] Bonazzola, S., Jaramillo, J. L. et Novak, J., (2007), *A fast stroboscopic spectral method for rotating systems in numerical relativity*, Class. Quantum Grav. **24**, 4037–4051.
- [75] Bonazzola, S. et Chevreton, M., (1973), *Possible Improvements of Gravitational Antennas*, Phys. Rev. D **8**, 359–361.

- [76] Bonazzola, S. etourgoulhon, E., (1994), *A virial identity applied to relativistic stellar models*, *Class. Quantum Grav.* **11**, 1775–1784.
- [77] Bonazzola, S. etourgoulhon, E., (1996), *Gravitational waves from pulsars : emission by the magnetic-field-induced distortion*, *Astron. Astrophys.* **312**, 675–690.
- [78] Bonazzola, S. et Marck, J.-A., (1986), *Pseudo-spectral technique applied to numerical solutions for stellar collapse*, *Astron. Astrophys.* **164**, 300–309.
- [79] Bonazzola, S. et Marck, J.-A., (1990), *Three-dimensional gas dynamics in a sphere*, *J. Comput. Phys.* **87**, 201–230.
- [80] Bonazzola, S. et Marck, J.-A., (1991), *A 1D exact treatment of shock waves within spectral methods in plane geometry*, *J. Comput. Phys.* **97**, 535–552.
- [81] Bonazzola, S. et Marck, J.-A., (1993), *Efficiency of gravitational radiation from axisymmetric and 3 D stellar collapse. I - Polytropic case*, *Astron. Astrophys.* **267**, 623–633.
- [82] Booth, I., (2005), *Black-hole boundaries*, *Can. J. Phys.* **83**, 1073–1099.
- [83] Boronski, P. et Tuckerman, L. S., (2007), *Poloidal toroidal decomposition in a finite cylinder. I : Influence matrices for the magnetohydrodynamic equations*, *J. Comput. Phys.* **227**, 1523–1543.
- [84] Boronski, P. et Tuckerman, L. S., (2007), *Poloidal toroidal decomposition in a finite cylinder. II : Discretization, regularisation and validation*, *J. Comput. Phys.* **227**, 1544–1566.
- [85] Boyd, J. B., (2001), *Chebyshev and Fourier Spectral Methods*, Dover Publications, Mineola, New York, 2^e édition.
- [86] Boyle, M., Lindblom, L., Pfeiffer, H. P., Scheel, M. A. et Kidder, L. E., (2007), *Testing the accuracy and stability of spectral methods in numerical relativity*, *Phys. Rev. D* **75**, 024006, 1–13.
- [87] Brandt, S. et Brüggmann, B., (1997), *A Simple Construction of Initial Data for Multiple Black Holes*, *Phys. Rev. Lett.* **78**, 3606–3609.
- [88] Brandt, S. R. et Seidel, E., (1995), *Evolution of distorted rotating black holes. I. Methods and tests*, *Phys. Rev. D* **52**, 856–869.
- [89] Brandt, S. R. et Seidel, E., (1995), *Evolution of distorted rotating black holes. II. Dynamics and analysis*, *Phys. Rev. D* **52**, 870–886.
- [90] Brandt, S. R. et Seidel, E., (1996), *Evolution of distorted rotating black holes. III. Initial data*, *Phys. Rev. D* **54**, 1403–1416.
- [91] Brill, D. R. et Lindquist, R. W., (1963), *Interaction Energy in Geometrostatics*, *Phys. Rev.* **131**, 471–476.
- [92] Brizuela, D., Martín-García, J. M. et Marugán, G. A. M., (2006), *Second- and higher-order perturbations of a spherical spacetime*, *Phys. Rev. D* **74**, 044039, 1–17.

-
- [93] Brun, A. S., Miesch, M. S. et Toomre, J., (2004), *Global-Scale Turbulent Convection and Magnetic Dynamo Action in the Solar Envelope*, *Astrophys. J.* **614**, 1073–1098.
- [94] Buchdahl, H. A., (1959), *General Relativistic Fluid Spheres*, *Phys. Rev.* **116**, 1027–1034.
- [95] Buchman, L. T. et Sarbach, O., (2007), *Improved outer boundary conditions for Einstein's field equations*, *Class. Quantum Grav.* **24**, S307–S326.
- [96] Buchman, L. T. et Sarbach, O. C. A., (2006), *Towards absorbing outer boundaries in general relativity*, *Class. Quantum Grav.* **23**, 6709–6744.
- [97] Buras, R., Rampp, M., Janka, H.-T. et Kifonidis, K., (2003), *Improved Models of Stellar Core Collapse and Still No Explosions : What Is Missing ?*, *Phys. Rev. Lett.* **90**, 241101.
- [98] Burrows, A. et Hayes, J., (1996), *Pulsar Recoil and Gravitational Radiation Due to Asymmetrical Stellar Collapse and Explosion*, *Phys. Rev. Lett.* **76**, 352–355.
- [99] Calabrese, G., Lehner, L. et Tiglio, M., (2002), *Constraint-preserving boundary conditions in numerical relativity*, *Phys. Rev. D* **65**, 104031, 1–13.
- [100] Calabrese, G., Pullin, J., Reula, O., Sarbach, O. et Tiglio, M., (2003), *Well Posed Constraint-Preserving Boundary Conditions for the Linearized Einstein Equations*, *Commun. Math. Phys.* **240**, 377–395.
- [101] Campanelli, M., Lousto, C. O., Marronetti, P. et Zlochower, Y., (2006), *Accurate Evolutions of Orbiting Black-Hole Binaries without Excision*, *Phys. Rev. Lett.* **96**, 111101.
- [102] Canuto, C., Hussaini, M. Y., Quarteroni, A. et Zang, T. A., (1988), *Spectral Methods in Fluid Dynamics*, Springer Series in Computational Physics, Springer, Berlin ; New York.
- [103] Canuto, C., Hussaini, M. Y., Quarteroni, A. et Zang, T. A., (2006), *Spectral Methods : Fundamentals in Single Domains*, Scientific Computation, Springer, Berlin ; New York.
- [104] Canuto, C., Hussaini, M. Y., Quarteroni, A. et Zang, T. A., (2007), *Spectral Methods : Evolution to Complex Geometries and Applications to Fluid Dynamics*, Scientific Computation, Springer, Berlin ; New York.
- [105] Cardall, C. Y., Prakash, M. et Lattimer, J. M., (2001), *Effects of Strong Magnetic Fields on Neutron Star Structure*, *Astrophys. J.* **554**, 322–339.
- [106] Carter, B., (1969), *Killing Horizons and Orthogonally Transitive Groups in Space-Time*, *J. Math. Phys.* **10**, 70–81.
- [107] Carter, B., (1970), *The commutation property of a stationary, axisymmetric system*, *Commun. Math. Phys.* **17**, 233–238.
- [108] Carter, B., (1971), *Axisymmetric black hole has only two degrees of freedom.*, *Phys. Rev. Lett.* **26**, 331–333.

- [109] Carter, B., (1983), dans *A Random Walk in General Relativity and Cosmology : Festschrift for Professors P.C. Vaidya & A.K. Raychaudhuri*, éd. Dadhich, N., Rao, J., Narlikar, J. et Vishveshwara, C., pp. 49–62, Wiley Eastern, New Delhi, India.
- [110] Carter, B., (1989), dans *Relativistic Fluid Dynamics*, éd. Anile, A. et Choquet-Bruhat, Y., tome 1385 de *Lecture Notes in Mathematics*, pp. 1–64, Berlin, Germany ; New York, U.S.A., Springer.
- [111] Carter, B., Langlois, D. et Sedrakian, D. M., (2000), *Centrifugal buoyancy as a mechanism for neutron star glitches*, *Astron. & Astrophys.***361**, 795–802.
- [112] Carter, B. et Langlois, D., (1998), *Relativistic models for superconducting-superfluid mixtures*, *Nucl. Phys. B* **531**, 478–504.
- [113] Caudill, M., Cook, G. B., Grigsby, J. D. et Pfeiffer, H. P., (2006), *Circular orbits and spin in black-hole initial data*, *Phys. Rev. D* **74**, 064011, 1–24.
- [114] Cerdá-Durán, P., Faye, G., Dimmelmeier, H., Font, J. A., Ibáñez, J. M., Müller, E. et Schäfer, G., (2005), *CFC+ : improved dynamics and gravitational waveforms from relativistic core collapse simulations*, *Astron. & Astrophys.***439**, 1033–1055.
- [115] Cerdá-Durán, P., Font, J. A. et Dimmelmeier, H., (2007), *General relativistic simulations of passive-magneto-rotational core collapse with microphysics*, *Astron. & Astrophys.***474**, 169–191.
- [116] Chao, N.-C., Clark, J. W. et Yang, C.-H., (1972), *Proton superfluidity in neutron-star matter*, *Nucl. Phys. A* **179**, 320–332.
- [117] Choptuik, M. W., (1993), *Universality and scaling in gravitational collapse of a massless scalar field*, *Phys. Rev. Lett.* **70**, 9–12.
- [118] Choptuik, M. W., Hirschmann, E. W., Liebling, S. L. et Pretorius, F., (2003), *An axisymmetric gravitational collapse code*, *Class. Quantum Grav.* **20**, 1857–1878.
- [119] Choquet-Bruhat, Y. et York, J. W., (1995), *Geometrical Well Posed Systems for the Einstein Equations*, *C. R. Acad. Sci. Paris, Sér. I Math.* **321**, 1089–1095, arXiv :gr-qc/9506071.
- [120] Choquet-Bruhat, Y. et York, J. W., (1996), *Mixed Elliptic and Hyperbolic Systems for the Einstein Equations*, arXiv :gr-qc/9606001.
- [121] Choquet-Bruhat, Y. et York, J. W., (1996), *Well Posed Reduced Systems for the Einstein Equations*, arXiv :gr-qc/9606001.
- [122] Christodoulou, D. L., (1971), *Investigations in Gravitational Collapse and the Physics of Black Holes*, Thèse de doctorat, Princeton University.
- [123] Cohen, J. M., Tiomno, J. et Wald, R. M., (1973), *Gyromagnetic ratio of a massive body*, *Phys. Rev. D* **7**, 998–1001.
- [124] Comer, G. L., (2004), *Slowly rotating general relativistic superfluid neutron stars with relativistic entrainment*, *Phys. Rev. D* **69**, 123009, 1–13.

-
- [125] Comer, G. L. et Joynt, R., (2003), *Relativistic mean field model for entrainment in general relativistic superfluid neutron stars*, Phys. Rev. D **68**, 023002, 1–12.
- [126] Comer, G. L. et Langlois, D., (1994), *Hamiltonian Formulation for Relativistic Superfluids*, Class. Quantum Grav. **11**, 709–721.
- [127] Cook, G., (2000), *Initial Data for Numerical Relativity*, Living Rev. Relativity **3**, lrr-2000-5, 5.
- [128] Cook, G. B., (1994), *Three-dimensional initial data for the collision of two black holes. II. Quasicircular orbits for equal-mass black holes*, Phys. Rev. D **50**, 5025–5032.
- [129] Cook, G. B., (2002), *Corotating and irrotational binary black holes in quasicircular orbits*, Phys. Rev. D **65**, 084003, 1–13.
- [130] Cook, G. B., Shapiro, S. L. et Teukolsky, S. A., (1994), *Rapidly rotating polytropes in general relativity*, Astrophys. J. **422**, 227–242.
- [131] Cook, G. B., Shapiro, S. L. et Teukolsky, S. A., (1996), *Testing a simplified version of Einstein's equations for numerical relativity*, Phys. Rev. D **53**, 5533–5540.
- [132] Cook, G. B. et Baumgarte, T. W., (2008), *Excision boundary conditions for the conformal metric*, Phys. Rev. D **78**, 104016, 1–10.
- [133] Cook, G. B. et Pfeiffer, H. P., (2004), *Excision boundary conditions for black-hole initial data*, Phys. Rev. D **70**, 104016, 1–24.
- [134] Cordero-Carrión, I., Ibáñez, J. M., Gourgoulhon, E., Jaramillo, J. L. et Novak, J., (2008), *Mathematical issues in a fully constrained formulation of Einstein equations*, Phys. Rev. D **77**, 084007, 1–13.
- [135] Cordero-Carrión, I., Cerdá-Durán, P., Dimmelmeier, H., Jaramillo, J. L., Novak, J. et Gourgoulhon, E., (2009), *Improved constrained scheme for the Einstein equations : An approach to the uniqueness issue*, Phys. Rev. D **79**, 024017, 1–17.
- [136] Cottam, J., Paerels, F. et Mendez, M., (2002), *Gravitationally redshifted absorption lines in the X-ray burst spectra of a neutron star*, Nature **420**, 51–54.
- [137] Courant, R. et Hilbert, D., (1953), *Methods of Mathematical Physics*, Interscience Publishers, New York, U.S.A..
- [138] Dahlquist, G. G., (1963), *A special stability problem for linear multistep methods*, BIT **3**, 27–43.
- [139] Dain, S., Lousto, C. O. et Takahashi, R., (2002), *New conformally flat initial data for spinning black holes*, Phys. Rev. D **65**, 104038, 1–7.
- [140] Dain, S., Jaramillo, J. L. et Krishnan, B., (2005), *Existence of initial data containing isolated black holes*, Phys. Rev. D **71**, 064003, 1–11.
- [141] Damour, T., (1979), *Quelques propriétés mécaniques, électromagnétiques, thermodynamiques et quantiques des trous noirs*, Thèse de doctorat d'état, Université Paris 6.

- [142] Damour, T., Gourgoulhon, E. et Grandclément, P., (2002), *Circular orbits of corotating binary black holes : Comparison between analytical and numerical results*, Phys. Rev. D **66**, 024007, 1–15.
- [143] Damour, T. et Esposito-Farèse, G., (1998), *Gravitational-wave versus binary-pulsar tests of strong-field gravity*, Phys. Rev. D **58**, 042001, 1–12.
- [144] de Donder, T., (1921), *La gravifique Einsteinienne*, Ann. Obs. R. Belg. .
- [145] Deser, S., (2004), *P.A.M. Dirac and the Development of Modern General Relativity*, International Journal of Modern Physics A **19**, 99–105.
- [146] Diener, P., (2003), *A new general purpose event horizon finder for 3D numerical spacetimes*, Class. Quantum Grav. **20**, 4901–4917.
- [147] Dimmelmeier, H., Font, J. A. et Müller, E., (2001), *Gravitational Waves from Relativistic Rotational Core Collapse*, Astrophys. J., Lett.**560**, L163–L166.
- [148] Dimmelmeier, H., Font, J. A. et Müller, E., (2002), *Relativistic simulations of rotational core collapse I. Methods, initial models, and code tests*, Astron. Astrophys. **388**, 917–935.
- [149] Dimmelmeier, H., Font, J. A. et Müller, E., (2002), *Relativistic simulations of rotational core collapse II. Collapse dynamics and gravitational radiation*, Astron. & Astrophys.**393**, 523–542.
- [150] Dimmelmeier, H., Cerdá-Durán, P., Cordero-Carrión, I. et Novak, J., (2004–2009), *CoCoNuT : Core-Collapse using Nu(new) Technologies*, <http://www.mpa-garching.mpg.de/hydro/COCONUT/intro.php>.
- [151] Dimmelmeier, H., Novak, J., Font, J. A., Ibáñez, J. M. et Müller, E., (2005), *Combining spectral and shock-capturing methods : A new numerical approach for 3D relativistic core collapse simulations*, Phys. Rev. D **71**, 064023, 1–30.
- [152] Dimmelmeier, H., Stergioulas, N. et Font, J. A., (2006), *Non-linear axisymmetric pulsations of rotating relativistic stars in the conformal flatness approximation*, Mon. Not. R. Astron. Soc. **368**, 1609–1630.
- [153] Dimmelmeier, H., Ott, C. D., Janka, H.-T., Marek, A. et Müller, E., (2007), *Generic Gravitational-Wave Signals from the Collapse of Rotating Stellar Cores*, Phys. Rev. Lett. **98**, 251101.
- [154] D’Inverno, R., (1997), dans *Relativistic Gravitation and Gravitational Radiation*, éd. Marck, J.-A. et Lasota, J.-P., pp. 191–211.
- [155] Dirac, P. A. M., (1958), *The Theory of Gravitation in Hamiltonian Form*, Proc. Roy. Soc. Lond. A **246**, 333–343.
- [156] Dirac, P. A. M., (1959), *Fixation of Coordinates in the Hamiltonian Theory of Gravitation*, Phys. Rev. **114**, 924–930.

-
- [157] Donat, R., (1998), *A Flux-Split Algorithm Applied to Relativistic Flows*, J. Comput. Phys. **146**, 58–81.
- [158] Dormy, E., Cardin, P. et Jault, D., (1998), *MHD flow in a slightly differentially rotating spherical shell, with conducting inner core, in a dipolar magnetic field*, Earth Planet. Sci. Lett. **160**, 15–30.
- [159] Dreyer, O., Krishnan, B., Shoemaker, D. et Schnetter, E., (2003), *Introduction to isolated horizons in numerical relativity*, Phys. Rev. D **67**, 024018, 1–14.
- [160] Dudley, M. et James, R., (1989), *Time-dependent kinematic dynamos with stationary flows*, Proc. Roy. Soc. London A **425**, 407–429.
- [161] Duez, M. D., Baumgarte, T. W., Shapiro, S. L., Shibata, M. et Uryū, K., (2002), *Comparing the inspiral of irrotational and corotational binary neutron stars*, Phys. Rev. D **65**, 024016, 1–8.
- [162] Engquist, B. et Majda, A., (1977), *Absorbing boundary conditions for the numerical solution of waves*, Math. Comput. **31**, 629.
- [163] Erdős, P., (1961), *Problems and Results on the Theory of Interpolation. II*, Acta Math. Acad. Sci. Hung. **12**, 235–244.
- [164] Evans, C. L., (1998), *Partial Differential Equations*, American Mathematical Society, Providence.
- [165] Evans, C. R., (1986), dans *Dynamical Spacetimes and Numerical Relativity*, éd. Centrella, J. M., pp. 3–39.
- [166] Evans, C. R., (1989), dans *Frontiers in Numerical Relativity*, éd. Evans, C. R., Finn, L. S. et Hobill, D. W., pp. 194–205.
- [167] Evans, C. R. et Hawley, J. F., (1988), *Simulation of magnetohydrodynamic flows : a constrained transport method*, Astrophys. J. **332**, 659–677.
- [168] Faber, G., (1914), *Über die interpolatorische Darstellung stetiger Funktionen*, Jahresber. Deutsch. Math.-Verein. **23**, 192–210.
- [169] Faber, J. A., Grandclément, P., Rasio, F. A. et Taniguchi, K., (2002), *Measuring Neutron-Star Radii with Gravitational-Wave Detectors*, Phys. Rev. Lett. **89**, 231102.
- [170] Faber, J. A., Grandclément, P. et Rasio, F. A., (2004), *Mergers of irrotational neutron star binaries in conformally flat gravity*, Phys. Rev. D **69**, 124036, 1–26.
- [171] Faber, J. A., Baumgarte, T. W., Shapiro, S. L., Taniguchi, K. et Rasio, F. A., (2006), *Dynamical evolution of black hole-neutron star binaries in general relativity : Simulations of tidal disruption*, Phys. Rev. D **73**, 024012, 1–31.
- [172] Fantina, A. F., Donati, P. et Pizzochero, P. M., (2009), *Systematic thermal reduction of neutronization in core-collapse supernovae*, Phys. Lett. B **676**, 140–145.
- [173] Ferrando, J. J. et Sáez, J. A., (2009), *An intrinsic characterization of the Kerr metric*, Class. Quantum Grav. **26**, 075013, 1–13.

- [174] Finn, L. S., (1989), dans *Frontiers in Numerical Relativity*, éd. Evans, C. R., Finn, L. S. et Hobill, D. W., pp. 126–145.
- [175] Finn, L. S. et Evans, C. R., (1990), *Determining gravitational radiation from Newtonian self-gravitating systems*, *Astrophys. J.* **351**, 588–600.
- [176] Font, J. A., (2003), *Numerical Hydrodynamics in General Relativity*, *Living Rev. Relativity* **6**, lrr-2003-4, 4, <http://www.livingreviews.org/lrr-2003-4>.
- [177] Font, J. A., (2007), *An introduction to relativistic hydrodynamics*, *J. Phys. Conf. Ser.* **91**, 012002, 1–25.
- [178] Font, J. A., Stergioulas, N. et Kokkotas, K. D., (2000), *Non-linear hydrodynamical evolution of rotating relativistic stars : numerical methods and code tests*, *Mon. Not. of the Royal Astron. Soc.* **313**, 678–688.
- [179] Font, J. A., Miller, M., Suen, W.-M. et Tobias, M., (2000), *Three-dimensional numerical general relativistic hydrodynamics : Formulations, methods, and code tests*, *Phys. Rev. D* **61**, 044011, 1–26.
- [180] Font, J. A., Dimmelmeier, H., Gupta, A. et Stergioulas, N., (2001), *Axisymmetric modes of rotating relativistic stars in the Cowling approximation*, *Mon. Not. of the Royal Astron. Soc.* **325**, 1463–1470.
- [181] Font, J. A., Goodale, T., Iyer, S., Miller, M., Rezzolla, L., Seidel, E., Stergioulas, N., Suen, W.-M. et Tobias, M., (2002), *Three-dimensional numerical general relativistic hydrodynamics. II. Long-term dynamics of single relativistic stars*, *Phys. Rev. D* **65**, 084024, 1–18.
- [182] Fornberg, B., (1995), *Practical Guide to Pseudospectral Methods*, tome 1 de *Cambridge Monographs on Applied and Computational Mathematics*, Cambridge University Press, Cambridge ; New York.
- [183] Foucart, F., Kidder, L. E., Pfeiffer, H. P. et Teukolsky, S. A., (2008), *Initial value problem for black hole-neutron star binaries : a flexible, high-accuracy spectral method*, *Phys. Rev. D* **77**, 124051, 1–20.
- [184] Fourès-Bruhat, Y., (1952), *Théorème d'existence pour certains systèmes d'équations aux dérivées partielles non linéaires*, *Acta Mathematica* **88**, 141.
- [185] Frauendiener, J., (1999), *Calculating initial data for the conformal Einstein equations by pseudospectral methods*, *J. Comput. Appl. Math.* **109**, 475–491.
- [186] Friedman, J. L., Uryū, K. et Shibata, M., (2002), *Thermodynamics of binary black holes and neutron stars*, *Phys. Rev. D* **65**, 064035, 1–20.
- [187] Friedrich, H., (1985), *On the hyperbolicity of Einstein's and other gauge field equations*, *Commun. Math. Phys.* **100**, 525–543.
- [188] Friedrich, H., (2006), *Is general relativity essentially understood ?*, *Ann. Phys.* **15**, 84–108.

- [189] Friedrich, H. et Nagy, G., (1999), *The Initial Boundary Value Problem for Einstein's Vacuum Field Equation*, Commun. Math. Phys. **201**, 619–655.
- [190] Friedrich, H. et Rendall, A., (2000), dans *Einstein's Field Equations and Their Physical Implications*, éd. Schmidt, B. G., tome 540 de *Lecture Notes in Physics*, Berlin Springer Verlag, p. 127.
- [191] Frittelli, S. et Gomez, R., (2000), *Ill-posedness in the Einstein equations*, J. Math. Phys. **41**, 5535.
- [192] Fryer, C. L., Holz, D. E. et Hughes, S. A., (2002), *Gravitational Wave Emission from Core Collapse of Massive Stars*, Astrophys. J. **565**, 430–446.
- [193] Fryer, C. L., Holz, D. E., Hughes, S. A. et Warren, M. S., (2002), *Stellar collapse and gravitational waves*, arXiv :astro-ph/0211609.
- [194] Fryer, C. L. et New, K. C. B., (2003), *Gravitational Waves from Gravitational Collapse*, Living Rev. Relativity **6**, lrr-2003-2, 2.
- [195] Funaro, D. et Gottlieb, D., (1988), *A New Method of Imposing Boundary Conditions in Pseudospectral Approximations of Hyperbolic Equations*, Math. Comput. **51**, 599–613.
- [196] Garat, A. et Price, R. H., (2000), *Nonexistence of conformally flat slices of the Kerr spacetime*, Phys. Rev. D **61**, 124011, 1–4.
- [197] Garching, groupe d'hydrodynamique relativiste, http://www.map-garching.mpg.de/rel_hydro/.
- [198] García-Parrado Gómez-Lobo, A. et Valiente Kroon, J. A., (2008), *Kerr initial data*, Class. Quantum Grav. **25**, 205018, 1–20.
- [199] Garfinkle, D., (2002), *Harmonic coordinate method for simulating generic singularities*, Phys. Rev. D **65**, 044029, 1–6.
- [200] Garfinkle, D. et Duncan, G. C., (2001), *Numerical evolution of Brill waves*, Phys. Rev. D **63**, 044011+, 1–8.
- [201] Garfinkle, D. et Traschen, J., (1990), *Gyromagnetic ratio of a black hole*, Phys. Rev. D **42**, 419–423.
- [202] Gentle, A. P., George, N. D., Kheyfets, A. et Miller, W. A., (2004), *The constraints as evolution equations for numerical relativity*, Class. Quantum Grav. **21**, 83–91.
- [203] Gondek-Rosińska, D., Bulik, T., Zdunik, J. L., Gourgoulhon, E., Ray, S., Dey, J. et Dey, M., (2000), *Rapidly rotating compact strange stars*, Astron. Astrophys. **363**, 1005–1012.
- [204] Gondek-Rosińska, D., Stergioulas, N., Bulik, T., Kluźniak, W. et Gourgoulhon, E., (2001), *Lower limits on the maximum orbital frequency around rotating strange stars*, Astron. Astrophys. **380**, 190–197.
- [205] Gondek-Rosińska, D., Gourgoulhon, E. et Haensel, P., (2003), *Are rotating strange quark stars good sources of gravitational waves ?*, Astron. Astrophys. **412**, 777–790.

- [206] Gondek-Rosińska, D., Bejger, M., Bulik, T., Gourgoulhon, E., Haensel, P., Limousin, F., Taniguchi, K. et Zdunik, J. L., (2007), *The final phase of inspiral of neutron stars : Realistic equations of state*, Adv. Space Res. **39**, 271–274.
- [207] Gondek-Rosińska, D. et Gourgoulhon, E., (2002), *Jacobi-like bar mode instability of relativistic rotating bodies*, Phys. Rev. D **66**, 044021, 1–11.
- [208] Gondek-Rosińska, D. et Limousin, F., (2008), *The final phase of inspiral of strange quark star binaries*, arXiv :0801.4829.
- [209] González, J. A., Hannam, M., Sperhake, U., Brüggmann, B. et Husa, S., (2007), *Supermassive Recoil Velocities for Binary Black-Hole Mergers with Antialigned Spins*, Phys. Rev. Lett. **98**, 231101.
- [210] Gottlieb, D. et Orszag, S. A., (1977), *Numerical Analysis of Spectral Methods : Theory and Applications*, tome 26 de *Regional Conference Series in Applied Mathematics*, SIAM, Philadelphia, U.S.A..
- [211] Gourgoulhon, E., (1991), *Simple equations for general relativistic hydrodynamics in spherical symmetry applied to neutron star collapse*, Astron. Astrophys. **252**, 651–663.
- [212] Gourgoulhon, E., (1992), *1D numerical relativity applied to neutron star collapse*, Class. Quantum Grav. **9**, S117–S125.
- [213] Gourgoulhon, E., (2005), *Generalized Damour-Navier-Stokes equation applied to trapping horizons*, Phys. Rev. D **72**, 104007, 1–16.
- [214] Gourgoulhon, E., (2007), *3+1 formalism and Bases of Numerical Relativity*, arXiv :gr-qc/0703035.
- [215] Gourgoulhon, E., Haensel, P. et Gondek, D., (1995), *Maximum mass instability of neutron stars and weak interaction processes in dense matter*, Astron. Astrophys. **294**, 747–756.
- [216] Gourgoulhon, E., Grandclément, P., Marck, J.-A. et Novak, J., (1997–2009), *LORENE : Langage Objet pour la RElativité Numérique*, <http://www.lorene.obspm.fr>.
- [217] Gourgoulhon, E., Haensel, P., Livine, R., Paluch, E., Bonazzola, S. et Marck, J.-A., (1999), *Fast rotation of strange stars*, Astron. Astrophys. **349**, 851–862.
- [218] Gourgoulhon, E., Grandclément, P., Taniguchi, K., Marck, J.-A. et Bonazzola, S., (2001), *Quasiequilibrium sequences of synchronized and irrotational binary neutron stars in general relativity : Method and tests*, Phys. Rev. D **63**, 064029, 1–27.
- [219] Gourgoulhon, E., Grandclément, P. et Bonazzola, S., (2002), *Binary black holes in circular orbits. I. A global spacetime approach*, Phys. Rev. D **65**, 044020, 1–19.
- [220] Gourgoulhon, E. et Bonazzola, S., (1994), *A formulation of the virial theorem in general relativity*, Class. Quantum Grav. **11**, 443–452.

-
- [221] Gourgoulhon, E. et Haensel, P., (1993), *Upper bounds on the neutrino burst from collapse of a neutron star into a black hole*, *Astron. Astrophys.* **271**, 187–208.
- [222] Gourgoulhon, E. et Jaramillo, J. L., (2006), *A 3+1 perspective on null hypersurfaces and isolated horizons*, *Phys. Rep.* **423**, 159–294.
- [223] Gourgoulhon, E. et Jaramillo, J. L., (2006), *Area evolution, bulk viscosity, and entropy principles for dynamical horizons*, *Phys. Rev. D* **74**, 087502, 1–4.
- [224] Goussard, J. O., Haensel, P. et Zdunik, J. L., (1997), *Rapid uniform rotation of protoneutron stars*, *Astron. Astrophys.* **321**, 822–834.
- [225] Goussard, J. O., Haensel, P. et Zdunik, J. L., (1998), *Rapid differential rotation of protoneutron stars and constraints on radio pulsars periods*, *Astron. Astrophys.* **330**, 1005–1016.
- [226] Grandclément, P., (2006), *Accurate and realistic initial data for black hole-neutron star binaries*, *Phys. Rev. D* **74**, 124002, 1–6.
- [227] Grandclément, P., (2009), *Kadath : a spectral solver for theoretical physics*, arXiv :0909.1228, submitted to *J. Comput. Phys.*
- [228] Grandclément, P., Bonazzola, S., Gourgoulhon, E. et Marck, J.-A., (2001), *A Multidomain Spectral Method for Scalar and Vectorial Poisson Equations with Noncompact Sources*, *J. Comput. Phys.* **170**, 231–260.
- [229] Grandclément, P., Gourgoulhon, E. et Bonazzola, S., (2002), *Binary black holes in circular orbits. II. Numerical methods and first results*, *Phys. Rev. D* **65**, 044021, 1–18.
- [230] Grandclément, P. et Novak, J., (2009), *Spectral methods for numerical relativity*, *Living Rev. Relativity* **12**, lrr-2009-1, 1, <http://www.livingreviews.org/lrr-2009-1>.
- [231] Gundlach, C., (1998), *Pseudospectral apparent horizon finders : An efficient new algorithm*, *Phys. Rev. D* **57**, 863–875.
- [232] Gundlach, C., Calabrese, G., Hinder, I. et Martín-García, J. M., (2005), *Constraint damping in the Z_4 formulation and harmonic gauge*, *Class. Quantum Grav.* **22**, 3767–3773.
- [233] Gundlach, C. et Martín-García, J. M., (2006), *Well-posedness of formulations of the Einstein equations with dynamical lapse and shift conditions*, *Phys. Rev. D* **74**, 024016, 1–19.
- [234] Gundlach, C. et Martín-García, J. M., (2007), *Critical Phenomena in Gravitational Collapse*, *Living Rev. Relativity* **10**, lrr-2007-5, 5, <http://www.livingreviews.org/lrr-2007-5>.
- [235] Guo, B.-Y., Ma, H.-P. et Tadmor, E., (2001), *Spectral Vanishing Viscosity Method For Nonlinear Conservation Laws*, *SIAM J. Numer. Anal.* **39**, 1254–1268.
- [236] Hairer, E., Norsett, S. D. et Wanner, G., (1987), *Ordinary Differential Equations I*, Springer-Verlag.
- [237] Hájíček, P., (1973), *Exact models of charged black holes. I. Geometry of totally geodesic null hypersurface*, *Comm. Math. Phys.* **34**, 37–52.

- [238] Hannam, M., Husa, S., Pollney, D., Brüggmann, B. et Murchadha, N. Ó., (2007), *Geometry and Regularity of Moving Punctures*, Phys. Rev. Lett. **99**, 241102.
- [239] Hannam, M. D., Evans, C. R., Cook, G. B. et Baumgarte, T. W., (2003), *Can a combination of the conformal thin-sandwich and puncture methods yield binary black hole solutions in quasiequilibrium ?*, Phys. Rev. D **68**, 064003, 1–7.
- [240] Hartle, J. B. et Thorne, K. S., (1968), *Slowly Rotating Relativistic Stars. II. Models for Neutron Stars and Supermassive Stars*, Astrophys. J. **153**, 807–834.
- [241] Hawke, I., Baiotti, L. et Montero, P., (2002–2009), *Whisky - the EU Network GR Hydrodynamics code*, <http://www.whiskycode.org/>.
- [242] Hawking, S. W. et Ellis, G. F. R., (1973), *The large scale structure of space-time*, Cambridge University Press.
- [243] Hawking, S. W. et Hartle, J. B., (1972), *Energy and angular momentum flow into a black hole.*, Communications in Mathematical Physics **27**, 283–290.
- [244] Hawley, S. H. et Choptuik, M. W., (2000), *Boson stars driven to the brink of black hole formation*, Phys. Rev. D **62**, 104024, 1–19.
- [245] Hayward, S. A., (1994), *General laws of black-hole dynamics*, Phys. Rev. D **49**, 6467–6474.
- [246] Hennig, J. et Ansorg, M., (2009), *A Fully Pseudospectral Scheme for Solving Singular Hyperbolic Equations on Conformally Compactified Space-Times*, J. Hyperbolic Diff. Eq. **6**, 161.
- [247] Herrmann, F., Hinder, I., Shoemaker, D. M., Laguna, P. et Matzner, R. A., (2007), *Binary black holes : Spin dynamics and gravitational recoil*, Phys. Rev. D **76**, 084032, 1–11.
- [248] Hesthaven, J. S., (1998), *On the analysis and construction of perfectly matched layers for the linearized Euler equations*, J. Comput. Phys. **142**, 129.
- [249] Hesthaven, J. S., (2000), *Spectral penalty methods*, Appl. Numer. Math. **33**, 23–41.
- [250] Hesthaven, J. S., Gottlieb, S. et Gottlieb, D., (2007), *Spectral Methods for Time-Dependent Problems*, tome 21 de *Cambridge Monographs on Applied and Computational Mathematics*, Cambridge University Press, Cambridge ; New York.
- [251] Hesthaven, J. S. et Gottlieb, D., (1996), *A Stable Penalty Method for the Compressible Navier-Stokes Equations : I. Open Boundary Conditions*, SIAM J. Sci. Comput. **17**, 579–612.
- [252] Hockney, R. W. et Eastwood, J. W., (1981), *Computer Simulations using Particles*, McGraw-Hill, New York.
- [253] Hollerbach, R., (2000), *A spectral solution of the magneto-convection equations in spherical geometry*, Int. J. Numer. Meth. Fluids **32**, 773–797.
- [254] Hollerbach, R. et Rüdiger, G., (2002), *The influence of Hall drift in the magnetic fields of neutron stars*, Mon. Not. of the Royal Astron. Soc. **337**, 216.

- [255] Holst, M., Lindblom, L., Owen, R., Pfeiffer, H. P., Scheel, M. A. et Kidder, L. E., (2004), *Optimal constraint projection for hyperbolic evolution systems*, Phys. Rev. D **70**, 084017, 1–17.
- [256] Hughes, S. A., Keeton, II, C. R., Walker, P., Walsh, K. T., Shapiro, S. L. et Teukolsky, S. A., (1994), *Finding black holes in numerical spacetimes*, Phys. Rev. D **49**, 4004–4015.
- [257] Ierley, G., Spencer, B. et Worthing, R., (1992), *Spectral Methods in Time for a Class of Parabolic Partial Differential Equations*, J. Comput. Phys. **102**, 88–97.
- [258] Imamura, J. N., Pickett, B. K. et Durisen, R. H., (2003), *The Nonlinear Evolution of Massive Stellar Core Collapses That “Fizzles”*, Astrophys. J. **587**, 341–355.
- [259] Isaacson, E. et Keller, H. B., (1966), *Analysis of Numerical Method*, John Wiley and Sons, New York.
- [260] Isenberg, J., (2008), *Waveless approximation theories of gravity*, Int. J. Mod. Phys. D **17**, 265–273, Première version de 1978 non-publiée.
- [261] Isenberg, J. et Nester, J., (1980), dans *General Relativity and Gravitation*, éd. Held, A., tome 1, p. 23, New York, Plenum.
- [262] Janka, H.-T., Zwerger, T. et Mönchmeyer, R., (1993), *Does artificial viscosity destroy prompt type-II supernova explosions?*, Astron. & Astrophys. **268**, 360–368.
- [263] Jaramillo, J. L., (2009), *Isolated horizon structures in quasiequilibrium black hole initial data*, Phys. Rev. D **79**, 087506, 1–4.
- [264] Jaramillo, J. L., Gourgoulhon, E. et Marugán, G. A., (2004), *Inner boundary conditions for black hole initial data derived from isolated horizons*, Phys. Rev. D **70**, 124036, 1–13.
- [265] Jaramillo, J. L., Ansorg, M. et Limousin, F., (2007), *Numerical implementation of isolated horizon boundary conditions*, Phys. Rev. D **75**, 024019, 1–11.
- [266] Jaramillo, J. L., Vasset, N. et Ansorg, M., (2008), dans *Proceedings of the Spanish Relativity Meeting 2007*, éd. Oscoz, A., Mediavilla, E. et Serra-Ricart, M., tome 30 de *EAS Publications Series*, pp. 257–260, arXiv :0712.1741.
- [267] Jaramillo, J. L., Valiente Kroon, J. A. et Gourgoulhon, E., (2008), *TOPICAL REVIEW : From geometry to numerics : interdisciplinary aspects in mathematical and numerical relativity*, Class. Quantum Grav. **25**, 093001, 1–66.
- [268] Jaramillo, J. L., Gourgoulhon, E., Cordero-Carrión, I. et Ibáñez, J. M., (2008), *Trapping horizons as inner boundary conditions for black hole spacetimes*, Phys. Rev. D **77**, 047501–+, 1–4.
- [269] Jennrich, O., (2009), *TOPICAL REVIEW : LISA technology and instrumentation*, Class. Quantum Grav. **26**, 153001, 1–32.
- [270] Kassam, A.-K. et Trefethen, L. N., (2005), *Fourth-Order Time-Stepping for Stiff PDEs*, SIAM J. Sci. Comput. **26**, 1214–1233.

- [271] Katsoulakis, M. A. et Jin, S., (2000), *Hyperbolic Systems with Supercharacteristic Relaxations and Roll Waves*, SIAM J. Appl. Math. **61**, 273–292.
- [272] Katz, J., Bičák, J. et Lynden-Bell, D., (1999), *Disc sources for conformastationary metrics*, Class. Quantum Grav. **16**, 4023–4034.
- [273] Kawamura, M., Oohara, K.-i. et Nakamura, T., (2003), *General Relativistic Numerical Simulation on Coalescing Binary Neutron Stars and Gauge-Invariant Gravitational Wave Extraction*, arXiv :astro-ph/0306481.
- [274] Kembell, A. J. et Bishop, N. T., (1991), *The numerical determination of apparent horizons.*, Class. Quantum Grav. **8**, 1361–1367.
- [275] Keppens, R. et Tóth, G., (1999), *Nonlinear dynamics of Kelvin-Helmholtz unstable magnetized jets : Three-dimensional effects*, Phys. Plasmas **6**, 1461–1469.
- [276] Kidder, L. E., Scheel, M. A., Teukolsky, S. A., Carlson, E. D. et Cook, G. B., (2000), *Black hole evolution by spectral methods*, Phys. Rev. D **62**, 084032, 1–20.
- [277] Kidder, L. E., Scheel, M. A. et Teukolsky, S. A., (2001), *Extending the lifetime of 3D black hole computations with a new hyperbolic system of evolution equations*, Phys. Rev. D **64**, 064017, 1–13.
- [278] Kidder, L. E., Lindblom, L., Scheel, M. A., Buchman, L. T. et Pfeiffer, H. P., (2005), *Boundary conditions for the Einstein evolution system*, Phys. Rev. D **71**, 064020, 1–22.
- [279] Kidder, L. E. et Finn, L. S., (2000), *Spectral methods for numerical relativity : The initial data problem*, Phys. Rev. D **62**, 084026, 1–13.
- [280] Klein, C., (2008), *Fourth-Order Time-Stepping for Low Dispersion Korteweg-de Vries and Non-linear Schrödinger Equation*, Electron. Trans. Numer. Anal. **29**, 116–135.
- [281] Kley, W. et Schäfer, G., (1999), *Relativistic dust disks and the Wilson-Mathews approach*, Phys. Rev. D **60**, 027501, 1–4.
- [282] Kokkotas, K. D. et Schmidt, B., (1999), *Quasi-Normal Modes of Stars and Black Holes*, Living Rev. Relativity **2**, lrr-1999-2, 2.
- [283] Komatsu, H., Eriguchi, Y. et Hachisu, I., (1989), *Rapidly rotating general relativistic stars. I - Numerical method and its application to uniformly rotating polytropes*, Mon. Not. of the Royal Astron. Soc. **237**, 355–379.
- [284] Korn, G. A. et Korn, T. M., (1961), *Mathematical Handbook for Scientists and Engineers : Definitions, Theorems, and Formulas for Reference and Review*, McGraw-Hill, New York.
- [285] Kotake, K., Yamada, S. et Sato, K., (2003), *Gravitational radiation from axisymmetric rotational core collapse*, Phys. Rev. D **68**, 044023, 1–7.
- [286] Kudoh, H. et Wiseman, T., (2005), *Connecting Black Holes and Black Strings*, Phys. Rev. Lett. **94**, 161102.

- [287] Langlois, D., Sedrakian, D. M. et Carter, B., (1998), *Differential Rotation of Relativistic Superfluids in Neutron Stars*, Mon. Not. R. Astron. Soc. **297**, 1189–1201.
- [288] Lau, S. R., (2004), *Rapid evaluation of radiation boundary kernels for time-domain wave propagation on blackholes : theory and numerical methods*, J. Comput. Phys. **199**, 376–422.
- [289] Lehner, L., (2001), *Numerical relativity : a review*, Class. Quantum Grav. **18**, R25–R86.
- [290] Libson, J., Massó, J., Seidel, E., Suen, W.-M. et Walker, P., (1996), *Event horizons in numerical relativity : Methods and tests*, Phys. Rev. D **53**, 4335–4350.
- [291] Lichnerowicz, A., (1944), *L'intégration des équations de la gravitation relativiste et le problème des n corps*, J. Math. Pures Appl. **23**, 37, reproduit dans *Choix d'œuvres mathématiques*, Hermann, Paris (1982) p. 4.
- [292] Limousin, F., Gondek-Rosińska, D. etourgoulhon, E., (2005), *Last orbits of binary strange quark stars*, Phys. Rev. D **71**, 064012, 1–11.
- [293] Lin, L.-M. et Novak, J., (2006), *Rotating star initial data for a constrained scheme in numerical relativity*, Class. Quantum Grav. **23**, 4545–4561.
- [294] Lin, L.-M. et Novak, J., (2007), *A new spectral apparent horizon finder for 3D numerical relativity*, Class. Quantum Grav. **24**, 2665–2676.
- [295] Lindblom, L., Tohline, J. E. et Vallisneri, M., (2002), *Numerical evolutions of nonlinear r -modes in neutron stars*, Phys. Rev. D **65**, 084039, 1–15.
- [296] Lindblom, L., Scheel, M. A., Kidder, L. E., Pfeiffer, H. P., Shoemaker, D. et Teukolsky, S. A., (2004), *Controlling the growth of constraints in hyperbolic evolution systems*, Phys. Rev. D **69**, 124025, 1–14.
- [297] Lindblom, L., Scheel, M. A., Kidder, L. E., Owen, R. et Rinne, O., (2006), *A new generalized harmonic evolution system*, Class. Quantum Grav. **23**, S447–S462.
- [298] Lindblom, L., Matthews, K. D., Rinne, O. et Scheel, M. A., (2008), *Gauge Drivers for the Generalized Harmonic Einstein Equations*, Phys. Rev. D **77**, 084001, 1–17.
- [299] Lindblom, L. et Scheel, M. A., (2003), *Dynamical gauge conditions for the Einstein evolution equations*, Phys. Rev. D **67**, 124005, 1–12.
- [300] Lindquist, R. W., (1963), *Initial-Value Problem on Einstein-Rosen Manifolds*, J. Math. Phys. **4**, 938–950.
- [301] Link, B., Epstein, R. I. et Lattimer, J. M., (2000), dans *Stellar Astrophysics*, éd. Cheng, K. S., Chau, H. F., Chan, K. L. et Leung, K. C., p. 117.
- [302] Lions, J.-L., Méttral, J. et Vacus, O., (2002), *Well-posed absorbing layer for hyperbolic problems*, Numer. Math. **92**, 535.
- [303] Liu, Y. T., Shapiro, S. L., Etienne, Z. B. et Taniguchi, K., (2008), *General relativistic simulations of magnetized binary neutron star mergers*, Phys. Rev. D **78**, 024012, 1–20.

- [304] Lockitch, K. H., Friedman, J. L. et Andersson, N., (2003), *Rotational modes of relativistic stars : Numerical results*, Phys. Rev. D **68**, 124010, 1–23.
- [305] Lovelace, G., Owen, R., Pfeiffer, H. P. et Chu, T., (2008), *Binary-black-hole initial data with nearly extremal spins*, Phys. Rev. D **78**, 084017, 1–28.
- [306] Løvgren, A. E., Maday, Y. et Rønquist, E. M., (2007), dans *Analysis and Simulation of Fluid Dynamics*, éd. Calgari, C., Coulombel, J.-F. et Goudon, T., Advances in Mathematical Fluid Mechanics, pp. 129–154, Birkhäuser, Basel ; Boston.
- [307] Mak, M. K., Dobson, Jr., P. N. et Harko, T., (2001), *Maximum mass-radius ratios for charged compact general relativistic objects*, Europhys. Lett. **55**, 310–316.
- [308] Marck, J. A., Lioure, A. et Bonazzola, S., (1996), *Numerical study of the tidal interaction of a star and a massive black hole*, Astron. & Astrophys. **306**, 666–674.
- [309] Marek, A., Dimmelmeier, H., Janka, H.-T., Müller, E. et Buras, R., (2006), *Exploring the relativistic regime with Newtonian hydrodynamics : an improved effective gravitational potential for supernova simulations*, Astron. & Astrophys. **445**, 273–289.
- [310] Marqués, F., (1990), *On boundary conditions for velocity potentials in confined flows : Application to Couette flow*, Phys. Fluid A **2**, 729–737.
- [311] Martí, J.-M. et Müller, E., (2003), *Numerical Hydrodynamics in Special Relativity*, Living Rev. Relativity **6**, lrr-2003-7, 7, <http://www.livingreviews.org/lrr-2003-7>.
- [312] Mathews, G. J. et Wilson, J. R., (2000), *Revised relativistic hydrodynamical model for neutron-star binaries*, Phys. Rev. D **61**, 127304–+.
- [313] Mathews, J., (1962), *Gravitational multipole radiation*, J. Soc. Ind. Appl. Math. **10**, 768–780.
- [314] Matzner, R. A., Huq, M. F. et Shoemaker, D. M., (1998), *Initial value problem and coordinates for multiple black hole systems.*, Phys. Rev. D **59**, 024015, 1–6.
- [315] May, M. M. et White, R. H., (1966), *Hydrodynamic Calculations of General-Relativistic Collapse*, Phys. Rev. **141**, 1232–1241.
- [316] Meinardus, G., (1967), *Approximation of Functions : Theory and Numerical Methods*, tome 13 de *Springer Tracts in Natural Philosophy*, Springer, Berlin ; New York.
- [317] Michell, J., (1784), *On the Means of Discovering the Distance, Magnitude, &c. of the Fixed Stars, in Consequence of the Diminution of the Velocity of Their Light, in Case Such a Diminution Should be Found to Take Place in any of Them, and Such Other Data Should be Procured from Observations, as Would be Farther Necessary for That Purpose. By the Rev. John Michell, B. D. F. R. S. In a Letter to Henry Cavendish, Esq. F. R. S. and A. S.*, R. Soc. London Philos. Trans. Series I **74**, 35–57.
- [318] Miniati, F. et Colella, P., (2007), *A modified higher order Godunov's scheme for stiff source conservative hydrodynamics*, J. Comput. Phys. **224**, 519–538.

-
- [319] Misner, C. W., (1963), *The Method of Images in Geometrostatics*, Ann. Phys. (New York) **24**, 102–117.
- [320] Misner, C. W., Thorne, K. S. et Wheeler, J. A., (1973), *Gravitation*, W.H. Freeman and Co., San Francisco.
- [321] Mönchmeyer, R., Schäfer, G., Müller, E. et Kates, R. E., (1991), *Gravitational waves from the collapse of rotating stellar cores*, Astron. & Astrophys.**246**, 417–440.
- [322] Moore, S., Healy, D., Rockmore, D. et Kostelec, P., (2004–2008), *Fast Spherical Harmonic Transforms : SpharmonicKit*, <http://www.cs.dartmouth.edu/geelong/sphere/>.
- [323] Morse, P. M. et Feshbach, H., (1953), *Methods of theoretical physics*, McGraw-Hill, New York.
- [324] Müller, E., (1982), *Gravitational radiation from collapsing rotating stellar cores*, Astron. & Astrophys.**114**, 53–59.
- [325] Müller, E., (1998), dans *Saas-Fee Advanced Course 27 : Computational Methods for Astrophysical Fluid Flow.*, éd. Steiner, O. et Gautschy, A., p. 343.
- [326] Müller, E., Rampp, M., Buras, R., Janka, H.-T. et Shoemaker, D. H., (2004), *Toward Gravitational Wave Signals from Realistic Core-Collapse Supernova Models*, Astrophys. J.**603**, 221–230.
- [327] Müller, E. et Janka, H.-T., (1997), *Gravitational radiation from convective instabilities in Type II supernova explosions.*, Astron. & Astrophys.**317**, 140–163.
- [328] Mustafa, E., Cohen, J. M. et Pechenick, K. R., (1987), *Angular Momentum, Magnetic Moment, and g-Factor in General Relativity*, Int. J. Theor. Phys. **26**, 1189–1217.
- [329] Nakamura, T., (1994), dans *Relativistic Cosmology, Proceedings of the 8th Nishinomiya-Yukawa Memorial Symposium*, éd. Sasaki, M., pp. 155–182.
- [330] Nakamura, T., Kojima, Y. et Oohara, K., (1984), *A method of determining apparent horizons in three-dimensional numerical relativity*, Phys. Lett. A **106**, 235–238.
- [331] Nakamura, T., Oohara, K. et Kojima, Y., (1987), *General Relativistic Collapse to Black Holes and Gravitational Waves from Black Holes*, Prog. Theor. Phys. Suppl. **90**, 1–218.
- [332] Nakamura, T. et Sato, H., (1981), *General Relativistic Collapse of Rotating Supermassive Stars*, Prog. Theor. Phys. **66**, 2038–2051.
- [333] Nakamura, T. et Sato, H., (1982), *General Relativistic Collapse of Non-Rotating, Axisymmetric Stars*, Prog. Theor. Phys. **67**, 1396–1405.
- [334] Neilsen, D. W. et Choptuik, M. W., (2000), *Critical phenomena in perfect fluids*, Class. Quantum Grav. **17**, 761–782.
- [335] Noble, S. C. et Choptuik, M. W., (2008), *Type II critical phenomena of neutron star collapse*, Phs. Rev. D **78**, 064059, 1–22.

- [336] Novak, J., (1998), *Neutron star transition to a strong-scalar-field state in tensor-scalar gravity*, Phys. Rev. D **58**, 064019, 1–7.
- [337] Novak, J., (1998), *Spherical neutron star collapse toward a black hole in a tensor-scalar theory of gravity*, Phys. Rev. D **57**, 4789–4801.
- [338] Novak, J., (2001), *Velocity-induced collapses of stable neutron stars*, Astron. & Astrophys. **376**, 606–613.
- [339] Novak, J., (2002), dans *Proceedings of the Ninth Marcel Grossman Meeting on General Relativity*, éd. Gurzadyan, V. G., Jantzen, R. T. et Ruffini, R., pp. 1705–1712, Singapore, World Scientific.
- [340] Novak, J., Cornou, J.-L. et Vasset, N., (2010), *A spectral method for the wave equation of divergence-free vectors and Symmetrics tensors inside a sphere*, J. Comput. Phys. **229**, 399–414.
- [341] Novak, J. et Bonazzola, S., (2004), *Absorbing boundary conditions for simulation of gravitational waves with spectral methods in spherical coordinates*, J. Comput. Phys. **197**, 186–196.
- [342] Novak, J. et Ibáñez, J. M., (2000), *Gravitational Waves from the Collapse and Bounce of a Stellar Core in Tensor-Scalar Gravity*, Astrophys. J. **533**, 392–405.
- [343] Novak, J. et Marcq, E., (2003), *The gyromagnetic ratio of rapidly rotating compact stars in general relativity*, Class. Quantum Grav. **20**, 3051–3060.
- [344] Nozawa, T., Stergioulas, N., Gourgoulhon, E. et Eriguchi, Y., (1998), *Construction of highly accurate models of rotating neutron stars - comparison of three different numerical schemes*, Astron. Astrophys. Suppl. **132**, 431–454.
- [345] Oechslin, R., Rosswog, S. et Thielemann, F.-K., (2002), *Conformally flat smoothed particle hydrodynamics application to neutron star mergers*, Phys. Rev. D **65**, 103005+, 1–15.
- [346] Oechslin, R. et Janka, H.-T., (2007), *Gravitational Waves from Relativistic Neutron-Star Mergers with Microphysical Equations of State*, Phys. Rev. Lett. **99**, 121102.
- [347] O’Murchadha, N. et York, J. W., (1973), *Existence and uniqueness of solutions of the Hamiltonian constraint of general relativity on compact manifolds*, J. Math. Phys. **14**, 1551–1557.
- [348] O’Murchadha, N. et York, J. W., (1974), *Initial - value problem of general relativity. I. General formulation and physical interpretation*, Phys. Rev. D **10**, 428–436.
- [349] Oppenheimer, J. R. et Snyder, H., (1939), *On Continued Gravitational Contraction*, Phys. Rev. **56**, 455–459.
- [350] Ott, C. D., Burrows, A., Livne, E. et Walder, R., (2004), *Gravitational Waves from Axisymmetric, Rotating Stellar Core Collapse*, Astrophys. J. **600**, 834–864.
- [351] Ott, C. D., Dimmelmeier, H., Marek, A., Janka, H.-T., Hawke, I., Zink, B. et Schnetter, E., (2007), *3D Collapse of Rotating Stellar Iron Cores in General Relativity Including Deleptonization and a Nuclear Equation of State*, Phys. Rev. Lett. **98**, 261101.

- [352] Ott, C. D., Dimmelmeier, H., Marek, A., Janka, H.-T., Zink, B., Hawke, I. et Schnetter, E., (2007), *Rotating collapse of stellar iron cores in general relativity*, *Class. Quantum Grav.* **24**, S139–S154.
- [353] Palenzuela, C., Anderson, M., Lehner, L., Liebling, S. L. et Neilsen, D., (2009), *Binary Black Holes' Effects on Electromagnetic Fields*, *Phys. Rev. Lett.* **103**, 081101.
- [354] Pan, Y., Buonanno, A., Baker, J. G., Centrella, J., Kelly, B. J., McWilliams, S. T., Pretorius, F. et van Meter, J. R., (2008), *Data-analysis driven comparison of analytic and numerical coalescing binary waveforms : Nonspinning case*, *Phys. Rev. D* **77**, 024014, 1–19.
- [355] Patera, A. T., (1984), *A spectral element method for fluid dynamics : Laminar flow in a channel expansion*, *J. Comput. Phys.* **54**, 468–488.
- [356] Penrose, R., (1965), *Gravitational Collapse and Space-Time Singularities*, *Phys. Rev. Lett.* **14**, 57–59.
- [357] Pfeiffer, H. P., (2003), *Initial value problem for black hole evolution*, Thèse de doctorat, Cornell University, Ithaca, New York.
- [358] Pfeiffer, H. P., (2005), *The initial value problem in numerical relativity*, *J. Hyperbolic Diff. Eq.* **2**, 497–520.
- [359] Pfeiffer, H. P., Teukolsky, S. A. et Cook, G. B., (2000), *Quasi-circular orbits for spinning binary black holes*, *Phys. Rev. D* **62**, 104018, 1–11.
- [360] Pfeiffer, H. P., Cook, G. B. et Teukolsky, S. A., (2002), *Comparing initial-data sets for binary black holes*, *Phys. Rev. D* **66**, 024047, 1–17.
- [361] Pfeiffer, H. P., Kidder, L. E., Scheel, M. A. et Teukolsky, S. A., (2003), *A multidomain spectral method for solving elliptic equations*, *Comput. Phys. Commun.* **152**, 253–273.
- [362] Pfeiffer, H. P., Kidder, L. E., Scheel, M. A. et Shoemaker, D. M., (2005), *Initial value problem for Einstein's equations with superposed gravitational waves*, *Phys. Rev. D* **71**, 024020, 1–9.
- [363] Pfeiffer, H. P., Brown, D. A., Kidder, L. E., Lindblom, L., Lovelace, G. et Scheel, M. A., (2007), *Reducing orbital eccentricity in binary black hole simulations*, *Class. Quantum Grav.* **24**, S59–S81.
- [364] Pfeiffer, H. P. et York, J. W., (2003), *Extrinsic curvature and the Einstein constraints*, *Phys. Rev. D* **67**, 044022, 1–8.
- [365] Pfeiffer, H. P. et York, J. W., (2005), *Uniqueness and Nonuniqueness in the Einstein Constraints*, *Phys. Rev. Lett.* **95**, 091101.
- [366] Pfister, H. et King, M., (2002), *Rotating charged mass shell : Dragging, antidragging, and the gyromagnetic ratio*, *Phys. Rev. D* **65**, 084033, 1–10.
- [367] Pfister, H. et King, M., (2003), *The gyromagnetic factor in electrodynamics, quantum theory and general relativity*, *Class. Quantum Grav.* **20**, 205–213.

- [368] Pollney, D., Reisswig, C., Rezzolla, L., Szilágyi, B. *et al.*, (2007), *Recoil velocities from equal-mass binary black-hole mergers : A systematic investigation of spin-orbit aligned configurations*, Phys. Rev. D **76**, 124002, 1–23.
- [369] Pons, J. A., Reddy, S., Ellis, P. J., Prakash, M. et Lattimer, J. M., (2000), *Kaon condensation in proto-neutron star matter*, Phys. Rev. C **62**, 035803, 1–20.
- [370] Postnov, K. A. et Yungelson, L. R., (2006), *The Evolution of Compact Binary Star Systems*, Living Rev. Relativity **9**, lrr-2006-6, 6.
- [371] Potter, D., (1973), *Computational Physics*, Wiley, Chichester, U.K..
- [372] Pradier, T., Arnaud, N., Bizouard, M.-A., Cavalier, F., Davier, M. et Hello, P., (2001), *Efficient filter for detecting gravitational wave bursts in interferometric detectors*, Phys. Rev. D **63**, 042002, 1–9.
- [373] Pretorius, F., (2005), *Evolution of Binary Black-Hole Spacetimes*, Phys. Rev. Lett. **95**, 121101.
- [374] Pretorius, F., (2005), *Numerical relativity using a generalized harmonic decomposition*, Class. Quantum Grav. **22**, 425–451.
- [375] Pretorius, F., (2009), *Physics of Relativistic Objects in Compact Binaries : From Birth to Coalescence*, tome 359 de *Astrophysics and Space Science Library*, chapitre Binary Black Hole Coalescence, pp. 305–369, Springer Netherlands.
- [376] Prix, R., (1999), *Slowly rotating two-fluid neutron star model*, Astron. & Astrophys.**352**, 623–631.
- [377] Prix, R., Comer, G. L. et Andersson, N., (2002), *Slowly rotating superfluid Newtonian neutron star model with entrainment*, Astron. & Astrophys.**381**, 178–196.
- [378] Prix, R., Novak, J. et Comer, G. L., (2002), dans *Proceedings of the Spanish relativity meeting 2002*, éd. Lobo, A., pp. 212–217, Barcelona, Spain, Universitat de Barcelona, arXiv :gr-qc/0211105.
- [379] Prix, R., Novak, J. et Comer, G. L., (2005), *Relativistic numerical models for stationary superfluid neutron stars*, Phys. Rev. D **71**, 043005, 1–18.
- [380] Prix, R. et Rieutord, M., (2002), *Adiabatic oscillations of non-rotating superfluid neutron stars*, Astron. & Astrophys.**393**, 949–963.
- [381] Protter, M. et Weinberger, H., (1967), *Maximum Principles in Differential Equations*, Prentice-Hall, Englewood Cliffs.
- [382] Quarteroni, A., Sacco, R. et Saleri, F., (2007), *Méthodes Numériques : Algorithmes, analyse et applications*, Springer Italia, Milano.
- [383] Rampp, M., Müller, E. et Ruffert, M., (1998), *Simulations of non-axisymmetric rotational core collapse*, Astron. & Astrophys.**332**, 969–983.

- [384] Regge, T. et Wheeler, J. A., (1957), *Stability of a Schwarzschild Singularity*, Phys. Rev. **108**, 1063–1069.
- [385] Reula, O., (1998), *Hyperbolic Methods for Einstein's Equations*, Living Rev. Relativity **1**, lrr-1998-1, 1.
- [386] Riazuelo, A., (2007), *Voyage au cœur d'un trou noir*, <http://www2.iap.fr/users/riazuelo/bh/index.html>.
- [387] Rinne, O., (2006), *Axisymmetric Numerical Relativity*, Thèse de doctorat, University of Cambridge, Cambridge, UK.
- [388] Rinne, O., (2006), *Stable radiation-controlling boundary conditions for the generalized harmonic Einstein equations*, Class. Quantum Grav. **23**, 6275–6300.
- [389] Rinne, O., (2008), *Constrained evolution in axisymmetry and the gravitational collapse of prolate Brill waves*, Class. Quantum Grav. **25**, 135009, 1–21.
- [390] Rinne, O., Lindblom, L. et Scheel, M. A., (2007), *Testing outer boundary treatments for the Einstein equations*, Class. Quantum Grav. **24**, 4053–4078.
- [391] Rinne, O., Buchman, L. T., Scheel, M. A. et Pfeiffer, H. P., (2009), *Implementation of high-order absorbing boundary conditions for the Einstein equations*, Class. Quantum Grav. **26**, 075009.
- [392] Rinne, O. et Stewart, J. M., (2005), *A strongly hyperbolic and regular reduction of Einstein's equations for axisymmetric spacetimes*, Class. Quantum Grav. **22**, 1143–1166.
- [393] Romero, J. V., Ibáñez, J. M., Martí, J. M. et Miralles, J. A., (1996), *A New Spherically Symmetric General Relativistic Hydrodynamical Code*, Astrophys. J. **462**, 839–854.
- [394] Rossmanith, J. A., Bale, D. S. et LeVeque, R. J., (2004), *A wave propagation algorithm for hyperbolic systems on curved manifolds*, J. Comput. Phys. **199**, 631–662.
- [395] Ruiz, M., Rinne, O. et Sarbach, O., (2007), *Outer boundary conditions for Einstein's field equations in harmonic coordinates*, Class. Quantum Grav. **24**, 6349–6377.
- [396] Sagert, I., Fischer, T., Hempel, M., Pagliara, G., Schaffner-Bielich, J., Mezzacappa, A., Thielemann, F.-K. et Liebendörfer, M., (2009), *Signals of the QCD Phase Transition in Core-Collapse Supernovae*, Phys. Rev. Lett. **102**, 081101.
- [397] Saijo, M., (2004), *The Collapse of Differentially Rotating Supermassive Stars : Conformally Flat Simulations*, Astrophys. J. **615**, 866–879.
- [398] Saijo, M. et Gourgoulhon, E., (2006), *Viscosity driven instability in rotating relativistic stars*, Phys. Rev. D **74**, 084006, 1–13.
- [399] Salgado, M., Bonazzola, S., Gourgoulhon, E. et Haensel, P., (1994), *High precision rotating neutron star models I. Analysis of neutron star properties*, Astron. Astrophys. **291**, 155–170.

- [400] Salgado, M., Bonazzola, S., Gourgoulhon, E. et Haensel, P., (1994), *High precision rotating neutron star models. II. Large sample of neutron star properties*, *Astron. Astrophys. Suppl.* **108**, 455–459.
- [401] Schäfer, G. et Gopakumar, A., (2004), *Minimal no-radiation approximation to Einstein's field equations*, *Phys. Rev. D* **69**, 021501, 1–4.
- [402] Scheel, M. A., Kidder, L. E., Lindblom, L., Pfeiffer, H. P. et Teukolsky, S. A., (2002), *Toward stable 3D numerical evolutions of black-hole spacetimes*, *Phys. Rev. D* **66**, 124005, 1–4.
- [403] Scheel, M. A., Erickcek, A. L., Burko, L. M., Kidder, L. E., Pfeiffer, H. P. et Teukolsky, S. A., (2004), *3D simulations of linearized scalar fields in Kerr spacetime*, *Phys. Rev. D* **69**, 104006, 1–11.
- [404] Scheel, M. A., Pfeiffer, H. P., Lindblom, L., Kidder, L. E., Rinne, O. et Teukolsky, S. A., (2006), *Solving Einstein's equations with dual coordinate frames*, *Phys. Rev. D* **74**, 104006, 1–13.
- [405] Scheel, M. A., Boyle, M., Chu, T., Kidder, L. E., Matthews, K. D. et Pfeiffer, H. P., (2009), *High-accuracy waveforms for binary black hole inspiral, merger, and ringdown*, *Phys. Rev. D* **79**, 024003, 1–15.
- [406] Schnetter, E., (2003), *Finding apparent horizons and other 2-surfaces of constant expansion*, *Class. Quantum Grav.* **20**, 4719–4737.
- [407] Schnetter, E., Krishnan, B. et Beyer, F., (2006), *Introduction to dynamical horizons in numerical relativity*, *Phys. Rev. D* **74**, 024028, 1–20.
- [408] Seidel, E. et Suen, W.-M., (1992), *Towards a singularity-proof scheme in numerical relativity*, *Phys. Rev. Lett.* **69**, 1845–1848.
- [409] Senovilla, J. M. M., (2009), dans *Proceedings of the Spanish Relativity Meeting 2008*, édés. Kunze, K. E., Mars, M. et Vázquez-Mozo, M. A., tome 1122 de *AIP Conf. Series*, pp. 72–87.
- [410] Shapiro, S. L. et Teukolsky, S. A., (1980), *Gravitational collapse to neutron stars and black holes - Computer generation of spherical spacetimes*, *Astrophys. J.* **235**, 199–215.
- [411] Shapiro, S. L. et Teukolsky, S. A., (1992), *Collisions of relativistic clusters and the formation of black holes*, *Phys. Rev. D* **45**, 2739–2750.
- [412] Shen, J., Tachim Medjo, T. et Wang, S., (1999), *On a Wind-Driven, Double-Gyre, Quasi-Geostrophic Ocean Model : Numerical Simulations and Structural Analysis*, *J. Comput. Phys.* **155**, 387–409.
- [413] Shibata, M., (1997), *Apparent horizon finder for a special family of spacetimes in 3D numerical relativity*, *Phys. Rev. D* **55**, 2002–2013.
- [414] Shibata, M., (1999), *Fully general relativistic simulation of coalescing binary neutron stars : Preparatory tests*, *Phys. Rev. D* **60**, 104052, 1–25.

- [415] Shibata, M., (2000), *Axisymmetric Simulations of Rotating Stellar Collapse in Full General Relativity – Criteria for Prompt Collapse to Black Holes –*, Prog. Theor. Phys. **104**, 325–358.
- [416] Shibata, M., (2003), *Axisymmetric general relativistic hydrodynamics : Long-term evolution of neutron stars and stellar collapse to neutron stars and black holes*, Phys. Rev. D **67**, 024033, 1–24.
- [417] Shibata, M., (2005), *Constraining Nuclear Equations of State Using Gravitational Waves from Hypermassive Neutron Stars*, Phys. Rev. Lett. **94**, 201101.
- [418] Shibata, M., Taniguchi, K. et Uryū, K., (2003), *Merger of binary neutron stars of unequal mass in full general relativity*, Phys. Rev. D **68**, 084020, 1–24.
- [419] Shibata, M., Uryū, K. et Friedman, J. L., (2004), *Deriving formulations for numerical computation of binary neutron stars in quasicircular orbits*, Phys. Rev. D **70**, 044044, 1–18.
- [420] Shibata, M., Liu, Y. T., Shapiro, S. L. et Stephens, B. C., (2006), *Magnetorotational collapse of massive stellar cores to neutron stars : Simulations in full general relativity*, Phys. Rev. D **74**, 104026, 1–28.
- [421] Shibata, M. et Nakamura, T., (1995), *Evolution of three-dimensional gravitational waves : Harmonic slicing case*, Phys. Rev. D **52**, 5428–5444.
- [422] Shibata, M. et Sekiguchi, Y.-I., (2003), *Gravitational waves from axisymmetrically oscillating neutron stars in general relativistic simulations*, Phys. Rev. D **68**, 104020, 1–14.
- [423] Shibata, M. et Sekiguchi, Y.-I., (2004), *Gravitational waves from axisymmetric rotating stellar core collapse to a neutron star in full general relativity*, Phys. Rev. D **69**, 084024, 1–16.
- [424] Shibata, M. et Uryū, K. ō., (2000), *Simulation of merging binary neutron stars in full general relativity : $\Gamma=2$ case*, Phys. Rev. D **61**, 064001, 1–18.
- [425] Shibata, M. et Uryū, K. ō., (2001), *Computation of gravitational waves from inspiraling binary neutron stars in quasiequilibrium circular orbits : Formulation and calibration*, Phys. Rev. D **64**, 104017, 1–26.
- [426] Shibata, M. et Uryū, K., (2006), *Merger of black hole-neutron star binaries : Nonspinning black hole case*, Phys. Rev. D **74**, 121503, 1–5.
- [427] Shibata, M. et Uryū, K., (2007), *Merger of black hole-neutron star binaries in full general relativity*, Class. Quantum Grav. **24**, S125–S137.
- [428] Shinkai, H.-A. et Yoneda, G., (2002), *Re-formulating the Einstein equations for stable numerical simulations : Formulation Problem in Numerical Relativity*, arXiv :gr-qc/0209111.
- [429] Shiromizu, T. et Shibata, M., (2000), *Black holes in the brane world : Time symmetric initial data*, Phys. Rev. D **62**, 127502, 1–4.
- [430] Shoemaker, D. M., Huq, M. F. et Matzner, R. A., (2000), *Generic tracking of multiple apparent horizons with level flow*, Phys. Rev. D **62**, 124005, 1–12.

- [431] Shu, C. W., (2002), dans *Collected Lectures on the Preservation of Stability under Discretization*, eds. Estep, D. et Tavener, S., pp. 51–65, SIAM, Philadelphia.
- [432] Siebel, F., Font, J. A., Müller, E. et Papadopoulos, P., (2003), *Axisymmetric core collapse simulations using characteristic numerical relativity*, Phys. Rev. D **67**, 124018, 1–16.
- [433] Sjöberg, O., (1976), *On the Landau effective mass in asymmetric nuclear matter.*, Nucl. Phys. A **265**, 511–516.
- [434] Smarr, L. et York, J. W., (1978), *Kinematical conditions in the construction of spacetime*, Phys. Rev. D **17**, 2529–2551.
- [435] Smarr, L. et York, J. W., (1978), *Radiation gauge in general relativity*, Phys. Rev. D **17**, 1945–1956.
- [436] Sommerfeld, A., (1949), *Partial Differential Equations in Physics*, Academic Press, New York, U.S.A..
- [437] Sorkin, E., Kol, B. et Piran, T., (2004), *Caged black holes : Black holes in compactified spacetimes. II. 5D numerical implementation*, Phys. Rev. D **69**, 064032, 1–23.
- [438] Sperhake, U., (2007), *Binary black-hole evolutions of excision and puncture data*, Phys. Rev. D **76**, 104015, 1–20.
- [439] Stark, R. F., (1989), dans *Frontiers in Numerical Relativity*, eds. Evans, C. R., Finn, L. S. et Hobill, D. W., pp. 281–296.
- [440] Stark, R. F. et Piran, T., (1985), *Gravitational-wave emission from rotating gravitational collapse*, Phys. Rev. Lett. **55**, 891–894.
- [441] Stephens, B. C., Duez, M. D., Liu, Y. T., Shapiro, S. L. et Shibata, M., (2007), *Collapse and black hole formation in magnetized, differentially rotating neutron stars*, Class. Quantum Grav. **24**, S207–S219.
- [442] Stergioulas, N., (2003), *Rotating Stars in Relativity*, Living Rev. Relativity **6**, Irr-2003-3, 3.
- [443] Stergioulas, N., Apostolatos, T. A. et Font, J. A., (2004), *Non-linear pulsations in differentially rotating neutron stars : mass-shedding-induced damping and splitting of the fundamental mode*, Mon. Not. of the Royal Astron. Soc. **352**, 1089–1101.
- [444] Stergioulas, N. et Font, J. A., (2001), *Nonlinear r-Modes in Rapidly Rotating Relativistic Stars*, Phys. Rev. Lett. **86**, 1148–1151.
- [445] Stergioulas, N. et Friedman, J. L., (1995), *Comparing models of rapidly rotating relativistic stars constructed by two numerical methods*, Astrophys. J. **444**, 306–311.
- [446] Stewart, J. M., (1998), *The Cauchy problem and the initial boundary value problem in numerical relativity*, Class. Quantum Grav. **15**, 2865–2889.
- [447] Swesty, F., (1996), *Thermodynamically Consistent Interpolation for Equation of State Tables*, J. Comput. Phys. **127**, 118–127.

- [448] Szilágyi, B., Pollney, D., Rezzolla, L., Thornburg, J. et Winicour, J., (2007), *An explicit harmonic code for black-hole evolution using excision*, *Class. Quantum Grav.* **24**, S275–S293.
- [449] Taniguchi, K., Gourgoulhon, E. et Bonazzola, S., (2001), *Quasiequilibrium sequences of synchronized and irrotational binary neutron stars in general relativity. II. Newtonian limits*, *Phys. Rev. D* **64**, 064012, 1–19.
- [450] Taniguchi, K., Baumgarte, T. W., Faber, J. A. et Shapiro, S. L., (2005), *Black hole-neutron star binaries in general relativity : Effects of neutron star spin*, *Phys. Rev. D* **72**, 044008, 1–26.
- [451] Taniguchi, K., Baumgarte, T. W., Faber, J. A. et Shapiro, S. L., (2006), *Quasiequilibrium sequences of black-hole–neutron-star binaries in general relativity*, *Phys. Rev. D* **74**, 041502, 1–5.
- [452] Taniguchi, K., Baumgarte, T. W., Faber, J. A. et Shapiro, S. L., (2007), *Quasiequilibrium black hole-neutron star binaries in general relativity*, *Phys. Rev. D* **75**, 084005, 1–17.
- [453] Taniguchi, K., Baumgarte, T. W., Faber, J. A. et Shapiro, S. L., (2008), *Relativistic black hole-neutron star binaries in quasiequilibrium : effects of the black hole excision boundary condition*, *Phys. Rev. D* **77**, 044003, 1–13.
- [454] Taniguchi, K. et Gourgoulhon, E., (2002), *Equilibrium sequences of synchronized and irrotational binary systems composed of different mass stars in Newtonian gravity*, *Phys. Rev. D* **65**, 044027, 1–16.
- [455] Taniguchi, K. et Gourgoulhon, E., (2002), *Quasiequilibrium sequences of synchronized and irrotational binary neutron stars in general relativity. III. Identical and different mass stars with $\gamma=2$* , *Phys. Rev. D* **66**, 104019, 1–14.
- [456] Taniguchi, K. et Gourgoulhon, E., (2003), *Various features of quasiequilibrium sequences of binary neutron stars in general relativity*, *Phys. Rev. D* **68**, 124025, 1–28.
- [457] Taylor, J. H., Wolszczan, A., Damour, T. et Weisberg, J. M., (1992), *Experimental constraints on strong-field relativistic gravity*, *Nature* **355**, 132–136.
- [458] Taylor, M. E., (1997), *Partial Differential Equations III. Nonlinear Equations*, tome 117 de *Applied Mathematical Sciences*, Springer-Verlag, New York, corrected reprint of the 1996 original.
- [459] Temperton, C., (1991), *On scalar and vector transform methods for global spectral models*, *Mon. Weather Rev.* **119**, 1303–1307.
- [460] Teukolsky, S. A., (1982), *Linearized quadrupole waves in general relativity and the motion of test particles.*, *Phys. Rev. D* **26**, 745–750.
- [461] Thornburg, J., (1987), *Coordinates and boundary conditions for the general relativistic initial data problem*, *Class. Quantum Grav.* **4**, 1119–1131.
- [462] Thornburg, J., (2004), *A fast apparent horizon finder for three-dimensional Cartesian grids in numerical relativity*, *Class. Quantum Grav.* **21**, 743–766.

- [463] Thornburg, J., (2007), *Event and Apparent Horizon Finders for 3+1 Numerical Relativity*, Living Rev. Relativity **10**, lrr-2007-3, 3.
- [464] Thorne, K. S., (1980), *Multipole expansions of gravitational radiation*, Rev. Mod. Phys. **52**, 299–339.
- [465] Thorne, K. S., Price, R. H. et MacDonald, D. A., (1986), *Black holes : The membrane paradigm*, Yale University Press, New Haven and London.
- [466] Tichy, W., (2006), *Black hole evolution with the BSSN system by pseudospectral methods*, Phys. Rev. D **74**, 084005, 1–10.
- [467] Tichy, W. et Marronetti, P., (2007), *Binary black hole mergers : Large kicks for generic spin orientations*, Phys. Rev. D **76**, 061502, 1–5.
- [468] Tiglio, M., Lehner, L. et Nielsen, D., (2004), *3D simulations of Einstein's equations : Symmetric hyperbolicity, live gauges, and dynamic control of the constraints*, Phys. Rev. D **70**, 104018, 1–22.
- [469] Toro, E. F., (1997), *Riemann Solvers and Numerical Methods for Fluid Dynamics – A Practical Introduction*, Springer, Berlin.
- [470] Tóth, G., (2000), *The $\nabla \cdot \mathbf{B} = 0$ constraint in shock capturing magnetohydrodynamics codes*, J. Comput. Phys. **161**, 605–652.
- [471] Uryū, K., Limousin, F., Friedman, J. L., Gourgoulhon, E. et Shibata, M., (2006), *Binary Neutron Stars : Equilibrium Models beyond Spatial Conformal Flatness*, Phys. Rev. Lett. **97**, 171101.
- [472] Uryū, K. et Eriguchi, Y., (2000), *New numerical method for constructing quasiequilibrium sequences of irrotational binary neutron stars in general relativity.*, Phys. Rev. D **61**, 124023, 1–19.
- [473] Valiente Kroon, J. A., (2004), *Nonexistence of Conformally Flat Slices in Kerr and Other Stationary Spacetimes*, Phys. Rev. Lett. **92**, 041101.
- [474] van Meter, J. R., Baker, J. G., Koppitz, M. et Choi, D.-I., (2006), *How to move a black hole without excision : Gauge conditions for the numerical evolution of a moving puncture*, Phys. Rev. D **73**, 124011, 1–8.
- [475] Vasset, N., Novak, J. et Jaramillo, J. L., (2009), *Excised black holes spacetimes : quasi-local horizon formalism applied to the Kerr example*, Phys. Rev. D **79**, 124010, 1–15.
- [476] Villain, L., Pons, J. A., Cerdá-Durán, P. et Gourgoulhon, E., (2004), *Evolutionary sequences of rotating protoneutron stars*, Astron. Astrophys. **418**, 283–294.
- [477] Villain, L., Bonazzola, S. et Haensel, P., (2005), *Inertial modes in stratified rotating neutron stars : An evolutionary description*, Phys. Rev. D **71**, 083001, 1–26.
- [478] Villain, L. et Bonazzola, S., (2002), *Inertial modes in slowly rotating stars : An evolutionary description*, Phys. Rev. D **66**, 123001, 1–25.

- [479] Wald, R. M., (1984), *General relativity*, University of Chicago Press, Chicago.
- [480] Walsh, D. M., (2007), *Non-uniqueness in conformal formulations of the Einstein constraints*, *Class. Quantum Grav.* **24**, 1911–1925.
- [481] Wilson, J. R., Mathews, G. J. et Marronetti, P., (1996), *Relativistic numerical model for close neutron-star binaries*, *Phys. Rev. D* **54**, 1317–1331.
- [482] Wilson, J. R. et Mathews, G. J., (1989), dans *Frontiers in Numerical Relativity*, éd. Evans, C. R., Finn, L. S. et Hobill, D. W., pp. 306–314.
- [483] Winicour, J., (2005), *Characteristic Evolution and Matching*, *Living Rev. Relativity* **8**, lrr-2005-10, 10.
- [484] Yamada, S. et Sato, K., (1995), *Gravitational Radiation from Rotational Collapse of a Supernova Core*, *Astrophys. J.* **450**, 245.
- [485] York, J. W., (1972), *Role of Conformal Three-Geometry in the Dynamics of Gravitation*, *Phys. Rev. Lett.* **28**, 1082–1085.
- [486] York, J. W., (1979), dans *Sources of Gravitational Radiation*, éd. Smarr, L. L., pp. 83–126, Cambridge; New York, Cambridge University Press.
- [487] York, J. W., (1999), *Conformal “Thin-Sandwich” Data for the Initial-Value Problem of General Relativity*, *Phys. Rev. Lett.* **82**, 1350–1353.
- [488] Yoshida, S. et Eriguchi, Y., (2004), *Rapidly rotating superfluid neutron stars in Newtonian dynamics*, *Mon. Not. of the Royal Astron. Soc.* **347**, 575–586.
- [489] Yoshino, H., Shiromizu, T. et Shibata, M., (2006), *Close-slow analysis for head-on collision of two black holes in higher dimensions : Bowen-York initial data*, *Phys. Rev. D* **74**, 124022, 1–15.
- [490] Zdunik, J. L., Haensel, P., Gondek-Rosińska, D. et Gourgoulhon, E., (2000), *Innermost stable circular orbits around strange stars and kHz QPOs in low-mass X-ray binaries*, *Astron. Astrophys.* **356**, 612–618.
- [491] Zdunik, J. L., Haensel, P. et Gourgoulhon, E., (2001), *The crust of rotating strange quark stars*, *Astron. Astrophys.* **372**, 535–543.
- [492] Zdunik, J. L., Haensel, P. et Gourgoulhon, E., (2002), *Recycling strange stars to millisecond periods*, *Astron. Astrophys.* **381**, 933–940.
- [493] Zdunik, J. L., Haensel, P., Gourgoulhon, E. et Bejger, M., (2004), *Hyperon softening of the EOS of dense matter and the spin evolution of isolated neutron stars*, *Astron. Astrophys.* **416**, 1013–1022.
- [494] Zdunik, J. L., Bejger, M., Haensel, P. et Gourgoulhon, E., (2006), *Phase transitions in rotating neutron stars cores : back bending, stability, corequakes, and pulsar timing*, *Astron. Astrophys.* **450**, 747–758.

- [495] Zdunik, J. L., Bejger, M., Haensel, P. et Gourgoulhon, E., (2007), *Energy release associated with a first-order phase transition in a rotating neutron star core*, *Astron. Astrophys.* **465**, 533–539.
- [496] Zdunik, J. L., Bejger, M., Haensel, P. et Gourgoulhon, E., (2008), *Strong first-order phase transition in a rotation neutron star core and the associated energy release*, *Astron. Astrophys.* **479**, 515–522.
- [497] Zdunik, J. L. et Gourgoulhon, E., (2001), *Small strange stars and marginally stable orbit in Newtonian theory*, *Phys. Rev. D* **63**, 087501, 1–4.
- [498] Zerilli, F. J., (1970), *Tensor Harmonics in Canonical Form for Gravitational Radiation and Other Applications*, *J. Math. Phys.* **11**, 2203–2208.
- [499] Zwerger, T. et Müller, E., (1997), *Dynamics and gravitational wave signature of axisymmetric rotational core collapse.*, *Astron. & Astrophys.* **320**, 209–227.